University of California
Santa Barbara

Many-body electronic structure theory: method development and applications in chemistry and materials

A dissertation submitted in partial satisfaction
of the requirements for the degree

Doctor of Philosophy
in
Chemistry

by

Guorong Weng

Committee in charge:

Professor Vojtěch Vlček, Chair
Professor Frank Brown
Professor Thuc-Quyen Nguyen
Professor Ram Seshadri

June 2023

The Dissertation of Guorong Weng is approved.

Professor Frank Brown

Professor Thuc-Quyen Nguyen

Professor Ram Seshadri

Professor Vojtěch Vlček, Committee Chair

May 2023

Many-body electronic structure theory: method development and applications in chemistry and materials

by

Guorong Weng

To my family, girlfriend, friends, and advisor without whose support I would not have been able to complete my Ph.D. degree.

Acknowledgements

Sitting on the couch on Coastal Starlight and staring at the US101, the freeway on which I have been driving for five years reminds me that my journey as a graduate student at UCSB is arriving at the destination.

There are so many memorable experiences during my Ph.D. study, but everything on my first date in Santa Barbara seem to just happen yesterday: my flight landed safely in Los Angeles and I took a connecting bus towards Goleta; my friend Xinpeng picked me up from the bus stop and took me to In-and-Out for dinner; I moved into the graduate housing apartment and spent my first night on the sofa ... Now I am finishing my dissertation and completing the honorable Ph.D. degree. I would like to thank UCSB and the chemistry department for giving me an opportunity to purse a Ph.D. degree and providing me with superior resources and robust support in my research. In addition, I want to express my gratefulness for the following genuine people upon the completion of my Ph.D. degree

My advisor, Professor Vojtěch, Vlček. Vojtěch entered the chemistry department in the same year as I did, and it is absolutely my pride and honor to become the first graduate student of a wise, knowledgeable, energetic, and young professor like him. Back to the October in 2018, I still remember the date I walked in his office and expressed my interest in simulating functional materials in the field of organic semiconducting solids. At that point I could never have imagined that I would end up working so much in the Green's function theory in physics. Or maybe it is my destiny since my initials "GW" happen to be the most popular electronic structure approach in this field. It is safe to say I had almost zero background in the field I was about to enter, except for just performing a few DFT calculations in the past. I am so grateful that Vojtěch did not care and was willing to train me from scratch, as he probably saw my passion and potential. At the

beginning, I was struggling so much with reading papers full of convoluted equations, most of which started to make sense to me only after I derived them 3000 times. My advisor has been patient and enthusiastic enough every time I came to him with questions. I enjoy so much having his detailed explanations with unexpected extensions on the white board, but I am feeling so sad that I am going to lose them soon. Vojtěch is also extremely hardworking in order to be supportive for us graduate students. Without his support in finance, I would not have been able to attend and present our research in the national meetings, like APS and ACS, and other fantastic conferences. And without his advice, criticisms, or hard work, I would never have been able to have such fruitful accomplishments in my research. As the first alumnus in the group, I wish Vojěch all the best in continuing his sacred mission, contributing more and more great scientists to the world.

My parents and grandma in China. Limited by their original family, my father and mother were not able to go to college. Therefore, they can hardly help me with my course work since I went to middle school. However, I never complained about this since they gave me adequate freedom to do whatever I want. In the meanwhile, they support me quietly and provide what I need. I can feel that they have tried their best to bring me up, and I cannot feel luckier to be their son. In the past five years, there have been numerous times I missed the days of living with them, having dinners together, and spending holidays together. I feel so sorry for not being able to visit them a few more times in these five years due to the pandemic and my research work. As a result, I treasure every online chat with them for their being so caring about my life in another country. I wish I can share my happiness and pride with them upon the completion of my Ph.D. degree in person shortly.

My girlfriend, Shuhua Guo at UC Davis. I lost all social activities and interactions with the outside world since the beginning of the pandemic. My life was messed up

and became disordered, as I was discouraged to step out of my room and ended up facing my cell phone and laptop all the time. Shuhua's appearance changed this situation immediately. She was so interested in everything about me, my life, my study, and my research. She is a perfect listener, showing curiosity about the quantum phenomena that I am researching. I was also encouraged to go further outside with her for a trip. She has been super supportive for me, even if she also has heavy course work to finish. Without her, I might have given up striving for my Ph.D. and left his country. Knowing Shuhua is one of the greatest fortune from God in my life. I wish her success in the pursuit of her career, and us a wonderful future.

Finally, I want to thank Professor Thuc-Quyen Nguyen for her suggestion in my research projects, being a member in my defense committee, and supporting me in my postdoc and fellowship applications; Professor Bernard Kirtman for teaching me fundamental quantum chemistry in his class, which turned out very useful in my research; Professors Ram Seshadri and Frank Brown for serving as committee members; Dr. Xinpeng Cheng and Dr. Leilai Shao for hosting me as an alumnus from Zhejiang University and helping me to start my graduate study; Dr. Mariya Romanova for joining our group as a Postdoc and a fantastic colleague to work with; Xiaohe Lei for her kind support to my work as a friend and colleague; Junjie Pan for being my roommate with immense mental support especially during the pandemic; all the other members from the Vlček group and friends from the chemistry department for showing up in my life.

Curriculum Vitæ

Guorong Weng

Education

2023	Ph.D. in Chemistry (Expected), University of California, Santa Barbara.
2018	B.S. in Chemistry, Zhejiang University, Hangzhou, China.

Publications

1. J. Brooks, G. Weng, S. Taylor, and V. Vlček, Stochastic many-body perturbation theory for moiré states in twisted bilayer phosphorene, Journal of Physics: Condensed Matter 32 (2020) 234001.
2. G. Weng and V. Vlček, Quasiparticles and band structures in organized nanostructures of donor–acceptor copolymers, The Journal of Physical Chemistry Letters 11 (2020) 7177–7183.
3. G. Weng and V. Vlček, Efficient treatment of molecular excitations in the liquid phase environment via stochastic many-body theory, The Journal of Chemical Physics 155 (2021) 054104.
4. C. Mejuto-Zaera, G. Weng, M. Romanova, S. J. Cotton, K. B. Whaley, N. M. Tubman, and V. Vlček, Are multi-quasiparticle interactions important in molecular ionization?, The Journal of Chemical Physics 154 (2021) 121101.
5. G. Weng, M. Romanova, A. Apelian, H. Song, and V. Vlček, Reduced scaling of optimal regional orbital localization via sequential exhaustion of the single-particle space, Journal of Chemical Theory and Computation 18 (2022) 4960–4972.
6. G. Weng, R. Mallarapu, and V. Vlček, Embedding vertex corrections in *GW* self-energy: theory, implementation, and outlook, The Journal of Chemical Physics 158 (2023) 144105.
7. M. Romanova, G. Weng, A. Apelian, and V. Vlček, Dynamical downfolding for localized quantum states, arXiv:2211.05966 (2022).
8. G. Weng, A. Pang, and V. Vlček, Spatial decay and limits of quantum solute-solvent interactions, The Journal of Physical Chemistry Letters 14 (2023) 2473-2480.

Abstract

Many-body electronic structure theory: method development and applications in chemistry and materials

by

Guorong Weng

Quantum mechanical calculations have revolutionized the study of matter by providing a powerful tool to access a wide range of material properties. In particular, gaining insight into the electronic structure of functional materials is crucial for understanding their work mechanisms in optoelectronic devices at the atomistic level, ultimately enabling the targeted design of materials with desired optical and electrical properties. However, achieving accurate first-principles predictions for direct comparison with photoelectron or optical spectroscopy experiments is challenging. Multilevel and advanced quantum theories are required to handle both ground and excited states accurately and efficiently. Although the widely-used density functional theory offers excellent accuracy in solving ground-state problems, it does not provide information on excited states, even in principle.

Many-body Green's function theory is becoming increasingly popular in describing single-particle excitations, i.e., electron and hole injections. Within this framework, the GW approximation has demonstrated significant improvement over density functional calculations in predicting the excited-state properties of molecules and solids. The recent implementation of stochastic sampling has made linear-scaling GW calculations feasible for nanoscale systems with tens of thousands of electrons.

This dissertation presents novel developments for solving electronic structure problems in practically important systems, including polymer solids, donor-acceptor molecular complexes, molecules in the liquid phase, and defects in a solid-state environment. Periodic

boundary conditions are implemented in many-body Green's function calculations for systems of all dimensions. The highly-ordered domains in stacking polymers are modeled by infinitely periodic systems, allowing detailed analysis of the quasiparticle band structures and describing the correlation effects in charge transport. In treating localized excitations of solvated molecules and defects in solids, localized orbitals are employed to precisely reconstruct molecular states and efficiently define electronic subspaces. To lower the cost of orbital localization, I introduce the ideas of fragmentation and sequential exhaustion of single-particle orbital space. The resulting algorithm scales linearly in computational cost, allowing efficient real-space and orbital-space partitioning. The established methods significantly improve the predictions of ionization energies, electron affinities, and band gaps for the investigated systems. Furthermore, the couplings between a molecule and its environment are discussed in detail in the context of quasiparticle excitations.

Contents

Chapter 1

Introduction

Since the discovery of electrons in 1897,[1] the atomic structure problem has captivated scientists with two fundamental and critical questions: why is an atom stable despite having oppositely charged subatomic particles, and why do atoms emit line spectra? The models proposed by Thomson[2] and Rutherford[3] illustrated the positions of the nucleus and electrons but failed to answer these two question quantitatively. Motivated by Rutherford's model and Nicholson's work on quantized angular momentum,[4] Niels Bohr proposed his "solar system" model, where electrons orbit the nucleus like planets orbiting the sun.[5, 6, 7, 8] Each electron orbital has a definite radius and a corresponding orbital energy characterized by a "quantum" number. These energy levels are discretized and quantized, with the lowest-energy orbital defining the smallest radius for the electrons. Bohr successfully explained the stability of atoms and recovered the Rydberg formula to describe all spectral series of lines for the hydrogen atom. In Bohr's model, the electromagnetic radiation of atomic hydrogen is caused by electronic transition between two orbitals, with the emitted photon energy being equal to the energy difference between these two states. Although Bohr's original model was later shown oversimplified for electronic motion, the concepts of orbitals, energy levels, and electronic transition are

inspiring. Particularly, they created a huge and profound impact on the development of *electronic structure theory*, which has become a powerful tool for gaining insights into spectroscopic properties of matter, such as absorption, emission, and photoelectron spectra. For systems beyond the hydrogen atom, where there are more than one electron, the electronic structure problems must be solved with electrons interacting and coupled to one another. The solution to these many-electron problems falls under the purview of *quantum mechanics*.

In the first three decades of the 20th century, the formulation of quantum mechanics has been completed by joint contributions from a group of brilliant theorists such as Werner Heisenberg,[9, 10, 11] Erwin Schrödinger,[12] and Paul Dirac,[13, 14, 15]. Schrödinger's wave equation formulation provided a fundamental way to study many-particle problems involving electrons and nuclei, which are the two common types of particles in chemistry. The solution of the wavefunction to the Schrödinger equation represents the probability amplitude of finding the system in a certain configuration at a certain time. Solving the time-independent Schrödinger equation provides the total energy of a stationary eigenstate representing the stability of a system. The lowest energy corresponds to the ground state of a system. Because of the significant difference in energy and mass scales between nuclei and electrons, the ground state of a system is largely determined by the ground state of the electrons.[16] To simplify a many-particle problem and focus on electronic properties, the Born-Oppenheimer approximation[17] is often used to reduce the problem to a many-electron problem, where the electrons move in a static potential field provided by a set of clamped nuclei.

Quantum mechanics provides a basic framework for description the behavior of nuclei and electrons at the subatomic level. However, finding the exact solution to the Schrödinger equation is almost impossible for systems with many electrons. Hence, approximations are required for solving many-electron problems in realistic systems such as atoms, molecules,

and solids. Focusing particularly on molecular electronic properties, quantum chemistry emerged as a branch of quantum mechanics. Early pioneers of this field, Hartree, Fock, and Slater[18, 19, 20, 21, 22], approximated the many-electron wavefunction with a single determinant (later named after Slater) composed of single-particle orbitals. The Slater determinant formulation results from enforcing the antisymmetry of the many-electron wavefunction. With the introduction of the atomic orbital basis[23, 24] and self-consistent field method,[19] the Hartree−Fock approximation became a systematic route to perform wavefunction calculations on the ground-state properties of atoms and molecules with no empirical parameter (also called first-principles or ab initio calculations). Typically, the Hartree–Fock ground-state wavefunction provides a set of optimized single-particle orbitals, each characterized by an eigenvalue. For a molecule with N electrons, the N states with the lowest eigenvalues are considered occupied molecular orbitals, while the rest are unoccupied/virtual. Such a diagram of orbitals characterized by energy resembled Bohr's model for the hydrogen atom and serves as the foundation of modern molecular electronic structure theory.

Although the advancement from single atoms to polyatomic molecules was groundbreaking, it was soon realized that the Hartree–Fock approach did not provide a quantitative description for electronic properties and could be even qualitatively wrong. The root cause of these failures is the lack of electron–electron correlation effects originating from the dynamically and instantaneously mutual influence of electrons on each other's movement.[25] One effective and common way to account for correlation effects is to correct/improve the Hartree–Fock solution through configuration interaction (CI),[26, 27, 28, 29] couple-cluster (CC),[30, 31, 32, 33, 34] and perturbation theory.[35, 36, 37, 38, 39, 40, 41] CI, CC, and related methods are commonly known as wavefunction methods in which more determinants are added to the Hartree–Fock wavefunction, and the correlation effects are represented and captured by single-particle excitations from occupied to virtual states

in the additional determinants. Wavefunction methods can significantly improve the ground-state energy and wavefunction with excellent chemical accuracy. However, their computational costs normally scale as high as $\mathcal{O}(e^N)$, which hinders their applications to large molecules such as DNA/RNA and proteins, and to nanoscale materials with thousands of electrons.

The development in quantum mechanics also stimulated major progress in solid-state physics. Sommerfeld[42] introduced the quantum mechanical principles to the classical Drude model[43, 44] and improved the classical descriptions of charge carriers, thermal conductivity, and heat capacity for metals. Other solid-state systems of interest include semicondutors, insulators, and superconductors; they are mostly crystals with a regularly repeating pattern of atoms or ions arranged in a three-dimensional lattice structure. The field potential in a crystalline solid follows from the periodicity of the nuclei. To solve the Schrödinger equation with a periodic potential, Bloch functions[45] provided a suitable basis for the single-particle orbitals in crystalline solids. More importantly, the representation of electrons using Bloch states leads to the well-known electronic energy band theory, which became a crucial tool for understanding the electronic properties of solids. However, solving the correlation problem of electrons was still challenging and practically intractable by wavefunction methods. In fact, capturing the correlation effects is even more important in solids to account for the dynamical screening among electrons. Finding an accurate and efficient approach to solve many-electron problems for atoms, molecules, and solids was in necessity.

In the 1940s, Feynman formulated quantum mechanics using the path integral approach, where the interactions between elementary particles are represented by diagrams.[46, 47] The Feynman diagrams provide intuitive insight into the structures of many-electron interactions, including classical repulsion and quantum effects. In the 1960s, Hohenberg and Kohn proved that the ground state of a quantum many-body system could be fully

determined by its charge density, and the total energy of the system is a functional of the charge density.[48] The Hohenberg–Kohn theorem established the density functional approach as an exact theory to solve many-body problems. The Thomas–Fermi model[49, 50] and Slater's exchange-hole[51] method can thus be viewed as particular approximations, which however did not include the correlation effects. This fundamental problem was further tackled by Kohn and Sham, leading to the Kohn–Sham (KS) approach to the density functional theory (DFT).[52] In KS-DFT, the fully interacting many-electron problem of a real system is mapped onto an auxiliary system with non-interacting particle – the particles exist in a field that mimics the presence of other particles at the mean-field level. By construction, only the ground-state density and energy are meaningful for interpretation, while the particles are fictitious, i.e., they are not physical electrons; among these single-particle states, only the energy of the highest occupied orbital corresponds to the binding energy of an electron (discussed in the following as ionization energy).[53, 54, 55, 56, 57, 25] By replacing the wavefunction with the charge density as the basic variable, KS-DFT significantly reduced the computational complexity and cost, allowing efficient electronic structure calculations for solid-state systems with periodic boundary conditions. In practice, the exchange–correlation (XC) functional in KS-DFT governs the accuracy of calculations and needs to be approximated, and the applications of KS-DFT to atoms and molecules relied on the development of more sophisticated XC functionals than the local density approximation (LDA).[58, 59, 60, 61, 62, 63, 64, 65, 66, 67, 68, 69] The quality of XC functionals is often evaluated by comparing the KS-DFT ground-state energy and density with benchmarking results obtained from wavefunction methods. However, recently developed XC functionals focused more on the energy agreement but overlooked the density, causing the approximated functional to stray away from the exact one.[70]

The theoretical approaches described above primarily deal with the ground-state properties of a system, such as equilibrium crystal or molecular structure, charge density,

magnetic order, and static dielectric and magnetic susceptibilities. However, the electrical and spectroscopic properties of matter involve both the ground and excited states. For example, the atomic line spectra come from the electronic transition from an excited state to the ground state. Another type of excited-state properties in spectroscopy is the excitation spectra for adding or removing electrons, which is the focus of this dissertation. The removal or addition of electrons can be observed through direct or inverse photoemission spectroscopy, and the measured energies correspond to the ionization potentials (IPs) or the electron affinities (EAs). Knowledge of these spectroscopic properties provides valuable insights into the electronic structure of matter of interests, and it is tempting to outline the electronic structure through quantum mechanical calculations. While the eigenvalues from Hartree–Fock calculations can be interpreted as IPs and EAs for charged excitation energies based on the Koopmans' theorem,[71] they generally overestimate IPs and underestimate EAs compared to experimental measurements. Similarly, the eigenvalues from KS-DFT calculations have also been widely interpreted as excitation energies.[72] However, these eigenvalues depend strongly on the choice of XC functionals that are in principle not exact. Other related issues include overestimated EAs, underestimated IPs, and too-small band gaps.

The failures of Hartree–Fock and KS-DFT above can be attributed to the nature of ground-state approaches: the electron–electron interactions are highly averaged and show little dependence on a specific single-particle state. This mean-field treatment might be sufficient to describe the collective properties of electrons, e.g., the total energy, but is inadequate to capture the nonlocal and dynamical interactions associated with a single-electron excitation. Hence, excited-state properties should not be expected from a ground-state calculation and should be treated by excited-state theories. Using the Hartree–Fock ground state as a starting point, wavefunction methods such as CI and CC can handle excited states to improve the results but suffer from steep scaling in cost.

Many-body Green's function theory is another alternative and ideal solution to excitation energies involving hole or electron injections. In Green's function theory, the ground-state of a system is treated as a Fermi vacuum, and the electron removal or addition corresponds to a particle (hole or electron) created in the Fermi vacuum. This created particle perturbs the surrounding environment, and the responding environment dresses the particle, leading to the formation of a *quasiparticle*. The dynamics of this quasiparticle in the system is described by the single-particle Green's function, associated with a self-energy term accounting for all the many-body effects, including Coulomb repulsion and exchange–correlation interactions. The Green's function formalism provides in principle single-quasiparticle energies corresponding exactly to ionization energies and electron affinities measured in photoemission spectroscopy. However, analogous to the XC functionals in KS-DFT, the exact XC self-energy is intractable and needs to be approximated. On the other hand, the XC self-energy is nonlocal, dynamical and state-specific, contrasting the local/semilocal and static XC functionals in KS-DFT. Within this framework, the GW approximation, where G denotes the Green's function and W the screened Coulomb interactions, has been widely used to compute charge excitation energies in solid-state and molecular systems,[73, 74, 75, 76, 77] and excellent agreements with experiments have been achieved.

The traditional GW approach outperforms the wavefunction methods with a scaling of N^4. Additionally, it provides better accuracy than the wavefunction methods particularly in tackling solid-state systems. However, the N^4 cost scaling still limits its applications to only small molecules and unit cells. By combining the stochastic sampling technique with GW, the scaling has been significantly reduced to linear, enabling GW calculations for systems with thousands of electrons.[78, 79, 80] The success of the stochastic GW formalism promises accurate predictions of electronic structure for large-scale systems. It also highlights the two rules of thumb in developing electronic structure methods:

accuracy and efficiency. The former determines the reliability of simulations, while the latter dictates the size of a system that can be handled. Both factors are essential for one to use first-principles calculations in aiding materials design or elucidating the work mechanism of functional materials.

Following the aforementioned rules of thumb, the methods developed in this dissertation are to solve the interacting many-electron problem with high efficiency and accuracy in electronic structure calculations. From investigating quasiparticle excitations and dynamics, this dissertation is dedicated to answering questions including but not limited to

(1) What are the effects of dynamically electronic couplings, e.g., van der Waals interactions, on the electronic properties of functional molecules and polymers in the condensed phase?

(2) What is the strategy for treating localized excitations of molecules or defects in an arbitrary environment?

(3) How to effectively and efficiently separate the electronic subspace for a molecule of interest from a multicomponent condensed system?

(4) How to quantify the environmental renormalization effects associated with single-quasiparticle excitations?

(5) How to perform GW and beyond-GW calculations on systems of all dimensions?

To achieve these, multilevel theoretical approaches are employed to search for various properties: equilibrium structures and geometries are generated by molecular dynamics simulations; electronic ground states are computed by KS-DFT; quasiparticle energies are obtained by the GW method and beyond. The remaining content of this dissertation

is organized as follows: Chapter 2 provides a detailed introduction to the theories mentioned above, Chapter 3 demonstrates how to perform deterministic and stochastic *GW* calculations to obtain quasiparticle energies in practice, Chapter 4 briefly introduces the six research projects listed in the following Chapters (Chapter 5-Chapter 10), and the motivation and background of each work can be found in each individual Chapter. Finally, Chapter 11 summarizes the achievements and significance of this dissertation.

Bibliography

[1] J. J. Thomson, *Xl. cathode rays*, *The London, Edinburgh, and Dublin Philosophical Magazine and Journal of Science* **44** (1897), no. 269 293–316.

[2] J. J. Thomson, *Xxiv. on the structure of the atom: an investigation of the stability and periods of oscillation of a number of corpuscles arranged at equal intervals around the circumference of a circle; with application of the results to the theory of atomic structure*, *The London, Edinburgh, and Dublin Philosophical Magazine and Journal of Science* **7** (1904), no. 39 237–265.

[3] E. Rutherford, *Lxxix. the scattering of α and β particles by matter and the structure of the atom*, *The London, Edinburgh, and Dublin Philosophical Magazine and Journal of Science* **21** (1911), no. 125 669–688.

[4] R. McCormmach, *The atomic theory of john william nicholson*, *Archive for History of Exact Sciences* **3** (1966) 160–184.

[5] N. Bohr, *I. on the constitution of atoms and molecules*, *The London, Edinburgh, and Dublin Philosophical Magazine and Journal of Science* **26** (1913), no. 151 1–25.

[6] N. Bohr, *Xxxvii. on the constitution of atoms and molecules*, *The London, Edinburgh, and Dublin Philosophical Magazine and Journal of Science* **26** (1913), no. 153 476–502.

[7] N. Bohr, *Lxxiii. on the constitution of atoms and molecules*, *The London, Edinburgh, and Dublin Philosophical Magazine and Journal of Science* **26** (1913), no. 155 857–875.

[8] N. Bohr, *The spectra of helium and hydrogen*, *Nature* **92** (1913), no. 2295 231–232.

[9] W. Heisenberg, *Über quantentheoretische umdeutung kinematischer und mechanischer beziehungen.*, *Zeitschrift für Physik* **33** (1925), no. 1 879–893.

[10] W. Heisenberg, *Über den anschaulichen inhalt der quantentheoretischen kinematik und mechanik*, *Zeitschrift für Physik* **43** (1927), no. 3 172–198.

[11] W. Heisenberg, C. Eckart, and F. Hoyt, *The Physical Principles of the Quantum Theory*. Dover books on advanced science. University of Chicago Press, 1930.

[12] E. Schrödinger, *An undulatory theory of the mechanics of atoms and molecules*, *Phys. Rev.* **28** (1926) 1049–1070.

[13] P. A. M. Dirac and R. H. Fowler, *The quantum theory of the electron*, *Proceedings of the Royal Society of London. Series A, Containing Papers of a Mathematical and Physical Character* **117** (1928), no. 778 610–624.

[14] P. A. M. Dirac and R. H. Fowler, *A theory of electrons and protons*, *Proceedings of the Royal Society of London. Series A, Containing Papers of a Mathematical and Physical Character* **126** (1930), no. 801 360–365.

[15] P. A. M. Dirac, *The principles of quantum mechanics*. Oxford, 4 ed., 1930.

[16] R. M. Martin, *Electronic Structure: Basic Theory and Practical Methods*. Cambridge University Press, 2 ed., 2020.

[17] M. Born and R. Oppenheimer, *Zur quantentheorie der molekeln*, *Annalen der Physik* **389** (1927), no. 20 457–484.

[18] D. R. Hartree, *The wave mechanics of an atom with a non-coulomb central field. part i. theory and methods*, *Mathematical Proceedings of the Cambridge Philosophical Society* **24** (1928), no. 1 89–110.

[19] J. C. Slater, *The self consistent field and the structure of atoms*, *Phys. Rev.* **32** (1928) 339–348.

[20] V. Fock, *Näherungsmethode zur lösung des quantenmechanischen mehrkörperproblems*, *Zeitschrift für Physik* **61** (1930), no. 1 126–148.

[21] J. C. Slater, *Note on hartree's method*, *Phys. Rev.* **35** (1930) 210–211.

[22] D. R. Hartree and W. Hartree, *Self-consistent field, with exchange, for beryllium*, *Proceedings of the Royal Society of London. Series A - Mathematical and Physical Sciences* **150** (1935), no. 869 9–33.

[23] J. C. Slater, *The theory of complex spectra*, *Phys. Rev.* **34** (1929) 1293–1322.

[24] J. E. Lennard-Jones, *The electronic structure of some diatomic molecules*, *Trans. Faraday Soc.* **25** (1929) 668–686.

[25] R. M. Martin, L. Reining, and D. M. Ceperley, *Interacting Electrons: Theory and Computational Approaches*. Cambridge University Press, 2016.

[26] W. Duch, *Configuration interaction method: the past and future perspectives*, *Journal of Molecular Structure: THEOCHEM* **234** (1991) 27–49.

[27] C. David Sherrill and H. F. Schaefer, *The configuration interaction method: Advances in highly correlated approaches*, vol. 34 of *Advances in Quantum Chemistry*, pp. 143–269. Academic Press, 1999.

[28] P. G. Szalay, T. Müller, G. Gidofalvi, H. Lischka, and R. Shepard, *Multiconfiguration self-consistent field and multireference configuration interaction methods and applications*, *Chemical Reviews* **112** (2012), no. 1 108–181. PMID: 22204633.

[29] D. Cremer, *From configuration interaction to coupled cluster theory: The quadratic configuration interaction approach*, *WIREs Computational Molecular Science* **3** (2013), no. 5 482–503.

[30] N. Oliphant and L. Adamowicz, *Multireference coupled cluster method for electronic structure of molecules*, *International Reviews in Physical Chemistry* **12** (1993), no. 2 339–362.

[31] R. J. Bartlett and M. Musiał, *Coupled-cluster theory in quantum chemistry*, *Rev. Mod. Phys.* **79** (2007) 291–352.

[32] P. Cársky, J. Paldus, and J. Pittner, *Recent Progress in Coupled Cluster Methods: Theory and Applications*. Challenges and Advances in Computational Chemistry and Physics. Springer Netherlands, 2012.

[33] D. I. Lyakh, M. Musiał, V. F. Lotrich, and R. J. Bartlett, *Multireference nature of chemistry: The coupled-cluster view*, *Chemical Reviews* **112** (2012), no. 1 182–243. PMID: 22220988.

[34] I. Y. Zhang and A. Grüneis, *Coupled cluster theory in materials science*, *Frontiers in Materials* **6** (2019) 1–13.

[35] C. Møller and M. S. Plesset, *Note on an approximation treatment for many-electron systems*, *Phys. Rev.* **46** (1934) 618–622.

[36] K. A. Brueckner, *Many-body problem for strongly interacting particles. ii. linked cluster expansion*, *Phys. Rev.* **100** (1955) 36–45.

[37] J. O. Hirschfelder, W. B. Brown, and S. T. Epstein, *Recent developments in perturbation theory*, vol. 1 of *Advances in Quantum Chemistry*, pp. 255–374. Academic Press, 1964.

[38] P.-O. Löwdin, *Studies in perturbation theory. x. lower bounds to energy eigenvalues in perturbation-theory ground state*, *Phys. Rev.* **139** (1965) A357–A372.

[39] K. F. Freed, *Many-body theories of the electronic structure of atoms and molecules*, *Annual Review of Physical Chemistry* **22** (1971), no. 1 313–346.

[40] M. Head-Gordon, J. A. Pople, and M. J. Frisch, *Mp2 energy evaluation by direct methods*, *Chemical Physics Letters* **153** (1988), no. 6 503–506.

[41] D. Cremer, *Møller–plesset perturbation theory: from small molecule methods to methods for thousands of atoms*, *WIREs Computational Molecular Science* **1** (2011), no. 4 509–530.

[42] A. Sommerfeld, *Zur elektronentheorie der metalle auf grund der fermischen statistik*, *Zeitschrift für Physik* **47** (1928), no. 1 1–32.

[43] P. Drude, *Zur elektronentheorie der metalle*, *Annalen der Physik* **306** (1900), no. 3 566–613.

[44] P. Drude, *Zur elektronentheorie der metalle; ii. teil. galvanomagnetische und thermomagnetische effecte*, *Annalen der Physik* **308** (1900), no. 11 369–402.

[45] F. Bloch, *Über die quantenmechanik der elektronen in kristallgittern*, *Zeitschrift für Physik* **52** (1929), no. 7 555–600.

[46] R. P. Feynman, *Space-time approach to quantum electrodynamics*, *Phys. Rev.* **76** (1949) 769–789.

[47] R. P. Feynman, *THE PRINCIPLE OF LEAST ACTION IN QUANTUM MECHANICS*, pp. 1–69. 1949.

[48] P. Hohenberg and W. Kohn, *Inhomogeneous electron gas*, *Physical Review* **136** (1964), no. 3B B864–B871.

[49] L. H. Thomas, *The calculation of atomic fields*, *Mathematical Proceedings of the Cambridge Philosophical Society* **23** (1927), no. 5 542–548.

[50] E. Fermi, *Statistical method to determine some properties of atoms*, *Rend. Accad. Naz. Lincei* **6** (1927), no. 602-607 5.

[51] J. C. Slater, *A simplification of the hartree-fock method*, *Phys. Rev.* **81** (1951) 385–390.

[52] W. Kohn and L. J. Sham, *Self-consistent equations including exchange and correlation effects*, *Physical Review* **140** (1965), no. 4A A1133–A1138.

[53] M. Levy, *Universal variational functionals of electron densities, first-order density matrices, and natural spin-orbitals and solution of the v-representability problem*, *Proceedings of the National Academy of Sciences* **76** (1979), no. 12 6062–6065.

[54] M. Levy, *Electron densities in search of hamiltonians*, *Phys. Rev. A* **26** (1982) 1200–1208.

[55] J. P. Perdew, R. G. Parr, M. Levy, and J. L. Balduz, *Density-functional theory for fractional particle number: Derivative discontinuities of the energy*, *Phys. Rev. Lett.* **49** (1982) 1691–1694.

[56] E. H. Lieb, *Density functionals for coulomb systems*, *International Journal of Quantum Chemistry* **24** (1983), no. 3 243–277.

[57] R. M. Dreizler and E. K. U. Gross, *Density functional theory: an approach to the quantum many-body problem*. Springer, Berlin, 1990.

[58] J. P. Perdew and A. Zunger, *Self-interaction correction to density-functional approximations for many-electron systems*, *Phys. Rev. B* **23** (1981) 5048–5079.

[59] C. Lee, W. Yang, and R. G. Parr, *Development of the colle-salvetti correlation-energy formula into a functional of the electron density*, *Phys. Rev. B* **37** (1988) 785–789.

[60] J. P. Perdew and Y. Wang, *Accurate and simple analytic representation of the electron-gas correlation energy*, *Phys. Rev. B* **45** (1992) 13244–13249.

[61] A. D. Becke, *Density-functional thermochemistry. III. The role of exact exchange*, *The Journal of Chemical Physics* **98** (1993), no. 7 5648–5652.

[62] J. P. Perdew, K. Burke, and M. Ernzerhof, *Generalized gradient approximation made simple*, *Phys. Rev. Lett.* **77** (1996) 3865–3868.

[63] C. Adamo and V. Barone, *Toward reliable density functional methods without adjustable parameters: The PBE0 model*, *The Journal of Chemical Physics* **110** (1999), no. 13 6158–6170.

[64] J. Heyd, G. E. Scuseria, and M. Ernzerhof, *Hybrid functionals based on a screened Coulomb potential*, *The Journal of Chemical Physics* **118** (2003), no. 18 8207–8215.

[65] T. Yanai, D. P. Tew, and N. C. Handy, *A new hybrid exchange–correlation functional using the coulomb-attenuating method (cam-b3lyp)*, *Chemical Physics Letters* **393** (2004), no. 1 51–57.

[66] R. Baer and D. Neuhauser, *Density functional theory with correct long-range asymptotic behavior*, *Phys. Rev. Lett.* **94** (2005) 043002.

[67] E. Livshits and R. Baer, *A well-tempered density functional theory of electrons in molecules*, *Physical Chemistry Chemical Physics* **9** (2007), no. 23 2932–2941.

[68] M. A. Rohrdanz and J. M. Herbert, *Simultaneous benchmarking of ground- and excited-state properties with long-range-corrected density functional theory*, *The Journal of Chemical Physics* **129** (2008), no. 3. 034107.

[69] J. Sun, A. Ruzsinszky, and J. P. Perdew, *Strongly constrained and appropriately normed semilocal density functional*, *Phys. Rev. Lett.* **115** (2015) 036402.

[70] M. G. Medvedev, I. S. Bushmarinov, J. Sun, J. P. Perdew, and K. A. Lyssenko, *Density functional theory is straying from the path toward the exact functional*, *Science* **355** (2017), no. 6320 49–52.

[71] T. Koopmans, *Über die zuordnung von wellenfunktionen und eigenwerten zu den einzelnen elektronen eines atoms*, *Physica* **1** (1934), no. 1 104–113.

[72] J. F. Janak, *Proof that $\frac{\partial e}{\partial n_i} = \epsilon$ in density-functional theory*, *Phys. Rev. B* **18** (1978) 7165–7168.

[73] F. Aryasetiawan and O. Gunnarsson, *The gw method*, *Reports on Progress in Physics* **61** (1998), no. 3 237.

[74] C. Friedrich and A. Schindlmayr, *Many-body perturbation theory: The GW approximation*, vol. 31 of *NIC Series*, p. 335–355. John von Neumann Institute for Computing, 2006.

[75] M. J. van Setten, F. Caruso, S. Sharifzadeh, X. Ren, M. Scheffler, F. Liu, J. Lischner, L. Lin, J. R. Deslippe, S. G. Louie, C. Yang, F. Weigend, J. B. Neaton, F. Evers, and P. Rinke, *Gw100: Benchmarking g0w0 for molecular systems*, *Journal of Chemical Theory and Computation* **11** (2015), no. 12 5665–5687.

[76] F. Caruso, M. Dauth, M. J. van Setten, and P. Rinke, *Benchmark of gw approaches for the gw100 test set*, *Journal of Chemical Theory and Computation* **12** (2016), no. 10 5076–5087.

[77] M. Govoni and G. Galli, *Gw100: Comparison of methods and accuracy of results obtained with the west code*, *Journal of Chemical Theory and Computation* **14** (2018), no. 4 1895–1909.

[78] D. Neuhauser, Y. Gao, C. Arntsen, C. Karshenas, E. Rabani, and R. Baer, *Breaking the theoretical scaling limit for predicting quasiparticle energies: The stochastic GW approach*, *Physical Review Letters* **113** (2014), no. 7 076402.

[79] V. Vlček, W. Li, R. Baer, E. Rabani, and D. Neuhauser, *Swift GW beyond 10,000 electrons using sparse stochastic compression*, *Physical Review B* **98** (2018), no. 7 075107.

[80] V. Vlček, *Stochastic vertex corrections: Linear scaling methods for accurate quasiparticle energies*, *Journal of Chemical Theory and Computation* **15** (2019), no. 11 6254–6266.

Chapter 2

Theory

2.1 Many-electron problem

Quantum mechanics provides a theoretical framework for understanding the behavior of atoms, molecules, and solids. In these systems, most chemical and physical phenomena, such as chemical bonding, charge transport, and excitations in spectroscopy, involve the positions and motions of subatomic quantum particles, i.e., nuclei and electrons. The desired information of such a *many-particle* quantum system is encoded in a quantum state $|\Psi\rangle$, from which one can extract observables like total energy, particle densities, forces, and many others. A stationary many-particle state $|\Psi\rangle$ satisfies the following time-independent Schrödinger equation

$$\hat{\mathcal{H}} |\Psi\rangle = \mathcal{E} |\Psi\rangle , \tag{2.1}$$

where $\hat{\mathcal{H}}$ is the Hamiltonian specifying the mutual interactions within a many-particle system , and $\mathcal{E}$ is the corresponding total energy. A seemingly concrete description of the quantum state can be provided in real space, where $|\Psi\rangle$ is projected onto a configuration

state of the system

$$\Psi(\mathbf{x}_1, \mathbf{x}_2, \ldots, \mathbf{x}_N, \mathbf{R}_1, \mathbf{R}_2, \ldots, \mathbf{R}_M) = \langle \mathbf{x}_1, \mathbf{x}_2, \ldots, \mathbf{x}_N; \mathbf{R}_1, \mathbf{R}_2, \ldots, \mathbf{R}_M | \Psi \rangle \,. \tag{2.2}$$

Here, the configuration state $|\mathbf{x}_1, \mathbf{x}_2, \ldots, \mathbf{x}_N, \mathbf{R}_1, \mathbf{R}_2, \ldots, \mathbf{R}_M\rangle$ refers to a particular set of coordinates of all the nuclei and electrons. $\Psi(\mathbf{x}_1, \mathbf{x}_2, \ldots, \mathbf{x}_N, \mathbf{R}_1, \mathbf{R}_2, \ldots, \mathbf{R}_M)$ is commonly known as a many-particle *wavefunction*. $\mathbf{x}_i = (\mathbf{r}_i, \sigma_i)$ represents the spatial and spin coordinates of the i^{th} electron, with $\mathbf{r}_i = (x_i, y_i, z_i)$ and $\sigma_i = \pm\frac{1}{2}$. $\mathbf{R}_A$ is the spatial coordinates of the A^{th} nucleus.

The Hamiltonian $\hat{\mathcal{H}}$ in Eq. (2.1) can also be expressed in real-space Cartesian coordinates

$$\begin{aligned} \hat{\mathcal{H}} = &- \sum_{i=1}^{N} \frac{\hbar^2}{2m_e} \nabla_i^2 - \sum_{A=1}^{M} \frac{\hbar^2}{2M_A} \nabla_A^2 - \sum_{i=1}^{N} \sum_{A=1}^{M} \frac{Z_A e^2}{4\pi\epsilon_0 r_{iA}} \\ &+ \frac{1}{2} \sum_{i \neq j}^{N} \sum_{j=1}^{N} \frac{e^2}{4\pi\epsilon_0 r_{ij}} + \frac{1}{2} \sum_{A \neq B}^{M} \sum_{B=1}^{M} \frac{Z_A Z_B e^2}{4\pi\epsilon_0 R_{AB}}. \end{aligned} \tag{2.3}$$

In Eq. (2.3), $\hbar$ denotes the reduced Planck constant (Planck constant divided by 2π), m_e represents the mass of an electron, M_A is the mass of nucleus A, e is the elementary charge, and Z_A is the atomic number of nucleus A. Additionally, r_{iA} represents the distance between electron i and nucleus A, r_{ij} is the interelectronic distance, and R_{AB} denotes the internuclear distance. Each term on the right-hand side of Eq. (2.3) contributes to the total energy of a system. The first term is the kinetic energy operator summing over all N electrons, where the Laplace operator ∇_i^2 takes the divergence of the gradient of the wavefunction with respect to electron i. Similarly, the second term is the kinetic energy operator for all M nuclei. The third term represents the Coulomb attraction between electrons and nuclei, while the last two terms are the Coulomb repulsion between electrons and between nuclei, respectively. The factor 1/2 in these terms cancels the

double-counting effects in the summation. The expression of Eq. (2.3) can be simplified using the atomic units

$$\begin{aligned}\hat{\mathcal{H}} = &-\sum_{i=1}^{N}\frac{1}{2}\nabla_i^2 - \sum_{A=1}^{M}\frac{1}{2M'_A}\nabla_A^2 - \sum_{i=1}^{N}\sum_{A=1}^{M}\frac{Z_A}{r_{iA}} \\ &+ \frac{1}{2}\sum_{i\neq j}^{N}\sum_{j=1}^{N}\frac{1}{r_{ij}} + \frac{1}{2}\sum_{A\neq B}^{M}\sum_{B=1}^{M}\frac{Z_A Z_B}{R_{AB}},\end{aligned} \tag{2.4}$$

where M'_A is defined as M_A/m_e. Expressions are assumed in atomic units throughout the rest of this dissertation unless otherwise stated.

For the main interest in electronic properties, it is desirable to disentangle the electronic motion from the nuclei. Based on the fact that the nuclei are much heavier and thus move much slower than the electrons, one can invoke the Born–Oppenheimer approximation[1] to study the motion of electrons with the nuclei fixed in space. In this approximation, the many-particle state collapses into states with well-defined nuclear positions. Assuming that the many-particle wavefunction is separable,[2, 3, 4] one can factor out the nuclear component and obtain the following product form of a wavefunction

$$\Psi(\mathbf{x}_1, \mathbf{x}_2, \ldots, \mathbf{x}_N, \mathbf{R}_1, \mathbf{R}_2, \ldots, \mathbf{R}_M) = \Psi^{\text{elec}}(\mathbf{x}_1, \mathbf{x}_2, \ldots, \mathbf{x}_N; \{\mathbf{R}_A\})\Psi^{\text{nucl}}(\{\mathbf{R}_A\}). \tag{2.5}$$

Here, $\Psi^{\text{elec}}(\{\mathbf{x}_i\})$ denotes the *many-electron* wavefunction, in which the set of nuclear coordinates $\{\mathbf{R}_A\}$ serve as parameters (i.e., known values) instead of variables. $\Psi^{\text{nucl}}(\{\mathbf{R}_A\})$ is the wavefunction that describes a state of well-defined positions of nuclei.

Upon the Born–Oppenheimer approximation and the separation of the wavefunction, one can effectively treat a many-particle system as a combination of "classical" and quantum particles. The nuclei are treated by classical mechanics, with the internuclear interactions computed as Coulomb repulsion between point charges and the kinetic energy

computed from particle velocity. Only the electrons are treated quantum mechanically by the following electronic Hamiltonian

$$\begin{aligned}\hat{H}^{\text{elec}} &= -\sum_{i=1}^{N}\frac{1}{2}\nabla_i^2 + \frac{1}{2}\sum_{i\neq j}^{N}\sum_{j=1}^{N}\frac{1}{r_{ij}} - \sum_{A=1}^{M}\sum_{i=1}^{N}\frac{Z_A}{r_{iA}} \\ &= \hat{T} + \hat{V}_{\text{ee}} + \hat{V}_{\text{ext}}.\end{aligned} \tag{2.6}$$

Here, the operators $\hat{T}$, $\hat{V}_{\text{ee}}$ are the shorthand notations for the kinetic energy and the electron interaction energy. $\hat{V}_{\text{ext}}$ represents the interaction with an static external field, which is provided by the fixed nuclei

$$\begin{aligned}\hat{V}_{\text{ext}} &= -\sum_{i}^{N}\sum_{A}^{M}\frac{Z_A}{|\mathbf{r}_i - \mathbf{R}_A|} \\ &= \sum_{i}^{N} v_{\text{ext}}(\mathbf{r}_i).\end{aligned} \tag{2.7}$$

Here, the external potential is purely the classical Coulomb attraction that acts the same on each electron

$$v_{\text{ext}}(\mathbf{r}) = -\sum_{A}^{M}\frac{Z_A}{|\mathbf{r} - \mathbf{R}_A|}. \tag{2.8}$$

As a result, the electron-nucleus attraction E_{en} can be written in terms of the electron density $n(\mathbf{r})$ interacting with the external field

$$E_{\text{en}} = \langle\Psi^{\text{elec}}|\hat{V}_{\text{ext}}|\Psi^{\text{elec}}\rangle = \int v_{\text{ext}}(\mathbf{r})n(\mathbf{r})\mathrm{d}\mathbf{r}. \tag{2.9}$$

This expression will be used very often when it comes to the density functional theory in Section 2.4. The electron density in Eq. (2.9) is given by

$$n(\mathbf{r}) = N\int \mathrm{d}\sigma\mathrm{d}\mathbf{x}_2\mathrm{d}\mathbf{x}_3\ldots\mathrm{d}\mathbf{x}_N|\Psi^{\text{elec}}(\mathbf{r}\sigma\mathbf{x}_2,\mathbf{x}_3,\ldots,\mathbf{x}_N)|^2, \tag{2.10}$$

where N is the renormalization factor to the number of electrons as the electronic wavefunction is normalized: $\langle \Psi^{\text{elec}} | \Psi^{\text{elec}} \rangle = 1$. The many-particle problem is formally reduced to a many-electron problem, where the many-electron state satisfies the following Schrödinger equation

$$\hat{H}^{\text{elec}} \left| \Psi^{\text{elec}}(\{\mathbf{R}_A\}) \right\rangle = E^{\text{elec}}(\{\mathbf{R}_A\}) \left| \Psi^{\text{elec}}(\{\mathbf{R}_A\}) \right\rangle . \tag{2.11}$$

Here, $|\Psi^{\text{elec}}\rangle$ is subject to $\{\mathbf{R}_A\}$, and the corresponding electronic energy E^{elec} is a function of $\{\mathbf{R}_A\}$. The total energy of a system is the sum of the electronic energy and the nuclear repulsion

$$E^{\text{tot}}(\{\mathbf{R}_A\}) = E^{\text{elec}}(\{\mathbf{R}_A\}) + \frac{1}{2} \sum_{A \neq B}^{M} \sum_{B=1}^{M} \frac{Z_A Z_B}{R_{AB}}. \tag{2.12}$$

This total energy E^{tot} is a function of $\{\mathbf{R}_A\}$, which is known as the adiabatic potential energy surface appearing in the nuclear Hamiltonian to describe the motion of the nuclei. The nuclear motion is responsible for the system's rotational, vibrational, and translational properties that can be coupled to the electronic properties. However, this dissertation does not address these coupling effects and focuses only on the electronic degrees of freedom, with the Born–Oppenheimer approximation applied to all the electronic problems. Furthermore, the superscript "elec" used in this section is omitted for all the wavefunctions, Hamiltonians, and energies for simplicity in the remaining content.

2.2 Mean-field solutions: an overview

The exact solution to Eq. (2.11) remains a perpetual challenge for systems beyond the hydrogen atom, i.e., systems with more than one electron. The reasons for it being difficult to solve are multiple. First of all, although the expression of the many-electron Hamiltonian is known, information about the wavefunction, such as its form and dimension, is not given.

Second, assuming that the electronic Hilbert space can be completely defined by M basis functions, the number of possible configuration (introduced later as a single determinant) for full interaction will be $\binom{M}{N}$, accompanied by a Hamiltonian matrix with a dimension of $\binom{M}{N}^2$. The computational cost scales exponentially with the number of electrons N. For a nanoscale system, which is often the case in chemistry and materials, the required computational time and memory for storage are expected to be astronomical. Third, the completeness of basis is not guaranteed in practice, and the computational results usually depend on the number and the type of basis functions. Given the intractability of the exact answer, numerous efforts have been devoted to finding approximate solutions for many-body problems in chemically important and materials systems.

Suppose that the system in question is a hydrogen atom for which an exact solution to the Schrödinger equation exists. The resulting wavefunctions can be interpreted as *atomic orbitals* that are characterized by a set of quantum numbers. These are orbitals describing the spatial distribution (motion) of an electron. When two hydrogen atoms are brought close together, they form an H_2 molecule, and the "bond" connecting these two atoms is indeed a pair of electrons whose motions are described by the so-called *molecular orbitals*. Since electrons are fermions, the Pauli exclusion principle states that an orbital can be occupied by two electrons if and only if they have opposite spins. For a doubly-occupied molecular orbital, one can multiply it by a spin function, which is either up (+1/2) or down (-1/2), to define a *spin orbital* for each electron. The relationship between atomic orbitals and molecular spin orbitals will be discussed later. This example alludes to the single-particle picture for solving a many-body problem, in which each individual electron is characterized by a spin orbital. The many-body wavefunction can then be expressed as a single or multiple determinants, which is constructed using N spin orbitals. When solving the ground-state single-particle spin orbitals, the Hamiltonian either uses explicitly or ends up with effective potentials, representing the average effects

of the surrounding particles. Hence, these approaches are also called *mean-field* methods.

The following content of this section provides an overview for the ground-state mean-field methods. Section 2.3 introduces the Hartree–Fock approximation, in which the many-body wavefunction is approximated as a single determinant with partially correlated electrons. Section 2.4 summarizes the principles in density functional theory and presents the Kohn-Sham approach, where a fully interacting quantum many-body system is mapped onto a non-interacting auxiliary system with fictitious particles moving in a mean field.

2.2.1 Search of ground state

The mean-field methods discussed in this section seek the solution to the ground state for Eq. (2.11)

$$\hat{H}\,|\Psi_0\rangle = \mathcal{E}_0\,|\Psi_0\rangle\,, \tag{2.13}$$

where $|\Psi_0\rangle$ denotes the *non-degenerate* ground state, and $\mathcal{E}_0$ is the exact ground-state energy

$$\mathcal{E}_0 < \langle\Psi|\hat{H}|\Psi\rangle = \mathcal{E}\,[\Psi] \quad \text{for } |\Psi\rangle \neq |\Psi_0\rangle\,. \tag{2.14}$$

In the mean-field formulation, the motion of an electron is represented by a single-particle state, and the mean-field total energy E is often writtend in terms of integrals using the set of orthonormal single-particle states

$$E = E\,[\psi_1, \psi_2, \ldots, \psi_N] \tag{2.15}$$

The orthonormality follows the form of the Kronecker delta function

$$\langle\psi_i|\psi_j\rangle = \delta_{ij}, \tag{2.16}$$

where δ_{ij} is defined as

$$\delta_{ij} = \begin{cases} 1 & \text{if } i = j, \\ 0 & \text{if } i \neq j. \end{cases} \tag{2.17}$$

In Eq. (2.15), the set of ψ_i are trial single-particle states to be optimized. The energy functional $E[\{\psi_i\}]$ is assumed *variational* and differentiable with respect to $\{\psi_i\}$, and the optimized E and $\{\psi_i\}$ are obtained at the stationary point

$$\frac{\delta E[\{\psi_i\}]}{\delta\{\psi_i\}} = 0, \tag{2.18}$$

The extremum of E is often found a minimum, which is denoted E_0 as the mean-field ground-state energy

$$E_0 = \min_{\{\psi_i\}} E[\{\psi_i\}]. \tag{2.19}$$

Note that the real ground-state energy $\mathcal{E}_0$ is usually unknow and provided by benchmarking calculations, e.g., using wavefunction methods. The mean-field E_0 is to approach $\mathcal{E}_0$, and this correspondence can be exact. However, practical approximations are usually empolyed, the quality of which is evaluated by comparing E_0 to benchmarking $\mathcal{E}_0$. In cases of large systems where a legitimate $\mathcal{E}_0$ is unavailable, the mean-field ground state is often evaluated together with other properties such as the electron density and experimental observables.

2.2.2 Single-particle eigenvalue equations

Note that the electronic Hamiltonian [Eq. (2.6)] in question is spin-independent, i.e., no operation is performed on the spin state. The spin-orbit coupling is not considered either. As a result, a spin orbital $\psi_i(\mathbf{x})$ can be written as a product of the spatial and the

spin function

$$\psi_i(\mathbf{x}) = \phi_i(\mathbf{r})\xi(\sigma), \tag{2.20}$$

where the function ξ has only two orthonormal states α and β, representing respectively spin up and down

$$\langle \xi(\sigma) | \xi(\sigma') \rangle = \delta_{\sigma\sigma'}. \tag{2.21}$$

With no dependence on spin in the Hamiltonian, the energy functional E in Eq. (2.18) can be fully expressed in terms of the spatial functions.

Generally, the constrained minimization of E in Eq. (2.18) with respect to the set of single-particle spatial functions leads to a set of eigenvalue equations of the following canonical form

$$\hat{h}^{\mathrm{mf}} \left| \phi_i \right\rangle = \varepsilon_i \left| \phi_i \right\rangle, \tag{2.22}$$

where ε_i is the Lagrange multiplier used in the constrained search. $\hat{h}^{\mathrm{mf}}$ denotes the mean-field single-particle Hamiltonian, which commonly reads

$$\hat{h}^{\mathrm{mf}} = -\frac{\nabla^2}{2} + \hat{v}_{\mathrm{eff}}. \tag{2.23}$$

Here, $\hat{v}_{\mathrm{eff}}$ is an effective potential acting on a single particle with a kinetic energy. $\hat{v}_{\mathrm{eff}}$ accounts for the average particle–particle interaction effects, and it can be local or nonlocal, depending on the actual construction.

Practical solutions to the spatial orbitals $\phi_i(\mathbf{r})$ in Eq. (2.22) employ basis functions for expansion. For molecules, the set of $\phi_i(\mathbf{r})$ are often constructed as linear combinations of atomic orbitals[5] (LCAO-MO)

$$\phi_i(\mathbf{r}) = \sum_{\mu} c_{\mu i} \chi_{\mu}(\mathbf{r}), \tag{2.24}$$

where $\chi_\mu(\mathbf{r})$ is an atomic orbital with a definite form, and $c_{\mu i}$ is the corresponding complex coefficient. $\phi_i(\mathbf{r})$ in this basis is called a molecular orbital.

The eigenvalue equations of the form in Eq. (2.22) are often non-linear since the Hamiltonian depends also on the set of $\phi_i(\mathbf{r})$ (demonstrated later in Section 2.3). Hence, these single-particle eigenvalue equations need to be solved self-consistently in practice. And this iteration procedure is called the *self-consistent-field* (SCF) approach, details of which are provided in Section 2.3.

2.2.3 Plane-wave expansion

For systems with periodic boundary conditions, such as three-dimensional solids or two-dimensional surfaces, the single-particle solutions to Eq. (2.22) satisfy the Bloch's theorem,[6] where the state is characterized by an additional wave vector $\mathbf{k}$

$$\phi_{i\mathbf{k}}(\mathbf{r}) = e^{\mathrm{i}\mathbf{k}\mathbf{r}} u(\mathbf{r}). \tag{2.25}$$

Here, $\phi_{i\mathbf{k}}(\mathbf{r})$ represents a Bloch state. $\mathbf{k}$ in the plane-wavefunction $e^{\mathrm{i}\mathbf{k}\mathbf{r}}$ determines its periodicity/wavelength, and i denotes the eigenvalue level solved for a particular $\mathbf{k}$. $u(\mathbf{r})$ is a periodic function appearing in each unit cell. This periodic function can also be expanded in terms of plane waves leveraging the periodicity of the lattice

$$u(\mathbf{r}) = \frac{1}{\sqrt{\Omega}} \sum_{\mathbf{G}_\alpha} c_\alpha e^{\mathrm{i}\mathbf{G}_\alpha \mathbf{r}}. \tag{2.26}$$

Generally, a three-dimensional box is constructed in computation by the lattice vectors $\mathbf{a}_1$, $\mathbf{a}_2$, and $\mathbf{a}_3$. Ω in Eq. (2.26) is the box volume computed from the lattice vectors

$$\Omega = |\mathbf{a}_1 \cdot (\mathbf{a}_2 \times \mathbf{a}_3)| \tag{2.27}$$

$\mathbf{G}_\alpha$ is a reciprocal lattice vector defined as

$$\mathbf{G}_\alpha = i \cdot \mathbf{b}_1 + j \cdot \mathbf{b}_2 + k \cdot \mathbf{b}_3, \tag{2.28}$$

where i, j, and k are integers, and α denotes a particular combination of (i, j, k). The reciprocal lattice constants are given by

$$\begin{aligned} \mathbf{b}_1 &= 2\pi \tfrac{\mathbf{a}_2 \times \mathbf{a}_3}{\Omega}, \\ \mathbf{b}_2 &= 2\pi \tfrac{\mathbf{a}_3 \times \mathbf{a}_1}{\Omega}, \\ \mathbf{b}_3 &= 2\pi \tfrac{\mathbf{a}_1 \times \mathbf{a}_2}{\Omega}. \end{aligned} \tag{2.29}$$

c_α in Eq. (2.26) is a complex coefficient similar to the one in LCAO.

By plugging Eq. (2.26) into Eq. (2.25), one obtains the expression of a single-particle orbital in the plane-wave basis

$$\phi_{i\mathbf{k}}(\mathbf{r}) = \frac{1}{\sqrt{\Omega}} \sum_{\mathbf{G}_\alpha} c_{\alpha i} e^{\mathrm{i}(\mathbf{G}_\alpha + \mathbf{k})\mathbf{r}}. \tag{2.30}$$

The exact plane-wave expansion of $u(\mathbf{r})$ requires the summation of G_α to infinity. However, in practical calculations, one would avoid this infinite summation by setting a cutoff kinetic energy

$$E_{\mathrm{cut}} = \frac{|\mathbf{G}_{\mathrm{cut}}|^2}{2}. \tag{2.31}$$

A large enough E_{cut} is often applicable to a vast variety of systems. To guarantee the results are independent of E_{cut}, one will need to increase it at a certain step to perform multiple calculations until the results do not vary. Finally, the optimization of $\{\phi_{i\mathbf{k}}(\mathbf{r})\}$ also follows the self-consistent field approach as mentioned for molecular orbitals.

Solutions to $\{\phi_i(\mathbf{r})\}$ or $\{\phi_{i\mathbf{k}}(\mathbf{r})\}$ come with a set of eigenvalues $\{\varepsilon_{i(\mathbf{k})}\}$, which are introduced as the Lagrange multipliers for constrained minimization (will be revisited

later on). These eigenvalues are purely mathematical tools and do not have any physical meaning in principle. However, due to the "Schrödinger-like" feature of Eq. (2.22), ε_i is often interpreted as the orbital energy characterizing the electron occupying $\phi_i(\mathbf{r})$. This interpretation, although risky, is straightforward, since the mean-field Hamiltonian $\hat{h}^{\mathrm{mf}}$ includes effectively all the energy ingredients describing the motion a single particle. Most importantly, the interpretation as single-particle energies contributes significantly to modern electronic structure theory. This dissertation is centered on the discussion of $\phi_i(\mathbf{r})$ and ε_i, and their relations with excited-state properties such as charged excitations.

Sections 2.3 and 2.4 review the formalism of the Hartree–Fock approximation and the density functional theory.

2.3 Hartree–Fock approximation

Taking advantage of the known electronic Hamiltonian, Hartree, Fock, and Slater in ∼1930 [7, 8, 9] attempted to solve directly the Schrödinger equation by approximating the many-body wavefunction for atoms and molecules. In principle, the true wavefunction $\Psi(\{\mathbf{x}_i\})$ for a system with N electrons should *at least* satisfy two conditions: antisymmetry and normalization. For fermionic systems, the wavefunction changes its sign upon a permutation operation

$$\hat{P}_{ij}\Psi(\mathbf{x}_1, \mathbf{x}_2, \ldots, \mathbf{x}_i, \mathbf{x}_j, \ldots, \mathbf{x}_N) = -\Psi(\mathbf{x}_1, \mathbf{x}_2, \ldots, \mathbf{x}_j, \mathbf{x}_i, \ldots, \mathbf{x}_N), \tag{2.32}$$

where $\hat{P}_{ij}$ $(i \neq j)$ is the permutation operator that swaps the coordinates between the electron i and the electron j. For $|\Psi(\{\mathbf{x}_i\})|^2$ being the probability density, Ψ must be normalized

$$\int \mathrm{d}\mathbf{x}^N |\Psi(\mathbf{x}_1, \mathbf{x}_2, \ldots, \mathbf{x}_N)|^2 = 1. \tag{2.33}$$

For any trial wavefunction $\widetilde{\Psi}(\{\mathbf{x}_i\})$ defined in a complete basis of $\Psi_j(\{\mathbf{x}_i\})$, the following variational principle is satisfied

$$E[\widetilde{\Psi}] = \langle \widetilde{\Psi} | \hat{H} | \widetilde{\Psi} \rangle \geq \mathcal{E}_0, \tag{2.34}$$

where $\widetilde{\Psi}(\{\mathbf{x}_i\})$ is a linear combination of $\Psi_j(\{\mathbf{x}_i\})$

$$\widetilde{\Psi}(\{\mathbf{x}_i\}) = \sum_j \alpha_j \Psi_j(\{\mathbf{x}_i\}). \tag{2.35}$$

Minimization of $E[\widetilde{\Psi}]$ with respect to $\widetilde{\Psi}(\{\mathbf{x}_i\})$ gives the solution to the ground-state energy and wavefunction of the system.

2.3.1 Restricted Hartree–Fock

Suppose that the system in question is a closed-shell molecule with N electrons. In the Hartree–Fock approximation, the trial wavefunction is constructed as a single determinant, later named after Slater

$$\begin{aligned}\Phi(\mathbf{x}_1, \mathbf{x}_2, \ldots, \mathbf{x}_N) &= \langle \mathbf{x}_1 \mathbf{x}_2 \ldots \mathbf{x}_N | \psi_1 \psi_2 \ldots \psi_a \ldots \psi_N \rangle \\ &= \frac{1}{\sqrt{N!}} \begin{vmatrix} \psi_1(\mathbf{x}_1) & \psi_2(\mathbf{x}_1) & \ldots & \psi_a(bx_1) & \ldots & \psi_N(\mathbf{x}_1) \\ \psi_1(\mathbf{x}_2) & \psi_2(\mathbf{x}_2) & \ldots & \psi_a(\mathbf{x}_2) & \ldots & \psi_N(\mathbf{x}_2) \\ \psi_1(\mathbf{x}_3) & \psi_2(\mathbf{x}_3) & \ldots & \psi_a(\mathbf{x}_3) & \ldots & \psi_N(\mathbf{x}_3) \\ \ldots & \ldots & \ldots & \ldots & \ldots & \ldots \\ \psi_1(\mathbf{x}_N) & \psi_2(\mathbf{x}_N) & \ldots & \psi_a(\mathbf{x}_N) & \ldots & \psi_N(\mathbf{x}_N) \end{vmatrix},\end{aligned} \tag{2.36}$$

where $\{\psi_a\}$ represent a set of orthonormal single-particle spin orbitals. Since the electronic Hamiltonian does not act on spin, the spin orbital can be simply written as a product of

the spatial orbital $\phi(\mathbf{r})$ and the spin function $\zeta(\sigma)$

$$\psi(\mathbf{r}, \sigma) = \phi(\mathbf{r})\zeta(\sigma), \tag{2.37}$$

where the value of $\zeta(\sigma)$ can be either α or β.

The factor $1/\sqrt{N!}$ along with the orthonormality of $\{\psi_a\}$ above ensures that $\Phi(\{\mathbf{x}_i\})$ is normalized. Furthermore, the determinantal form of $\Phi(\{\mathbf{x}_i\})$ satisfies the permutation symmetry, as interchanging any two rows of a determinant changes its sign.

With the explicit form of $\Phi(\{\mathbf{x}_i\})$ in Eq. (2.36), the total energy can now be expressed in terms of the set of spin orbitals

$$\begin{aligned} E &= \langle \Phi | \hat{H} | \Phi \rangle \\ &= \sum_{a=1}^{N} h_a + \frac{1}{2} \sum_{a=1}^{N} \sum_{b=1}^{N} \left([aa|bb] - [ab|ba] \right). \end{aligned} \tag{2.38}$$

Here, the shorthand notation h_a denotes the one-body integral consisting of the kinetic energy and electron–nucleus attraction

$$\begin{aligned} h_a &= \langle \psi_a | \hat{h} | \psi_a \rangle \\ &= \langle \psi_a | -\frac{\nabla^2}{2} + \hat{v}_{\text{ext}} | \psi_a \rangle, \end{aligned} \tag{2.39}$$

where the external potential is simply a scalar potential given by all the nuclei

$$v_{\text{ext}}(\mathbf{r}) = -\sum_{A}^{M} \frac{Z_A}{|\mathbf{R}_A - \mathbf{r}|}. \tag{2.40}$$

$[aa|bb]$ in Eq. (2.38) is a two-body integral of the following form

$$[aa|bb] = \int\int \frac{\psi_a^*(\mathbf{x})\psi_a(\mathbf{x})\psi_b^*(\mathbf{x}')\psi_b(\mathbf{x}')}{|\mathbf{r} - \mathbf{r}'|} \mathrm{d}\mathbf{x}\mathrm{d}\mathbf{x}'. \tag{2.41}$$

Note that the electron density $n(\mathbf{r})$ derived from $\Phi(\{\mathbf{x}_i\})$ is simply the sum over all N singly-occupied orbital density

$$n(\mathbf{r}) = \sum_{a}^{N} \sum_{\sigma} |\psi_a(\mathbf{r}\sigma)|^2. \tag{2.42}$$

The summation of all $[aa|bb]$ terms can then be written in terms of $n(\mathbf{r})$

$$\begin{aligned} E_H &= \frac{1}{2} \sum_{a=1}^{N} \sum_{b=1}^{N} [aa|bb] \\ &= \frac{1}{2} \int \int \frac{n(\mathbf{r}) n(\mathbf{r}')}{|\mathbf{r} - \mathbf{r}'|} \mathrm{d}\mathbf{r} \mathrm{d}\mathbf{r}'. \end{aligned} \tag{2.43}$$

This series of integrals add up to the classical electron density–density repulsion, which is known as the Hartree energy E_H.

The other two-body integral in Eq. (2.38), $[ab|ba]$, shares the same form as $[aa|bb]$

$$[ab|ba] = \int \int \frac{\psi_a^*(\mathbf{x}) \psi_b(\mathbf{x}) \psi_b^*(\mathbf{x}') \psi_a(\mathbf{x}')}{|\mathbf{r} - \mathbf{r}'|} \mathrm{d}\mathbf{x} \mathrm{d}\mathbf{x}'. \tag{2.44}$$

Analogous to $n(\mathbf{r})$, one can define the one-body density matrix as follows

$$\rho(\mathbf{x}, \mathbf{x}') = \sum_{a=1}^{N} \psi_a(\mathbf{x}) \psi_a^*(\mathbf{x}'). \tag{2.45}$$

The summation of all $[ab|ba]$ terms can thus be expressed by $\rho(\mathbf{x}, \mathbf{x}')$

$$\begin{aligned} E_{\mathrm{X}} &= -\frac{1}{2} \sum_{a=1}^{N} \sum_{b=1}^{N} [ab|ba] \\ &= -\frac{1}{2} \int \int \frac{\rho(\mathbf{x}, \mathbf{x}') \rho(\mathbf{x}', \mathbf{x})}{|\mathbf{r} - \mathbf{r}'|} \mathrm{d}\mathbf{x} \mathrm{d}\mathbf{x}'. \end{aligned} \tag{2.46}$$

These terms thus represent density matrix–matrix interaction, which is called the exchange

energy E_{X} stemming from the antisymmetry of the wavefunction.

The factor 1/2 above avoids double counting the classical Coulomb or exchange interaction. Note that the exchange energy has an opposite sign to the Hartree term, indicating that inclusion of exchange lowers the total energy and stabilizes the many-body electron. Furthermore, the $[aa|aa]$ term in E_H represents the interactions of an electron with itself, i.e., the *self-interaction error*. However, this error is eliminated by exactly the same $[aa|aa]$ term with an opposite sign in E_{X}. That is to say, parts of the exchange interactions are to cancel the self-interaction errors. This issue will be revisited in the topic of density functional theory.

For closed-shell systems, one can apply a restriction that two electrons of opposite spins form a pair and occupy the same spatial orbital, leading to the restricted Hartree–Fock (RHF) approach

$$\begin{aligned}\Phi^R(\mathbf{x}_1,\mathbf{x}_2,\ldots,\mathbf{x}_N) &= \langle \mathbf{x}_1\mathbf{x}_2\ldots\mathbf{x}_N|\phi_1\alpha\phi_1\beta\ldots\phi_{N_{\mathrm{occ}}}\alpha\phi_{N_{\mathrm{occ}}}\beta\rangle \\ &= \frac{1}{\sqrt{N!}}\begin{vmatrix} \phi_1(\mathbf{r}_1)\alpha & \phi_1(\mathbf{r}_1)\beta & \ldots & \ldots & \phi_{N_{\mathrm{occ}}}(\mathbf{r}_1)\alpha & \phi_{N_{\mathrm{occ}}}(\mathbf{r}_1)\beta \\ \phi_1(\mathbf{r}_2)\alpha & \phi_1(\mathbf{r}_2)\beta & \ldots & \ldots & \phi_{N_{\mathrm{occ}}}(\mathbf{r}_2)\alpha & \phi_{N_{\mathrm{occ}}}(\mathbf{r}_2)\beta \\ \phi_1(\mathbf{r}_3)\alpha & \phi_1(\mathbf{r}_3)\beta & \ldots & \ldots & \phi_{N_{\mathrm{occ}}}(\mathbf{r}_3)\alpha & \phi_{N_{\mathrm{occ}}}(\mathbf{r}_3)\beta \\ \ldots & \ldots & \ldots & \ldots & \ldots & \ldots \\ \phi_1(\mathbf{r}_N)\alpha & \phi_1(\mathbf{r}_N)\beta & \ldots & \ldots & \phi_{N_{\mathrm{occ}}}(\mathbf{r}_N)\alpha & \phi_{N_{\mathrm{occ}}}(\mathbf{r}_N)\beta \end{vmatrix}. \end{aligned} \tag{2.47}$$

Here, N_{occ} equals $N/2$ representing the number of doubly occupied spatial orbitals.

Invoking the double occupation restriction in Eq. (2.47), the one-body and two-body integrals for the total energy in Eq. (2.38) can be written in terms of the spatial orbitals

only

$$\begin{aligned} E &= \langle \Phi^R | \hat{H} | \Phi^R \rangle \\ &= \sum_{a=1}^{N_{\text{occ}}} \sum_{\sigma} h_a + \frac{1}{2} \sum_{a=1}^{N_{\text{occ}}} \sum_{b=1}^{N_{\text{occ}}} \sum_{\sigma} \sum_{\sigma'} \left([aa|bb] - [ab|ba] \right) \\ &= 2 \sum_{a=1}^{N_{\text{occ}}} h_a + \sum_{a=1}^{N_{\text{occ}}} \sum_{b=1}^{N_{\text{occ}}} \left(2[aa|bb] - [ab|ba] \right). \end{aligned} \tag{2.48}$$

Here, indices a and b represent spatial orbitals $\phi(\mathbf{r})$ only. Note that the number of terms in the exchange energy is half of that in the Hartree term. This is due to fact that the classical Coulomb repulsion is allowed between any two particle densities disregarding their spins. However, the exchange interactions exist only between two electrons of the same spin. For opposite spins, α and β, the two-body integral vanishes due to spin orthogonality

$$[ab|ba]_{\alpha\beta} = \int \int \frac{\phi_a^*(\mathbf{r}) \phi_b(\mathbf{r}) \phi_b^*(\mathbf{r}') \phi_a(\mathbf{r}')}{|\mathbf{r} - \mathbf{r}'|} \mathrm{d}\mathbf{r} \mathrm{d}\mathbf{r}' \langle \alpha | \beta \rangle \langle \beta | \alpha \rangle = 0. \tag{2.49}$$

For the systems of interest in this dissertation, doubly occupied orbitals and closed-shell electronic configuration are assumed. In the following, the singlet Hartree–Fock ground state is derived using the variational principle, and the extension to open-shell systems will be briefly commented on.

2.3.2 Hartree–Fock equations

Given that the energy expression in the restricted form of Hartree–Fock approximation (RHF) depends only on the spatial orbitals, the total energy E is then minimized with respect to $\{\phi_a\}$. Furthermore, the minimization is constrained through the following

Lagrangian

$$\mathcal{L}_{RHF} = E\left[\{\phi_a\}\right] - 2\sum_{a=1}^{N_{\rm occ}}\sum_{b=1}^{N_{\rm occ}}\varepsilon_{ab}\left(\langle\phi_a|\phi_b\rangle - \delta_{ab}\right), \tag{2.50}$$

where ε_{ab} is a Lagrange multiplier to subject the minimization to the orthonormality of $\{\phi_a\}$. Through the variational, the RHF ground state is attained at the stationary point of $\mathcal{L}_{RHF}$

$$\frac{\delta\mathcal{L}_{RHF}}{\delta\{\phi_c^*\}} = 0, \tag{2.51}$$

which results in a set of coupled eigenvalue equations known as the Hartree–Fock equations

$$\hat{h}\phi_i(\mathbf{r}) + 2\sum_{b=1}^{N_{\rm occ}}\int\frac{|\phi_b(\mathbf{r}')|^2}{|\mathbf{r}-\mathbf{r}'|}\mathrm{d}\mathbf{r}'\phi_i(\mathbf{r}) - \sum_{b=1}^{N_{\rm occ}}\int\frac{\phi_b^*(\mathbf{r}')\phi_i(\mathbf{r}')}{|\mathbf{r}-\mathbf{r}'|}\mathrm{d}\mathbf{r}'\phi_b(\mathbf{r}) = \sum_j\varepsilon_{ji}\phi_i(\mathbf{r}). \tag{2.52}$$

Here, $i, j, k, \ldots$ denote general orbitals that can be either occupied or unoccupied (explained later), while $a, b, c, \ldots$ refer to occupied orbitals only. $\hat{h}$ is the operator for the one-body term [Eq. (2.39)]. The second term in Eq. (2.52) stems from the classical Coulomb repulsion, which can be represented by a Hartree potential operator as follows

$$\begin{aligned}\hat{v}_H &= 2\sum_{b=1}^{N_{\rm occ}}\int\frac{|\phi_b(\mathbf{r}')|^2}{|\mathbf{r}-\mathbf{r}'|}\mathrm{d}\mathbf{r}' \\ &= \int\frac{n(\mathbf{r}')}{|\mathbf{r}-\mathbf{r}'|}\mathrm{d}\mathbf{r}',\end{aligned} \tag{2.53}$$

Analogously, an exchange operator $\hat{v}_{\rm x}$ can be defined for the third term based on its effect when operated on $\phi_i(\mathbf{r})$

$$\hat{v}_{\rm x}\phi_i(\mathbf{r}) = -\sum_{b=1}^{N_{\rm occ}}\int\frac{\phi_b^*(\mathbf{r}')\phi_i(\mathbf{r}')}{|\mathbf{r}-\mathbf{r}'|}\mathrm{d}\mathbf{r}'\phi_b(\mathbf{r}) \tag{2.54}$$

In a more compact form, the Hartree–Fock equations [Eq. (2.52)] can then be written as

$$\hat{f}\phi_i(\mathbf{r}) = \sum_j \varepsilon_{ji}\phi_i(\mathbf{r}), \tag{2.55}$$

where $\hat{f}$ is the Fock operator resembling the single-particle mean-field Hamiltonian

$$\hat{f} = \hat{h} + \hat{v}_H + \hat{v}_{\mathrm{x}}. \tag{2.56}$$

Here, $\hat{v}_H$ corresponds to a static local potential created by *all* the electrons. $\hat{v}_{\mathrm{x}}$ represents the nonlocal exchange interactions between the electron occupying $\phi_i(\mathbf{r})$ and all the same-spin electrons in the system. The total effective potential is the sum of the external potential and the Hartree–Fock potential $\hat{v}_{HF}$

$$\begin{aligned} \hat{v}_{\mathrm{eff}} &= \hat{v}_{\mathrm{ext}} + \hat{v}_H + \hat{v}_{\mathrm{x}} \\ &= \hat{v}_{\mathrm{ext}} + \hat{v}_{HF}. \end{aligned} \tag{2.57}$$

Solutions to $\{\phi_i\}$ give the RHF ground-state wavefunction Φ_0 and the corresponding RHF ground-state energy E_0. Note that observables like E_0 are invariant to any *unitary transformation* of the spin orbital basis. This allows the freedom for one to choose the set of orbitals that diagonalizes the Fock matrix (which is Hermitian due to imposed symmetries mentioned below). The diagonalization leads to a set of eigenvalue equations that are known as the *canonical* Hartree–Fock equations

$$\hat{f}\phi_i(\mathbf{r}) = \varepsilon_i\phi_i(\mathbf{r}), \tag{2.58}$$

where ε_i can be interpreted as the energy associated with an electron occupying the orbital $\phi_i(\mathbf{r})$ and moving in an effective field.

The derivations above show that using a single Slater determinant as an approximation to the many-body wavefunction, the search of the ground state is reduced to solving the restricted Hartree–Fock equations. The restrcited form of the Slater determinant enforces time-reversal and spin-rotation symmetries.[10, 11] As a result, the RHF ground-state Φ_0 requires solutions to the spatial orbitals only.

Note that the $\hat{v}_H$ and $\hat{v}_\mathrm{x}$ operators in Eq. (2.58) depend on the set of orbitals in question, making the eigenvalue equations non-linear. The explicit form of $\phi(\mathbf{r})$ is still unknown. As mentioned in Section 2.2, a single-particle orbital $\phi_a(\mathbf{r})$ can be expanded in terms of basis functions χ, either atomic orbitals or plane waves, with a set of coefficients $\{c_{\mu a}\}$. The index μ sums over all N_a basis functions, which in fact determine the dimension of the electronic Hilbert space in question ($N_a > N_\mathrm{occ}$). In practice, the total energy E needs to be converged with respect to N_a.

The self-consistent iteration is initialized by a set of coefficients $\{c^0_{\mu a}\}$ for the trial occupied orbitals $\{\phi^0_a\}$, leading to an initial guess for the Hartree–Fock potential $\hat{v}^0_{HF}$. The initial Fock matrix element F^0_{ab} reads

$$\begin{aligned} F^0_{ab} &= \langle\phi_a|\hat{f}^0|\phi_b\rangle \\ &= \sum_\mu \sum_\nu c^*_{\mu i} c_{\nu j} \langle\chi_\mu|\hat{f}^0|\chi_\nu\rangle \\ &= \sum_\mu \sum_\nu c^*_{\mu a} f^0_{\mu\nu} c_{\nu b}. \end{aligned} \tag{2.59}$$

With spin-rotation and time-reversal symmetries imposed in derivation, the Fock matrix is Hermitian by construction. Further, the Fock matrix $\underset{\sim}{F}^0$ can be written as a matrix product

$$\underset{\sim}{F}^0 = \underset{\sim}{C}^\dagger \underset{\sim}{F}^{\prime 0} \underset{\sim}{C}, \tag{2.60}$$

where $\underset{\sim}{F}^{\prime 0}$ is the Fock matrix in the atomic or plane-wave basis, and $\underset{\sim}{C}$ denotes the

coefficient matrix.

The right-hand side of Eq. (2.58) with a bra state $\langle\phi_a|$ is derived as

$$\begin{aligned}\langle\phi_a|\varepsilon_b|\phi_b\rangle &= \sum_\mu \sum_\nu c^*_{\mu a} c_{\nu b} \varepsilon_b \langle\chi_\mu|\chi_\nu\rangle \\ &= \sum_\mu \sum_\nu c^*_{\mu a} S_{\mu\nu} c_{\nu b} \varepsilon_b.\end{aligned} \tag{2.61}$$

The equivalence of Eqs. (2.59) and (2.61) gives the matrix (product) form of the canonical Hartree–Fock equations

$$\underset{\sim}{F}'^0 \underset{\sim}{C} = \underset{\sim}{S}\underset{\sim}{C}\underset{\sim}{\varepsilon}, \tag{2.62}$$

where $\underset{\sim}{S}$ represents the overlap matrix of the basis functions, and $\underset{\sim}{\varepsilon}$ is a diagonal matrix of the eigenvalues. With the expansion in atomic basis sets, the set of coupled equations in Eq. (2.62) are also known as Roothaan equations,[12] providing a numerical solution to molecular orbitals.

Note that, although only N_{occ} orbitals are being sought, solutions to Eq. (2.62) give more than N_{occ} canonical orbitals, say N_a, which conserves the dimension of the Hilbert space. A simple example is the simultaneous formation of bonding and antibonding orbitals from linear combinations of two atomic orbitals. There are also N_a corresponding ε_i that can be ranked in the following order

$$\varepsilon_1 \leq \varepsilon_2 \leq \cdots \leq \varepsilon_a \leq \cdots \leq \varepsilon_{N/2} < \varepsilon_{(N/2+1)} \leq \cdots \leq \varepsilon_r \leq \cdots \leq \varepsilon_{N_a}. \tag{2.63}$$

From this ranking, the lowest N_{occ} orbitals are considered occupied, and the rest are unoccupied or virtual orbitals (denoted by $r, s, t, \dots$). For molecules, the $N^{\text{th}}_{\text{occ}}$ orbital is denoted the highest occupied molecular orbital (HOMO), and the $(N_{\text{occ}}+1)^{\text{th}}$ one is called the lowest unoccupied molecular orbital (LUMO); the energy difference between

these two states is the so-called HOMO/LUMO gap

$$E_{\mathrm{g}} = \varepsilon_{\mathrm{L}} - \varepsilon_{\mathrm{H}}. \tag{2.64}$$

The identified N_{occ} occupied orbitals above correspond to a new set of coefficients $\{c^1_{\nu i}\}$ and an updated $\hat{v}^1_{HF}$, which enter Eq. (2.59) for the next iteration. This procedure is called "self-consistent field" since the iteration ends when the potential field $\hat{v}_{HF}$ reaches self-consistence, i.e., the set of orbitals that creates $\hat{v}_{HF}$ produces the same set of orbitals after solving Eq. (2.62). In practice, the self-consistency can also be determined by comparing the change of the energy ($\Delta E = E^n - E^{n-1}$) with a predefined convergence threshold.

For open-shell systems where the number of α electrons different from that of β, the Hartree–Fock equations are separated into two sets with orbitals of the same spin function

$$\underset{\sim}{F}^{\prime\alpha}\underset{\sim}{C}^{\alpha} = \underset{\sim}{S}\underset{\sim}{C}^{\alpha}\underset{\sim}{\varepsilon}^{\alpha}, \tag{2.65}$$

and

$$\underset{\sim}{F}^{\prime\beta}\underset{\sim}{C}^{\beta} = \underset{\sim}{S}\underset{\sim}{C}^{\beta}\underset{\sim}{\varepsilon}^{\beta}. \tag{2.66}$$

Here, the Fock operators $\hat{f}^{\alpha}$ and $\hat{f}^{\beta}$ are spin-dependent because the exchange term $\hat{v}_{\mathrm{x}}$ contains contributions from orbitals of the same spin only.

For the pairs of electrons with opposite spins in an open-shell system, they are still allowed to have the same spatial orbital in construction. While for unpaired electrons with the same spin, distinct spatial orbitals are required. This hybrid treatment of paired and unpaired electrons lead to the restricted open-shell Hartree–Fock (ROHF) approach.[13] However, two electrons with opposite spins do not necessarily occupy the same spatial orbital, and the double occupation can thus be uplifted. This construction corresponds

to the *unrestricted* Hartree–Fock (UHF) method[14] that applies in principle to both closed-shell and open-shell systems.

To sum up, the Hartree–Fock approximation attempts to solve the many-body Schrödinger equation by using a single Slater determinant as an approximation to the many-body wavefunction, and the approximated solution is limited to the ground state only depending on the nature of the variational principle. Ultimately, the many-body problem is broken down to solving a set of Hartree–Fock equations for N_{occ} "optimal" single-particle orbitals through, e.g., the SCF-LCAO-MO approach. The convoluted electronic problems have been simplified to a huge extent, allowing practical applications to atoms and, most importantly, polyatomic molecules. However, the Hartree–Fock method suffers from the lack of dynamical electron–electron correlation effects, especially for electrons of opposite spins.

The correlation among electronic motions is supposed to be captured by the many-body wavefunction, which is however oversimplified as a single determinant in the Hartree–Fock approach. Particularly, the electron–electron interactions derived from the Hartree–Fock approximation differ from the classical Coulomb repulsion by simply the exchange interactions, which stems from the antisymmetry of the Slater determinant. Although the exchange interactions can be considered as a special type of "correlation" between electrons of the same spin, a lot of other dynamical effects are still missing.

The deficiency of the Hartree–Fock approximation defines the correlation energy E_{corr}

$$E_{\text{corr}} = \mathcal{E}_0 - E_0, \tag{2.67}$$

where $\mathcal{E}_0$ is the exact ground-state energy, while E_0 is instead the minimized energy in Hartree–Fock. Quantitative description of E_{corr} becomes a new pursuit for the community following the wavefunction approximation. Post Hartree–Fock methods for solving the

correlation problem mainly include configuration interaction (CI),[15, 16, 17, 18] coupled-cluster (CC),[19, 20, 21, 22, 23] and Moller–Plesset related perturbation theory.[24, 25, 26, 27, 28, 29, 30] Readers with particular interest are recommended to consult the references indicated above. However, this dissertation will not extend to the discussion of these methods. Instead, Section 2.6 introduces an alternative formalism for capturing correlation interactions in the context of single-particle excitations.

Section 2.4 discusses the reformulation of the many-electron problem in the framework of density functional theory. Despite the change of topic, many equations derived in this section are indeed universal and applicable in other mean-field approaches.

2.4 Density functional theory

The Hartree–Fock approximation introduced in Section 2.3 set up the basis for wavefunction approaches. The idea is to solve the many-body wavefunction in the form of determinants and obtain all the information and properties of a system. The wavefunction methods are known for their accuracy but are practically limited to small systems, since the size and dimension of the wavefunction scales rapidly (as high as e^N) with the system's size. Finding an alternative basic variable to replace the wavefunction in formulating the many-body problem is in necessity for tackling systems where a massive number of electrons are present.

2.4.1 Early density functional model

The electron density $n(\mathbf{r})$, depending on three variables only, appears to be an appropriate choice for reformulating properties such as the total electronic energy

$$E[n] = \int \bar{\epsilon}(\mathbf{r}) n(\mathbf{r}) \mathrm{d}\mathbf{r}, \tag{2.68}$$

where $\bar{\epsilon}(\mathbf{r})$ denotes the average energy per electron within the unit volume d$\mathbf{r}$. As introduced in Section 2.1, the total energy in question should contain the kinetic energy, electron–nucleus attraction, and electron–electron interaction. The expression for the electron–nucleus term is straightforward upon the Born–Oppenheimer approximation

$$E_{en}[n] = \int v_{\text{ext}}(\mathbf{r}) n(\mathbf{r}) \mathrm{d}\mathbf{r}. \tag{2.69}$$

And the expression for the classical Coulomb repulsion, the Hartree energy, is also explicit

$$E_H[n] = \frac{1}{2} \int \int \frac{n(\mathbf{r}) n(\mathbf{r}')}{|\mathbf{r} - \mathbf{r}'|} \mathrm{d}\mathbf{r} \mathrm{d}\mathbf{r}'. \tag{2.70}$$

The kinetic part and the non-classical quantum effects are still missing to finalize the expression for the full energy functional.

The exploration of kinetic energy functional for many-electron systems can date back to 1920s by Thomas and Fermi,[31, 32] who assumed that the energy of the homogeneous electron gas depends only on the distribution of electrons – the electron density. For inhomogeneous electron gas such as atoms, the major problem tackled in the Thomas–Fermi (TF) model was the kinetic energy functional, which reads

$$T_{TF}[n] = C_F \int n^{5/3}(\mathbf{r}) \mathrm{d}\mathbf{r}. \tag{2.71}$$

Here, $C_F = 2.871$ is a constant. This expression is derived based on the local density approximation, which assumes that an inhomogeneous electron gas can be divided into many small volume elements d$\mathbf{r}$. In each d$\mathbf{r}$, the electrons are distributed *uniformly* and follow locally from the properties of a homogeneous electron gas. Neglecting the quantum effects from electron–electron interactions, all the energy terms can now be

written explicitly as a functional of $n(\mathbf{r})$, leading to the TF energy functional

$$\begin{aligned} E_{TF}[n] &= C_F \int n^{5/3}(\mathbf{r})\mathrm{d}\mathbf{r} + \int v_{\text{ext}}(\mathbf{r})n(\mathbf{r})\mathrm{d}\mathbf{r} + \frac{1}{2}\int\int \frac{n(\mathbf{r})n(\mathbf{r}')}{|\mathbf{r}-\mathbf{r}'|}\mathrm{d}\mathbf{r}\mathrm{d}\mathbf{r}' \\ &= T_{TF}[n] + E_{en}[n] + E_H[n]. \end{aligned} \tag{2.72}$$

To search for the ground state, one can construct a Lagrangian to minimize E_{TF} with the constraint of $n(\mathbf{r})$ being integrated to the number of electrons N

$$\mathcal{L}_{TF}[n] = E_{TF}[n] - \mu_{TF}\left(\int n(\mathbf{r})\mathrm{d}\mathbf{r} - N\right), \tag{2.73}$$

where μ_{TF} is the Lagrangian multiplier. The variation of $\mathcal{L}_{TF}$ with respect to $n(\mathbf{r})$ at the stationary point satisfies

$$\frac{\delta\mathcal{L}_{TF}[n]}{\delta n(\mathbf{r})} = 0, \tag{2.74}$$

which further leads to the Thomas–Fermi equation

$$\begin{aligned} \mu_{TF} &= \frac{\delta E_{TF}[n]}{\delta n(\mathbf{r})} \\ &= \frac{5}{3}C_F n^{2/3}(\mathbf{r}) + v_{\text{ext}}(\mathbf{r}) + \int \mathrm{d}\mathbf{r}'\frac{n(\mathbf{r}')}{|\mathbf{r}-\mathbf{r}'|}. \end{aligned} \tag{2.75}$$

The Thomas–Fermi ground-state density is obtained by solving Eq. (2.75) with the constraint in Eq. (2.73), and the ground-state energy is calculated by inserting the resulting density in Eq. (2.72).

The TF model remarkably reduced the computational complexity by formulating the energy in terms of the density, and can be applied to atoms, molecules, and solids. However, this model did not guarantee any accuracy for chemical properties. First, it was not a fully quantum-mechanical model since it did not consider the electron quantum effects, later known as the exchange and correlation interactions. Second, the kinetic

energy functional is shown oversimplified by the local density approximation. Most importantly, it was not proved whether the ground-state energy is truly a functional of the density or not, although the construction of energy functional in Eq. (2.68) is intuitive. This fundamental question was answered by Hohenberg and Kohn in 1964,[33] establishing the modern density functional theory. Based on this theoretical foundation, Kohn and Sham further proposed an exact mapping approach[34] to solve the ground state in practice.

2.4.2 Hohenberg–Kohn theorems

In 1964, Hohenberg and Kohn (HK) addressed the concern about whether the ground-state energy $\mathcal{E}_0$ can be expressed as a functional of the ground-state $n_0(\mathbf{r})$.[33] This is proved in their first Hobenberg–Kohn theorem, which states that a quantum many-body system is fully defined by its groun-state electron density.

In principle, all the information of a quantum many-body system can be obtained by solving the Schrödinger equation, where the external potential $\hat{V}_{\text{ext}}$ in the Hamiltonian uniquely determines the system. Hohenberg and Kohn demonstrated that there exists a one-to-one correspondence between $\hat{V}_{\text{ext}}$ [equivalent to $v_{\text{ext}}(\mathbf{r})$] and the ground state density $n_0(\mathbf{r})$. That is to say, $n_0(\mathbf{r})$ can be used as the basic variable to define a system, since knowing $n_0(\mathbf{r})$ is equivalent to knowing $\hat{V}_{\text{ext}}$ and then all the other properties (see Figure 2.1), including the ground-state wavefunction $\Psi_0(\{\mathbf{x}_i\})$. One can immediately show the $\mathcal{E}_0$ is functional of $n_0(\mathbf{r})$

$$\mathcal{E}_0 = \langle \Psi_0[n_0] | \hat{H} | \Psi_0[n_0] \rangle = E[n_0] \tag{2.76}$$

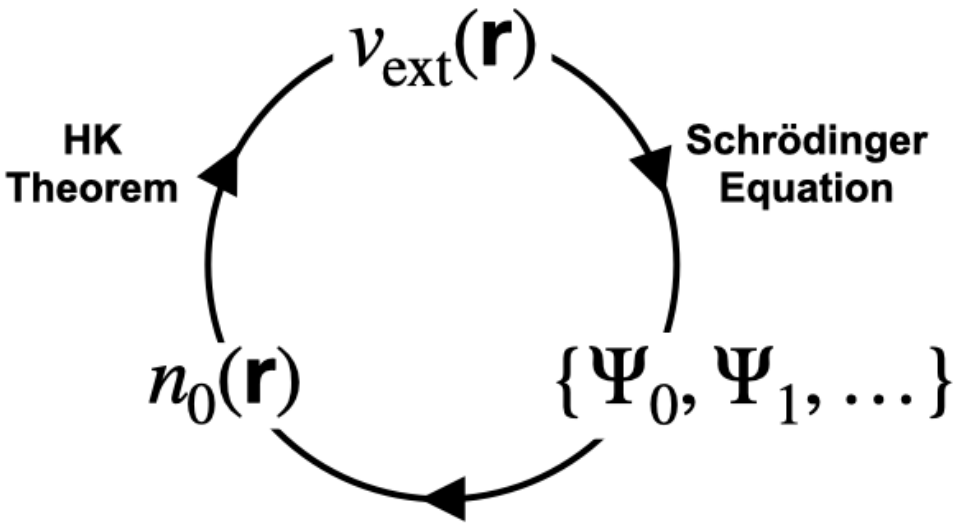

Figure 2.1: Schematic representation of the one-to-one correspondence between v_{ext} and $n_0(\mathbf{r})$. The system is uniquely determined by v_{ext} (and N), with which one can (in principle) solve the Schrödinger equation for all the many-body eigenstates. The ground-state wavefunction Ψ_0 gives the ground-state electron density $n_0(\mathbf{r})$. Hohenberg and Kohn proved that the v_{ext} is uniquely determined by $n_0(\mathbf{r})$, which closes the loop.

The first HK theorem above justified the expression of ground-state energy as a functional of the ground-state density. The second HK theorem then provided the variational principle for finding the ground state energy and density through minimizing the following energy functional

$$\mathcal{E}_0 = \min_n E[n], \tag{2.77}$$

where the energy functional $E[n]$ reads

$$\begin{aligned} E[n] &= \langle \Psi[n] | \hat{H} | \Psi[n] \rangle \\ &= F_{HK}[n] + \int v_{\text{ext}}(\mathbf{r}) n(\mathbf{r}) \mathrm{d}\mathbf{r}. \end{aligned} \tag{2.78}$$

Here, the HK functional $F_{HK}[n]$ is defined as

$$\begin{aligned} F_{HK}[n] &= \langle \Psi[n] | \hat{T} + \hat{V}_{ee} | \Psi[n] \rangle \\ &= T[n] + E_{ee}[n], \end{aligned} \tag{2.79}$$

which is a functional for the kinetic energy $T[n]$ and the electron interaction energy $E_{ee}[n]$. $F_{HK}[n]$ is a universal functional that applies to all systems, while the external field functional in Eq. (2.78) is system-dependent.

For details about proving the two HK theorems above, please refer to Refs. 35, 36, 37.

Note that the HK functional $F_{HK}[n]$ is defined only for v-representable density $n(\mathbf{r})$, i.e., $n(\mathbf{r})$ is not arbitrary and must be the ground-state density of some external potential $v_{\text{ext}}(\mathbf{r})$. In other words, the minimization of $E[n]$ in Eq. (2.78) can be performed only discretely on the set of v-representable $n(\mathbf{r})$. This limitation causes troubles in processing $E[n]$ mathematically due to the constraint of v-representability for $n(\mathbf{r})$. Such a set of densities is not known *a priori*. Furthermore, for an arbitrary "well-behaved" $n(\mathbf{r})$ – smooth and non-negative, there is no clear criterium to determine whether it is v-representable or not.

2.4.3 Levy–Lieb constrained search

The limitation of v-representability was uplifted by the work of Levy and Lieb [38, 39, 40] around the year 1980. The input density is extended to all N-representable $n(\mathbf{r})$ following the normalization condition

$$\int n(\mathbf{r}) \mathrm{d}\mathbf{r} = N. \tag{2.80}$$

Here, $n(\mathbf{r})$ is a non-negative density that integrate to the number of electrons N in the system.

The extension to N-representability is rationalized by a two-step constrained search for the ground-state energy, starting with the following

$$\mathcal{E}_0 = \inf_{\Psi} \langle \Psi | \hat{T} + \hat{V}_{ee} + \hat{V}_{\text{ext}} | \Psi \rangle \,, \tag{2.81}$$

which searches over all antisymmetric and normalized many-body wavefunction $\Psi(\{\mathbf{x}\})$. All these wavefunctions have a corresponding density generated from

$$n(\mathbf{r}) = N \int \mathrm{d}\sigma \mathrm{d}\mathbf{x}_2 \mathrm{d}\mathbf{x}_3 \ldots \mathrm{d}\mathbf{x}_N |\Psi(\mathbf{r}\sigma, \mathbf{x}_2, \mathbf{x}_3, \ldots, \mathbf{x}_N)|^2. \tag{2.82}$$

$\Psi(\{\mathbf{x}_i\})$ can be categorized by the density they produce, i.e., $\Psi(\{\mathbf{x}_i\})$ that gives the same $n(\mathbf{r})$ is grouped together. For any given $n(\mathbf{r})$, the search of the infimum is constrained to the corresponding set of $\Psi(\{\mathbf{x}_i\})$

$$\mathcal{E}_0 = \inf_{n} \left[\inf_{\Psi \to n} \langle \Psi | \hat{T} + \hat{V}_{ee} \rangle + \int v_{\text{ext}}(\mathbf{r}) n(\mathbf{r}) \mathrm{d}\mathbf{r} \right]. \tag{2.83}$$

The exhaustion of all possible $n(\mathbf{r})$ then guarantees the constrained search leads to the correct ground state, since such a two-step constrained search is equivalent to that in Eq. (2.81). The LL universal functional is defined from Eq. (2.83) as

$$F_{LL}[n] = \inf_{\Psi \to n} \langle \Psi | \hat{T} + \hat{V}_{ee} | \Psi \rangle \,, \tag{2.84}$$

in which the infimum is searched over all $\Psi(\{\mathbf{x}_i\})$ that (i) are antisymmetric, (ii) integrate to N electrons, (iii) and produce the same prescribed density $n(\mathbf{r})$ ($\Psi \to n$). The resulting

Levy-Lieb energy functional reads

$$E[n] = F_{LL}[n] + \int v_{\text{ext}}(\mathbf{r}) n(\mathbf{r}) \mathrm{d}\mathbf{r}. \tag{2.85}$$

Here, the densities being searched over just need to be N-representable. For any v-representable $n(\mathbf{r})$ entering F_{LL}, F_{LL} will be the same as F_{HK}. Therefore, the LL universal functional is an extension of the HK universal functional.

In summary, the many-body problem has been reformulated by Hohenberg and Kohn using the three-dimensional ground state electron density $n(\mathbf{r})$ as the basic variable. The ground state energy $\mathcal{E}_0$ of a quantum many-body system has been proven to be a functional of $n(\mathbf{r})$. $\mathcal{E}_0$ can be determined by minimizing the HK energy functional with respect to all v-representable densities only. Levy and Lieb then solved the v-representability problem and extended the search to all N-representable densities.

Although the theoretical foundation has been set up for using density functional theory to find the exact ground state energy and density. However, the explicit form of the exact F_{LL} or F_{HK} is not provided. Therefore, more information and even approximations are needed in order to search for the ground state in practice. In addition, the Thomas–Fermi model provides an explicit but crude approximation to the universal functional for solving the problem, where the kinetic energy functional is approximated as $T_{TF}[n]$ using the homogeneous electron gas model, and the electron interaction energy takes the classical Coulomb repulsions $E_H[n]$ only. Although these approximations do not guarantee high accuracy, they are informative for constructing explicit kinetic energy functionals and electron–electron interaction functionals. A systematic way to improve the description for the kinetic energy and the electron interaction energy was proposed by Kohn and Sham in 1965.[34]

2.4.4 Kohn–Sham approach to DFT

Kohn and Sham addressed the concerns about the universal functionals,[34] leading to the Kohn–Sham approach in the density functional theory (KS-DFT). The novelty distinguishing KS-DFT from the previous work[31, 32, 41] is the mapping of an interacting many-electron system onto an auxiliary system with non-interacting fictitious particles. The mapping offers the exact solution to the ground-state energy $\mathcal{E}_0$ and density $n_0(\mathbf{r})$ by solving the ground state of this auxiliary KS system. The particles in this system are non-interacting in the sense that they are moving independently in an effective field mimicking the *average* effects created by real interacting electrons.

In a KS auxiliary system, each particle is represented by a single-particle orbital $\phi_i(\mathbf{r})$. The system is assumed closed shell and $\phi_i(\mathbf{r})$ is doubly occupied. The following Kohn–Sham eigenvalue equations are satisfied,

$$\hat{h}^{ks}\phi_i(\mathbf{r}) = \varepsilon_i\phi_i(\mathbf{r}), \tag{2.86}$$

where the KS Hamiltonian reads

$$\hat{h}^{ks} = -\frac{\nabla^2}{2} + v_{ks}(\mathbf{r}). \tag{2.87}$$

Here, $v_{ks}(\mathbf{r})$ is the Kohn–Sham potential that depends on the system.

The N-particle Hamiltonian for the KS non-interacting system is simply given by the sum of $\hat{h}^{ks}$ for each particle j

$$\begin{aligned}\hat{H}^{ks} &= \sum_j^N \hat{h}^{ks}(j) \\ &= \sum_j^N \hat{T}_j + \sum_j^N v_{ks}(\mathbf{r}_j),\end{aligned} \tag{2.88}$$

where $\hat{T}_j$ is the Laplace operator in Eq. (2.87). To enforce antisymmetry and the normalization condition, the N-particle wavefunction $\Phi(\{\mathbf{r}_i\})$ is simply a single Slater determinant constructed by $\{\phi_i\}$. It can be shown that $\Phi(\{\mathbf{r}_i\})$ is the eigenstate of $\hat{H}^{ks}$ by construction. The particle density $n(\mathbf{r})$ is given by the sum over all single-particle states

$$n(\mathbf{r}) = 2\sum_{i}^{N_{\text{occ}}} |\phi_i(\mathbf{r})|^2. \tag{2.89}$$

In this auxiliary system, it can be shown that the first Hohenberg–Kohn theorem applies to $n(\mathbf{r})$, $\hat{H}^{ks}$ and its eigenstate $\Phi_0(\{\mathbf{r}_i\})$: the ground state KS density $n_0(\mathbf{r})$ uniquely determines $\hat{H}^{ks}$ and the ground state determinant $\Phi_0(\{\mathbf{r}_i\})$. Noticing that $\hat{H}^{ks}$ is defined by $v_{ks}(\mathbf{r})$, one can conclude that there exist a one-to-one correspondence between $n(\mathbf{r})$ and $v_{ks}(\mathbf{r})$. The exact mapping for the ground state of the non-interacting system onto that of the real many-body system depends on the choice of $v_{ks}(\mathbf{r})$, which needs to provide the exact ground state energy by construction.

To investigate the condition for the exact mapping, it is necessary to analyze the energy functional of the KS auxiliary system. The ground state kinetic energy of the KS system follows that

$$T_{ks}[\Phi_0] = 2\sum_{i}^{N} \langle\phi_i| - \frac{\nabla^2}{2}|\phi_i\rangle\,. \tag{2.90}$$

Since $\Phi_0(\{\mathbf{r}_i\})$ is uniquely determined by $n_0(\mathbf{r})$, T_{ks} is thus an implicit functional of $n_0(\mathbf{r})$

$$T_{ks}[\Phi_0] = T_{ks}[n_0]. \tag{2.91}$$

There exist an effective particle interaction energy for the KS non-interacting system in order to complete the mapping. The particle interaction energy mimics the electron–electron interactions in the real quantum many-body system, and the functional can be

divided into two terms as

$$\begin{aligned} E_{\mathrm{ee}}^{ks}[n] &= E_H[n] + E_{\mathrm{xc}}[n] \\ &= \frac{1}{2}\int\int \frac{n(\mathbf{r})n(\mathbf{r}')}{|\mathbf{r}-\mathbf{r}'|} + E_{\mathrm{xc}}[n], \end{aligned} \tag{2.92}$$

where the two contributions correspond to the Hartree energy $E_H[n]$ and the exchange–correlation (XC) energy $E_{\mathrm{xc}}[n]$. The former is an explicit functional of $n(\mathbf{r})$ accounting for classical Coulomb repulsions. The latter is an functional of $n(\mathbf{r})$ by construction, the meaning of which is explained below.

Combing the external field interaction term with T_{ks} and E_{ee}^{ks} gives the total energy functional of the KS system,

$$E_{ks}[n] = T_{ks}[n] + E_H[n] + E_{\mathrm{xc}}[n] + \int v_{\mathrm{ext}}(\mathbf{r})n(\mathbf{r})\mathrm{d}\mathbf{r}. \tag{2.93}$$

To have the following equality

$$T_{ks}[n] + V_H[n] + E_{\mathrm{xc}}[n] = F_{HK}[n], \tag{2.94}$$

the XC energy functional must be constructed in the following way

$$\begin{aligned} E_{\mathrm{xc}}[n] &= F_{HK}[n] - T_{ks}[n] - E_H[n] \\ &= T[n] - T_{ks}[n] + E_{ee}[n] - E_H[n]. \end{aligned} \tag{2.95}$$

In other words, the XC energy functional constructed in KS-DFT is to correct the non-interacting kinetic energy and capture the non-classical quantum effects of electron–electron interactions beyond the Hartree energy. $E_{\mathrm{xc}}[n]$ is the key quantity that completes the map of the ground state energy between the KS auxiliary system and the real many-body quantum system.

Assuming that $E_{\mathrm{xc}}[n]$ is known at this point, the ground-state energy and density can be determined by minimizing $E_{ks}[n]$ in Eq. (2.93) with respect to $n(\mathbf{r})$

$$E_{ks}[n] = \min_{n} \left\{ T_{ks}[n] + E_H[n] + E_{\mathrm{xc}}[n] + \int v_{\mathrm{ext}}(\mathbf{r}) n(\mathbf{r}) \mathrm{d}\mathbf{r} \right\}. \tag{2.96}$$

Here, the N-representable $n(\mathbf{r})$ suffices for minimization following from the Levy and Lieb's two-step constrained search. Given that the expression for $T_{ks}[n]$ is written explicitly using the single-particle orbitals, it is more convenient to express the rest in terms of $\{\phi_i\}$ via Eq. (2.89). And the variation of $E_{ks}[n]$ can then be done with respect to $\{\phi_i\}$. A constrained minimization of $E_{ks}[\{\phi_i\}]$ is performed through constructing a Lagrangian as described in Section 2.3, which ends up with the Kohn–Sham equations in Eq. (2.86) shown at the beginning of this section.

The effective potential $v_{ks}(\mathbf{r})$ in Eq. (2.87) is a mean-field potential consisting of the following terms

$$\begin{aligned} v_{ks}(\mathbf{r}) &= \frac{\delta E_{en}[n]}{\delta n(\mathbf{r})} + \frac{\delta E_H[n]}{\delta n(\mathbf{r})} + \frac{\delta E_{\mathrm{xc}}[n]}{\delta n(\mathbf{r})} \\ &= v_{\mathrm{ext}}(\mathbf{r}) + \int \frac{n(\mathbf{r}')}{|\mathbf{r} - \mathbf{r}'|} \mathrm{d}\mathbf{r}' + v_{\mathrm{xc}}(\mathbf{r}) \\ &= v_{\mathrm{ext}}(\mathbf{r}) + v_H(\mathbf{r}) + v_{\mathrm{xc}}(\mathbf{r}). \end{aligned} \tag{2.97}$$

Analogous to the Hartree–Fock equations, the Kohn–Sham equations are coupled and non-linear, which need to be solved self-consistently with $\{\phi_i\}$ expanded in terms of basis functions, either atomic orbitals for molecules or plane waves for periodic systems. The XC potential $v_{\mathrm{xc}}(\mathbf{r})$ is a key component that dictates the success of mapping. While the exact XC functional is practically intractable, numerous efforts have been devoted to approximating it, as briefly introduced below.

2.4.5 Exchange–Correlation functionals

As mentioned above, $E_{\mathrm{xc}}[n]$ governs the success in mapping a many-electron interacting system onto a non-interacting fictitious system. Whether the exact ground state energy and density can be reproduced or not depends on the choice of $E_{\mathrm{xc}}[n]$. Although an exact and universal E_{xc} should exist, approximations are inevitable. The accuracy of DFT calculations depends strongly on the quality of the XC functional, as shown in the Jacob's ladder[42] in Figure 2.2. A brief explanation is provided for each level of the ladder below. Detailed evaluations and references of different functionals can be found in Ref. 43, but will not provided here in this topic.

The lowest level of the Jacob's ladder is the Hartree approach, where only classical Coulomb repulsion is included with no exchange or correlation interaction. In the local (spin) density approximation (LDA), the exchange and correlation interactions are introduced as a functional of the density only, and the XC potential $v_{\mathrm{xc}}(\mathbf{r})$ are based on the density at a space point $\mathbf{r}$ where the local density is assumed uniform. The density gradient (∇n) is then added as a new variable together with $n(\mathbf{r})$, leading to the generalized gradient approximation (GGA). The DFT calculations done in this dissertation employ the GGA functional, particularly the PBE functional. meta-GGA further includes the second gradient of $n(\mathbf{r})$ ($\nabla^2 n$) and the kinetic energy density as the functional variables.

In hyper/hybrid-GGA, the nonlocal exchange interaction, analogous to the exchange operator defined in the Hartree–Fock approximation, is combined with local/semilocal GGA functionals, leading to the so-called hybrid functionals. The nonlocal exchange involves the one-body density matrix, which is beyond the density argument and leads to a generalized Kohn–Sham approach in KS-DFT (GKS-DFT). Including the nonlocal exchange can mitigate the self-interaction errors found in local/semilocal functionals, improving significantly the prediction of energy gap. More importantly, the inclusion

of nonlocal exchange provides a correct asymptotic behavior describing the decay of electron–electron interactions. In most local/semilocal XC functionals, the tail of the interacting potential decays nearly exponentially, which is too rapid. The introduction of nonlocal exchange corrects the decaying behavior to $1/r$ in the long range. The highest level in Figure 2.2 is the state-of-the-art method within the KS- and GKS-DFT framework. The random phase approximation (RPA) is meant to evaluate the dynamical response of the density to a perturbation. RPA is able to capture the screening effects as an important class of electron correlation.

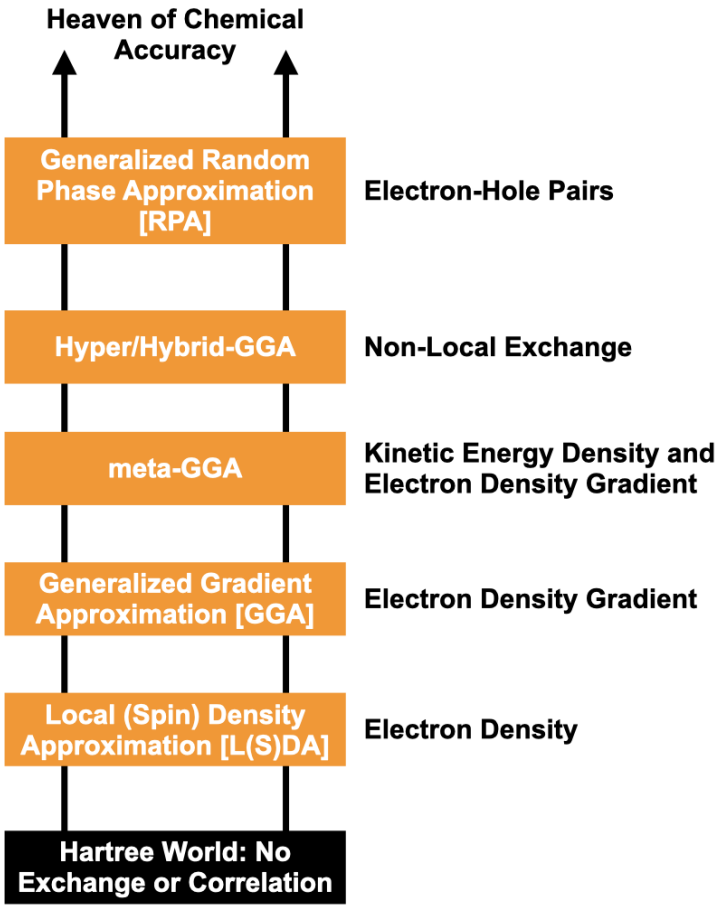

Figure 2.2: Evolution of density functionals toward the heaven of chemical accuracy. The texts on the right denote the new variable introduced at the corresponding level with respect to the lower one. This figure is adapted from Ref. 43.

For more in-depth discussions in DFT, readers are recommended to Refs. 35 and Refs. 36. In Section 2.5, I will discuss the interpretation of eigenvalues from mean-field calculations and their failures in describing excited-state properties.

2.5 Excited-state properties: interpretation and failure

2.5.1 Photoemission and charged excitations

The explorations of electronic structure of atoms can be traced back to the discovery of the photoelectric effect and the line spectrum of atomic emission. The latter has been successfully rationalized by Niels Bohr, who postulated that the energy of an electron is quantized into discrete levels, and the atomic line spectrum stems from the transitions between energy levels. Despite the fact that Bohr's explanations were incorrect, it paved the way for the electron orbital treatment and the interpretation of orbital energy in electronic structure calculations.

The photoelectric phenomenon has also evolved into photoemission spectroscopic techniques for measuring the energetics associated with charged excitations, i.e., electron and hole injections. For molecules, the energy required to remove an electron (inject a hole) is called the ionization potential (IP); the addition of an electron to a bound state causes stabilization in energy, and this change in energy is defined as the electron affinity (EA). For solids, the measurements of hole and electron injections probe respectively the valence and the conduction band structures. Photoemission spectroscopy has become a powerful tool to explore single-particle energy levels, provdining insights into the electronic structure of matter.

The direct and inverse photoemission spectroscopies (PES) for measuring the energetics associated with hole or electron injections are schematically depicted in Figure 2.3. The

density of states are plotted in terms of single-particle energy levels, where the Fermi energy E_F separates the occupied states (valence band) from the unoccupied ones (conduction band). The vacuum level sets the border between bound and unbound states, beyond which an electron becomes a free particle with a detectable kinetic energy E_{kin}.

In direct PES, a beam of photons with energy $h\nu$ shines on the sample (which can be gaseous atoms and molecules, liquid droplets, or solid-state materials) and ejects electrons, whose kinetic energy is subsequently measured by the detector. In inverse PES, electrons with a kinetic energy E_{kin} are first injected into the continuum states of the sample and then jump to a bound state (if available) by emitting photons; the detector measures the photon energy $h\nu$. The IP and EA can then be derived based on the collected E_{kin} or $h\nu$

$$\text{IP}_a = h\nu - E_{\text{kin}}, \tag{2.98}$$

$$\text{EA}_r = E_{\text{kin}} - h\nu. \tag{2.99}$$

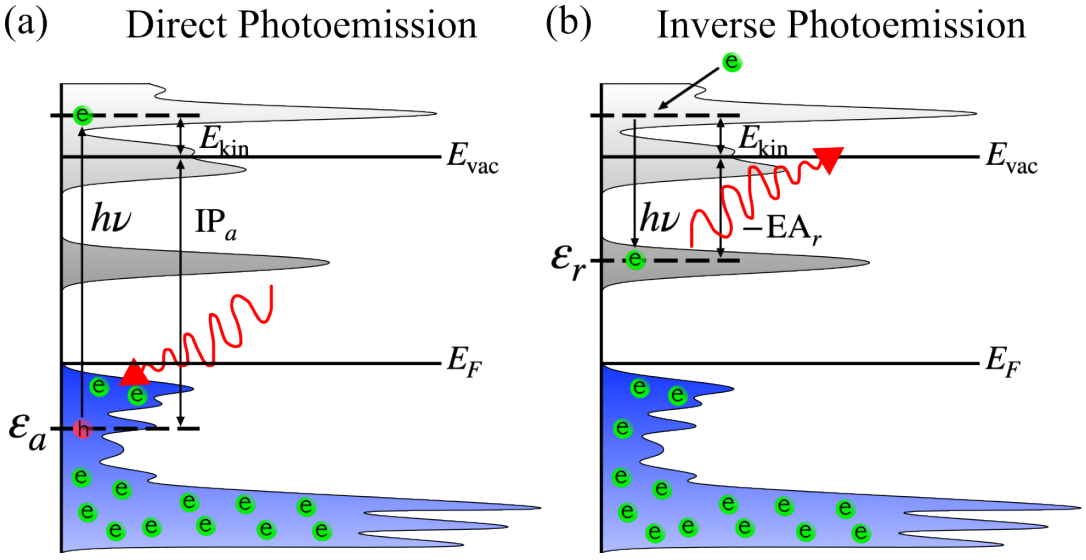

Figure 2.3: Schematic representations of the direct photoemission spectroscopy (a) for IP measurements and the inverse photoemission spectroscopy (b) for EA measurements. This figure is adapted from Ref. 44.

In Figure 2.3, the injected holes or electrons are described by single-particle energy levels, where a hole can be injected into an available occupied state labeled by "a", and an electron can occupied a bound unoccupied state labeled by "r". The measurability of IPs and EAs from a continuum of states is particularly significant in angle-resolved PES (ARPES) experiements for solid-state materials. Using the law of energy conservation, the IPs and EAs of a N-electron system can also be expressed as the energy difference between the positively/negatively charged system and the neutral one

$$\mathrm{IP}_a = E_a^{N-1} - E_0^N, \tag{2.100}$$

$$\mathrm{EA}_r = E_0^N - E_r^{N+1}. \tag{2.101}$$

Here, E_0^N refers to the ground-state energy of the neutral system. The energies of the charged systems $E^{\mathrm{N}\pm1}$ in Eqs (2.100) and (2.101) account for the induced relaxation effects of the system, i.e., electrons are attracted by the created hole or are repelled by the additional electron, and these effects are also captured in the measured IPs and EAs from PES. Furthermore, both the measurements of IPs and EAs measurements involve energy flowing into the neutral system, i.e., the N-electron system is excited to another higher-energy state from the ground state. Therefore, IPs and EAs belong to the *excited-state* properties of a system.

The formulations of IPs and EAs above indicate two possible ways to simulate these two processes (properties) using quantum mechanical methods: (1) compute the total electronic energies of the neutral and charged systems, and then take the difference in energies as shown in Eqs. (2.100) and (2.101); (2) use the one-particle approximation and find the energy level which the electron is removed from or injected into. The energy-difference approach requires total energy calculations, which mainly employ high-accuracy

wavefunction methods such as truncated CI or CC. These methods suffer from steep scaling in cost and are thus prohibitive for large-scale systems. Furthermore, this finite difference approach is mostly limited to the first IP and the largest EA, corresponding to the highest occupied state and the lowest unoccupied state. Such a limitation prevents access from band structures of solid-state materials. On the other hand, the second approach offers a more direct description for single-particle excitations, and is able to access a continuum of energy levels in solids as well as discrete molecular energy levels.

2.5.2 Interpretation of orbital energy

In practice, it is very tempting and common to interpret the eigenvalues from mean-field calculations as the energy levels for electron removal and addition. Recall the Hartree–Fock equations [Eq. (2.58)] in Section 2.3

$$\left(-\frac{\nabla^2}{2} + \hat{v}_{\text{ext}} + \hat{v}_H + \hat{v}_{\text{x}}\right) |\phi_i\rangle = \varepsilon_i |\phi_i\rangle \,, \tag{2.102}$$

and the Kohn–Sham equations [Eq. (2.86)] in Section 2.4

$$\left(-\frac{\nabla^2}{2} + \hat{v}_{\text{ext}} + \hat{v}_H + \hat{v}_{\text{xc}}\right) |\phi_i\rangle = \varepsilon_i |\phi_i\rangle \,. \tag{2.103}$$

The first three terms between these two mean-field single-particle Hamiltonians have the same form; the difference is embodied in the non-classical electron–electron interactions terms: the Hartree–Fock approximation contains only exchange interaction that is nonlocal, while the Kohn–Sham scheme includes both approximated exchange and correlation interactions that can be local, semilocal, or hybrid. Given the Schrödinger-like form of the Hamiltonian, the eigenvalue ε_i represents the single-particle energy level associated with the electron moving in a mean field in the state $\phi_i(\mathbf{r})$.

The first attempt to connect ε_i to IPs/EAs was done by Koopmans in 1933,[45] leading to the well known Koopmans' theorem within the Hartree–Fock approximation

$$\mathrm{IP}_a = E_a^{N-1} - E^N = -\varepsilon_a, \tag{2.104}$$

$$\mathrm{EA}_r = E^N - E_r^{N+1} = -\varepsilon_r. \tag{2.105}$$

The proof of the Koopmans' theorem is straightforward, as one just needs to express the total energies and eigenvalues in terms of the single-particle orbital basis. Readers who are interested in the proof are recommended to Chapter 3 in Ref. 46. The Koopmans' theorem applies to electron removal from any occupied state and electron addition to any bound unoccupied (virtual) state, which promises a convenient way to predict IPs and EAs. However, a critical approximation, namely the *frozen orbital* approximation, is made to enable the equal signs in Eqs. (2.104) and (2.105). That is to say, the estimated IPs and EAs by ε_i do not include the relaxation effects of the remaining/existing electrons, which are against the experimental measurements. Although it has been proposed that this error can be canceled out by the lack of correlation in ε_i, the Hartree–Fock eigenvalues are commonly found to overestimate IPs and underestimate EAs.

In KS-DFT, the ε_i of the highest occupied state can be interpreted as the first IP. This interpretation is supported by the Janak's theorem,[47] which states that the eigenvalue is the energy derivative with respect to the fractional particle number f_i

$$\varepsilon_i = \frac{\partial E}{\partial f_i}, \tag{2.106}$$

where $0 \leq f_i \leq 1$. It can be shown that the highest occupied eigenvalue ε_N satisfies the following equation

$$E^N - E^{N-1} = \int_0^1 \mathrm{d}f_N \frac{\partial E}{\partial f_N} = \varepsilon_N. \tag{2.107}$$

The Janak's theorem is sometimes called the DFT Koopmans' theorem. However, the Janak's theorem is much weaker since only the eigenvalue of the highest occupied (N^{th}) state in DFT is interpretable

$$\text{IP}(N) = -\varepsilon_N(N). \tag{2.108}$$

Here, the N in parenthesis emphasizes that the eigenvalue is obtained from the DFT calculation of the N-electron system. Analogously, the largest electron affinity of the N-electron system corresponds to the highest occupied eigenvalue of the $(N+1)$-electron system

$$\text{EA}(N) = -\varepsilon_{N+1}(N+1). \tag{2.109}$$

Despite the caveat that only the highest occupied eigenvalue is physically meaningful, KS-DFT has become the most popular and practical approach in electronic structure calculations for molecules and solids. But inevitably, the inappropriate interpretations caused problems including but not limited to (1) overestimated bandwidths for evaluating band transport properties of charge carriers in metallic solids; (2) highly underestimated bandgaps for semiconductors and fundamental gaps (HOMO/LUMO gaps) for molecules; (3) disagreement on density of states with experiments; (4) strongly underestimated IPs compared to experiments. The significant bandgap problems for a wide range of materials are presented in Figure 2.4.

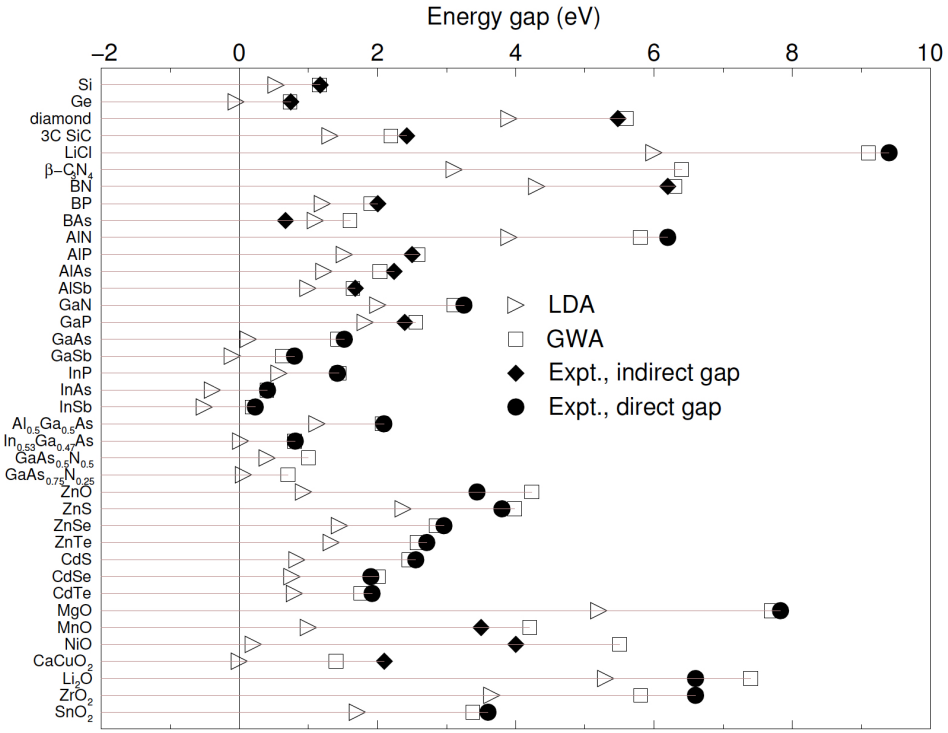

Figure 2.4: Comparisons of the bandgaps for a wide range of materials. The bandgap values are obtained from KS-DFT calculations (with LDA functional), many-body perturbation calculations (the *GW* approximation), and experiments. This figure is taken from Ref. 48.

The failures of KS-DFT mentioned above can be partly attributed to the density functional approximation used in practical implementations and the self-interaction error.[36] Even if the density functional reproduces exactly the same ground-state energy and density, the derivative discontinuity[49, 35] still exists in the exchange–correlation functional, causing fundamental problems in deriving IPs, EAs, and bandgaps from DFT eigenvalues. Most importantly, the underlying reason is the overinterpretations of the DFT eigenvalues. In principle, the optimized single-particle orbitals and eigenvalues in mean-field methods, including the Hartree–Fock approximation and KS-DFT, represent only the (approximated) ground state, while IPs, EAs, and energy gaps involved also excited states. Ground-state mean-field calculations are thus inappropriate for evaluating excited-state properties such as charged excitation energies. Although the generalized

KS-DFT with ad-hoc hybrid functionals are able to reproduce properties like the IP or the bandgaps, these methods are still within the static and mean-field framework, which does not account for the excited-state dynamics.

In Section 2.6, I will introduce the many-body perturbation theory based on the Green's function formalism. This class of theory, especially the *GW* approximation (GWA), excels at describing single-particle excitations that correspond to the IP, EA, and the resulting bandgaps (see Figure 2.4).

2.6 Many-body Green's function theory

Although the mean-field approaches fail to access excited-state properties, it is still tempting to describe charged excitations (i.e., IPs and EAs) using single-particle energy levels. And the success in mapping ε_i onto IPs/EAs is dictated by the ability of capturing the excited-state dynamics induced by electron removal/addition. A closer look at the example of electron removal is depicted in the upper half of Figure 2.5. After injecting a hole/electron, the $(N \pm 1)$-electron system is in its excited state, and the remaining/preexisting electrons react to the created hole/electron, constituting the excited-state dynamics. In principle, one can find the ground states energies of both the neutral and charged systems using wavefunction methods like truncated CI or CC, and then compute the change in energy as the first IP or the largest EA. This approach accounts for the dynamics of the $(N \pm 1)$-system. However, this energy-difference method is limited to small systems (tens of electrons) only because of the steep cost-scaling with respect to N.

Many-body perturbation theory within the Green's function formalism[50] offers a reformulated picture to describe the ionization process (the lower half Figure 2.5): the ground state is treated as a *Fermi vacuum*, where no *effective particle* is present; the

ejection of an electron is equivalent to the injection of a hole to the Fermi vacuum, upon which the electrons are *perturbed* and start interacting with the hole and each other; the excited-state dynamics is downfolded from tracking $(N-1)$ electrons to tracking only one hole "dressed" by surrounding electrons. This dressed hole is defined as a *quasi-hole*, and the concept of single *quasiparticle* (QP) refers to either an injected hole or electron to the Fermi vacuum. The following derivations are mainly based on References 51 and 52.

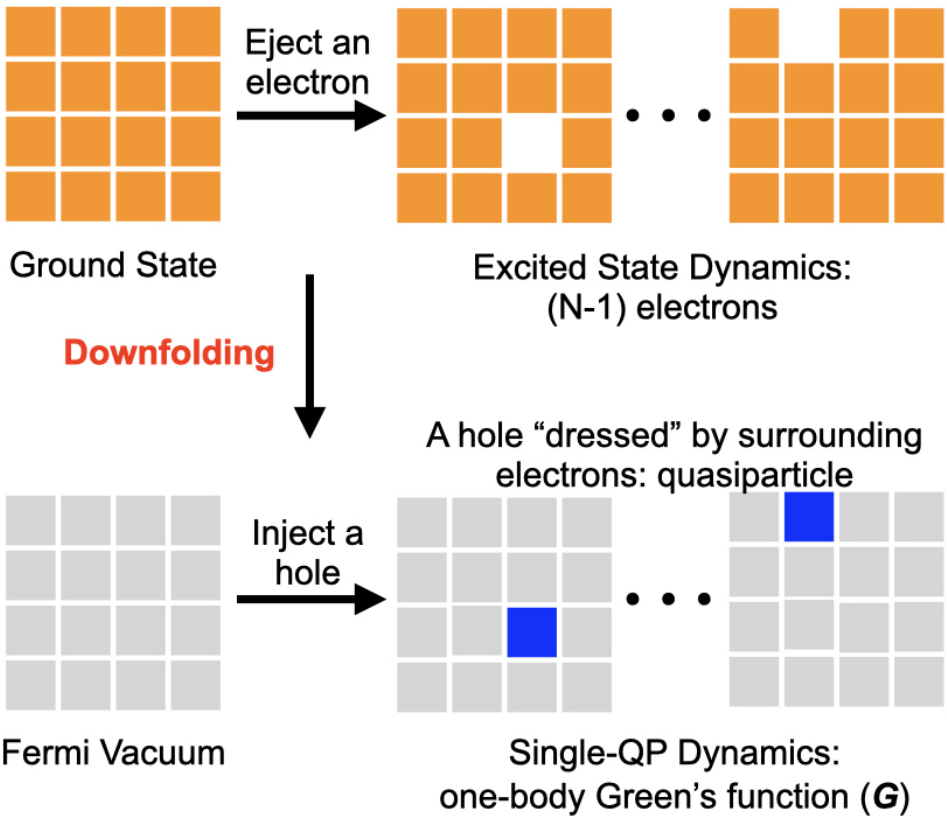

Figure 2.5: Schematic representations of the excited-state dynamics using the many–electron picture (upper half) and the quasiparticle picture (lower half), exemplified on the case where an electron is ejected from an N-electron system.

Mathematically, the dynamics of a single QP is described by the one-body equilibrium

Green's function (G) at 0K

$$\begin{aligned} \mathrm{i}G(1,2) &= \langle \Psi_0^N | \hat{\mathcal{T}} \left[\hat{\psi}(1) \hat{\psi}^\dagger(2) \right] | \Psi_0^N \rangle \\ &= \begin{cases} \langle \Psi_0^N | \hat{\psi}(1) \hat{\psi}^\dagger(2) | \Psi_0^N \rangle & \text{if } t_1 > t_2 \\ -\langle \Psi_0^N | \hat{\psi}^\dagger(2) \hat{\psi}(1) | \Psi_0^N \rangle & \text{if } t_1 < t_2 \end{cases} . \end{aligned} \tag{2.110}$$

Here, shorthand notations are used for the space-time coordinates: $1 \equiv (\mathbf{r}_1, t_1)$. $\hat{\psi}$ is the electron-annihilation operator while $\hat{\psi}^\dagger$ is the electron-creation operator. Ψ_0^N is the ground-state many-body wavefunction of the N-electron system. $\hat{\mathcal{T}}$ denotes the time-ordering operator arranging $\hat{\psi}$ and $\hat{\psi}^\dagger$ in the order of time: for $t_1 < t_2$, the Green's function represents the probability amplitude that a hole is created at $(\mathbf{r}_1, t_1)$ and then annihilated at $(\mathbf{r}_2, t_2)$; for $t_1 > t_2$, the Green's function represents instead the probability amplitude that an electron is created at $(\mathbf{r}_2, t_2)$ and then annihilated at $(\mathbf{r}_1, t_1)$. In this definition, the Green's function is also called a propagator for the hole propagation ($t_1 < t_2$) or the electron propagation ($t_1 > t_2$).

The Green's function in Eq. (2.110) satisfies the following equation of motion

$$\left[\mathrm{i}\frac{\partial}{\partial t} - \hat{h}_0 \right] G(1,2) - \int \mathrm{d}3 \Sigma(1,3) G(3,2) = \delta(1-2), \tag{2.111}$$

where $\hat{h}_0$ is the one-body interaction term containing the kinetic energy and the external potential; Σ is the total *self-energy*, which only exists after a quasiparticle is introduced to the Fermi vacuum. Therefore, Σ exists because of the QP itself and is thus called

self-energy. The integral that involves Σ in Eq. (2.111) has the following form

$$\int \mathrm{d}3\Sigma(1,3)G(3,2) = \\ -\mathrm{i}\int \mathrm{d}\mathbf{r}_3 \nu(\mathbf{r}_1-\mathbf{r}_3)\left\langle \Psi_0^N|\hat{\mathcal{T}}\left[\hat{\psi}^\dagger(\mathbf{r}_3,t_1)\hat{\psi}(\mathbf{r}_3,t_1)\hat{\psi}(\mathbf{r}_1,t_1)\hat{\psi}^\dagger(\mathbf{r}_2,t_2)\right]|\Psi_0^N\right\rangle, \tag{2.112}$$

where the intricate term on the right-hand side is related to the two-body Green's function

$$G_2(12;34) = (\mathrm{i})^2\left\langle \Psi_0^N|\hat{\mathcal{T}}\left[\hat{\psi}^\dagger(4)\hat{\psi}(2)\hat{\psi}(1)\hat{\psi}^\dagger(3)\right]|\Psi_0^N\right\rangle. \tag{2.113}$$

Our discussion here does not extend to G_2. However, it will be useful for the derivation of Σ. The time-dependent density and density matrix can be expressed in terms of the Green's function

$$n(1) = -\mathrm{i}G(1,1^+), \tag{2.114}$$

$$\rho(1,2^+) = -\mathrm{i}G(1,2^+), \tag{2.115}$$

where the plus sign of 1^+ or 2^+ is infinitesimally after 1: $t_1^+ = t_1 + \eta$ (η is an infinitesimal positive number).

The Green's function $G(1,2)$ can be simplified as $G(\mathbf{r}_1,\mathbf{r}_2;t)$ by setting $t_2 = 0$ and $t = t_1 - t_2$. For the $N \pm 1$ charged system, one can assume that a complete basis of many-body wavefunctions fully span the electronic space, leading to the following closure relations

$$\hat{I} = \sum_a |\Psi_a^{N-1}\rangle\langle\Psi_a^{N-1}|, \tag{2.116}$$

$$\hat{I} = \sum_r |\Psi_r^{N+1}\rangle\langle\Psi_r^{N+1}|. \tag{2.117}$$

Inserting Eq. (2.116) into the hole Green's function ($t < 0$) in Eq. (2.110), one can obtain

$$\begin{aligned} \mathrm{i}G^h(\mathbf{r}_1, \mathbf{r}_2; t) &= -\sum_a \langle \Psi_0^N | \hat{\psi}^\dagger(\mathbf{r}_2) \, | \Psi_a^{N-1} \rangle \, \langle \Psi_a^{N-1} | \, \hat{\psi}(\mathbf{r}_1, t) | \Psi_0^N \rangle \\ &= -\sum_a \langle \hat{\psi}(\mathbf{r}_2) \Psi_0^N \, | \Psi_a^{N-1} \rangle \, \langle \Psi_a^{N-1} | \, \hat{\psi}(\mathbf{r}_1, t) | \Psi_0^N \rangle \, . \end{aligned} \tag{2.118}$$

To further simplify the equation above, one can define a time-dependent *Dyson* orbital $\phi_a^h(\mathbf{r}_1, t)$ for a quasi-hole as

$$\phi_a^h(\mathbf{r}_1, t) = \langle \Psi_a^{N-1} | \hat{\psi}(\mathbf{r}_1, t) | \Psi_0^N \rangle = e^{-\mathrm{i}\varepsilon_a^h t} \phi_a^h(\mathbf{r}_1), \tag{2.119}$$

where ε_a^h is the quasiparticle energy associated with the state ϕ_a^h. The conjugated term in Eq. (2.118) is given by

$$\phi_a^{h*}(\mathbf{r}_2) = \langle \hat{\psi}(\mathbf{r}_2) \Psi_0^N | \Psi_a^{N-1} \rangle = \phi_a^{h*}(\mathbf{r}_2), \tag{2.120}$$

where ε_a^h is the QP energy associated with the state ϕ_a^h. Plugging Eqs. (2.119) and (2.120) into Eq. (2.118), the hole Green's function G^h can be written in terms of the Dyson orbitals

$$\mathrm{i}G^h(\mathbf{r}_1, \mathbf{r}_2; t) = -\sum_a \phi_a^h(\mathbf{r}_1) \phi_a^{h*}(\mathbf{r}_2) e^{-\mathrm{i}\varepsilon_a^h t}. \tag{2.121}$$

Following the same derivation of G^h, the electron Green's function ($t > 0$) can also be written in terms of the Dyson orbitals

$$\mathrm{i}G^e(\mathbf{r}_1, \mathbf{r}_2; t) = \sum_r \phi_r^e(\mathbf{r}_1) \phi_r^{e*}(\mathbf{r}_2) e^{-\mathrm{i}\varepsilon_r^e t}, \tag{2.122}$$

where ϕ_r^e for a quasi-electron is defined in a way similar to that for a quasi-hole

$$\phi_r^e(\mathbf{r}_1, t) = \langle \hat{\psi}^\dagger(\mathbf{r}_1, t)\Psi_0^N | \Psi_r^{N+1} \rangle = e^{-\mathrm{i}\varepsilon_r^e t}\phi_r^e(\mathbf{r}_1), \tag{2.123}$$

$$\phi_r^{e*}(\mathbf{r}_2) = \langle \Psi_r^{N+1} | \hat{\psi}^\dagger(\mathbf{r}_2) | \Psi_0^N \rangle . \tag{2.124}$$

Using a step function, the combined Green's function in terms of the Dyson orbital reads

$$\begin{aligned} \mathrm{i}G(\mathbf{r}_1, \mathbf{r}_2; t) = &- \sum_a \phi_a^h(\mathbf{r}_1)\phi_a^{h*}(\mathbf{r}_2)e^{-\mathrm{i}\varepsilon_a^h t}\theta(-t) \\ &+ \sum_r \phi_r^e(\mathbf{r}_1)\phi_r^{e*}(\mathbf{r}_2)e^{-\mathrm{i}\varepsilon_r^e t}\theta(t), \end{aligned} \tag{2.125}$$

where the Heaviside step function θ is defined as

$$\theta(t) = \begin{cases} 0, & \text{for } t < 0 \\ 1, & \text{for } t > 0 \end{cases} . \tag{2.126}$$

Note that one can perform a Laplace transformation on Eq. (2.125) to obtain the expression of G in the frequency domain. It is more straightforward to analyze single-quasiparticle excitation energies from the frequency-dependent Green's function

$$G(\mathbf{r}_1, \mathbf{r}_2; \omega) = \sum_a \frac{\phi_a^h(\mathbf{r}_1)\phi_a^{h*}(\mathbf{r}_2)}{\omega - \varepsilon_a^h - \mathrm{i}\eta} + \sum_r \frac{\phi_r^e(\mathbf{r}_1)\phi_r^{e*}(\mathbf{r}_2)}{\omega - \varepsilon_r^e + \mathrm{i}\eta}. \tag{2.127}$$

Here, η represents an infinitesimally small positive number. Eq. (2.127) indicates that poles will be observed from $G(\mathbf{r}_1, \mathbf{r}_2; \omega)$ at $\omega = \varepsilon_a^h$ and $\omega = \varepsilon_r^e$, and these frequencies (energies) correspond exactly to the excitation energies from Ψ_0^N to Ψ_a^{N-1} and Ψ_r^{N+1}, respectively. And hence, the poles of $G(\mathbf{r}_1, \mathbf{r}_2; \omega)$ represent the negative of IPs and EAs.

Furthermore, the spectral function $A(\mathbf{r}_1, \mathbf{r}_2; \omega)$ can be obtained from $G(\mathbf{r}_1, \mathbf{r}_2; \omega)$

$$\begin{aligned} A(\mathbf{r}_1, \mathbf{r}_2; \omega) &= \frac{1}{\pi} \mathrm{Im} G(\mathbf{r}_1, \mathbf{r}_2; \omega) \mathrm{sgn}(\varepsilon_F - \omega) \\ &= \sum_j \phi_j(\mathbf{r}_1) \phi_j{}^*(\mathbf{r}_2) \frac{P_j}{(\omega - \varepsilon_j)^2 + P_j^2}. \end{aligned} \tag{2.128}$$

Here, ε_F is the Fermi energy separating the hole (occupied) and electron (unoccupied) states; sgn is the sign function, assigning a "1" to the frequency domain below ε_F and a "-1" to the domain beyond ε_F; the absolute value of P_j is the width of the peak at $\omega = \varepsilon_j$. From the spectral function, one can determine the QP excitation energy as well as extracting the QP lifetime, which is inversely proportional to $|P_j|$.

The single-quasiparticle orbitals in Eq. (2.128) are the solutions to the following non-linear eigenvalue equations

$$\hat{h}_0 \phi_j(\mathbf{r}) + \int \mathrm{d}\mathbf{r}' \Sigma(\mathbf{r}, \mathbf{r}'; \omega = \varepsilon_j) \phi_j(\mathbf{r}') = \varepsilon_j \phi_j(\mathbf{r}) \tag{2.129}$$

Different from the eigenvalue equations in the mean-field approaches, the electron–electron interaction term here is frequency (energy)-dependent. In fact, the Σ term in Eq. (2.129) is a very critical and interesting quantity in the Green's function theory, as all the many-body effects are downfolded into this nonlocal and dynamical self-energy. In Section 2.7, I will present the derivation of Σ and important approximations in practical applications.

2.7 Approximations to the self-energy: GW and beyond

The total self-energy Σ is central for quasiparticle excitation energies in the Green's function formalism.[51, 52, 53] Applying an inverse Green's function G^{-1} to the definition

of Σ in Eq. (2.112), one can extract the following expression for the exact total self-energy

$$\Sigma(1,2) = -\mathrm{i}\nu(1,\bar{3}^+)G_2(1\bar{3};\bar{4}\bar{3}^+)G^{-1}(\bar{4},2), \tag{2.130}$$

Here, the two-body Green's function G_2 is defined in Eq. (2.113), and the bar over a number represents integrating over that space-time coordinates: $\bar{3} = \int\int \mathrm{d}\mathbf{r}_3\mathrm{d}t_3$. $\nu(1,3^+)$ denotes the instantaneous Coulomb kernel

$$\nu(1,3^+) = \frac{1}{|\mathbf{r}_1 - \mathbf{r}_3|}\delta(t_1 - t_3). \tag{2.131}$$

To manipulate the two-body Green's function in Eq. (2.130) for further processing, one can introduce an external perturbing potential U_{ext} such that[53]

$$G_2(13;43^+;[U_{\mathrm{ext}}])\big|_{U_{\mathrm{ext}}=0} = G(1,4)G(3,3^+) - \frac{\delta G(1,4)}{\delta U_{\mathrm{ext}}(3)}\bigg|_{U_{\mathrm{ext}}=0}, \tag{2.132}$$

where G_2 is broken down into a product of two one-body Green's functions plus the functional derivative of G with respect to U_{ext}. In the following, it is assumed that the functional derivative takes the value at $U_{\mathrm{ext}} = 0$. Combining Eqs. (2.130) and (2.132), the self-energy can be written as

$$\Sigma(1,2) = -\mathrm{i}\nu(1,\bar{3}^+)G(1,\bar{4})G^{-1}(\bar{4},2)G(\bar{3},\bar{3}^+) + \mathrm{i}\nu(1,\bar{3}^+)\frac{\delta G(1,\bar{4})}{\delta U_{\mathrm{ext}}(\bar{3})}G^{-1}(\bar{4},2). \tag{2.133}$$

Here, the first term on the right-hand side can be simplified as

$$\begin{aligned}\Sigma_H(1,2) &= -\mathrm{i}\nu(1,\bar{3}^+)G(\bar{3},\bar{3}^+)\delta(1-2)\\ &= v_H(1)\delta(1-2),\end{aligned} \tag{2.134}$$

given that

$$G(1,\bar{4})G^{-1}(\bar{4},2) = \delta(1-2), \tag{2.135}$$

and

$$n(3) = -\mathrm{i}G(3,3^{+}). \tag{2.136}$$

That is to say, the first term of $\Sigma(1,2)$ in Eq. (2.133) turns out to be the instantaneous and local classical Coulomb repulsion stemming from the electron density. This term is denoted as the Hartree self-energy Σ_H. Conventionally, the second term in Eq. (2.133) is defined as the exchange–correlation self-energy Σ_{XC}

$$\Sigma_{\mathrm{XC}}(1,2) = \mathrm{i}\nu(1,\bar{3}^{+})\frac{\delta G(1,\bar{4})}{\delta U_{\mathrm{ext}}(\bar{3})}G^{-1}(\bar{4},2). \tag{2.137}$$

Using the fact that

$$\frac{\delta\left[G(1,\bar{4})G^{-1}(\bar{4},2)\right]}{\delta U_{\mathrm{ext}}(3)} = G(1,\bar{4})\frac{\delta G^{-1}(\bar{4},2)}{\delta U_{\mathrm{ext}}(3)} + \frac{\delta G(1,\bar{4})}{\delta U_{\mathrm{ext}}(3)}G^{-1}(\bar{4},2) = 0, \tag{2.138}$$

one can substitute the functional derivative in Eq. (2.137) and obtain

$$\Sigma_{\mathrm{XC}}(1,2) = -\mathrm{i}\nu(1,\bar{3}^{+})G(1,\bar{4})\frac{\delta G^{-1}(\bar{4},2)}{\delta U_{\mathrm{ext}}(\bar{3})}. \tag{2.139}$$

The inverse Green's function G^{-1} in the functional derivative of Eq. (2.139) is more processable. Note that in perturbation theory, auxiliary calculations with approximations are prerequisite. In practice, mean-field methods such as KS-DFT can serve as the starting points for many-body perturbation theory calculations. The *non-interacting* Green's function G_0 is associated with some mean-field Hamiltonian $\hat{H}_0$

$$\hat{G}_0^{-1} = \mathrm{i}\frac{\partial}{\partial t} - \hat{H}_0, \tag{2.140}$$

where $\hat{H}_0$ reads

$$\hat{H}_0 = \hat{T} + \hat{v}_{\text{ext}} + \hat{v}_{\text{H}} + \hat{v}_{\text{xc}}. \tag{2.141}$$

Analogously, the *interacting* Green's function G is associated with the fully interacting Hamiltonian $\hat{H}$

$$\hat{G}^{-1} = \mathrm{i}\frac{\partial}{\partial t} - \hat{H}, \tag{2.142}$$

with $\hat{H}$ written as

$$\hat{H} = \hat{T} + \hat{v}_{\text{ext}} + \hat{\Sigma}_H + \hat{\Sigma}_{\text{XC}}. \tag{2.143}$$

The only difference between $\hat{H}_0$ and $\hat{H}$ is the nonlocal and dynamical $\hat{\Sigma}_{\text{XC}}$ versus the local/semilocal and static $\hat{v}_{\text{xc}}$. Subtracting Eq. (2.142) from Eq. (2.140) gives rise to

$$\hat{G}_0^{-1} - \hat{G}^{-1} = \Delta\hat{\Sigma}_{\text{XC}}, \tag{2.144}$$

where $\Delta\hat{\Sigma}_{\text{XC}} = \hat{\Sigma}_{\text{XC}} - \hat{v}_{\text{xc}}$. Eq. (2.144) is known as a form of the Dyson equation connecting the non-interacting and interacting Green's functions. The Dyson equation in the recurring form can be obtained by simply rearranging the terms in Eq. (2.144)

$$\hat{G} = \hat{G}_0 + \hat{G}_0\Delta\hat{\Sigma}_{\text{XC}}\hat{G}. \tag{2.145}$$

2.7.1 Hedin's equations

Let us first proceed with the Hedin's formulation for Σ_{XC}. By introducing the following classical potential U_{cls}

$$U_{\text{cls}}(1) = U_{\text{ext}}(1) + v_H(1), \tag{2.146}$$

the functional derivative in Eq. (2.139) can be rewritten using the chain rule

$$\frac{\delta G^{-1}(4,2)}{\delta U_{\text{ext}}(3)} = \frac{\delta G^{-1}(4,2)}{\delta U_{\text{cls}}(\bar{5})} \frac{\delta U_{\text{cls}}(\bar{5})}{\delta U_{\text{ext}}(3)}. \tag{2.147}$$

The three-point function $\delta G^{-1}(4,2)/\delta U_{\text{cls}}(5)$ is defined as the vertex function Γ

$$\Gamma(4,2,5) := -\frac{\delta G^{-1}(4,2)}{\delta U_{\text{cls}}(5)}. \tag{2.148}$$

The inverse dielectric function is given by

$$\epsilon^{-1}(5,3) = \frac{\delta U_{\text{cls}}(5)}{\delta U_{\text{ext}}(3)}. \tag{2.149}$$

Σ_{XC} in Eq. (2.139) can be expressed in terms of Γ

$$\Sigma_{\text{XC}}(1,2) = \mathrm{i} G(1,\bar{4}) W(1,\bar{5}) \Gamma(\bar{4},2,\bar{5}), \tag{2.150}$$

where the screened Coulomb potential W defined through ϵ^{-1}

$$W(1,5) = \epsilon^{-1}(5,\bar{3}) \nu(1,\bar{3}^{+}). \tag{2.151}$$

Eq. (2.150) belongs to the set of coupled integral equations known as the Hedin's equations, which are summarized as the Hedin's pentagon in Figure 2.6. The integral form of the Dyson equation for the Green's function reads

$$G(1,2) = G_0(1,2) + G_0(1,\bar{3}) \Delta\Sigma_{\text{XC}}(\bar{3},\bar{4}) G(\bar{4},2). \tag{2.152}$$

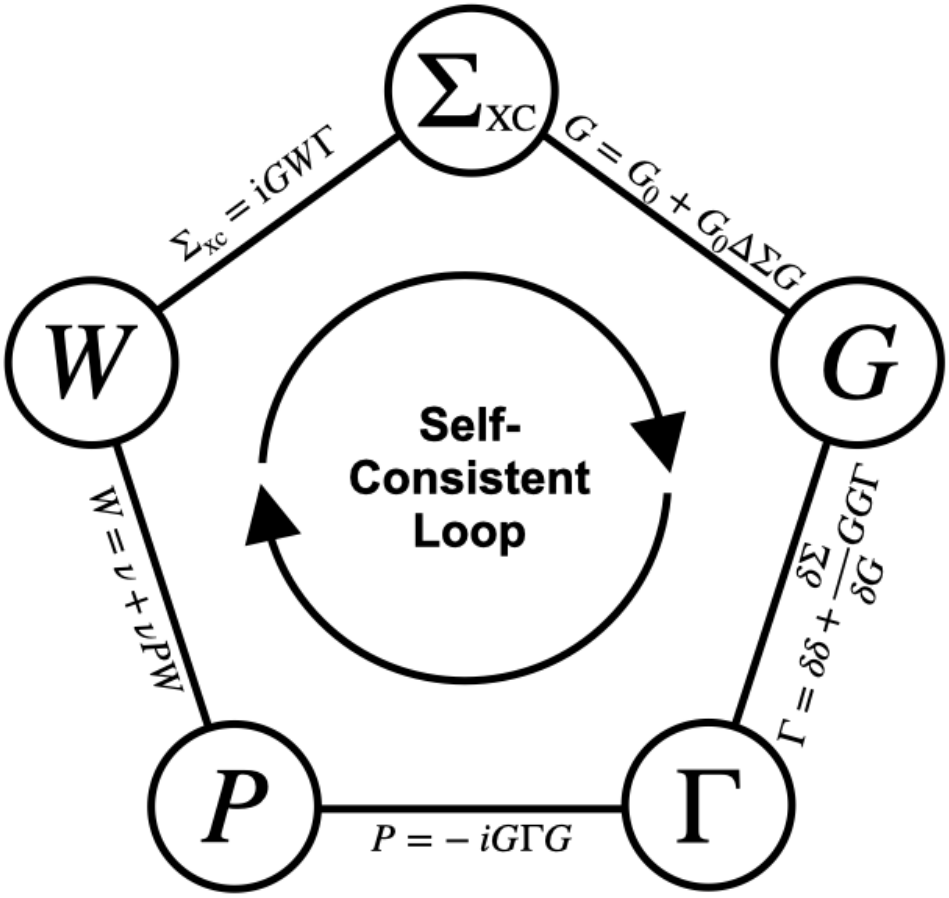

Figure 2.6: Hedin's equations in a pentagonal self-consistent loop.

The expression for W can be also rewritten in an integral and recurring form. First, the inverse dielectric function can be expanded as follows

$$\begin{aligned}
\epsilon^{-1}(1,2) &= \frac{\delta U_{\text{cls}}(1)}{\delta U_{\text{ext}}(2)} \\
&= \frac{\delta U_{\text{ext}}(1)}{\delta U_{\text{ext}}(2)} + \frac{\delta v_H(1)}{\delta U_{\text{ext}}(2)} \\
&= \delta(1-2) + \nu(1,\bar{3}) \frac{\delta n(\bar{3})}{\delta U_{\text{ext}}(2)} \\
&= \delta(1-2) + \nu(1,\bar{3}) \frac{\delta n(\bar{3})}{\delta U_{\text{cls}}(\bar{4})} \frac{\delta U_{\text{cls}}(\bar{4})}{\delta U_{\text{ext}}(2)}.
\end{aligned} \tag{2.153}$$

Next, the response function $R(1,2)$ is defined as

$$R(1,2) = \frac{\delta n(1)}{\delta U_{\text{ext}}(2)}, \tag{2.154}$$

and the polarization function $P(1,2)$ reads

$$P(1,2) = \frac{\delta n(1)}{\delta U_{\text{cls}}(2)}. \tag{2.155}$$

It can be shown that the ϵ, R, and P functions are inter-related by

$$\epsilon^{-1}(1,2) = \delta(1-2) + \nu(1,\bar{3})R(\bar{3},2), \tag{2.156}$$

$$R(1,2) = P(1,2) + P(1,\bar{3})\nu(\bar{3},\bar{4})R(\bar{4},2). \tag{2.157}$$

Finally, the Dyson form of the screened Coulomb potential W reads

$$W(1,2) = \nu(1,2) + \nu(1,\bar{3})P(\bar{3},\bar{4})W(\bar{4},2). \tag{2.158}$$

Given the relationship between the density n and the Green's function G [Eq. (2.114)] and $GG^{-1} = \delta$, the polarization function P can be expanded as

$$P(1,2) = -\mathrm{i}G(1,\bar{3})\Gamma(\bar{3},\bar{4},2)G(\bar{4},1^{+}). \tag{2.159}$$

The last Dyson-like equation to find is for the vertex function Γ. Using the Dyson equation for G^{-1} [Eq. (2.144)], Γ can be written as

$$\Gamma(1,2,3) = \delta(1-3)\delta(2-3) + \frac{\delta\Sigma_{H\text{XC}}(1,2)}{\delta G(\bar{4},\bar{5})}G(\bar{4},\bar{6})G(\bar{7},\bar{5})\Gamma(\bar{6},\bar{7},3), \tag{2.160}$$

where $\Sigma_{H\mathrm{XC}}$ is the total self-energy equivalent to the Σ introduced before

$$\Sigma_{H\mathrm{XC}}(1,2) = \Sigma_H(1,2) + \Sigma_{\mathrm{XC}}(1,2). \tag{2.161}$$

To sum up, the following five coupled integral equations constitute the renowned set of Hedin's equations

$$\begin{aligned}
\Sigma_{\mathrm{XC}}(1,2) &= \mathrm{i}G(1,\bar{4})W(1,\bar{5})\Gamma(\bar{4},2,\bar{5}) \\
G(1,2) &= G_0(1,2) + G_0(1,\bar{3})\Delta\Sigma_{\mathrm{XC}}(\bar{3},\bar{4})G(\bar{4},2) \\
W(1,2) &= \nu(1,2) + \nu(1,\bar{3})P(\bar{3},\bar{4})W(\bar{4},2) \\
P(1,2) &= -\mathrm{i}G(1,\bar{3})\Gamma(\bar{3},\bar{4},2)G(\bar{4},1^+) \\
\Gamma(1,2,3) &= \delta(1-3)\delta(2-3) + \frac{\delta\Sigma_{H\mathrm{XC}}(1,2)}{\delta G(\bar{4},\bar{5})}G(\bar{4},\bar{6})G(\bar{7},\bar{5})\Gamma(\bar{6},\bar{7},3)
\end{aligned}$$

In principle, the Hedin's equations can be solved self-consistently starting from a given approximation to Σ_{XC}. Ref. 54 is recommended for readers interested in the self-consisent solultion. However, it is exceptionally challenging to find the exact solutions, and the applications to realistic systems (e.g., atoms and molecules) remain to be explore. In practice, approximations are made, especially to the sophisticated vertex function Γ, among which the GW approximation has become a widely-used approach for calculating quasiparticle excitation energies of molecules and solids.[51, 52, 55, 56, 57]

In the GW approximation, the vertex function is truncated to the delta functions only

$$\Gamma(1,2,3) \approx \delta(1-3)\delta(2-3). \tag{2.162}$$

The exchange–correlation self-energy thus becomes

$$\Sigma_{\mathrm{XC}}(1,2) \approx \mathrm{i}G(1,2)W(1,2), \tag{2.163}$$

which represents the so-called GW self-energy and is denoted $\Sigma_{\mathrm{XC}}^{\mathrm{GW}}$ in the following. The polarization function is also simplified as

$$P(1,2) \approx -\mathrm{i}G(1,2)G(2,1^{+}). \tag{2.164}$$

The product of two Green's functions here indeed corresponds to the electron-hole pairs in the "bubble" diagrams in the diagrammatic representation of the Green's function. This class of interactions is related to the induced charge density fluctuations. In this context, the screened Coulomb potential W can be written as

$$W(1,2) = \nu(1,2) + \delta n(1,\bar{3})\nu(\bar{3},2), \tag{2.165}$$

which represents the effective potential at $(\mathbf{r}_2, t_2)$ induced by a quasiparticle at $(\mathbf{r}_1, t_1)$. In the GW approximation, the bare Coulomb potential $\nu(1,2)$ is screened by the effective positive charges stemming from the induced charge density fluctuations δn. In Chapter 3, this concept will be revisited in practical QP energy calculations.

Within the GW framework, one can start from the one-shot GW (G_0W_0) approximation with $G = G_0$. The W is one-shot in the sense that the polarization function, or effectively the induced charge density fluctuations, is computed by the random phase approximation (RPA) using the mean-field Hamiltonian $\hat{H}_0$. After the first shot, one can update G and W and iterate the calculation until self-consistence, leading to the so-called self-consistent GW (scGW).[58, 59, 60, 61] scGW can be regarded as an improvement or a correction to G_0W_0, to which I will not extend further in this dissertation. For the corrections to G_0W_0, I will consider instead the effects from the leftover part in Γ, i.e., the second term on the right-hand side of Eq. (2.160). These effects are known as the vertex corrections, which will be derived them in the following.

2.7.2 Derivation of vertex corrections

Given that the vertex function Γ appears in both Σ_{XC} and P, there are two types of vertex corrections: referencing to the GW self-energy ($\Sigma_{\mathrm{XC}}^{\mathrm{GW}}$), one vertex correction applies directly to the self-energy that is outside $\Sigma_{\mathrm{XC}}^{\mathrm{GW}}$, the other one applying to P is inside $\Sigma_{\mathrm{XC}}^{\mathrm{GW}}$.

First of all, the outside vertex correction can be introduced to $\Sigma_{\mathrm{XC}}^{\mathrm{GW}}$ by reformulating the expression for Σ_{XC}. In Eq. (2.139), one can substitute the G^{-1} using Eq. (2.144) and obtain

$$\Sigma_{\mathrm{XC}}(1,2) = -\mathrm{i}\nu(1,\bar{3}^{+})G(1,\bar{4})\frac{\delta G_0^{-1}(\bar{4},2)}{\delta U_{\mathrm{ext}}(\bar{3})} + \mathrm{i}\nu(1,\bar{3}^{+})G(1,\bar{4})\frac{\delta \Delta\Sigma_{\mathrm{XC}}(\bar{4},2)}{\delta U_{\mathrm{ext}}(\bar{3})}. \tag{2.166}$$

Furthermore, the v_{xc} and Σ_H terms can be separated from G_0^{-1} and combined with Σ_{XC} to reproduce the total self-energy $\Sigma_{H\mathrm{XC}}$ (the same as Σ introduced before)

$$\begin{aligned}\hat{G}_0^{-1} &= \mathrm{i}\frac{\partial}{\partial t} - \hat{h}_0 - \hat{\Sigma}_H - \hat{v}_{\mathrm{xc}} \\ &= \hat{G'}_0^{-1} - \hat{\Sigma}_H - \hat{v}_{\mathrm{xc}}.\end{aligned} \tag{2.167}$$

Plugging Eq. (2.167) into Eq. (2.166) leads to

$$\Sigma_{\mathrm{XC}}(1,2) = -\mathrm{i}\nu(1,\bar{3}^{+})G(1,\bar{4})\frac{\delta G'^{-1}_0(\bar{4},2)}{\delta U_{\mathrm{ext}}(\bar{3})} + \mathrm{i}\nu(1,\bar{3}^{+})G(1,\bar{4})\frac{\delta \Sigma_{H\mathrm{XC}}(\bar{4},2)}{\delta U_{\mathrm{ext}}(\bar{3})}. \tag{2.168}$$

Given the fact that

$$\frac{\delta G'^{-1}_0(4,2)}{\delta U_{\mathrm{ext}}(3)} = -\delta(2-3)\delta(4-3), \tag{2.169}$$

the first term on the right-hand side of Eq. (2.168) becomes

$$\begin{aligned}\Sigma_{\mathrm{X}}(1,2) &= \mathrm{i}\nu(1,\bar{3}^{+})G(1,\bar{4})\delta(2-\bar{3})\delta(\bar{4}-\bar{3}) \\ &= \mathrm{i}\nu(1,2^{+})G(1,2).\end{aligned} \tag{2.170}$$

This term, denoted Σ_{X}, is similar to the nonlocal exchange interaction in the Hartree–Fock approximation since $\rho(1,2^{+}) = -\mathrm{i}G(1,2)\delta(t_1 - t_2)$ [Eq. (2.115)].

With the identification of Σ_{X}, the second term on the right-hand side of Eq. (2.168) is thus defined as the correlation self-energy

$$\Sigma_{\mathrm{C}} = \mathrm{i}\nu(1,\bar{3}^{+})G(1,\bar{4})\frac{\delta\Sigma_{H\mathrm{XC}}(\bar{4},2)}{\delta U_{\mathrm{ext}}(\bar{3})}. \tag{2.171}$$

Through inserting a Green's function and introducing a generalized polarizability, Σ_{C} can be rewritten using the chain rule

$$\Sigma_{\mathrm{C}}(1,2) = -\nu(1,\bar{3}^{+})G(1,\bar{4})\frac{\delta\Sigma_{H\mathrm{XC}}(\bar{4},2)}{\delta G(\bar{6},\bar{5})}{}^{3}\chi(\bar{6},\bar{5},\bar{3}), \tag{2.172}$$

where the three-point generalized polarizability ${}^{3}\chi$ is defined as

$${}^{3}\chi(6,5,3) := -\mathrm{i}\frac{\delta G(6,5)}{\delta U_{\mathrm{ext}}(3)}. \tag{2.173}$$

Given that $\Sigma_{H\mathrm{XC}} = \Sigma_H + \Sigma_{\mathrm{X}} + \Sigma_{\mathrm{C}}$, the correlation self-energy Σ_{C} appears on both sides of Eq. (2.172) and needs to be solved self-consistently, which is equivalent to solving the Hedin's pentagon. However, there are two seemingly possible approximations to make: (1) $\Sigma_{H\mathrm{XC}} \approx \Sigma_H$; (2) $\Sigma_{H\mathrm{XC}} \approx \Sigma_H + \Sigma_{\mathrm{X}}$. In this following, I will show that the first approximation is equivalent to the GW approximation, while the second approximation is beyond GW and introduces the outside vertex correction.

The truncation from Σ_{HXC} to Σ_H reads

$$\Sigma_{HXC}(1,2) \approx \Sigma_H(1)\delta(1-2). \tag{2.174}$$

Inserting Eqs. (2.174) and (2.134) to Eq. (2.172), the functional derivative is approximated as

$$\frac{\delta\Sigma_{HXC}(4,2)}{\delta G(6,5)} \approx -\mathrm{i}\nu(2,5)\delta(6-5)\delta(4-2). \tag{2.175}$$

With $\delta(6-5)$, the three-point polarizability is simplified to a two point reducible polarizability

$$\begin{aligned}\delta(\bar{6}-5)^3\chi(\bar{6},5,3) &= -\mathrm{i}\frac{\delta G(5,5^+)}{\delta U_{\mathrm{ext}}(3)} \\ &:= \chi(5,3),\end{aligned} \tag{2.176}$$

which is indeed equivalent to the response function R in Eq. (2.154). Plugging Eqs. (2.175) and (2.176) back into Eq. (2.172), the correlation self-energy is simplified as

$$\Sigma_{\mathrm{C}}(1,2) = \mathrm{i}G(1,2)\nu(2,\bar{5})\chi(\bar{5},\bar{3})\nu(\bar{3},1). \tag{2.177}$$

Combining Eq. (2.170) with Eq. (2.177) gives rise to

$$\begin{aligned}\Sigma_{\mathrm{XC}}(1,2) &= \mathrm{i}\nu(1,2^+)G(1,2) + \mathrm{i}G(1,2)\nu(2,\bar{5})\chi(\bar{5},\bar{3})\nu(\bar{3},1) \\ &= \mathrm{i}G(1,2)\left[\nu(1,2^+) + \nu(2,\bar{5})\chi(\bar{5},\bar{3})\nu(\bar{3},1)\right],\end{aligned} \tag{2.178}$$

where the sum in the square brackets is simply the screened Coulomb potential $W(1,2)$ in Eq. (2.163). Therefore, the truncation of Σ_{HXC} to Σ_H is equivalent to the GW approximation presented in the Hedin's formulation.

Next, in order to introduce vertex correction to the GW correlation self-energy, Σ_{X} is

included in the approximation

$$\Sigma_{H\mathrm{XC}}(1,2) \approx \Sigma_H(1)\delta(1-2) + \Sigma_{\mathrm{X}}(1,2). \tag{2.179}$$

Plugging the expression of Σ_{X} in Eq. (2.170) into the functional derivative, one can obtain[62]

$$\frac{\delta\Sigma_{H\mathrm{XC}}(4,2)}{\delta G(6,5)} \approx -\mathrm{i}\nu(2,5)\delta(6-5)\delta(4-2) + \mathrm{i}\nu(4,2)\delta(5-2)\delta(6-4). \tag{2.180}$$

The main difference between the first and the second term on the right-hand side of Eq. (2.180) is that the second term keeps the three-point polarizability. Therefore, the corresponding correlation self-energy reads

$$\Sigma_{\mathrm{C}}(1,2) = \mathrm{i}G(1,2)\nu(2,\bar{5})\chi(\bar{5},\bar{3})\nu(\bar{3},1) - \mathrm{i}G(1,\bar{4})\nu(\bar{4},2)^3\chi(\bar{4},2,\bar{3})\nu(\bar{3},1). \tag{2.181}$$

Here, the additional term on the right-hand side with respect to Eq. (2.177) is the outside vertex correction applying directly to the correlation self-energy. As it is derived from the nonlocal exchange interaction Σ_{X}, I denote this correction as Γ_{X}, and the approach is denoted $G_0W_0\Gamma_{\mathrm{X}}$.

Given the fact that $\rho(4,2^+) = -\mathrm{i}G(4,2)\delta(t_4 - t_2)$, this outside vertex correction actually corresponds to the induced density matrix fluctuations $\delta\rho$. Chapter 3 discusses how to calculate δn and $\delta\rho$ by implementing real space-time representations in practice. In summary, the correlation self-energy in Eq. (2.181) accounts for the particle-density and particle-density matrix interactions in a quasiparticle excitation.

For the inside vertex correction, i.e., the correction to P in Eq. (2.164), the key step is to go beyond the random phase approximation used in the G_0W_0 approximation. The approach that includes both the inside and outside vertex corrections is denoted $G_0W_0^{\mathrm{tc}}\Gamma_{\mathrm{X}}$,

where the superscript "tc" stands for "test charge" used to probe the charge density response as an external source. More details can be found in References 63, 64, 65, 66. and the elaboration on this topic will not be provided here. One effective step to go beyond RPA is to include the time-dependent density matrix in addition to the time-dependent density when computing the induced charge density fluctuations using, for instance, real-time propagation approaches. A practical implementation of the time-dependent density matrix in real-time propagation is demonstrated in Chapter 10.

Bibliography

[1] M. Born and R. Oppenheimer, *Zur quantentheorie der molekeln*, *Annalen der Physik* **389** (1927), no. 20 457–484.

[2] A. Abedi, N. T. Maitra, and E. K. U. Gross, *Exact factorization of the time-dependent electron-nuclear wave function*, *Phys. Rev. Lett.* **105** (2010) 123002.

[3] A. Abedi, N. T. Maitra, and E. K. U. Gross, *Correlated electron-nuclear dynamics: Exact factorization of the molecular wavefunction*, *The Journal of Chemical Physics* **137** (2012), no. 22.

[4] F. Agostini and E. K. U. Gross, *Ultrafast dynamics with the exact factorization*, *The European Physical Journal B* **94** (2021), no. 9 179.

[5] F. Jensen, *Atomic orbital basis sets*, *WIREs Computational Molecular Science* **3** (2013), no. 3 273–295.

[6] F. Bloch, *Über die quantenmechanik der elektronen in kristallgittern*, *Zeitschrift für Physik* **52** (1929), no. 7 555–600.

[7] V. Fock, *Näherungsmethode zur lösung des quantenmechanischen mehrkörperproblems*, *Zeitschrift für Physik* **61** (1930), no. 1 126–148.

[8] J. C. Slater, *Note on hartree's method*, *Phys. Rev.* **35** (1930) 210–211.

[9] D. R. Hartree and W. Hartree, *Self-consistent field, with exchange, for beryllium*, *Proceedings of the Royal Society of London. Series A - Mathematical and Physical Sciences* **150** (1935), no. 869 9–33.

[10] H. Fukutome, *Unrestricted hartree–fock theory and its applications to molecules and chemical reactions*, *International Journal of Quantum Chemistry* **20** (1981), no. 5 955–1065.

[11] J. Stuber and J. Paldus, *Symmetry Breaking in the Independent Particle Model*, vol. 1, pp. 67–139. 2003.

[12] C. C. J. Roothaan, *New developments in molecular orbital theory*, *Rev. Mod. Phys.* **23** (1951) 69–89.

[13] C. C. J. Roothaan, *Self-consistent field theory for open shells of electronic systems*, *Rev. Mod. Phys.* **32** (1960) 179–185.

[14] J. A. Pople and R. K. Nesbet, *Self-Consistent Orbitals for Radicals*, *The Journal of Chemical Physics* **22** (1954), no. 3 571–572.

[15] W. Duch, *Configuration interaction method: the past and future perspectives*, *Journal of Molecular Structure: THEOCHEM* **234** (1991) 27–49.

[16] C. David Sherrill and H. F. Schaefer, *The configuration interaction method: Advances in highly correlated approaches*, vol. 34 of *Advances in Quantum Chemistry*, pp. 143–269. Academic Press, 1999.

[17] P. G. Szalay, T. Müller, G. Gidofalvi, H. Lischka, and R. Shepard, *Multiconfiguration self-consistent field and multireference configuration interaction methods and applications*, *Chemical Reviews* **112** (2012), no. 1 108–181. PMID: 22204633.

[18] D. Cremer, *From configuration interaction to coupled cluster theory: The quadratic configuration interaction approach*, *WIREs Computational Molecular Science* **3** (2013), no. 5 482–503.

[19] N. Oliphant and L. Adamowicz, *Multireference coupled cluster method for electronic structure of molecules*, *International Reviews in Physical Chemistry* **12** (1993), no. 2 339–362.

[20] R. J. Bartlett and M. Musiał, *Coupled-cluster theory in quantum chemistry*, *Rev. Mod. Phys.* **79** (2007) 291–352.

[21] P. Cársky, J. Paldus, and J. Pittner, *Recent Progress in Coupled Cluster Methods: Theory and Applications*. Challenges and Advances in Computational Chemistry and Physics. Springer Netherlands, 2012.

[22] D. I. Lyakh, M. Musiał, V. F. Lotrich, and R. J. Bartlett, *Multireference nature of chemistry: The coupled-cluster view*, *Chemical Reviews* **112** (2012), no. 1 182–243. PMID: 22220988.

[23] I. Y. Zhang and A. Grüneis, *Coupled cluster theory in materials science*, *Frontiers in Materials* **6** (2019) 1–13.

[24] C. Møller and M. S. Plesset, *Note on an approximation treatment for many-electron systems*, *Phys. Rev.* **46** (1934) 618–622.

[25] K. A. Brueckner, *Many-body problem for strongly interacting particles. ii. linked cluster expansion*, *Phys. Rev.* **100** (1955) 36–45.

[26] J. O. Hirschfelder, W. B. Brown, and S. T. Epstein, *Recent developments in perturbation theory*, vol. 1 of *Advances in Quantum Chemistry*, pp. 255–374. Academic Press, 1964.

[27] P.-O. Löwdin, *Studies in perturbation theory. x. lower bounds to energy eigenvalues in perturbation-theory ground state*, *Phys. Rev.* **139** (1965) A357–A372.

[28] K. F. Freed, *Many-body theories of the electronic structure of atoms and molecules*, *Annual Review of Physical Chemistry* **22** (1971), no. 1 313–346.

[29] M. Head-Gordon, J. A. Pople, and M. J. Frisch, *Mp2 energy evaluation by direct methods*, *Chemical Physics Letters* **153** (1988), no. 6 503–506.

[30] D. Cremer, *Møller–plesset perturbation theory: from small molecule methods to methods for thousands of atoms*, *WIREs Computational Molecular Science* **1** (2011), no. 4 509–530.

[31] L. H. Thomas, *The calculation of atomic fields*, *Mathematical Proceedings of the Cambridge Philosophical Society* **23** (1927), no. 5 542–548.

[32] E. Fermi, *Statistical method to determine some properties of atoms*, *Rend. Accad. Naz. Lincei* **6** (1927), no. 602-607 5.

[33] P. Hohenberg and W. Kohn, *Inhomogeneous electron gas*, *Physical Review* **136** (1964), no. 3B B864–B871.

[34] W. Kohn and L. J. Sham, *Self-consistent equations including exchange and correlation effects*, *Physical Review* **140** (1965), no. 4A A1133–A1138.

[35] R. M. Dreizler and E. K. U. Gross, *Density functional theory: an approach to the quantum many-body problem*. Springer, Berlin, 1990.

[36] R. G. Parr and Y. Weitao, *Density-Functional Theory of Atoms and Molecules*. Oxford University Press, USA, 1994.

[37] R. M. Martin, *Electronic Structure: Basic Theory and Practical Methods*. Cambridge University Press, 2 ed., 2020.

[38] M. Levy, *Universal variational functionals of electron densities, first-order density matrices, and natural spin-orbitals and solution of the v-representability problem*, *Proceedings of the National Academy of Sciences* **76** (1979), no. 12 6062–6065.

[39] M. Levy, *Electron densities in search of hamiltonians*, *Phys. Rev. A* **26** (1982) 1200–1208.

[40] E. H. Lieb, *Density functionals for coulomb systems*, *International Journal of Quantum Chemistry* **24** (1983), no. 3 243–277.

[41] J. C. Slater, *A simplification of the hartree-fock method*, *Phys. Rev.* **81** (1951) 385–390.

[42] J. P. Perdew, A. Ruzsinszky, J. Tao, V. N. Staroverov, G. E. Scuseria, and G. I. Csonka, *Prescription for the design and selection of density functional approximations: More constraint satisfaction with fewer fits*, *The Journal of Chemical Physics* **123** (2005), no. 6 062201.

[43] N. Mardirossian and M. Head-Gordon, *Thirty years of density functional theory in computational chemistry: an overview and extensive assessment of 200 density functionals*, *Molecular Physics* **115** (2017), no. 19 2315–2372.

[44] D. Golze, M. Dvorak, and P. Rinke, *The gw compendium: A practical guide to theoretical photoemission spectroscopy*, *Frontiers in Chemistry* **7** (2019) 1–66.

[45] T. Koopmans, *Über die zuordnung von wellenfunktionen und eigenwerten zu den einzelnen elektronen eines atoms*, *Physica* **1** (1934), no. 1 104–113.

[46] A. Szabo and N. S. Ostlund, *Modern Quantum Chemistry: Introduction to Advanced Electronic Structure Theory*. Dover Publications, Inc., Mineola, first ed., 1996.

[47] J. F. Janak, *Proof that* $\frac{\partial e}{\partial n_i} = \epsilon$ *in density-functional theory*, *Phys. Rev. B* **18** (1978) 7165–7168.

[48] W. G. Aulbur, L. Jönsson, and J. W. Wilkins, *Quasiparticle calculations in solids*, vol. 54 of *Solid State Physics*, pp. 1–218. Academic Press, 2000.

[49] P. Mori-Sánchez and A. J. Cohen, *The derivative discontinuity of the exchange–correlation functional*, *Physical Chemistry Chemical Physics* **16** (2014), no. 28 14378–14387.

[50] R. M. Martin, L. Reining, and D. M. Ceperley, *Interacting Electrons: Theory and Computational Approaches*. Cambridge University Press, 2016.

[51] F. Aryasetiawan and O. Gunnarsson, *The gw method*, *Reports on Progress in Physics* **61** (1998), no. 3 237.

[52] C. Friedrich and A. Schindlmayr, *Many-body perturbation theory: The GW approximation*, vol. 31 of *NIC Series*, p. 335–355. John von Neumann Institute for Computing, 2006.

[53] P. Romaniello, F. Bechstedt, and L. Reining, *Beyond the gw approximation: Combining correlation channels*, *Phys. Rev. B* **85** (2012) 155131.

[54] C. Mejuto-Zaera and V. c. v. Vlček, *Self-consistency in gw*Γ *formalism leading to quasiparticle-quasiparticle couplings*, *Phys. Rev. B* **106** (2022) 165129.

[55] M. J. van Setten, F. Caruso, S. Sharifzadeh, X. Ren, M. Scheffler, F. Liu, J. Lischner, L. Lin, J. R. Deslippe, S. G. Louie, C. Yang, F. Weigend, J. B. Neaton, F. Evers, and P. Rinke, *Gw100: Benchmarking g0w0 for molecular systems*, *Journal of Chemical Theory and Computation* **11** (2015), no. 12 5665–5687.

[56] F. Caruso, M. Dauth, M. J. van Setten, and P. Rinke, *Benchmark of gw approaches for the gw100 test set*, *Journal of Chemical Theory and Computation* **12** (2016), no. 10 5076–5087.

[57] M. Govoni and G. Galli, *Gw100: Comparison of methods and accuracy of results obtained with the west code*, *Journal of Chemical Theory and Computation* **14** (2018), no. 4 1895–1909.

[58] C. Rostgaard, K. W. Jacobsen, and K. S. Thygesen, *Fully self-consistent gw calculations for molecules*, *Physical Review B* **81** (2010), no. 8 085103.

[59] Y.-W. Chang and B.-Y. Jin, *Correlation effects of π electrons on the band structures of conjugated polymers using the self-consistent gw approximation with vertex corrections*, *The Journal of Chemical Physics* **136** (2012), no. 2 024110.

[60] W. Chen and A. Pasquarello, *Band-edge positions in gw: Effects of starting point and self-consistency*, *Phys. Rev. B* **90** (2014) 165133.

[61] C. Mejuto-Zaera and V. Vlček, *Self-consistency in gwΓ formalism leading to quasiparticle-quasiparticle couplings*, *Phys. Rev. B* **106** (2022) 165129.

[62] V. Vlček, *Stochastic vertex corrections: Linear scaling methods for accurate quasiparticle energies*, *Journal of Chemical Theory and Computation* **15** (2019), no. 11 6254–6266.

[63] M. S. Hybertsen and S. G. Louie, *Ab initio static dielectric matrices from the density-functional approach. i. formulation and application to semiconductors and insulators*, *Phys. Rev. B* **35** (1987) 5585–5601.

[64] R. Del Sole, L. Reining, and R. W. Godby, *GwΓ approximation for electron self-energies in semiconductors and insulators*, *Phys. Rev. B* **49** (1994) 8024–8028.

[65] F. Bruneval, F. Sottile, V. Olevano, R. Del Sole, and L. Reining, *Many-body perturbation theory using the density-functional concept: Beyond the gw approximation*, *Phys. Rev. Lett.* **94** (2005) 186402.

[66] P. Romaniello, S. Guyot, and L. Reining, *The self-energy beyond gw: Local and nonlocal vertex corrections*, *The Journal of Chemical Physics* **131** (2009), no. 15 154111.

Chapter 3

Methodology

3.1 Perturbative corrections to mean-field eigenvalues

Chapter 2 introduces the one-body Green's function, which encapsulates information about quasiparticles and QP excitation energies appearing in the Lehmann representation

$$G(\mathbf{r}_1, \mathbf{r}_2; \omega) = \sum_j \frac{\phi_j(\mathbf{r}_1)\phi_j{}^*(\mathbf{r}_2)}{\omega - \varepsilon_j^{\mathrm{QP}} + \mathrm{i}\eta \mathrm{sgn}(\varepsilon_j^{\mathrm{QP}} - \mu)}, \tag{3.1}$$

where μ denotes the chemical potential, and η is an infinitesimally small number. Depending on the sign of $(\varepsilon_j^{\mathrm{QP}} - \mu)$, the sign function "sgn", stemming from the transformation of the Heaviside step function in Eq. (2.126), gives "1" for states above μ (electron) and "-1" for states below μ (hole). The QP states ϕ_j (either quasi-hole or quasi-electron) in the numerator above satisfy the following eigenvalue equation

$$\left[-\frac{\nabla^2}{2} + \hat{v}_{\mathrm{ext}} + \hat{\Sigma}_H + \hat{\Sigma}_{\mathrm{XC}}(\omega = \varepsilon_j^{\mathrm{QP}})\right] |\phi_j\rangle = \varepsilon_j^{\mathrm{QP}} |\phi_j\rangle \,, \tag{3.2}$$

where all quantum many-body effects are accounted in the nonlocal and dynamical exchange–correlation self-energy $\hat{\Sigma}_{\mathrm{XC}}$.

To access the QP excitation spectrum, one can solve the frequency-dependent Green's function directly with the many-body wavefunctions of the neutral (N-electron) and the charged ($N \pm 1$-electron) systems; Chapter 9 presents a collaborative work where the full valence spectrum is obtained from the Green's function solved by the adaptive-sampling configuration interaction approach. The approach is equivalent to solving the ground- and excited-state wavefunction using nearly full CI, which is limited to small molecules due to steep scaling in computational cost.

An alternative and practical way to obtain quasiparticle energies is applying perturbative corrections to the mean-field eigenvalues ε^0 from an auxiliary starting point, e.g., Hartree–Fock or KS-DFT calculations. The issue plaguing the eigenvalues is attributed to the insufficient mean-field description of electron–electron interactions embodied in the local/semical exchange–correlation (XC) potential $\hat{v}_{\mathrm{xc}}$. The corrections replace $\hat{v}_{\mathrm{xc}}$ in ε_j^0 with the nonlocal and dynamical XC self-energy operator $\hat{\Sigma}_{\mathrm{XC}}(\omega)$, yielding the following QP energy

$$\varepsilon_j^{\mathrm{QP}} = \langle \phi_j^0 | \varepsilon_j^0 - \hat{v}_{\mathrm{xc}} + \hat{\Sigma}_{\mathrm{XC}}(\omega = \varepsilon_j^{\mathrm{QP}}) | \phi_j^0 \rangle \,. \tag{3.3}$$

Here, the GW approximation (see Section 2.7 in Chapter 2) is employed to compute the expectation value of $\hat{\Sigma}_{\mathrm{XC}}$ in the real-time domain

$$\langle \phi_j^0 | \hat{\Sigma}_{\mathrm{XC}}(t) | \phi_j^0 \rangle = \langle \phi_j^0 | \mathrm{i}\hat{G}(t)\hat{W}(t) | \phi_j^0 \rangle \,, \tag{3.4}$$

where the mean-field eigenstate ϕ_j^0 is a legitimate approximation to the real quasiparticle Dyson orbital, and only the diagonal terms of the XC self-energy matrix are considered. Note that in the Hedin's pentagon (Figure 2.6), all the five quantities, including $\hat{\Sigma}_{\mathrm{XC}}$,

need to be solved self-consistently. However, this dissertation focuses on the one-shot approximation (G_0W_0) only and does not consider self-consistency due to the non-linearity of the problem.

Note that the time-dependent correlation self-energy $\hat{\Sigma}_{\mathrm{XC}}(t)$ above needs to be time-ordered i.e., t spans both the negative and positive axes. This requires both $\hat{G}_0(t)$ and $\hat{W}_0(t)$ to be time-ordered.

Similar to the fully interacting Green's function in Eq. (2.125), the non-interacting Green's function $\hat{G}_0$ has the following form

$$G_0(\mathbf{r}_1, \mathbf{r}_2; t) = \begin{cases} \mathrm{i} \sum_a^{N_{\mathrm{occ}}} \phi_a^0(\mathbf{r}_1, t) \phi_a^{0*}(\mathbf{r}_2) & t < 0 \\ -\mathrm{i} \sum_r^{N_{\mathrm{uno}}} \phi_r^0(\mathbf{r}_1, t) \phi_r^{0*}(\mathbf{r}_2) & t > 0 \end{cases}, \tag{3.5}$$

where $\phi_k^0(\mathbf{r}, t) = e^{-\mathrm{i}\varepsilon_k^0 t} \phi_k^0(\mathbf{r})$. The time-ordering of $\hat{G}_0(t)$ is simply done by flipping the sign in the time-evolution operator for the Trotter propagation

$$|\phi_a^0(t - \mathrm{d}t)\rangle = e^{\mathrm{i}\varepsilon_a^0 \mathrm{d}t} |\phi_a^0(t)\rangle \,, \tag{3.6}$$

$$|\phi_r^0(t + \mathrm{d}t)\rangle = e^{-\mathrm{i}\varepsilon_r^0 \mathrm{d}t} |\phi_r^0(t)\rangle \,. \tag{3.7}$$

Here, the hole (occupied) states fill the negative time domain, while the electron (unoccupied) states fill the positive time domain. This discrepancy follows simply the time-ordering of the field operators in Eq. (2.110).

$\hat{W}_0(t)$ denotes the screened Coulomb potential with the two-point polarizability χ_0 computed at the random phase approximation (RPA) level

$$W_0(\mathbf{r}_1, \mathbf{r}_2; t) = \nu(\mathbf{r}_1, \mathbf{r}_2)\delta(t) + \int\int \nu(\mathbf{r}_1, \mathbf{r}_3)\chi_0(\mathbf{r}_4, \mathbf{r}_3; t)\nu(\mathbf{r}_4, \mathbf{r}_2)\mathrm{d}\mathbf{r}_3\mathrm{d}\mathbf{r}_4. \tag{3.8}$$

Here, $\nu(\mathbf{r}_1, \mathbf{r}_2)$ is the bare Coulomb kernel. The convolution with $\hat{G}_0(t)$ yields the instantaneous and static exchange interaction

$$\langle \phi_j^0 | \hat{G}_0(t) \hat{\nu} \delta(t) | \phi_j^0 \rangle = - \int \int \frac{\phi_j^{0*}(\mathbf{r}_1) \rho(\mathbf{r}_1, \mathbf{r}_2) \phi_j^0(\mathbf{r}_2)}{|\mathbf{r}_1 - \mathbf{r}_2|} \mathrm{d}\mathbf{r}_1 \mathrm{d}\mathbf{r}_2, \tag{3.9}$$

where $\rho(\mathbf{r}_1, \mathbf{r}_2)$ is the non-interacting one-body density matrix

$$\rho(\mathbf{r}_1, \mathbf{r}_2) = \langle \mathbf{r}_1 | \sum_a^{N_{\mathrm{occ}}} | \phi_a^0 \rangle \langle \phi_a^0 | \mathbf{r}_2 \rangle . \tag{3.10}$$

The exchange interaction in Eq. (3.9) is equivalent to the nonlocal exchange in the Fock operator in the Hartree–Fock approximation.

In the second term on the right-hand side of Eq. (3.8), $\chi_0(\mathbf{r}_4, \mathbf{r}_3; t)$ is the time-ordered non-interacting two-point polarizability resulting in the following time-ordered polarization potential u_{P}

$$u_{\mathrm{P}}(\mathbf{r}_1, t; k) = \int \int \int \nu(\mathbf{r}_1, \mathbf{r}_3) \chi_0(\mathbf{r}_4, \mathbf{r}_3; t) \nu(\mathbf{r}_4, \mathbf{r}_2) \phi_k^{0*}(\mathbf{r}_2) \phi_j^0(\mathbf{r}_2) \mathrm{d}\mathbf{r}_2 \mathrm{d}\mathbf{r}_3 \mathrm{d}\mathbf{r}_4, \tag{3.11}$$

where ϕ_k^0 comes from the convolution with $\hat{G}_0$. The polarization potential here is induced by an external charge $(\phi_k^{0*} \phi_j^0)$ at $\mathbf{r}_2$ and $t = 0$. In this dissertation, only the linear response is considered in u_{P}, and the time-ordered u_{P} is obtained from a *retarded* potential u_{P}^R

$$u_{\mathrm{P}}^R(\mathbf{r}, t; k) = \frac{v_H^\lambda(\mathbf{r}, t; k) - v_H^0(\mathbf{r})}{\lambda}, \tag{3.12}$$

where λ is a small real number representing the strength of perturbation induced by the external charge at $\mathbf{r}_2$ and $t = 0$. The static and time-dependent Hartree potentials, $v_H^0(\mathbf{r})$

and $v_H^\lambda(\mathbf{r}, t; k)$ above, are given by

$$v_H^0(\mathbf{r}) = \int \nu(\mathbf{r}, \mathbf{r}') n_0(\mathbf{r}') \mathrm{d}\mathbf{r}', \tag{3.13}$$

and

$$v_H^\lambda(\mathbf{r}, t) = \int \nu(\mathbf{r}, \mathbf{r}') n^\lambda(\mathbf{r}', t; k) \mathrm{d}\mathbf{r}'. \tag{3.14}$$

Here, $n_0(\mathbf{r})$ is simply the ground-state charge density

$$n_0(\mathbf{r}) = \sum_a^{N_{\mathrm{occ}}} \phi_a^{0*}(\mathbf{r}) \phi_a^0(\mathbf{r}). \tag{3.15}$$

The perturbed and time-evolved charge density $n^\lambda(\mathbf{r}, t; k)$ is computed through the following procedure

(1) at $t = 0$, the single-particle states are perturbed by the electron removal (or addition)

$$|\phi_j^\lambda\rangle = e^{-\mathrm{i}\lambda \hat{v}_{\mathrm{pert}} \delta(t)} |\phi_j^0\rangle, \tag{3.16}$$

where the perturbing potential is given by $v_{\mathrm{pert}}(\mathbf{r}) = \int \nu(\mathbf{r}, \mathbf{r}') \phi_k^{0*}(\mathbf{r}') \phi_j^0(\mathbf{r}') \mathrm{d}\mathbf{r}'$.

(2) the perturbed states are then propagated in time using a Trotter split-operator technique

$$|\phi_j^\lambda(t + \mathrm{d}t)\rangle = e^{-\mathrm{i}\hat{H}(t)\mathrm{d}t} |\phi_j^\lambda(t)\rangle, \tag{3.17}$$

where t starts from 0, and the Hamiltonian $\hat{H}$ is time-dependent (detailed in the following).

(3) analogous to $n_0(\mathbf{r})$, $n(\mathbf{r},t)$ is derived from the time-evolved single-particle states

$$n^{\lambda}(\mathbf{r},t;k) = \sum_{a}^{N_{\mathrm{occ}}} |\phi_a^{\lambda}(\mathbf{r},t)|^2. \tag{3.18}$$

Using Eqs. (3.13) and (3.14), the retarded polarization potential can be written as

$$u_{\mathrm{P}}^{R}(\mathbf{r},t;k) = \int \nu(\mathbf{r},\mathbf{r}')\delta n(\mathbf{r}',t;k)\mathrm{d}\mathbf{r}', \tag{3.19}$$

which in fact corresponds to the induced dipole–dipole interactions. $\delta n(\mathbf{r}',t;k)$ is the induced density fluctuations renormalized by λ

$$\delta n(\mathbf{r},t;k) = \frac{1}{\lambda}\left[n^{\lambda}(\mathbf{r},t;k) - n_0(\mathbf{r})\right]. \tag{3.20}$$

In the real-time propagation procedure shown above, the time-dependent Hamiltonian $\hat{H}(t)$ in Eq. (3.17) plays a critical role in the dynamical response of the charge density to the electron removal/addition. At the G_0W_0 level, $\hat{H}(t)$ contains a time-dependent Hartree potential $\hat{v}_H(t)$ [Eq. (3.14)] only

$$\hat{H}(t) = \hat{T} + \hat{v}_{\mathrm{ext}} + \hat{v}_H[n^{\lambda}(t),t] + \hat{v}_{\mathrm{xc}}[n_0], \tag{3.21}$$

where $\hat{v}_{\mathrm{xc}}$ is simply the static mean-field exchange–correlation potential depending on the ground-state density. This time-dependent Hartree approach is also known as RPA mentioned in Chapter 2.

The retarded potential $u_{\mathrm{P}}^{R}(\mathbf{r},t;k)$ is only defined in the positive time domain. To obtain the time-ordered polarization potential $u_{\mathrm{P}}(\mathbf{r},t;k)$, a Fourier transformation is first

performed on $u_{\mathrm{P}}^{R}(\mathbf{r},t;k)$

$$u_{\mathrm{P}}^{R}(\mathbf{r},\omega;k)=\int_{0}^{\infty}e^{-\frac{1}{2}\alpha^{2}t^{2}}e^{-\mathrm{i}\omega t}u_{\mathrm{P}}^{R}(\mathbf{r},t;k)\mathrm{d}t. \tag{3.22}$$

Next, the frequency-dependent non-retarded potential $u_{\mathrm{P}}(\mathbf{r},\omega;k)$ is given by

$$u_{\mathrm{P}}(\mathbf{r},\omega;k)=\begin{cases}u_{\mathrm{P}}^{R}(\mathbf{r},\omega;k) & \omega\geq 0\\ [u_{\mathrm{P}}^{R}(\mathbf{r},\omega;k)]^{*} & \omega<0\end{cases}. \tag{3.23}$$

Finally, $u_{\mathrm{P}}(\mathbf{r},t;k)$ in the positive and negative time domain is obtained by Fourier transforming $u_{\mathrm{P}}(\mathbf{r},\omega;k)$

$$u_{\mathrm{P}}(\mathbf{r},t;k)=\frac{1}{2\pi}\int_{-\infty}^{\infty}e^{\mathrm{i}\omega t}u_{\mathrm{P}}(\mathbf{r},\omega;k)\mathrm{d}\omega. \tag{3.24}$$

After u_{P} is time-ordered, the time-dependent G_0W_0 correlation self-energy for a specific state ϕ_j^0 reads

$$\Sigma_{\mathrm{C},j}(t)=\sum_{k}\mathrm{sgn}(\varepsilon_k^0-\mu)\int\phi_j^0(\mathbf{r})\phi_k^0(\mathbf{r},t)u_{\mathrm{P}}(\mathbf{r},t;k)\mathrm{d}\mathbf{r}. \tag{3.25}$$

In practice, $\Sigma_{\mathrm{C},j}(t)$ is Fourier transformed to the frequency domain for solving the QP energy

$$\Sigma_{\mathrm{C},j}(\omega)=\int_{-\infty}^{\infty}e^{-\mathrm{i}\omega t}\Sigma_{\mathrm{C},j}(t)\mathrm{d}t. \tag{3.26}$$

Next, the outside vertex correction $\Sigma_{\mathrm{C},j}^{\Gamma}(t)$ can be introduced to the G_0W_0 self-energy in a similar way. The derivation of $\Sigma_{\mathrm{C},j}^{\Gamma}(t)$ is similar to that of $\Sigma_{\mathrm{C},j}(t)$, starting from a bare nonlocal exchange

$$\Sigma_{\mathrm{X}}(\mathbf{r}_1,\mathbf{r}_2)=-\nu(\mathbf{r}_1,\mathbf{r}_2)\rho(\mathbf{r}_1,\mathbf{r}_2). \tag{3.27}$$

$\Sigma^{\Gamma}_{\mathrm{C},j}(t)$ is given by the following equation

$$\Sigma^{\Gamma}_{\mathrm{C},j}(t) = \sum_k \mathrm{sgn}(\varepsilon^0_k - \mu)\, \langle \phi^0_j \phi^0_k(t) | \hat{\nu}\ {}^3\hat{\chi}(t) \hat{\nu} | \phi^0_k \phi^0_j \rangle\,, \tag{3.28}$$

where ${}^3\hat{\chi}(t)$ is the time-ordered three-point polarizability derived from the functional derivative of Σ_{X} with respect to G (see Section 2.7 in Chapter 2).

In the real space-time representation, the individual term in the sum of Eq. (3.28) reads

$$\Sigma^{\Gamma}_{\mathrm{C},j}(t;k) = \int\int \phi^{0*}_j(\mathbf{r}_2)\phi^0_k(\mathbf{r}_1,t) u_{\mathrm{X}}(\mathbf{r}_1,\mathbf{r}_2,t;k) \mathrm{d}\mathbf{r}_1 \mathrm{d}\mathbf{r}_2, \tag{3.29}$$

where u_{X} is the time-ordered induced-exchange potential given by

$$u_{\mathrm{X}}(\mathbf{r}_1,\mathbf{r}_2,t;k) = \int\int \nu(\mathbf{r}_1,\mathbf{r}_3)\ {}^3\chi(\mathbf{r}_4,\mathbf{r}_2,\mathbf{r}_3;t)\nu(\mathbf{r}_4,\mathbf{r}_2)\phi^{0*}_k(\mathbf{r}_4)\phi^0_j(\mathbf{r}_4)\mathrm{d}\mathbf{r}_3\mathrm{d}\mathbf{r}_4. \tag{3.30}$$

Analogous to $u_{\mathrm{P}}(\mathbf{r},t;k)$, $u_{\mathrm{X}}(\mathbf{r}_1,\mathbf{r}_2,t;k)$ is obtained from a retarded potential in the linear response regime

$$u^R_{\mathrm{X}}(\mathbf{r}_1,\mathbf{r}_2,t;k) = \frac{\rho^{\lambda}(\mathbf{r}_1,\mathbf{r}_2,t;k) - \rho_0(\mathbf{r}_1,\mathbf{r}_2)}{\lambda}\nu(\mathbf{r}_1,\mathbf{r}_2), \tag{3.31}$$

where $\rho_0(\mathbf{r}_1,\mathbf{r}_2)$ is the ground-state one-body density matrix [Eq. (3.10)]. The set of perturbed and time-evolved single-particle states [Eqs. (3.16)-(3.18)] used in $n^{\lambda}(\mathbf{r},t;k)$ also applies to the construction of the time-dependent density matrix

$$\rho^{\lambda}(\mathbf{r}_1,\mathbf{r}_2,t;k) = \sum_a^{N_{\mathrm{occ}}} \phi^{\lambda}_a(\mathbf{r}_1,t)\phi^{\lambda\,*}_a(\mathbf{r}_2,t), \tag{3.32}$$

where ϕ^{λ}_a is a state perturbed by the external potential associated with ϕ^0_k.

The time-ordered induced-exchange potential $u_{\mathrm{X}}(\mathbf{r}_1,\mathbf{r}_2,t;k)$ is then generated by the

procedure in Eqs. (3.22)-(3.24). The induced-exchange potential can also be written in term of the renormalized induced density matrix fluctuation

$$u_{\mathrm{X}}^{R}(\mathbf{r}_1, \mathbf{r}_2; t) = \nu(\mathbf{r}_1, \mathbf{r}_2)\delta\rho(\mathbf{r}_1, \mathbf{r}_2, t; k), \tag{3.33}$$

where

$$\delta\rho(\mathbf{r}_1, \mathbf{r}_2; t) = \frac{\rho^{\lambda}(\mathbf{r}_1, \mathbf{r}_2, t; k) - \rho_0(\mathbf{r}_1, \mathbf{r}_2)}{\lambda}. \tag{3.34}$$

Physically, $\delta\rho(\mathbf{r}_1, \mathbf{r}_2, t; k)$ can cancel the self-polarization error appearing in $\delta n(\mathbf{r}, t; k)$, similar to the cancellation of self-interaction error in Σ_H by Σ_{X}.

Note that the outside vertex correction above can also be derived from other forms of nonlocal exchange than the bare Hartree–Fock form, e.g, range-separated hybrid exchange functionals.[1, 2, 3] In a general way, the exchange interaction is split into two parts by

$$\begin{aligned} \frac{1}{r_{12}} &= \frac{1 - \{\alpha + \beta[1 - \mathrm{erfc}(\gamma r_{12})]\}}{r_{12}} + \frac{\alpha + \beta[1 - \mathrm{erfc}(\gamma r_{12})]}{r_{12}} \\ &= \nu_{\mathrm{S}}^{\alpha,\beta,\gamma}(\mathbf{r}_1, \mathbf{r}_2) + \nu_{\mathrm{L}}^{\alpha,\beta,\gamma}(\mathbf{r}_1, \mathbf{r}_2). \end{aligned} \tag{3.35}$$

Here, the Coulomb kernel $1/r_{12} = \nu(\mathbf{r}_1, \mathbf{r}_2)$ is partitioned into the short-range part $\nu_{\mathrm{S}}^{\alpha,\beta,\gamma}(\mathbf{r}_1, \mathbf{r}_2)$ and the long-range part $\nu_{\mathrm{L}}^{\alpha,\beta,\gamma}(\mathbf{r}_1, \mathbf{r}_2)$; α and β are empirical mixing parameters that can be related to dielectric screening properties; erfc(x) is the complementary error function that connect smoothly the long-range and short-range parts; γ denotes the range separation parameter that is either constant or optimally tuned based on the ionization potential (IP) theorem. The nonlocal exchange interaction appears only in the long-range part, while the short-range part is treated with local/semilocal exchange functionals. Hence, only the long-range nonlocal exchange contributes to the outside

vertex correction, and the retarded induced-exchange potential is written as

$$u_{\mathrm{LX}}^{R}(\mathbf{r}_1, \mathbf{r}_2; t) = \nu_{\mathrm{L}}^{\alpha,\beta,\gamma}(\mathbf{r}_1, \mathbf{r}_2)\delta\rho(\mathbf{r}_1, \mathbf{r}_2; t). \tag{3.36}$$

The inclusion of inside vertex correction to the GW correlation self-energy requires evaluating the vertex function in the polarization function P (see Eq. (2.154) in Chapter 2), leading to the GW^{tc} approximation. In our real space-time approach, the GW^{tc} approach is equivalent to evaluating the time-dependent induced density fluctuation $\delta n(\mathbf{r}, t)$ beyond the random phase approximation (RPA). As the evaluation of $\delta n(\mathbf{r}, t)$ hinges upon the real-time propagation process, the time-dependent Hamiltonian contains only a time-dependent Hartree term [see Eq. (3.21)] in the RPA approach. An effective way to introduce vertex correction in the real-time formalism to $\delta n(\mathbf{r}, t)$ is to introduce a time-dependent exchange term in the Hamiltonian. In practice, one can consider using the time-dependent Hartree–Fock or the time-dependent generalized KS-DFT Hamiltonian shown below

$$\hat{H}(t) = \hat{T} + \hat{v}_{\mathrm{ext}} + \hat{v}_H\left[n^{\lambda}(t), t\right] + \hat{\Sigma}_{\mathrm{X}}\left[\rho^{\lambda}(t), t\right], \tag{3.37}$$

or

$$\hat{H}(t) = \hat{T} + \hat{v}_{\mathrm{ext}} + \hat{v}_H\left[n^{\lambda}(t), t\right] + \hat{\Sigma}_{\mathrm{X}}^{\alpha,\beta,\gamma}\left[\rho^{\lambda}(t), t\right] + \hat{v}_{\mathrm{x}}^{\alpha,\beta,\gamma}[n_0] + \hat{v}_{\mathrm{c}}[n_0]. \tag{3.38}$$

In Eq. (3.37), the time-dependent exchange interaction is unscreened (bare). In Eq. (3.38), the generalized Kohn–Sham DFT Hamiltonian employs a hybrid form of exchange functionals where the exchange kernel is partitioned by Eq. (3.35). Only the long-range exchange interaction is time-dependent, and it depends on the α and β parameters as introduced above. Chapter 10 is recommended for readers who are interested in introducing both inside and outside vertex corrections in the real-time formalism.

In summary, this section demonstrates how to obtain QP energies by adding the

nonlocal and dynamical exchange–correlation self-energy as a perturbative correction to a mean-field eigenvalue. Furthermore, the calculations of G_0W_0 correlation self-energy and the inclusion of vertex corrections (both inside and outside) are presented using the real space-time approach. In Section 3.2, I will introduce the stochastic GW and beyond formalism as a linear-scaling method applying to systems with thousands of electrons.

3.2 Stochastic formalism of correlation self-energy

The GW method introduced in the previous section has been widely used in electronic structure calculations, providing significantly improved results for ionization potentials, electron affinities, and fundamental gaps. Although the GW approach scales less rapidly as N^4 than the comparable wavefunction approaches (N^6 or higher), its applications are still highly limited to simple solids and small molecules. The cost of GW can be analyzed from the two following perspectives in the real space-time approach

(1) the sum of all states in the non-interacting Green's function in Eq. (3.25). The summation over k here spans the entire Hilbert space, including both occupied and virtual states. The number of occupied states is definite, while the number of virtual states is not. In pratice, the number of states constituting G_0 needs to be converged by setting an energy cutoff. In real-space implementations, the dimension of the summation corresponds to the grid size, which can be over 10 million for nanoscale systems.

(2) the stepwise time evolution of each single-particle state for the time-dependent induced density fluctuation $\delta n(\mathbf{r}, t)$. This procedure involves the occupied states only and depends on the number of discrete propagation steps and the length of propagation time. The cost of propagation becomes much higher if the time-

dependent exchange interaction is also included in the Hamiltonian.

Recent developments in high-performance computing[4, 5, 6] and algorithm optimization[7, 8, 9, 10, 11, 12, 13, 14, 15, 16, 17, 18] have remarkably accelerated the GW calculations and make GW more affordable for large molecules and realistic materials. In the following, I review the linear-scaling stochastic formalism for computing GW correlation self-energy and beyond.[19, 20, 21, 22, 23, 24, 25, 26, 27, 28] Particularly, the derivations focus on the stochastic non-interacting Green's function $G_0(t)$ and the induced density and density matrix fluctuations $\delta n(\mathbf{r}, t)$ and $\delta\rho(\mathbf{r}, \mathbf{r}'; t)$.

In a real-space GW calculation, the grid size N_g is given by the following product

$$N_\mathrm{g} = N_x \times N_y \times N_z, \tag{3.39}$$

where N_x, N_y, and N_z represent the number of grid points in the three orthogonal directions of a rectangular box, respectively. The unit volume is the product of the grid spacing in each direction

$$\mathrm{d}V = \mathrm{d}x \times \mathrm{d}y \times \mathrm{d}z. \tag{3.40}$$

The core step to perform a stochastic sampling is to generate a real-value random function in the real-space grid of the following form

$$\bar{\zeta}(\mathbf{r}) = \pm\frac{1}{\sqrt{\mathrm{d}V}}, \tag{3.41}$$

where the $\pm$ sign embodies the randomness as each sign is of an equal probability, and $\sqrt{\mathrm{d}V}$ is the renormalization factor leading to

$$\int |\bar{\zeta}(\mathbf{r})|^2 \mathrm{d}V = N_\mathrm{g}, \tag{3.42}$$

which corresponds to the dimension of the entire Hilbert space.

The random function $\bar{\zeta}(\mathbf{r})$ can also be written in the following vector form

$$|\bar{\zeta}\rangle = \frac{1}{\sqrt{\mathrm{d}V}} \left[\pm 1, \pm 1, \pm 1, \ldots, \pm 1\right]^{\mathrm{T}}, \tag{3.43}$$

the dimension of which is N_{g}. Furthermore, the following random matrix can be generated from such a random vector

$$|\bar{\zeta}\rangle \langle\bar{\zeta}| = \frac{1}{\mathrm{d}V} \begin{bmatrix} 1 & \pm 1 & \pm 1 & \ldots & \pm 1 \\ \pm 1 & 1 & \pm 1 & \ldots & \pm 1 \\ \pm 1 & \pm 1 & 1 & \ldots & \pm 1 \\ \ldots & \ldots & \ldots & \ldots & \ldots \\ \pm 1 & \pm 1 & \pm 1 & \ldots & 1 \end{bmatrix}. \tag{3.44}$$

In this matrix, the diagonal elements are definitely "1." However, the off-diagonal elements are indefinite, with an equal probability of being "1" or "-1" depending on the actual $\bar{\zeta}$. Based on the distinct features between the diagonal and off-diagonal elements, it can be deduced that the sum of infinitely many random matrices of this form reads

$$\lim_{N_{\bar{\zeta}} \to \infty} \sum_{i=1}^{N_{\bar{\zeta}}} |\bar{\zeta}_i\rangle \langle\bar{\zeta}_i| = \frac{N_{\bar{\zeta}}}{\mathrm{d}V} \begin{bmatrix} 1 & 0 & 0 & \ldots & 0 \\ 0 & 1 & 0 & \ldots & 0 \\ 0 & 0 & 1 & \ldots & 0 \\ \ldots & \ldots & \ldots & \ldots & \ldots \\ 0 & 0 & 0 & \ldots & 1 \end{bmatrix}. \tag{3.45}$$

Eq. (3.45) can be expressed in a shorthand version

$$\langle\mathbf{r}| \left\{ |\bar{\zeta}_i\rangle \langle\bar{\zeta}_i| \right\} |\mathbf{r}'\rangle = \frac{1}{\mathrm{d}V} \delta_{\mathbf{r},\mathbf{r}'}, \tag{3.46}$$

where $\delta_{\mathbf{r},\mathbf{r}'}$ is a Kronecker delta function; the curly brackets $\{\dots\}$ denote taking a statistical average over $N_{\bar{\zeta}}$ random matrices

$$\left\{|\bar{\zeta}_i\rangle\langle\bar{\zeta}_i|\right\} = \frac{1}{N_{\bar{\zeta}}}\lim_{N_{\bar{\zeta}}\to\infty}\sum_{i=1}^{N_{\bar{\zeta}}}|\bar{\zeta}_i\rangle\langle\bar{\zeta}_i|\,. \tag{3.47}$$

In short, the random vectors are constructed to satisfy the following stochastic resolution of identity (neglecting the trivial prefactor $\mathrm{d}V$)

$$\hat{I} = \left\{|\bar{\zeta}_i\rangle\langle\bar{\zeta}_i|\right\}, \tag{3.48}$$

where the dimension of the identity matrix is N_{g}^2. The stochastic resolution of identity here is a critical and useful expression derived from a set of random vectors, as $\hat{I}$ can be inserted in front of, in between, or after any operators without changing the operations. First of all, the ground-state density can be recovered by a set of random vectors using $\hat{I}$ in Eq. (3.48) in the following procedure

(1) the ground-state density can be written in terms of the occupied space operator

$$n_0(\mathbf{r}) = \langle\mathbf{r}|\hat{P}^{\mathrm{occ}}|\mathbf{r}\rangle\,. \tag{3.49}$$

Using the idempotency of $\hat{P}^{\mathrm{occ}}$, it holds that

$$n_0(\mathbf{r}) = \langle\mathbf{r}|\hat{P}^{\mathrm{occ}}\hat{P}^{\mathrm{occ}}|\mathbf{r}\rangle\,. \tag{3.50}$$

(2) the stochastic resolution of identity can be inserted in between the two $\hat{P}^{\mathrm{occ}}$ operators in Eq. (3.50)

$$n_0(\mathbf{r}) = \left\{\langle\mathbf{r}|\hat{P}^{\mathrm{occ}}|\bar{\zeta}_i\rangle\langle\bar{\zeta}_i|\hat{P}^{\mathrm{occ}}|\mathbf{r}\rangle\right\}. \tag{3.51}$$

(3) a random ket state projected onto the occupied space can then be defined based on Eq. (3.51)

$$|\zeta_i\rangle = \hat{P}^{\text{occ}} |\bar{\zeta}_i\rangle = \sum_a^{N_{\text{occ}}} \langle \phi_a^0 | \bar{\zeta}_i \rangle \, |\phi_a^0\rangle = \sum_a^{N_{\text{occ}}} \beta_{ai} \, |\phi_a^0\rangle \, . \tag{3.52}$$

Similarly, the corresponding bra state is given by

$$\langle \bar{\zeta}_i | \, \hat{P}^{\text{occ}} = \sum_a^{N_{\text{occ}}} \langle \phi_a^0 | \, \langle \bar{\zeta}_i | \phi_a^0 \rangle = \sum_a^{N_{\text{occ}}} \langle \phi_a^0 | \, \beta_{ia}^* = \langle \zeta_i | \, . \tag{3.53}$$

(4) plugging Eqs. (3.52) and (3.53) into Eq. (3.51), the stochastic resolution of the ground-state density reads

$$n_0(\mathbf{r}) = \{ \langle \mathbf{r} | \zeta_i \rangle \, \langle \zeta_i | \mathbf{r} \rangle \} = \{ \zeta_i^*(\mathbf{r}) \zeta_i(\mathbf{r}) \} \, . \tag{3.54}$$

The stochastic expression for $n_0(\mathbf{r})$ can be generalized to the perturbed and time-evolved density

$$n^\lambda(\mathbf{r}, t) = \left\{ \zeta_i^{\lambda *}(\mathbf{r}, t) \zeta_i^\lambda(\mathbf{r}, t) \right\} , \tag{3.55}$$

where the set of random functions $\zeta_i(\mathbf{r})$ is perturbed and propagated in time using Eqs. (3.16) and (3.17). Note that the time-dependent Hamiltonian e.g., for RPA, is constructed using the stochastic time-dependent density. Due to the stochastic nature, the ground-state density also shows a time-dependency

$$n_0(\mathbf{r}, t) = \{ \zeta_i{}^*(\mathbf{r}, t) \zeta_i(\mathbf{r}, t) \} \, , \tag{3.56}$$

where the set of random functions are **not** perturbed and are directly evolved in time.

It is also trivial to extend the stochastic sampling to the first order density matrix for

the inclusion of vertex corrections

$$\rho_0(\mathbf{r},\mathbf{r}';t) = \{\zeta_i{}^*(\mathbf{r}',t)\zeta_i(\mathbf{r},t)\}\,, \tag{3.57}$$

and

$$\rho^\lambda(\mathbf{r},\mathbf{r}';t) = \left\{\zeta_i^{\lambda\,*}(\mathbf{r}',t)\zeta_i^\lambda(\mathbf{r},t)\right\}. \tag{3.58}$$

The time-dependent Hamiltonian that introduces the inside vertex correction is constructed using both the stochastic time-dependent density and density matrix. Eqs. (3.55) and (3.56) produce the time-dependent induced density fluctuation $\delta n(\mathbf{r},t)$ that enters Eq. (3.19) for the polarization potential; Eqs. (3.57) and (3.58) generate $\delta\rho(\mathbf{r},\mathbf{r}';t)$ entering Eq. (3.33) for the induced-exchange potential.

Next, to avoid summing over the dimension of the entire Hilbert space, the non-interacting Green's function $G_0(t)$ can also be sampled by another set of random vectors $\bar{\eta}$. For $t<0$, the expression of the hole Green's function reads

$$G_0^h(\mathbf{r},\mathbf{r}';t) = \langle\mathbf{r}|e^{-\mathrm{i}\hat{H}_0 t}\hat{P}^{\mathrm{occ}}|\mathbf{r}'\rangle\,, \tag{3.59}$$

where $\hat{H}_0$ denotes the ground-state mean-field Hamiltonian for the single-particle eigenvalue equations. Using the idempotency of $\hat{P}^{\mathrm{occ}}$ and the stochastic resolution of identity, G_0^h can also be written as

$$\begin{aligned} G_0^h(\mathbf{r},\mathbf{r}';t) &= \langle\mathbf{r}|e^{-\mathrm{i}\hat{H}_0 t}\hat{P}^{\mathrm{occ}}\hat{I}\hat{P}^{\mathrm{occ}}|\mathbf{r}'\rangle \\ &= \left\{\langle\mathbf{r}|e^{-\mathrm{i}\hat{H}_0 t}\hat{P}^{\mathrm{occ}}\,|\bar{\eta}_i\rangle\,\langle\bar{\eta}_i|\,\hat{P}^{\mathrm{occ}}|\mathbf{r}'\rangle\right\} \\ &= \{\langle\mathbf{r}|\eta_i(t)\rangle\,\langle\eta_i|\mathbf{r}'\rangle\}\,, \end{aligned} \tag{3.60}$$

where the projected vectors are defined as

$$|\eta_i\rangle = \hat{P}^{\text{occ}} |\bar{\eta}_i\rangle \,, \tag{3.61}$$

and

$$|\eta_i(t)\rangle = e^{-\mathrm{i}\hat{H}_0 t} \hat{P}^{\text{occ}} |\bar{\eta}_i\rangle \,. \tag{3.62}$$

For the electron Green's function ($t > 0$), the derivation of the stochastic expression is analogous, starting from

$$G_0^e(\mathbf{r}, \mathbf{r}'; t) = \langle \mathbf{r} | e^{-\mathrm{i}\hat{H}_0 t} \hat{P}^{\text{uno}} | \mathbf{r}' \rangle \,, \tag{3.63}$$

where the unoccupied subspace operator is the complement of $\hat{P}^{\text{occ}}$

$$\hat{I} = \hat{P}^{\text{occ}} + \hat{P}^{\text{uno}}. \tag{3.64}$$

As $\hat{P}^{\text{uno}}$ is idempotent, the following expression holds

$$\begin{aligned} G_0^h(\mathbf{r}, \mathbf{r}'; t) &= \langle \mathbf{r} | e^{-\mathrm{i}\hat{H}_0 t} \hat{P}^{\text{uno}} \hat{I} \hat{P}^{\text{uno}} | \mathbf{r}' \rangle \\ &= \left\{ \langle \mathbf{r} | e^{-\mathrm{i}\hat{H}_0 t} \hat{P}^{\text{uno}} |\bar{\eta}_i\rangle \langle \bar{\eta}_i | \hat{P}^{\text{uno}} | \mathbf{r}' \rangle \right\} \\ &= \left\{ \langle \mathbf{r} | \eta_i'(t) \rangle \langle \eta_i' | \mathbf{r}' \rangle \right\} , \end{aligned} \tag{3.65}$$

where the projected vectors are defined as

$$|\eta_i'\rangle = \hat{P}^{\text{uno}} |\bar{\eta}_i\rangle \,, \tag{3.66}$$

and

$$|\eta_i'(t)\rangle = e^{-\mathrm{i}\hat{H}_0 t} \hat{P}^{\text{uno}} |\bar{\eta}_i\rangle \,. \tag{3.67}$$

Note that $|\bar{\eta}_i\rangle = |\eta_i\rangle + |\eta_i'\rangle$, the total $G_0(t)$ can be written in a more compact form

$$G_0(\mathbf{r}, \mathbf{r}'; t) = \{\eta_i(\mathbf{r}, t)\bar{\eta}_i^*(\mathbf{r}')\}\,, \tag{3.68}$$

where the time-evolved random function is given by

$$\eta_i(\mathbf{r}, t) = \begin{cases} \langle \mathbf{r}|e^{-\mathrm{i}\hat{H}_0 t}\hat{P}^{\mathrm{occ}}|\bar{\eta}_i\rangle & t < 0 \\ \langle \mathbf{r}|e^{-\mathrm{i}\hat{H}_0 t}(\hat{I} - \hat{P}^{\mathrm{occ}})|\bar{\eta}_i\rangle & t > 0 \end{cases}. \tag{3.69}$$

Through the procedure above, the stochastic $\hat{G}_0(t)$ is time-ordered, and the time-ordered polarization potential can also be prepared from $\delta n(\mathbf{r}, t)$ in the stochastic form. Hence, the resulting stochastic G_0W_0 correlation self-energy for a specific state ϕ_j^0 reads

$$\Sigma_{\mathrm{C},j}(t) = \left\{ \int \phi_j^{0*}(\mathbf{r})\eta_i(\mathbf{r}, t)u_{\mathrm{P}}^{\bar{\zeta},\bar{\eta}_i}(\mathbf{r}, t)\mathrm{d}\mathbf{r} \right\}. \tag{3.70}$$

Here, the statistical average is performed on two different sets of random functions, $\bar{\zeta}$ and $\bar{\eta}$; the time-dependent induced density fluctuation $\delta n(\mathbf{r}, t)$ that leads to $u_{\mathrm{P}}^{\bar{\zeta},\bar{\eta}_i}(\mathbf{r}, t)$ is sampled by the set of random vectors ζ [see Eqs. (3.55) and (3.56)], while $\bar{\eta}_i$ appears in the external potential that perturbs the ζ states

$$v_{\mathrm{pert}}^{\bar{\eta}_i}(\mathbf{r}) = \int \mathrm{d}\mathbf{r}'\nu(\mathbf{r}, \mathbf{r}')\bar{\eta}_i^*(\mathbf{r}')\phi_j^0(\mathbf{r}'). \tag{3.71}$$

The outside vertex correction to $\Sigma_{\mathrm{C},j}$ can also be written in the following stochastic form

$$\Sigma_{\mathrm{C},j}^{\Gamma}(t) = \left\{ \int\int \phi_j^{0*}(\mathbf{r}')\eta_i(\mathbf{r}, t)u_{\mathrm{X}}^{\bar{\zeta},\bar{\eta}_i}(\mathbf{r}, \mathbf{r}'; t)\mathrm{d}\mathbf{r}\mathrm{d}\mathbf{r}' \right\}, \tag{3.72}$$

where $u_{\mathrm{X}}^{\bar{\zeta},\bar{\eta}_i}(\mathbf{r}, \mathbf{r}'; t)$ is given by the stochastic $\delta\rho(\mathbf{r}, \mathbf{r}'; t)$ from Eqs. (3.57) and (3.58).

This section finishes introducing the stochastic framework for the GW correlation self-energy and the outside vertex correction, especially the application of the stochastic resolution of identity. In case any readers are interested in more technical details, please refer to References 19, 21, 23, 29.

Bibliography

[1] J. M. Seminario, *Recent developments and applications of modern density functional theory*. Elsevier, 1996.

[2] T. Leininger, H. Stoll, H.-J. Werner, and A. Savin, *Combining long-range configuration interaction with short-range density functionals*, *Chemical Physics Letters* **275** (1997), no. 3 151–160.

[3] H. Iikura, T. Tsuneda, T. Yanai, and K. Hirao, *A long-range correction scheme for generalized-gradient-approximation exchange functionals*, *The Journal of Chemical Physics* **115** (2001), no. 8 3540–3544.

[4] M. Del Ben, F. H. da Jornada, A. Canning, N. Wichmann, K. Raman, R. Sasanka, C. Yang, S. G. Louie, and J. Deslippe, *Large-scale gw calculations on pre-exascale hpc systems*, *Computer Physics Communications* **235** (2019) 187–195.

[5] M. D. Ben, C. Yang, Z. Li, F. H. d. Jornada, S. G. Louie, and J. Deslippe, *Accelerating large-scale excited-state gw calculations on leadership hpc systems*, in *SC20: International Conference for High Performance Computing, Networking, Storage and Analysis*, SC20: International Conference for High Performance Computing, Networking, Storage and Analysis, pp. 1–11, 2020.

[6] V. W.-z. Yu and M. Govoni, *Gpu acceleration of large-scale full-frequency gw calculations*, *Journal of Chemical Theory and Computation* **18** (2022), no. 8 4690–4707.

[7] T. A. Pham, H.-V. Nguyen, D. Rocca, and G. Galli, *gw calculations using the spectral decomposition of the dielectric matrix: Verification, validation, and comparison of methods*, *Phys. Rev. B* **87** (2013) 155148.

[8] M. Govoni and G. Galli, *Large scale gw calculations*, *Journal of Chemical Theory and Computation* **11** (2015), no. 6 2680–2696.

[9] F. Bruneval, *Optimized virtual orbital subspace for faster gw calculations in localized basis*, *The Journal of Chemical Physics* **145** (2016), no. 23 234110.

[10] P. Liu, M. Kaltak, J. c. v. Klimeš, and G. Kresse, *Cubic scaling gw: Towards fast quasiparticle calculations*, *Phys. Rev. B* **94** (2016) 165109.

[11] J. Wilhelm, D. Golze, L. Talirz, J. Hutter, and C. A. Pignedoli, *Toward gw calculations on thousands of atoms*, *The Journal of Physical Chemistry Letters* **9** (2018), no. 2 306–312.

[12] H. Yang, M. Govoni, and G. Galli, *Improving the efficiency of g0w0 calculations with approximate spectral decompositions of dielectric matrices*, *The Journal of Chemical Physics* **151** (2019), no. 22 224102.

[13] A. Förster and L. Visscher, *Low-order scaling g0w0 by pair atomic density fitting*, *Journal of Chemical Theory and Computation* **16** (2020), no. 12 7381–7399.

[14] M. Kim, G. J. Martyna, and S. Ismail-Beigi, *Complex-time shredded propagator method for large-scale gw calculations*, *Phys. Rev. B* **101** (2020) 035139.

[15] W. Gao and J. R. Chelikowsky, *Accelerating time-dependent density functional theory and gw calculations for molecules and nanoclusters with symmetry adapted interpolative separable density fitting*, *Journal of Chemical Theory and Computation* **16** (2020), no. 4 2216–2223.

[16] J. Wilhelm, P. Seewald, and D. Golze, *Low-scaling gw with benchmark accuracy and application to phosphorene nanosheets*, *Journal of Chemical Theory and Computation* **17** (2021), no. 3 1662–1677.

[17] A. Förster and L. Visscher, *Low-order scaling quasiparticle self-consistent gw for molecules*, *Frontiers in Chemistry* **9** (2021) 1–14.

[18] P. Umari, *A fully linear response g0w0 method that scales linearly up to tens of thousands of cores*, *The Journal of Physical Chemistry A* **126** (2022), no. 21 3384–3391.

[19] D. Neuhauser, Y. Gao, C. Arntsen, C. Karshenas, E. Rabani, and R. Baer, *Breaking the theoretical scaling limit for predicting quasiparticle energies: The stochastic GW approach*, *Physical Review Letters* **113** (2014), no. 7 076402.

[20] V. Vlček, E. Rabani, D. Neuhauser, and R. Baer, *Stochastic gw calculations for molecules*, *Journal of Chemical Theory and Computation* **13** (2017), no. 10 4997–5003.

[21] V. Vlček, W. Li, R. Baer, E. Rabani, and D. Neuhauser, *Swift GW beyond 10,000 electrons using sparse stochastic compression*, *Physical Review B* **98** (2018), no. 7 075107.

[22] V. Vlček, E. Rabani, and D. Neuhauser, *Quasiparticle spectra from molecules to bulk*, *Physical Review Materials* **2** (2018), no. 3 030801.

[23] V. Vlček, *Stochastic vertex corrections: Linear scaling methods for accurate quasiparticle energies*, *Journal of Chemical Theory and Computation* **15** (2019), no. 11 6254–6266.

[24] J. Brooks, G. Weng, S. Taylor, and V. Vlcek, *Stochastic many-body perturbation theory for moiré states in twisted bilayer phosphorene*, *Journal of Physics: Condensed Matter* **32** (2020), no. 23 234001.

[25] G. Weng and V. Vlček, *Quasiparticles and band structures in organized nanostructures of donor–acceptor copolymers*, *The Journal of Physical Chemistry Letters* **11** (2020), no. 17 7177–7183.

[26] M. Romanova and V. Vlček, *Decomposition and embedding in the stochastic gw self-energy*, *The Journal of Chemical Physics* **153** (2020), no. 13 134103.

[27] G. Weng and V. Vlček, *Efficient treatment of molecular excitations in the liquid phase environment via stochastic many-body theory*, *The Journal of Chemical Physics* **155** (2021), no. 5 054104.

[28] M. Romanova and V. Vlček, *Stochastic many-body calculations of moiré states in twisted bilayer graphene at high pressures*, *npj Computational Materials* **8** (2022), no. 1 11.

[29] G. Weng, R. Mallarapu, and V. Vlček, *Embedding vertex corrections in gw self-energy: Theory, implementation, and outlook*, *The Journal of Chemical Physics* **158** (2023), no. 14 144105.

Chapter 4

Research overview

The previous two chapters summarize the fundamental knowledge in electronic structure theories. The following chapters introduce the new development in my research projects in an accumulative form. Applications of the developed methods focus on the electronic structures of molecules and condensed-phase systems. All the six publications included in this dissertation are peer-reviewed and available online. The default affiliation for the authors in each chapter is Department of Chemistry and Biochemistry at UCSB unless otherwise stated.

The first project (Chapter 5) investigates the quasiparticle band structures of a donor-acceptor copolymer and its assembilies.[1] Periodic boundary conditions are implemented to the stochastic *GW* source code, enabling calculations of low-dimensional (1D and 2D) periodic systems. The semiconducting polymer itself is modeled by a 1D finitely periodic strand, while the 2D single-layer system is built by strands stacking in the π–π direction. Furthermore, the 3D polymer solids are constrcucted with stacking 2D layers in the edge-on direction. All system geometries are optimized by DFT calculations with the PBE functional and the van der Waals correction. The same density functional approxiamtion is also used to obtain the electronic ground state of each optimized system, which is

followed by many-body GW calculations for the quasiparticle energies of three signature bands. Large supercells are employed in the real-space calculations, and the steep scaling in cost is overcome by the stochastic formalism. The GW method provides significantly improved results for the bandgaps and band structures of the investigated systems.

The quasiparticle excitation studied in my first work is assumed delocalized in highly-ordered π-conjugated systems (modeled by periodic systems), where the electronic states are represented by Bloch states. However, in disordered systems, e.g., molecules in the liquid phase, localized molecular excitations are more intuitive. These solvated systems are commonly separated into the solute and the solvent environment, and the environment is considered to renormalize the molecular excitations, i.e., shifts the excitation energies and changes the quasiparticle lifetimes. In practice, the solute–solvent separation utilizes a localized orbital basis, which is often obtained by unitarily transforming the canonical eigenstates. In the second project (Chapter 6), I developed a linear scaling orbital localization method[2] based on the Pipek–Mezey localization scheme. This method excels at generating directly regionally localized states on an arbitrary fragment (subsystem) in a giant system. The fragmentation treatment disregards the localization outside the chosen region and thus avoids the necessary cost overhead. The entire orbital space, which can have a dimension of up to 5000 single-particle states, is transformed sequentially until the cost function reaches the maximum for the fragment. This sequential exhaustion technique is the key to reduce the cost scaling from hyperquadratic to linear. The resulting localization method is first exemplified on the negatively charged nitrogen-vacancy (NV^-) center in diamond solids. Four daggling bonds are successfully obtained from orbital localization and used as localized basis in Hubbard model calculations for the optical transition energies of the NV^- center. Excellent agreement is achieved with previously reported results, and significant improvement of the localized basis is observed when using the proposed sequential localization on the fragment (NV^- center).

Chapter 7 introduces the third project where the established regional orbital localization approach is applied to study molecular ionization energies in the liquid phase.[3] Three representative solute molecules, phenol, thymine, and phenyalanine, are chosen with the solvent, water, for molecular dynamics simulations. Five uncorrelated snapshots are extracted from the trajectory to sample the dynamics of each solvated system. Using a set of occupied localized orbitals, the electronic subspace for the solute is then separated from the solvent environment. The localized ionization states of the solute are then reconstructed from the localized basis, for which there exists a one-to-one correspondence between the solvated molecule and the isolated one. The isolated molecule, possessing the same structure as the solvated one, serves as an auxiliary system for evaluating the solvation electronic effects – the energy shifts of the molecular ionization potentials. For phenol, the computed result agrees excellently with the experimental value. The same agreement is achieved for the solvated thymine with a comparable computed value. The proposed method is also able to generate the full valence spectrum of photoemission, where consistent solvation effects are observed in shifting the quasiparticle energies and shortening the lifetimes.

The fourth work extends the investigation of molecular excitations to various polarizable solvent environments,[4] including water, acetonitrile, dichloromethane, tetrahydrofuran, and benzene. The computed IP shifts are further campared to the macroscopic polarizability of the five solvents. These comparisons show that the explicit IP shifts do not depend solely on the solvent polarizability but are also relatd to the decay of solute–solvent interactions, at least at the density–density interacting (GW) level. To probe the distance-dependent solvation effects, the solvent environment is fragmented into shells, followed by the decompostion of the correlation self-energy stemming from the induced density fluctuation on each solvent shell. The fragment correlation energy at the quasiparticle energy solution is then plotted as a function of the distance characterizing

each solvent shell. As expected, the solute–solvent correlation decays with an increasing distance and practically vanishes at about 9 Å. Surprisingly, the decaying pattern is independent of the solvent type. The 9 Å distance appears to be the common cutoff radius, within which the solvent molecules are considered effectively screening the interactions. Hence, the number of effective solvent molecules is found another important factor contributing to the explicit IP shifts. Finally, the averaged IP shift over the number of effective solvent molecules is found proportional to the macroscopic solvent polarizability.

The previous four projects are based on the correlation method up to the GW approximation, which captures the electrodynamical screening effects. However, in the low-density or strong correlation limit, e.g., molecular or d-electron systems, the GW method may fail to capture the electron–electron correlation sufficiently. One effective way to improve the one-shot GW (G_0W_0) approach is to including the vertex corrections, which capture higher-order electronic correlation such as particle–hole ladder diagrams and density matrix interactions. Chapter 9 presents a collaborative work with a research group from Berkeley on comparing and benchmarking the vertex-corrected G_0W_0 (vxG_0W_0) results with respect to a nearlt full CI method – adaptive sampling configuration interaction (ASCI).[5] The linearly scaling vxG_0W_0 approach agrees excellently with ACSI on the shake-up satellites appearing in the spectral functions for the excitations of bottom valence states. These secondary peaks, which are missing in the G_0W_0 spectra, correspond to multi-quasiparticle interactions induced by the creation of a high-energy hole. Compared to the steep scaling of ASCI, the vxG_0W_0 is more hopeful to tackle large-scale systems and provide more accurate quasiparticle energies.

Chapter 10 introduces an embedding scheme to include vertex corrections in the stochastic GW correlation self-energy.[6] First, an orbital subspace is defined by a projector consisting of electron–hole states with low optical transition energy, e.g., the highest occupied and lowest unoccupied states. Such an electronic subspace is denoted as the

active space, which can also be constructed by the π and π^* bonds of π-conjugated systems. Using this active space projector, the embedding is then performed through a "separation–propagation–recombination" procedure for the real-time proagation of stochastic electronic states. An effective Hamiltonian with rescaled time-dependent exchange interactions is determined specifically for each electron and hole state in the active space. Only components within the active space are treated by this effective time-dependent Hamiltonian, while the rest at the random phase approximation level. Based on the resclaed exchange approximation to the correlation effects, a coefficient-self-consistent circle is further proposed to update the rescaling factor and the vertex-corrected self-energy. This methodology is exemplied on computing the frontier orbital energies of practical donor–acceptor materials with up to 2500 electrons. The fundamental gaps of these charge-transfer systems have been significantly improved upon the G_0W_0 results by the embedded vertex corrections. This enhancement is found consistent among systems of various dimensions.

The supporting information for each work is also provided as appendices. Technical details and supplementary figures and tables indicated in the main text can be found there.

Bibliography

[1] G. Weng and V. Vlček, *Quasiparticles and band structures in organized nanostructures of donor–acceptor copolymers*, *The Journal of Physical Chemistry Letters* **11** (2020), no. 17 7177–7183.

[2] G. Weng, M. Romanova, A. Apelian, H. Song, and V. Vlček, *Reduced scaling of optimal regional orbital localization via sequential exhaustion of the single-particle space*, *Journal of Chemical Theory and Computation* **18** (2022), no. 8 4960–4972.

[3] G. Weng and V. Vlček, *Efficient treatment of molecular excitations in the liquid phase environment via stochastic many-body theory*, *The Journal of Chemical Physics* **155** (2021), no. 5 054104.

[4] G. Weng, A. Pang, and V. Vlček, *Spatial decay and limits of quantum solute–solvent interactions*, *The Journal of Physical Chemistry Letters* **14** (2023), no. 10 2473–2480.

[5] C. Mejuto-Zaera, G. Weng, M. Romanova, S. J. Cotton, K. B. Whaley, N. M. Tubman, and V. Vlček, *Are multi-quasiparticle interactions important in molecular ionization?*, *The Journal of Chemical Physics* **154** (2021), no. 12 121101.

[6] G. Weng, R. Mallarapu, and V. Vlček, *Embedding vertex corrections in gw self-energy: Theory, implementation, and outlook*, *The Journal of Chemical Physics* **158** (2023), no. 14 144105.

Chapter 5

Quasiparticles and Band Structures in Organized Nanostructures of Donor−Acceptor Copolymers

Guorong Weng, Vojtěch Vlček

ABSTRACT

The performance of organic semiconductor devices is linked to highly-ordered nanostructures of self-assembled molecules and polymers. The many-body perturbation theory is employed to study the excited states in bulk copolymers. The results show that acceptors in the polymer scaffold introduce a, hitherto unrecognized, conduction impurity band that leads to electron localization. The donor states are responsible for the formation of conjugated bands, which are only mildly perturbed by the presence of the acceptors. Along the polymer axis, the nonlocal electronic correlations among copolymer strands hinder efficient band transport, which is, however, strongly enhanced across individual

chains. Holes are most effectively transported in the $\pi-\pi$ stacking, while electrons in the impurity band follow the edge-to-edge directions. The copolymers exhibit regions with inverted transport polarity, in which electrons and holes are efficiently transported in mutually orthogonal directions.

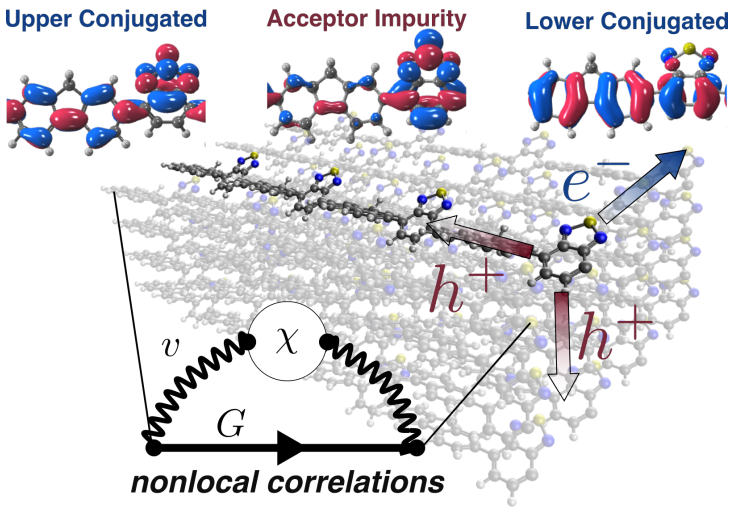

5.1 LETTER

Donor−acceptor (D−A) semiconducting copolymers represent arguably the most variable class of semiconducting materials in organic electronics.[1, 2, 3, 4] The wide range of possible donors and acceptors provides an unmatched tunability of the system's electronic and optical properties.[5, 6, 7] Rational device design is, however, hampered by the complicated relationship between electronic properties and the arrangement of the molecular chains in the condensed phase (e.g., in spin-coated thin films).[8, 9, 10, 11] Experiments showed that highly ordered nanodomains, i.e., highly organized nanometer-scale regions, are widely present in solution-processed thin films. The nanodomains are composed of nanowires,[12] nanosheets,[13] and crystallites.[14, 15, 16, 17] Face-on

($\pi-\pi$) or edge-on stacking is the dominant arrangement of conjugated molecules leading to high charge mobilities and excellent device performance.[12, 13, 14, 15, 16, 17] The nanodomains exhibit quasiparticle bands observed by angle-resolved photoemission.[18] Hence, the high hole mobilities are explained by band-like transport[19, 20] in the $\pi-\pi$ direction.[14, 16, 21] However, a detailed microscopic understanding of how the structure and composition of the copolymers impact the electronic excitations is currently missing.

Answering these questions requires a theoretical investigation of the copolymers' electronic structure in the condensed phase. In principle, such simulations need to capture the nonlocal *inter*molecular interactions [22] of electrons delocalized along the π-conjugated backbone.[18] The individual polymer chains are highly polarizable and held together by van der Waals (vdW) forces. Even in the limit of ideally crystalline systems, quantitative theoretical predictions of electronic excitations are prohibitive, and they have been limited to crystals of small molecules.[23, 24, 25, 26, 27, 28, 29, 30, 31, 32, 33] For polymers, the computational efforts have considered only isolated oligomers [34, 35] or one-dimensional (1D) periodic systems[36, 37, 38, 39, 40] treated by mean-field approaches, which are less expensive but do not take into account the nonlocal electronic correlations (governed by polarization effects). [41] Further, the geometries of the polymer strands are typically forced to be planar, i.e., they disregard actual arrangements in the highly organized domains.[35, 39] Finally, the mean-field methods do not, in principle, provide access to quasiparticle (injected electron and hole) energies and tend to underestimate excitation energies grossly.[42]

In this work, we overcome these limitations and apply state-of-the-art theoretical approaches to explain the key features of the electronic structure of D−A copolymers. Our calculations employ many-body perturbation theory[42] within the stochastic GW approach[43, 44, 45, 46] (where G represents the Green's function and W the screened Coulomb interactions). The electron−electron interactions are computed for each excita-

tion. In the *GW* approximation, the interaction term takes into account a selected classes of Feynman diagrams describing the electrodynamic screening, i.e., the induced charge density fluctuations. Electrons thus interact via a screened Coulomb interaction, which is nonlocal and time-dependent. In practice, the *GW* method yields quasiparticle (QP) excitation energies in excellent agreement with available experimental data.[47, 42, 44]

The electronic structure and QP energies of the condensed phase is determined by the properties of the constituting moieties as well as by mutual interactions among individual copolymer strands. While these contributions are nontrivial, relations among a few key parameters govern the system's overall behavior. To illustrate this, we consider a prototypical example: "FBT" and related D−A copolymers[48, 49, 50] (see the Supporting Information for details). Here, the fluorene moiety (F) acts as a "donor" (D), and benzothiadiazole (BT) acts as an "acceptor" (A). The isolated molecules are illustrated in the inset of Figure 5.1 and the Supporting Information. To focus only on the interactions among the conjugated backbones and to relate to previous literature,[35, 38, 39] we replaced the long alkyl chains of FBT with H atoms. The D units are the source of delocalized electronic states. In contrast, acceptors are typically chosen so that they have a higher electron affinity than donors,[51, 52] acting as strong potential wells for electrons (see Figure A.2). Hence, the A unit is a source of localized electrons whose wave functions have a limited spatial extent.

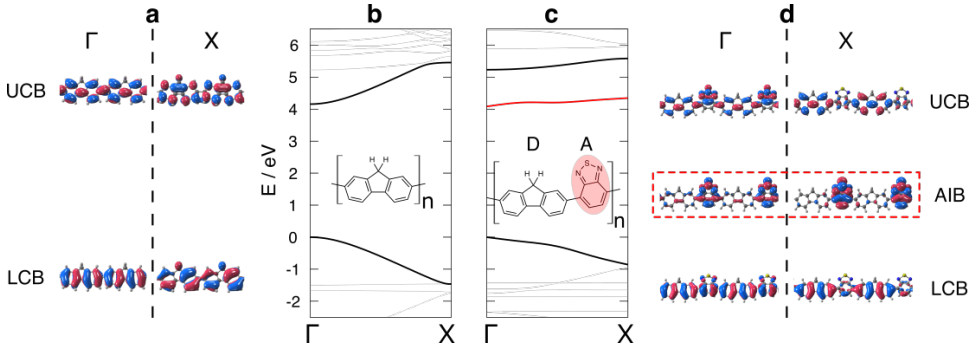

Figure 5.1: Quasiparticle band structures and orbitals of selected states of a fluorene (a, b) and FBT (c, d) strands. The monomer units are shown in the inset of panels b and c. The electronic states that are delocalized over the entire polymer backbone are denoted lower and upper conjugated bands (LCB and UCB), for the highest valence and lowest conduction band. The band-edge states in fluorene (a) are formed by the LCB and UCB illustrated for the Brillouin zone center, Γ, and its boundary, X. The corresponding bands are highlighted in panel b. FBT is D−A copolymer, with the individual subunits labeled in the inset of panel c. Due to the presence of A, the bandstructure contains an acceptor impurity band (AIB) highlighted in red (c). Panel d depicts the LCB, AIB, and UCB for two points in the Brillouin zone; the AIB is strongly localized on the acceptor subunit. Red and blue colors distinguish the wave function phase.

In a single copolymer strand (i.e., 1D periodic system with repeated D and A subunits), the quantum confinement is reduced in the direction of the polymer axis. Consequently, the fundamental gap of the infinite chain decreases with the polymerization length; for an infinite system, it is 4.08 ± 0.04 eV, which is 1.48 ± 0.05 eV less than for an isolated monomer (Figure A.3). In a condensed phase (either 2D slab or 3D bulk), the presence of neighboring strands eliminates the quantum confinement in the directions orthogonal to the polymer axis. Hence, the fundamental band gap further decreases (Figure A.3b).

For quantitative predictions of the band gaps in the condensed phase, many-body methods turn out to be indispensable as dynamical electron−electron interactions are responsible for the nonlocal (interchain) interactions. Indeed, the ionization potential for the 2D slab computed with the sGW method is 5.48 ± 0.02 eV (Figure A.3a), in excellent agreement with thin-film experiments that provide an estimate of 5.4−5.5 eV.[49] The

fundamental band gaps of the surface and the bulk are 3.33 and 2.23 eV (Figure A.3b), and the latter is in good agreement with the experimental value of 2.32−2.44 eV.[49]

The periodic copolymer arrangement supports the formation of band structures (observed experimentally, as discussed above). To characterize the principal features of the electronic states, we start with the 1D system shown in Figure 5.1c. The crystal momentum is imprinted on the individual wave functions (Figure 5.1d), which, however, retain much of their molecular character (Figure A.4). It is thus possible to separate the contributions of D and A to the highest valence and lowest conduction bands that are responsible for the charge transport.

The donor behavior dominates the highest valence state; it has conjugated character and delocalized π orbitals (see more details in Figure A.5). The top valence band is broad (its bandwidth is 0.86 ± 0.04 eV) with a parabolic dispersion near the extrema that occur at the critical points of the Brillouin zone. The near-band-edge character, together with the large bandwidth, translates to a low effective mass of $\sim$0.22 m_e^*. Such a low value is consistent with experimental results for similar (semi)conducting copolymers.[18] We denote the highest conduction band and the lower conjugated band (LCB). The complementary "upper" conjugated band (UCB) is formed from π^* orbitals, and it has much higher energy (Figure 5.1d). Both the LCB and UCB are qualitatively analogous to the band edge states in a *pure* fluorene chain (Figure 5.1a), i.e., the conjugated bands are only mildly perturbed by the presence of acceptor subunits. The correspondence between the electronic structures of D−A and pure donor polymers has not been noticed until now.

In contrast, the lowest conduction band of the copolymer comprises states localized only on the acceptors (Figure A.5). The acceptor band has significantly reduced width (Figure 5.1c), and it appears between the LCB and UCB.

In calculations with distinct A molecules, we found that the exact energy separation

between the conjugated and localized states depends only a little on the choice of acceptors (see Figure A.6 for details). In FBT, the separation of the conduction states is 1.11 eV; the oxygen- and selenium- substituted copolymers show slightly larger separations [1.38 eV and 1.16 eV, respectively (see Figure A.6)]. In all cases studied, the localized state is characteristically inserted between the two conjugated bands. On the basis of the conceptual analogy to charge-trapping "in-gap" states, we denote the lowest conduction states as the acceptor impurity band (AIB). The formation of the localized and flat impurity band has not been described previously. One of the key findings of this letter is the recognition and distinction between the conjugated and impurity bands.

The LCB, AIB, and UCB are present in the same order in 1D and in the condensed phases. While the van der Waals forces only weakly bond the individual copolymer strands, the interchain interactions change the band structures significantly. Besides the shift of the QP gaps (discussed above), the charge transport is critically influenced by the changes in the bandwidth. The dispersion of LCB and AIB determines the charge transport polarity. Further, the bandwidth is directly related to the charge carrier effective mass. To investigate the physical origin of the of the band structure changes, we will separate two main contributions: (i) the one-body electronic interactions[53] including the (classical) density−density Coulomb repulsion (Table A.6), and (ii) the electron−electron interactions, which represent highly nonlocal and dynamical (time-dependent) quantum effects.

The first contribution derives from the local[54] properties of the copolymer. In this case, the electronic structure and charge transport are related to the bond arrangement between the donor and acceptor subunits.[37] The existence of a single bond between adjacent donors and acceptors implies large rotational freedom. In practice, the mutual orientation of the A and D units depends on the environment. The rotational angle varies between 43° and 56° in the relaxed structures with 1D, 2D, or 3D topology (Figure A.9).

Other structural variations are insignificant as the rest of the copolymer backbone is rigid, and we disregard them in the analysis.

As noted above, the AIB is composed of localized states centered on the acceptor subunits. The corresponding wave function does not extend to the D−A joint appreciably (Figure 5.1d). Hence, the AIB is practically insensitive to the torsion angle. In contrast to the AIB, rotation away from the ideally planar geometry leads to the narrowing of conjugated states (Figure 5.2b). Since the torsion angle is larger in the condensed phase than in a free-standing polymer, the hole effective mass in the LCB is thus increased in bulk compared to a prediction from the 1D model.

The sensitivity of the LCB is directly related to the character of the wave function near the D−A bond. Going from the low energy part of the LCB (near the X point of the Brillouin zone) to the band edge, the wave function develops a nodal plane across the D−A joint (Figure 5.2c). The presence of the nodes is associated with increased QP kinetic energy. A close inspection of various torsion angles reveals that the nodes across the D−A bond are suppressed when going from 1D to 3D conformation. The band edge is kinetically stabilized (Figure 5.2a), while the bottom LCB is insensitive to the rotation. As a result, the single-electron interactions promote bandwidth reduction in the condensed phase.

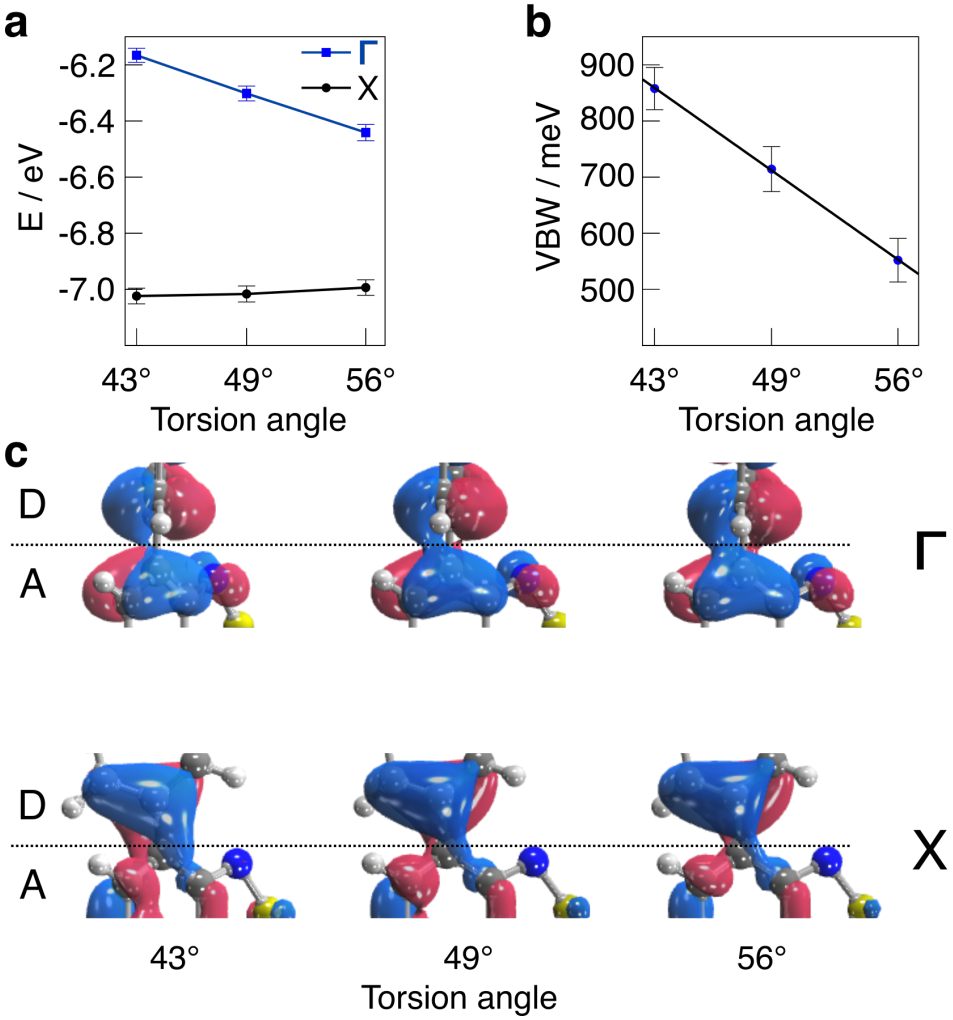

Figure 5.2: The effect of the characteristic torsion angles between D and A subunits found in various condensed phases of FBT: (a) The QP energies of the LCB at the Brillouin zone center, Γ, and its boundary, X as a function of the torsion angle. The QP energy of LCB is more sensitive to torsion at Γ than that at X. (b) The QP valence bandwidth linearly decreases with the torsion angle. (c) LCB wave function at the donor (D) and the acceptor (A) joint for Γ and X points of the Brillouin zone. Red and blue colors distinguish the wave function phase. At Γ, the torsion gradually destroys a nodal plane between D and A, leading to kinetic stabilization of the QP energy. Conversely, the "bridging character" of the LCB at the X point is little affected by the increased torsion. The error bars in panels a and b represent the statistical error of the stochastic many-body calculation.

While the local properties are clearly responsible for the electronic structure modification, the nonlocal many-body effects are equally important and influence the excited

states. These electron−electron interactions are decomposed into two principal contributions: (i) nonlocal exchange (due to the fermionic nature of the charge carriers), and (ii) time-dependent correlations among electrons and holes (which include vdW interactions responsible for the cohesive energy of the bulk). The significance of the many-body treatment is illustrated by the fact that LCB and AIB widths increase by ∼25% and ∼46% if the nonlocal and dynamic description is used instead of the common mean-field approach [e.g., in local and static density functional theory (see Table A.6)].

We first inspect the behavior of the conjugated states. While the exchange interaction typically drives electron localization,[55] it surprisingly enhances the dispersion of the delocalized bands along the polymer axis. The energies of states near the valence band maximum are stabilized much less than at the Brillouin zone boundary, i.e., the X-point (Figure A.7a). In the latter case, there is an increased spatial overlap with a large number of occupied orbitals, leading to a QP energy decrease. The exchange-driven band widening is a signature of the conjugated bands, and it is not observed otherwise (e.g., in AIB). To document this, we provide complementary calculations for additional polymer strands (polyacetylene and polyethylene, with and without conjugated bonds) in Table A.9.

In general, this effect is dramatic for copolymer systems. In the absence of electronic correlation (which reduces the exchange through dynamical screening), the LCB would widen by an additional 40%. This increase can be paralleled with a (spurious) infinite-range response to hole localization observed for bare exchange interactions.[56]

The screening contribution, governed by the reducible polarizability related to charge density fluctuations,[42] changes the picture qualitatively. These correlation effects are dominated by optical (plasmon) excitation that shifts to lower energy as the crystal momentum increases (Figure A.8). The states away from the band edge (i.e., closer to the Brillouin zone boundary) have energies approaching the resonant frequency of the collective charge density oscillations. For the corresponding quasiparticle excitations,

exchange is strongly attenuated and becomes short range; the QP energies shift up, and the LCB consequently narrows (Figure A.7b). The polarization effects thus reduce both the conduction and valence bandwidths, indicating that charge carriers are stabilized (localized) by the intra- and interchain charge density fluctuations.

In the condensed systems, the LCB and UCB remain delocalized only along the polymer, not across the individual strands (illustrated in Figure 5.3c). As a result, the conjugated bands further flatten. Along the edge-to-edge direction ($\Gamma \rightarrow Z$ Figure 5.3a), both the LCB and UCB are extremely narrow and effectively "molecular" in nature. Neither nonlocal exchange nor correlation effects contribute significantly to the quasiparticle energies in this case. In practice, any band-transport of holes in LCB is significantly hampered along the edge-to-edge stacking direction.

However, the localization does not imply that the conjugated bands behave like those in an isolated strand. Here, the band dispersion is reduced by as much as 60% along the polymer axis compared to a free-standing copolymer. The flattening is most prominent in the 2D case (Table A.7). Nonlocal interchain correlations govern the decrease of the LCB width; they are almost twice as big as the effect of torsion between the D and A subunits. In slabs, the strong polarization effects lead to the formation of local maxima in LCB and dispersion narrowing near the Γ point (Figure A.10b). This indicates that in near-surface regions, the valence band edge may not be characterized by a single crystal momentum vector, and the fundamental band gap is likely indirect.

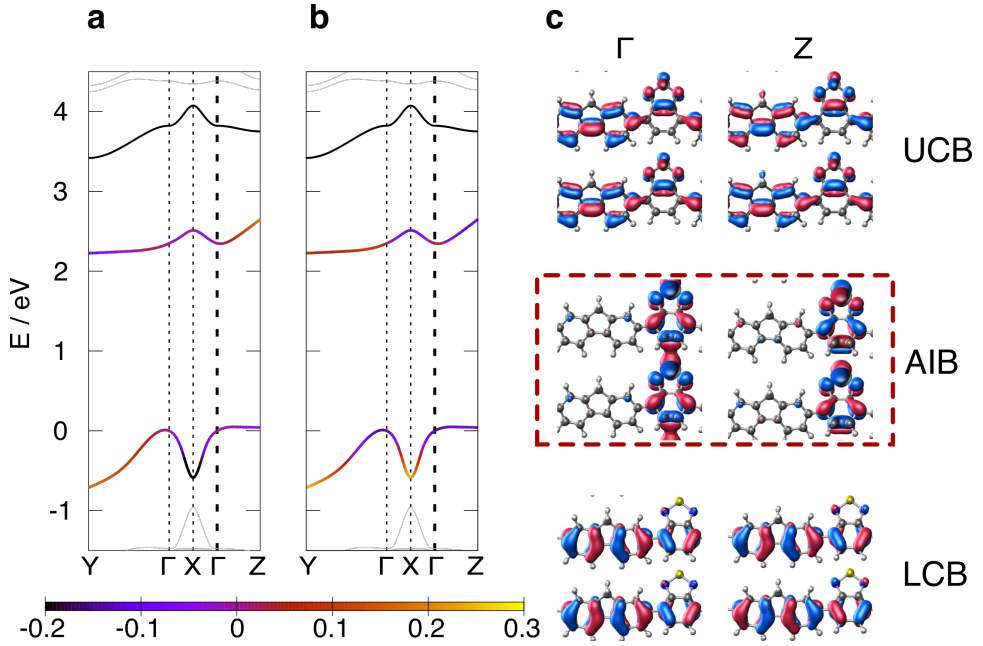

Figure 5.3: Quasiparticle band structure of FBT in a 3D crystalline domain with relative contributions of electronic (a) exchange and (b) correlation energies for the LCB and AIB. The contributions are given by the color code and are plotted relative to the band average. The $\Gamma \rightarrow$ Y branch corresponds to the band in the $\pi-\pi$ stacking direction; the $\Gamma \rightarrow$ X and $\Gamma \rightarrow$ Z branches correspond to the intrachain and edge-on stacking directions. The inverted polarity regime is in the $\Gamma \rightarrow$ Z, where the band dispersion of AIB is much higher than for the conjugated bands. (c) Local wave function character is of the selected states at two distinct points in the Brillouin zone along the $\Gamma \rightarrow$ Z direction. The two molecules are depicted in the edge-on stacking. Both the LCB and UCB remain localized on individual strands, but AIB bridges the polymer chains. Red and blue colors distinguish the wave function phase.

In contrast, cooperative interchain interactions appear along the $\pi-\pi$ stacking ($\Gamma \rightarrow Y$ branch in Figure 5.3). As a result, the LCB dispersion is the largest along this face-on direction ($\leq$710 meV). The significant bandwidth suggests a high propensity for efficient band-like transport of holes within LCB. The reason (despite the strong on-chain localization) is twofold: first, the packing of chains in bulk is tighter; second, the high efficient screening allows greater delocalization of the π (and π^*) orbitals above and below the conjugated framework. Both effects enhance the interchain "communication," which leads to an enlarged bandwidth. In the 3D condensed phase, the LCB width is largest

along the $\pi-\pi$ stacking compared to any other direction (Figures 5.3a and 5.3b), and indicates an efficient band transport of holes.

The lowest conduction band is very different. The impurity states are strongly localized along the copolymer axis. As a result, local and nonlocal interactions are insensitive to crystal momentum, and the band is narrow. Further, there are no increased interactions along the $\pi-\pi$ stacking, and the AIB electronic states thus appear to be molecule-like. Hence, the acceptor band is flat along $\Gamma \rightarrow$ Y as well. There is a low likelihood of electron band-transport in the face-on or polymer axis directions.

Unexpectedly, the AIB exhibits cooperative effects along the edge-to-edge stacking (Figure 5.3c). For states near the band minimum (i.e., near Γ), the impurity wave function delocalizes across individual copolymer chains. In contrast, a nodal plane appears between every adjacent polymer for higher crystal momenta due to the increase of the kinetic energy towards the Brillouin zone boundary (i.e., near Z). The associated QP energy variation leads to a relatively wide[57] dispersion of $\sim$300 meV in the $\Gamma \rightarrow Z$ direction. Besides the kinetic contribution, the band widening is also driven by a large variation of the exchange energy. Along $\Gamma \rightarrow Z$, the AIB thus behaves like the conjugated states in the polymer axis. These properties indicate that the AIB can sustain electron transport along the edge-to-edge stacking direction.

In summary, we investigated a prototypical example of D−A copolymers, FBT, and explained its electronic structure and the propensity to band transport in the condensed phase. Our many-body calculations are in excellent agreement with available experimental data, and, for the first time, they provide insight into the quasiparticle (added hole and electron) states of bulk copolymers. The results show that acceptors, which typically act as strong potential wells for electrons, form a previously unrecognized "impurity" band. In contrast, the donor groups are responsible for delocalized lower (valence) and upper (conduction) conjugated bands. The delocalized states surround the acceptor band, but

they only mildly affect each other.

The intrachain transport is negatively impacted by the condensed phase stacking, which affects the rotation between the donor and acceptors. This is compensated by electron delocalization across the copolymer strands, leading to the formation of wide bands that likely support efficient transport. Electronic correlations (responsible for the cohesive van der Waals forces) universally suppress band dispersion, but nonlocal exchange interactions drive it in some directions.

The large width of valence bands along the $\pi-\pi$ stacking indicates that hole transport is possible in the face-on direction. Surprisingly, we observe a strong propensity for electron transport along the edge-on stacking within the acceptor impurity band. Hence, our calculations predict that D−A copolymers sustain an orthogonal ambipolar transport network. So far, such transport behavior have been reported only in heterogeneous mixtures of p-type polymer and a small n-type molecule.[58, 59] In contrast, our results suggest that the transport of electrons and holes can be achieved in pure D−A copolymers merely through molecular packing.

SUPPORTING INFORMATION

The Supporting Information provides additional texts, figures and tables listed below.

Texts: computational methods and details.

Figures: 1D, 2D, and 3D supercells in computations, QP energy diagrams of molecular and periodic systems, hybridization of FBT frontier orbitals, selected orbitals of UCB, AIB, and LCB in the 1D system, Comparison of band structures of D−A copolymers with different acceptors, QP band structures with exchange and correlation energy as functions of the momentum, graphical solutions to the QP and correlation energies, represnetaion of the D−A torsion angle.

Tables: parameters in DFT and MBPT calculations, measurements of geometrical constants for different polymers, decomposition of the contribution to the valence bandwidth, bandwidths of the LCB and AIB, exchange contribution to the valence bandwidth, measurements of torsion angle for FBT strands, convergence of the IP, EA, and gap to the supercell's size.

ACKNOWLEDGMENTS

The authors want to acknowledge Prof. Thuc-Quyen Nguyen and Prof. Guillermo Bazan for fruitful discussions. This work was supported by the NSF CAREER award through Grant No. DMR-1945098. The calculations were performed as part of the XSEDE computational Project No. TG-CHE180051. Use was made of computational facilities purchased with funds from the National Science Foundation (CNS-1725797) and administered by the Center for Scientific Computing (CSC). The CSC is supported by the California NanoSystems Institute and the Materials Research Science and Engineering Center (MRSEC; NSF DMR 1720256) at UC Santa Barbara.

Bibliography

[1] S. Günes, H. Neugebauer, and N. S. Sariciftci, *Conjugated polymer-based organic solar cells*, *Chemical Reviews* **107** (2007), no. 4 1324–1338.

[2] A. J. Heeger, *Semiconducting polymers: the third generation*, *Chem. Soc. Rev.* **39** (2010) 2354–2371.

[3] A. Facchetti, *π-conjugated polymers for organic electronics and photovoltaic cell applications*, *Chemistry of Materials* **23** (2011), no. 3 733–758.

[4] C. Wang, H. Dong, W. Hu, Y. Liu, and D. Zhu, *Semiconducting π-conjugated systems in field-effect transistors: A material odyssey of organic electronics*, *Chemical Reviews* **112** (2012), no. 4 2208–2267.

[5] J. D. Yuen, J. Fan, J. Seifter, B. Lim, R. Hufschmid, A. J. Heeger, and F. Wudl, *High performance weak donor-acceptor polymers in thin film transistors: Effect of the acceptor on electronic properties, ambipolar conductivity, mobility, and thermal stability*, *Journal of the American Chemical Society* **133** (2011), no. 51 20799–20807.

[6] Y. Li, *Molecular design of photovoltaic materials for polymer solar cells: Toward suitable electronic energy levels and broad absorption*, *Accounts of Chemical Research* **45** (2012), no. 5 723–733.

[7] X. Zhang, H. Bronstein, A. J. Kronemeijer, J. Smith, Y. Kim, R. J. Kline, L. J. Richter, T. D. Anthopoulos, H. Sirringhaus, K. Song, M. Heeney, W. Zhang, I. McCulloch, and D. M. DeLongchamp, *Molecular origin of high field-effect mobility in an indacenodithiophene-benzothiadiazole copolymer*, *Nature Communications* **4** (2013), no. 1 2238.

[8] B. J. Schwartz, *Conjugated polymers as molecular materials: How chain conformation and film morphology influence energy transfer and interchain interactions*, *Annual Review of Physical Chemistry* **54** (2003), no. 1 141–172. PMID: 12524429.

[9] R. Noriega, J. Rivnay, K. Vandewal, F. P. V. Koch, N. Stingelin, P. Smith, M. F. Toney, and A. Salleo, *A general relationship between disorder, aggregation and charge transport in conjugated polymers*, *Nature Materials* **12** (2013), no. 11 1038–1044.

[10] S. Nagasawa, E. Al-Naamani, and A. Saeki, *Computer-aided screening of conjugated polymers for organic solar cell: Classification by random forest*, *The Journal of Physical Chemistry Letters* **9** (2018), no. 10 2639–2646.

[11] L. Ye, H. Hu, M. Ghasemi, T. Wang, B. A. Collins, J.-H. Kim, K. Jiang, J. H. Carpenter, H. Li, Z. Li, T. McAfee, J. Zhao, X. Chen, J. L. Y. Lai, T. Ma, J.-L. Bredas, H. Yan, and H. Ade, *Quantitative relations between interaction parameter, miscibility and function in organic solar cells*, *Nature Materials* **17** (2018), no. 3 253–260.

[12] J. H. Oh, H. W. Lee, S. Mannsfeld, R. M. Stoltenberg, E. Jung, Y. W. Jin, J. M. Kim, J.-B. Yoo, and Z. Bao, *Solution-processed, high-performance n-channel organic microwire transistors*, *Proceedings of the National Academy of Sciences* **106** (2009), no. 15 6065–6070.

[13] H. R. Barzegar, C. Larsen, N. Boulanger, A. Zettl, L. Edman, and T. Wågberg, *Self-assembled pcbm nanosheets: A facile route to electronic layer-on-layer heterostructures*, *Nano Letters* **18** (2018), no. 2 1442–1447.

[14] H. Sirringhaus, P. J. Brown, R. H. Friend, M. M. Nielsen, K. Bechgaard, B. M. W. Langeveld-Voss, A. J. H. Spiering, R. A. J. Janssen, E. W. Meijer, P. Herwig, and D. M. de Leeuw, *Two-dimensional charge transport in self-organized, high-mobility conjugated polymers*, *Nature* **401** (1999), no. 6754 685–688.

[15] D. Venkateshvaran, M. Nikolka, A. Sadhanala, V. Lemaur, M. Zelazny, M. Kepa, M. Hurhangee, A. J. Kronemeijer, V. Pecunia, I. Nasrallah, I. Romanov, K. Broch, I. McCulloch, D. Emin, Y. Olivier, J. Cornil, D. Beljonne, and H. Sirringhaus, *Approaching disorder-free transport in high-mobility conjugated polymers*, *Nature* **515** (2014), no. 7527 384–388.

[16] C. Luo, A. K. K. Kyaw, L. A. Perez, S. Patel, M. Wang, B. Grimm, G. C. Bazan, E. J. Kramer, and A. J. Heeger, *General strategy for self-assembly of highly oriented nanocrystalline semiconducting polymers with high mobility*, *Nano Letters* **14** (2014), no. 5 2764–2771.

[17] M. Li, C. An, T. Marszalek, M. Baumgarten, H. Yan, K. Müllen, and W. Pisula, *Controlling the surface organization of conjugated donor-acceptor polymers by their aggregation in solution*, *Advanced Materials* **28** (2016), no. 42 9430–9438.

[18] B. B.-Y. Hsu, C.-M. Cheng, C. Luo, S. N. Patel, C. Zhong, H. Sun, J. Sherman, B. H. Lee, L. Ying, M. Wang, G. Bazan, M. Chabinyc, J.-L. Brédas, and A. Heeger, *The density of states and the transport effective mass in a highly oriented semiconducting polymer: Electronic delocalization in 1d*, *Advanced Materials* **27** (2015), no. 47 7759–7765.

[19] T. Sakanoue and H. Sirringhaus, *Band-like temperature dependence of mobility in a solution-processed organic semiconductor*, *Nature Materials* **9** (2010), no. 9 736–740.

[20] Y. Yamashita, J. Tsurumi, F. Hinkel, Y. Okada, J. Soeda, W. Zajaczkowski, M. Baumgarten, W. Pisula, H. Matsui, K. Müllen, and J. Takeya, *Transition between band and hopping transport in polymer field-effect transistors*, *Advanced Materials* **26** (2014), no. 48 8169–8173.

[21] G. Kim, S.-J. Kang, G. K. Dutta, Y.-K. Han, T. J. Shin, Y.-Y. Noh, and C. Yang, *A thienoisoindigo-naphthalene polymer with ultrahigh mobility of 14.4 cm2/v·s that substantially exceeds benchmark values for amorphous silicon semiconductors*, *Journal of the American Chemical Society* **136** (2014), no. 26 9477–9483.

[22] C. Sutton, C. Risko, and J.-L. Brédas, *Noncovalent intermolecular interactions in organic electronic materials: Implications for the molecular packing vs electronic properties of acenes*, *Chemistry of Materials* **28** (2016), no. 1 3–16.

[23] J. E. Norton and J.-L. Brédas, *Polarization energies in oligoacene semiconductor crystals*, *Journal of the American Chemical Society* **130** (2008), no. 37 12377–12384.

[24] P. K. Nayak and N. Periasamy, *Calculation of electron affinity, ionization potential, transport gap, optical band gap and exciton binding energy of organic solids using 'solvation' model and dft*, *Organic Electronics* **10** (2009), no. 7 1396–1400.

[25] S. Difley, L.-P. Wang, S. Yeganeh, S. R. Yost, and T. V. Voorhis, *Electronic properties of disordered organic semiconductors via qm/mm simulations*, *Accounts of Chemical Research* **43** (2010), no. 7 995–1004.

[26] S. M. Ryno, S. R. Lee, J. S. Sears, C. Risko, and J.-L. Brédas, *Electronic polarization effects upon charge injection in oligoacene molecular crystals: Description via a polarizable force field*, *The Journal of Physical Chemistry C* **117** (2013), no. 27 13853–13860.

[27] S. Refaely-Abramson, S. Sharifzadeh, M. Jain, R. Baer, J. B. Neaton, and L. Kronik, *Gap renormalization of molecular crystals from density-functional theory*, *Physical Review B* **88** (2013), no. 8 081204.

[28] C. Poelking, M. Tietze, C. Elschner, S. Olthof, D. Hertel, B. Baumeier, F. Würthner, K. Meerholz, K. Leo, and D. Andrienko, *Impact of mesoscale order on open-circuit voltage in organic solar cells*, *Nature Materials* **14** (2015), no. 4 434–439.

[29] Y. Kang, S. H. Jeon, Y. Cho, and S. Han, *Ab initio calculation of ionization potential and electron affinity in solid-state organic semiconductors*, *Phys. Rev. B* **93** (2016) 035131.

[30] J. Li, G. D'Avino, I. Duchemin, D. Beljonne, and X. Blase, *Combining the many-body gw formalism with classical polarizable models: Insights on the electronic structure of molecular solids*, *The Journal of Physical Chemistry Letters* **7** (2016), no. 14 2814–2820.

[31] H. Sun, S. Ryno, C. Zhong, M. K. Ravva, Z. Sun, T. Körzdörfer, and J.-L. Brédas, *Ionization energies, electron affinities, and polarization energies of organic molecular crystals: Quantitative estimations from a polarizable continuum model (pcm)-tuned range-separated density functional approach*, *Journal of Chemical Theory and Computation* **12** (2016), no. 6 2906–2916.

[32] J. Li, G. D'Avino, I. Duchemin, D. Beljonne, and X. Blase, *Accurate description of charged excitations in molecular solids from embedded many-body perturbation theory*, *Phys. Rev. B* **97** (2018) 035108.

[33] S. Bhandari, M. S. Cheung, E. Geva, L. Kronik, and B. D. Dunietz, *Fundamental gaps of condensed-phase organic semiconductors from single-molecule calculations using polarization-consistent optimally tuned screened range-separated hybrid functionals*, *Journal of Chemical Theory and Computation* **14** (2018), no. 12 6287–6294.

[34] J. J. M. Halls, J. Cornil, D. A. dos Santos, R. Silbey, D.-H. Hwang, A. B. Holmes, J. L. Brédas, and R. H. Friend, *Charge- and energy-transfer processes at polymer/polymer interfaces: A joint experimental and theoretical study*, *Phys. Rev. B* **60** (1999) 5721–5727.

[35] J. Cornil, I. Gueli, A. Dkhissi, J. C. Sancho-Garcia, E. Hennebicq, J. P. Calbert, V. Lemaur, D. Beljonne, and J. L. Brédas, *Electronic and optical properties of polyfluorene and fluorene-based copolymers: A quantum-chemical characterization*, *The Journal of Chemical Physics* **118** (2003), no. 14 6615–6623.

[36] J. L. Brédas, B. Thémans, J. G. Fripiat, J. M. André, and R. R. Chance, *Highly conducting polyparaphenylene, polypyrrole, and polythiophene chains: An ab initio study of the geometry and electronic-structure modifications upon doping*, *Phys. Rev. B* **29** (1984) 6761–6773.

[37] J. L. Brédas, G. B. Street, B. Thémans, and J. M. André, *Organic polymers based on aromatic rings (polyparaphenylene, polypyrrole, polythiophene): Evolution of the electronic properties as a function of the torsion angle between adjacent rings*, *The Journal of Chemical Physics* **83** (1985), no. 3 1323–1329.

[38] C. Cheng, H. Geng, Y. Yi, and Z. Shuai, *Super-exchange-induced high performance charge transport in donor-acceptor copolymers*, *Journal of Materials Chemistry C* **5** (2017), no. 13 3247–3253.

[39] F. He, C. Cheng, H. Geng, Y. Yi, and Z. Shuai, *Effect of donor length on electronic structures and charge transport polarity for dtdpp-based d-a copolymers: a computational study based on a super-exchange model*, *Journal of Materials Chemistry A* **6** (2018), no. 25 11985–11993.

[40] J.-L. Brédas, Y. Li, H. Sun, and C. Zhong, *Why can high charge-carrier mobilities be achieved along p-conjugated polymer chains with alternating donor-acceptor moieties?*, *Advanced Theory and Simulations* **1** (2018), no. 7 1800016.

[41] L. M. Woods, D. A. R. Dalvit, A. Tkatchenko, P. Rodriguez-Lopez, A. W. Rodriguez, and R. Podgornik, *Materials perspective on casimir and van der waals interactions*, *Rev. Mod. Phys.* **88** (2016) 045003.

[42] R. M. Martin, L. Reining, and D. M. Ceperley, *Interacting Electrons: Theory and Computational Approaches*. Cambridge University Press, 2016.

[43] D. Neuhauser, Y. Gao, C. Arntsen, C. Karshenas, E. Rabani, and R. Baer, *Breaking the theoretical scaling limit for predicting quasiparticle energies: The stochastic gw approach*, *Phys. Rev. Lett.* **113** (2014) 076402.

[44] V. Vlček, E. Rabani, D. Neuhauser, and R. Baer, *Stochastic gw calculations for molecules*, *Journal of Chemical Theory and Computation* **13** (2017), no. 10 4997–5003. PMID: 28876912.

[45] V. Vlček, W. Li, R. Baer, E. Rabani, and D. Neuhauser, *Swift gw beyond 10,000 electrons using sparse stochastic compression*, *Phys. Rev. B* **98** (2018) 075107.

[46] V. Vlček, *Stochastic vertex corrections: Linear scaling methods for accurate quasiparticle energies*, *Journal of Chemical Theory and Computation* **15** (2019), no. 11 6254–6266.

[47] X. Blase, C. Attaccalite, and V. Olevano, *First-principles GW calculations for fullerenes, porphyrins, phtalocyanine, and other molecules of interest for organic photovoltaic applications*, *Phys. Rev. B* **83** (2011) 115103.

[48] C.-K. Mai, H. Zhou, Y. Zhang, Z. B. Henson, T.-Q. Nguyen, A. J. Heeger, and G. C. Bazan, *Facile doping of anionic narrow-band-gap conjugated polyelectrolytes during dialysis*, *Angewandte Chemie International Edition* **52** (2013), no. 49 12874–12878.

[49] C.-K. Mai, B. Russ, S. L. Fronk, N. Hu, M. B. Chan-Park, J. J. Urban, R. A. Segalman, M. L. Chabinyc, and G. C. Bazan, *Varying the ionic functionalities of conjugated polyelectrolytes leads to both p- and n-type carbon nanotube composites for flexible thermoelectrics*, *Energy & Environmental Science* **8** (2015), no. 8 2341–2346.

[50] Q. Cui and G. C. Bazan, *Narrow band gap conjugated polyelectrolytes*, *Accounts of Chemical Research* **51** (2018), no. 1 202–211.

[51] H. Zhou, L. Yang, and W. You, *Rational design of high performance conjugated polymers for organic solar cells*, *Macromolecules* **45** (2012), no. 2 607–632.

[52] C. Duan, F. Huang, and Y. Cao, *Recent development of push-pull conjugated polymers for bulk-heterojunction photovoltaics: rational design and fine tailoring of molecular structures*, *Journal of Materials Chemistry* **22** (2012), no. 21 10416–10434.

[53] The one-body terms include the single particle non-interacting kinetic energy and external as well as the Hartree potential energies.

[54] The external and Hartree potentials are manifestedly local; the non-interacting kinetic energy is determined purely by a Kohn-Sham map using a local potential. Note that the many-body calculations use a perturbative correction with the Kohn-Sham results as a starting point. The non-local contributions are included in the self-energy term, i.e., it is part of the electron-electron interaction.

[55] P. Mori-Sánchez, A. J. Cohen, and W. Yang, *Localization and delocalization errors in density functional theory and implications for band-gap prediction*, *Phys. Rev. Lett.* **100** (2008) 146401.

[56] V. Vlček, H. R. Eisenberg, G. Steinle-Neumann, D. Neuhauser, E. Rabani, and R. Baer, *Spontaneous charge carrier localization in extended one-dimensional systems*, *Phys. Rev. Lett.* **116** (2016) 186401.

[57] For comparison, this value is practically identical to the dispersion of the conjugated bands along the polymer chain in the 2D system (c.f., Figure A.10).

[58] W. Huang, J. C. Markwart, A. L. Briseno, and R. C. Hayward, *Orthogonal ambipolar semiconductor nanostructures for complementary logic gates*, *ACS Nano* **10** (2016), no. 9 8610–8619.

[59] W. Huang and R. C. Hayward, *Orthogonal ambipolar semiconductors with inherently multi-dimensional responses for the discriminative sensing of chemical vapors*, *ACS Applied Materials & Interfaces* **10** (2018), no. 39 33353–33359.

Chapter 6

Reduced Scaling of Optimal Regional Orbital Localization via Sequential Exhaustion of the Single-Particle Space

Guorong Weng, Mariya Romanova, Arsineh Apelian,[a] Hanbin Song,[b] Vojtěch Vlček

ABSTRACT

Wannier functions have become a powerful tool in the electronic structure calculations of extended systems. The generalized Pipek−Mezey Wannier functions exhibit appealing characteristics (e.g., reaching an optimal localization and the separation of the $\sigma-\pi$ orbitals) compared with other schemes. However, when applied to giant nanoscale systems, the orbital localization suffers from a large computational cost overhead if one is interested in localized states in a small fragment of the system. Herein we present a swift, efficient,

[a]Materials Department, University of California, Santa Barbara, CA 93106, USA
[b]Current institution: University of California, Berkeley, Berkeley, CA 94720, USA

and robust approach for obtaining regionally localized orbitals of a subsystem within the generalized Pipek−Mezey scheme. The proposed algorithm introduces a reduced work space and sequentially exhausts the entire orbital space until the convergence of the localization functional. It tackles systems with ∼10000 electrons within 0.5 h with no loss in localization quality compared to the traditional approach. Regionally localized orbitals with a higher extent of localization are obtained via judiciously extending the subsystem's size. Exemplifying on large bulk and a 4 nm wide slab of diamond with NV^- center, we demonstrate the methodology and discuss how the choice of the localization region affects the excitation energy of the defect. Furthermore, we show how the sequential algorithm is easily extended to stochastic methodologies that do not provide individual single-particle eigenstates. It is thus a promising tool to obtain regionally localized states for solving the electronic structure problems of a subsystem embedded in giant condensed systems.

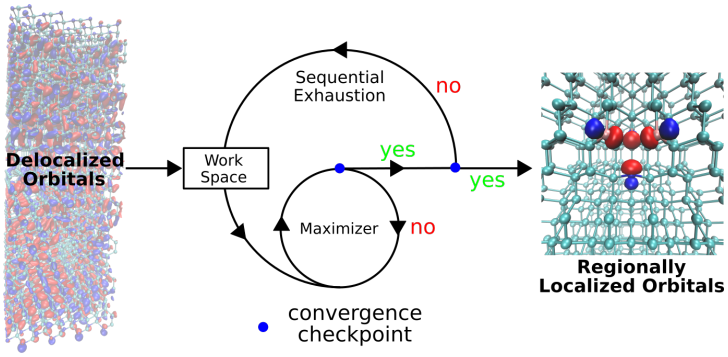

6.1 INTRODUCTION

Localized orbitals are widely used in electronic structure computations for multiple purposes: conceptually, they can provide valuable information about chemical bonding and chemical properties of molecules and materials. More importantly, they allow the evaluation of nonlocal two-body interaction integrals at a significantly reduced cost due to the reduced spatial overlaps. Hence, they represent a powerful tool in mean-field and

postmean-field electronic structure calculations such as hybrid functional calculations,[1, 2] density functional theory with the Hubbard correction term,[3, 4] or many-body calculations.[5, 6] In the same vein, the maximally localized orbital descriptions are optimal for treating correlation phenomena since (due to the locality) the number of "inter-site" interactions is minimal, and the effective size of the problem is smaller. As a result, optimally localized states are essential in the context of embedding and downfolding for many-electron problems.[7, 8, 9, 10]

Orbital localization approaches can be categorized by whether a cost function is optimized or not. The selected columns of the density matrix (SCDM)[11] method and projection with a minimal atomic basis[12, 10] are representative localization schemes without optimizing a cost function. Within the optimization techniques, several functionals have been proposed: the Foster−Boys (FB) scheme[13, 14, 15] minimizes the spatial extension of the orbitals and leads to maximally localized Wannier functions (MLWF)[16, 17] in periodic solids, while the Edmiston−Ruedenberg (ER) approach[18, 19, 15] maximizes the self-repulsion energy. von Niessen[20] introduced another functional that maximizes the charge-density overlap. Pipek−Mezey (PM)[21] proposed to minimize the mean delocalization measure (defined later). Arguably, the most popular approaches are the FB scheme for molecules and the MLWF for periodic solids due to their $\mathcal{O}(N^3)$ scaling (N is the number of electrons). But these schemes suffer from the mixture of $\sigma-\pi$ bonds, commonly known as "banana" orbitals.[21, 22] The ER approach provides more localized orbitals than the FB and supports the $\sigma-\pi$ separation. However, its computational cost scales as steeply as $\mathcal{O}(N^5)$, preventing it from practical applications in large systems.

Among these functional-optimization approaches, PM localization is the most appealing approach. It can provide high spatial localization and the separation of $\sigma-\pi$ characters of chemical bonds compared with the FB counterpart. At the same time, the scaling of PM localization is $\mathcal{O}(N^3)$ only, i.e., significantly lower than the ER counterpart. Because

of the mathematically ill-defined Mulliken charges[23] in the original scheme, the PM localization has been generalized to various partial charge schemes.[24, 25] The generalized PM approach is robust with respect to the choice of the partial charge.[25] Recently, the PM localized molecular orbital formalism has been further expanded to periodic systems.[22] This generalized Pipek−Mezey Wannier Functions (G-PMWF) approach retains the advantages (particularly stronger localization) compared with MLWF.

The iterative optimization with $\mathcal{O}(N^3)$ scaling per iteration, however, still translates to a relatively high computational cost and requires that all single-particle states are known. This becomes a bottleneck for giant systems: the overhead is substantial when one is interested only in a small fraction of the system, such as maximally localized orbitals associated with a point defect in solids, an adsorbate molecule on a surface, or molecular states in a complex environment. Here, handling the entire problem is often necessary, despite only a fraction of localized states being sought. Such nanoscale problems involve thousands of electrons. To generate PMWFs or localized orbitals with comparable quality, the prevalent strategy is to lower the number of iteration steps necessary to reach the optimum, e.g., by a robust solver.[26, 27] Although the proposed scheme is either iteration-free[26] or can effectively lower the iteration steps towards convergence,[27] an auxiliary set of functions or atomic basis is still required in the localization process. The computational scaling to the system's size is not seen improved either. Further, for truly large systems with thousands of electrons, one would employ techniques that avoid the use (or knowledge) of all single-particle states.[28, 29, 30, 31, 32, 33, 34, 35, 36, 37, 38, 39, 40, 41, 42, 43, 44, 45]

Herein, we present a new and complementary top-down approach leading to a fast, efficient, and robust orbital localization algorithm via sequentially exhausting the entire orbital space. It is beneficial for obtaining regionally localized orbitals for a subsystem within the G-PMWF scheme. In contrast to other methods, the problem's dimensionality is reduced from the outset by partitioning the orbital space. As our work space is effectively

compressed, the dimensionality of the relevant matrices in the G-PMWF scheme is much smaller and therefore, the time per iteration step is shortened by orders of magnitude. The unitary transform is performed iteratively until convergence. The transformation starts directly either with: (i) the canonical real-space delocalized orbitals without any external or auxiliary atomic basis set;[46, 26, 27] or (ii) an initial guess of the subspace of localized single-particle orbitals (which can be obtained by, e.g., by filtering[28, 30, 31, 33, 41, 43]). The compression of dimensionality helps to reduce the scaling of the method with the number of electrons to be linear. The completeness of sequentially exhausting the orbital space is demonstrated by the converged localization functional. We test the quality of the localized basis by constructing an effective Hubbard model for the negatively charged nitrogen-vacancy (NV^-) defect center in diamond and computing its optical transition energies in bulk supercells and a large (4 nm thick) slab containing nearly 10,000 electrons. Excellent agreement between the sequential exhausting approach and the full space approach is achieved for the computation of optical transition energies. The accuracy of Hubbard model calculations is further improved by the Wannier function basis obtained from the subsystem with an extended size. In the last section, we provide a thorough discussion of how the choice of localization affects the excitation energies of the embedded NV^- center.

6.2 THEORY

6.2.1 Generalized Pipek−Mezey Wannier Functions

In this subsection, we briefly revisit the G-PMWF formalism[22] to clarify the motivation for this work. The G-PMWF seeks to minimize the mean delocalization measure $\mathcal{D}$

defined as[21]

$$\frac{1}{\mathcal{D}} = \frac{1}{N_s}\sum_{i=1}^{N_s}\sum_{A=1}^{N_A}[Q_{ii}^{A}(\mathbf{U})]^2 \tag{6.1}$$

where i denotes the i^{th} state, and N_s represents the number of states that spans a particular orbital space. A is the A^{th} atom in the system, and N_A is the number of atoms in the system. Q is termed the atomic partial charge matrix (defined below). In practice, Q_{ii}^{A} represents the partial charge on atom A contributed by state i. $\mathbf{U}$ is the unitary matrix that transforms the orbitals. Minimizing $\mathcal{D}$ is equivalent to maximizing the following functional $\mathcal{P}$

$$\mathcal{P}(\mathbf{U}) = \sum_{i=1}^{N_s}\sum_{A=1}^{N_A}[Q_{ii}^{A}(\mathbf{U})]^2 \tag{6.2}$$

The stationary point of $\mathcal{P}$ corresponds to the unitary matrix $\mathbf{U}$ that transforms the canonical states into Pipek−Mezey localized states

$$|\psi_j^{PM}\rangle = \sum_{k=1}^{N_s}\mathbf{U}_{jk}\,|\phi_k\rangle \tag{6.3}$$

where $|\phi_k\rangle$ represents the canonical state.

Generally, the value of $\mathcal{P}$ is iteratively maximized until reaching convergence. In the n^{th} iteration step, the Q matrix can be calculated by

$$Q_{ij}^{A,n} = \int \psi_i^{n*}(\mathbf{r})w_A(\mathbf{r})\psi_j^{n}(\mathbf{r})\mathrm{d}\mathbf{r} \tag{6.4}$$

Here $\psi_i^n(\mathbf{r})$ represents either the transformed state ($n > 0$) or the canonical state ($n = 0$). In the G-PMWF formalism, w_A denotes the atomic weight function using real-space partitioning,[25, 22] e.g., Gaussian weight.[47]

For $n \geq 1$, the Q matrix can also be transformed by

$$Q_{ij}^{A,n} = \sum_{k=1}^{N_s} \sum_{l=1}^{N_s} (\mathbf{U}^{n\dagger})_{ik} Q_{kl}^{A,n-1} \mathbf{U}_{lj}^{n} \tag{6.5}$$

Note that in practice, the Q matrix has a dimensionality of $N_A \times N_s^2$. The number of elements reaches 10^9 for a system with 10^3 atoms and 10^3 occupied states. Furthermore, in our real-space implementation, the theoretical scaling of the method is $N_g \times N_A \times N_s^2$, where N_g denotes the number of grid points in real space. Our numerical results for the defect center in diamond are close to this theoretical behavior, as discussed in the Results and Discussion section.

6.2.2 Fragmentation and Sequential Variant of G-PMWF

This subsection presents an efficient algorithm to obtain a subset of PMWFs localized on a specific set of atoms.

Fragmentation Treatment

Conventionally, one has to localize all N_s states and then identify N_{rl} states that are regionally localized on the selected atoms. For instance, for a CH_4 molecule surrounded by other atoms/molecules, N_{rl} will be four if considering only the valence electrons and doubly occupancy. When $N_{rl} \ll N_s$, this approach suffers from a significant overhead. This is quite limiting when nanoscale systems are considered: the dimensionality of matrix Q and the computational scaling make it challenging to work with thousands of electrons. Previously, we introduced a modified form of the PM functional to account for N'_A ($N'_A \ll N_A$) selected atoms only and search for the N_{rl} states directly.[6] Such a modification is equivalent to the search of a local maximum of $\mathcal{P}$ on the selected atoms, and it reduces the dimensionality to $N'_A \times N_s^2$. In this work, we further compress the

N'_A to simply 1 by creating a single fragment from the subset of atoms. Unlike the "fragment" proposed in the FB scheme,[46] our definition of a fragment uses the atomic weight function w_A

$$w_f(\mathbf{r}) = \sum_{A=1}^{N'_A} w_A(\mathbf{r}) \tag{6.6}$$

where f denotes the fragment of interest. The localization functional thus becomes

$$\mathcal{P}'(\mathbf{U}) = \sum_{i=1}^{N_{rl}} [Q_{ii}^f(\mathbf{U})]^2 \tag{6.7}$$

where $\mathcal{P}'$ is the modified PM functional for the fragment.

Note that: (i) the unitary transform is still performed on *all* N_s states that need to be known, and (ii) the N_{rl} states are identified from N_s by evaluating the partial charge on the selected fragment. In this context, we define the measure of the locality of a specific state on the fragment as

$$L_i^f = \int \psi_i{}^*(\mathbf{r}) w_f(\mathbf{r}) \psi_i(\mathbf{r}) \mathrm{d}\mathbf{r} \tag{6.8}$$

Its value ranges from 0 (not localized) to 1 (most localized). Only the top N_{rl} states of the N_s states in the decreasing order of L_i^f are considered the regionally localized Wannier functions on the fragment. In the following text, we denote this fragmentation variant of G-PMWF as "F-PMWF."

Next, the F-PMWF approach is broken into two steps: (1) maximize $\mathcal{P}'$ (eq 6.7) and find the N_{rl} states that are localized on the fragment; (2) maximize the canonical $\mathcal{P}$ defined as

$$\mathcal{P}(\mathbf{U}) = \sum_{i=1}^{N_{rl}} \sum_{A=1}^{N'_A} [Q_{ii}^A(\mathbf{U})]^2$$

using the N_{rl} states from step 1 and obtain localized states on each individual atom of the fragment.

Essentially, the first step is a "folding" step where the electron density is effectively localized on the fragment disregarding the individual atoms. The second step is instead an "unfolding" step where the electronic states obtained from step 1 are unfolded onto each individual atom in the fragment.

The Q matrix is reduced to N_s^2 in step 1 and to $N'_A \times N_{rl}^2$ in step 2, respectively. The second step is trivial in cost since N_{rl} is often much smaller than N_s. However, the first step can still be expensive when working with thousands of electrons, and the knowledge of N_s eigenstates is necessary.

Sequential Exhausting of the Full Orbital Space

To further compress the N_s in the maximization process and, in principle, avoid the knowledge of N_s states altogether, we introduce a *sequential variant* of F-PMWF, sF-PMWF. We first review the approach which assumes N_s states are available, and at the end of this section, we extend it to a more generalized case when the eigenstates do not need to be known *a priori*.

The sF-PMWF approach incorporates an additional iterative loop ("outer-loop") to maximize the functional $\mathcal{P}'$ successively. The idea is schematically presented in Figure 6.1a. A generalized original (entire) space, either occupied or unoccupied, is spanned by N_s orthonormal canonical states. The initial matrix that contains the canonical states is the identity matrix, and each row of the matrix contains the coefficients of a single-particle state in the canonical basis. The number of rows represents the number of states used in the Q matrix. The black lines and arrows stand for the initialization of the localization procedure. The outer-loop is guided by the blue lines and arrows, while the magenta lines and arrows guide the inner-loop (maximizer). The red points denote the convergence checkpoints.

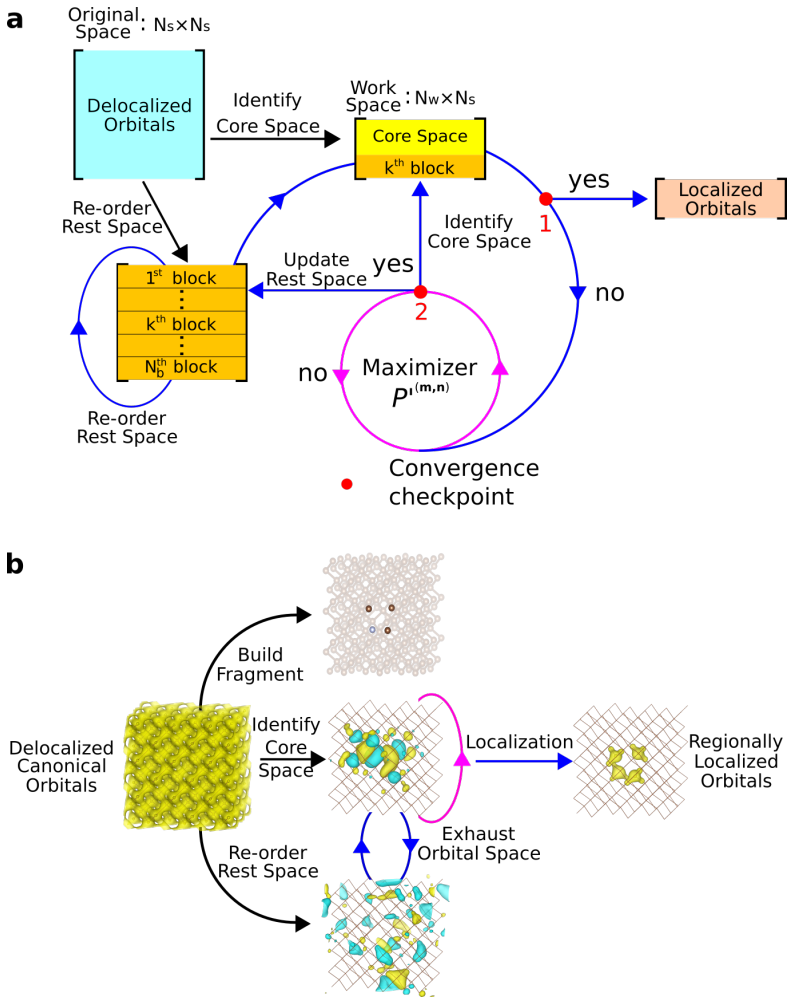

Figure 6.1: (a) Schematic illustration of the sF-PMWF method. Each row of the matrix represents a single-particle state in the canonical $|\phi_j\rangle$ basis. N_s represents the number of states that define the original space while N_w represents the number of states in the actual work space. P' is the modified PM objective functional. The index m denotes the iterative step of the outer-loop (blue). The index n denotes the iterative step of the inner-loop (magenta). (b) sF-PMWF method exemplified on the NV^- center in diamond. The electron density represents the occupied space consisting of N_s delocalized canonical orbitals. The fragment is built with four selected atoms. The core space is first defined by N_c relatively localized canonical states and then sequentially localized on the selected fragment. The rest space is represented by $N_s - N_c$ delocalized states over the whole system. The output is a set of regionally localized Wannier functions on the selected fragment. The isosurface value is set at 0.1 for the electron density and 0.05 for the single-paricle orbital.

Our goal is to find only N_{rl} states that are spatially localized on a selected fragment.

We seek to minimize the cost of the calculation by neglecting the localization in the other regions of the systems. The general procedure is as follows:

First, we assume that in practical calculations, it may be necessary to account for a "buffer," i.e., we search for $N_c \geq N_{rl}$ states (where N_c is typically similar to N_{rl} in magnitude). We denote the N_c most localized orbitals chosen based on the value of L_i^f (eq 6.8) as "core states." And the "core space" is spanned by such N_c states. The original space is essentially split into two, the core and its complement (denoted "rest space"). The states in the rest space are then reordered upon their locality (eq 6.8) for the next step.

Second, a work space is built with a dimensionality of $N_w \times N_s$, where $N_c < N_w \ll N_s$. The first part of the work space is filled by the core states (the yellow region). On the other hand, the rest space is partitioned into N_b blocks according to the value of N_r, which is an arbitrary integer parameter ($1 \leq N_r \leq N_s - N_c$) that denotes the number of states from the rest space. And note that the states in the rest space have been reordered in the decreasing order of L_i^f. The number of states in each block satisfies the following equations

$$N_s^k = N_r \quad \text{if } k < N_b \tag{6.9}$$

and

$$N_s^k \leq N_r \quad \text{if } k = N_b \tag{6.10}$$

Here N_s^k represents the actual number of states in the k^{th} block. The rest space is sequentially updated (explained in the next step) and can be reaccessed during the localization process. The index m denotes the m^{th} iteration step in the outer-loop and

the m ($m > 0$) and k are connected by

$$k = \begin{cases} N_b & \text{if } \mathrm{mod}(m, N_b) = 0 \\ \mathrm{mod}(m, N_b) & \text{if } \mathrm{mod}(m, N_b) \neq 0 \end{cases} \tag{6.11}$$

Here we define one "macro-cycle" when the outer-loop exhausts all the blocks in the rest space once, i.e., the full orbital space is transformed once.

Third, the initial ($m = 0$) objective functional value (eq 6.7) is calculated for the work space and the change of the PM functional in the outer-loop is defined as

$$\Delta\mathcal{P}'^{(m)} = \mathcal{P}'^{(m,0)} - \mathcal{P}'^{(m-1,0)} \quad \text{for } m \geq 1 \tag{6.12}$$

The convergence checkpoint 1 in Figure 6.1a evaluates the $\Delta\mathcal{P}'^{(m)}$ as well as the accumulative step m. The iteration will exit the outer-loop if either

$$\Delta\mathcal{P}'^{(m)} \leq \lambda_1 \tag{6.13}$$

or

$$m = \text{maximal outer-loop iterations} \tag{6.14}$$

is satisfied. Here λ_1 is a convergence threshold. The λ_1 value and the maximal outer-loop iterations are carefully chosen to converge the localization (see the next section). If the iteration does not exit the loop, the index m will become $m + 1$, and the corresponding k^{th} (eq 6.11) block will fill the second part of the work space. The constructed work space then enters the maximization solver (the inner-loop in magenta). The change of the PM

functional in the inner-loop is defined as

$$\Delta\mathcal{P}'^{(n)} = \mathcal{P}'^{(m,n)} - \mathcal{P}'^{(m,n-1)} \quad \text{for } n \geq 1 \tag{6.15}$$

Here n denotes the iteration step (if iterative maximization is needed) in the inner-loop. The convergence checkpoint 2 evaluates the $\Delta\mathcal{P}'^{(n)}$ as well as the accumulative step n. The iteration will exit the inner-loop if either

$$\Delta\mathcal{P}'^{(n)} \leq \lambda_2 \tag{6.16}$$

or

$$n = \text{maximal inner-loop iterations} \tag{6.17}$$

is satisfied. Here λ_2 is another convergence threshold. The λ_2 value and the maximal inner-loop iterations are carefully chosen to allow the work space to reach the maximum smoothly (see the next section). Once exiting, the core space is identified from the transformed work space, and the residues of work space replace the N_s^k states in the k^{th} block. This operation is denoted as "the update of the rest space" since both the core and rest spaces are dynamic during the maximization. The index n is reset to 0, and the $\Delta\mathcal{P}'^{(m)}$ arrives at the convergence checkpoint 1. If the iteration does not exit the loop, the next block then fills the work space to re-enter the maximizer. With all the N_b blocks exhausted and updated, the states in the rest space will be reordered again for the next macro-cycle.

In Figure 6.1b, we provide a concrete example where the sF-PMWF algorithm is applied to search for $N_{rl} = 16$ regionally localized Wannier functions on the NV^- center in diamond. The original space is the occupied space consisting of $N_s = 432$ delocalized canonical orbitals, represented by the electron density. The fragment is built with the

four atoms at the NV^- center, and then $N_c \geq N_{rl}$ relatively localized (based on eq 6.8) canonical states are identified from the original space to form the core space. The complementary $N_s - N_c$ states are reordered and form the rest space. The rest space is then sequentially exhausted and updated at a step of N_r until convergence. The output is N_{rl} Wannier functions that are regionally localized on the selected fragment (represented by the electron density).

In practice, the outer-loop (identify the core space, construct the work space, maximization, and update the rest space) has to be iterated multiple times until the $\mathcal{P}'$ is converged. In general, each iteration step in the outer-loop feeds the core space with the ingredients to localize itself and sequentially exhaust the full orbital space until convergence. However, the cost of the calculation depends primarily on the size of the work space N_w. A small N_r might require extra outer-loop iterations, but the cost of each maximization ("inner-loop") should be orders of magnitude smaller than the traditional full-space approach.

So far, we have assumed that a basis of individual single-particle states is known (e.g., obtained by a deterministic DFT calculation). However, this procedure is trivially extended even to other cases, e.g., when stochastic DFT is employed.[28, 29, 30, 31, 32, 33] For simplicity (and without loss of generality), we assume the localization is performed in the occupied subspace. Here, the sF-PMWF calculation is initialized by constructing a guess of N_c random vectors $|\zeta\rangle$, which are projected onto the occupied subspace as $|\zeta_c\rangle = \hat{P}^o |\zeta\rangle$. These N_c random states then enter the core space in Figure 6.1a. Here, the projector $\hat{P}^o$ is a low-pass filter constructed from the Fermi operator leveraging the knowledge of the chemical potential.[28, 29, 30, 31, 32, 33, 41, 43] Next, in each outer-loop step, one creates a block of random vectors $|\zeta_r^m\rangle$, which have to be mutually orthogonal as well as orthogonal to the N_c core states via, e.g., Gram−Schmidt process. Here r denotes the rest space and m denotes the m^{th} step in the outer-loop. This block of random states

follows the procedure in Figure 6.1a to fill the work space. Note that this block of random vectors represents the entire orthogonal complement to the core space.

Combined with the fragmentation treatment, the number of elements in Q is reduced from $N_A \times N_s^2$ to N_w^2. And the unitary matrices are also reduced from N_s^2 to N_w^2. Such a reduction in dimensionality is expected to shorten the time spent on each iteration step as long as $N_w \ll N_s$. The cost of the stochastic method (which does not require the knowledge of the N_s eigenstates) is higher due to the additional orthogonalization process. In the Results and Discussion section, we show that the total wall time spent on a job becomes much shorter, especially for large systems, at the expense of more inner-loop steps. Most importantly, the localized states obtained from sF-PMWF are practically identical to those obtained from the traditional F-PMWF approach.

6.3 COMPUTATIONAL DETAILS

6.3.1 F-PMWF and sF-PMWF

A shared memory approach is employed to parallelize the do-loops (via OpenMP). Several real-space partitioning schemes[47, 48, 49, 50, 51] for the atomic weight function in eq 6.4 have been tested within the PM localization framework.[25] It turns out the resulting localized orbitals are insensitive[25, 22] to its choice. This robustness of the G-PMWF approach allows choosing the weight function for computational convenience;[25, 22] in this work, Hirshfeld partitioning[47] is used to calculate the Q matrix in eq 6.4. The actual implementation can be found in ref 22. For simplicity, we employ the steepest ascent (SA) algorithm[52, 53, 54] to maximize the PM functional $\mathcal{P}$ and $\mathcal{P}'$. Note that other extremization procedures will likely further reduce the cost of the inner-loop, but they do not have a decisive effect on the overall scaling. The ascending step is set at 5.0 in

the beginning and is divided by 1.1 each time the change of PM functional $\Delta\mathcal{P}'^{(n)}$ appears negative. In calculations using a stochastic basis, the random states are constructed using Fortran random number generator. The random number generator employs seeds that change in each outer-loop step. These random states are then orthogonalized by the Gram−Schmidt process detailed in the Supporting Information (SI).

In F-PMWF calculations, the λ_2 is set at 5×10^{-7}, and it has to be consecutively hit three times to ensure smooth convergence. In sF-PMWF calculations, the λ_2 is set at 1×10^{-7} in the inner-loop, which also has to be hit three times consecutively. The λ_1 is set at 5×10^{-7} for the outer-loop. The maximal iteration step is set at 2000 for n and 5000 for m.

To avoid the spurious convergence or local maximum issue, a special criterion is devised for the sF-PMWF. The principle comes from the full-space F-PMWF. When the core space reaches the maximum localization, the whole rest space should no longer increase the $\mathcal{P}'$ by $>\lambda_1$, and neither should a subspace in the rest space contribute further. And thus, the $\Delta\mathcal{P}'^{(m)}$ of each block in one complete macro-cycle are evaluated simultaneously. Only the maximal $\Delta\mathcal{P}'^{(m)}$ satisfies the criterion ($<\lambda_1$) will the $\mathcal{P}'^{(m)}$ be considered converged. This also means that once the 1$^{\text{st}}$ block re-enters the work space, all the blocks must be exhausted to decide the convergence. This might lead to a slight increase in cost but guarantees that the sF-PMWF reaches the convergence in the same manner as the F-PMWF.

The sF-PMWF calculation can be easily restarted as long as one keeps the checkpoint file at the m^{th} step and sets the outer-loop to start with $m+1$. The source code is posted on git-hub and available for download.

6.3.2 Model Systems

As a test case, we investigate the NV^- center in 3D periodic diamond supercells and a 2D slab. The relaxed chemical structures of the investigated systems are provided in Figure B.1. The atomic relaxations of the NV^- defect center in 3D periodic diamond supercells with 215, 511, and 999 atoms are performed using QuantumESPRESSO package[55] employing the Tkatchenko-Scheffler's total energy corrections.[56] For the 111 nitrogen terminated surface slab 2D periodic calculations, the surface relaxation also employs the Effective Screening Medium correction.[57] The atom relaxation of the surface terminated with nitrogen atoms is performed on a smaller slab with 24 atoms, which corresponds to the $1 \times 1 \times 2$ supercell. The relaxed top and bottom surfaces were then substituted into a large $4 \times 4 \times 6$ ($1.5 \times 1.7 \times 4.7$ nm) supercell containing 2303 atoms. The 111 surface is set normal to the z-direction. The relaxed structure of the NV^- center is cut out from a 511-atom supercell in a way that the N–V axis is normal to the 111 surface. This supercell is then substituted in the middle of the 111 nitrogen terminated surface $4 \times 4 \times 6$ slab at the 2 nm depth from the surface.

The starting-point calculations for all systems are performed with a real-space DFT implementation, employing regular grids, Troullier−Martins pseudopotentials,[58] and the PBE[59] exchange−correlation functional. For 3D periodic structures, we use a kinetic energy cutoff of 26 Hartree to converge the eigenvalue variation to <5 meV. The real-space grids of $68 \times 68 \times 68$; $92 \times 92 \times 92$; and $112 \times 112 \times 112$ with the spacing of 0.3 a_0 are used for 215-atom, 511-atom, and 999-atom supercells, respectively. The grid of $70 \times 82 \times 338$ with the spacing of 0.4 a_0 is used for 2303 atoms slab supercell. The generated canonical Kohn−Sham eigenstates are used for the subsequent orbital localization.

6.4 RESULTS AND DISCUSSION

The full-space F-PMWF and the proposed sF-PMWF methods are applied to obtain regionally localized states on the NV^- center in diamond. The NV^- center is composed of three carbon atoms and one nitrogen atom that are mutually nonbonded. The fragment in the actual calculations is constructed with these four atoms (see Figure 6.1b) unless stated otherwise. The number of regionally localized states, N_{rl}, is 16 on the constructed fragment. Two types of systems, solids and slab, are studied. For the solids, three supercells of different sizes are investigated. The number of occupied states, N_s, for each system is 432, 1024, and 2000, respectively. For the slab, the regionally localized states are identified from a supercell with 2303 atoms and 4656 occupied states.

6.4.1 Completeness of sF-PMWF

First, we investigate the completeness of the sequential exhausting approach, i.e., whether the sF-PMWF can reproduce the same results as the F-PMWF. To contrast the sF-PMWF method, we perform F-PMWF localization on the 511-atom system using a truncated orbital space. This is a common technique to lower the cost by filtering out a portion of canonical states upon the eigenenergy (eigenvalue). Only eigenstates within a specific energy range (termed as the "energy window") are selected for localization. We tested two energy windows (10 eV and 20 eV below the Fermi level, respectively) on obtaining the localized Wannier function basis. Upon visual inspection, the results do not look too different, but when applied to compute the optical transitions in the NV^- center (see "Excited states of the NV^- center" in the SI), we see considerable differences in the energies (Table B.1). The results from the truncated space are highly underestimated compared with the results from the full space. The energy-windowing technique fails since, to reach optimal localization, the maximum possible Bloch states are needed to be

transformed, i.e., *all* the occupied states are necessary. To localize electronic states on a selected fragment, choosing states with significant spatial distribution on the fragment is more critical than the choice of the energy window for the F-PMWF technique. The degree of localization critically depends on what fraction of states that overlap with the selected fragment are included. Note that this is not necessarily related to the energy of the corresponding canonical mean-field state or the size of the energy window, i.e., even states energetically far from the defect state can be important and may plague the frozen window approach. The proposed sF-PMWF method does not have this issue, and we demonstrate its completeness below.

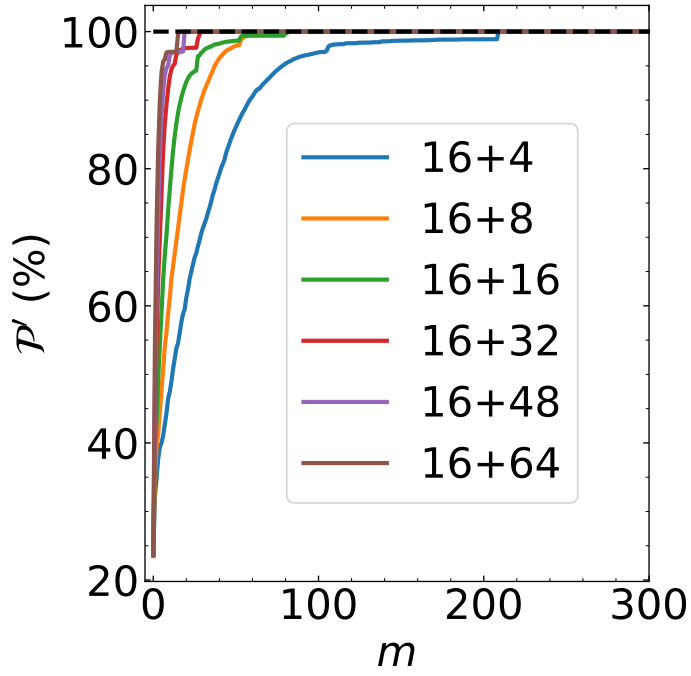

Figure 6.2: Convergence of the functional $\mathcal{P}'$ with respect to the outer-loop step m for the NV^- center of the 215-atom system. Each curve is labelled by the combination of N_c and N_r.

We first illustrate the completeness in detail using the 215-atom system. To initialize the sF-PMWF calculations, the N_c parameter takes 16 (minimum), i.e., we take no "buffer."

For convenience, we only consider combinations with N_r being an integer multiple of N_c and vice versa. Several N_r ranging from 4 to 64 are tested. Figure 6.2 shows the maximized $\mathcal{P}'$, which measures the degree of localization (eq 6.7) relative to the converged maximized value using the full space ($\mathcal{P}'/\mathcal{P}'_{full}$), as a function of the accumulative outer-loop step m. It can be clearly seen that 100% of the $\mathcal{P}'_{full}$ is sequentially recovered regardless of the (N_c, N_r) combination. The maximization of each curve presented in Figure 6.2 is not smooth, i.e., spikes are observed at the step where the iteration enters a new macro-cycle. In fact, at least 94% of the converged $\mathcal{P}'$ has been gained after the first macro-cycle (see Table B.2). As the N_r increases, fewer and fewer iteration steps (N_{it}^{outer}) are required to reach convergence (Figure 6.3a). And theoretically, the N_{it}^{outer} should be reduced to two (the second step is to exit the outer-loop) if one takes $N_r = N_s - N_c$ to work directly in the full space. However, the reduction in N_{it}^{outer} does not necessarily lead to a shorter job time. Note that the time per outer-loop iteration (t^{outer}) increases with a scaling of $\mathcal{O}(N_w^{1.53})$ (see Figure B.3) for the 215-atom system. Figure 6.3b shows the total wall time of each job as a function of the N_w with N_c fixed at 16. The N_{it}^{outer} dominates the total wall time when N_w is small (<48). In this regime, reducing the number of iterations lowers the total wall time effectively. When the N_w is larger, however, the t^{outer} becomes the dominating factor and the total wall time increases even though the N_{it}^{outer} decreases. The trade-off between N_{it}^{outer} and t^{outer} suggests there exists an optimal combination of N_c and N_r for a specific system to minimize the total cost.

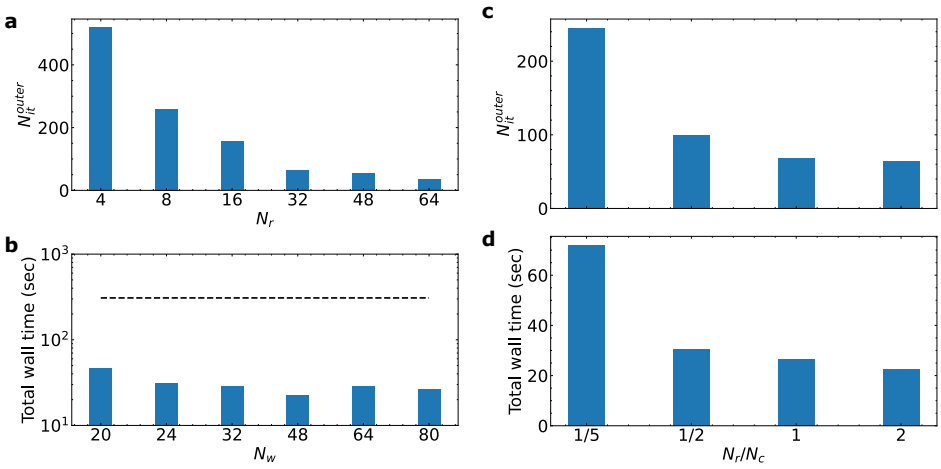

Figure 6.3: Left: Investigation of different combinations of N_c and N_r for the localization on the NV^- center of the 215-atom cell. N_c is fixed at 16. (a) Number of iteration steps in the outer-loop as a function of the N_r. (b) Total wall time of the calculation as a function of N_w. The dashed line indicates the total wall time from the F-PMWF method using the full orbital space. Right: Investigation of different combinations of N_c and N_r for the localization on the NV^- center of the 215-atom cell. N_w is fixed at 48. (c) Number of iteration steps in the outer-loop as a function of the N_r/N_c ratio; (d) The total wall time as a function of the N_r/N_c ratio.

We also test the sF-PMWF calculation employing a set of stochastic basis that represents the rest space. The same parameter combination (16, 32) is used. The 16 core states are taken directly from the canonical eigenstates based on the locality, while the 32 stochastic states are constructed in a three-step manner (see "Preparation of stochastic basis" in the SI). Compared with the (16, 32) calculation using the deterministic basis, the stochastic approach exhibits the same completeness in exhausting the full orbital space, as seen from the converged $\mathcal{P}'$ and $\mathcal{P}$. Nevertheless, more outer-loop iterations are needed due to the randomized search. And the time per iteration also becomes longer (3.47 seconds versus 0.32 seconds) due to the Gram−Schmidt orthogonalization process. And therefore, the total wall time increases to 729 seconds (see the last row in Table B.2). For the evolution of the objective functional in comparison with the deterministic counterpart, the stochastic approach converges more smoothly (see Figure 6.4). The stochastic basis

search does not show competitive efficiency versus the full-space approach (308 seconds) for such a small system. In the following section, we show the stochastic basis approach becomes more efficient than the full-space counterpart for a larger system. However, we emphasize that the advantage of sF-PMWF does not hinge on this stochastic extension but enables it. In most of our results, we will focus on the fully deterministic approach in which the knowledge of N_s states is assumed.

The behavior of the sF-PMWF method discussed above is also observed for the 511-atom system (Figure B.5 and Table B.3 in the SI), confirming the generality of the completeness.

6.4.2 Optimization of Work Space

In the previous section, we observe a trade-off between N_{it}^{outer} and t^{outer}, which implies a possibly optimal parameter combination. To further understand the choices of N_c and N_r, several other combinations with $N_c > 16$ are tested on the 215-atom system. The maximal $\mathcal{P}'$ and $\mathcal{P}$ are secured regardless of the (N_c, N_r) combination, indicating that the convergence of $\mathcal{P}'$ is insensitive to the choices of these two parameters. For N_c fixed at 16, the time-to-solution reaches a minimum when $N_w = 48$, as shown in Figure 6.3b. For N_w fixed at 48, different ratios of N_r/N_c are tested. The results suggest that the larger the N_r, the smaller the N_{it}^{outer} (Figure 6.3c). Note that the t^{outer} depends solely on the N_w (Table B.2). And therefore, a smaller N_{it}^{outer} translates directly to a shorter wall time (Figure 6.3d). The numerical results are summarized in Table B.2. This behavior is further observed in the 511-atom system (see Figure B.6).

Table 6.1: Timing data of orbital localization performed on the 215-atom system using sF-PMWF.

$(Nc,\ Nr)$	t^{tot} (s)	t^{macro} (s)	n^{macro}
(16, 4)	47	9.07	5
(16, 8)	31	5.87	5
(16, 16)	29	4.65	6
(16, 32)	22	4.19	5
(16, 48)	28	4.51	6
(16, 64)	27	5.09	5

To further quantify our observations above, we examine the time per macro-cycle (t^{macro}) and the number of macro-cycle (n^{macro}) shown in Table 6.1. The variation of the total wall time (t^{tot}) agrees well with the t^{macro} among different (N_c, N_r) combinations since the n^{macro} in each trial does not differ too much from one another ($n^{macro} = 5 \pm 1$). The total wall time is essentially very close to $n^{macro} \times t^{macro}$. The scaling of t^{macro}, in our sF-PMWF algorithm, can be approximately expressed as

$$\mathcal{O}(N_w^2 * \frac{N_s - N_c}{N_r}) = \mathcal{O}\left[(\frac{N_c^2}{N_r} + N_r + 2N_c)(N_s - N_c)\right] \tag{6.18}$$

With N_s and N_c fixed, the right-hand side (RHS) of eq 6.18 is a function of N_r with a theoretical minimum for some nonzero N_r. And thus, eq 6.18 explains the existence of an optimal (N_c, N_r) combination as observed. We note that the RHS of eq 6.18 is also crucial in explaining the scaling of our sF-PMWF method with respect to N_s as discussed in the following section.

To conclude, the "buffer" seems to be unnecessary for the core space, i.e., N_c can be set directly as N_{rl} for a specific fragment. The work space optimization then depends

solely on the choice of N_r, and there exists an optimal N_r. Nevertheless, the cost of the investigated sF-PMWF calculations without optimization is already absolutely lower than that of F-PMWF regardless of the N_r (see Figure 6.3b and Figure B.5b). The protocol of choosing N_c and N_r is suggested to be $N_c = N_{rl}$ and $N_r = 2N_c$ since it leads to a local minimum in the total wall time.

This protocol is then applied to the 999-atom system and two additional combinations of N_c and N_r are also tested. The (16, 32) combination still leads to a cost minimum and is 85 times faster than the F-PMWF (see Table B.4). Further, we also test the stochastic basis search with the 999-atom employing the (16, 32) combination. The completeness of the stochastic exhausting is again confirmed by the converged $\mathcal{P}'$ and $\mathcal{P}$. Although the stochastic approach is still more costly than the deterministic sequential counterpart, it is more efficient than F-PMWF (by roughly 50%) when applied to this system with ∼4000 electrons (see the last row of Table B.4). Furthermore, ∼74% of the cost in the stochastic search comes from the Gram-Schmidt process, which advanced orthogonalization techniques can optimize. When combined with stochastic DFT, the total cost of orbital localization is expected to be much lower than the deterministic approach that requires the knowledge of the eigenstates in a system with tens of thousands of electrons.

For the 2303-atom system, the (16, 32) combination successfully converges the $\mathcal{P}'$ and produces localized states. Note that the cost can be lowered by 10% if the (16, 48) combination is used. And if one searches further for the optimal N_r (or N_w), it is possible to lower the cost further. However, for a fair comparison between one system and another, we use the timing from the (16, 32) combination for the slab, which is already 412 times faster than the F-PMWF. The numerical results are provided in Table B.5.

We also compare the time spent on folding and the unfolding steps, respectively (see Table B.6). In each system, the cost of the unfolding step is merely 1∼2% of the folding

one since only N_{rl} states are transformed in the unfolding step. And thus, it is sufficient to evaluate just the cost of the unfolding step as the total cost of the orbital localization.

Finally, we remark that the (16, 32) combination is stable and efficient for a given fragment regardless of the precise environment. This indicates that sF-PMWF is robust. Further, the consistent parameter combination clearly demonstrates the scaling of the sF-PMWF calculation with respect to the N_s as discussed in the next section.

6.4.3 Scaling Analysis of sF-PMWF vs F-PMWF

To investigate the scaling of the sF-PMWF method, we normalize the timing data to the largest grid by

$$t_n = \frac{N_g^{max}}{N_g} t \tag{6.19}$$

where t_n represents the normalized time, N_g^{max} denotes the number of grid points of the largest system (the 2303-atom system), and N_g is the grid of each investigated system. The numeric data is summarized in Table 6.2. We report the results with a precision of 1 second for the total wall time and 0.01 second for the time per iteration/cycle. Here we note that t_n^{tot} represents the normalized total wall time, t_n^{SA} and n^{SA} denote the normalized time per SA step and the number of SA steps in F-PMWF, t_n^{outer} denotes the normalized time per outer-loop in sF-PMWF, t_n^{macro} and n^{macro} represent the normalized time per macro-cycle and number of macro-cycles in sF-PMWF.

Table 6.2: Normalized timing data of orbtial localization performed on the four investigated systems using F-PMWF and sF-PMWF, respectively

System	F-PMWF			sF-PMWF			
	t_n^{tot} (s)	t_n^{SA} (s)	n^{SA}	t_n^{tot} (s)	t_n^{outer} (s)	t_n^{macro} (s)	n^{macro}
215-atom	1903	1.81	637	139	1.99	25.83	5
511-atom	18339	21.43	700	284	2.08	66.45	4
999-atom	58007	85.01	586	675	2.07	128.16	5
2303-atom	695370	1056.26	650	1683	1.89	266.02	6

In Figure 6.4a, the log of t_n^{tot} is plotted as a function of the log of N_s for the four investigated systems. The scaling of the F-PMWF using the full orbital space is $\mathcal{O}(N_s^{2.43})$ (black line and square points). This is a bit higher than the theoretical $\mathcal{O}(N_s^2)$ due to the other $\mathcal{O}(N_s)$ do-loops, tasks related to parallelization, and practical executions (e.g., reading and writing of files). The sequential method, sF-PMWF, reduces the scaling from $\mathcal{O}(N_s^{2.43})$ to $\mathcal{O}(N_s^{1.07})$ (red line and circle points). This linear scaling is observed when the same protocol (16, 32) applies to the four systems. Such an order of magnitude reduction in the scaling promises the efficiency of sF-PMWF when applied to much larger systems. In our largest system with 4656 states, the total wall time is shortened from 8 days to < 0.5 hours (Table 6.2, on a workstation with 2.5 GHz CPUs and parallelization on 60 cores).

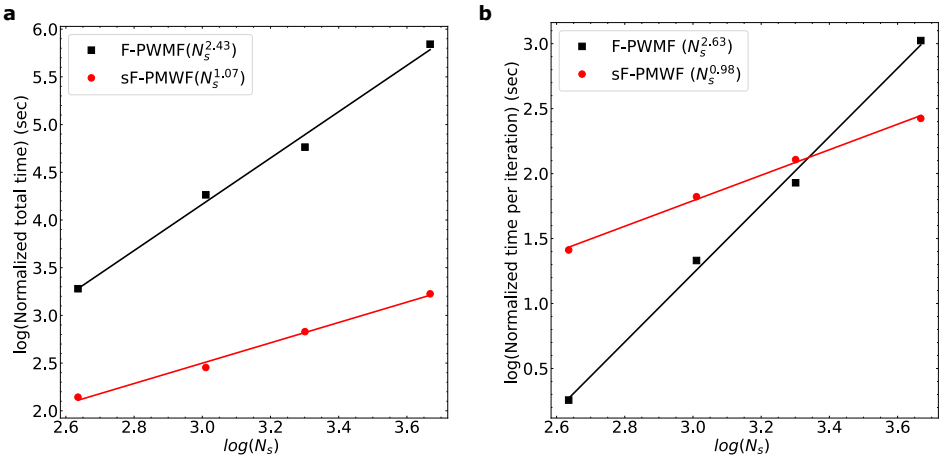

Figure 6.4: (a) The log of the normalized total job time plotted as a function of the log of N_s. (b) The log of the normalized time per macro-cycle plotted as a function of the log of N_s. The black line and square points represent results obtained from the F-PMWF method transforming the full orbital space at once. The red line and circle points represent results obtained from the sF-PMWF method sequentially transforming the orbital space. The scaling is derived from the slope of each fitting using the numeric data in Table 6.2.

The reduced scaling of sF-PMWF is largely attributed to the reduction of dimensionality during the maximization process. The efficiency is reflected mainly in the time per inner-loop iteration, t^{inner} in sF-PMWF and t^{SA} in F-PMWF. From 432 states to 4656 states, the t_n^{SA} of the F-PMWF approach scales rapidly from 1.81 seconds to 1056.26 seconds (Table 6.2). As shown in Figure 6.4b, the scaling of t_n^{SA} in F-PMWF is $\mathcal{O}(N_s^{2.63})$. Further, Table 6.2 shows that the numbers of inner-loop iterations N_{it}^{inner} in F-PMWF are reasonably large (600∼700) and translate to a total scaling of $\mathcal{O}(N_s^{2.43})$ shown in Figure 6.4a.

In sF-PMWF, however, the t^{inner} remains constant and as low as $\sim 5 \times 10^{-4}$ seconds regardless of the N_s (see Table B.9). Although more SA iteration steps are required relative to the F-PMWF calculations (Figure B.8 and B.9), 1000 iterations now take as low as 0.5 seconds. And therefore, in sF-PMWF, the time spent in the maximizer is no more the dominating factor within an outer-loop step. It is more convenient to evaluate

the efficiency of sF-PMWF by t_n^{outer} and t_n^{macro}. We first study the scaling of the time per outer-loop step (t_n^{outer}) with respect to the N_s. It is shown that the t_n^{outer} hardly scales with respect to N_s when the same (N_c, N_r) combination is applied (see Figure B.10). In addition, the N_{it}^{outer} scales almost linearly with N_s and gives a total scaling of $\mathcal{O}(N_s^{1.07})$.

A more direct derivation of linear-scaling is by evaluating the t_n^{macro} and n^{macro} summarized in Table 6.2. Interestingly, the n^{macro} is very close between any two systems, being 5 ± 1. The total wall time is approximately the product of t_n^{macro} and n^{macro}; hence, it is sufficient to evaluate t_n^{macro} only. In the previous section, eq 6.18 actually suggests that the scaling of t^{macro} depends linearly on N_s. The normalized time per macro-cycle (t_n^{macro}, Table 6.2) is plotted as a function of N_s in Figure 6.4b. Note that the t_n^{macro} for F-PMWF coincides with the t_n^{SA} since the full orbital space is transformed at once in a single SA step. Here we can clearly see the linear dependence $\mathcal{O}(N_s^{0.98})$ in sF-PMWF versus the $\mathcal{O}(N_s^{2.63})$ in F-PMWF. Although t_n^{macro} for a specific system in sF-PMWF can be higher than that in F-PMWF, the evaluation of the number of macro-cycles, n^{macro} or n^{SA}, is ∼5 for sF-PMWF while ∼650 for the conventional F-PMWF. To conclude, eq 6.18 quantitatively explains the observed linear-scaling when the same (N_c, N_r) combination is applied to systems of different sizes.

6.4.4 Localization Quality of sF-PMWF vs F-PMWF

Visualization of Localized Orbitals and Density

In the previous section, the completeness of sF-PMWF has been demonstrated for the maximization of the modified PM functional $\mathcal{P}'$ (eq 6.7). These 16 resulting states are localized on the fragment and serve as a subspace to further maximize the $\mathcal{P}$, which unfolds the states on each individual atom. The converged $\mathcal{P}'$ and $\mathcal{P}$ between F-PMWF and sF-PMWF differ by no more than 0.0001 (<0.002%, see Tables B.11 and B.12) .

Graphically, the 16 regional Wannier functions correspond to 9 C−C bonds, 3 C−N bonds, and 4 "p"-like states. The electron density constructed from these 16 localized states are shown to be visually identical between the sF-PMWF and F-PMWF calculations (see Figures B.11 to B.13). The same agreement is also seen for the four selected individual "p"-like states (Figures B.14 to B.16) that are used in the following excited-state calculations. Figure 6.5a highlights the NV^- center in the slab using the regionally localized electron density. The obtained electron density conserves the spatial symmetry across the C−C−C plane and the C−C−N plane (Figure 6.5b). The left panels of Figure 6.5b show the electron density constructed from the 16 most localized canonical states, while the right panels present the maximized results from the sF-PMWF calculation. It can be clearly seen that electron density distribution becomes much more concentrated on the selected atoms, indicating the effectiveness of the localization.

To demonstrate that the sF-PMWF localization is subsystem-independent, an arbitrary carbon atom is chosen from each investigated system, and four regionally localized states are sought. The electron density around the selected C atom is successfully reproduced for each system (see Figure B.17), confirming the generality of the sF-PMWF approach.

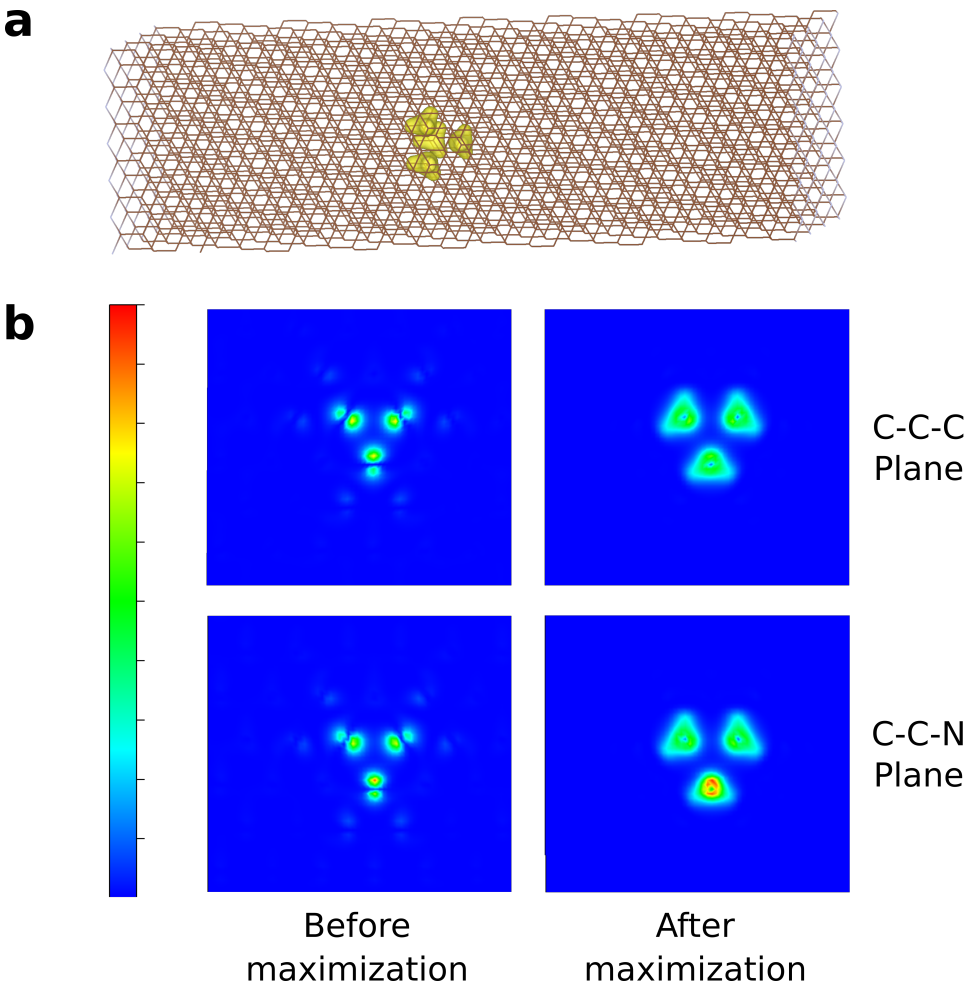

Figure 6.5: (a) Electron density constructed from the 16 regionally localized states around the NV^- center. The isosurface value is set at 0.05. (b) density distribution sliced through the C−C−C plane (upper panels) and the C−C−N plane (lower panels) of the NV^- center in the slab. The left panels are constructed from the 16 most localized canonical states before the sF-PMWF calulation and the right panels are constructed from the 16 regionally localized states after the sF-PMWF maximization.

Excited States of the NV^- Center

To further demonstrate the practical application and quality of the sF-PMWF approach, we investigate the optical transitions in the NV^- center using the "p"-like Wannier functions (see Figure 6.6) that form a minimal basis. To model the excited states of the NV^- center,

we solve the Hubbard Hamiltonian written as

$$\begin{aligned}\hat{H} = &\sum_{i\sigma} \varepsilon_i \hat{c}^\dagger_{i\sigma} \hat{c}_{i\sigma} - \sum_{i\neq j,\sigma} t_{ij} \hat{c}^\dagger_{i\sigma} \hat{c}_{j\sigma} + \\ &+ \sum_{i\sigma} U \hat{n}^\dagger_{i\uparrow} \hat{n}_{i\downarrow} + \sum_{i>j,\sigma,\sigma'} V \hat{n}^\dagger_{i\sigma} \hat{n}_{j\sigma'}\end{aligned} \tag{6.20}$$

where $\hat{c}^\dagger_{i\sigma}$ and $\hat{c}_{i,\sigma}$ are creation and annihilation operators in site i with spin σ and $\hat{n}^\dagger_{i\sigma}$ is a particle number operator. The ε_i and t_{ij} are the on-site and hopping energies. U and V represent the on-site and intersite Coulomb interaction, respectively. It is a minimal model of the NV^- center that is commonly used [60, 61, 62, 63] to describe its low-lying excited states. Note, although including screening is important to capture the physics of the system correctly and has been extensively studied,[61, 63, 64] only bare interactions are considered in this work to focus on the sensitivity to the variations of the Wannier basis. In this section, we will particularly comment on the selection of the fragment on which the electronic states are localized. Note that the fragment size is independent of the sF-PMWF methodology, but it represents an important parameter.

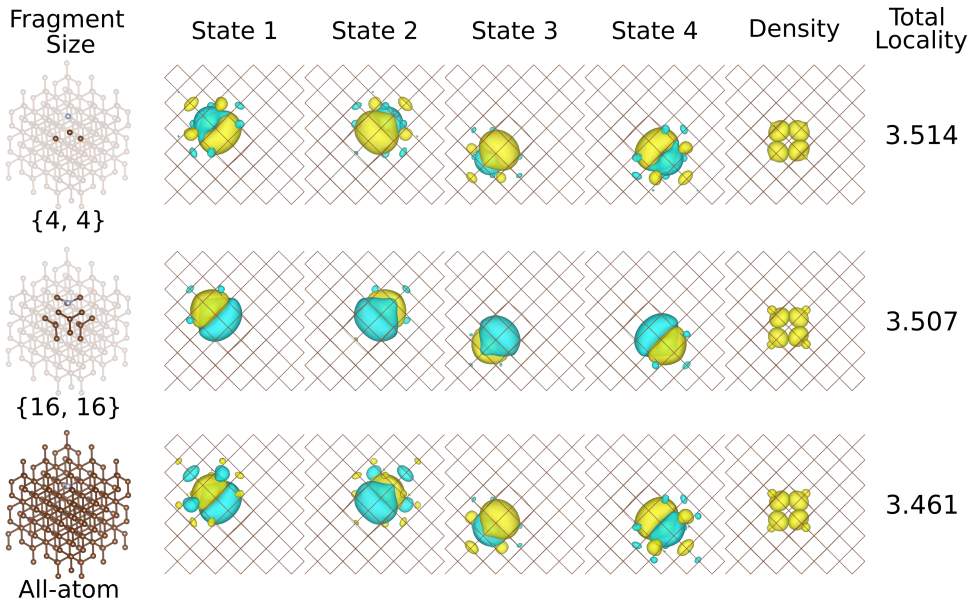

Figure 6.6: "p"-like Wannier function basis used in the Hubbard model calculations. Each row provides the fragment model, the corresponding set of PMWFs obtained from this fragment, the electron density constructed from these four PMWFs, and the total locality computed from eq 6.21. Here the {4, 4} fragment represents the minimal model and the {16, 16} one is found the optimal fragment size. The isosurface value is set at 0.02.

First, we focus on the results computed from the sF-PMWF Wannier basis of the four-atom fragment shown in Figure 6.6. The three lowest energy transitions are given in Table 6.3 in parentheses. For the 3D periodic systems, the two small cells slightly underestimate the ^3E – $^3A_2$ transition energy and overestimate the $^1A_1$ – $^3A_2$ one. Instead, the ^1E – $^3A_2$ transition converges well to the supercell size. The ^3E – $^3A_2$ and $^1A_1$ – ^1E transition energies are underestimated with respect to the experimental values of 1.95 eV and 1.19 eV, respectively. However, these results agree well with other theoretical calculations that employ PBE functionals to compute the bare Hubbard model parameters.[65, 66, 67, 68, 69, 70] The ^1E – $^3A_2$ transition energy fluctuates mildly with respect to the supercell size but maintains a comparable magnitude. The results computed in bulk systems from the sF-PMWF basis agree perfectly with the F-PMWF ones (see the F-PMWF results in Table B.15), confirming the equivalency of the two sets of localized

orbitals. In contrast, the F-PMWF and sF-PMWF differ slightly more from each other for the slab results. To investigate this difference in transition energies, we first examine the equivalence of the two sets of "p"-like Wannier functions: the orbitals from sF-PMWF has >99.99% overlap with their counterparts from F-PMWF, i.e., these two sets of states are practically identical. The numerical results are provided in Table B.16. By subtracting corresponding sF-PMWF and F-PMWF Wannier orbitals, we observe seemingly negligible difference (slightly higher than the numerical noise), which however affects the Hubbard model calculations. Comparing the Hamiltonian computed with the two basis sets, we found that the discrepancy in transition energies stems only from the ionic part of the t parameters (see the definition of t parameters in eq B.2 in the SI). In contrast, the kinetic part, sensitive to the small variation of the Wannier functions, is practically identical, confirming that both orbitals should be considered as equivalent. The small, $\ll 0.01\%$ difference, is distributed over the real-space grid and it becomes sizable enough for the slab calculation because of the system size (which is significantly larger than the bulk systems).

Furthermore, the slab results are strikingly different from the bulk, i.e., the transition energies are up to $70\%-80\%$ lower than those in bulk. As we show below, this is due to the selection of the fragment size and independent of the completeness of the orbital space. To the best of our knowledge, we note that no calculations for shallow NV^- centers in slabs have been done previously. Hence it is not possible to compare our results with any reference.

Table 6.3: Excited-state transition energies of the NV^- center in the four investigated systems using the Wannier function basis obtained from sF-PMWF calculations. The numbers with and without the parenthesis correspond to the {4, 4} and {16, 16} fragment, respectively.

Transition	Energy (eV)			
symmetry	215-atom cell	511-atom cell	999-atom cell	slab
$^3E - {}^3A_2$	2.108 (1.560)	2.277 (1.695)	2.312 (1.710)	1.343 (0.363)
$^1A_1 - {}^3A_2$	1.433 (1.325)	1.310 (1.270)	1.202 (1.193)	1.159 (0.292)
$^1E - {}^3A_2$	0.447 (0.378)	0.435 (0.381)	0.413 (0.368)	0.329 (0.091)

The situation is remedied when the fragment size effects are considered. As noted earlier, the fragment studied in the previous sections is actually a minimal model, i.e., the orbital localization is considered only on the 4 atoms where the "p"-like states are located, and the total number of orbitals on these four atoms is 16. However, neglecting the neighboring atoms might lead to a mixed character of "p"-like states and C−C (or N−C) covalent bonds. To test this, we investigate four combinations of $\{N'_A, N''_A\}$ fragments: for instance, {4, 16} represents the case where 4 atoms are considered in the folding step while 16 atoms (including the bonded atoms) are considered in the unfolding step. A detailed investigation of the various parameters is performed on the 215-atom system. The corresponding fragments are presented in Figure B.2. The four Wannier functions used for the Hubbard model are illustrated in Figure 6.6, where we compare the {4, 4} fragment, the {16, 16} fragment, and the all-atom case.

For a better comparison among different sets of PMWFs (Figure B.18), we also provide the spatial overlaps between the fragmentation approaches and the all-atom calculation, $|\langle\psi_i|\psi_j\rangle|$, in Table B.13. The all-atom calculation refers to orbital localization on all atoms at once using G-PMWF. Numerically, the {4, 16} combination gives the closest solutions to the all-atom ones. Note that in the all-atom case, the optimization does not

preferentially localize single-electron states near the defect; rather, it seeks globally most localized states. Such an approach is not guaranteed to generate transformed PMWFs that are optimal for the mapping onto the Hubbard model. Indeed, we discuss this point in detail below.

In contrast, the results for the {4, 4} combination represent the minimal fragment where the optimization is performed for 16 orbitals on four atoms neighboring the defect center. These PMWFs from the minimal model are shown in Figure 6.6 and display over-localization of the "p"-like states in the NV^- center, i.e., the orbitals are less centered on the atoms and tend to merge at the geometric center. This is a purely numerical artifact of a too-small optimization space which is alleviated (Figure B.18) when the 12 bonded atoms are included to compete with the geometric center for the electron density. Due to this, we disregard the {4, 4} case further.

Upon visual inspection, the {16, 16} combination *graphically* gives the most localized "p"-like orbitals (the second row in Figure 6.6). To provide a quantitative measure of localization, we calculate the locality of each "p"-like state on the corresponding atom plus its neighboring bonded atoms to account for the environment

$$L_i = \sum_{A=1}^{4} \langle \psi_i | w_A | \psi_i \rangle \tag{6.21}$$

where i denote the i^{th} "p"-like state and A sums over the 4 atoms (1 center atom + 3 bonded atoms). The value for each individual state is summarized in Table B.14, where we use the sum, $\sum_{i=1}^{4} L_i$, to represent the whole set of PMWFs. In agreement with the visual analysis (Figure 6.6), the {16, 16} combination exhibits the strongest localization attributed to the modification of the objective functional (eq 6.7). As commented by Jónsson[22] et al., the solutions to "maximally localized Wannier functions" are actually not unique and sometimes ambiguous since the resulting localized orbitals are determined by

the objective functional. We emphasize that the traditional G-PMWF approach evaluates the overall orbital localization on all the atoms, but it does not necessarily reach maximal localization on a specific subsystem (fragment). Instead, the proposed fragmentation treatment in this work leads to an objective functional for regionally localized orbitals. We surmise that this approach is more beneficial for effective embedding and downfolding.

To further analyze the results, we use the four sets of PMWFs and compute the optical transition energies for the 215-atom system (Table 6.4). We see that the $^3E - {}^3A_2$ is the most sensitive to the basis while the other two are less. The {4, 16} combination provides results that are closest to the all-atom calculations. Compared with the most localized case ({16, 16}), the other results are consistently underestimated by up to 0.55 eV. From these results, it is clear that the extent of orbital localization affects various observables differently. While some optical transitions for a given system are insensitive, others can be highly dependent on the basis. The sensible strategy is to search for a fragment that provides the maximal localization on each atom of interest and seek convergence of the observables of interest.

Table 6.4: Excited-state transition energies of the NV^- center in the 215-atom system using the Wannier function basis obtained from different sizes of the fragment as well as the all-atom calculation.

Transition	Energy (eV)				
symmetry	{4, 4}	{4, 16}	{16, 16}	{40, 40}	all-atom
$^3E - {}^3A_2$	1.560	1.770	2.108	1.860	1.715
$^1A_1 - {}^3A_2$	1.325	1.373	1.433	1.384	1.355
$^1E - {}^3A_2$	0.378	0.407	0.447	0.417	0.398
$\sum_{i=1}^{4} L_i$	3.514	3.464	3.507	3.411	3.461

In the rest of the paper, we employ the {16, 16} fragment to obtain the PMWF basis. The parameter study of orbital localization using this fragment is provided in Tables B.17−B.20. The excited-state transition energies are summarized in Table 6.3. For the bulk systems with the new "p"-like basis, ^3E – $^3A_2$ transition gap is enlarged by up to 0.6 eV from the less localized basis, while the other two transition energies are relatively less sensitive to the change of basis.

The effect of the fragment size is most pronounced for the slab. If the {16, 16} fragment is used, the results are similar to those for the bulk systems. In detail: the ^3E – $^3A_2$ transition is predicted ∼1 eV lower than that in bulk, while the other two are only slightly lower (by ∼0.1 eV) compared to the 999-atom cell. Here, the significant lowering of the triplet−triplet transition energy in the slab can be attributed to the interplay with the surface states of nitrogen-atom passivation layer. The surface states dive below the conduction band minimum of the bulk states and are located inside the band gap and affect the position of the in-gap defect states. Finally, we remark that these observations underline the importance of fragment selection. However, they are completely independent of the proposed sequential exhausting methodology. Indeed, the results obtained with the sF-PMWF and F-PMWF methods agree excellently (Table B.15) in each case, while the results depend on the fragment size.

6.5 CONCLUSIONS AND PERSPECTIVE

By introducing the fragmentation treatment and the sequential exhaustion of the orbital space to the traditional F-PMWF method, we develop a swift, efficient, and robust algorithm, sF-PMWF, to obtain a set of regionally localized states on a subsystem of interest. The completeness and efficiency are insensitive to the choice of input parameters. The core idea is to reduce the dimensionality of matrices during the maximization process.

The resulting scaling is reduced from being hyper-quadratic to linear. For the applications of localized basis to the Hubbard model, the excited-state calculations are sensitive to the localized basis. While the Pipek-Mezey scheme is an ideal candidate to provide localized states with optimal localization for the whole system, it does not necessarily lead to "maximally" localized orbitals on a specific subsystem. But in our fragmentation treatment, one can carefully select the atoms (the strategy is mentioned above) to reach "maximally" localized orbitals on the subsystem and avoid the over-localization issue.

The resulting sF-PMWF method has five primary benefits: (1) largely shortens the time per SA iteration and makes it easier to monitor the progress of localization; (2) significantly lowers the total job time and scaling for systems with thousands of electrons; (3) provides regionally localized orbitals with higher extent of localization; (4) less demanding for computing resources, e.g., memory and CPUs; (5) can be performed without the knowledge of canonical eigenstates if it is coupled with stochastic methods (e.g., stochastic DFT). The stochastic basis search approach exhibits higher efficiency than the traditional method for systems with over 4000 electrons.

Furthermore, we want to comment on the following prospective applications of the sequential exhausting method: (1) this method can be generalized to obtain localized states of the whole system. Given that the rest space can always be updated or reconstructed by Gram−Schmidt orthogonalization, the sF-PMWF calculation can then be sequentially applied to all the fragments in the entire system; (2) this method can be coupled with other maximizers, e.g., conjugated gradient and BFGS approach, to further facilitate the convergence of the PM functional; (3) the idea of sequentially exhausting the orbital space can be also implemented in other localization schemes, e.g., Foster−Boys, for a suitably defined fragment and an associated cost function.

We believe that the sF-PMWF method will find numerous applications in condensed matter problems, either in chemistry, materials science, or computational materials

physics.

ACKNOWLEDGMENTS

The authors acknowledge Dr. Susi Lehtola for the fruitful discussion on the atomic weight function and partial charge schemes, which are discussed in the manuscript. The authors also thank the reviewer's comments on the quantification of our observations in timing via eq 6.18. This material is based upon work supported by the U.S. Department of Energy, Office of Science, Office of Advanced Scientific Computing Research, Scientific Discovery through Advanced Computing (SciDAC) program under Award Number DE-SC0022198. This research used resources of the National Energy Research Scientific Computing Center, a DOE Office of Science User Facility supported by the Office of Science of the U.S. Department of Energy under Contract No. DE-AC02-05CH11231 using NERSC award BES-ERCAP0020089. This material is based upon work supported by the National Science Foundation Graduate Research Fellowship under Grant No. (2139319).

SUPPROTING INFORMATION

The Supporting Information provides additional texts, figures and tables listed below.

Texts: Downfolded effective Hamiltonian for the Hubbard Model; Excited states of the NV^- center; Preparation of stochastic basis using deterministic eigenstates.

Figures: three fragments of different sizes and the all-atom system exemplied by the 215-atom cell; scaling of t^{outer} with respect to N_w, evolution of the objective functional with respect to the outer-loop step using deterministic and stochastic basis, investigations of (N_c, N_r) on the 511-atom system, total wall time of orbital localization on the four investigated systems, relative number of SA iterations in the sF-PMWF calculations for

215- and 511-atom systems, scaling of time per iteration with respect to N_s, electron density localized on the NV^- center of the three solid systems, four "p"-like localized Wannier functions on the NV^- center of the three solid systems, electron density localized on an arbitrary carbon atom of the four investigated systems, four "p"-like localized Wannier functions as well as the resulting electron density on the NV^- center of the 215-atom system using different sizes of fragments;

Tables: transition energies obatined from different Wannier functions basis using energy-windowing truncated space, comparison of F-PMWF and sF-PMWF calculations with different N_c and N_r for the four investigated systems using the 4-atom fragment, comparison of the time spent on the folding and unfolding steps; time per outer-loop iteration and normalized time per outer-loop iteration in the sF-PMWF calculations of the four investigated systems, time per macro-cycle iteration and normalized time per macro-cycle iteration in the sF-PMWF calculations of the four investigated systems, total wall time and normalized total wall time of F-PMWF and sF-PMWF calculations for the four investigated systems, time per steep-ascent step in the F-PMWF and sF-PMWF calculations, number of iterations required to reach convergence for the four investigated systems, converged maximized PM functional values, spatial overlap between the Wannier functions obtained from F-PMWF and sF-PMWF calculations for the 2303-atom slab, spatial overlap between the Wannier functions obtained from the fragment approaches with those obtained from the all-atom calculation, transition energies of the four investigated systems using the Wannier functions basis obtained from the F-PMWF calculations, comparison of F-PMWF and sF-PMWF calculations with different N_c and N_r for the four investigated systems using the 16-atom fragment.

Bibliography

[1] X. Wu, A. Selloni, and R. Car, *Order-n implementation of exact exchange in extended insulating systems*, *Phys. Rev. B* **79** (2009) 085102.

[2] F. Gygi and I. Duchemin, *Efficient computation of hartree–fock exchange using recursive subspace bisection*, *Journal of Chemical Theory and Computation* **9** (2013), no. 1 582–587. PMID: 26589056.

[3] T. Miyake, F. Aryasetiawan, and M. Imada, *Ab initio procedure for constructing effective models of correlated materials with entangled band structure*, *Phys. Rev. B* **80** (2009) 155134.

[4] J. M. Tomczak, T. Miyake, R. Sakuma, and F. Aryasetiawan, *Effective coulomb interactions in solids under pressure*, *Phys. Rev. B* **79** (2009) 235133.

[5] S. Choi, M. Jain, and S. G. Louie, *Mechanism for optical initialization of spin in nv^- center in diamond*, *Phys. Rev. B* **86** (2012) 041202.

[6] G. Weng and V. Vlček, *Efficient treatment of molecular excitations in the liquid phase environment via stochastic many-body theory*, *The Journal of Chemical Physics* **155** (2021), no. 5 054104.

[7] F. Aryasetiawan, J. M. Tomczak, T. Miyake, and R. Sakuma, *Downfolded self-energy of many-electron systems*, *Phys. Rev. Lett.* **102** (2009) 176402.

[8] E. Pavarini, E. Koch, D. Vollhardt, and A. Lichtenstein (eds), *The LDA+DMFT approach to strongly correlated materials*. 2011.

[9] D. R. Bowler and T. Miyazaki, *$\mathcal{O}(n)$ methods in electronic structure calculations*, *Reports on Progress in Physics* **75** (2012), no. 3 036503.

[10] B. T. G. Lau, G. Knizia, and T. C. Berkelbach, *Regional embedding enables high-level quantum chemistry for surface science*, *The Journal of Physical Chemistry Letters* **12** (2021), no. 3 1104–1109. PMID: 33475362.

[11] A. Damle, L. Lin, and L. Ying, *Compressed representation of kohn–sham orbitals via selected columns of the density matrix*, *Journal of Chemical Theory and Computation* **11** (2015), no. 4 1463–1469. PMID: 26574357.

[12] E. R. Sayfutyarova, Q. Sun, G. K.-L. Chan, and G. Knizia, *Automated construction of molecular active spaces from atomic valence orbitals*, *Journal of Chemical Theory and Computation* **13** (2017), no. 9 4063–4078.

[13] S. F. Boys, *Construction of some molecular orbitals to be approximately invariant for changes from one molecule to another*, *Rev. Mod. Phys.* **32** (1960) 296–299.

[14] J. M. Foster and S. F. Boys, *Canonical configurational interaction procedure*, *Rev. Mod. Phys.* **32** (1960) 300–302.

[15] P.-O. Löwdin, *Quantum Theory of Atoms, Molecules, and the Solid State A Tribute to John C. Slater*. 1966.

[16] N. Marzari and D. Vanderbilt, *Maximally localized generalized wannier functions for composite energy bands*, *Phys. Rev. B* **56** (1997) 12847–12865.

[17] N. Marzari, A. A. Mostofi, J. R. Yates, I. Souza, and D. Vanderbilt, *Maximally localized wannier functions: Theory and applications*, *Rev. Mod. Phys.* **84** (2012) 1419–1475.

[18] C. Edmiston and K. Ruedenberg, *Localized atomic and molecular orbitals*, *Rev. Mod. Phys.* **35** (1963) 457–464.

[19] C. Edmiston and K. Ruedenberg, *Localized atomic and molecular orbitals. ii*, *The Journal of Chemical Physics* **43** (1965), no. 10 S97–S116.

[20] W. von Niessen, *Density localization of atomic and molecular orbitals. i*, *The Journal of Chemical Physics* **56** (1972), no. 9 4290–4297.

[21] J. Pipek and P. G. Mezey, *A fast intrinsic localization procedure applicable for ab initio and semiempirical linear combination of atomic orbital wave functions*, *The Journal of Chemical Physics* **90** (1989), no. 9 4916–4926.

[22] E. Ö. Jónsson, S. Lehtola, M. Puska, and H. Jónsson, *Theory and applications of generalized pipek–mezey wannier functions*, *Journal of Chemical Theory and Computation* **13** (2017), no. 2 460–474.

[23] R. S. Mulliken, *Electronic population analysis on lcao–mo molecular wave functions. ii. overlap populations, bond orders, and covalent bond energies*, *The Journal of Chemical Physics* **23** (1955), no. 10 1841–1846.

[24] G. Knizia, *Intrinsic atomic orbitals: An unbiased bridge between quantum theory and chemical concepts*, *Journal of Chemical Theory and Computation* **9** (2013), no. 11 4834–4843. PMID: 26583402.

[25] S. Lehtola and H. Jónsson, *Pipek–mezey orbital localization using various partial charge estimates*, *Journal of Chemical Theory and Computation* **10** (2014), no. 2 642–649.

[26] A. Heßelmann, *Local molecular orbitals from a projection onto localized centers*, *Journal of Chemical Theory and Computation* **12** (2016), no. 6 2720–2741.

[27] M. C. Clement, X. Wang, and E. F. Valeev, *Robust pipek–mezey orbital localization in periodic solids*, *Journal of Chemical Theory and Computation* **17** (2021), no. 12 7406–7415. PMID: 34739235.

[28] R. Baer, D. Neuhauser, and E. Rabani, *Self-averaging stochastic kohn-sham density-functional theory*, *Phys. Rev. Lett.* **111** (2013) 106402.

[29] Y. Cytter, E. Rabani, D. Neuhauser, and R. Baer, *Stochastic density functional theory at finite temperatures*, *Phys. Rev. B* **97** (2018) 115207.

[30] M. Chen, R. Baer, D. Neuhauser, and E. Rabani, *Energy window stochastic density functional theory*, *The Journal of Chemical Physics* **151** (2019), no. 11 114116.

[31] M. D. Fabian, B. Shpiro, E. Rabani, D. Neuhauser, and R. Baer, *Stochastic density functional theory*, *WIREs Computational Molecular Science* **9** (2019), no. 6 e1412.

[32] M. Nguyen, W. Li, Y. Li, E. Rabani, R. Baer, and D. Neuhauser, *Tempering stochastic density functional theory*, *The Journal of Chemical Physics* **155** (2021), no. 20 204105.

[33] R. Baer, D. Neuhauser, and E. Rabani, *Stochastic vector techniques in ground-state electronic structure*, *Annual Review of Physical Chemistry* **73** (2022), no. 1 null. PMID: 35081326.

[34] D. Neuhauser, E. Rabani, and R. Baer, *Expeditious stochastic calculation of random-phase approximation energies for thousands of electrons in three dimensions*, *The Journal of Physical Chemistry Letters* **4** (2013), no. 7 1172–1176.

[35] M. Romanova and V. Vlček, *Stochastic many-body calculations of moiré states in twisted bilayer graphene at high pressures*, *npj Computational Materials* **8** (2022), no. 1 1–10.

[36] D. Neuhauser, E. Rabani, and R. Baer, *Expeditious stochastic approach for mp2 energies in large electronic systems*, *Journal of Chemical Theory and Computation* **9** (2013), no. 1 24–27.

[37] Q. Ge, Y. Gao, R. Baer, E. Rabani, and D. Neuhauser, *A guided stochastic energy-domain formulation of the second order møller–plesset perturbation theory*, *The Journal of Physical Chemistry Letters* **5** (2014), no. 1 185–189.

[38] D. Neuhauser, R. Baer, and D. Zgid, *Stochastic self-consistent second-order green's function method for correlation energies of large electronic systems*, *Journal of Chemical Theory and Computation* **13** (2017), no. 11 5396–5403.

[39] W. Dou, T. Y. Takeshita, M. Chen, R. Baer, D. Neuhauser, and E. Rabani, *Stochastic resolution of identity for real-time second-order green's function: Ionization potential and quasi-particle spectrum*, *Journal of Chemical Theory and Computation* **15** (2019), no. 12 6703–6711.

[40] T. Y. Takeshita, W. Dou, D. G. A. Smith, W. A. de Jong, R. Baer, D. Neuhauser, and E. Rabani, *Stochastic resolution of identity second-order matsubara green's function theory*, *The Journal of Chemical Physics* **151** (2019), no. 4 044114.

[41] D. Neuhauser, Y. Gao, C. Arntsen, C. Karshenas, E. Rabani, and R. Baer, *Breaking the Theoretical Scaling Limit for Predicting Quasiparticle Energies: The Stochastic GW Approach*, *Phys. Rev. Lett.* **113** (2014), no. 7 076402.

[42] V. Vlček, E. Rabani, D. Neuhauser, and R. Baer, *Stochastic GW calculations for molecules*, *J. Chem. Theory Comput.* **13** (2017), no. 10 4997–5003.

[43] V. Vlček, W. Li, R. Baer, E. Rabani, and D. Neuhauser, *Swift GW beyond 10,000 electrons using sparse stochastic compression*, *Phys. Rev. B* **98** (2018) 075107.

[44] M. Romanova and V. Vlček, *Decomposition and embedding in the stochastic GW self-energy*, *J. Chem. Phys.* **153** (2020), no. 13 134103.

[45] V. Vlček, *Stochastic vertex corrections: Linear scaling methods for accurate quasiparticle energies*, *J. Chem. Theory Comput.* **15** (2019), no. 11 6254–6266.

[46] C. Zhang and S. Li, *An efficient localization procedure for large systems using a sequential transformation strategy*, *The Journal of Chemical Physics* **141** (2014), no. 24 244106.

[47] F. L. Hirshfeld, *Bonded-atom fragments for describing molecular charge densities*, *Theoretica chimica acta* **44** (1977), no. 2 129–138.

[48] A. D. Becke, *A multicenter numerical integration scheme for polyatomic molecules*, *The Journal of Chemical Physics* **88** (1988), no. 4 2547–2553.

[49] R. Bader, *Atoms in Molecules: A Quantum Theory*. International Ser. of Monogr. on Chem. Clarendon Press, 1994.

[50] T. C. Lillestolen and R. J. Wheatley, *Redefining the atom: atomic charge densities produced by an iterative stockholder approach*, *Chem. Commun.* (2008) 5909–5911.

[51] T. C. Lillestolen and R. J. Wheatley, *Atomic charge densities generated using an iterative stockholder procedure*, *The Journal of Chemical Physics* **131** (2009), no. 14 144101.

[52] P. L. Silvestrelli, N. Marzari, D. Vanderbilt, and M. Parrinello, *Maximally-localized wannier functions for disordered systems: Application to amorphous silicon*, *Solid State Communications* **107** (1998), no. 1 7–11.

[53] P. L. Silvestrelli, *Maximally localized wannier functions for simulations with supercells of general symmetry*, *Phys. Rev. B* **59** (1999) 9703–9706.

[54] K. S. Thygesen, L. B. Hansen, and K. W. Jacobsen, *Partly occupied wannier functions: Construction and applications*, *Phys. Rev. B* **72** (2005) 125119.

[55] P. Giannozzi, O. Andreussi, T. Brumme, O. Bunau, M. Buongiorno Nardelli, M. Calandra, R. Car, C. Cavazzoni, D. Ceresoli, M. Cococcioni, N. Colonna, I. Carnimeo, A. Dal Corso, S. de Gironcoli, P. Delugas, R. A. DiStasio, A. Ferretti, A. Floris, G. Fratesi, G. Fugallo, R. Gebauer, U. Gerstmann, F. Giustino, T. Gorni, J. Jia, M. Kawamura, H.-Y. Ko, A. Kokalj, E. Küçükbenli, M. Lazzeri, M. Marsili, N. Marzari, F. Mauri, N. L. Nguyen, H.-V. Nguyen, A. Otero-de-la Roza, L. Paulatto, S. Poncé, D. Rocca, R. Sabatini, B. Santra, M. Schlipf, A. P. Seitsonen, A. Smogunov, I. Timrov, T. Thonhauser, P. Umari, N. Vast, X. Wu, and S. Baroni, *Advanced capabilities for materials modelling with quantum espresso*, *Journal of Physics: Condensed Matter* **29** (2017), no. 46 465901.

[56] A. Tkatchenko and M. Scheffler, *Accurate molecular van der waals interactions from ground-state electron density and free-atom reference data*, *Phys. Rev. Lett.* **102** (2009) 073005.

[57] M. Otani and O. Sugino, *First-principles calculations of charged surfaces and interfaces: A plane-wave nonrepeated slab approach*, *Phys. Rev. B* **73** (2006) 115407.

[58] N. Troullier and J. L. Martins, *Efficient pseudopotentials for plane-wave calculations*, *Phys. Rev. B* **43** (1991), no. 3 1993.

[59] J. P. Perdew and Y. Wang, *Accurate and simple analytic representation of the electron-gas correlation energy*, *Phys. Rev. B* **45** (1992), no. 23 13244–13249.

[60] S. Choi, M. Jain, and S. G. Louie, *Mechanism for optical initialization of spin in nv-center in diamond*, *Physical Review B* **86** (2012), no. 4 041202.

[61] M. Bockstedte, F. Schütz, T. Garratt, V. Ivády, and A. Gali, *Ab initio description of highly correlated states in defects for realizing quantum bits*, *npj Quantum Materials* **3** (2018), no. 1 1–6.

[62] H. Ma, M. Govoni, and G. Galli, *Quantum simulations of materials on near-term quantum computers*, *npj Computational Materials* **6** (2020), no. 1 1–8.

[63] H. Ma, N. Sheng, M. Govoni, and G. Galli, *Quantum embedding theory for strongly correlated states in materials*, *Journal of Chemical Theory and Computation* **17** (2021), no. 4 2116–2125.

[64] L. Muechler, D. I. Badrtdinov, A. Hampel, J. Cano, M. Rösner, and C. E. Dreyer, *Quantum embedding methods for correlated excited states of point defects: Case studies and challenges*, *Phys. Rev. B* **105** (2022) 235104.

[65] J. P. Goss, R. Jones, S. J. Breuer, P. R. Briddon, and S. Öberg, *The twelve-line 1.682 eV luminescence center in diamond and the vacancy-silicon complex*, *Phys. Rev. Lett.* **77** (1996).

[66] A. Gali, M. Fyta, and E. Kaxiras, *Ab initio supercell calculations on nitrogen-vacancy center in diamond: Electronic structure and hyperfine tensors*, *Phys. Rev. B* **77** (2008).

[67] P. Delaney and J. A. Larsson, *Small cluster model of the NV centre in diamond*, *Phys. Procedia* **3** (2010).

[68] Y. Ma, M. Rohlfing, and A. Gali, *Excited states of the negatively charged nitrogen-vacancy color center in diamond*, *Phys. Rev. B* **81** (2010).

[69] L. Gordon, J. R. Weber, J. B. Varley, A. Janotti, D. D. Awschalom, and C. G. Van De Walle, *Quantum computing with defects*, *MRS Bull.* **38** (2013).

[70] A. Alkauskas, B. B. Buckley, D. D. Awschalom, and C. G. Van De Walle, *First-principles theory of the luminescence lineshape for the triplet transition in diamond NV centres*, *New J. Phys.* **16** (2014).

Chapter 7

Efficient treatment of molecular excitations in the liquid phase environment via stochastic many-body theory

Guorong Weng, Vojtěch Vlček

ABSTRACT

Accurate predictions of charge excitation energies of molecules in the disordered condensed phase are central to the chemical reactivity, stability, and optoelectronic properties of molecules and critically depend on the specific environment. Herein, we develop a stochastic GW method for calculating these charge excitation energies. The approach employs maximally localized electronic states to define the electronic subspace of a molecule and the rest of the system, both of which are randomly sampled. We test

the method on three solute−solvent systems: phenol, thymine, and phenylalanine in water. The results are in excellent agreement with the previous high-level calculations and available experimental data. The stochastic calculations for supercells containing up to 1000 electrons representing the solvated systems are inexpensive and require $\leq$1000 central processing unit hrs. We find that the coupling with the environment accounts for $\sim$40% of the total correlation energy. The solvent-to-solute feedback mechanism incorporated in the molecular correlation term causes up to 0.6 eV destabilization of the QP energy. Simulated photo-emission spectra exhibit red shifts, state-degeneracy lifting, and lifetime shortening. Our method provides an efficient approach for an accurate study of excitations of large molecules in realistic condensed phase environments.

7.1 INTRODUCTION

The charged excited states of molecules in the condensed phase are critical for understanding the molecular electronic structure under realistic conditions. Experimentally, developments in photo-emission spectroscopy (PES) have enabled direct measurement of ionization in the liquid[1, 2, 3, 4, 5, 6, 7] or the solid phase.[8, 9, 10, 11, 12, 13, 14] PES characterizes individual quasiparticles (QP), i.e., holes and electrons that are "dressed" by interactions with their surroundings and have finite (excitation) lifetimes. In principle, the spectra thus provide a direct route to estimate how the environment affects the molecular electronic structure. However, understanding the role of the environmental couplings requires PES with a high energetic and spatio-temporal resolution to differentiate the origin of individual QPs. In practice, the theory thus remains the primary route to uncover the details of the couplings.

Multiple approaches have been proposed for the computational treatment of molecules in realistic environments. The methodologies range from polarizable continuum models

(PCM)[15, 16, 17, 18] to quantum embedding methods.[19, 20, 21, 22, 23, 24, 25] In either of these, the condensed phase is not captured uniformly: the (small) system of interest is typically treated by a high-level quantum mechanical (QM) theory, and the remainder, i.e., the surrounding environment, is represented by an affordable and approximate approach, e.g., classical molecular mechanics. Embedding of the density functional theory (DFT) is computationally inexpensive and, especially the emerging optimally tuned range-separation hybrid (OT-RSH) approach,[26, 27, 28, 29, 30, 31] yields accurate frontier eigenvalues corresponding to ionization potentials (IP) and electron affinities (EA). However, the single-particle levels obtained by DFT do not correspond to QP energies and also contain no information about excited-state lifetimes.[32] The state-of-the-art quantum chemistry approaches, e.g., CCSD(T)[33, 34] and EOM-CC[35, 36, 37, 38, 39, 40, 41, 42] provide accurate predictions for IP and EA. However, they do not capture QP lifetimes either and suffer from a high computational cost. Hence, these methods are applied to either small clusters or within an embedding scheme. Matching of multiple approaches is non-trivial and may lead to artifacts, e.g., blue shifts of the ionization energies rather than red shifts.[43]

Green's function (GF) techniques[44] are becoming more widespread in chemistry and provide an appealing alternative to other methods. In principle, the GF formalism fully captures QPs and their lifetimes, and it is widely applied to condensed matter problems.[45, 46, 47, 48, 49, 50, 51, 52, 53, 54, 55, 56, 57, 58, 59, 60] Further, the methodology is open for systematic improvements; embedding within the GF framework[21, 48, 49, 44, 55, 61] is conceptually straightforward and "seamless." Finally, recent developments of stochastic GF methods[62, 63, 64, 65, 61] enabled calculations for giant systems with thousands of electrons, practically treating large and inhomogeneous systems on equal footing.

In this work, we develop and implement a new computational technique that employs the stochastic approach to many-body calculations combined with the decomposition of

the electron−electron interaction terms. We demonstrate the first-principles QM approach on a set of molecules in the liquid water environment. The method is applied to the *entire* condensed phase; the description of the electronic states in the solute and the solvent is thus consistent. We analyze the dynamical couplings and show that the interactions between the molecule and environment are sensitive to the local molecular geometry and orientation. The non-local correlations are responsible for state reordering; the feedback from the solvent leads to significant changes in the simulated PES spectra of the solutes compared to their isolated counterparts. The methodology captures the red shifts in energy, lifting electronic state-degeneracy, and significant QP lifetime shortening. The results are in excellent agreement with experimental data, and the approach thus provides a unique tool to address the electronic properties in realistic environments.

7.2 METHODOLOGIES

7.2.1 Quasiparticle and decomposition of the self-energy

The GF formalism conveniently describes the dynamics of the QP excitation and directly yields experimentally accessible observables.[66] In practice, the excitation energies and lifetimes are identified from the *spectral function* $A(\omega) = \mathrm{Im}G(\omega)$, where $G(\omega)$ is the GF (representing the time-ordered product of electron creation and annihilation operators). Conceptually, the GF represents the probability amplitude associated with addition or removal at two distinct space-time points; hence it captures the *propagation* of the excitation through the system.

The maxima in $A(\omega)$, i.e., the excitation energies, correspond to the poles of $G(\omega)$ (on real axis). The QP propagator G is "dressed" by many-body interactions and it is related to a (mean-field) non-interacting GF, G_0, via the Dyson equation: $G^{-1} = G_0^{-1} - \Sigma$, where the

self-energy, Σ, emerges as the the central quantity representing *all* many-body effects. It is a complex valued quantity whose real part captures the QP energy *renormalization* (i.e., energy shifts) and its imaginary part is proportional to the inverse of the QP lifetime.[67]

To uncover the role of the solvent environment on the QP excitations, we *formally* decompose the self-energy into the the term stemming from interaction within the molecule (e.g., solute) and outside (i.e., in the environment), denoted Σ^m and Σ^{env}. In this *ansatz*, the QP energy of the j^{th} molecular state is

$$\varepsilon_j = \varepsilon_j^0 + \langle\phi_j| \Sigma^m(\omega = \varepsilon_j) + \Sigma^{env}(\omega = \varepsilon_j) - \hat{v}_{xc} |\phi_j\rangle \,, \tag{7.1}$$

where ε_j^0 is the single particle energy containing all the single-electron and local effective terms in the underlying mean-field Hamiltonian, including the Hartree term and the exchange−correlation potential, v_{xc} (e.g., formulated as a density functional). Hence ε_j^0 corresponds to the j^{th} pole of G_0. To facilitate the comparison between the excitation in an isolated and solvated molecule, the mean-field result is taken from the calculations in the absence of the surrounding solvent molecules. Hence ε_j^0 accounts for the molecular geometry effects, while the solute−solvent interactions are embodied in the remaining terms. In practice, the self-energy is further split into the static and dynamical parts, corresponding to the exchange and the correlation interactions. Here, Σ is constructed using the GW approximation, presented in Secs. 7.2.3 and 7.2.3, and contributions of the environment are analyzed in the results and discussion Sec. 7.3. We emphasize that the decomposition of the self-energy is formal; we treat the environment and the molecule on the same footing, i.e., no approximations beyond those in GW are applied in this work.

For simplicity, we here assume that the molecular states $|\phi_j\rangle$ already represent the Dyson orbitals. This corresponds to the diagonal approximation to the self-energy, which holds in common cases.[68, 69, 70] Our approach can be easily generalized and include also

off-diagonal contributions, e.g., when self-consistent GW treatment is sought.[70] Further, note that the set $|\phi_j\rangle$ does not generally correspond to the single particle eigenstates of the underlying mean-field calculations in the condensed phase (see the end of Sec. 7.2.2). In practice, we first reconstruct $|\phi_j\rangle$ using Wannier functions as detailed in Sec. 7.2.2 and use them to define the occupied subspace that is sampled by the stochastic formalism described later. This approach allows to consistently characterize the charged excitations in the molecule and hence comparing the QPs in isolated and solvated systems.

7.2.2 Separation subspaces: Wannier functions

Our goal is to analyze the effect of the environment on the molecular states $\{|\phi_j\rangle\}$ via Eq. (7.1). Without loss of generality, we will first focus only on charge removal, and $|\phi_j\rangle$ will thus represent an occupied electronic state. We first separate the space spanned by single-particle states into molecular and environmental subspaces. Note that the separation and its construction is rather arbitrary, but as long as there is a map between the subspace of the isolated molecule and the molecule in the condensed phase, we consider this decomposition as complete. Further, the stochastic approach (discussed in Sec. 7.2.3) is applicable regardless of choice for the basis vectors; hence, the goal is to provide a practical route to define the molecular subspace.

Here, we employ the maximally localized Pipek−Mezey Wannier (PMW) functions[71, 72, 73, 74], $\{|\psi_j\rangle\}$, obtained from a unitary transformation of the canonical Kohn−Sham (KS) occupied eigenstates. Let $\{|\psi_j^m\rangle\}$ correspond to states localized on the molecule (i.e., forming the molecular subspace) that are found via the procedure described below. The occupied subspace of the environment is spanned by vectors $\{|\phi^{env}\rangle\}$ obtained through projection:

$$|\phi_j^{env}\rangle = \left(\hat{I} - \hat{P}^m\right) \hat{P}^{occ} |\phi_j^c\rangle \,. \tag{7.2}$$

Here $\hat{I}$ is the identity and $\{|\phi_j^c\rangle\}$ are the *canonical* KS eigenstates of the entire system (i.e., the molecule plus the environment). $\hat{P}^{occ}$ projects onto the occupied subspace, i.e.,

$$\hat{P}^{occ} = \sum_{i}^{N_{occ}} |\phi_i^c\rangle \langle\phi_i^c| . \tag{7.3}$$

Here, N_{occ} is the number of occupied states per the simulation cell of the system (including the target molecule). Further, the $\hat{P}^m$ projector is defined using the PMW states:

$$\hat{P}^m \equiv \sum_{j=1}^{N'_{occ}} |\psi_j^m\rangle \langle\psi_j^m| , \tag{7.4}$$

where N'_{occ} is the number of occupied states on the molecule of interest.

The calculation of the PMW states is iterative and maximizes the following objective function using the steepest descent algorithm[75, 76, 77] (see the supplementary material for details):

$$\mathcal{P} = \sum_{i}^{N_{occ}} \sum_{\mathcal{A}}^{N_{\mathcal{A}}} [Q_{ii}^{\mathcal{A}}]^2, \tag{7.5}$$

where $N_{\mathcal{A}}$ represents the number of atoms in the simulation cell. The Q matrix is defined as

$$Q_{ij}^{\mathcal{A}} = \langle\psi_i| w_{\mathcal{A}} |\psi_j\rangle \tag{7.6}$$

Here, $w_{\mathcal{A}}$ represents the weight function for each atom type $\mathcal{A}$:

$$w_{\mathcal{A}}(\mathbf{r}) = \frac{\bar{n}_{\mathcal{A}(\mathbf{r})}}{\sum_{\mathcal{A}'}^{N_{\mathcal{A}'}} \bar{n}_{\mathcal{A}'}(\mathbf{r})}, \tag{7.7}$$

where $\bar{n}_{\mathcal{A}}(\mathbf{r})$ is the density function of atom type $\mathcal{A}$ using the simple Gaussian model

density.[78] Finally, $\{|\psi_j\rangle\}$ in Eq. (7.6) are

$$|\psi_j\rangle = \sum_{i}^{N_{occ}} W_{ij} \, |\phi_i^c\rangle \, , \tag{7.8}$$

where W is the unitary matrix defined as the exponential of an anti-Hermitian matrix (see the supplementary material). The W matrix is iteratively updated, and PMW orbitals correspond to the solutions $\{|\psi_j\rangle\}$ which maximize $\mathcal{P}$.

In practice, we search only for states localized on the molecule of interest. The program with "locally searching for localized states" feature is available on Github.[79] The sums in Eq. (7.5) thus contain N'_{occ} and $N'_{\mathcal{A}}$ instead of N_{occ} and $N_{\mathcal{A}}$, where the first set of quantities refer to the target molecule. Similarly, the objective function is

$$\mathcal{P}' = \sum_{i}^{N'_{occ}} \sum_{\mathcal{A}}^{N'_{\mathcal{A}}} [Q_{ii}^{\mathcal{A}}]^2. \tag{7.9}$$

Note that the unitary transform is still performed on all (N_{occ}). However, in each iteration step, N'_{occ} states are identified by having the largest expectation value of the weight function:

$$L_j = \sum_{\mathcal{A}}^{N_{\mathcal{A}'}} \langle \psi_j | \, w_{\mathcal{A}} \, |\psi_j\rangle \, . \tag{7.10}$$

The N'_{occ} states with largest L values are used in Eq. (7.9). The resulting PMW states localized on the target molecule and are denoted as $\{|\psi_j^m\}\rangle$.

Using the set of PMWs, we reconstruct the molecular state $|\phi_j\rangle$ in the condensed phase. *First*, we make an auxiliary calculation for an isolated molecule and obtain its N'_{occ} PMWs, $|\psi_j^{iso}\rangle$. The desired molecular state (corresponding to the KS eigenstate of

an isolated system), $|\phi_j^{iso}\rangle$ is represented in the PMW basis:

$$|\phi_j^{iso}\rangle = \sum_i^{N'_{occ}} \alpha_{ij} |\psi_i^{iso}\rangle \,. \tag{7.11}$$

Next, we use the molecular PMW basis in the condensed phase, $|\psi_l^m\rangle$, to reconstruct the molecular orbital:

$$|\phi_j\rangle = \sum_k^{N'_{occ}} \sum_l^{N'_{occ}} \alpha_{ij}\beta_{li} |\psi_l^m\rangle \,, \tag{7.12}$$

where α_{ij} are taken from the Eq. (7.11) and $\beta_{jk} \equiv \langle\psi_j^m|\psi_k^{iso}\rangle$. The underlying assumption is that the occupied molecular subspace in the isolated and solvated molecules are the same. Note that for strongly interacting solvent−solute systems the molecular states may be hybridized with the environment. However, if the occupied subspace remains similar, one can establish a map between $|\psi_j^m\rangle$ and $|\psi_j^{iso}\rangle$. Consequently, Eq. (7.12) imposes that the charged excitation is constrained to be within a particular state ϕ_j localized on the molecule. In this way, we can directly compare the ionization of isolated and solvated systems. Such a treatment is also readily applicable in the context of GF and self-energy embedding.[80, 81, 82, 83, 84]

For the systems described in Sec. 7.3, we found one-to-one correspondence between the PMW orbitals, i.e., $\beta_{jk} \simeq \delta_{jk}$, and Eq. (7.12) is considerably simplified. In all the cases studied, the solute/solvent molecules do not strongly hybridize, and we reconstruct individual molecular states, as presented in Sec. 7.3.1.

Finally, despite we focused on the occupied states, the methodology can be applied to reconstruct the bound empty molecular orbitals. The critical part is the identification of the *bound* unoccupied subspace first for the isolated molecule and then the molecule in the condensed phase. Once done, the reconstruction follows the same steps explained above.

7.2.3 Stochastic calculation of the self-energy

For calculations of the QP energies, we employ the *GW* approximation in which the non-local and dynamical $\Sigma(\omega)$ derives from charge density fluctuations (induced by particle removal or addition) that screens the exchange interactions. This approach is typically in good agreement with experiments.[85, 86, 44] Nevertheless, the *GW* correlation neglects the quantum fluctuations, which may become important for high energy excitations and/or for unoccupied states.[65, 87] The method of subspace separations is, however, general and applicable to beyond-*GW* approaches; it will be explored in the future. Here, a single-shot perturbative correction is computed within the random phase approximation (RPA) on top of a density functional theory (DFT) starting point (see the supplementary material for details).

To overcome the high cost of conventional implementations, we employ the recently developed stochastic formalism, which can be applied to extremely large systems owing to its linear scaling.[62, 63, 64, 57, 65, 59, 60, 61, 87] This approach to the one-shot perturbative correction (typically denoted G_0W_0) seeks the QP energy by randomly sampling the single-particle states and decomposing the operators in the real-time domain. The stochastic formalism has been described in detail in previous work[62, 63, 64] and it is briefly revisited in the supplementary material. In Subsections 7.2.3 and 7.2.3, we describe the connection between random sampling and the decomposition of the correlation and exchange self-energies.

Correlation contribution

As stated above, the correlation part of the *GW* self-energy, Σ_c, is governed by the charge density fluctuations. Recently, we have formulated a stochastic approach to decompose Σ_c (Ref. 61), which is also applied to the calculations of the Σ_c^m and Σ_c^{env} in

this work. Here, m and env denote the molecule and the environment.

Within the stochastic formalism, we employ random states ζ to decompose the GF. The resulting expression for the correlation self-energy $\Sigma_c(t)$ explicitly depends on the induced charge density potential $u_{\bar{\zeta}}(\mathbf{r},t)$

$$\langle\phi_j|\,\Sigma_c(t)\,|\phi_j\rangle \simeq \frac{1}{N_\zeta}\sum_{\zeta}\int \phi(\mathbf{r})\zeta(\mathbf{r},t)u_{\bar{\zeta}}(\mathbf{r},t)\mathrm{d}\mathbf{r}, \tag{7.13}$$

where $u_{\bar{\zeta}}(\mathbf{r},t)$ is in practice computed from the retarded response potential due to the $\delta n(t)$:

$$\tilde{u}_{\zeta}(\mathbf{r},t) = \int \nu(\mathbf{r},\mathbf{r}')\delta n(\mathbf{r}',t)\mathrm{d}\mathbf{r}'. \tag{7.14}$$

The definitions of $u_{\bar{\zeta}}(\mathbf{r},t)$ and $\tilde{u}_{\zeta}(\mathbf{r},t)$ are provided in the supplementary material.

Next, we separate the induced time-dependent charge density $\delta n(\mathbf{r},t) = n(\mathbf{r},t) - n(\mathbf{r},0)$ into two terms: for the time-dependent density of the molecule, i.e., solute, and the environment, i.e., solvent (distinguished by superscripts):

$$n(\mathbf{r},t) = n^m(\mathbf{r},t) + n^{env}(\mathbf{r},t). \tag{7.15}$$

Both densities are expressed via the linear combination of PMW states (Sec. 7.2.2). In our stochastic approach, the time-dependent n^m and n^{env} are sampled using a set of random vectors $\{\eta^k\}$ confined to the corresponding (and mutually orthogonal) subspaces k ($k = m, env$):

$$n^k(\mathbf{r},t) = \frac{1}{N_\eta}\sum_{l}^{N_\eta}|\eta_l^k(\mathbf{r},t)|^2. \tag{7.16}$$

Here, N_η represents the number of random vectors used in the sampling (we employ $N_\eta = 16$; see the supplmentary material for details). The random vector is prepared by

projections:

$$|\eta^k\rangle = \hat{P}^k \hat{P}^{occ} |\eta\rangle \,, \tag{7.17}$$

where the case of $\hat{P}^m$ is given by Eq. (7.4) and $\hat{P}^{env} = \hat{I} - \hat{P}^m$. The projector $\hat{P}^{occ}$ is defined by Eq. (7.3).

The time propagated random vector $|\eta^k(t)\rangle$ in Eq. (7.16) is:

$$|\eta^k(t)\rangle = U_{0,t}[n(t)] \, |\eta^k\rangle \,, \tag{7.18}$$

where $U_{0,t}$ is the time evolution operator defined as

$$U_{0,t}[n(t)] = e^{-iH_0[n^m, n^{env}]t}. \tag{7.19}$$

Here, H_0 is the mean-field Hamiltonian that is a functional of the total time-dependent charge density (i.e., containing contributions of both subspaces). Propagation using the full charge density ensures that the correlated dynamics between the two subsystems is captured.

Exchange contribution

The exchange self-energy is clearly defined via the non-local integral involving the density matrix, ρ, and the bare Coulomb interaction, ν:

$$\Sigma_x = \iint \varphi_j{}^*(\mathbf{r}) \nu(\mathbf{r}, \mathbf{r}') \rho(\mathbf{r}, \mathbf{r}') \varphi_j(\mathbf{r}') \mathrm{d}\mathbf{r}' \mathrm{d}\mathbf{r}, \tag{7.20}$$

where φ_j is a single-particle state. The density matrix is

$$\rho(\mathbf{r}, \mathbf{r}') = \sum_i^{N'_{occ}} \varphi_i(\mathbf{r}) \varphi_i^*(\mathbf{r}'). \tag{7.21}$$

In practice, we disentangle the contributions from various parts of the system similar to the procedure applied to the correlation self-energy. Due to the orthogonality of the molecular and environment states, the density matrix is simply decomposed into the corresponding contributions ρ^m and ρ^{env}. The former is analogous to the solution for an isolated molecule. The contribution of the environment is employs states $\{|\phi_j^{env}\rangle\}$ obtained by the projection in Eq. (7.2).

7.3 RESULTS AND DISCUSSIONS

We now demonstrate the methodology and investigate the role of solute−solvent interactions on the PES of phenol, thymine, and phenylalanine in water. The molecules are selected based on their relevance in chemistry and (variable) structural complexity. Phenol in water is a ubiquitous motif in biological chromophores, and hence this system has attracted interest in the past.[36, 6] Thymine and phenylalanine are studied in the context of DNA molecules[88, 89, 2, 35, 40] and amino acids.[90, 91, 92, 41, 42] While phenol is the simplest and represents a "rigid" system (only a hydroxyl group is attached to the benzene ring), thymine has a methyl group attached to the ring, which can freely rotate. Phenylalanine has a much longer amino-acid group attached to the benzene ring. The molecular structures are provided in Figure C.1.

The system geometries are obtained using Molecular Dynamics simulations (see the supplementary material). From the trajectory of the calculation, we extract five uncorrelated solute−solvent structures and perform the stochastic many-body calculations. Ground state DFT is used to obtain the starting point for GW: the calculations are performed on a regular real-space grid with generalized gradient approximation to exchange and correlation in combination with the Troullier Martins norm-conserving pseudopotentials.[93] The computations for isolated molecules are denoted as *iso* henceforth; the full QP spectra

are computed for the solvated systems (see the discussion below) captured by simulation cells with the periodic boundary condition with up to 1056 electrons. The stochastic calculations of QP energies are converged with respect to the number of stochastic samples such that the errors are $\leq$0.07 eV for the frontier state. The random sampling is efficient – to reach this level of statistical error, the simulation took only 438, 988, and 1315 central processing unit (CPU) hrs for phenol, thymine, and phenylalanine on a cluster computer equipped with CPUs with a clock speed of 2.40GHz.

In the rest of this section, we first discuss the orbital reconstruction, followed by the analysis of the QP renormalization in the liquid phase. Finally, we show the full theoretical PES.

7.3.1 One-to-one correspondence of occupied subspace

Following the ground state DFT calculations, we determine the PMW states for both the isolated and solvated solute molecules. Figure 7.1, shows the typical PMW functions for phenol molecule. In the rest of this paper, we consider only the occupied subspace; a similar approach is, however, applicable to empty states as discussed in Sec. 7.2.2.

The PMW functions have highly localized spatial distribution, and it is appealing to interpret them as bonding orbitals that characterize the entire occupied subspace. In this (convenient) framework, one can expect that PMW functions of the isolated and solvated systems are related. Indeed, our calculations indicate that we can directly map the isolated and solvated system PMW functions onto each other in all the cases studied (Figure C.3). The spatial overlap between the corresponding PMW functions is at least 99% for all the three molecules (Table C.3).

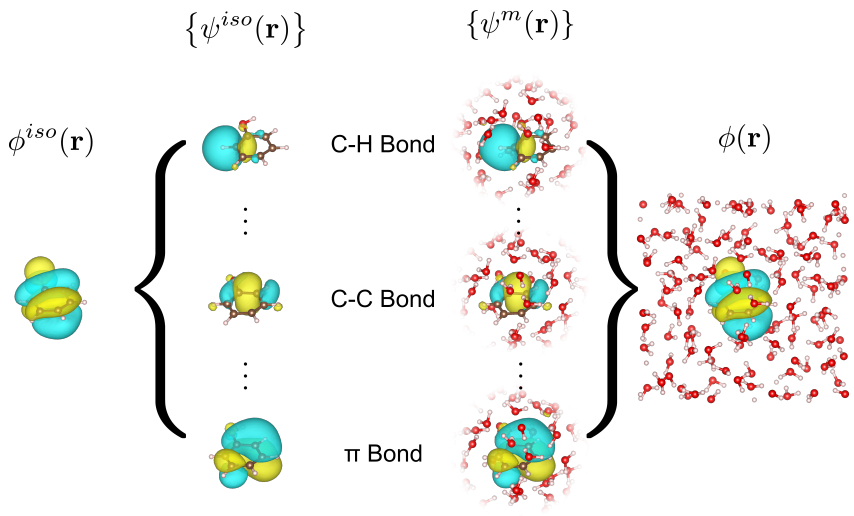

Figure 7.1: Three typical PMW functions of isolated and solvated phenol molecule, respectively (Middle). The PMW functions are labelled by chemical bonds due to their spatial distribution. The eigenstate, e.g., HOMO, of the isolated molecule is expressed as a linear combination of $|\psi_j^{iso}\rangle$ (Left). Using the same set of coefficients, the molecular state of the solvated molecule is constructed as a linear combination of $|\psi_j^{m}\rangle$ (Right).

The correspondence between PMWs of isolated and embedded systems is likely common, and PMWs can thus be leveraged to reconstruct the molecular orbitals. As discussed in Sec. 7.2.2, it is not, however, necessary that there is a one-to-one map. Instead, the only underlying assumption is that the selected subspace is the same for both the solvated and isolated molecules. In particular, this is one of the advantages of the stochastic methods, which merely require the knowledge of the molecular *subspace* (not the states).

Figure 7.1 shows the reconstructed highest occupied molecular orbital (HOMO) for the phenol in water (the right panel) versus the counterpart of the isolated one (the left panel). The reconstructed $|\phi\rangle$ enters Eq. (7.1), and it is used to evaluate the role of the environmental effects.

7.3.2 HOMO QP energies and energy shifts

The QP energies of frontier states are of primary interest in the charge transfer process as they correspond to the negative of the first ionization/detachment energy. We employ the reconstructed orbitals discussed above. The solvent affects the QP energy [Eq. (7.1)] via (i) variation of the molecular (solute) geometry and (ii) changes in the total self-energy and presence of the Σ^{env} term for the solvated molecule.

We first quantify the effects of the solute structure as changes of the QP energy purely due to the geometry variation in the absence of the environment. In practice, we compare the average of the QP energies for isolated molecules (with geometries extracted from the MD trajectory) against the results for the system in its ground state geometry in the gas phase (see Table C.4). On average, the absolute differences between the two are merely 0.05, 0.22, and 0.15 eV for phenol, thymine, and phenylalanine, respectively. Surprisingly, the *GW* values appear to be less sensitive to the structural changes than the underlying DFT (Table C.6). More importantly, the *GW* method provides results that are in good agreement with experimental gas-phase IP measurements (albeit with a systematic shift, see Table C.4).

Although the HOMO QP energies do not deviate significantly from the gas-phase values *on average*, they can markedly differ for a particular configuration (Figure C.4). The standard deviations (σ) stemming from structural variations of isolated molecules are 0.08, 0.11, and 0.28 eV for phenol, thymine, and phenylalanine (Table C.4), respectively. Clearly, the spread of the results (captured by σ) increases with the molecular complexity (i.e., from phenol to phenylalanine). Furthermore, the structural changes are associated with electronic state reordering, i.e., the QP energies associated with particular states are (de)stabilizing various states differently and QP HOMO is not identical to the DFT HOMO orbital. Hence, the non-local dynamical correlations in Σ^m are responsible for

significant energy renormalization. For instance, the HOMO orbital is not the same as predicted by DFT in the majority of the calculations for phenylalanine (see Table C.5 for details).

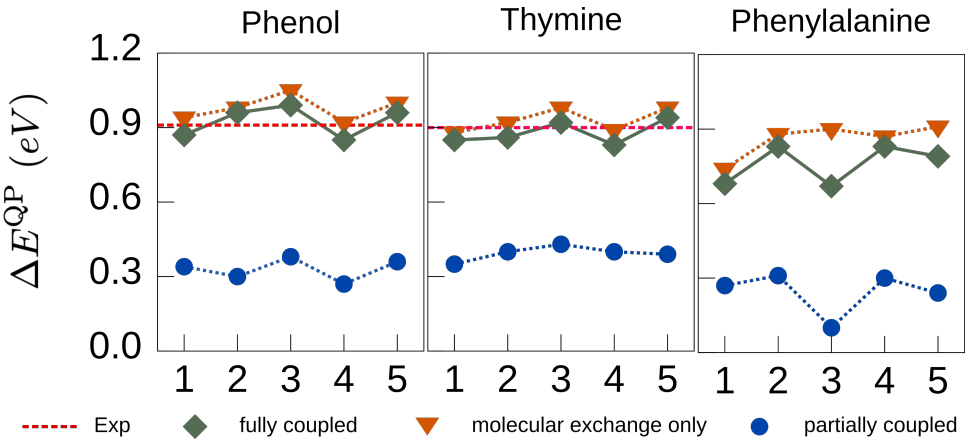

Figure 7.2: HOMO QP energy shifts with respect to the snapshots along the MD trajectory of the three solvated molecules. The red dashed lines represent the experimental results for phenol[36] and quantum chemistry calculations for thymine[35].

In the remaining part, we focus on the QP energy renormalization stemming purely from the electron−electron interactions due to the water solvent. Again, we quantify them as QP energy shifts relative to the QP energy of isolated molecules. The results are presented in Figure 7.2 (the dark green solid lines) and Table C.9, where the averaged QP energy shifts over 5 snapshots are $+0.92 \pm 0.06$, $+0.88 \pm 0.05$, and $+0.76 \pm 0.08$ eV for phenol, thymine, and phenylalanine, respectively. The QP energies are significantly destabilized, and the ionization potential thus decreases. Reference data from previous studies are summarized in Table C.8. The predicted QP energy shift of phenol is in excellent agreement with previous PES measurements[6] and OT-RSH-DFT calculations.[28] The shift of thymine also agrees well with previous quantum chemistry calculations.[35] For phenylalanine, the experimental IP in the gas phase ranges from 8.80 to 9.15 eV, which depends on the molecular conformation.[94, 90] Our calculations for the five geometries of isolated phenylalanine along the MD trajectory also reflect such conformational dependency

(see Figure C.4). The available aqueous-phase measurements give the IP as 8.7/8.8 eV,[95] resulting in an IP shift of 0-0.45 eV by experiments. These values, however, contrast other commonly reported estimates of the solvent shifts (∼1 eV).[96] The uncertainty of the experimental data can be interpreted at least in two ways: either by a strong conformation-dependence of the IP (yet to be explored), or potential inconsistency between the gas-phase and aqueous-phase measurements. For these reasons, we do not validate our results for phenylalanine against experiments. Further, the only available calculations of phenylalanine using DFT and non-equilibrium PCM method suggest a 1.06 eV shift in IP between two phases,[92] which is higher than our value. Since DFT is a mean-field method, we do not use it to validate the results computed using the many-body perturbation theory.

The environment affects the QPs more than by just rigidly shifting the excitation energies. Indeed, the QP energy variation for phenol and phenylalanine in water increases by 75% and 18% (to 0.14 and 0.33 eV). In contrast, σ for thymine in water slightly decreases by 11%. The numerical results are provided in Table C.7. This indicates that the many-body interactions between the solute and solvent can strongly depend on the actual molecular arrangements, and the effects are further analyzed in Subsection 7.3.3.

7.3.3 "Fully coupled" correlation vs. "partially coupled" correlation

To understand the changes in the QP energies, we decompose the self-energy into exchange and correlation terms stemming from the molecule and the environment. The exchange interaction generally leads to the QP stabilization, and it is governed by solute molecular states. The contribution of Σ_x due to the solvent is small ($\leq$0.16 eV, Table C.10) due to the limited spatial overlap between the the molecular orbitals and the remainder

of the system (Figure 7.2, the dark orange dotted line and Table C.10). In practice, the non-local and dynamical correlation self-energy thus captures the key aspects of mutual coupling between the solute and solvent.

To understand the effect of the environment on Σ_c, we will, for simplicity, consider the first ionization energies, i.e., HOMO states. First, we note that the relative contribution of environment correlation Σ_c^{env} (i.e., the fraction of the total Σ_c) ranges between 30% and 47% (Table C.11) and the remaining portion, Σ_c^m, is due to the dynamical interactions of electrons localized in the molecule.

The environmental effects are, however, not represented solely by Σ^{env}. In fact, the charge removal from a molecular state, $|\phi_j\rangle$, leads to dynamical interactions with electrons in the surrounding water molecules. Besides the "direct" effect (i.e., solute-to-solvent), the induced charge density fluctuations in water also create a solvent-to-solute feedback mechanism. Hence, the induced charge density in the environment leads to secondary fluctuations in the molecule and so on. This coupling is inherently captured by the charge density in each subsystem, $n^k(\mathbf{r}, t)$, which is subject to the time evolution governed by the *total* charge density [Eq. (7.19)]. In this case, the real-time formalism is particularly appealing as it enables capturing strong (i.e., even non-linear) couplings.[97, 98, 99, 100]

We now compare the self-energies of the molecule in the environment, Σ_c^m, with an isolated one, Σ_c^{iso}, i.e., without the environmental feedback.[101] The comparison provides an estimate of the solvent-to-solute coupling magnitude. The real parts of the HOMO self-energy Σ_c^{iso} and Σ_c^m are shown in Figure 7.3 for one of the snapshots along the MD trajectory. The observed shift with respect to each other is due to the solvent. In practice, the spectral features are shifted closer to QP energy and generally enhance the correlation energy contribution. The changes do not correspond merely to a rigid shift of the self-energy and distinct, i.e., various maxima of the curve are affected differently.

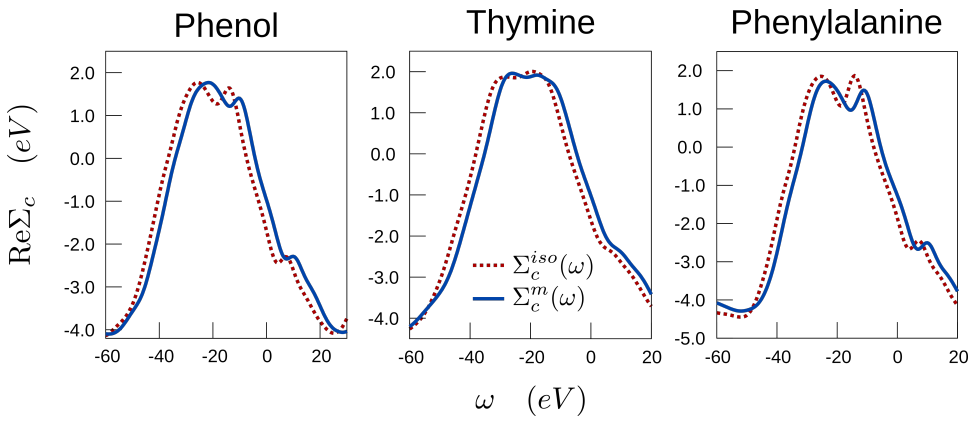

Figure 7.3: Comparisons of the real-part of the correlation self-energy with (solid line) and without (dotted line) the solvent-to-solute feedback for the three molecules. When the solute-to-solvent feedback is accounted, the self-energy curves derived from the charge density fluctuations on the solvated molecules (δn^m) are unanimously shifted to lower frequency region with respect to that of the isolated molecules.

If we recompute the QP energy by combining Σ_c^{env} with Σ_c^{iso}, the correlations contain only screening stemming either from the molecule or the environment but the indirect solvent-to-solute contributions are missing. To distinguish this result, we label this QP energy as "partially-coupled." Figure 7.2 shows that in this case the QP energy shifts decrease by as much as 68% (to 0.33, 0.39, and 0.24 eV for phenol, thymine, and phenylalanine, respectively, Table C.12). Hence, the induced interactions between the charge densities represent a significant component of the QP renormalization. This observation illustrates the need for a fully coupled description of the molecule and the environment.

Note that the approach proposed here is distinct from the previous calculations employing GW only for a molecular subsystem, and relied on the QM/MM embedding approach,[48, 55] which was further combined with an electrostatic reaction field based on the classical charge response model.[102] This embedding accounts for the environment response in the screened Coulomb interaction term (W) through the inclusion of the solvent polarizability. In practice, the correlation term contains contributions from the

induced charge density on the molecule and the environment, but their dynamical coupling (i.e., secondary solvent-to-solute interaction) is neglected except for structural changes of the solute molecule and its orbitals. In contrast, the approach proposed here treats both subspaces consistently and fully coupled (within the GW approximation). Further, the environmental effects are present in all the terms entering the self-energy evaluation, i.e., not only W. This is particularly important for calculations that include higher-level treatment beyond GW.[65, 87]

7.3.4 Simulated photo-emission spectra

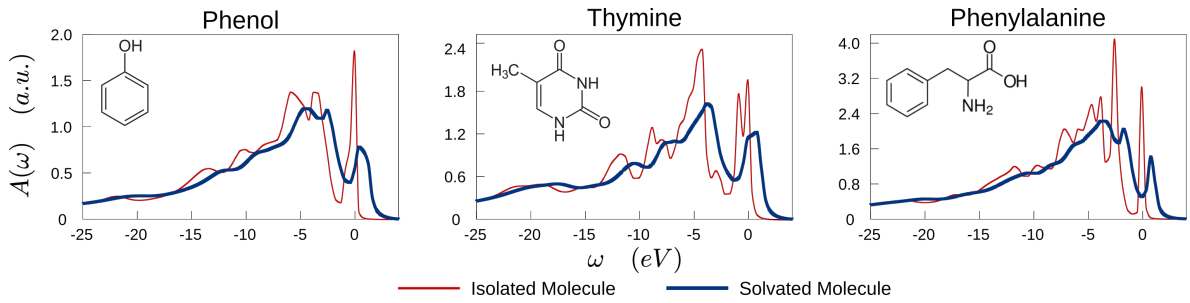

Figure 7.4: Simulated photo-emission spectra of the three molecules depicted in the insets. The spectral functions for an isolated molecule and its solvated counterpart are distinguished by color.

In the final step, we turn to the prediction of the entire photo-emission spectra of the solvated molecules represented by the spectral function $A(\omega)$ (Sec. 7.2.1). Here, the total $A(\omega)$ curve is a sum over the imaginary components of the GFs from each valence state.[103] Figure 7.4 shows a comparison between $A(\omega)$ for the isolated and solvated molecules. The zero on the frequency (energy) axis is aligned with the HOMO QP energy of the isolated system. The common feature is the destabilization of the molecular states, i.e., shifts to higher energies.

For phenol, the profiles of the PES in two phases are similar, although the height of the frontier state's peak is significantly reduced and simultaneously broadened. This

indicates a strong QP lifetime decrease due to the electron−electron interactions with the water solvent. Note that for the spectra of isolated molecules, the peak width is artificially widened by the finite time evolution employed when computing Σ_c^{iso}; since this finite broadening affects the spectrum uniformly, we consider only the relative changes in the peak width with respect to the HOMO state. Further, note that we consider only the *electron−electron scattering*, but, in practice, additional broadening will be observed due to vibrational couplings. The results presented in Figure C.6 clearly indicate that even if only electronic degrees of freedom are considered, the QP lifetime shortening is significant for all valence states and the spectral broadening progresses with the hole energy (i.e., the deep valence holes correspond to wide peaks).

For thymine, besides the energy shift, the overall spectrum is much smoother as molecular distortions and solvent couplings lift the QP state degeneracy. In general, the peak widths of the solvated systems are on average 50% increased (see also Table C.16). These effects are most obvious in the PES of phenylalanine: the spectral function is destabilized, the QP lifetime decreases, and we observe almost complete smearing of the entire spectrum below the HOMO level. The QP lifetime of phenylalanine's frontier state is shortened most significantly, by as much as 90%, leading to a drastically reduced peak height in Figure 7.4.

For completeness, we analyze the energy shifts ΔE^{QP} of all valence states (see Tables C.13−C.15). For phenol and phenylalanine, ΔE^{QP} is practically constant (on average 0.94 and 0.86 eV). For thymine, the bottom valence states are more destabilized compared to the top valence region; yet the average shift for each state is comparable to the other two molecules (0.87 eV). For a specific system configuration, the environmental effect is consistent for all valence states.

7.4 CONCLUSION

In summary, a fully ab-initio stochastic many-body method is established to calculate QP energy for molecules in the condensed phase. Here, the separation between the electronic states is general, and the methodology treats the entire system at the same level of theory. We adopt the *GW* approximation to describe the QP excitations. The approach combines the random sampling of operators in mutually orthogonal subspaces corresponding to the molecule and the environment. We presented a practical route to reconstruct the molecular subspace in liquid water via a linear combination of localized PMW functions. Owing to the linear scaling of the stochastic methodology, realistic calculations for systems with thousands of electrons are thus possible.

The approach is tested on three solute−solvent combinations. By separating the interactions, we find that the environment correlation energy Σ_c^{env} accounts for ∼40% of the QP renormalization. Further, the solvent effects are responsible for dynamical coupling to the correlations within the molecular subspace and contribute by up to 68% of the overall energy shift. The simulated PES of solutes shows the following characteristic features: destabilization (i.e., red shift) of the peaks, smearing of the entire spectrum, and significant QP lifetime shortening.

The methodology is general and can be applied to liquid and solid phases. It provides direct access to the charge excitation energies as well as the photo-emission spectra and their changes due to the interactions with the environment. Thus, this approach provides a new perspective on ionization and charge transfer processes. Our subspace approach can be further applied in (real-time) TDDFT calculations to simulate photo-absorption spectra accounting for the environmental effects on the embedded molecules. And ultimately, our method will contribute to understanding the chemical reactivity and opto-electronic properties of molecules in complex systems.

SUPPLEMENTARY MATERIAL

The supplementary material provides the supporting information for the details of DFT and GW calculations, Pipek−Mezey wannier functions, and spectral functions. Supplementary tables and figures indicated in the texts are also provided in this document.

ACKNOWLEDGMENTS

The authors would like to acknowledge Professor Thuc-Quyen Nguyen for fruitful discussions. This work was supported by the NSF CAREER award through Grant No. DMR-1945098. The calculations were performed as part of the XSEDE computational Project No. TG-CHE180051. Use was made of computational facilities purchased with funds from the National Science Foundation (CNS-1725797) and administered by the Center for Scientific Computing (CSC). The CSC is supported by the California NanoSystems Institute and the Materials Research Science and Engineering Center (MRSEC; NSF DMR 1720256) at UC Santa Barbara.

DATA AVAILABILITY

The data that support the findings of this study are available from the corresponding author upon reasonable request.

Bibliography

[1] B. Winter and M. Faubel, *Photoemission from liquid aqueous solutions*, *Chemical Reviews* **106** (2006), no. 4 1176–1211.

[2] P. Slavíček, B. Winter, M. Faubel, S. E. Bradforth, and P. Jungwirth, *Ionization energies of aqueous nucleic acids: Photoelectron spectroscopy of pyrimidine nucleosides and ab initio calculations*, *Journal of the American Chemical Society* **131** (2009), no. 18 6460–6467.

[3] R. Seidel, S. Thürmer, and B. Winter, *Photoelectron spectroscopy meets aqueous solution: Studies from a vacuum liquid microjet*, *The Journal of Physical Chemistry Letters* **2** (2011), no. 6 633–641.

[4] E. Pluhařová, C. Schroeder, R. Seidel, S. E. Bradforth, B. Winter, M. Faubel, P. Slavíček, and P. Jungwirth, *Unexpectedly small effect of the dna environment on vertical ionization energies of aqueous nucleobases*, *The Journal of Physical Chemistry Letters* **4** (2013), no. 21 3766–3769.

[5] P. R. Tentscher, R. Seidel, B. Winter, J. J. Guerard, and J. S. Arey, *Exploring the aqueous vertical ionization of organic molecules by molecular simulation and liquid microjet photoelectron spectroscopy*, *The Journal of Physical Chemistry B* **119** (2015), no. 1 238–256.

[6] J. W. Riley, B. Wang, J. L. Woodhouse, M. Assmann, G. A. Worth, and H. H. Fielding, *Unravelling the role of an aqueous environment on the electronic structure and ionization of phenol using photoelectron spectroscopy*, *The Journal of Physical Chemistry Letters* **9** (2018), no. 4 678–682.

[7] T. Suzuki, *Ultrafast photoelectron spectroscopy of aqueous solutions*, *The Journal of Chemical Physics* **151** (2019), no. 9 090901.

[8] K. Seki, *Ionization energies of free molecules and molecular solids*, *Molecular Crystals and Liquid Crystals Incorporating Nonlinear Optics* **171** (1989), no. 1 255–270.

[9] K. Seki, T. Tani, and H. Ishii, *Electronic structures of organic-inorganic interfaces studied by uv photoemission*, *Thin Solid Films* **273** (1996), no. 1 20–26.

[10] K. Seki, T. Furuyama, T.-o. Kawasumi, Y. Sakurai, H. Ishii, K. Kajikawa, Y. Ouchi, and T. Masuda, *Uv photoelectron spectroscopy of substituted polyacetylenes*, *The Journal of Physical Chemistry B* **101** (1997), no. 45 9165–9169.

[11] I. G. Hill and A. Kahn, *Energy level alignment at interfaces of organic semiconductor heterostructures*, *Journal of Applied Physics* **84** (1998), no. 10 5583–5586.

[12] K. Sugiyama, D. Yoshimura, T. Miyamae, T. Miyazaki, H. Ishii, Y. Ouchi, and K. Seki, *Electronic structures of organic molecular materials for organic electroluminescent devices studied by ultraviolet photoemission spectroscopy*, *Journal of Applied Physics* **83** (1998), no. 9 4928–4938.

[13] B. W. D'Andrade, S. Datta, S. R. Forrest, P. Djurovich, E. Polikarpov, and M. E. Thompson, *Relationship between the ionization and oxidation potentials of molecular organic semiconductors*, *Organic Electronics* **6** (2005), no. 1 11–20.

[14] K. Seki and K. Kanai, *Development of experimental methods for determining the electronic structure of organic materials*, *Molecular Crystals and Liquid Crystals* **455** (2006), no. 1 145–181.

[15] J. Tomasi and M. Persico, *Molecular interactions in solution: An overview of methods based on continuous distributions of the solvent*, *Chemical Reviews* **94** (1994), no. 7 2027–2094.

[16] C. J. Cramer and D. G. Truhlar, *Implicit solvation models: equilibria, structure, spectra, and dynamics*, *Chemical Reviews* **99** (1999), no. 8 2161–2200.

[17] M. Orozco and F. J. Luque, *Theoretical methods for the description of the solvent effect in biomolecular systems*, *Chemical Reviews* **100** (2000), no. 11 4187–4226.

[18] J. Tomasi, B. Mennucci, and R. Cammi, *Quantum mechanical continuum solvation models*, *Chemical Reviews* **105** (2005), no. 8 2999–3094.

[19] M. S. Gordon, D. G. Fedorov, S. R. Pruitt, and L. V. Slipchenko, *Fragmentation methods: A route to accurate calculations on large systems*, *Chemical Reviews* **112** (2012), no. 1 632–672.

[20] S. R. Pruitt, C. Bertoni, K. R. Brorsen, and M. S. Gordon, *Efficient and accurate fragmentation methods*, *Accounts of Chemical Research* **47** (2014), no. 9 2786–2794.

[21] W. Chibani, X. Ren, M. Scheffler, and P. Rinke, *Self-consistent green's function embedding for advanced electronic structure methods based on a dynamical mean-field concept*, *Physical Review B* **93** (2016), no. 16 165106.

[22] Q. Sun and G. K.-L. Chan, *Quantum embedding theories*, *Accounts of Chemical Research* **49** (2016), no. 12 2705–2712.

[23] L. O. Jones, M. A. Mosquera, G. C. Schatz, and M. A. Ratner, *Embedding methods for quantum chemistry: Applications from materials to life sciences*, *Journal of the American Chemical Society* **142** (2020), no. 7 3281–3295.

[24] Z. Tóth, J. Kubečka, E. Muchová, and P. Slavíček, *Ionization energies in solution with the qm:qm approach*, *Physical Chemistry Chemical Physics* **22** (2020), no. 19 10550–10560.

[25] H. Ma, N. Sheng, M. Govoni, and G. Galli, *Quantum embedding theory for strongly correlated states in materials*, *Journal of Chemical Theory and Computation* **17** (2021), no. 4 2116–2125.

[26] H. Sun, S. Ryno, C. Zhong, M. K. Ravva, Z. Sun, T. Körzdörfer, and J.-L. Brédas, *Ionization energies, electron affinities, and polarization energies of organic molecular crystals: Quantitative estimations from a polarizable continuum model (pcm)-tuned range-separated density functional approach*, *Journal of Chemical Theory and Computation* **12** (2016), no. 6 2906–2916.

[27] H. Sun, Z. Hu, C. Zhong, S. Zhang, and Z. Sun, *Quantitative estimation of exciton binding energy of polythiophene-derived polymers using polarizable continuum model tuned range-separated density functional*, *The Journal of Physical Chemistry C* **120** (2016), no. 15 8048–8055.

[28] M. Rubešová, E. Muchová, and P. Slavíček, *Optimal tuning of range-separated hybrids for solvated molecules with time-dependent density functional theory*, *Journal of Chemical Theory and Computation* **13** (2017), no. 10 4972–4983.

[29] L. Kronik and S. Kümmel, *Dielectric screening meets optimally tuned density functionals*, *Advanced Materials* **30** (2018), no. 41 1706560.

[30] S. Bhandari, M. S. Cheung, E. Geva, L. Kronik, and B. D. Dunietz, *Fundamental gaps of condensed-phase organic semiconductors from single-molecule calculations using polarization-consistent optimally tuned screened range-separated hybrid functionals*, *Journal of Chemical Theory and Computation* **14** (2018), no. 12 6287–6294.

[31] A. Boruah, M. P. Borpuzari, and R. Kar, *Performance of range separated density functional in solvent continuum: Tuning long-range hartree–fock exchange for improved orbital energies*, *Journal of Computational Chemistry* **41** (2020), no. 4 295–304.

[32] The eigenvalues of the Kohn-Sham states are stationary solutions with infinite lifetimes and they, by construction, do not correspond to the QPs.

[33] B. Winter, R. Weber, I. V. Hertel, M. Faubel, P. Jungwirth, E. C. Brown, and S. E. Bradforth, *Electron binding energies of aqueous alkali and halide ions: euv photoelectron spectroscopy of liquid solutions and combined ab initio and molecular dynamics calculations*, *Journal of the American Chemical Society* **127** (2005), no. 19 7203–7214.

[34] P. Dedíková, P. Neogrády, and M. Urban, *Electron affinities of small uracil-water complexes: A comparison of benchmark ccsd(t) calculations with dft*, *The Journal of Physical Chemistry A* **115** (2011), no. 11 2350–2358.

[35] D. Ghosh, O. Isayev, L. V. Slipchenko, and A. I. Krylov, *Effect of solvation on the vertical ionization energy of thymine: From microhydration to bulk*, *The Journal of Physical Chemistry A* **115** (2011), no. 23 6028–6038.

[36] D. Ghosh, A. Roy, R. Seidel, B. Winter, S. Bradforth, and A. I. Krylov, *First-principle protocol for calculating ionization energies and redox potentials of solvated molecules and ions: Theory and application to aqueous phenol and phenolate*, *The Journal of Physical Chemistry B* **116** (2012), no. 24 7269–7280.

[37] S. Bose, S. Chakrabarty, and D. Ghosh, *Effect of solvation on electron detachment and excitation energies of a green fluorescent protein chromophore variant*, *The Journal of Physical Chemistry B* **120** (2016), no. 19 4410–4420.

[38] S. Ren, J. Harms, and M. Caricato, *An eom-ccsd-pcm benchmark for electronic excitation energies of solvated molecules*, *Journal of Chemical Theory and Computation* **13** (2017), no. 1 117–124.

[39] D. Ghosh, *Hybrid equation-of-motion coupled-cluster/effective fragment potential method: A route toward understanding photoprocesses in the condensed phase*, *The Journal of Physical Chemistry A* **121** (2017), no. 4 741–752.

[40] R. Chakraborty, S. Bose, and D. Ghosh, *Effect of solvation on the ionization of guanine nucleotide: A hybrid qm/efp study*, *Journal of Computational Chemistry* **38** (2017), no. 29 2528–2537.

[41] A. Sadybekov and A. I. Krylov, *Coupled-cluster based approach for core-level states in condensed phase: Theory and application to different protonated forms of aqueous glycine*, *The Journal of Chemical Physics* **147** (2017), no. 1 014107.

[42] A. Barrozo, B. Xu, A. O. Gunina, M. I. Jacobs, K. Wilson, O. Kostko, M. Ahmed, and A. I. Krylov, *To be or not to be a molecular ion: The role of the solvent in photoionization of arginine*, *The Journal of Physical Chemistry Letters* **10** (2019), no. 8 1860–1865.

[43] E. Cauët, M. Valiev, and J. H. Weare, *Vertical ionization potentials of nucleobases in a fully solvated dna environment*, *The Journal of Physical Chemistry B* **114** (2010), no. 17 5886–5894.

[44] R. M. Martin, L. Reining, and D. M. Ceperley, *Interacting Electrons: Theory and Computational Approaches*. Cambridge University Press, 2016.

[45] S. Y. Quek, J. B. Neaton, M. S. Hybertsen, E. Kaxiras, and S. G. Louie, *First-principles studies of the electronic structure of cyclopentene on si(001): density functional theory and gw calculations*, *physica status solidi (b)* **243** (2006), no. 9 2048–2053.

[46] I. Tamblyn, P. Darancet, S. Y. Quek, S. A. Bonev, and J. B. Neaton, *Electronic energy level alignment at metal-molecule interfaces with a gw approach*, *Physical Review B* **84** (2011), no. 20 201402.

[47] N. Kharche, J. T. Muckerman, and M. S. Hybertsen, *First-principles approach to calculating energy level alignment at aqueous semiconductor interfaces*, *Physical Review Letters* **113** (2014), no. 17 176802.

[48] J. Li, G. D'Avino, I. Duchemin, D. Beljonne, and X. Blase, *Combining the many-body gw formalism with classical polarizable models: Insights on the electronic structure of molecular solids*, *The Journal of Physical Chemistry Letters* **7** (2016), no. 14 2814–2820.

[49] Y. Kang, S. H. Jeon, Y. Cho, and S. Han, *Ab initio calculation of ionization potential and electron affinity in solid-state organic semiconductors*, *Physical Review B* **93** (2016), no. 3 035131.

[50] A. P. Gaiduk, M. Govoni, R. Seidel, J. H. Skone, B. Winter, and G. Galli, *Photoelectron spectra of aqueous solutions from first principles*, *Journal of the American Chemical Society* **138** (2016), no. 22 6912–6915.

[51] T. Rangel, K. Berland, S. Sharifzadeh, F. Brown-Altvater, K. Lee, P. Hyldgaard, L. Kronik, and J. B. Neaton, *Structural and excited-state properties of oligoacene crystals from first principles*, *Physical Review B* **93** (2016), no. 11 115206.

[52] G. Li, T. Rangel, Z.-F. Liu, V. R. Cooper, and J. B. Neaton, *Energy level alignment of self-assembled linear chains of benzenediamine on au(111) from first principles*, *Physical Review B* **93** (2016), no. 12 125429.

[53] T. A. Pham, M. Govoni, R. Seidel, S. E. Bradforth, E. Schwegler, and G. Galli, *Electronic structure of aqueous solutions: Bridging the gap between theory and experiments*, *Science Advances* **3** (2017), no. 6 e1603210.

[54] L. Blumenthal, J. M. Kahk, R. Sundararaman, P. Tangney, and J. Lischner, *Energy level alignment at semiconductor–water interfaces from atomistic and continuum solvation models*, *RSC Advances* **7** (2017), no. 69 43660–43670.

[55] J. Li, G. D'Avino, I. Duchemin, D. Beljonne, and X. Blase, *Accurate description of charged excitations in molecular solids from embedded many-body perturbation theory*, *Physical Review B* **97** (2018), no. 3 035108.

[56] A. P. Gaiduk, T. A. Pham, M. Govoni, F. Paesani, and G. Galli, *Electron affinity of liquid water*, *Nature Communications* **9** (2018), no. 1 247.

[57] V. c. v. Vlček, E. Rabani, and D. Neuhauser, *Quasiparticle spectra from molecules to bulk*, *Phys. Rev. Materials* **2** (2018) 030801.

[58] Z.-F. Liu, F. H. da Jornada, S. G. Louie, and J. B. Neaton, *Accelerating gw-based energy level alignment calculations for molecule–metal interfaces using a substrate screening approach*, *Journal of Chemical Theory and Computation* **15** (2019), no. 7 4218–4227.

[59] J. Brooks, G. Weng, S. Taylor, and V. Vlček, *Stochastic many-body perturbation theory for moiré states in twisted bilayer phosphorene*, *Journal of Physics: Condensed Matter* **32** (2020), no. 23 234001.

[60] G. Weng and V. Vlček, *Quasiparticles and band structures in organized nanostructures of donor–acceptor copolymers*, *The Journal of Physical Chemistry Letters* **11** (2020), no. 17 7177–7183.

[61] M. Romanova and V. Vlček, *Decomposition and embedding in the stochastic gw self-energy*, *The Journal of Chemical Physics* **153** (2020), no. 13 134103.

[62] D. Neuhauser, Y. Gao, C. Arntsen, C. Karshenas, E. Rabani, and R. Baer, *Breaking the theoretical scaling limit for predicting quasiparticle energies: The stochastic gw approach*, *Phys. Rev. Lett.* **113** (2014) 076402.

[63] V. Vlček, E. Rabani, D. Neuhauser, and R. Baer, *Stochastic gw calculations for molecules*, *Journal of Chemical Theory and Computation* **13** (2017), no. 10 4997–5003. PMID: 28876912.

[64] V. Vlček, W. Li, R. Baer, E. Rabani, and D. Neuhauser, *Swift gw beyond 10,000 electrons using sparse stochastic compression*, *Phys. Rev. B* **98** (2018) 075107.

[65] V. Vlček, *Stochastic vertex corrections: Linear scaling methods for accurate quasiparticle energies*, *Journal of Chemical Theory and Computation* **15** (2019), no. 11 6254–6266.

[66] D. Golze, M. Dvorak, and P. Rinke, *The gw compendium: A practical guide to theoretical photoemission spectroscopy*, *Frontiers in Chemistry* **7** (2019) 377.

[67] G. D. Mahan, *Many Particle Physics, Third Edition.* Plenum, New York, 2000.

[68] F. Kaplan, F. Weigend, F. Evers, and M. J. van Setten, *Off-diagonal self-energy terms and partially self-consistency in gw calculations for single molecules: Efficient implementation and quantitative effects on ionization potentials*, *Journal of Chemical Theory and Computation* **11** (2015), no. 11 5152–5160.

[69] F. Kaplan, M. E. Harding, C. Seiler, F. Weigend, F. Evers, and M. J. van Setten, *Quasi-particle self-consistent gw for molecules*, *Journal of Chemical Theory and Computation* **12** (2016), no. 6 2528–2541.

[70] M. Romanova and V. Vlček, *Stochastic many-body calculations of moiré states in twisted bilayer graphene at high pressures*, *npj Computational Materials* **8** (2022), no. 1 11.

[71] J. Pipek and P. G. Mezey, *A fast intrinsic localization procedure applicable for ab initio and semiempirical linear combination of atomic orbital wave functions*, *The Journal of Chemical Physics* **90** (1989), no. 9 4916–4926.

[72] I.-M. Høyvik, B. Jansik, and P. Jørgensen, *Pipek–mezey localization of occupied and virtual orbitals*, *Journal of Computational Chemistry* **34** (2013), no. 17 1456–1462.

[73] S. Lehtola and H. Jónsson, *Pipek–mezey orbital localization using various partial charge estimates*, *Journal of Chemical Theory and Computation* **10** (2014), no. 2 642–649.

[74] E. Ö. Jónsson, S. Lehtola, M. Puska, and H. Jónsson, *Theory and applications of generalized pipek–mezey wannier functions*, *Journal of Chemical Theory and Computation* **13** (2017), no. 2 460–474.

[75] P. L. Silvestrelli, N. Marzari, D. Vanderbilt, and M. Parrinello, *Maximally-localized wannier functions for disordered systems: Application to amorphous silicon*, *Solid State Communications* **107** (1998), no. 1 7–11.

[76] P. L. Silvestrelli, *Maximally localized wannier functions for simulations with supercells of general symmetry*, *Physical Review B* **59** (1999), no. 15 9703–9706.

[77] K. S. Thygesen, L. B. Hansen, and K. W. Jacobsen, *Partly occupied wannier functions: Construction and applications*, *Physical Review B* **72** (2005), no. 12 125119.

[78] H. Oberhofer and J. Blumberger, *Charge constrained density functional molecular dynamics for simulation of condensed phase electron transfer reactions*, *The Journal of Chemical Physics* **131** (2009), no. 6 064101.

[79] G. Weng and V. Vlček, *Pipek-mezey wannier functions with local and subspace wannierzation*, 2021.

[80] A. Georges, G. Kotliar, W. Krauth, and M. J. Rozenberg, *Dynamical mean-field theory of strongly correlated fermion systems and the limit of infinite dimensions*, *Rev. Mod. Phys.* **68** (1996) 13–125.

[81] V. I. Anisimov, A. I. Poteryaev, M. A. Korotin, A. O. Anokhin, and G. Kotliar, *First-principles calculations of the electronic structure and spectra of strongly correlated systems: dynamical mean-field theory*, *J. Phys.: Condens. Matter* **9** (1997), no. 35 7359.

[82] T. Nguyen Lan, A. A. Kananenka, and D. Zgid, *Rigorous ab initio quantum embedding for quantum chemistry using green's function theory: Screened interaction, nonlocal self-energy relaxation, orbital basis, and chemical accuracy*, *Journal of Chemical Theory and Computation* **12** (2016), no. 10 4856–4870.

[83] A. A. Rusakov, S. Iskakov, L. N. Tran, and D. Zgid, *Self-energy embedding theory (seet) for periodic systems*, *Journal of Chemical Theory and Computation* **15** (2019), no. 1 229–240.

[84] Z.-H. Cui, T. Zhu, and G. K.-L. Chan, *Efficient implementation of ab initio quantum embedding in periodic systems: Density matrix embedding theory*, *Journal of Chemical Theory and Computation* **16** (2020), no. 1 119–129.

[85] F. Aryasetiawan and O. Gunnarsson, *Thegwmethod*, *Reports on Progress in Physics* **61** (1998), no. 3 237–312.

[86] C. Friedrich and A. Schindlmayr, *Many-body perturbation theory: The gw approximation*, *NIC Series* **31** (2006) 335.

[87] C. Mejuto-Zaera, G. Weng, M. Romanova, S. J. Cotton, K. B. Whaley, N. M. Tubman, and V. Vlček, *Are multi-quasiparticle interactions important in molecular ionization?*, *The Journal of Chemical Physics* **154** (2021), no. 12 121101.

[88] D. M. Close, *Calculation of the ionization potentials of the dna bases in aqueous medium*, *The Journal of Physical Chemistry A* **108** (2004), no. 46 10376–10379.

[89] C. E. Crespo-Hernández, R. Arce, Y. Ishikawa, L. Gorb, J. Leszczynski, and D. M. Close, *Ab initio ionization energy thresholds of dna and rna bases in gas phase and in aqueous solution*, *The Journal of Physical Chemistry A* **108** (2004), no. 30 6373–6377.

[90] K. T. Lee, J. Sung, K. J. Lee, S. K. Kim, and Y. D. Park, *Conformation-dependent ionization of l-phenylalanine: structures and energetics of cationic conformers*, *Chemical Physics Letters* **368** (2003), no. 3 262–268.

[91] P. Papp, P. Shchukin, J. Kočíšek, and Š. Matejčík, *Electron ionization and dissociation of aliphatic amino acids*, *The Journal of Chemical Physics* **137** (2012), no. 10 105101.

[92] D. M. Close, *Calculated vertical ionization energies of the common α-amino acids in the gas phase and in solution*, *The Journal of Physical Chemistry A* **115** (2011), no. 13 2900–2912.

[93] N. Troullier and J. L. Martins, *Efficient pseudopotentials for plane-wave calculations*, *Phys. Rev. B* **43** (1991) 1993–2006.

[94] K. T. Lee, J. Sung, K. J. Lee, Y. D. Park, and S. K. Kim, *Conformation-dependent ionization energies of l-phenylalanine*, *Angewandte Chemie International Edition* **41** (2002), no. 21 4114–4117.

[95] A. Roy, R. Seidel, G. Kumar, and S. E. Bradforth, *Exploring redox properties of aromatic amino acids in water: Contrasting single photon vs resonant multiphoton ionization in aqueous solutions*, *The Journal of Physical Chemistry B* **122** (2018), no. 14 3723–3733.

[96] E. Pluhařová, P. Slavíček, and P. Jungwirth, *Modeling photoionization of aqueous dna and its components*, *Accounts of Chemical Research* **48** (2015), no. 5 1209–1217.

[97] E. Runge and E. K. U. Gross, *Density-functional theory for time-dependent systems*, *Physical Review Letters* **52** (1984), no. 12 997–1000.

[98] M. Cossi and V. Barone, *Time-dependent density functional theory for molecules in liquid solutions*, *The Journal of Chemical Physics* **115** (2001), no. 10 4708–4717.

[99] M. A. L. Marques and E. K. U. Gross, *Time-dependent density functional theory*, *Annual Review of Physical Chemistry* **55** (2004), no. 1 427–455.

[100] C. Adamo and D. Jacquemin, *The calculations of excited-state properties with time-dependent density functional theory*, *Chemical Society Reviews* **42** (2013), no. 3 845–856.

[101] The calculations for the isolated molecule make use of the geometry extracted from the MD trajectory of the solvated system.

[102] E. V. Tsiper and Z. G. Soos, *Charge redistribution and polarization energy of organic molecular crystals*, *Physical Review B* **64** (2001), no. 19 195124.

[103] Only one selected system snapshot along the MD trajectory is considered in this section.

Chapter 8

Spatial Decay and Limits of Quantum Solute–Solvent Interactions

Guorong Weng, Amanda Pang,[a] Vojtěch Vlček

ABSTRACT

Molecular excitations in the liquid-phase environment are renormalized by the surrounding solvent molecules. Herein, we employ the *GW* approximation to investigate the solvation effects on the ionization energy of phenol in various solvent environments. The electronic effects differ by up to 0.4 eV among the five investigated solvents. This difference depends on both the macroscopic solvent polarizability and the spatial decay of the solvation effects. The latter is probed by separating the electronic subspace and the *GW* correlation self-energy into fragments. The fragment correlation energy decays with increasing intermolecular distance and vanishes at ∼9 Å, and this pattern is independent of the type of solvent environment. The 9 Å cutoff defines an effective interacting volume within which the ionization energy shift per solvent molecule is proportional to the

[a]Present address: University of Pennsylvania, PA, 19104, USA

macroscopic solvent polarizability. Finally, we propose a simple model for computing the ionization energies of molecules in an arbitrary solvent environment.

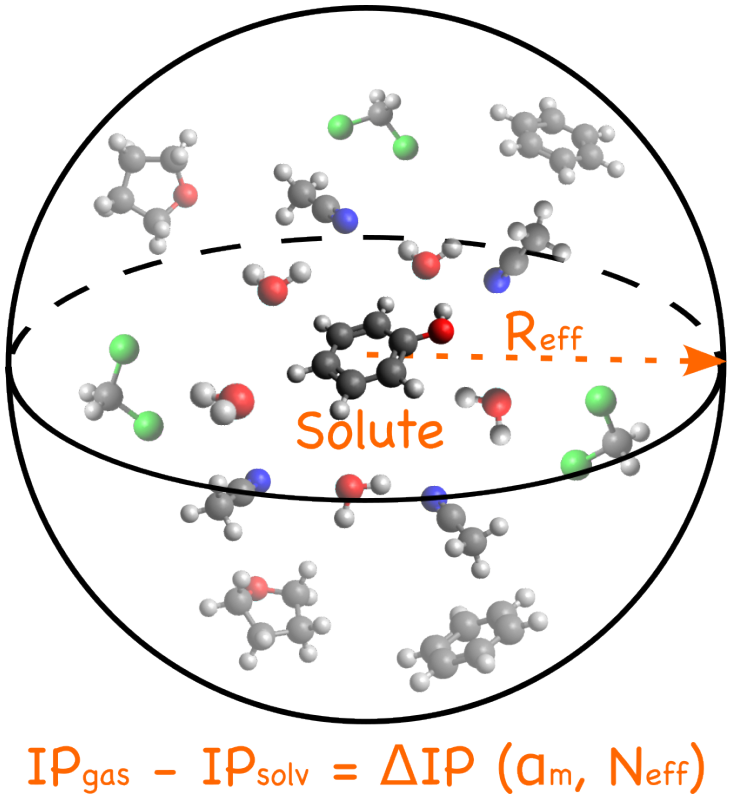

8.1 LETTER

Liquid phase is the most practical environment for treating multicomponent chemical systems. Applications in synthetic chemistry and material processing rely on the dissolving ability, primarily linked to the solvent's permanent dipole, i.e., the polarity. In the context of electronic excitations (e.g., in spectroscopy) or charge transport, the dynamical electric polarizability represents another fundamental property characterizing the solvent medium; it is related to the dynamically induced dipoles that screen the electron−electron interactions. The charge carriers are "dressed" by mutual interactions, forming quasiparticles (QP),[1, 2] and the electronic structure is renormalized. Specifically, the presence

of solvent shifts the excitation energies of the solute molecule and leads to their finite excitation lifetimes. The effects on molecular energy levels of chromophores are commonly known as *solvatochromic shifts*.[3, 4] In experiments, these shifts can be measured by light absorption and emission spectroscopy as well as photoelectron spectroscopy.

The detailed microscopic understanding of solvatochromic shifts requires efficient and accurate first-principles simulations. State-of-the-art theoretical approaches for simulating solute−solvent systems are mainly formulated within the embedding framework: quantum mechanical approaches, including quantum chemistry methods[5, 6, 7, 8, 9, 10, 11, 12, 13, 14, 15, 16, 17, 18, 19, 20, 21] and time-dependent density functional theory (TDDFT),[22, 23, 24, 25, 26, 27, 28, 29, 30, 31, 32, 33, 34] apply only to the "core region," which consists of the solute molecule and sometimes a small number of proximal solvent molecules;[22, 5, 8, 29, 11, 14, 18, 20, 21] the solvent environment is treated most often with either the polarizable continuum model[35, 36, 37, 38] (PCM) or classical molecular mechanics.[39, 40] However, high-accuracy quantum chemistry approaches are limited to small molecules due to the steep cost-scaling; TDDFT results from practical implementations strongly depend on the choice of the exchange−correlation functional. For the environment, the use of implicit solvent models (e.g., PCM) does not allow detailed investigations, for instance, about the spatial decay of the solute−solvent interactions. Furthermore, current studies[5, 6, 7, 9, 10, 13, 14, 17, 18, 20, 21, 22, 24, 25, 27, 28, 29, 30, 31, 33, 34, 41] focus mainly on the optical absorption and emission processes but do not provide direct information about the absolute energies of electronic levels, i.e., ionization potential (IP) and electron affinity (EA). These levels represent the electron-donating and accepting abilities of the solute molecule. The development of liquid microjet photoelectron spectroscopy[42, 43, 44, 45] allows direct IP measurements for solvated molecules. However, this technique applies mainly to aqueous solutions due to the volatility of most organic solvents. An affordable and accurate theoretical approach is

in demand for predicting the IP and EA of molecules in diverse liquid environments.

Many-body Green's function methods[1, 2] provide direct access to single-quasiparticle energies, provided that the system is weakly or moderately correlated. Indeed, the *GW* approximation,[46, 47, 48, 49, 50] even at the lowest order expansion in which the electronic correlation is described merely through charge density fluctuations, yields IPs that agree with experiments for most molecular systems.[51, 52, 53] Recent developments in efficient algorithms[54, 55, 56, 57, 58, 59, 60, 61, 62, 63, 64, 65] and high-performance computing,[66, 67, 68] especially the linear-scaling stochastic formalism,[69, 70, 71, 72, 73, 74, 75, 76, 77, 78] have enabled large-scale *GW* calculations for systems with thousands of electrons. Within the stochastic *GW* framework,[69, 71, 72] our previous work[77] established an efficient approach for computing the photoemission spectra (i.e., IPs) of various solvated molecules, in which the solute and the solvent environment (containing ∼1000 electrons) are treated on the same footing. Excellent agreements with experiments and other comparable methods have been achieved for molecules solvated by water.

In this work, we investigate the molecular ionization in various polarizable solvents and the spatial decay of the solvation electronic effects on the ionization energy. We use regionally-localized[79] Pipek−Mezey[80, 81, 82] orbitals to separate the electronic subspaces and decompose the correlation contributions into fragments. The methodology is exemplified on a phenol molecule in five different solvents, with geometric structures generated from molecular dynamics (MD) simulations (details are provided in the supporting information). The energy shifts of the phenol's IP are computed and related to the macroscopic solvent polarizability. The rapid convergence of the IP shifts with respect to the number of surrounding solvent molecules indicates that the solute−solvent interactions vanish at some distance, which is fairly uniform across vastly different types of solvents. From the decay of the *GW* correlation self-energy, we identify an effective interacting radius for the solute molecule to interact with the induced charge density from

the environment. Within the effective interacting volume, we find that the IP shift per solvent molecule is proportional to the polarizability volume calculated for each solvent. Finally, a simple solvation model is proposed for computing the IP of molecules in an arbitrary solvent environment.

In the Green's function formalism,[1, 2] the electron−electron interactions are represented by the nonlocal and dynamical exchange−correlation self-energy, Σ_{X} and Σ_{C}. In practice, we compute Σ_{X} and Σ_{C} as perturbative corrections to the mean-field eigenvalue yielding the following QP energy

$$\varepsilon_j^{\mathrm{QP}} = \langle\phi_j|\varepsilon_j^0 - \hat{v}_{\mathrm{xc}} + \hat{\Sigma}_{\mathrm{X}} + \hat{\Sigma}_{\mathrm{C}}(\omega = \varepsilon_j^{\mathrm{QP}})|\phi_j\rangle \tag{8.1}$$

Here, ϕ_j is a reconstructed molecular state on the solute,[77] and ε_j^0 comes from an auxiliary density functional theory[83, 84] (DFT) calculation of the isolated solute;[77] $\hat{v}_{\mathrm{xc}}$ is the PBE exchange−correlation potential,[85] and $\hat{\Sigma}_{\mathrm{X}}$ is the nonlocal exchange interaction equivalent to the Fock operator;[2] $\hat{\Sigma}_{\mathrm{C}}(\omega)$ is the frequency-dependent correlation self-energy. This work employs the one-shot GW (G_0W_0) approach, in which the correlation corresponds to the potential due to charge density fluctuations. In the following, we use Σ_{C} to denote the expectation value $\langle\phi_j|\hat{\Sigma}_{\mathrm{C}}|\phi_j\rangle$, where the spatial coordinates are integrated out.

We demonstrated the separation of Σ_{C} into the molecular and the environmental contributions in ref 77. In this work, we generalize this separation to multifragments in the solute−solvent systems. The definition of a fragment is arbitrary and in the remainder of this text, a fragment refers to a solvation shell consisting of one or multiple solvent molecules. The electronic subspace of a fragment is represented by the following projector

$$\hat{P}^k = \sum_i^{N_{\mathrm{s}}} |\psi_i^k\rangle \langle\psi_i^k| \tag{8.2}$$

where ψ^k form a localized basis, and N_s includes all the valence electrons of the k^{th} fragment. The corresponding electronic subspace is sufficiently defined by the full set of occupied states based on the "local density fluctuations" assumption: the perturbed and time-evolved ψ^k stay localized on the k^{th} fragment. In other words, we assume no intermolecular charge transfer happens, and all the density fluctuations remain on the fragment. This assumption is reasonable when no apparent donor−acceptor character is found in a van der Waals-bound molecular system. It follows that the time-dependent charge-density fluctuations $\delta n(\mathbf{r}, t)$ are decomposed into fragments

$$\delta n(\mathbf{r}, t) = \sum_{k}^{N_{\text{frag}}} \delta n^k(\mathbf{r}, t) \tag{8.3}$$

where N_{frag} denotes the number of fragments, and $\delta n^k(\mathbf{r}, t)$ is the density fluctuations contributed by the k^{th} fragment.

Since the G_0W_0 correlation self-energy stems from the charge density−density interactions (i.e., induced dipole interactions), the Σ_{C} can be immediately written as

$$\Sigma_{\text{C}}[\delta n(t), t] = \sum_{k}^{N_{\text{frag}}} \Sigma_{\text{C}}^k[\delta n^k(\mathbf{r}, t), t] \tag{8.4}$$

In this work, we use the stochastic GW method[69, 71, 72] to compute the correlation self-energy contributed from a specific fragment, e.g., a solvation shell at distance $\mathbf{R}^k$, and then study the decay of Σ_{C}^k as a function of $\mathbf{R}^k$.

The construction of $\hat{P}^k$, the decomposition of $\delta n(\mathbf{r}, t)$, and the calculation of Σ_{C}^k are detailed in the Theory and Methodology section in the Supporting Information.

To practically investigate the energy shifts contributed by the solvent environment, we explore the vertical ionization potential (corresponding to the negative of the HOMO QP energy) of phenol in five different solvents: water (H_2O), acetonitrile (ACN), dichloromethane

(DCM), tetrahydrofuran (THF), and benzene (BEN). The solute−solvent systems are constructed and propagated using a cubic cell with lateral dimensions of 18−21 Å in MD simulations (see Figure D.2 and Table D.7). The solvent environment contributes to the solute's electronic structure in two ways: direct electron−electron interactions and structural relaxations. The latter also involves direct electron/hole-vibrational couplings, which are, however, not considered in this work. The structural effects are thus reduced to conformational changes and the corresponding QP energies of the isolated phenol molecule (ε^{iso}), with molecular structures extracted from snapshots (Figure D.1 and Figure D.2) of the MD trajectories. Figure 8.1a shows the HOMO of an isolated phenol molecule, which is obtained by simply removing all the solvent molecules (Figure 8.1b). The ε^{iso} results do not differ too much among the five solvents (see Table D.2), i.e., the solvent-induced structural changes of phenol are consistent regardless of the actual chemical environment in the liquid phase. Note that flexible molecules, e.g., phenylalanine with a chain group attached to the aromatic ring, will display a more pronounced dependence on the structural variation (see our reported results in ref 77). Since we focus on the purely electronic contributions stemming from the dynamical electronic interactions with the solvent environment, phenol thus appears to be an appropriate choice as a test system.

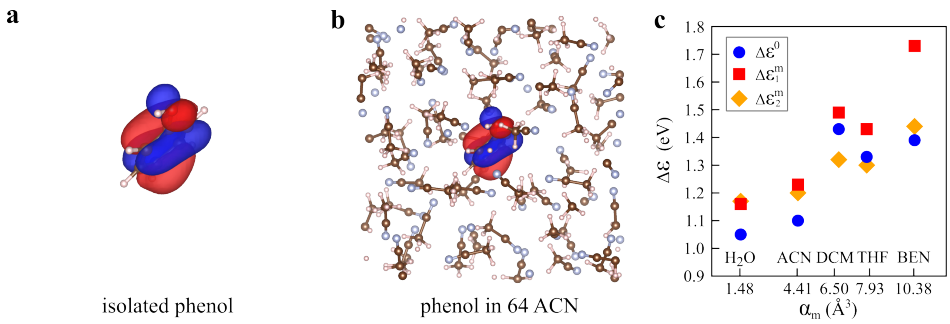

Figure 8.1: (a) HOMO of the isolated phenol molecule. (b) Reconstructed HOMO of the phenol molecule surrounded by 64 ACN molecules in the simulation cell. (c) IP shifts $\Delta\varepsilon$ plotted as a function of the mean polarizability volume: $\Delta\varepsilon^0$ represents the first-principles results calculated as $\varepsilon^{\text{solv}} - \varepsilon^{\text{iso}}$; $\Delta\varepsilon_1^{\text{m}}$ and $\Delta\varepsilon_2^{\text{m}}$ are derived from the proposed solvation model, where $\Delta\varepsilon_1^{\text{m}}$ uses N_{eff} derived from the solvent mass density, while $\Delta\varepsilon_2^{\text{m}}$ uses the average N_{eff} over five selected snapshots from the MD trajectory.

The solvation many-body effects on the IP of phenol correspond to the energy shifts, $\Delta\varepsilon$, defined as the QP energy difference between the solvated and the isolated HOMO ($\varepsilon^{\text{solv}} - \varepsilon^{\text{iso}}$). For each solvent environment, we sample $\Delta\varepsilon$ using five snapshots and obtain the average value (see Figure D.4). The standard deviation of $\Delta\varepsilon$ is lower than that of $\varepsilon^{\text{solv}}$, indicating that the sampling of $\Delta\varepsilon$ represents the average solvation effects along the MD trajectory. A significant part of these effects is due to the dynamical screening by the induced charge density fluctuations of the solvent environment.[77] Hence, it stands to reason that $\Delta\varepsilon$ is related to the macroscopic solvent polarizability, which is further related to the refractive index n_r of the liquid by the Lorentz-Lorenz equation, $\alpha_m = 3({n_r}^2 - 1)/4\pi({n_r}^2 + 2)$. α_m is the mean polarizability volume, and N_v is the number of molecules per unit volume. The derivation of N_v takes the solvent's mass density at 293 K. Both n_r and mass density data are readily accessible in the CRC Handbook of Chemistry and Physics.[86] In Figure 8.1c, the $\Delta\varepsilon^0$ (blue circles, first-principles values) averaged over five snapshots of each solvated system is plotted with respect to the corresponding α_m. While there is a general trend, the dependence is not straightforward: most importantly, the DCM environment exhibits the largest $\Delta\varepsilon^0$

(IP shifts), despite its polarizability volume being in the middle of the range. The results in Figure 8.1c are then compared with simulations using a smaller cell and fewer solvent molecules (see Figures D.1 and D.3). Even though the numbers of solvent molecules are (nearly) doubled (Table D.7), the $\Delta\varepsilon^0$ are increased by at most 15% (see Figure D.5). It implies that the solute−solvent many-body interactions are converging rapidly with an increasing number of solvent molecules, at least at the GW level. In fact, we expect that these intermolecular interactions decay with distance, and the decay is governed by the polarizability of the solvent molecules.

Next, we investigate the distance ($\mathbf{R}^k$)-dependence of the correlation self-energy (Σ_{C}^k) contributed from the liquid environment. At the G_0W_0 level, this corresponds to the polarization screening effects stemming from the induced time-dependent dipoles on the solvent molecules. The solvent environment is fragmented into solvation shells (Figure D.6), each of which is represented by a set of localized orbitals (eq 8.2). Note that the shell in this work is constructed by a cluster of solvent molecules at a similar distance (±0.2 Å). We set integer distances ranging from 3 to 10 Å for the fragment selection, while the actual distance $\mathbf{R}^k$ is derived by averaging the distances of all molecules within the same shell. In total, six shells are chosen from a typical snapshot of each solvated system, and most of them contain more than one molecule in order to cancel out the solvent orientation effects (Figure D.6).

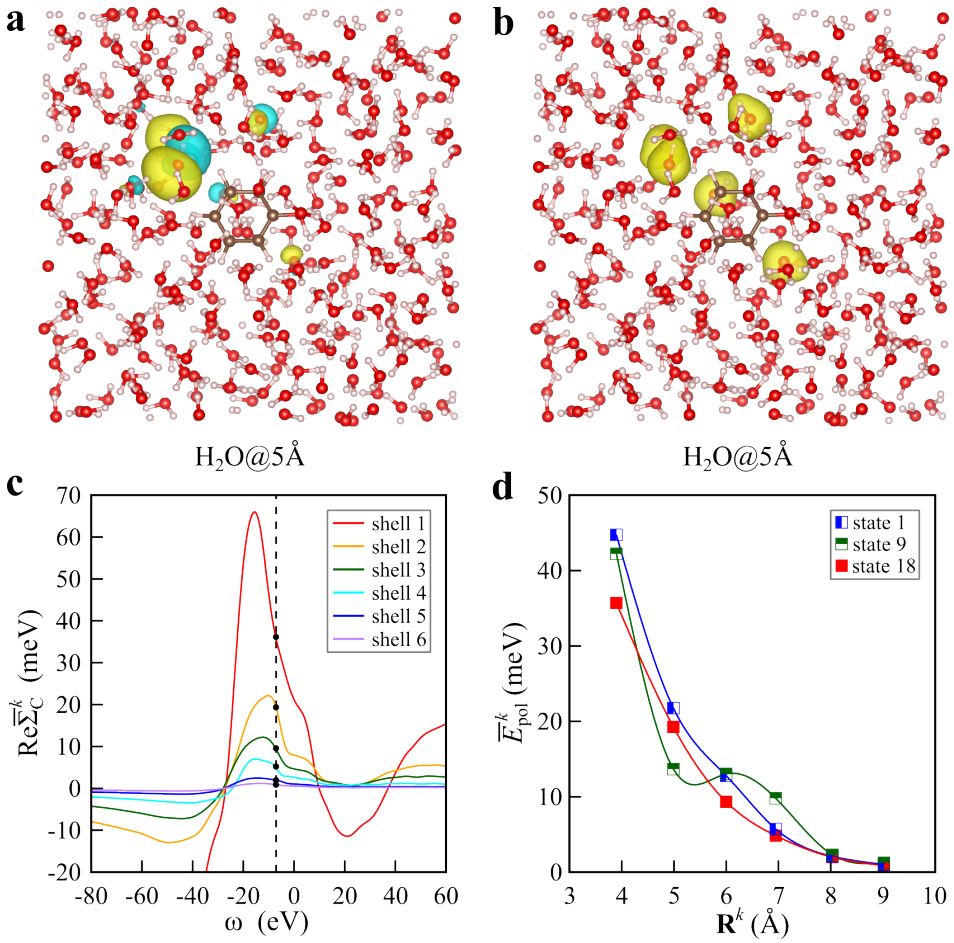

Figure 8.2: (a) A typical localized orbital on the fragment with 5 H_2O molecules at ∼5 Å. (b) Localized electron density on the fragment with 5 H_2O molecules at ∼5 Å. (c) Real part of the normalized fragment correlation self-energy for each H_2O shell. The dashed line indicates the HOMO QP energy. (d) Normalized fragment polarization energy plotted as a function of the shell distance for the three chosen valence states of phenol.

First, we focus on the investigation of the H_2O environment. Figure 8.2a shows one of the localized orbitals on the H_2O molecules at ∼5 Å. This is a hybridized state distributed on five molecules that are spatially separated. The total charge density for this H_2O shell (Figure 8.2b) then enters the G_0W_0 calculation and leads to the fragment correlation self-energy Σ_C^k. As Σ_C^k is computed for multiple solvent molecules, we divide it by the number of solvent molecules in the shell and obtain a normalized fragment correlation

self-energy $\overline{\Sigma}^k_{\mathrm{C}}$. The real part of $\overline{\Sigma}^k_{\mathrm{C}}$ for each H_2O shell is presented in Figure 8.2c. The labels from 1 to 6 correspond to the actual distances from 4 to 9 Å. Around the peak of $\overline{\Sigma}^k_{\mathrm{C}}$ (the plasmon pole), the magnitude decays as the solvent molecules get further away. The vertical dashed line indicates the frequency where $\omega = \varepsilon_j$, i.e., the HOMO QP energy; the vertical coordinate of each intersection represents the actual polarization contribution from each shell to the QP energy. This derived polarization energy is denoted as $\overline{E}^k_{\mathrm{pol}}$. In Figure 8.2d, the solid red squares are the plot of the $\overline{E}^k_{\mathrm{pol}}$ induced by the HOMO (the 18^{th} valence state of phenol) at each distance, and the red line is fitted to this data set. The $\overline{E}^k_{\mathrm{pol}}$ decreases with increasing $\mathbf{R}^k$ and practically vanishes at ∼9 Å.

Surprisingly, this is a very robust decaying pattern, as we observe a similar behavior from the first or the ninth valence state of phenol (half-filled squares with fitted lines in Figure 8.2d). All three $\overline{E}^k_{\mathrm{pol}}$ vanish at ∼9 Å. The decaying pattern shows little dependence on the state's QP energy or its spatial distribution (Figure D.7) on the solute molecule. We surmise that this pattern also applies to other small molecules similar to phenol, and further explanations are provided after discussing the nonaqueous solvents.

The same fragmentation analysis is performed on the HOMO of the other four solvated systems (Figure D.6), in which the decays of $\overline{\Sigma}^k_{\mathrm{C}}$ of each individual solvent with respect to $\mathbf{R}^k$ are consistent (Figure D.9). Further, we compare the $\overline{\Sigma}^k_{\mathrm{C}}$ from the shell at the same distance (∼5 Å) of each solvent, as shown in Figure 8.3a: around the solvent plasmon pole (i.e., a polarizability resonance), the magnitude of $\overline{\Sigma}^k_{\mathrm{C}}$ has its maximum. At the same time, the pole shifts gradually to a higher frequency (indicated by the dashed arrow line), which corresponds to a faster response sustained by a more polarizable solvent. Further, the overall magnitude of $\overline{\Sigma}^k_{\mathrm{C}}$ increases with the polarizability volume of the liquid environment. In Figure 8.3b, the normalized polarization energy $\overline{E}^k_{\mathrm{pol}}$ is plotted with respect to $\mathbf{R}^k$ for each solvent. Within 7 Å, the magnitude of $\overline{E}^k_{\mathrm{pol}}$ along the vertical axis represents the strength of the interactions, which follows the order of α_m in Figure 8.1c.

However, the decay of $\overline{E}^k_{\rm pol}$ along the horizontal axis does not differ too much among various solvents: particularly, the 9 Å distance appears to be the common point at which the $\overline{E}^k_{\rm pol}$ for all the five solvents vanishes ($\overline{E}^k_{\rm pol} < 10$ meV).

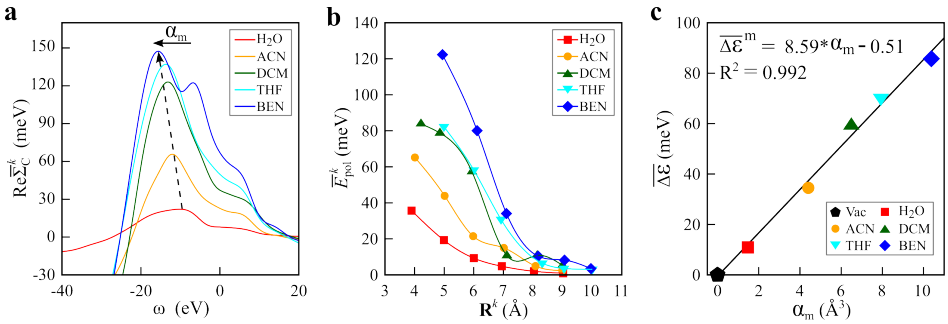

Figure 8.3: (a) Real part of the normalized fragment correlation self-energy for the shell at ∼5 Å of each solvent. The dashed arrow indicates the shift of the pole, and the solid arrow denotes the order of α_m. (b) Normalized fragment polarization energy plotted as a function of the shell distance for the HOMO state of phenol in each solvent. (c) Averaged IP shifts plotted as a function of the mean polarizability volume. The straight line is fitted using the linear regression model, where the slope is 8.59 meV/Å^3 with an intercept of −0.51 meV at $\alpha_m = 0$.

From the observations above, we find that the macroscopic solvent polarizability dictates the temporal behavior (i.e., how fast the response is) and the strength of the response (i.e., the magnitude of the nonlocal correlation self-energy). A common cutoff distance, within which the solvent molecules are considered *effective*, is found at ∼9 Å away from the phenol solute. This effective interacting radius depends neither on the ionization state nor the solvent type, and this phenomenon, as we believe, can be attributed to the localized molecular excitation on phenol. In practice, electronic states on the solvent molecules are only mildly perturbed by the excitation of the solute. For solvent molecules at long distances, the perturbation is even weaker. Hence, the 9 Å cutoff should be a consequence of the localized molecular excitation and applies likely to other molecules of similar size to phenol.

Based on the effective interacting radius, we identify the number of *effective solvent*

molecules N_{eff} for each solvated system (see Table D.9). From H_2O to BEN (as ordered in Figure 8.1c), the N_{eff} (averaged over five snapshots) are found to be 97, 32, 24, 19, and 16. This will help to explain the apparent contradiction observed for the DCM solvent (Figure 8.1c): although DCM is less polarizable than THF and BEN, it leads to stronger energy shifts because of a larger N_{eff} (i.e., more effective solvent molecules). The difference in N_{eff} originates from the molecular size and mass density difference among various solvents. Moreover, we divide the QP energy shifts $\Delta\varepsilon$ by the number of effective solvent molecules N_{eff} and denote the result as $\overline{\Delta\varepsilon}$. The $\overline{\Delta\varepsilon}$ represents the IP shift per effective solvent molecule. In Figure 8.3c, the derived $\overline{\Delta\varepsilon}$ is plotted as a function of α_m, with $\alpha_m = \overline{\Delta\varepsilon} = 0$ representing the solvent-free (i.e., solute placed in a vacuum) case. This data set is fitted to the linear regression model, resulting in a determination $R^2 > 0.99$. The $\overline{\Delta\varepsilon}$ is shown to depend linearly on α_m with a slope of 8.59 meV/Å^3 and an interception of -0.51 meV at $\alpha_m = 0$.

The linear relationship between $\overline{\Delta\varepsilon}$ and α_m shown in Figure 8.3c can lead to a potential solvation model for computing the QP excitation energies, corresponding to the ionization potentials in this particular case, of molecules in an arbitrary solvent environment. The current work presents a model parameterization for phenol, and its generalization to different solutes is discussed below

$$\begin{aligned} \varepsilon^{\text{solv}} &= \varepsilon^{\text{iso}} + \Delta\varepsilon^m \\ &= \varepsilon^{\text{iso}} + N_{\text{eff}}\overline{\Delta\varepsilon}^m \end{aligned} \tag{8.5}$$

where ε^{iso} denotes the QP energy of the isolated molecule from first-principles calculations, and $\Delta\varepsilon^m$, derived as a product of N_{eff} and $\overline{\Delta\varepsilon}^m$, is the QP energy shifts (i.e., the IP shifts) induced by the solvent environment. Using the 9 Å cutoff radius, the number of effective solvent molecules N_{eff} can be determined by sampling snapshots from MD

simulations (denoted N_{eff}^{0}), or estimated by the solvent's mass density and the solute's exclusion volume[87] (denoted N_{eff}^{m}). The $\overline{\Delta\varepsilon}^{m}$ in eq 8.5 is obtained by inserting the solvent polarizability volume α_m (derived from n_r) into the linear equation shown in Figure 8.3c. The $\Delta\varepsilon^{m}$ in eq 8.5 can thus be derived from only classical solvent properties, which are accessible for most of the common solvents. Although we hypothesize that the linear equation shown in Figure 8.3c should be universal, the exact proportionality coefficient would likely change for another solute molecule since the solute−solvent interactions are coupled. For instance, a more polarizable solute might cause a stronger response from the solvent environment, leading to a larger coefficient than the one found in Figure 8.3c.

We use the proposed solvation model to compute the IP shifts for phenol in the five investigated solvents and compare them with the first-principles results. The α_m listed in Figure 8.1c are inserted into the linear equation in Figure 3c to derive $\overline{\Delta\varepsilon}^{m}$, which show differences from the first-principles values (Figure D.11). For the number of effective solvent molecules, we consider both N_{eff}^{m} and N_{eff}^{0} (defined above). Numerical details are provided in Table D.10. The computed results using the combination of N_{eff}^{m} and $\overline{\Delta\varepsilon}^{m}$ are plotted in Figure 8.1c ($\Delta\varepsilon_1^{m}$, red squares). For the first four solvents, the derived trend agrees well with the first-principles one (blue circles), despite a common overestimation of ∼0.1 eV. The deviation of $\Delta\varepsilon_1^{m}$ for BEN is more significant due to an overestimated N_{eff}^{m}. By replacing N_{eff}^{m} with N_{eff}^{0} ($\Delta\varepsilon_2^{m}$, orange diamonds), the derived IP shifts for the BEN solvent become closer to the first-principles result. For the DCM solvent, $\Delta\varepsilon_2^{m}$ underestimates the IP shifts due to a smaller $\overline{\Delta\varepsilon}^{m}$ than the first-principles $\overline{\Delta\varepsilon}^{0}$ (Figure D.11). However, the agreement with the first-principles results is generally improved when the N_{eff} is estimated by MD simulations.

For further development and optimization of this simple solvation model, we note that (1) the full parameterization relies on exploring multiple solute molecules to elucidate the solute-dependence discussed above; (2) the linear equation in Figure 8.3c can be improved,

e.g., by sampling more solvent cases and averaging over more MD snapshots.

In summary, this work introduces a generalized decomposition scheme of the *GW* correlation self-energy based on the fragmentation of a multimolecule system. This methodology is employed to investigate the energy shifts of single-(quasi)particle excitations in various solvent environments. The fragmentation (decomposition) of the correlation self-energy is formulated upon the assumption that the induced density fluctuations, represented by Pipek−Mezey localized orbitals, are local on each fragment.

We sample molecular dynamics simulations using water and four other organic solvents together with the phenol solute. The first observation is that the explicit IP shifts do not follow the order of the mean polarizability volume computed for each solvent. To investigate this disagreement, we apply the self-energy fragmentation scheme to explore the solvation many-body effects in these systems. Specifically, we compute the fragment correlation contributions for solvation shells at various distances away from the solute molecule. The fragment correlation self-energy decays monotonically as a function of the shell distance. At the distance of ∼9 Å, the correlation contribution practically vanishes. This distance corresponds to an effective interacting radius for considering the solvent response stemming from the induced dipole interactions. The 9 Å effective interacting radius depends neither on the ionization state of the solute nor on the solvent type. This phenomenon can be attributed to the localized feature of QP excitations on the solute.

Comparing the correlation self-energies among various environments, we find that the macroscopic solvent polarizability is directly related to the temporal behavior and the correlation strength. However, the apparent 9 Å cutoff radius is unaffected by the polarizability of the solvent. This existing cutoff radius indicates that the explicit solvation many-body effects on the ionization energy depend not only on the polarizability but also on the number of effective solvent molecules. The latter can be extremely sensitive to practical experimental conditions. Indeed, if both the polarizability and the number of

solvent molecules within the effective volume are considered together, the average IP shift is perfectly reflected by the mean polarizability volume and exhibits a linear dependence. Based on this connection, we further propose a possible solvation model to compute the QP energies of solvated molecules. This model requires only classical parameters that are readily accessible.

Although further explorations are needed to confirm the universality of the effective interacting radius and the solvation model, rich information about the solvation many-body effects has been unveiled by the proposed self-energy fragmentation method. We believe this approach will provide a powerful tool for understanding and analyzing the interactions and couplings between specific fragments in composite condensed systems.

SUPPORTING INFORMATION

Texts: details of computations and methodologies; Tables: parameters in the DFT and *GW* calculations, number of solvent molecules in the small and large simulation cells, QP energies and IP shifts of each snapshot in each solvated system, number of effective solvent molecules in each snapshot of each solvated system; Figures: extracted snapshots from the MD trajectories, fluctuations of the QP energies and IP shifts with respect to the MD snapshot, IP shifts as a function of the mean polarizability, solvation shells at various distances, fragment correlation self-energy of different ionization states and solvents, graphical solutions to the QP energy of the isolated and solvated phenol.

ACKNOWLEDGMENTS

This work was supported by the NSF CAREER award through Grant No. DMR-1945098. The calculations were performed as part of the XSEDE computational Project

No. TG-CHE180051. Use was made of computational facilities purchased with funds from the National Science Foundation (CNS-1725797) and administered by the Center for Scientific Computing (CSC). The CSC is supported by the California NanoSystems Institute and the Materials Research Science and Engineering Center (MRSEC; NSF DMR 1720256) at UC Santa Barbara.

Bibliography

[1] A. Fetter and J. Walecka, *Quantum Theory of Many-particle Systems*. Dover Books on Physics. Dover Publications, 2003.

[2] R. M. Martin, L. Reining, and D. M. Ceperley, *Interacting Electrons: Theory and Computational Approaches*. Cambridge University Press, Cambridge, 2016.

[3] E. Buncel and S. Rajagopal, *Solvatochromism and solvent polarity scales*, *Accounts of Chemical Research* **23** (1990), no. 7 226–231.

[4] C. Reichardt, *Solvatochromic dyes as solvent polarity indicators*, *Chemical Reviews* **94** (1994), no. 8 2319–2358.

[5] D. Kosenkov and L. V. Slipchenko, *Solvent effects on the electronic transitions of p-nitroaniline: A qm/efp study*, *The Journal of Physical Chemistry A* **115** (2011), no. 4 392–401.

[6] C. M. Isborn, N. Luehr, I. S. Ufimtsev, and T. J. Martínez, *Excited-state electronic structure with configuration interaction singles and tamm–dancoff time-dependent density functional theory on graphical processing units*, *Journal of Chemical Theory and Computation* **7** (2011), no. 6 1814–1823.

[7] C. Bistafa and S. Canuto, *Solvent effects on the two lowest-lying singlet excited states of 5-fluorouracil*, *Theoretical Chemistry Accounts* **132** (2012), no. 1 1299.

[8] D. Ghosh, A. Roy, R. Seidel, B. Winter, S. Bradforth, and A. I. Krylov, *First-principle protocol for calculating ionization energies and redox potentials of solvated molecules and ions: Theory and application to aqueous phenol and phenolate*, *The Journal of Physical Chemistry B* **116** (2012), no. 24 7269–7280.

[9] M. Caricato, *Absorption and emission spectra of solvated molecules with the eom-ccsd-pcm method*, *Journal of Chemical Theory and Computation* **8** (2012), no. 11 4494–4502.

[10] T. Schwabe, K. Sneskov, J. M. Haugaard Olsen, J. Kongsted, O. Christiansen, and C. Hättig, *Peri–cc2: A polarizable embedded ri-cc2 method*, *Journal of Chemical Theory and Computation* **8** (2012), no. 9 3274–3283.

[11] S. Bose, S. Chakrabarty, and D. Ghosh, *Effect of solvation on electron detachment and excitation energies of a green fluorescent protein chromophore variant*, *The Journal of Physical Chemistry B* **120** (2016), no. 19 4410–4420.

[12] A. Sadybekov and A. I. Krylov, *Coupled-cluster based approach for core-level states in condensed phase: Theory and application to different protonated forms of aqueous glycine*, *The Journal of Chemical Physics* **147** (2017), no. 1 014107.

[13] D. Ghosh, *Hybrid equation-of-motion coupled-cluster/effective fragment potential method: A route toward understanding photoprocesses in the condensed phase*, *The Journal of Physical Chemistry A* **121** (2017), no. 4 741–752.

[14] S. Ren, J. Harms, and M. Caricato, *An eom-ccsd-pcm benchmark for electronic excitation energies of solvated molecules*, *Journal of Chemical Theory and Computation* **13** (2017), no. 1 117–124.

[15] R. Chakraborty, S. Bose, and D. Ghosh, *Effect of solvation on the ionization of guanine nucleotide: A hybrid qm/efp study*, *Journal of Computational Chemistry* **38** (2017), no. 29 2528–2537.

[16] D. Hršak, J. M. H. Olsen, and J. Kongsted, *Polarizable density embedding coupled cluster method*, *Journal of Chemical Theory and Computation* **14** (2018), no. 3 1351–1360.

[17] S.-I. Lu and L.-T. Gao, *Calculations of electronic excitation energies and excess electric dipole moments of solvated p-nitroaniline with the eom-ccsd-pcm method*, *The Journal of Physical Chemistry A* **122** (2018), no. 29 6062–6070.

[18] S. Ren, F. Lipparini, B. Mennucci, and M. Caricato, *Coupled cluster theory with induced dipole polarizable embedding for ground and excited states*, *Journal of Chemical Theory and Computation* **15** (2019), no. 8 4485–4496.

[19] M. Caricato, *Coupled cluster theory in the condensed phase within the singles-t density scheme for the environment response*, *WIREs Computational Molecular Science* **10** (2020), no. 5 e1463.

[20] S. D. Folkestad and H. Koch, *Multilevel cc2 and ccsd methods with correlated natural transition orbitals*, *Journal of Chemical Theory and Computation* **16** (2020), no. 1 179–189.

[21] L. Goletto, T. Giovannini, S. D. Folkestad, and H. Koch, *Combining multilevel hartree–fock and multilevel coupled cluster approaches with molecular mechanics: a study of electronic excitations in solutions*, *Physical Chemistry Chemical Physics* **23** (2021), no. 7 4413–4425.

[22] F. Santoro, V. Barone, T. Gustavsson, and R. Improta, *Solvent effect on the singlet excited-state lifetimes of nucleic acid bases: a computational study of 5-fluorouracil and uracil in acetonitrile and water*, *Journal of the American Chemical Society* **128** (2006), no. 50 16312–16322.

[23] V. Barone, R. Improta, and N. Rega, *Quantum mechanical computations and spectroscopy: From small rigid molecules in the gas phase to large flexible molecules in solution*, *Accounts of Chemical Research* **41** (2008), no. 5 605–616.

[24] F. Santoro, V. Barone, A. Lami, and R. Improta, *The excited electronic states of adenine-guanine stacked dimers in aqueous solution: a pcm/td-dft study*, *Physical Chemistry Chemical Physics* **12** (2010), no. 19 4934–4948.

[25] S. Sok, S. Y. Willow, F. Zahariev, and M. S. Gordon, *Solvent-induced shift of the lowest singlet $\pi \rightarrow \pi^*$ charge-transfer excited state of p-nitroaniline in water: An application of the tddft/efp1 method*, *The Journal of Physical Chemistry A* **115** (2011), no. 35 9801–9809.

[26] M. Dargiewicz, M. Biczysko, R. Improta, and V. Barone, *Solvent effects on electron-driven proton-transfer processes: adenine–thymine base pairs*, *Physical Chemistry Chemical Physics* **14** (2012), no. 25 8981–8989.

[27] R. Improta, *Photophysics and photochemistry of thymine deoxy-dinucleotide in water: A pcm/td-dft quantum mechanical study*, *The Journal of Physical Chemistry B* **116** (2012), no. 49 14261–14274.

[28] C. M. Isborn, A. W. Götz, M. A. Clark, R. C. Walker, and T. J. Martínez, *Electronic absorption spectra from mm and ab initio qm/mm molecular dynamics: Environmental effects on the absorption spectrum of photoactive yellow protein*, *Journal of Chemical Theory and Computation* **8** (2012), no. 12 5092–5106.

[29] A. V. Marenich, C. J. Cramer, and D. G. Truhlar, *Electronic absorption spectra and solvatochromic shifts by the vertical excitation model: Solvated clusters and molecular dynamics sampling*, *The Journal of Physical Chemistry B* **119** (2015), no. 3 958–967.

[30] C. A. Guido, D. Jacquemin, C. Adamo, and B. Mennucci, *Electronic excitations in solution: The interplay between state specific approaches and a time-dependent density functional theory description*, *Journal of Chemical Theory and Computation* **11** (2015), no. 12 5782–5790.

[31] T.-J. Bi, L.-K. Xu, F. Wang, M.-J. Ming, and X.-Y. Li, *Solvent effects on excitation energies obtained using the state-specific td-dft method with a polarizable continuum model based on constrained equilibrium thermodynamics*, *Physical Chemistry Chemical Physics* **19** (2017), no. 48 32242–32252.

[32] M. Rubešová, E. Muchová, and P. Slavíček, *Optimal tuning of range-separated hybrids for solvated molecules with time-dependent density functional theory*, *Journal of Chemical Theory and Computation* **13** (2017), no. 10 4972–4983.

[33] J. Preiss, D. Kage, K. Hoffmann, T. J. Martínez, U. Resch-Genger, and M. Presselt, *Ab initio prediction of fluorescence lifetimes involving solvent environments by means of cosmo and vibrational broadening*, *The Journal of Physical Chemistry A* **122** (2018), no. 51 9813–9820.

[34] C. Chakravarty, H. Aksu, J. A. Martinez B., P. Ramos, M. Pavanello, and B. D. Dunietz, *Role of dielectric screening in calculating excited states of solvated azobenzene: A benchmark study comparing quantum embedding and polarizable continuum model for representing the solvent*, *The Journal of Physical Chemistry Letters* **13** (2022), no. 22 4849–4855.

[35] C. J. Cramer and D. G. Truhlar, *Implicit solvation models: equilibria, structure, spectra, and dynamics*, *Chemical Reviews* **99** (1999), no. 8 2161–2200.

[36] J. Tomasi, B. Mennucci, and R. Cammi, *Quantum mechanical continuum solvation models*, *Chemical Reviews* **105** (2005), no. 8 2999–3094.

[37] B. Mennucci, *Polarizable continuum model*, *WIREs Computational Molecular Science* **2** (2012), no. 3 386–404.

[38] F. Lipparini and B. Mennucci, *Perspective: Polarizable continuum models for quantum-mechanical descriptions*, *The Journal of Chemical Physics* **144** (2016), no. 16 160901.

[39] M. S. Gordon, D. G. Fedorov, S. R. Pruitt, and L. V. Slipchenko, *Fragmentation methods: A route to accurate calculations on large systems*, *Chemical Reviews* **112** (2012), no. 1 632–672.

[40] S. R. Pruitt, C. Bertoni, K. R. Brorsen, and M. S. Gordon, *Efficient and accurate fragmentation methods*, *Accounts of Chemical Research* **47** (2014), no. 9 2786–2794.

[41] T. J. Zuehlsdorff and C. M. Isborn, *Modeling absorption spectra of molecules in solution*, *International Journal of Quantum Chemistry* **119** (2019), no. 1 e25719.

[42] B. Winter and M. Faubel, *Photoemission from liquid aqueous solutions*, *Chemical Reviews* **106** (2006), no. 4 1176–1211.

[43] R. Seidel, S. Thürmer, and B. Winter, *Photoelectron spectroscopy meets aqueous solution: Studies from a vacuum liquid microjet*, *The Journal of Physical Chemistry Letters* **2** (2011), no. 6 633–641.

[44] P. R. Tentscher, R. Seidel, B. Winter, J. J. Guerard, and J. S. Arey, *Exploring the aqueous vertical ionization of organic molecules by molecular simulation and liquid microjet photoelectron spectroscopy*, *The Journal of Physical Chemistry B* **119** (2015), no. 1 238–256.

[45] T. Suzuki, *Ultrafast photoelectron spectroscopy of aqueous solutions*, *The Journal of Chemical Physics* **151** (2019), no. 9 090901.

[46] L. Hedin, *New method for calculating the one-particle green's function with application to the electron-gas problem*, *Physical Review* **139** (1965), no. 3A A796–A823.

[47] F. Aryasetiawan and O. Gunnarsson, *The gw method*, *Reports on Progress in Physics* **61** (1998), no. 3 237.

[48] G. Onida, L. Reining, and A. Rubio, *Electronic excitations: density-functional versus many-body green's-function approaches*, *Reviews of Modern Physics* **74** (2002), no. 2 601–659.

[49] C. Friedrich and A. Schindlmayr, *Many-body perturbation theory: The GW approximation*, vol. 31 of *NIC Series*, p. 335–355. John von Neumann Institute for Computing, 2006.

[50] D. Golze, M. Dvorak, and P. Rinke, *The gw compendium: A practical guide to theoretical photoemission spectroscopy*, *Frontiers in Chemistry* **7** (2019).

[51] M. J. van Setten, F. Caruso, S. Sharifzadeh, X. Ren, M. Scheffler, F. Liu, J. Lischner, L. Lin, J. R. Deslippe, S. G. Louie, C. Yang, F. Weigend, J. B. Neaton, F. Evers, and P. Rinke, *Gw100: Benchmarking g0w0 for molecular systems*, *Journal of Chemical Theory and Computation* **11** (2015), no. 12 5665–5687.

[52] F. Caruso, M. Dauth, M. J. van Setten, and P. Rinke, *Benchmark of gw approaches for the gw100 test set*, *Journal of Chemical Theory and Computation* **12** (2016), no. 10 5076–5087.

[53] M. Govoni and G. Galli, *Gw100: Comparison of methods and accuracy of results obtained with the west code*, *Journal of Chemical Theory and Computation* **14** (2018), no. 4 1895–1909.

[54] T. A. Pham, H.-V. Nguyen, D. Rocca, and G. Galli, *gw calculations using the spectral decomposition of the dielectric matrix: Verification, validation, and comparison of methods*, *Phys. Rev. B* **87** (2013) 155148.

[55] M. Govoni and G. Galli, *Large scale gw calculations*, *Journal of Chemical Theory and Computation* **11** (2015), no. 6 2680–2696.

[56] F. Bruneval, *Optimized virtual orbital subspace for faster gw calculations in localized basis*, *The Journal of Chemical Physics* **145** (2016), no. 23 234110.

[57] P. Liu, M. Kaltak, J. c. v. Klimeš, and G. Kresse, *Cubic scaling gw: Towards fast quasiparticle calculations*, *Phys. Rev. B* **94** (2016) 165109.

[58] J. Wilhelm, D. Golze, L. Talirz, J. Hutter, and C. A. Pignedoli, *Toward gw calculations on thousands of atoms*, *The Journal of Physical Chemistry Letters* **9** (2018), no. 2 306–312.

[59] H. Yang, M. Govoni, and G. Galli, *Improving the efficiency of g0w0 calculations with approximate spectral decompositions of dielectric matrices*, *The Journal of Chemical Physics* **151** (2019), no. 22 224102.

[60] A. Förster and L. Visscher, *Low-order scaling g0w0 by pair atomic density fitting*, *Journal of Chemical Theory and Computation* **16** (2020), no. 12 7381–7399.

[61] M. Kim, G. J. Martyna, and S. Ismail-Beigi, *Complex-time shredded propagator method for large-scale gw calculations*, *Phys. Rev. B* **101** (2020) 035139.

[62] W. Gao and J. R. Chelikowsky, *Accelerating time-dependent density functional theory and gw calculations for molecules and nanoclusters with symmetry adapted interpolative separable density fitting*, *Journal of Chemical Theory and Computation* **16** (2020), no. 4 2216–2223.

[63] J. Wilhelm, P. Seewald, and D. Golze, *Low-scaling gw with benchmark accuracy and application to phosphorene nanosheets*, *Journal of Chemical Theory and Computation* **17** (2021), no. 3 1662–1677.

[64] A. Förster and L. Visscher, *Low-order scaling quasiparticle self-consistent gw for molecules*, *Frontiers in Chemistry* **9** (2021).

[65] P. Umari, *A fully linear response g0w0 method that scales linearly up to tens of thousands of cores*, *The Journal of Physical Chemistry A* **126** (2022), no. 21 3384–3391.

[66] M. Del Ben, F. H. da Jornada, A. Canning, N. Wichmann, K. Raman, R. Sasanka, C. Yang, S. G. Louie, and J. Deslippe, *Large-scale gw calculations on pre-exascale hpc systems*, *Computer Physics Communications* **235** (2019) 187–195.

[67] M. D. Ben, C. Yang, Z. Li, F. H. d. Jornada, S. G. Louie, and J. Deslippe, *Accelerating large-scale excited-state gw calculations on leadership hpc systems*, in *SC20: International Conference for High Performance Computing, Networking, Storage and Analysis*, SC20: International Conference for High Performance Computing, Networking, Storage and Analysis, pp. 1–11, 2020.

[68] V. W.-z. Yu and M. Govoni, *Gpu acceleration of large-scale full-frequency gw calculations*, *Journal of Chemical Theory and Computation* **18** (2022), no. 8 4690–4707.

[69] D. Neuhauser, Y. Gao, C. Arntsen, C. Karshenas, E. Rabani, and R. Baer, *Breaking the theoretical scaling limit for predicting quasiparticle energies: The stochastic GW approach*, *Physical Review Letters* **113** (2014), no. 7 076402.

[70] V. Vlček, E. Rabani, D. Neuhauser, and R. Baer, *Stochastic gw calculations for molecules*, *Journal of Chemical Theory and Computation* **13** (2017), no. 10 4997–5003.

[71] V. Vlček, W. Li, R. Baer, E. Rabani, and D. Neuhauser, *Swift GW beyond 10,000 electrons using sparse stochastic compression*, *Physical Review B* **98** (2018), no. 7 075107.

[72] V. Vlček, *Stochastic vertex corrections: Linear scaling methods for accurate quasiparticle energies*, *Journal of Chemical Theory and Computation* **15** (2019), no. 11 6254–6266.

[73] V. Vlček, E. Rabani, and D. Neuhauser, *Quasiparticle spectra from molecules to bulk*, *Physical Review Materials* **2** (2018), no. 3 030801.

[74] J. Brooks, G. Weng, S. Taylor, and V. Vlcek, *Stochastic many-body perturbation theory for moiré states in twisted bilayer phosphorene*, *Journal of Physics: Condensed Matter* **32** (2020), no. 23 234001.

[75] G. Weng and V. Vlček, *Quasiparticles and band structures in organized nanostructures of donor–acceptor copolymers*, *The Journal of Physical Chemistry Letters* **11** (2020), no. 17 7177–7183.

[76] M. Romanova and V. Vlček, *Decomposition and embedding in the stochastic gw self-energy*, *The Journal of Chemical Physics* **153** (2020), no. 13 134103.

[77] G. Weng and V. Vlček, *Efficient treatment of molecular excitations in the liquid phase environment via stochastic many-body theory*, *The Journal of Chemical Physics* **155** (2021), no. 5 054104.

[78] M. Romanova and V. Vlček, *Stochastic many-body calculations of moiré states in twisted bilayer graphene at high pressures*, *npj Computational Materials* **8** (2022), no. 1 11.

[79] G. Weng, M. Romanova, A. Apelian, H. Song, and V. Vlček, *Reduced scaling of optimal regional orbital localization via sequential exhaustion of the single-particle space*, *Journal of Chemical Theory and Computation* **18** (2022), no. 8 4960–4972.

[80] J. Pipek and P. G. Mezey, *A fast intrinsic localization procedure applicable for ab initio and semiempirical linear combination of atomic orbital wave functions*, *The Journal of Chemical Physics* **90** (1989), no. 9 4916–4926.

[81] S. Lehtola and H. Jónsson, *Pipek–mezey orbital localization using various partial charge estimates*, *Journal of Chemical Theory and Computation* **10** (2014), no. 2 642–649.

[82] E. Ö. Jónsson, S. Lehtola, M. Puska, and H. Jónsson, *Theory and applications of generalized pipek–mezey wannier functions*, *Journal of Chemical Theory and Computation* **13** (2017), no. 2 460–474.

[83] P. Hohenberg and W. Kohn, *Inhomogeneous electron gas*, *Phys. Rev.* **136** (1964) B864–B871.

[84] W. Kohn and L. J. Sham, *Self-consistent equations including exchange and correlation effects*, *Phys. Rev.* **140** (1965) A1133–A1138.

[85] J. P. Perdew, K. Burke, and M. Ernzerhof, *Generalized gradient approximation made simple*, *Phys. Rev. Lett.* **77** (1996) 3865–3868.

[86] For experimental data of the investigated solvents, see the CRC Handbook of Chemistry and Physics Online. Accessed January 10, 2022.

[87] The solute exclusion volume by phenol is calculated as the volume of a sphere with a 3.5 Å radius.

Chapter 9

Are multi-quasiparticle interactions important in molecular ionization?

Carlos Mejuto-Zaera,[a] Guorong Weng, Mariya Romanova, Stephen J. Cotton,[b,c] K. Birgitta Whaley,[1] Norm M. Tubman,[d] Vojtěch Vlček

ABSTRACT

Photo-emission spectroscopy directly probes individual electronic states, ranging from single excitations to high-energy satellites, which simultaneously represent multiple quasiparticles (QPs) and encode information about electronic correlation. First-principles description of the spectra requires an efficient and accurate treatment of all many-body effects. This is especially challenging for inner valence excitations where the single QP picture breaks down. Here, we provide the full valence spectra of small closed-shell

[a]University of California, Berkeley, California 94720, USA
[b]Quantum Artificial Intelligence Laboratory (QuAIL), Exploration Technology Directorate, NASA Ames Research Center, Moffett Field, California 94035, USA
[c]KBR, 601 Jefferson St., Houson, Texas 77002, USA
[d]Quantum Artificial Intelligence Laboratory (QuAIL), Exploration Technology Directorate, NASA Ames Research Center, Moffett Field, California 94035, USA

molecules, exploring the independent and interacting quasiparticle regimes, computed with the fully-correlated adaptive sampling configuration interaction (ASCI) method. We critically compare these results to calculations with the many-body perturbation theory, based on the GW and vertex corrected $GW\Gamma$ approaches. The latter explicitly accounts for two-QP quantum interactions, which have been often neglected. We demonstrate that for molecular systems, the vertex correction universally improves the theoretical spectra, and it is crucial for accurate prediction of QPs as well as capturing the rich satellite structures of high-energy excitations. $GW\Gamma$ offers a unified description across all relevant energy scales. Our results suggest that the multi-QP regime corresponds to dynamical correlations, which can be described via perturbation theory.

9.1 COMMUNICATION

The quantitative understanding of electronic excitations in complex molecular extended systems is one of the most fundamental open challenges in modern theoretical chemistry. Perhaps the most direct experimental probe of the excited state manifold is given by photo-emission spectra (PES), which directly access individual electronic states [1, 2, 3, 4] and, in principle, access information on the single-particle orbitals [5, 6, 7]. Theoretical approaches are meant to provide an interpretative connection between measured spectral features and chemical concepts, thus helping design systems with tailored (opto)electronic properties. An accurate realization of this ideal often requires a treatment beyond effective one-body theories, such as Hartree−Fock or Kohn−Sham density-funcitonal theory, to capture all interactions that renormalize single electron properties and lead to the formation of quasiparticles (QPs).

Traditional gold-standard wave function approaches, such as the configuration interaction or coupled cluster methods, can yield highly accurate predictions, and they have

been extensively applied to describe the outer valence and core electron spectra of small molecules [8, 9, 10, 11, 12, 13], which fundamentally behave as individual QPs. However, the description of the inner valence region is more complicated: multiple excitation mechanisms are available, and ionization can be accompanied by simultaneous neutral excitation of the system. At the energy scales associated with inner valence PES, the single QP (SQP) picture breaks down, and the spectra exhibit a multitude of features [14, 15], which we refer to as the multi-QP (MQP) regime. In analyzing PES, these are typically referred to as shake-up satellites. Describing these ionized states requires accounting for the nontrivial interactions among many excited states. The inner valence excitations in the MQP regime thus represents an unambiguous measure of electron correlation [16]. This correlation may be dynamic or static in nature, and, depending of this distinction, it may be captured by different approximations: dynamical correlation would correspond to a frequency dependent potential on top of an effective one-body theory, and can (in principle) be described by perturbation theory. On the other hand, static correlation requires an intrinsically many-body description, i.e., it cannot be qualitatively approximated by a single effective one-body hamiltonian and its perturbation.

Ab-initio wave function methods capture both types or correlations, they, in principle, describe the high energy holes, but often require extensive exploration of the exponentially large Hilbert space, limiting their application to small molecular systems. However, while convenient from a computational perspective, the formulation of these methods in terms of determinants makes a definite distinction between dynamic and static correlation complicated in most cases. In particular, it is unclear whether MQP features in PES belong to the former or latter class. On the one hand, they are intrinsically many-body effects which cannot be captured by a single Slater determinant. On the other hand, they often arise from neutral excitations weakly coupled to holes, which suggests they should be amenable to perturbative description.

In the pursuit of an accurate but scalable theoretical description of PES, many-body perturbation theory (MBPT) has proven a viable alternative for computing QP excitations. It offers a systematically improvable theoretical framework for capturing *dynamical* correlations. MBPT relies on physically motivated concepts such as screening, while retaining a polynomial computational scaling. In particular, the popular GW approximation is extensively applied to treat molecules and solids, and it predicts outer valence and core electron spectra with good accuracy [17, 18, 19, 20, 21, 22]. With recent algorithmic developments, GW can be applied to systems with thousands of electrons [23, 20, 24, 25, 26, 27, 28]. Unfortunately, the GW framework is fundamentally limited to systems where classical electrodynamics dominates the electronic correlation. Hence, the description of the MQP regime is beyond the GW capabilities [29, 30, 31, 32, 33, 34, 35, 36]. Within the MBPT framework, the missing higher-order quantum interactions are represented by the vertex term Γ, which encodes dynamical two-particle correlations. The inclusion of Γ leads to the $GW\Gamma$ approach, which for molecular systems has been studied only on first ionization energies and electron affinities[37, 38, 39, 40, 30, 31]. However, the role of Γ on the entire valence states and the MQP excitations has not been explored up to now.

In this communication, we demonstrate that MBPT with vertex terms successfully captures the correlations necessary for a qualitative the description of the MQP regime of PES, suggesting them to be dynamic in nature. By comparison with explicitly correlated and numerically exact methods, namely the adaptive sampling configuration interaction (ASCI) approach [41, 42, 43, 44], we show that the $GW\Gamma$ approach yields superior results compared to GW throughout all energy scales. Moreover, we discover that the non-local quantum interactions play a significant role for all valence electron excitations and correctly captures the breakdown of the SQP picture, eliminating spurious artifacts of GW in the shake-up region of PES. We choose as case study the PES of selected closed

shell molecules (NH_3, H_2O, CH_4, C_2H_2, and N_2), which as we show present rich MQP character in the inner valence region.

The spectral function $A(\omega)$ computed with ASCI and MBPT is the figure of merit. This corresponds to the physical observable (i.e., PES), and is given as the trace over the imaginary part of the Green's function (GF) $G_{i,j}(\omega)$ [32], i.e., $A(\omega) = \frac{1}{\pi}\mathrm{Tr}\,|\mathrm{Im}\,G(\omega)|$. The i, j sub-indices correspond to a chosen single particle basis. The peaks in $A(\omega)$ correspond to the poles of G [45] and for a particular hole component:

$$G_{i,i}(\omega) = \sum_m \frac{\left|\langle \Psi_m^{N-1}|c_i|\Psi_0^N\rangle\right|^2}{\omega + (E_m^{N-1} - E_0^N) - i\eta}, \tag{9.1}$$

where $|\Psi_m^N\rangle$ is the m-th eigenstate of the N particle system, with energy E_m^N. Further, c_i is the i-th annihilation operator and η is an integrating factor. In the mean-field and SQP regimes, we expect only *one* non-vanishing overlap $\left|\langle \Psi_m^{N-1}|c_i|\Psi_0^N\rangle\right|^2$ per single-particle state i, corresponding to a dressed hole with energy $E_m^{N-1} - E_0^N$. However, *multiple* states $|\Psi_m^{N-1}\rangle$ with distinct E_m^{N-1} exist in the MQP regime.

First, we evaluate Eq. (9.1) without further approximations via the ASCI algorithm [41, 42, 46, 43, 44], which captures both SQP and MQP regimes, regardless of the degree of correlation of the excited states. ASCI provides accurate Green's functions in model systems [43, 47]; here, we compute Green's functions of *ab initio* Hamiltonians using ASCI for the first time. The spectral features calculated from Eq. (9.1) represent a series of infinitely sharp peaks due to the use of finite atomic basis sets and a Hermitian Hamiltonian. As a result, no scattering states are considered and the finite lifetimes of individual excitations (arising due to the coupling to continuum) are neglected. While the MBPT calculations also discretize the state space, this is performed in the converged real space grid which enables the description of the continuum states as well (for the details of the calculations see the supplementary material). To facilitate comparison with

the MBPT results, which thus include lifetimes due to electron−electron scattering, the ASCI-computed spectra have been artificially broadened using the η parameter in Eq. (9.1). For the heuristics and technical details of ASCI, including basis set extrapolation, see the supplementary material.

MBPT is based on the conceptually different approach of obtaining the QP energies through the Dyson equation [32]. This relates the Green's function of the fully interacting QPs $G_{i,j}(\omega)$ and a reference (mean-field) Green's function $G_{0,i,j}(\omega)$, through the self-energy $\Sigma_{i,j}(\omega)$. The latter, in principle, contains all many-body effects. The poles of $G_{i,j}(\omega)$ are subject to the QP fixed point equation:

$$\epsilon_j = \epsilon_j^0 + \mathrm{Re}\left[\Sigma_{j,j}(\omega = \epsilon_j)\right] + \mathrm{Re}\left[\Delta_j(\omega = \epsilon_j)\right]. \tag{9.2}$$

Here ϵ_j^0 is a pole of G_0 and $\Delta_j(\omega)$ comprises the coupling due to the off-diagonal elements of $\Sigma_{i,j}(\omega)$. In this work, we adopt the common diagonal self-energy approximation, i.e. we assume $\Delta_j(\omega) = 0$ in Eq. (9.2). In the SQP regime, $\Sigma(\omega)_{i,j}$ merely shifts the poles of G with respect to G_0, and Eq. (9.2) only has one solution per orbital. For MQPs, the structure of the self-energy is necessarily more complex and, in principle, yields multiple solutions to Eq. (9.2). To capture such correlated states, $\Sigma(\omega)_{i,j}$ must account for the interactions between the particle−hole pairs and ionized holes (or injected electrons) in the system. It is often helpful to represent the solutions of Eq. (9.2) graphically as done in the discussion below.

In this work, we base the perturbation expansion on top of the Hartree−Fock (HF) Hamiltonian employing a one-step iteration in building the self-energy. In principle, the correlation self-energy, Σ_c, is derived from the equation of motion of the QP Green's function and the non-interacting reference (i.e., HF in this case). The full (self-consistently

renormalized) expression reads [32]:

$$\Sigma_c(1,2) = -\nu(1,\bar{4})G(1,\bar{3})\frac{\delta\Sigma_{Hxc}(\bar{3},2)}{\delta G(\bar{6},\bar{5})}{}^3\chi(\bar{6},\bar{5},\bar{4}), \tag{9.3}$$

where we employ a short-hand notation for space-time coordinates $1 \equiv (r_1, t_1)$ and bar indicates a coordinate that is integrated over. Here, Σ_{Hxc} contains Hartree, exchange, and correlation interactions, and $\nu(1,2) = \delta(t_1 - t_2)/|r_1 - r_2|$ is the bare Coulomb interaction. Further, we introduce a generalized response function connecting the induced Green's function to a perturbing potential $U(1)$ as ${}^3\chi(1,2,3) = -i\delta G(1,2)/\delta U(3)$.[31] To lower the computational cost, it is common to approximate $\delta\Sigma_{Hxc}/\delta G$, the two-particle interaction kernels [33, 32, 34, 35, 36]. In particular, taking $\delta\Sigma_{Hxc}/\delta G \approx \delta\Sigma_H/\delta G$ leads to the popular GW approximation [48, 49], which describes the correlations as induced time-dependent density fluctuations. In contrast, $GW\Gamma$ evaluates Eq. (9.3) in full and captures the QP couplings. The additional terms (compared to GW) stemming from $\delta\Sigma_{xc}/\delta G$ are referred to as vertex corrections, and they are responsible for mutual coupling of MQP interactions [29, 30, 31, 32, 35]. In particular, it has been shown that including vertex corrections is necessary for self-consistent renormalization[50] and to capture satellite spectral features for simple models of core electrons [51]. While the computational cost of Γ is large [52, 30], a recent stochastic formalism introduced a linear-scaling algorithm, which we apply here [31] to study the effect of vertex corrections on the satellite features in the valence spectrum.

In practice, we resort to the single step correction scheme for both GW and $GW\Gamma$. In this approximation, the two-particle kernel derives from the mean-field Hamiltonian, i.e., it becomes $\delta\Sigma_H/\delta G$ for GW. For $GW\Gamma$, the kernel is $\delta\Sigma_{Hx}/\delta G$, i.e., it also includes the HF exchange term [31]. Thus, the $GW\Gamma$ implementation contains, on top of induced Hartree potentials, also the dynamical induced exchange interactions. The latter are introduced

through an additional term in the self-energy (see the supplementary material for details) that is responsible for additional oscillations in $\Sigma_c(\omega)$ and, hence, for additional solutions to Eq. (9.2). Further, as common, we employ the random-phase approximation (RPA) in GW; however it is avoided in $GW\Gamma$, where the time evolution of states is governed by the full Hamiltonian (by the time-dependent Hartree−Fock approximation in this particular case). Hence, the propagated states incorporate excitonic effects through the dynamical exchange potential[33]. Effectively, our $GW\Gamma$ implementation corresponds to performing one full iteration through Hedin's pentagon. An alternative formulation based on the T-matrix formalism allows to incorporate other channels of correlations[29, 32, 53], which would be accounted for if the Hedin's pentagon (with Σ_{xc} defined by Eq. (9.3)) was run to self-consistency. The use of GW without RPA is possible, but it worsens the quality of $A(\omega)$ [31]. Further, we deliberately choose HF as the starting point as it often lacks spurious multiple solutions to Eq. (9.3) [54] and HF single-particle states are close to true Dyson orbitals.[55]

The computed spectral functions with the different theoretical approaches are illustrated in the top panel of Figure 9.1 for the CH_4, NH_3, and H_2O molecules. The frontier orbitals appear at the lowest absolute frequencies, an thus we henceforth refer to the orbitals with energy close to zero frequency as *low* energy, or outer valence, and those with energy far away from zero as *high* energy, or inner valence. The distinction between the SQP and MQP regimes is evident: the highest occupied molecular orbitals (HOMO) and states energetically close to these are composed of a single sharp peak per orbital, consistent with the SQP picture. In contrast, excitations far away from the HOMO exhibit broader peaks; their spectral intensity is often redistributed to multiple satellite features. This is a signature of the MQP regime. These results alone however do not indicate whether the satellites represent a weak coupling of, in principle, distinguishable QPs, and to what extent the MQP couplings can be captured perturbatively using single

particle states forming only one Slater determininant.

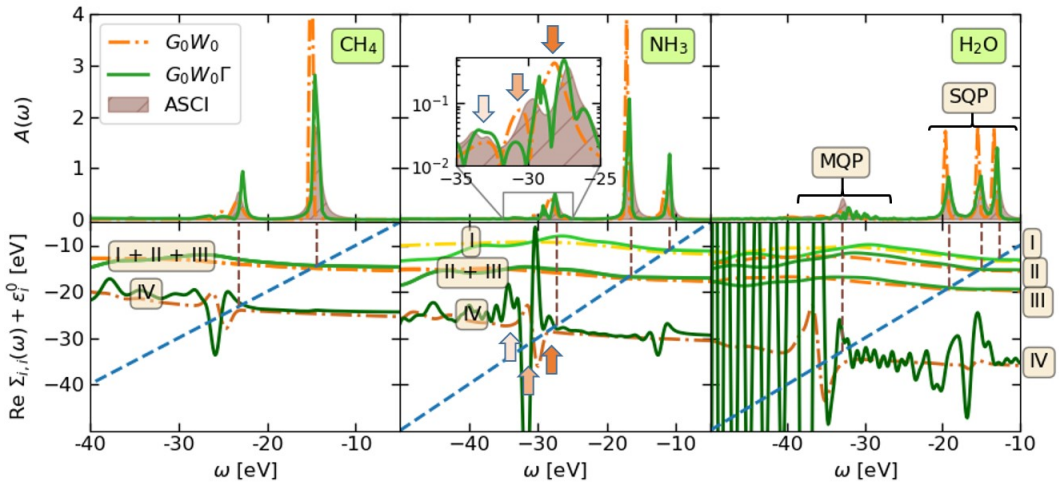

Figure 9.1: Upper panels: Spectral functions for CH_4, NH_3 and H_2O as computed with ASCI (filled curve), G_0W_0 (dot-dashed line) and $G_0W_0\Gamma$ (solid line). Note that the inset in the central panel is in log scale. We mark the SQP and MQP regimes explicitly for H_2O. Lower panels: Corresponding real part of the diagonal self-energy terms from G_0W_0 and $G_0W_0\Gamma$, one curve per orbital numbered starting with I for the HOMO, shifted by corresponding Hartree−Fock QP energy ϵ_i^0. Symmetry induced degeneracies reduce the number of peaks and self-energy curves in CH_4 and NH_3. The former has a three-fold degenerate HOMO at ~ -14 eV, and the latter a two-fold degenerate at ~ -17 eV. The vertical dashed lines mark the position of the ASCI QP energies, and the blue dashed line corresponds to the frequency line $y(\omega) = \omega$. The intercepts of the self-energy curves with the blue dashed line correspond to graphical solutions of the QP equation (9.2). The arrows point at the features in the G_0W_0 highest energy curve which create maxima in the spectral function, see text for discussion.

To answer this, we compare the ASCI and MBPT calculations. We show the QP energies for all valence excitations and all methods in Figure 9.2. As expected [33, 52, 30, 31, 34, 35, 36], $GW\Gamma$ is closest to ASCI results (compared to HF and GW) and we find the best agreement for the holes of the HOMO states, which are in the SQP regime. For HOMO, the self-energy is merely responsible for shifting the poles of the Green's function, but the presence of the vertex corrections is important, as illustrated in the inset of Figure 9.2. The one-shot GW approach performs only slightly better than HF; the mean absolute deviation (MAD) with respect to ASCI is 1.0 eV and 0.8 eV for HF

and GW, respectively. Upon inclusion of vertex terms, however, the MAD decreases to 0.3 eV. The presence of Γ is responsible for the excitonic effects in W, and these are likely non-negligible in small systems, where electrons and holes have large spatial overlaps. Further, the vertex correction cancels, at least partially, the spurious self-polarization in GW [56, 57]. The latter is possibly the major driving force of the improvement, because the electron−hole interactions in the screening tend to have little or (surprisingly) negative impact on the QP energy predictions [30, 58, 31].

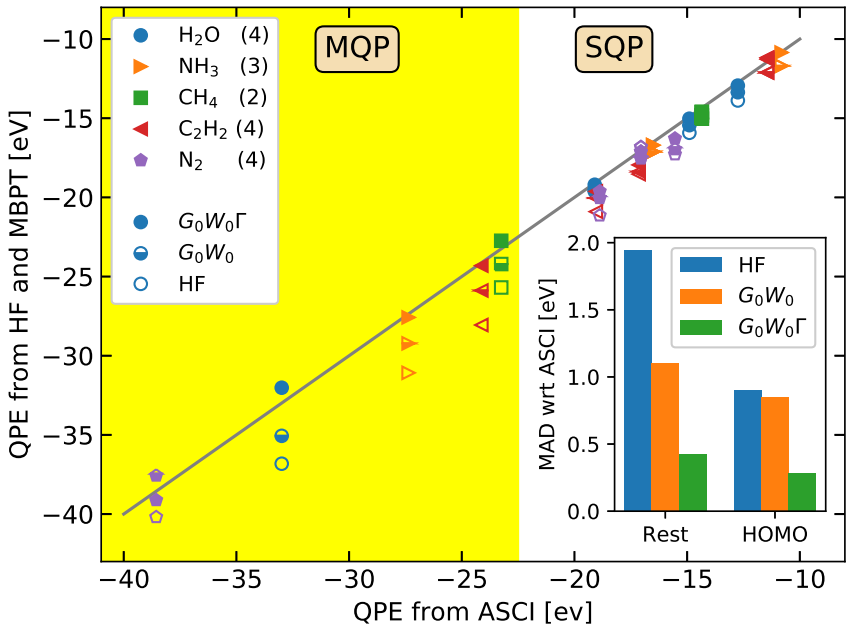

Figure 9.2: Quasiparticle energies (QPE) for the different molecular systems computed from ASCI vs the QPEs computed with the many-body pertubation theory. The symbols correspond to: Hartree−Fock (HF, empty), G_0W_0 (half-filled), and the vertex corrected $G_0W_0\Gamma$ (solid). The energy region where the excitations present MQP character is shaded yellow. The number of QPEs per molecule is given in the legend. The inset shows the mean average deviation (MAD) between the ASCI results and the three perturbative approaches.

Unlike previous studies, we go beyond the HOMO and also examine higher energy excitations, which exhibit MQP behavior. Due to the lack of correlation, the HF ionization

potentials deviate significantly from the ASCI QP energies (MAD $\sim$ 2 eV), as illustrated in Figure 9.2. Even here, the ASCI spectral function retains a dominant peak (in Figure 9.1 at -23 eV for CH_4, -27 eV for NH_3 and -33 eV for H_2O); yet, a fraction of the spectral weight is redistributed to satellite features. This departure from the SQP regime progresses with the increasing excitation energy. For the highest energy valence states of H_2O and N_2 (at -33 eV and -39 eV respectively), $A(\omega)$ shows multitude of sizeable satellites located > 10 eV away from the main peak. Unsurprisingly, the MBPT QPEs deviate more strongly from ASCI in this regime, see inset of Figure 9.2. Nevertheless, for these higher energy states the vertex correction again significantly improves the QPEs of the most prominent peaks, bringing the MAD below 0.5 eV. Considering the main QP signatures alone, the vertex corrections seem necessary for an accurate description throughout all studied energy scales, suggesting that MQP effects are important even for the simple orbital ionization energies.

We now turn to address the satellites in the MQP regime. Processes at this energy scale are characterized by the presence of neutral (e.g. optical) excitations interacting with the ionized hole. However, the strength of their mutual "hybridization" (i.e., the degree of entanglement in Eq. (9.1)) is not encoded in $A(\omega)$. The spectral function only provides information about the *probability* of the given (SQP or MQP) excitation, as given by the overlaps $\langle \Psi_m^{N-1} | c_i | \Psi_0^N \rangle$ in Eq. (9.1). In the rest of this paper, we explore how the MBPT methods may offer some clarification by investigating the properties of $\Sigma(\omega)$, since the poles of $A(\omega)$ are related to $\Sigma(\omega)$ through Eq. (9.2).

A graphical solution to Eq. (9.2) is illustrated in the lower panels of Figure 9.1 for each orbital explicitly. We realize that the distinction between SQP and MQP regime made in the upper panels is evident in the lower panels as well. Indeed, for the HOMO and two subsequent orbitals (labeled I, II and III), the self-energy crosses the $y = \omega$ line exactly once, while for the inner valence orbital (IV) there may be multiple crossings,

giving rise to satellite features. The *GW* $A(\omega)$ in the MQP regime shows a common simple structure: besides the main peak, there are two other smaller peaks accompanying it (see the arrows in the inset of Figure 9.1). This three-peak feature corresponds to the self-energy with only a single true pole (middle arrow in lower central panel of Figure 9.1), but having two nearby frequencies where Eq. (9.2) is approximately fulfilled (left and right arrows). In almost all of the molecules, the main maximum corresponds one of these two "pseudo-poles" (rightmost arrow). This same three-peak structure has been discussed in the context of solids as an artifact of *GW*. [59, 60, 61]. Note that due to the finite real-time propagation employed in our stochastic implementation [23, 20, 25, 24, 31], some of the *GW* "pseudo-poles" may correspond to actual poles. Only for N_2, does Eq. (9.2) have two solutions (i.e., two poles). Here the resulting $A(\omega)$ features only a single prominent peak associated with the low-energy QP; see the supplementary material. In general, neither the main QP peaks nor the "secondary" solutions in *GW* appear at the correct energy and the overall spectrum is on average shifted to too high energies. To summarize, ASCI shows a complex satellite structure, whereas *GW* only presents a regular three-peak spectra for the bottom valence states.

Clearly, *GW* can provide multiple solutions, in principle, though they do not match the fully correlated results.[62, 32, 61] The QPs predicted by *GW* in closed shell systems is consistent with a *surmised* "plasmaron," representing a resonantly bound hole and a collective neutral excitation. In solids, this was interpreted as an electron−plasmon state. However this was eventually identified as an artifact of *GW* [63]. In practice, the *GW* approximation spuriously substitutes the multiple satellites with a single secondary QP that does not correspond to a physical excited state. Nevertheless, for *weakly* interacting MQPs, the absence of satellites can be remedied by reconstructing the Green's function [and $A(\omega)$] via the cumulant expansion technique [25, 61]. This method reproduces MQP structures, but in its common linear order formulation assumes the presence of a *distinguishable*

neutral excitation, which corresponds to a pole in the (classical) polarizability, which describes the charge density fluctuations. This in turn implies that $|\Psi_m^{N-1}\rangle$ in Eq. (9.1) has a direct product state of an ionized hole and excited state determinant; the total energy of such a state is merely the sum of the ionization potential and the neutral excitation energy. If true, the $A(\omega)$ would exhibit a regular satellite structure, in which peaks appear at energies corresponding to the multiples of the "plasmon" energy. In other words, the n-th satellite maximum represents the energy of a single hole plus n excited plasmons. The weak coupling regime is justified for localized holes in the presence of delocalized neutral excitations [63]. However, this separation is hard to conceive in small finite systems and cannot be readily justified for molecules. Furthermore, the fully correlated ASCI results do *not* exhibit a regular pattern of satellite peaks, suggesting that the MQP regime comprises at least some entangled $|\Psi_m^{N-1}\rangle$ states. A recent extension of the cumulant approximation [64, 65] includes non-linear contributions and it is not limited to the regular satellite structure (important, e.g., for molecular core spectra). Unlike core holes, the energy scale of inner valence holes is comparable to that of the valence neutral excitations. As a result a high degree of "hybridization" between the two QPs is expected, requiring an explicitly inclusion of MQP interactions through the vertex Γ.

The two particle interactions present in $GW\Gamma$ enable mutual couplings between holes and neutral excitations. Hence, if the MQP regime stems from the dynamical correlation, the frequency dependence of the self-energy should capture it. Indeed, the $GW\Gamma$ yields *multiple peaks* in $A(\omega)$, recovering the same kind of rich satellite structure present in the ASCI spectra. In general, the maxima in $A(\omega)$ are close to the excitations predicted from ASCI. From the current results it appears that there is no common tendency to shift the spectrum (toward neither higher nor lower frequency). To understand the origin of the multi-peak structure, we illustrate $GW\Gamma$ self-energy in Figure 9.1 for CH_4, NH_3 and H_2O. By inspecting the results closely, we see that the distant satellites appear either: (i) due

to the small denominator in Eq. (9.1),[66] or (ii) because Eq. (9.2) is satisfied at multiple frequencies.

Regardless of the system, the vertex correction is responsible for new features in Σ, especially in the inner-most valence energy regions. For NH_3, the double peak in the ~ -30 eV region is accompanied by small satellites at lower energies stemming from the rapid variation of Σ. The oscillatory behavior increases with the energy of the excited holes. This is clearly seen for the bottom valence region in H_2O and N_2: their inner valence states are at lower energies than NH_3 and the self-energy indeed exhibits stronger oscillations leading to a plethora of poles (more than ten) with energies almost 30 eV below the main QP peak (see Figure 9.1 and the supplementary material).[67] Further, we observe that the vertex corrections introduce "pseudo-poles" in the self-energy of the highest energy hole states that are resonant with the QP peaks of the lower energy holes; c.f. the "pseudo-pole" at -11 eV in the highest energy hole state (IV) of NH_3, resonant with the HOMO (I) QPE. This seems to underline the inter-orbital couplings arising from the vertex correction, which may be further related to a mixed orbital character that appears in the ASCI treatment, see the supplementary material. As of now, it is not possible to verify the nature of the $GW\Gamma$ poles as true poles or pseudo-poles, since as mentioned above the ASCI Green's functions are artificially broadened. A reliable classification of satellites in this regard would provide valuable information on the strength of the multi-quasiparticle interactions generating them.

In this communication, we theoretically investigated the electronic correlation which affects valence ionization energies and is directly linked to photoemission experiments. We provided virtually-exact ab-initio valence spectra for small molecular systems and explored whether and how many-body perturbation theory captures the various excitations. Namely, we compared the spectral functions computed with one-shot GW and single-iteration $GW\Gamma$ to adaptive-sampling CI. For the first time, we provide such a comparison for the

entire range of valence excitations, i.e., the outer and inner valence holes and shake-up satellites.

We show that the neglect of explicit two-particle interactions in GW leads to substantial errors. In contrast, $GW\Gamma$ results are close to the fully correlated calculations and exhibit a rich structure of multi-quasiparticle excitations stemming from the coupling between holes and optically excited states. While GW yields spurious solutions, the presence of vertex terms removes the artifacts and correctly reproduces the peak structure in $A(\omega)$.

The high-energy regime is typically associated with the breakdown of the quasiparticle picture. However, our results clearly show that the shake-up satellite features arise due to dynamical correlations. In other words, they can be described perturbatively using single-particle states of only one Slater determinant. Our findings should encourage the further development of perturbative methods that explicitly account for mutual multi-quasiparticle excitations via vertex terms. Beyond small molecular systems, this will have a decisive effect on the path towards a first-principles understanding of excited states, photoactivated chemical reactions, and quantum materials.

SUPPLEMENTARY MATERIAL

See supplementary material for a detailed description of the ASCI, G_0W_0 and $G_0W_0\Gamma$ implementation, completed with a convergence discussion. We further provide tables with the QPE's for all main peaks of the valence orbitals, and details of the extrapolation to the complete basis set limit.

ACKNOWLEDGMENTS

This work was supported by the NSF CAREER award through Grant No. DMR-1945098 (V.V.). In part, this work was supported by the NSF Quantum Foundry through QAMASE-i program Award No. DMR-1906325 (V.V). This work was partially supported by a *Obra Social "La Caixa"* graduate fellowship (ID 100010434), with code LCF/BQ/AA16/11580047 (C.M.Z.). N.M.T. and S.C. are grateful for support from NASA Ames Research Center and support from the AFRL Information Directorate under Grant No. F4HBKC4162G001. The calculations were performed as part of the XSEDE computational Project No. TG-CHE180051 and TG-MCA93S030. Use was made of computational facilities purchased with funds from the National Science Foundation (CNS-1725797) and administered by the Center for Scientific Computing (CSC). The CSC is supported by the California NanoSystems Institute and the Materials Research Science and Engineering Center (MRSEC; NSF DMR 1720256) at UC Santa Barbara. We thank Mark Babin, Blake Erickson and Diptarka Hait for helpful discussions.

DATA AVAILABILITY

The data that support the findings of this study are available from the corresponding author upon reasonable request.

Bibliography

[1] S. Hüfner, J. Osterwalder, T. Riesterer, and F. Hulliger, *Photoemission and inverse photoemission spectroscopy of nio*, *Solid state communications* **52** (1984), no. 9 793–796.

[2] M. Sander, L. Chewter, K. Müller-Dethlefs, and E. Schlag, *High-resolution zero-kinetic-energy photoelectron spectroscopy of nitric oxide*, *Physical Review A* **36** (1987), no. 9 4543.

[3] L. Chewter, M. Sander, K. Müller-Dethlefs, and E. Schlag, *High resolution zero kinetic energy photoelectron spectroscopy of benzene and determination of the ionization potential*, *The Journal of chemical physics* **86** (1987), no. 9 4737–4744.

[4] G. Wu, P. Hockett, and A. Stolow, *Time-resolved photoelectron spectroscopy: from wavepackets to observables*, *Phys. Chem. Chem. Phys.* **13** (2011) 18447.

[5] P. Puschnig, S. Berkebile, A. J. Fleming, G. Koller, K. Emtsev, T. Seyller, J. D. Riley, C. Ambrosch-Draxl, F. P. Netzer, and M. G. Ramsey, *Reconstruction of molecular orbital densities from photoemission data*, *Science* **326** (2009), no. 5953 702–706.

[6] D. Lüftner, T. Ules, E. M. Reinisch, G. Koller, S. Soubatch, F. S. Tautz, M. G. Ramsey, and P. Puschnig, *Imaging the wave functions of adsorbed molecules*, *Proceedings of the National Academy of Sciences* **111** (2014), no. 2 605–610.

[7] C. Vozzi, M. Negro, F. Calegari, G. Sansone, M. Nisoli, S. De Silvestri, and S. Stagira, *Generalized molecular orbital tomography*, *Nature Physics* **7** (2011), no. 10 822–826.

[8] P. S. Bagus and E.-K. Viinikka, *Origin of satellite structure in the valence x-ray photoelectron spectrum of co: A theoretical study*, *Physical Review A* **15** (1977), no. 4 1486.

[9] A. Lisini, P. Decleva, and G. Fronzoni, *Theoretical study of the satellite structure in the valence photoelectron spectra of the second and third row hydrides*, *Journal of Molecular Structure: THEOCHEM* **228** (1991) 97–116.

[10] N. Honjou, T. Sasajima, and F. Sasaki, *Theoretical study of the satellite bands in the valence shell xps spectra of n2, co, o2 and no molecules*, *Chemical Physics* **57** (1981), no. 3 475–485.

[11] B. Peng and K. Kowalski, *Green's function coupled-cluster approach: Simulating photoelectron spectra for realistic molecular systems*, *Journal of Chemical Theory and Computation* **14** (2018), no. 8 4335–4352.

[12] H. Nishi, T. Kosugi, Y. Furukawa, and Y.-i. Matsushita, *Quasiparticle energy spectra of isolated atoms from coupled-cluster singles and doubles (ccsd): Comparison with exact ci calculations*, *The Journal of Chemical Physics* **149** (2018), no. 3 034106.

[13] J. J. Rehr, F. D. Vila, J. J. Kas, N. Hirshberg, K. Kowalski, and B. Peng, *Equation of motion coupled-cluster cumulant approach for intrinsic losses in x-ray spectra*, *The Journal of chemical physics* **152** (2020), no. 17 174113.

[14] L. S. Cederbaum, J. Schirmer, W. Domcke, and W. von Niessen, *Complete breakdown of the quasiparticle picture for inner valence electrons*, *J. Phys. B: At. Mol. Phys.* **10** (1977), no. 15 L549.

[15] L. S. Cederbaum, W. Domcke, J. Schirmer, and W. von Niessen, *Many-body effects in valence and core photoionization of molecules*, *Phys. Scr.* **21** (1980), no. 3-4 481.

[16] J. S. Zhou, L. Reining, A. Nicolaou, A. Bendounan, K. Ruotsalainen, M. Vanzini, J. Kas, J. Rehr, M. Muntwiler, V. N. Strocov, *et. al.*, *Unraveling intrinsic correlation effects with angle-resolved photoemission spectroscopy*, *Proceedings of the National Academy of Sciences* (2020).

[17] D. Golze, M. Dvorak, and P. Rinke, *The gw compendium: A practical guide to theoretical photoemission spectroscopy*, *Frontiers in chemistry* **7** (2019) 377.

[18] F. Bruneval and M. A. Marques, *Benchmarking the starting points of the gw approximation for molecules*, *Journal of chemical theory and computation* **9** (2013), no. 1 324–329.

[19] X. Blase, C. Attaccalite, and V. Olevano, *First-principles gw calculations for fullerenes, porphyrins, phtalocyanine, and other molecules of interest for organic photovoltaic applications*, *Physical Review B* **83** (2011), no. 11 115103.

[20] V. Vlček, D. Neuhauser, E. Rabani, and R. Baer, *Stochastic GW calculations for molecules*, *J. Chem. Theory Comput.* **13** (2017) 4997.

[21] M. J. van Setten, F. Caruso, S. Sharifzadeh, X. Ren, M. Scheffler, F. Liu, J. Lischner, L. Lin, J. R. Deslippe, S. G. Louie, *et. al.*, *Gw 100: Benchmarking g 0 w 0 for molecular systems*, *Journal of chemical theory and computation* **11** (2015), no. 12 5665–5687.

[22] D. Golze, J. Wilhelm, M. J. van Setten, and P. Rinke, *Core-level binding energies from GW: An efficient full-frequency approach within a localized basis*, *J. Chem. Theory Comput.* **14** (2018) 4856.

[23] D. Neuhauser, Y. Gao, C. Arntsen, C. Karshenas, E. Rabani, and R. Baer, *Breaking the theoretical scaling limit for predicting quasiparticle energies: The stochastic GW approach*, *Phys. Rev. Lett.* **113** (2014) 076402.

[24] V. Vlček, W. Li, R. Baer, E. Rabani, and D. Neuhauser, *Swift GW beyond 10,000 electrons using sparse stochastic compression*, *Phys. Rev. B* **98** (2018) 075107.

[25] V. Vlček, E. Rabani, and D. Neuhauser, *Quasiparticle spectra from molecules to bulk*, *Phys. Rev. Materials* **2** (2018) 030801(R).

[26] M. Romanova and V. Vlček, *Decomposition and embedding in the stochastic gw self-energy*, *The Journal of Chemical Physics* **153** (2020), no. 13 134103.

[27] J. Brooks, G. Weng, S. Taylor, and V. Vlcek, *Stochastic many-body perturbation theory for moiré states in twisted bilayer phosphorene*, *Journal of Physics: Condensed Matter* **32** (2020), no. 23 234001.

[28] G. Weng and V. Vlcek, *Quasiparticles and band structures in organized nanostructures of donor–acceptor copolymers*, *The Journal of Physical Chemistry Letters* **11** (2020), no. 17 7177–7183.

[29] P. Romaniello, F. Bechstedt, and L. Reining, *Beyond GW approximation: Combining correlation channels*, *Phys. Rev. B* **85** (2012) 155131.

[30] E. Maggio and G. Kresse, *GW vertex corrected calculations for molecular systems*, *J. Chem. Theory Comput.* **13** (2017) 4765.

[31] V. Vlček, *Stochastic vertex corrections: Linear scaling methods for accurate quasiparticle energies*, *J. Chem. Theory Comput.* **15** (2019) 6254.

[32] R. M. Martin, L. Reining, and D. M. Ceperley, *Interacting Electrons: Theory and Computational Approaches*. Cambridge University Press, 2016.

[33] G. Onida, L. Reining, and A. Rubio, *Electronic excitations: density-functional versus many-body green's-function approaches*, *Rev. Mod. Phys.* **74** (2002) 601.

[34] A. Marini and A. Rubio, *Electron linewidths of wide-gap insulators: Excitonic effects in LiF*, *Phys. Rev. B* **70** (2004) 081103(R).

[35] F. Bruneval, F. Sottile, V. Olevano, R. D. Sole, and L. Reining, *Many-body perturbation perturbation theory using the density-functional concept: Beyond the GW approximation*, *Phys. Rev. Lett.* **94** (2005) 186402.

[36] A. Schindlmayr and R. W. Godby, *Systematic vertex corrections through iterative solution of hedin's equations beyond the GW approximation*, *Phys. Rev. Lett.* **80** (1998) 1702.

[37] R. D. Sole, L. Reining, and R. W. Godby, *GWΓ approximation for electron self-energies in semiconductors and insulators*, *Phys. Rev. B* **49** (1994) 8024.

[38] M. Shishkin, M. Marsman, and G. Kresse, *Accurate quasiparticle spectra from self-consistent GW calculations with vertex corrections*, *Phys. Rev. Lett.* **99** (2007) 246403.

[39] M. Hellgren, N. Colonna, and S. de Gironcoli, *Beyond the random phase approximation with a local exchange vertex*, *Phys. Rev. A* **98** (2018) 045117.

[40] M. Springer, F. Aryasetiawan, and K. Karlsson, *First-principles T-matrix theory with application to the 6 ev satellite in Ni*, *Phys. Rev. Lett.* **80** (1998) 2389.

[41] N. M. Tubman, J. Lee, T. Y. Takeshita, M. Head-Gordon, and K. B. Whaley, *A deterministic alternative to the full configuration interaction quantum monte carlo method*, *J. Chem. Phys.* **145** (2016), no. 4 044112.

[42] N. M. Tubman, D. S. Levine, D. Hait, M. Head-Gordon, and K. B. Whaley, *An efficient deterministic perturbation theory for selected configuration interaction methods*, *arXiv preprint arXiv:1808.02049v1* (2018).

[43] C. Mejuto-Zaera, N. M. Tubman, and K. B. Whaley, *Dynamical Mean-Field Theory Simulations with the Adaptive Sampling Configuration Interaction Method*, *Phys. Rev. B* **100** (2019) 125165.

[44] N. M. Tubman, C. D. Freeman, D. S. Levine, D. Hait, M. Head-Gordon, and K. B. Whaley, *Modern approaches to exact diagonalization and selected configuration interaction with the adaptive sampling ci method*, *Journal of chemical theory and computation* **16** (2020), no. 4 2139–2159.

[45] A. L. Fetter and J. D. Walecka, *Quantum Theory of Many-Particle Systems*. Dover Publications, 2003.

[46] N. M. Tubman, C. Mejuto-Zaera, J. M. Epstein, D. Hait, D. S. Levine, W. Huggins, Z. Jiang, J. R. McClean, R. Babbush, M. Head-Gordon, and K. B. Whaley, *Postponing the orthogonality catastrophe: efficient state preparation for electronic structure simulations on quantum devices*, *ArXiv e-prints* (2018).

[47] C. Mejuto-Zaera, L. Zepeda-Núñez, M. Lindsey, N. Tubman, B. Whaley, and L. Lin, *Efficient hybridization fitting for dynamical mean-field theory via semi-definite relaxation*, *Physical Review B* **101** (2020), no. 3 035143.

[48] L. Hedin, *New method for calculating the one-particle green's function with application to the electron-gas problem*, *Phys. Rev.* **139** (1965) A796–A823.

[49] F. Aryasetiawan and O. Gunnarsson, *The GW method.*, *Rep. Prog. Phys.* **61** (1998) 237.

[50] E. L. Shirley, *Self-consistent gw and higher-order calculations of electron states in metals*, *Physical Review B* **54** (1996), no. 11 7758.

[51] H. Ness, L. Dash, M. Stankovski, and R. Godby, *G w approximations and vertex corrections on the keldysh time-loop contour: Application for model systems at equilibrium*, *Physical Review B* **84** (2011), no. 19 195114.

[52] A. Grüeneis, G. Kresse, Y. Hinuma, and F. Oba, *Ionization potentials of solids: The importance of vertex corrections*, *Phys. Rev. Lett.* **112** (2014) 096401.

[53] D. Zhang, N. Q. Su, and W. Yang, *Accurate quasiparticle spectra from the t-matrix self-energy and the particle–particle random phase approximation*, *The journal of physical chemistry letters* **8** (2017), no. 14 3223–3227.

[54] D. Golze, L. Keller, and P. Rinke, *Accurate absolute and relative core-level binding energies from GW*, *J. Phys. Chem. Lett.* **11** (2020) 1840.

[55] M. Díaz-Tinoco, H. H. Corzo, F. Pawłowski, and J. V. Ortiz, *Do dyson orbitals resemble canonical hartree–fock orbitals?*, *Mol. Phys.* **117** (2019) 2275.

[56] W. Nelson, P. Bokes, P. Rinke, and R. W. Godby, *Self-interaction in green's-function of the hydrogen atom*, *Phys. Rev. A* **75** (2007) 032505.

[57] F. Aryasetiawan, R. Sakuma, and K. Karlsson, *GW approximation with self-screening correction*, *Phys. Rev. B* **85** (2012) 035106.

[58] A. M. Lewis and T. C. Berkelbach, *Vertex corrections to the polarizability do not improve the GW approximation for the ionization potential of molecules*, *J. Chem. Theory Comput.* **15** (2019) 2925.

[59] F. Aryasetiawan, L. Hedin, and K. Karlsson, *Multiple plasmon satellits in Na and Al spectral functions from* ab initio *cumulant expansion*, *Phys. Rev. Lett.* **77** (1996) 2268.

[60] J. Lischner, D. Vigil-Fowler, and S. G. Louie, *Physical origin of satellites in photoemission of doped graphene: An* ab initio *GW plus cumulant study*, *Phys. Rev. Lett.* **110** (2013) 146801.

[61] J. Lischner, G. K. Pálsson, D. Vigil-Fowler, S. Nemsak, J. Avila, M. C. Asensio, C. S. Fadley, and S. G. Louie, *Satellite band structure in silicon caused by electron-plasmon coupling*, *Phys. Rev. B* **91** (2015) 205113.

[62] M. Guzzo, G. Lani, F. Sottile, P. Romaniello, M. Gatti, J. J. Kas, J. J. Rehr, M. G. Silly, F. Sirotti, and L. Reining, *Valence electron photoemission spectrum of semiconductors:* Ab Initio *description of multiple satellites*, *Phys. Rev. Lett.* **107** (2011) 166401.

[63] D. C. Langreth, *Singularities in the x-ray spectra of metals*, *Phys. Rev. B* **1** (1970) 471.

[64] F. D. Vila, J. J. Rehr, J. J. Kas, K. Kowalski, and B. Peng, *Real-time coupled-cluster approach for the cumulant green's function*, *Journal of Chemical Theory and Computation* **16** (2020), no. 11 6983–6992.

[65] M. Tzavala, J. J. Kas, L. Reining, and J. J. Rehr, *Nonlinear response in the cumulant expansion for core-level photoemission*, *Physical Review Research* **2** (2020), no. 3 033147.

[66] The distant peak stem from a combination of the small denominator in Eq. (9.1) in combination with the small imaginary part of Σ, which is not shown in Figure 9.1. Further note that the finite real-time propagation leads to numerical broadening; as a result, some of the features in the self-energy may not appear in the graphical solution as true poles, but only "pseudopoles.".

[67] Note that the effect of the vertex is possibly overestimated due to the absence of self-consistency. The self-consistent solution contains screened Coulomb interactions in Γ [36, 33]. This renormalization will weaken the MQP couplings, reducing the oscillatory behavior shown in H_2O and N_2, retaining the envelope of their $A(\omega)$ and resulting in a smooth behavior, like for the other molecules.

Chapter 10

Embedding vertex corrections in *GW* self-energy: Theory, implementation, and outlook

Guorong Weng, Rushil Mallarapu,[a] Vojtěch Vlček

ABSTRACT

The vertex function (Γ) within the Green's function formalism encapsulates information about all higher-order electron−electron interaction beyond those mediated by density fluctuations. Herein, we present an efficient approach that embeds vertex corrections in the one-shot *GW* correlation self-energy for isolated and periodic systems. The vertex-corrected self-energy is constructed through the proposed separation−propagation−recombination procedure: the electronic Hilbert space is separated into an active space and its orthogonal complement denoted as the "rest;" the active component is propagated by a space-specific effective Hamiltonian different from the rest. The vertex corrections are introduced by

[a]Current address: Harvard University, Cambridge, MA, 02138, USA

a rescaled time-dependent nonlocal exchange interaction. The direct Γ correction to the self-energy is further updated by adjusting the rescaling factor in a self-consistent post-processing cycle. Our embedding method is tested mainly on donor−acceptor charge-transfer systems. The embedded vertex effects consistently and significantly correct the quasiparticle energies of the gap-edge states. The fundamental gap is generally improved by 1−3 eV upon the one-shot GW approximation. Furthermore, we provide an outlook for applications of (embedded) vertex corrections in calculations of extended solids.

10.1 INTRODUCTION

Predicting optoelectronic properties of functional materials hinges upon the availability of accurate and efficient first-principles methods.[1, 2, 3, 4, 5, 6, 7, 8, 9] Particularly, excitation energies obtained from electron structure calculations are directly related to the charge-transfer processes and optical transitions in practical materials. This requires the ability to capture excited-state properties, especially the nonlocal and dynamical electron−electron interactions. Many-body perturbation theory (MBPT) within the Green's function formalism[10, 11] provide a powerful tool for solving electron correlation problems. The GW approximation[12, 13, 14, 15, 16] assumes that the many-body interactions (nonlocal and dynamical electron−electron exchange and correlation) are represented by the exchange−correlation self-energy: $\Sigma_{\mathrm{XC}} = \mathrm{i}GW$, which is a convolution of the single-particle excitation propagator, i.e., Green's function (G), and the screened Coulomb interaction (W). In practice, the correlation stems from nonlocal and time-dependent charge density−density interactions. The GW method provides direct access to quasiparticle (QP) energies and has been widely applied to molecular and condensed systems.[17, 18, 19, 20, 21, 22, 23, 24, 25, 26, 27, 28, 29, 30, 31, 32, 33, 34, 35, 36, 37] The emerging stochastic GW approach[38, 39, 40] further enables its application to systems

with up to thousands of electrons.[41, 42, 43, 44, 45, 46] In these approaches, the QP energy is obtained by applying the Σ_{XC} as a perturbative correction to the mean-field eigenvalue, typically computed using Kohn−Sham density functional theory (KS-DFT).[47, 48]

Although significant improvement upon the mean-field results has been achieved, the GW approximation suffers from large errors in predicting QP energies of unoccupied states[32] and fails to capture the satellite peaks in the photoemission spectra.[49, 50] These failures can be attributed (at least in part) to the self-polarization error.[51, 52] They are remedied by the inclusion of the vertex correction, which is completely neglected by the GW approximation. Only recently, vertex-corrected methods have started to emerge in practical calculations.[53, 54, 55, 56, 57, 58, 59, 60, 61, 62, 63, 64, 65, 66, 67, 68, 69, 70, 71, 72, 73, 74] The vertex corrections are applied to two places of Σ_{XC}: one enters the irreducible polarizability in the W term and the other is a term explicitly included in the expression of Σ_{XC}. Within the random phase approximation (RPA), the W term is computed using the independent particle picture, where $P = -\mathrm{i}GG$ (P denotes the polarizability). P computed by RPA neglects electron−hole ladder diagrams and higher-order interactions for the W term. The vertex correction, Γ, to the polarizability amounts to $P = -\mathrm{i}GG\Gamma$, which is in principle an exact formulation for P. This leads to the so-called GW^{tc} approximation.[53, 75, 76] The vertex function Γ entering Σ_{XC} leads to $\Sigma_{\mathrm{XC}} = \mathrm{i}GW^{tc}\Gamma$. Due to the intractability of the full vertex function, low-order[77, 53, 78, 57, 60, 64, 63, 69, 71] and local vertex[76, 54, 55, 79, 80, 62, 65, 67, 81] approximations are often employed. The vertex correction to the W term is shown to minimally improve the GW results for molecular ionization potentials (IPs).[69] In contrast, electron affinity (EA) predictions are enhanced in several cases.[64, 65, 68] Fundamentally, the inclusion of vertex in the self-energy (i.e., the $GW^{tc}\Gamma$ approach) successfully captures multi-quasiparticle interactions and satellite peaks in molecular photoemission spectra of all valence electrons,[72, 82] agreeing excellently with the adaptive sampling (nearly full)

configuration interaction approach.[83, 84, 85, 86]

Despite the success of $GW^{tc}\Gamma$ in molecules, extending it to condensed systems, e.g., solids or low-dimensional materials, is still challenging. The polarizability evaluated with electron−hole ladders can be paralleled with employing a Hamiltonian with a nonlocal exchange interaction in the time-dependent density functional theory (TDDFT) calculation. The spatial nonlocality of the electron−electron interactions is (to the lowest order) analogous to the Hartree−Fock (HF) approximation or the generalized Kohn−Sham (GKS) DFT. Furthermore, this nonlocal exchange should be screened corresponding to the nonlocal correlation, which is especially critical for semiconducting systems. A practical approach is to use a statically screened exchange interaction in parallel with the optimally tuned GKS functionals.[87, 88, 89, 90, 91, 92, 93, 94, 95, 96] This approach has been successfully used as the GW starting points for molecules,[29, 33, 32, 64, 97, 35, 98] and the optimized GKS Hamiltonian often yields excellent optical spectra.[99, 91, 92, 95] However, the optimal tuning of the range−separation parameter is non-trivial for extended (periodic) systems.[100, 101, 102, 103] In addition, the optimally tuning process based on the Koopman's[104] or Janak's[105] theorem involves only frontier states. The resulting parametrization is not necessarily "optimal" for other electronic states (e.g., in the bottom valence region). For the nonlocal vertex in extended systems, several attempts have been explored to compute the exchange−correlation kernel, including the use of ad hoc[56, 59] (e.g., Heyd−Scuseria−Ernzerhof hybrid functional) or dielectric-dependent[70] hybrid functionals and the approximate bootstrap iteration.[61]

To tackle the computational cost of including the nonlocal vertex in large extended systems, we propose an efficient embedding method that includes vertex corrections in the G_0W_0 correlation self-energy (here computed using stochastic sampling). We use an active space projector[44, 45] to separate electronic states into two components: the active part and its orthogonal complement denoted as the "rest." The active space projector is

composed of either canonical KS states or localized orbitals that are energetically favored in optical transitions. In this scheme, the electron−hole interactions are selectively "turned on" for the active space. A *space-specific* effective Hamiltonian is constructed with a stochastically sampled and *rescaled* time-dependent nonlocal exchange interaction. The active space component is specifically propagated using this effective Hamiltonian, while the evolution of the rest is treated by a mean-field one. The recombination of these two components produces the embedded states that enter the correlation self-energy. Furthermore, we propose a simple self-consistent post-processing cycle for rescaling the vertex contribution.

The proposed embedding method is mainly tested on π-conjugated donor−acceptor systems with significant electron−hole interactions. The investigated systems include isolated small molecules and donor−acceptor dimers, one-dimensional (1D) charge-transfer copolymer, and two-dimensional (2D) donor−acceptor double layers. Different sizes and representations of the active space are also explored. The embedded vertex corrections show consistent and non-trivial effects on the computed QP energies. We find that the vertex correction to the polarizability is critical to avoid overbound unoccupied states. The fundamental gaps are 1−3 eV greater than the G_0W_0 ones, hence improving upon the G_0W_0 results. More importantly and in contrast with previous findings, the vertex corrections significantly affect the QP energies of the occupied gap-edge states.

The following content contains three major parts: Section 10.2 focuses on the theory and methodology; Section 10.3 presents the computed charge excitation energies and the fundamental gaps of various systems; Section 10.4 summarizes the findings and comments on possible further improvement.

10.2 THEORY AND METHODOLOGY

In this section, the concept of QP self-energy is revisited and various forms of vertex-corrected self-energy are introduced. Second, we demonstrate the definition and construction of an active space. Finally, the vertex-embedding scheme is presented.

10.2.1 Quasiparticle self-energy

The QP Hamiltonian is written as

$$\hat{H}^{QP} = \hat{T} + \hat{V}_{\text{ext}} + \hat{\Sigma}_{\text{H}} + \hat{\Sigma}_{\text{XC}}(\omega), \tag{10.1}$$

where $\hat{T}$, $\hat{V}_{\text{ext}}$, and $\hat{\Sigma}_{\text{H}}$ represent the kinetic energy operator, external field potential, and classical Coulomb repulsion, respectively. All nonlocal and dynamical particle interactions are included in the frequency-dependent exchange−correlation self-energy $\hat{\Sigma}_{\text{XC}}$. Next, we separate the exchange and correlation interactions into two individual terms and focus on the correlation part. The perturbatively-corrected QP energy reads

$$\varepsilon_j^{QP} = \langle \phi_j | \varepsilon_j^0 - \hat{v}_{\text{xc}} + \hat{\Sigma}_{\text{X}} + \hat{\Sigma}_{\text{C}}(\omega = \varepsilon_j^{QP}) | \phi_j \rangle \, . \tag{10.2}$$

Here, ϕ_j is an eigenstate of the KS-DFT Hamiltonian with the corresponding eigenvalue ε_j^0 and exchange−correlation potential $\hat{v}_{\text{xc}}$. As a starting point, our DFT calculations employ the PBE functional.[106] Other starting points are also applicable but out of the scope of this work since we focus on demonstrating the embedding scheme. The nonlocal exchange $\hat{\Sigma}_{\text{X}}$ is equivalent to the Fock operator in the Hartree−Fock approximation.[11] The frequency-dependent correlation self-energy $\hat{\Sigma}_{\text{C}}(\omega)$ is obtained from the Fourier-transformed time-dependent $\hat{\Sigma}_{\text{C}}(t)$, which is approximated and computed by the stochastic methods.[38, 40, 68] Only diagonal terms of the self-energy are considered.

In the $GW^{tc}\Gamma$ formalism, the temporally and spatially nonlocal correlation self-energy (Σ_{C}) is derived from the derivative of the total self-energy (Σ_{T}) with respect to the Green's function (G).[68, 72, 82] The total self-energy reads

$$\Sigma_{\mathrm{T}} = \Sigma_{\mathrm{H}} + \Sigma_{\mathrm{X}} + \Sigma_{\mathrm{C}}. \tag{10.3}$$

Since the right-hand side (RHS) of Eq. (10.3) also contains the Σ_{C} term, the correlation self-energy thus needs to be solved self-consistently. Here, we expand the simplified approach presented in previous work[66, 68], where the variation of Σ_{C} is neglected. We derive the vertex (Γ) from a statically rescaled nonlocal exchange interaction. Hence, the exchange and correlation terms in Eq. (10.3) are combined as

$$\Sigma_{\mathrm{X}} + \Sigma_{\mathrm{C}} \approx \beta\Sigma_{\mathrm{X}}, \tag{10.4}$$

where β is simply a prefactor multiplied by the nonlocal exchange interaction. The *rescaling* factor β, derived in Sec. 10.2.4, is similar to the state-dependent screened exchange constant used in previous work.[97]

Based on the approximation above [Eq. (10.4)], the vertex is introduced in a greatly simplified way that preserves the spatial nonlocality of Γ (full derivation is provided in the supplementary material). In the time-dependent formalism, it is convenient to decompose the correlation self-energy into two terms:

$$\Sigma_{\mathrm{C}}^{G_0W_0^{tc}\Gamma_\beta}(t) = \Sigma_{\mathrm{C}}^{G_0W_0^{tc}}[\delta n(t), t] + \Sigma_{\mathrm{C}}^{\Gamma_\beta}[\delta\rho(t), t]. \tag{10.5}$$

The first term on the RHS of Eq. (10.5) comes from the derivative of the Hartree term (Σ_{H}) with respect to the Green's function (G), and it is a functional of the induced density δn. This is nothing else but the $G_0W_0^{tc}$ self-energy representing the correlation

stemming from density−density interactions. Here, the vertex correction is introduced to W by applying a Hamiltonian with a time-dependent nonlocal exchange interaction in the propagation process (see Sec. 10.2.3). The second contribution, $\Sigma_{\mathrm{C}}^{\Gamma_\beta}$, comes from the derivative of the rescaled nonlocal exchange ($\beta\Sigma_{\mathrm{X}}$) with respect to the Green's function (G). In practice, the correlation due to density matrix fluctuations is thus a functional of the induced density matrix ($\delta\rho$). Since β is simply a prefactor, we extract it from the derivative and have

$$\Sigma_{\mathrm{C}}^{\Gamma_\beta}[\delta\rho(t), t] = \beta\Sigma_{\mathrm{C}}^{\Gamma_{\mathrm{X}}}[\delta\rho(t), t], \tag{10.6}$$

where $\Sigma_{\mathrm{C}}^{\Gamma_{\mathrm{X}}}$ is derived from a bare Σ_{X} in this work. In the remainder of this article, we use Γ_W to denote the vertex correction to the W term (i.e., the polarizability) and the direct vertex correction to the self-energy is denoted as either Γ_{X} or Γ_β depending on the precise definition detailed below.

10.2.2 Electronic active space

In the real-time G_0W_0 formalism, the induced density is computed by the time-dependent Hartree (TDH) approximation, which corresponds to RPA. The TDH Hamiltonian does not couple the electron−hole pairs. Upon excitation, electron and hole states at low excitation energies are preferably populated and are expected to contribute predominantly to the polarizability. The gap-edge states, i.e., the highest occupied molecular orbital (HOMO) and the lowest occupied molecular orbital (LUMO), are mostly responsible for electron−hole pair formation captured by the ladders in vertex-corrected polarizability (detailed in Sec. 10.2.3). For π-conjugated molecules, the π−π^* transition is considered the governing element in the optical absorption spectrum. π and π^* bonds thus represent another type of highly-populated electron−hole states.

Here, we first identify the low-energy states (e.g., HOMO/LUMO or π/π^*). An

electronic active space is then formed by these states based on their population (occupation) during excitation, and we denote its orthogonal complement as the "rest." The active space is then treated differently from the rest (see Sec. 10.2.3).

Mathematically, the active space is defined by

$$\hat{P}^A = \sum_i^{N_{\text{act}}} |\psi_i\rangle \langle\psi_i| \,, \tag{10.7}$$

where $\hat{P}^A$ is a projector onto the active space, and N_{act} represents the number of projector states ψ.

This work explores two different representations of ψ: canonical KS eigenstates and localized orbitals. The first representation straightforwardly chooses canonical eigenstates, e.g., the HOMO and the LUMO, based on their mean-field eigenvalues. In contrast, the localized basis allows the selection of a specific type of chemical bonds, especially the π and π^* bonds mentioned above. We employ Pipek−Mezey (PM) localized orbitals[107] because they easily separate the σ and π characters.[107, 108] Analogously, for periodic systems, the top valence band (TVB) and the bottom conduction band (BCB) provide the gap-edge states, which can be represented by either Bloch states (canonical eigenstates) or combinations of Wannier functions. The regionally localized orbitals for molecular systems are obtained using the sequential PM localization on the chosen molecules.[109]. In Sec. 10.2.3, we demonstrate the embedding of vertex corrections using the defined active space.

10.2.3 Embedded vertex corrections

This section demonstrates the embedded vertex corrections in the correlation self-energy [Eq. (10.5)]. In the GW approximation, the polarizability computed by RPA includes only the electron−hole "bubble" diagrams but neglects higher-order interac-

tions. In the following, we go beyond the GW approximation and selectively turn on electron−hole interactions (vertex in the polarizability) for the active space by applying a space-specific effective Hamiltonian, which governs the real-time dynamics mimicking the time-dependent solution to the Bethe−Salpeter equation[110]

$$\hat{H}^{\text{eff}}(t) = \hat{T} + \hat{V}_{\text{ext}} + \hat{\Sigma}_{\text{H}}[n(t)] + \alpha\hat{\Sigma}_{\text{X}}[\rho(t)]. \tag{10.8}$$

The rest of the electronic Hilbert space is instead treated by

$$\hat{H}^{0}(t) = \hat{T} + \hat{V}_{\text{ext}} + \hat{v}_{\text{xc}} + \hat{\Sigma}_{\text{H}}[n(t)]. \tag{10.9}$$

Compared to $\hat{H}^0$, $\hat{H}^{\text{eff}}$ contains a rescaled time-dependent nonlocal exchange interaction, constituting the lowest-order vertex correction to the polarizability. The coefficient α is another rescaling factor analogous to the screening factor. Similar to β defined above, it is derived from the expectation values of the underlying self-energy (see Sec. 10.2.4). The α factor represents the averaged rescaling behavior for the entire active space, while β is used for a specific state.

In practice, the Hamiltonian separation is employed in the real-time evolution of electronic states yielding the time-dependent induced density $\delta n(t)$ and density matrix $\delta\rho(t)$ in Eq. (10.5). To make this approach efficient even for large systems, we employ the stochastic approach that samples these two quantities using a set of random vectors instead of the deterministic single-particle states. Technical details of the stochastic formalism are provided in the supplementary material. Here, we only emphasize the quantities that are directly related to the embedding.

The time-dependent density $n(t)$ and density matrix $\rho(t)$ are sampled by a set of

random states η [defined in Eqs. (F.28) and (F.34)]

$$n(\mathbf{r},t) = \{\eta^*(\mathbf{r},t)\eta(\mathbf{r},t)\}, \tag{10.10}$$

and

$$\rho(\mathbf{r}_1,\mathbf{r}_2,t) = \{\eta^*(\mathbf{r}_2,t)\eta(\mathbf{r}_1,t)\}. \tag{10.11}$$

Here, the brackets $\{\dots\}$ denote an average over the whole set of random functions. The time-evolution of η gives $n(t)$ and $\rho(t)$, which produce $\delta n(t)$ and $\delta\rho(t)$ for Eq. (10.5). The core procedure of vertex-embedding is to prepare η^{emb} by the following *separation−propagation−recombination* (SPR) treatment (Fig. 10.1).

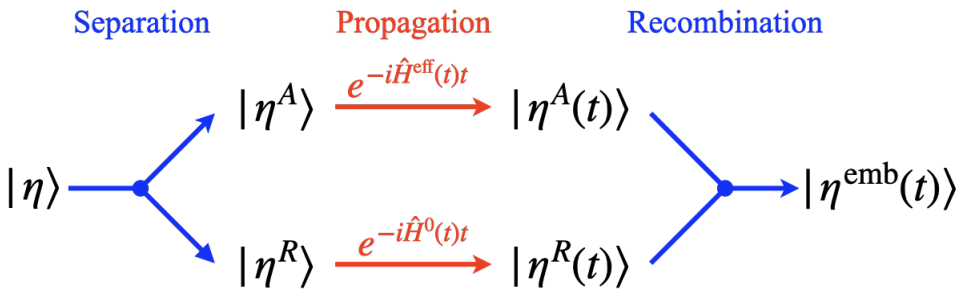

Figure 10.1: Schematic representation of the separation−propagation−recombination technique for the embedded time-evolved random vectors. The separation and recombination steps are colored in blue and the propagation step is colored in red.

At $t = 0$, the random vector η is projected onto the occupied subspace. The electron removal/addition rotates η to the full Hilbert space, i.e., it also represents electrons excited into the unoccupied subspace. The component in the active space, η^A, of the perturbed η is obtained by projection following Eq. (10.7),

$$|\eta^A\rangle = \hat{P}^A\,|\eta\rangle = \sum_i^{N_{\text{act}}} \langle\psi_i|\eta\rangle\,|\psi_i\rangle\,. \tag{10.12}$$

The rest component η^R is then given by

$$|\eta^R\rangle = |\eta\rangle - |\eta^A\rangle\,. \tag{10.13}$$

The two separated components are propagated using two different operators

$$|\eta^A(t)\rangle = \hat{U}^A(t)\,|\eta^A\rangle\,, \tag{10.14}$$

and

$$|\eta^R(t)\rangle = \hat{U}^R(t)\,|\eta^R\rangle\,. \tag{10.15}$$

The two time-evolution operators above correspond to the two forms of Hamiltonian in Eqs. (10.8) and (10.9), which (adiabatically) depend on the density (and density matrix) at time t,

$$\hat{U}^A(t) = e^{-\mathrm{i}\hat{H}^{\mathrm{eff}}(t)t}, \tag{10.16}$$

and

$$\hat{U}^R(t) = e^{-\mathrm{i}\hat{H}^{0}(t)t}. \tag{10.17}$$

Finally, the embedded time-evolved random vector $\eta^{\mathrm{emb}}(t)$ is given by recombining the two components

$$|\eta^{\mathrm{emb}}(t)\rangle = |\eta^A(t)\rangle + |\eta^R(t)\rangle\,. \tag{10.18}$$

The SPR scheme above is demonstrated in a two-component case, and the extension to three or more components is trivial. The three-component case, in which the active space is further divided into the occupied and unoccupied parts, is applied in this work as shown below. In practice, the propagation in time is discretized. In each time step, the separation treatment is repeated to ensure that $\eta^A(t)$ and $\eta^R(t)$ are orthogonal before

they are propagated. Refer to Eqs. (F.55)-(F.57) in the supplementary material for more details.

The embedded vector $\eta^{\mathrm{emb}}(t)$ generates the embedded density $n^{\mathrm{emb}}(t)$ via Eq. (10.10) and density matrix $\rho^{\mathrm{emb}}(t)$ via Eq. (10.11). Finally, $n^{\mathrm{emb}}(t)$ and $\rho^{\mathrm{emb}}(t)$ lead to the embedded self-energy [Eq. (10.5)]. The time-evolution behavior of η is modified, but the total number of electronic states sampled is conserved. Therefore, there is no double-counting error in this embedding scheme.

The SPR procedure also applies to the random vectors that sample the Green's function G_0. In this case, the time evolution is simplified as G_0 is the non-interacting propagator depending on a static form of the Hamiltonian. More details are provided in the "Embedded Vertex Correction" section of the supplementary material.

10.2.4 Rescaling factors

In the following, we comment on the working definition of the two rescaling factors: β in Eq. (10.4) and α in Eq. (10.8). In practice, they are derived simply as a fraction of the nonlocal exchange interaction that mimics the expectation value of the full exchange−correlation self-energy. In particular, we first derive them from the G_0W_0 approximation though; as we show below, they can be generalized to a simple self-consistent post-processing approach.

For a QP state ϕ_j, the initial rescaling factor β_j^0 is given by

$$\beta_j^0 = \frac{\Sigma_{\mathrm{X,j}} + \Sigma_{\mathrm{C}}^0(\omega = \varepsilon_j^{QP})}{\Sigma_{\mathrm{X,j}}}, \tag{10.19}$$

where $\Sigma_{\mathrm{X,j}} = \langle\phi_j|\hat{\Sigma}_{\mathrm{X}}|\phi_j\rangle$, and the correlation self-energy Σ_{C}^0 is an expectation value computed at the G_0W_0 level. Note that due to the definition of Σ_{X} in Eq. (10.2), the value of $\Sigma_{\mathrm{X,j}}$ is always negative throughout this work. The computed Σ_{C}, as shown in Sec. 10.3,

can have either the same or an opposite sign with/against $\Sigma_{\mathrm{X,j}}$. In the same-sign case, the derived β_j from Eq. (10.19) is greater than 1, and we define this effect as correlation stabilization. The opposite-sign case gives $\beta_j < 1$, which is instead defined as correlation destabilization.

For the rescaling factor α [Eq. (10.8)] that represents the entire active space, we first compute β_i^0 of each state ψ_i in Eq. (10.7) via Eq. (10.19). α for the entire active space takes the average value of β_i^0s,

$$\alpha = \frac{1}{N_{\mathrm{act}}} \sum_{i=1}^{N_{\mathrm{act}}} \beta_i^0. \tag{10.20}$$

As shown in Sec. 10.3, the states ψ_i within one active space have very similar character and consistent rescaling behavior. It is thus sufficient to use a single averaged α to describe the entire active space. From the correlation self-energy perspective, the parameters α and β play two different roles: α representing an active space enters the effective Hamiltonian in Eq. (10.8) that governs the time evolution and determines the electron−hole coupling strength; β_j of a state ϕ_j in Eq. (10.2) rescales Σ_{X} and thus the $\Sigma_{\mathrm{C}}^{\Gamma\mathrm{X}}$ term in Eq. (10.6).

With α and β_j^0 computed by G_0W_0, we solve the vertex-corrected self-energy in Eq. (10.5). β_j acts as a factor only in front of the $\Sigma_{\mathrm{C}}^{\Gamma\mathrm{X}}$ [see Eq. (10.6)]. We thus compute $\Sigma_{\mathrm{C}}^{\Gamma\mathrm{X}}(t)$ only once and use it to update β_j through the self-consistent cycle in Fig. 10.2,

$$\beta_j^n = \frac{\Sigma_{\mathrm{X,j}} + \Sigma_{\mathrm{C}}^{n-1}[\beta_j^{n-1}](\omega = \varepsilon_j^{QP})}{\Sigma_{\mathrm{X,j}}}, \tag{10.21}$$

where $\Sigma_{\mathrm{C}}^{n-1}$ is the vertex-corrected correlation self-energy using the prefactor β_j^{n-1} in Eq. (10.5). Note that this self-consistency comes at a negligible computational cost as β_j only rescales one (additive) component of the self-energy. In principle, the factor α can also be updated self-consistently, but this instead requires re-evaluating the time evolution. We avoid this step for simplicity here.

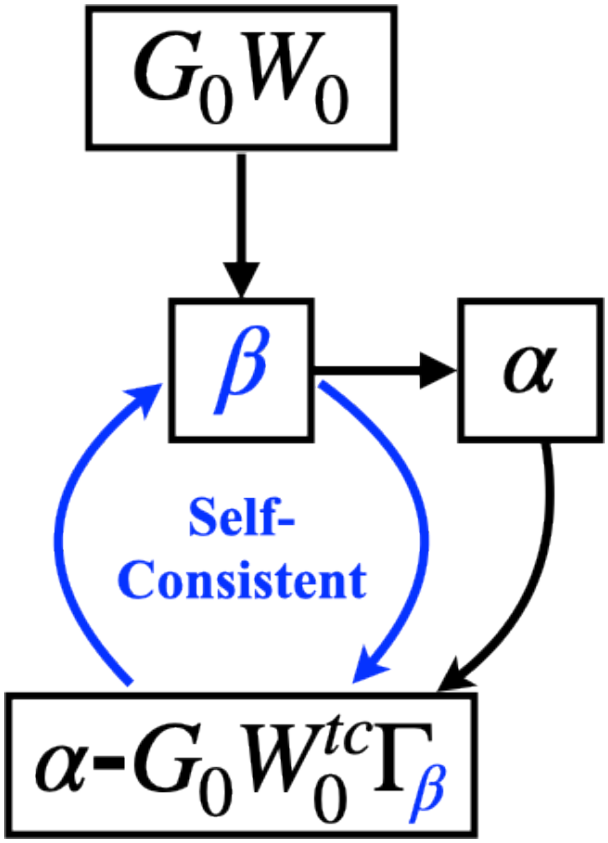

Figure 10.2: Schematic representation of the self-consistent α-$G_0W_0^{tc}\Gamma_\beta$ correlation self-energy. The self-consistent cycle is colored in blue.

In the remainder of this work, α-$G_0W_0^{tc}$ denotes the correlation self-energy with only Γ_W correction; α-$G_0W_0^{tc}\Gamma_{\beta^0}$ and α-$G_0W_0^{tc}\Gamma_{\beta^{sc}}$ represent the correlation self-energy with both Γ_W and Γ_β corrections, and the latter includes self-consistency in β_j.

10.3 RESULTS AND DISCUSSION

In the Secs. 10.3.1−10.3.3, we demonstrate and test the performance of the proposed methodology on selected practically important materials. Specifically, we focus on calculating QP energies of the gap-edge states for molecules and band-edge states for periodic systems. We choose to study isolated and low-dimensional (1D and 2D) periodic

systems so that for each case we can determine the absolute QP energy with respect to vacuum (in contrast, for 3D periodic systems only QP energy differences are meaningful). Investigated systems include tetracyanoethylene (TCNE) and tetracyanoquinodimethane (TCNQ) acceptors, 1,4-benzenediamine-TCNE (B−T) dimer, tetracene-C_{60} (Tc−C) dimer, poly-fluorene-benzothiadiazole (p-FBT) polymer, and tetracene-C_{60} (Tc−C) double layers. The structures of the isolated molecules, molecular dimers, and polymers are prepared or taken from Refs. 111, 43, 112. The double-layer system is constructed by using the dimer geometry with the periodic boundary conditions of the C_{60} crystal.

For isolated systems, the active space is constructed by either canonical frontier orbitals, i.e., the HOMO and LUMO, or π/π^* bonds. For periodic systems, the active space is represented by either Bloch states or Wannier functions. The stochastic G_0W_0 and α-$G_0W_0^{tc}$ results are reported with <0.05 eV statistical errors. The statistical erros for the α-$G_0W_0^{tc}\Gamma_\beta$ results are slightly larger (<0.07 eV) due to additional fluctuations in sampling the induced density matrix. All the numeric results in this work are supported by the graphical solutions on the self-energy curves (see Figs. F.7-F.12 in the supplementary material).

10.3.1 Single acceptor molecules

TCNE and TCNQ are ideal molecules to benchmark EA predictions due to their strongly bound LUMO.[60, 64, 113] To test the performance of our method on these two acceptors, we use the π+π^* active space. For TCNE, nine π bonds and nine π^* bonds are identified from the PM localized orbitals (Fig. F.1). The computed rescaling factors α and the representative orbitals for the active occupied and unoccupied spaces are listed in Fig. 10.3. The ratio $\Sigma_{\mathrm{XC}}/\Sigma_{\mathrm{X}}$ (α) is smaller than 1 for the π bonds but greater than 1 for the π^* bonds, i.e., the value of Σ_{C} is positive for occupied states but negative for

unoccupied states. This illustrates the role of the correlation self-energy component, which attenuates the nonlocal exchange and destabilizes occupied states but leads to the energetic stabilization of unoccupied states. The latter corresponds to the apparent "strengthening" of the nonlocal exchange interaction, and the α is counterintuitively greater than 1. These rescaling factors α are used in the time evolution [Eq. (10.8)] for the active space component. Note that this approach attempts to include the correlation via rescaling the exchange interaction Σ_{X} so that the QP energies are reproduced. Such an approach is undoubtedly a crude simplification, yet it enables an efficient proof of principle calculations described here; we comment on the shortcomings of this implementation in the following.

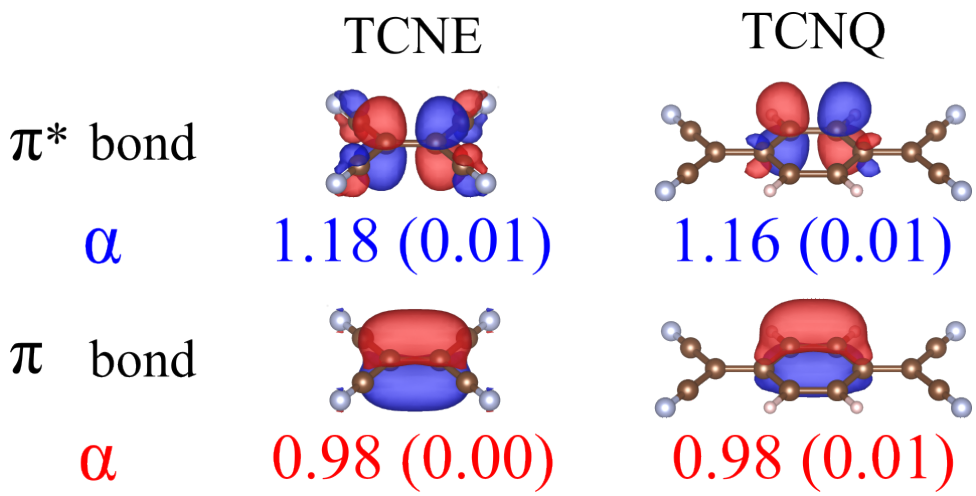

Figure 10.3: Representative π and π^* bonds of the TCNE and TCNQ molecules. The rescaling factor is averaged over 9 and 12 states for the TCNE and TCNQ, respectively, with the standard deviations provided in parentheses.

The computed HOMO/LUMO energies and fundamental gaps are summarized in Table 10.1. Our G_0W_0 QP energies agree perfectly with previously reported results,[60, 64] and the corresponding HOMO/LUMO gap increases to 7.38 eV. When the Γ_W is applied, the gap is further corrected by α-$G_0W_0^{tc}$: the HOMO energy is shifted down by $\sim$0.6 eV, and the LUMO energy is shifted up by $\sim$1 eV. These corrections to IP and EA are more

significant than the comparable G_0W_0+SOSEX[60, 64] approach (see Tables F.7 and F.8). The corrected results agree better with experiments,[114, 115] especially with the electron affinity. We note that the 2.30-eV result in Table 10.1 cited from Ref. 115 represents the *vertical* EA,[113] while the *adiabatic* EA from experiments is ∼3.16 eV.[116, 113, 117, 60] Our results are compared with the former since the QP energies correspond to vertical charge excitations. The G_0W_0 result highly overestimates the EA by ∼1.5 eV, and the inclusion of Γ_W improves it by ∼1 eV. In other words, the vertex correction to the polarizability is providing a significant improvement. This contrasts some previous observations,[69, 68] indicating that the effect of Γ_W is not universal.

Table 10.1: HOMO/LUMO energies and fundamental gaps of the single TCNE and TCNQ molecules computed by various methods. All energy values are in eV unit.

	TCNE					TCNQ				
	DFT	G_0W_0	α-$G_0W_0^{tc}$	α-$G_0W_0^{tc}\Gamma_\beta$	Exp.[1]	DFT	G_0W_0	α-$G_0W_0^{tc}$	α-$G_0W_0^{tc}\Gamma_\beta$	Exp.[a]
HOMO	−8.63	−11.15	−11.82	$-12.91^b/-13.02^c$	−11.79	−7.78	−9.63	−9.46	$-10.70^b/-10.71^c$	−9.61
LUMO	−5.85	−3.77	−2.73	-0.45^d	−2.30	−6.27	−4.96	−3.59	-1.47^d	−2.80
Gap	2.76	7.38	9.09	$10.18^e/10.29^f$	9.49	1.51	4.66	5.86	$7.11^e/7.12^f$	6.81

[a] experimental results are reported as −IP and −EA and are taken from Refs. 114, 115, 118, 119

[b] $\Sigma_C^{\Gamma_X}$ term is rescaled by β^0

[c] $\Sigma_C^{\Gamma_X}$ term is rescaled by β^{sc}

[d] $\Sigma_C^{\Gamma_X}$ term is rescaled by 1

[e] gap is calculated by the HOMO with β^0 and the LUMO taken from α-$G_0W_0^{tc}$

[f] gap is calculated by the HOMO with β^{sc} and the LUMO taken from α-$G_0W_0^{tc}$

When Γ_β is added, the HOMO level is stabilized by ∼1 eV, and the β-self-consistency contributes another ∼0.1 eV. Furthermore, the inclusion of Γ_β shifts the LUMO level up to a higher energy. However, the quantitative effect appears too strong when using the rescaled nonlocal exchange approach: when Γ_β is applied with $\beta = 1$, i.e., Γ_X, the LUMO

energy is strongly destabilized to -0.45 eV. The result worsens with $\beta > 1$, as suggested by the oversimplified approach based on the ratio of the self-energy expectation values. The nearly unbound value is incorrect and is against the acceptor nature of TCNE and the experiment. The derived Γ_β from a simple rescaled exchange interaction fails for the LUMO.

To further understand the Γ_β contribution, we neglect the rescaling effect by setting $\beta = 1$ and examine the real part of frequency-dependent $\Sigma_{\mathrm{C}}^{\Gamma_{\mathrm{X}}}$. By varying the components of the active space, we obtain several $\Sigma_{\mathrm{C}}^{\Gamma_{\mathrm{X}}}$ presented in Fig. 10.4, from which we discuss the *qualitative* Γ_{X} effect on the QP energy. We emphasize that this self-energy represents the vertex correction part to the self-energy only ($\Sigma_{\mathrm{C}}^{G_0W_0^{tc}\Gamma_{\mathrm{X}}} - \Sigma_{\mathrm{C}}^{G_0W_0^{tc}}$). The total self-energy curves (Fig. F.6) show $\frac{\mathrm{d}\Sigma\omega}{\mathrm{d}\omega} \leq 0$ at the QP energy, as indicated by the QP renormalization.[10, 11]. However, the individual components of the self-energy may not satisfy this inequality.

In Fig. 10.4a, the dashed line indicates the α-$G_0W_0^{tc}$ QP energy, which crosses the blue curve at a negative vertical coordinate. This means the value of $\Sigma_{\mathrm{C}}^{\Gamma_{\mathrm{X}}}$ around the QP energy is negative. Given that β is positive, the negative $\Sigma_{\mathrm{C}}^{\Gamma_{\mathrm{X}}}$ corresponds to the stabilization effect on the HOMO energy of TCNE shown in Table 10.1. When the π bonds are excluded from the active space, this stabilization effect disappears as the dashed line crosses the red curve at a positive vertical coordinate. Furthermore, we assume that the states in the full Hilbert space can be propagated by the effective Hamiltonian with $\alpha = 1$, i.e., no active space is constructed and the exchange interaction is unscreened. As indicated by the black curve in Fig. 10.4a, the stabilization effect is restored. The difference among the three $\Sigma_{\mathrm{C}}^{\Gamma_{\mathrm{X}}}$ suggests that the occupied states are required in the active space to cause the stabilization effect on the QP energy.

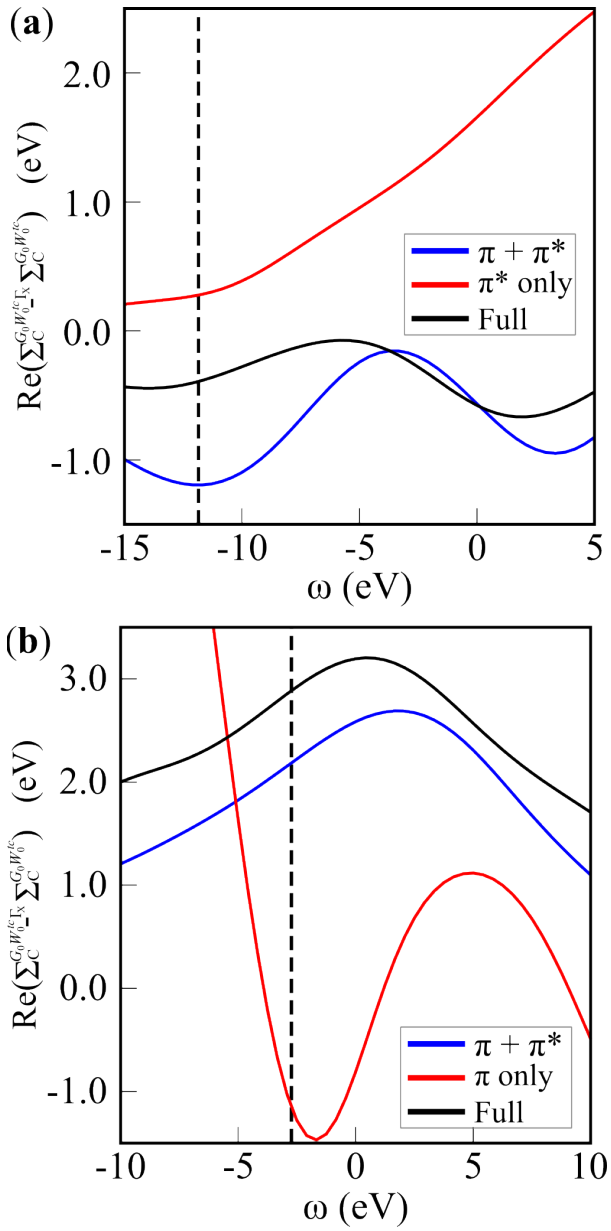

Figure 10.4: Real parts of the $\Sigma_C^{\Gamma_X}$ calculated for the (a) HOMO and the (b) LUMO using different active spaces. The black curve represents the full Hilbert space, the red curve denotes the π or π^* only space, and the blue curve is the $\pi + \pi^*$ active space. The dashed line indicates the QP energy from the α-$G_0W_0^{tc}$ results.

Analogously, the crossing between the blue curve and the dashed line in Fig. 10.4b indicates a positive value of $\Sigma_C^{\Gamma_X}$, corresponding to the destabilization effect of Γ_X on the LUMO energy. However, when the π^* bonds are excluded (the red curve) from the

active space, this destabilization effect vanishes. The expansion to the full Hilbert space (equivalent to having no active space) recovers this destabilization effect (black curve in Fig. 10.4b). In contrast with the HOMO case, the unoccupied states are necessary in the active space for destabilizing the LUMO energy.

The observations above imply that the Γ_{X} effect on the HOMO energy depends mainly on the occupied (hole) states that are "turned on" in the active space. On the other hand, Γ_{X} for the LUMO stems primarily from the unoccupied (electron) states included in the active space. This delivers an important message for the failure of simple rescaled Γ_{X} correction to the LUMO QP energy. The static exchange Σ_{X} is calculated using only the occupied (hole) states, while the LUMO state (corresponding to an injected electron) interacts mainly with the states above the Fermi level. The derived Γ_{X} should be dynamically screened, and its fraction cannot be trivially estimated based on the nonlocal exchange. In fact, to reproduce the experimental value of -2.30 eV,[115] one would need to set $\beta = 0.2$, which implies a substantial "exchange reduction" compared to its bare strength. Nevertheless, electrodynamic screening is apparently not delivering that. We surmise that the culprit is in the restriction to only density and density matrix interactions: it is likely that in small-scale systems with relatively low electron density, other types of explicit QP$-$QP interactions (i.e., classes of explicit two-body scatterings that are neglected here) become more important.[82] This direction will be explored in the future.

For the TCNQ molecule, 12 π and 12 π^* bonds constitute the active space. The representative orbitals are shown in Fig. 10.3, and the entire set of basis is provided in Fig. F.1. The computed rescaling factors for the occupied and unoccupied states are consistent with the TCNE case. Compared to the G_0W_0 result, the inclusion of Γ_W (α-$G_0W_0^{tc}$) slightly shifts the HOMO energy up, while the rescaled $\Sigma_{\mathrm{C}}^{\Gamma_{\mathrm{X}}}$ pulls the energy down by $\sim$1 eV. Similar to the TCNE case, the G_0W_0 approach overestimates the EA

by more than 2 eV (Table 10.1). The Γ_W correction in α-$G_0W_0^{tc}$ improves it by $\sim$1.4 eV, and the remaining part is attributed to the Γ_X term. However, the fraction of Γ_X is still not quantitatively determined through the simple rescaling approach. The LUMO energy becomes -1.47 eV with $\beta = 1$, which underestimates the EA by >1 eV. When using $\beta = 0.2$, the value (-3.22 eV) differs from the experiment[119] (-2.80 eV), indicating the uniqueness of β in each system.

Given the challenge of determining the fraction of Γ_X for the LUMO state, we do not seek to describe its effect on the LUMO QP energy quantitatively. When referring to the fundamental gaps estimated with α-$G_0W_0^{tc}\Gamma_\beta$, we consider the HOMO value from the α-$G_0W_0^{tc}\Gamma_\beta$ results and the LUMO energy from the α-$G_0W_0^{tc}$ ones. Even though further exploration on the type of explicit QP$-$QP couplings is warranted, the fundamental gaps of the two test systems are already improved by more than 2 eV upon the G_0W_0 ones and agree well with the experiments, indicating the importance of the embedded vertex corrections.

10.3.2 Donor$-$acceptor dimers

In the next step, we explore systems containing two weakly bound donor$-$acceptor molecules, in which the active space needs to account for the charge-transfer excitation. Acene compounds and tetracyanoethylene (TCNE) derivatives have been used in computations as charge-transfer dimer models.[120, 99, 112] In practice, acenes and C_{60} are popular donor$-$acceptor materials used in electronic devices.[121, 122, 123, 124] This section reports computational results for two donor$-$acceptor combinations: 1,4-benzenediamine-TCNE (B$-$T) dimer and tetracene-C_{60} (Tc$-$C) dimer. Electron and hole states participating in the charge-transfer process are chosen for the active space. The simplest choice for the charge-transfer active space is the construction from the HOMO

and LUMO states, constituting the minimal charge-transfer active space. The orbitals and their rescaling factors are shown in Fig. 10.5a. The nonlocal exchange is only slightly attenuated for the HOMO, while significant exchange-strengthening is observed for the LUMO state. The results are sensitive to the precise amount of exchange rescaling: a 10% change in the nonlocal exchange interaction corresponds to about 1 eV change in energy due to the magnitude of Σ_{X}. Therefore, the correlation contribution is especially significant for the unoccupied states.

To define an active space based on localized orbitals, we use the regional orbital localization[109] on the donor and acceptor for the occupied and unoccupied subspaces. Fig. 10.5b presents one π bond on the donor and one π^* bond on the acceptor. In total, five π bonds and nine π^* bonds constitute the charge-transfer active space (Fig. F.2). This new construction includes all π components on the donor and π^* components on the acceptor, which can be considered an "*augmented*" active space compared to the minimal one. The π and π^* bonds (Fig. 10.5b) are visually more localized than the canonical orbitals (Fig. 10.5a), and these bonds are fundamentally equivalent in terms of their atomic-orbital components. Indeed, the factor α is averaged over the π or π^* bonds, and the standard deviations are negligible. The values are also very close to the ones in the minimal space ($<$0.05 difference).

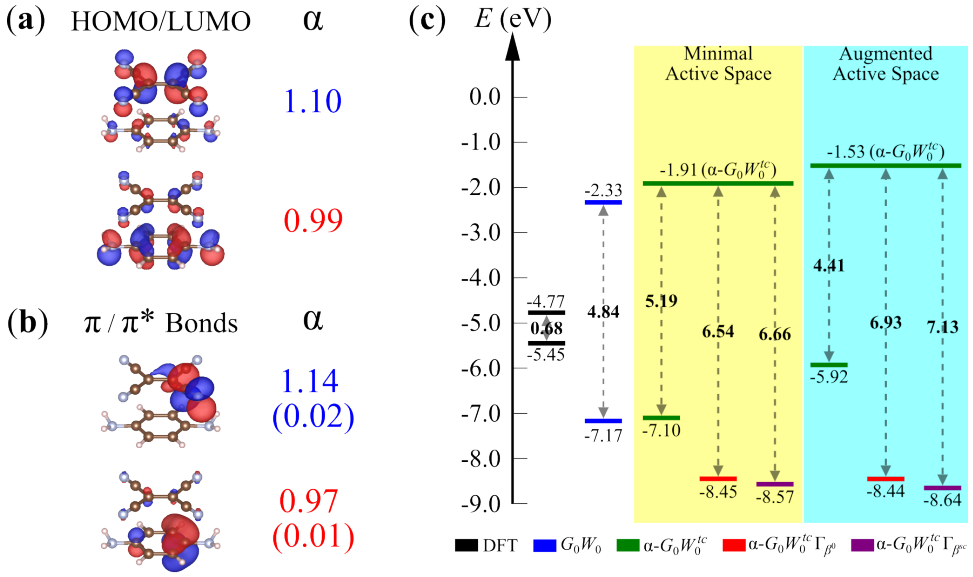

Figure 10.5: Computational results of the B−T dimer: (a) HOMO (lower) and LUMO (upper) states constructing the minimal active space and their rescaling factors, (b) representative π (lower) and π^* (upper) bonds constructing the augmented active space, and their average rescaling factors with standard deviations in parentheses, and (c) HOMO/LUMO energies and fundamental gaps computed by different methods. The yellow and blue regions denote the two different active spaces.

The resulting HOMO/LUMO energies and fundamental gaps are listed in Fig. 10.5c. The DFT (PBE) method, as expected, highly underestimates the gap. The G_0W_0 gap increases notably from 0.68 to 4.84 eV, as the HOMO and LUMO energies are shifted respectively down and up in energy. The yellow region in Fig. 10.5c highlights the results using the minimal active space. Compared to G_0W_0, a slight energy destabilization is caused by the Γ_W effect on the HOMO level. In contrast, the inclusion of Γ_β strongly stabilizes the HOMO level by ∼1.4 eV. The self-consistency in β makes a slight difference. The LUMO energy changes more than the HOMO level upon the inclusion of Γ_W; it is shifted up by ∼0.4 eV. The Γ_X contributes further destabilization (Fig. F.9b), which is consistent with our observations in the TCNE and TCNQ cases. The resulting fundamental gap from α-$G_0W_0^{tc}\Gamma_\beta$ is ∼1.8 eV greater than the G_0W_0 one.

When the active space is augmented (the cyan region), a larger portion of the single-

particle space is treated by the effective Hamiltonian. The changes caused by Γ_W to the QP energies become much more noticeable. The HOMO energy with Γ_W is increased by $\sim$1.2 eV compared to G_0W_0. Note that when the minimal active space is used, the change is merely 0.07 eV. The following Γ_β counters this contribution and stabilizes the HOMO energy to -8.44 eV (with β^0) and -8.64 eV (with β^{sc}). The energy change from -7.17 eV (G_0W_0) to -8.64 eV (α-$G_0W_0^{tc}\Gamma_\beta$) agrees excellently with the self-consistent field localized orbital scaling correction (SCF-LOSC) approach[112] for this dimer system. The LUMO energy with Γ_W is also shifted up to -1.53 eV, rendering a 2-eV larger gap (the red and purple bars in Fig. 10.5c) than the G_0W_0 one.

Next, we apply the same active space construction strategy to the Tc$-$C dimer. Similar to the B$-$T dimer, the minimal active space consists of the HOMO and LUMO states (Fig. 10.6a), which are localized respectively on the donor and the acceptor. The rescaling factors for these two states are both greater than 1. Unlike the previous cases, the HOMO state exhibits correlation stabilization, i.e., the QP energy decreases due to both exchange and correlation interactions. However, this picture depends strongly on the active space definition: when the space size is expanded to all π components, a more common situation arises, in which the nonlocal exchange decreases the QP energy while the correlation counterbalances that. The factor α averaged over five π bonds becomes smaller than 1 with a negligible standard deviation. For C_{60}, the averaged α is sampled by six π^* bonds using the geometric symmetry. The standard deviation is merely 0.01, and the average value (1.15) is thus sufficient to represent the entire set of 30 π^* bonds (see Fig. F.3 in the supplementary material).

The computed energies of the Tc$-$C dimer are summarized in Fig. 10.6c. When using the minimal active space (the yellow region) in α-$G_0W_0^{tc}$, the HOMO energy is hardly affected by Γ_W and the LUMO level is shifted up by 0.09 eV only. The Γ_β effect is found the same as in the B$-$T dimer: the HOMO state is profoundly stabilized, resulting in a

gap 1.5-eV larger than the G_0W_0 one; the self-consistency in β mildly affects the gap by <0.2 eV.

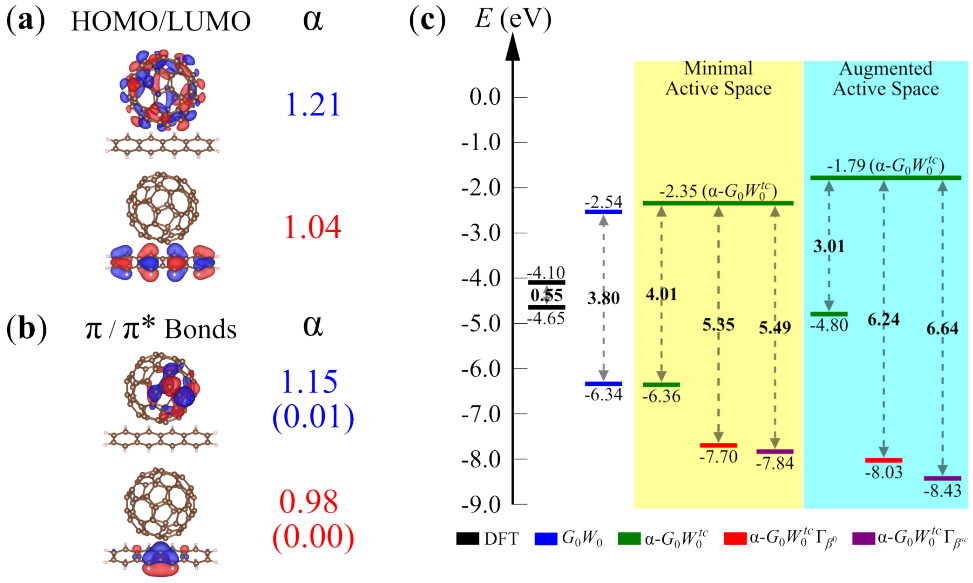

Figure 10.6: Computational results of the Tc−C dimer: (a) HOMO (lower) and LUMO (upper) states constructing the minimal active space and their rescaling factors, (b) representative π (lower) and π^* (upper) bonds constructing the augmented active space, and their average rescaling factors with standard deviations in parentheses, and (c) HOMO/LUMO energies and fundamental gaps computed by different methods. The yellow and blue regions denote the two different active spaces.

The cyan region in Fig. 10.6c highlights the results using the π+π^* active space. The Tc−C dimer behaves consistently with the B−T dimer when changing from the minimal active space to the augmented one: the HOMO energy predicted by α-$G_0W_0^{tc}$ is significantly elevated by ∼1.6 eV from G_0W_0 due to Γ_W; the LUMO energy increases by ∼0.8 eV. The α-$G_0W_0^{tc}$ gap (the green bar in Fig. 10.6c) is thus ∼0.8 eV smaller than the G_0W_0 one. However, Γ_β contributes oppositely to the gap by shifting the HOMO level down to −8.03 and −8.43 eV (with self-consistent β). The Γ_X effect on the LUMO energy behaves consistently with the previous systems (Fig. F.10b). In total, the fundamental gap of the Tc−C dimer is increased by ∼2.5 eV from the G_0W_0 one.

To conclude from the donor−acceptor dimer studies, the embedded vertex shows

a clear and non-trivial dependence on the active space size, significantly affecting the fundamental gap; yet some important generalizations can be already deduced. For the HOMO state, the minimal active space implementation of Γ_W makes little difference (compared to G_0W_0), while the augmented space notably corrects the QP energies. The Γ_β contribution is critical to generate quantitative predictions for the HOMO QP energy. Compared to HOMO, the LUMO QP energy exhibits a more pronounced dependence on the active space size. In general, the vertex-corrected fundamental gaps are more than 2 eV larger than the G_0W_0 ones. Most importantly, the results of the B−T dimer show a remarkable agreement between the HOMO QP energies obtained with α-$G_0W_0^{tc}\Gamma_\beta$ for the two very distinct definitions of the active space. Based on this, it seems that when the vertex corrections are applied consistently to both the W term and the self-energy, the dependence on the active space definition diminishes. Further investigation is necessary to clarify if this is a universal feature of the α-$G_0W_0^{tc}\Gamma_\beta$ approach.

10.3.3 *p*-FBT polymer and Tc−C double layers

The embedded vertex corrections consistently and significantly change the QP energies of the small molecules and molecular dimers investigated above. The embedding approach with two distinct active space selections is further applied to periodic systems, particularly 1D and 2D materials. Poly-fluorene-benzothiadiazole (p-FBT) is a typical donor−acceptor copolymer widely used in organic electronics.[125, 126, 127] Charge excitation energies and fundamental gaps of these functional materials are crucial parameters in understanding their opto-electronic properties. Furthermore, we extend the Tc−C dimer in Sec. 10.3.2 to a 2D double-layer model, which is closer to the solid-state thin-film environment and represents a minimal surface model of an organic heterojunction. For fair comparisons, the inter-layer distance takes the same value as that of the Tc−C dimer. Unlike isolated

molecules, the states form band structures, and the active space is represented by energy bands. Note that for these two periodic systems, we consider only the top valence band (TVB) and bottom conduction band (BCB) for simplicity when constructing the active space. Due to our real-space implementation, the TVB or BCB is represented by a set of (more than one) orbitals, which is equivalent to the k-point sampling in the reciprocal space. We illustrate the methodology with two distinct representations: Bloch states and PM Wannier functions. The latter is obtained by unitary transforming the former. The orbital space is thus identical in dimensions, but the rescaling factors α, in principle, differ and lead to distinct effective Hamiltonians [Eq. (10.8)].

First, we exemplify the embedding scheme with the p-FBT system. Fig. 10.7a shows a fraction of the polymer supercell, and in fact, eight repeated units are used for converging the real-space calculations. On the plot of density-of-states (Fig. 10.7a), the highlighted regions correspond to the TVB (red) and BCB (blue) in the band structure. Due to the supercell size, eight canonical KS states are found in each band with distinct crystal momentum within the first Brillouin zone, forming the Bloch representation. Orbital localization generates eight Wannier functions.

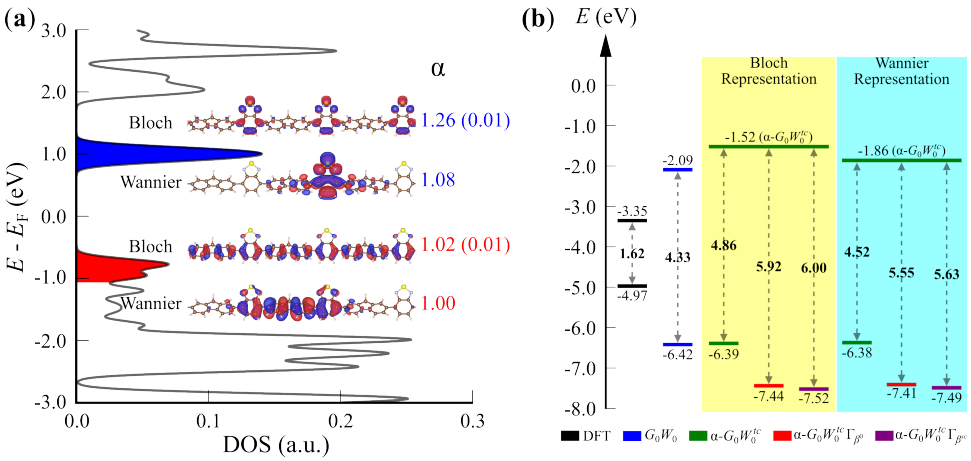

Figure 10.7: Computational results of the p-FBT polymer: (a) density of states with the top valence band colored in red and the bottom conduction band colored in blue. Active spaces are represented by either Bloch states or Wannier functions with the corresponding (averaged) rescaling factors and standard deviations in parentheses. (b) Valence band maximum/conduction band minimum energies and fundamental gaps computed by different methods. The yellow and blue regions denote the two different representations of the active space.

Typical Bloch and Wannier states are shown in Fig. 10.7a, and the entire set of orbitals is provided in Fig. F.4. In the Bloch representation, the TVB states are delocalized along the π-conjugated backbone, while the BCB states are localized on the acceptor units. The factor α is averaged over eight states with negligible standard deviations (0.01). For the TVB, α is slightly greater than 1, while the BCB one is much larger. These results agree with the calculations for molecules in Secs. 10.3.1 and 10.3.2. In the Wannier basis, the functions are localized in each unit cell. Within the cell, the TVB Wannier function is delocalized, while the BCB one is mainly localized on the acceptor. Due to the translational symmetry, only one Wannier function is needed to represent a band when computing the factor α. Yet, all the eight Wannier functions are needed for the active space projector [Eq. (10.7)]. α of Wannier representation is very close to the Bloch one for the TVB (1.00 vs. 1.02) but not for the BCB (1.08 vs 1.26). In the Wannier basis, the degree of exchange rescaling is less dependent on the particular orbital type.

Fig. 10.7b summarizes the computed results for the valence band maximum (VBM) and conduction band minimum (CBM) states of the p-FBT system. In the Bloch representation (the yellow region), the VBM remains nearly unchanged by Γ_W (α-$G_0W_0^{tc}$), while the CBM is shifted up by $\sim$0.5 eV. Consistent with the previous results, the Γ_β term corrects the VBM energy by $\sim$1 to -7.44 eV, and the self-consistency does not make a sizable difference ($<$0.1 eV). The results in the Wannier representation (the cyan region) show explicit α-dependence: the VBM energy does not differ too much from the Bloch one, while the CBM becomes lower in energy due to a smaller α being used for the unoccupied active space. The fundamental gap computed with α-$G_0W_0^{tc}\Gamma_\beta$ (the red and purple bars in the cyan region of Fig. 10.7b) is predicted to be 1.2$-$1.6 eV larger than the one obtained from the G_0W_0 calculation.

Similar rescaling results to the p-FBT are observed for the Tc$-$C double layers: the exchange interaction of the TVB is hardly rescaled in either representation; the averaged α of the BCB over eight Bloch states (Fig. F.5) is greater than that using the Wannier function. However, the differences in α do not markedly affect the energy diagram, i.e., the computed results do not depend on the representation or the rescaling factors. We thus focus only on the yellow region in Fig. 10.8b. The VBM energies given by α-$G_0W_0^{tc}$ and G_0W_0 are statistically the same. Moreover, the CBM of this system is also hardly affected by Γ_W. The Γ_β correction then stabilizes the VBM by $\sim$1 eV, resulting in a $\sim$4.6 eV gap (the red and purple bars in Fig. 10.8b) that is $\sim$1.2 eV greater than the G_0W_0 one. The self-consistency in β slightly shifts the energy further down. Compared with the Tc$-$C dimer, the solid-state renormalization of the gap is predicted to be $\sim$0.4 eV by G_0W_0 and $\sim$2 eV by α-$G_0W_0^{tc}\Gamma_\beta$. This difference suggests that the G_0W_0 approach underestimates the gap renormalization in condensed systems.

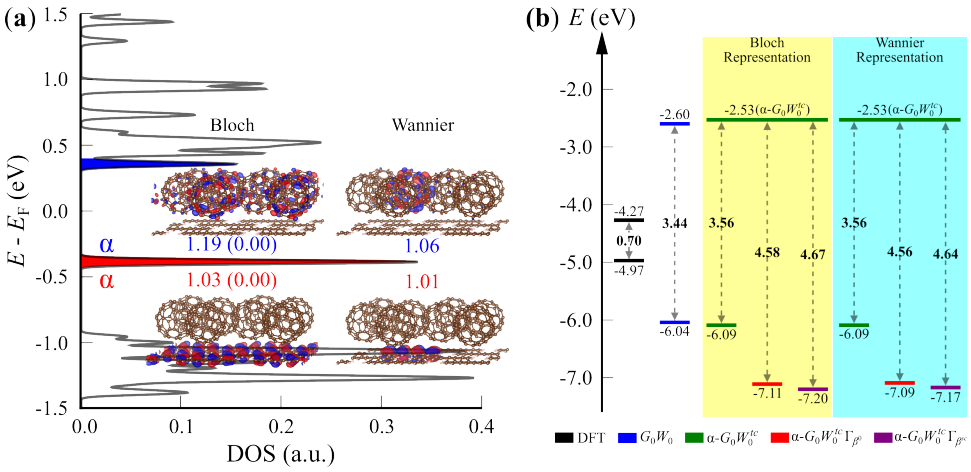

Figure 10.8: Computational results of Tc−C double layers: (a) density of states with the top valence band colored in red and the bottom conduction band colored in blue. Active spaces are represented by either Bloch states (left two states) or Wannier functions (right two states) with the corresponding (averaged) rescaling factors and standard deviations in parentheses. (b) Valence band maximum and conduction band minimum energies and fundamental gaps computed by different methods. The yellow and blue regions denote the two different representations of the active space.

The optical absorption spectrum of the tetracene-C_{60} blended thin film indicates a ∼3 eV optical gap,[122] which is similar to the G_0W_0 gap but deviates from the 4.6 eV result obtained from the α-$G_0W_0^{tc}\Gamma_\beta$ approach. However, the optical and fundamental gaps cannot be directly compared since several intrinsic and critical factors are not included. First of all, the exciton-binding energy significantly decreases the optical gap compared to the fundamental gap. For charge-transfer excitation in donor−acceptor systems, the exciton-binding energy follows the $1/R$ asymptotic behavior[128, 99, 129] (R is the distance between two separated charges). To estimate the exciton-binding energy, we approximate R by the distance between two respective geometric centers of the donor and acceptor layers; the bare Coulomb attraction is ∼2 eV between two integer charges separated by ∼12 bohrs. If this estimated energy is subtracted from the 4.6 eV result, the computed gap (∼2.6 eV) becomes much closer to the measured optical gap. Second, the neglected electron−phonon couplings in the solid-state thin-film environment also make non-trivial

contributions to the gap renormalization, in which the fundamental gap often becomes smaller.[130, 131, 132, 133] To limit the scope of this work, we do not seek to quantify the contributions above; but this rudimentary analysis demonstrates a straightforward fact that the computed fundamental gap should be significantly larger than the measured optical gap. For the double-layer system, we can compare our predictions to the scanning tunneling microscopic (STM) measurement of C_{60} nanochains on bilayer pentacene.[134] A $\sim$4 eV charge-transfer fundamental gap can be inferred from the spectra, which is also over 2 eV larger than the corresponding optical gap.[123] It is thus suggestive that the embedded vertex corrections improve the fundamental gap for this tetracene-C_{60} double-layer system.

10.4 CONCLUSIONS AND PERSPECTIVE

This work demonstrates a real-time approach to embed vertex corrections in the G_0W_0 correlation self-energy. The key procedure of the proposed methodology is to perform the separation−propagation−recombination treatment on the random vectors that sample the correlation self-energy. The separation step uses an electronic active space projector to divide electron states into two components: the active part and the rest. Fundamentally, the approach is applicable to any arbitrarily chosen active space definition, as demonstrated in this work; in particular, we construct the subspace with either canonical frontier orbitals (bands) or localized orbitals concerning the electron−hole pair formation. In the propagation step, the active space component is treated by a space-specific effective Hamiltonian, while the rest is treated at the RPA level. We employ a rescaled time-dependent nonlocal exchange interaction in the effective Hamiltonian, which approximates the correlation contribution and emulates the QP Hamiltonian. The use of effective Hamiltonian in time evolution introduces nonlocal vertex to the

polarizability. The last step recombines the two separately time-evolved components to generate embedded vertex-corrected states that lead to correlation self-energy with vertex corrections. The effective Hamiltonian constructed in the propagation step is a crude simplification but represents a convenient and efficient way to perform the embedding. The extension of this framework is straightforward and will be explored in the near future. In the current setup, the method is successfully applied to systems ranging from small molecules to large-scale extended systems, here exemplified on 2D double layers with up to 2500 electrons.

The vertex corrections to the polarizability (i.e., the inclusion of excitonic effects in the screening) and to the entire self-energy (including optical couplings and mitigating self-polarization errors) are discussed separately as Γ_W and Γ_β. Upon the G_0W_0 results, Γ_W is found to destabilize both the HOMO and LUMO energies in most investigated molecules. The change in QP energy exhibits strong dependence on the active space size: results from the minimal active space differ slightly from G_0W_0, especially for the HOMO; the destabilization effect is strongly enhanced when the active space is augmented. In the periodic systems, the frontier bands are represented by either Bloch states or Wannier functions; the latter allows an efficient evaluation of the rescaling factor for an energy band. The changes of active space representation and the corresponding exchange rescaling show contrasting influences: the CBM energy of p-FBT exhibits a clear dependence on the rescaling magnitude between two representations, while the results of the double-layer system are hardly affected.

Γ_β, in contrast, enters the self-energy and is also derived from the rescaled nonlocal exchange approximation. An appealing advantage of the scheme proposed here is the possibility to update the rescaling factor in Γ_β in a self-consistent post-processing step, which incurs no increase of the computational cost. In general, the inclusion of Γ_β stabilizes the HOMO energy but destabilizes the LUMO level. For the former, the Γ_β correction

reaches a quantitative agreement with the previous work on the B−T dimer.[112] The self-consistency in β leads to additional stabilization of the QP energy.

For the LUMO state, the simplistic approach based on the rescaled nonlocal exchange interaction fails to reach a quantitative description. Further investigations on the components of the active space imply that the unoccupied (electron) states play a dominating role in the $\Sigma_{\mathrm{C}}^{\Gamma\mathrm{x}}$ self-energy for the LUMO. However, the rescaling approximation involves only occupied (hole) states when calculating the exchange interaction, which is the surmised culprit. Further exploration is needed to approximate the correlation contribution for deriving the vertex function. Generally, the fundamental gaps of the investigated systems are increased by 1−3 eV. This improvement is especially significant in our donor−acceptor double-layer system, as the results agree excellently with the related experiments.

Finally, we note that if the vertex corrections are used internally and consistently in both the W term and the self-energy, the results exhibit a much weaker dependence on the choice of the active space. Ref. 82 points out that the vertex corrections arise naturally as a consequence of functional self-consistency, in which new classes of interactions (embodies by the vertex term) appear by evaluating the functional derivatives of the self-energy in *both* terms, i.e., W and Σ_{C}. This observation warrants further exploration to determine if indeed the inclusion of both Γ_W and Γ_β help to mitigate the active space selection conundrum.

In summary, our proposed methodology combines the concepts of stochastic sampling, Pipek−Mezey localized orbitals, space-specific Hamiltonian, and separation–propagation–recombination treatment. It provides an efficient and direct way to include nonlocal vertex corrections to the GW self-energy. We believe that this work on embedding methods within the Green's function framework will stimulate more attempts to handle vertex corrections in large condensed matter systems.

SUPPLEMENTARY MATERIAL

The supplementary material provides the details of theory and computation, as well as supplementary tables and figures indicated in the texts.

ACKNOWLEDGMENTS

The authors would like to acknowledge Professor Thuc-Quyen Nguyen for useful discussions on the donor and acceptor molecules. This work was supported by the NSF CAREER award through Grant No. DMR-1945098. The calculations were performed as part of XSEDE computational Project No. TG-CHE180051. Use was made of computational facilities purchased with funds from the National Science Foundation (Grant No. CNS-1725797) and administered by the Center for Scientific Computing (CSC). The CSC is supported by the California NanoSystems Institute and the Materials Research Science and Engineering Center (MRSEC; NSF Grant No. DMR 1720256) at UC Santa Barbara.

DATA AVAILABILITY

The data that support the findings of this study are available from the corresponding author upon reasonable request.

Bibliography

[1] S. Goedecker, *Linear scaling electronic structure methods*, *Reviews of Modern Physics* **71** (1999), no. 4 1085–1123.

[2] S. Goedecker and G. E. Scuserza, *Linear scaling electronic structure methods in chemistry and physics*, *Computing in Science & Engineering* **5** (2003), no. 4 14–21.

[3] C.-K. Skylaris, P. D. Haynes, A. A. Mostofi, and M. C. Payne, *Introducing onetep: Linear-scaling density functional simulations on parallel computers*, *The Journal of Chemical Physics* **122** (2005), no. 8 084119.

[4] J. VandeVondele, M. Krack, F. Mohamed, M. Parrinello, T. Chassaing, and J. Hutter, *Quickstep: Fast and accurate density functional calculations using a mixed gaussian and plane waves approach*, *Computer Physics Communications* **167** (2005), no. 2 103–128.

[5] Y. Zhou, Y. Saad, M. L. Tiago, and J. R. Chelikowsky, *Self-consistent-field calculations using chebyshev-filtered subspace iteration*, *Journal of Computational Physics* **219** (2006), no. 1 172–184.

[6] F. Neese, F. Wennmohs, A. Hansen, and U. Becker, *Efficient, approximate and parallel hartree–fock and hybrid dft calculations. a 'chain-of-spheres' algorithm for the hartree–fock exchange*, *Chemical Physics* **356** (2009), no. 1 98–109.

[7] Y. Saad, J. R. Chelikowsky, and S. M. Shontz, *Numerical methods for electronic structure calculations of materials*, *SIAM Review* **52** (2010), no. 1 3–54.

[8] R. Baer, D. Neuhauser, and E. Rabani, *Self-averaging stochastic kohn-sham density-functional theory*, *Physical Review Letters* **111** (2013), no. 10 106402.

[9] D. Neuhauser, R. Baer, and E. Rabani, *Communication: Embedded fragment stochastic density functional theory*, *The Journal of Chemical Physics* **141** (2014), no. 4 041102.

[10] A. Fetter and J. Walecka, *Quantum Theory of Many-particle Systems*. Dover Books on Physics. Dover Publications, 2003.

[11] R. M. Martin, L. Reining, and D. M. Ceperley, *Interacting Electrons: Theory and Computational Approaches*. Cambridge University Press, Cambridge, 2016.

[12] L. Hedin, *New method for calculating the one-particle green's function with application to the electron-gas problem*, *Physical Review* **139** (1965), no. 3A A796–A823.

[13] F. Aryasetiawan and O. Gunnarsson, *The gw method*, *Reports on Progress in Physics* **61** (1998), no. 3 237.

[14] G. Onida, L. Reining, and A. Rubio, *Electronic excitations: density-functional versus many-body green's-function approaches*, *Reviews of Modern Physics* **74** (2002), no. 2 601–659.

[15] C. Friedrich and A. Schindlmayr, *Many-body perturbation theory: The GW approximation*, vol. 31 of *NIC Series*, p. 335–355. John von Neumann Institute for Computing, 2006.

[16] D. Golze, M. Dvorak, and P. Rinke, *The gw compendium: A practical guide to theoretical photoemission spectroscopy*, *Frontiers in Chemistry* **7** (2019) 1–66.

[17] G. Strinati, H. J. Mattausch, and W. Hanke, *Dynamical correlation effects on the quasiparticle bloch states of a covalent crystal*, *Physical Review Letters* **45** (1980), no. 4 290–294.

[18] G. Strinati, H. J. Mattausch, and W. Hanke, *Dynamical aspects of correlation corrections in a covalent crystal*, *Physical Review B* **25** (1982), no. 4 2867–2888.

[19] M. S. Hybertsen and S. G. Louie, *First-principles theory of quasiparticles: Calculation of band gaps in semiconductors and insulators*, *Physical Review Letters* **55** (1985), no. 13 1418–1421.

[20] M. S. Hybertsen and S. G. Louie, *Electron correlation in semiconductors and insulators: Band gaps and quasiparticle energies*, *Physical Review B* **34** (1986), no. 8 5390–5413.

[21] R. W. Godby, M. Schlüter, and L. J. Sham, *Self-energy operators and exchange-correlation potentials in semiconductors*, *Physical Review B* **37** (1988), no. 17 10159–10175.

[22] W. G. Aulbur, L. Jönsson, and J. W. Wilkins, *Quasiparticle Calculations in Solids*, vol. 54, pp. 1–218. Academic Press, 2000.

[23] C. Rostgaard, K. W. Jacobsen, and K. S. Thygesen, *Fully self-consistent gw calculations for molecules*, *Physical Review B* **81** (2010), no. 8 085103.

[24] F. Hüser, T. Olsen, and K. S. Thygesen, *Quasiparticle gw calculations for solids, molecules, and two-dimensional materials*, *Physical Review B* **87** (2013), no. 23 235132.

[25] M. J. van Setten, F. Weigend, and F. Evers, *The gw-method for quantum chemistry applications: Theory and implementation*, *Journal of Chemical Theory and Computation* **9** (2013), no. 1 232–246.

[26] S. Körbel, P. Boulanger, I. Duchemin, X. Blase, M. A. L. Marques, and S. Botti, *Benchmark many-body gw and bethe–salpeter calculations for small transition metal molecules*, *Journal of Chemical Theory and Computation* **10** (2014), no. 9 3934–3943.

[27] W. Chen and A. Pasquarello, *Band-edge positions in gw: Effects of starting point and self-consistency*, *Phys. Rev. B* **90** (2014) 165133.

[28] M. Govoni and G. Galli, *Large scale gw calculations*, *Journal of Chemical Theory and Computation* **11** (2015), no. 6 2680–2696.

[29] L. Gallandi and T. Körzdörfer, *Long-range corrected dft meets gw: Vibrationally resolved photoelectron spectra from first principles*, *Journal of Chemical Theory and Computation* **11** (2015), no. 11 5391–5400.

[30] F. Caruso, M. Dauth, M. J. van Setten, and P. Rinke, *Benchmark of gw approaches for the gw100 test set*, *Journal of Chemical Theory and Computation* **12** (2016), no. 10 5076–5087.

[31] Y. Kang, S. H. Jeon, Y. Cho, and S. Han, *Ab initio calculation of ionization potential and electron affinity in solid-state organic semiconductors*, *Physical Review B* **93** (2016), no. 3 035131.

[32] T. Rangel, S. M. Hamed, F. Bruneval, and J. B. Neaton, *Evaluating the gw approximation with ccsd(t) for charged excitations across the oligoacenes*, *Journal of Chemical Theory and Computation* **12** (2016), no. 6 2834–2842.

[33] L. Gallandi, N. Marom, P. Rinke, and T. Körzdörfer, *Accurate ionization potentials and electron affinities of acceptor molecules ii: Non-empirically tuned long-range corrected hybrid functionals*, *Journal of Chemical Theory and Computation* **12** (2016), no. 2 605–614.

[34] L. Hung, F. Bruneval, K. Baishya, and S. Öğüt, *Benchmarking the gw approximation and bethe–salpeter equation for groups ib and iib atoms and monoxides*, *Journal of Chemical Theory and Computation* **13** (2017), no. 5 2135–2146.

[35] J. Bois and T. Körzdörfer, *Size-dependence of nonempirically tuned dft starting points for g0w0 applied to π-conjugated molecular chains*, *Journal of Chemical Theory and Computation* **13** (2017), no. 10 4962–4971.

[36] M. Govoni and G. Galli, *Gw100: Comparison of methods and accuracy of results obtained with the west code*, *Journal of Chemical Theory and Computation* **14** (2018), no. 4 1895–1909.

[37] Z. Ergönenc, B. Kim, P. Liu, G. Kresse, and C. Franchini, *Converged GW quasiparticle energies for transition metal oxide perovskites*, *Physical Review Materials* **2** (2018), no. 2 024601.

[38] D. Neuhauser, Y. Gao, C. Arntsen, C. Karshenas, E. Rabani, and R. Baer, *Breaking the theoretical scaling limit for predicting quasiparticle energies: The stochastic GW approach*, *Physical Review Letters* **113** (2014), no. 7 076402.

[39] V. Vlček, E. Rabani, D. Neuhauser, and R. Baer, *Stochastic gw calculations for molecules*, *Journal of Chemical Theory and Computation* **13** (2017), no. 10 4997–5003.

[40] V. Vlček, W. Li, R. Baer, E. Rabani, and D. Neuhauser, *Swift GW beyond 10,000 electrons using sparse stochastic compression*, *Physical Review B* **98** (2018), no. 7 075107.

[41] V. Vlček, E. Rabani, and D. Neuhauser, *Quasiparticle spectra from molecules to bulk*, *Physical Review Materials* **2** (2018), no. 3 030801(R).

[42] J. Brooks, G. Weng, S. Taylor, and V. Vlcek, *Stochastic many-body perturbation theory for moiré states in twisted bilayer phosphorene*, *Journal of Physics: Condensed Matter* **32** (2020), no. 23 234001.

[43] G. Weng and V. Vlček, *Quasiparticles and band structures in organized nanostructures of donor–acceptor copolymers*, *The Journal of Physical Chemistry Letters* **11** (2020), no. 17 7177–7183.

[44] M. Romanova and V. Vlček, *Decomposition and embedding in the stochastic gw self-energy*, *The Journal of Chemical Physics* **153** (2020), no. 13 134103.

[45] G. Weng and V. Vlček, *Efficient treatment of molecular excitations in the liquid phase environment via stochastic many-body theory*, *The Journal of Chemical Physics* **155** (2021), no. 5 054104.

[46] M. Romanova and V. Vlček, *Stochastic many-body calculations of moiré states in twisted bilayer graphene at high pressures*, *npj Computational Materials* **8** (2022), no. 1 11.

[47] P. Hohenberg and W. Kohn, *Inhomogeneous electron gas*, *Physical Review* **136** (1964), no. 3B B864–B871.

[48] W. Kohn and L. J. Sham, *Self-consistent equations including exchange and correlation effects*, *Physical Review* **140** (1965), no. 4A A1133–A1138.

[49] L. S. Cederbaum, J. Schirmer, W. Domcke, and W. von Niessen, *Complete breakdown of the quasiparticle picture for inner valence electrons*, *Journal of Physics B: Atomic and Molecular Physics* **10** (1977), no. 15 L549.

[50] L. S. Cederbaum, W. Domcke, J. Schirmer, and W. von Niessen, *Many-body effects in valence and core photoionization of molecules*, *Physica Scripta* **21** (1980), no. 3-4 481.

[51] W. Nelson, P. Bokes, P. Rinke, and R. W. Godby, *Self-interaction in green's-function theory of the hydrogen atom*, *Phys. Rev. A* **75** (2007) 032505.

[52] F. Aryasetiawan, R. Sakuma, and K. Karlsson, *gw approximation with self-screening correction*, *Phys. Rev. B* **85** (2012) 035106.

[53] R. Del Sole, L. Reining, and R. W. Godby, *$GW\Gamma$ approximation for electron self-energies in semiconductors and insulators*, *Phys. Rev. B* **49** (1994) 8024–8028.

[54] M. L. Tiago and J. R. Chelikowsky, *Optical excitations in organic molecules, clusters, and defects studied by first-principles green's function methods*, *Physical Review B* **73** (2006), no. 20 205334.

[55] A. J. Morris, M. Stankovski, K. T. Delaney, P. Rinke, P. García-González, and R. W. Godby, *Vertex corrections in localized and extended systems*, *Physical Review B* **76** (2007), no. 15 155106.

[56] M. Shishkin, M. Marsman, and G. Kresse, *Accurate quasiparticle spectra from self-consistent gw calculations with vertex corrections*, *Phys. Rev. Lett.* **99** (2007) 246403.

[57] A. Grüneis, M. Marsman, J. Harl, L. Schimka, and G. Kresse, *Making the random phase approximation to electronic correlation accurate*, *The Journal of Chemical Physics* **131** (2009), no. 15 154115.

[58] Y.-W. Chang and B.-Y. Jin, *Correlation effects of π electrons on the band structures of conjugated polymers using the self-consistent gw approximation with vertex corrections*, *The Journal of Chemical Physics* **136** (2012), no. 2 024110.

[59] A. Grüneis, G. Kresse, Y. Hinuma, and F. Oba, *Ionization potentials of solids: The importance of vertex corrections*, *Phys. Rev. Lett.* **112** (2014) 096401.

[60] X. Ren, N. Marom, F. Caruso, M. Scheffler, and P. Rinke, *Beyond the GW approximation: A second-order screened exchange correction*, *Physical Review B* **92** (2015), no. 8 081104.

[61] W. Chen and A. Pasquarello, *Accurate band gaps of extended systems via efficient vertex corrections in gw*, *Phys. Rev. B* **92** (2015) 041115.

[62] L. Hung, F. H. da Jornada, J. Souto-Casares, J. R. Chelikowsky, S. G. Louie, and S. Öğüt, *Excitation spectra of aromatic molecules within a real-space GW-bse formalism: Role of self-consistency and vertex corrections*, *Physical Review B* **94** (2016), no. 8 085125.

[63] R. Kuwahara, Y. Noguchi, and K. Ohno, GWΓ + *bethe-salpeter equation approach for photoabsorption spectra: Importance of self-consistent* GWΓ *calculations in small atomic systems*, *Phys. Rev. B* **94** (2016) 121116.

[64] J. W. Knight, X. Wang, L. Gallandi, O. Dolgounitcheva, X. Ren, J. V. Ortiz, P. Rinke, T. Körzdörfer, and N. Marom, *Accurate ionization potentials and electron affinities of acceptor molecules iii: A benchmark of gw methods*, *Journal of Chemical Theory and Computation* **12** (2016), no. 2 615–626.

[65] P. S. Schmidt, C. E. Patrick, and K. S. Thygesen, *Simple vertex correction improves GW band energies of bulk and two-dimensional crystals*, *Physical Review B* **96** (2017), no. 20 205206.

[66] E. Maggio and G. Kresse, *Gw vertex corrected calculations for molecular systems*, *Journal of Chemical Theory and Computation* **13** (2017), no. 10 4765–4778.

[67] M. Hellgren, N. Colonna, and S. de Gironcoli, *Beyond the random phase approximation with a local exchange vertex*, *Physical Review B* **98** (2018), no. 4 045117.

[68] V. Vlček, *Stochastic vertex corrections: Linear scaling methods for accurate quasiparticle energies*, *Journal of Chemical Theory and Computation* **15** (2019), no. 11 6254–6266.

[69] A. M. Lewis and T. C. Berkelbach, *Vertex corrections to the polarizability do not improve the gw approximation for the ionization potential of molecules*, *Journal of Chemical Theory and Computation* **15** (2019), no. 5 2925–2932.

[70] H. Ma, M. Govoni, F. Gygi, and G. Galli, *A finite-field approach for gw calculations beyond the random phase approximation*, *Journal of Chemical Theory and Computation* **15** (2019), no. 1 154–164.

[71] Y. Pavlyukh, G. Stefanucci, and R. van Leeuwen, *Dynamically screened vertex correction to gw*, *Phys. Rev. B* **102** (2020) 045121.

[72] C. Mejuto-Zaera, G. Weng, M. Romanova, S. J. Cotton, K. B. Whaley, N. M. Tubman, and V. Vlček, *Are multi-quasiparticle interactions important in molecular ionization?*, *The Journal of Chemical Physics* **154** (2021), no. 12 121101.

[73] Y. Wang, P. Rinke, and X. Ren, *Assessing the g0w0γ0(1) approach: Beyond g0w0 with hedin's full second-order self-energy contribution*, *Journal of Chemical Theory and Computation* **17** (2021), no. 8 5140–5154.

[74] Y. Wang and X. Ren, *Vertex effects in describing the ionization energies of the first-row transition-metal monoxide molecules*, 2022.

[75] F. Bruneval, F. Sottile, V. Olevano, R. Del Sole, and L. Reining, *Many-body perturbation theory using the density-functional concept: Beyond the gw approximation*, *Phys. Rev. Lett.* **94** (2005) 186402.

[76] P. Romaniello, S. Guyot, and L. Reining, *The self-energy beyond gw: Local and nonlocal vertex corrections*, *The Journal of Chemical Physics* **131** (2009), no. 15 154111.

[77] D. L. Freeman, *Coupled-cluster expansion applied to the electron gas: Inclusion of ring and exchange effects*, *Physical Review B* **15** (1977), no. 12 5512–5521.

[78] H. J. de Groot, R. T. M. Ummels, P. A. Bobbert, and W. v. Haeringen, *Lowest-order corrections to the rpa polarizability and gw self-energy of a semiconducting wire*, *Physical Review B* **54** (1996), no. 4 2374–2380.

[79] P. Romaniello, F. Bechstedt, and L. Reining, *Beyond the gw approximation: Combining correlation channels*, *Physical Review B* **85** (2012), no. 15 155131.

[80] T. Ayral, P. Werner, and S. Biermann, *Spectral properties of correlated materials: Local vertex and nonlocal two-particle correlations from combined GW and dynamical mean field theory*, *Physical Review Letters* **109** (2012), no. 22 226401.

[81] M. Hellgren, *Local vertex corrections from exchange-correlation kernels with a discontinuity*, *The European Physical Journal B* **91** (2018), no. 7 155.

[82] C. Mejuto-Zaera and V. Vlček, *Self-consistency in gwΓ formalism leading to quasiparticle-quasiparticle couplings*, *Phys. Rev. B* **106** (2022) 165129.

[83] N. M. Tubman, J. Lee, T. Y. Takeshita, M. Head-Gordon, and K. B. Whaley, *A deterministic alternative to the full configuration interaction quantum monte carlo method*, *The Journal of Chemical Physics* **145** (2016), no. 4 044112.

[84] N. M. Tubman, D. S. Levine, D. Hait, M. Head-Gordon, and K. B. Whaley, *An efficient deterministic perturbation theory for selected configuration interaction methods*, 2018.

[85] C. Mejuto-Zaera, N. M. Tubman, and K. B. Whaley, *Dynamical mean field theory simulations with the adaptive sampling configuration interaction method*, *Phys. Rev. B* **100** (2019) 125165.

[86] N. M. Tubman, C. D. Freeman, D. S. Levine, D. Hait, M. Head-Gordon, and K. B. Whaley, *Modern approaches to exact diagonalization and selected configuration interaction with the adaptive sampling ci method*, *Journal of Chemical Theory and Computation* **16** (2020), no. 4 2139–2159.

[87] T. Stein, L. Kronik, and R. Baer, *Prediction of charge-transfer excitations in coumarin-based dyes using a range-separated functional tuned from first principles*, *The Journal of Chemical Physics* **131** (2009), no. 24 244119.

[88] T. Stein, H. Eisenberg, L. Kronik, and R. Baer, *Fundamental gaps in finite systems from eigenvalues of a generalized kohn-sham method*, *Phys. Rev. Lett.* **105** (2010) 266802.

[89] L. Kronik, T. Stein, S. Refaely-Abramson, and R. Baer, *Excitation gaps of finite-sized systems from optimally tuned range-separated hybrid functionals*, *Journal of Chemical Theory and Computation* **8** (2012), no. 5 1515–1531.

[90] S. Refaely-Abramson, S. Sharifzadeh, N. Govind, J. Autschbach, J. B. Neaton, R. Baer, and L. Kronik, *Quasiparticle spectra from a nonempirical optimally tuned range-separated hybrid density functional*, *Phys. Rev. Lett.* **109** (2012) 226405.

[91] S. Refaely-Abramson, M. Jain, S. Sharifzadeh, J. B. Neaton, and L. Kronik, *Solid-state optical absorption from optimally tuned time-dependent range-separated hybrid density functional theory*, *Phys. Rev. B* **92** (2015) 081204.

[92] A. K. Manna, S. Refaely-Abramson, A. M. Reilly, A. Tkatchenko, J. B. Neaton, and L. Kronik, *Quantitative prediction of optical absorption in molecular solids from an optimally tuned screened range-separated hybrid functional*, *Journal of Chemical Theory and Computation* **14** (2018), no. 6 2919–2929.

[93] L. Kronik and S. Kümmel, *Dielectric screening meets optimally tuned density functionals*, *Advanced Materials* **30** (2018), no. 41 1706560.

[94] S. Bhandari, M. S. Cheung, E. Geva, L. Kronik, and B. D. Dunietz, *Fundamental gaps of condensed-phase organic semiconductors from single-molecule calculations using polarization-consistent optimally tuned screened range-separated hybrid functionals*, *Journal of Chemical Theory and Computation* **14** (2018), no. 12 6287–6294.

[95] D. Wing, J. B. Haber, R. Noff, B. Barker, D. A. Egger, A. Ramasubramaniam, S. G. Louie, J. B. Neaton, and L. Kronik, *Comparing time-dependent density*

functional theory with many-body perturbation theory for semiconductors: Screened range-separated hybrids and the gw plus bethe-salpeter approach, *Phys. Rev. Materials* **3** (2019) 064603.

[96] G. Prokopiou, M. Hartstein, N. Govind, and L. Kronik, *Optimal tuning perspective of range-separated double hybrid functionals*, *Journal of Chemical Theory and Computation* **18** (2022), no. 4 2331–2340.

[97] N. P. Brawand, M. Vörös, M. Govoni, and G. Galli, *Generalization of dielectric-dependent hybrid functionals to finite systems*, *Phys. Rev. X* **6** (2016) 041002.

[98] T. Rangel, S. M. Hamed, F. Bruneval, and J. B. Neaton, *An assessment of low-lying excitation energies and triplet instabilities of organic molecules with an ab initio bethe-salpeter equation approach and the tamm-dancoff approximation*, *The Journal of Chemical Physics* **146** (2017), no. 19 194108.

[99] T. Stein, L. Kronik, and R. Baer, *Reliable prediction of charge transfer excitations in molecular complexes using time-dependent density functional theory*, *Journal of the American Chemical Society* **131** (2009), no. 8 2818–2820.

[100] V. Vlček, H. R. Eisenberg, G. Steinle-Neumann, L. Kronik, and R. Baer, *Deviations from piecewise linearity in the solid-state limit with approximate density functionals*, *The Journal of Chemical Physics* **142** (2015), no. 3 034107.

[101] D. Wing, G. Ohad, J. B. Haber, M. R. Filip, S. E. Gant, J. B. Neaton, and L. Kronik, *Band gaps of crystalline solids from wannier-localization–based optimal tuning of a screened range-separated hybrid functional*, *Proceedings of the National Academy of Sciences* **118** (2021), no. 34 e2104556118.

[102] S. E. Gant, J. B. Haber, M. R. Filip, F. Sagredo, D. Wing, G. Ohad, L. Kronik, and J. B. Neaton, *Optimally tuned starting point for single-shot gw calculations of solids*, *Phys. Rev. Materials* **6** (2022) 053802.

[103] G. Ohad, D. Wing, S. E. Gant, A. V. Cohen, J. B. Haber, F. Sagredo, M. R. Filip, J. B. Neaton, and L. Kronik, *Band gaps of halide perovskites from a wannier-localized optimally tuned screened range-separated hybrid functional*, *Phys. Rev. Materials* **6** (2022) 104606.

[104] T. Koopmans, *Über die zuordnung von wellenfunktionen und eigenwerten zu den einzelnen elektronen eines atoms*, *Physica* **1** (1934), no. 1 104–113.

[105] J. F. Janak, *Proof that* $\frac{\partial e}{\partial n_i} = \epsilon$ *in density-functional theory*, *Phys. Rev. B* **18** (1978) 7165–7168.

[106] J. P. Perdew, K. Burke, and M. Ernzerhof, *Generalized gradient approximation made simple*, *Phys. Rev. Lett.* **77** (1996) 3865–3868.

[107] J. Pipek and P. G. Mezey, *A fast intrinsic localization procedure applicable for ab initio and semiempirical linear combination of atomic orbital wave functions*, *The Journal of Chemical Physics* **90** (1989), no. 9 4916–4926.

[108] E. Ö. Jónsson, S. Lehtola, M. Puska, and H. Jónsson, *Theory and applications of generalized pipek–mezey wannier functions*, *Journal of Chemical Theory and Computation* **13** (2017), no. 2 460–474.

[109] G. Weng, M. Romanova, A. Apelian, H. Song, and V. Vlček, *Reduced scaling of optimal regional orbital localization via sequential exhaustion of the single-particle space*, *Journal of Chemical Theory and Computation* **18** (2022), no. 8 4960–4972.

[110] E. Rabani, R. Baer, and D. Neuhauser, *Time-dependent stochastic bethe-salpeter approach*, *Phys. Rev. B* **91** (2015) 235302.

[111] C.-R. Zhang, J. S. Sears, B. Yang, S. G. Aziz, V. Coropceanu, and J.-L. Brédas, *Theoretical study of the local and charge-transfer excitations in model complexes of pentacene-c60 using tuned range-separated hybrid functionals*, *Journal of Chemical Theory and Computation* **10** (2014), no. 6 2379–2388.

[112] Y. Mei, Z. Chen, and W. Yang, *Self-consistent calculation of the localized orbital scaling correction for correct electron densities and energy-level alignments in density functional theory*, *The Journal of Physical Chemistry Letters* **11** (2020), no. 23 10269–10277.

[113] V. G. Zakrzewski, O. Dolgounitcheva, and J. V. Ortiz, *Electron binding energies of tcnq and tcne*, *The Journal of Chemical Physics* **105** (1996), no. 14 5872–5877.

[114] K. N. Houk and L. L. Munchausen, *Ionization potentials, electron affinities, and reactivities of cyanoalkenes and related electron-deficient alkenes. a frontier molecular orbital treatment of cyanoalkene reactivities in cycloaddition, electrophilic, nucleophilic, and radical reactions*, *Journal of the American Chemical Society* **98** (1976), no. 4 937–946.

[115] L. Lyons and L. Palmer, *The electron affinity of tetracyanoethylene and other organic electron acceptors*, *Australian Journal of Chemistry* **29** (1976), no. 9 1919–1929.

[116] S. Chowdhury and P. Kebarle, *Electron affinities of di- and tetracyanoethylene and cyanobenzenes based on measurements of gas-phase electron-transfer equilibria*, *Journal of the American Chemical Society* **108** (1986), no. 18 5453–5459.

[117] D. Khuseynov, M. T. Fontana, and A. Sanov, *Photoelectron spectroscopy and photochemistry of tetracyanoethylene radical anion in the gas phase*, *Chemical Physics Letters* **550** (2012) 15–18.

[118] I. Ikemoto, K. Samizo, T. Fujikawa, K. Ishii, T. Ohta, and H. Kuroda, *Photoelectron spectra of tetracyanoethylene(tcne) and tetracyanoquinodimethane (tcnq)*, *Chemistry Letters* **3** (1974), no. 7 785–790.

[119] C. E. Klots, R. N. Compton, and V. F. Raaen, *Electronic and ionic properties of molecular ttf and tcnq*, *The Journal of Chemical Physics* **60** (1974), no. 3 1177–1178.

[120] M. Hayashi, T.-S. Yang, J. Yu, A. Mebel, and S. H. Lin, *On the theoretical investigation on spectroscopy of the electron donor-acceptor complex tcne-hmb*, *The Journal of Physical Chemistry A* **101** (1997), no. 23 4156–4162.

[121] S. Yoo, B. Domercq, and B. Kippelen, *Efficient thin-film organic solar cells based on pentacene/c60 heterojunctions*, *Applied Physics Letters* **85** (2004), no. 22 5427–5429.

[122] C.-W. Chu, Y. Shao, V. Shrotriya, and Y. Yang, *Efficient photovoltaic energy conversion in tetracene-c60 based heterojunctions*, *Applied Physics Letters* **86** (2005), no. 24 243506.

[123] J. Yang and T.-Q. Nguyen, *Effects of thin film processing on pentacene/c60 bilayer solar cell performance*, *Organic Electronics* **8** (2007), no. 5 566–574.

[124] Z. Zhang and Y. Lin, *Organic semiconductors for vacuum-deposited planar heterojunction solar cells*, *ACS Omega* **5** (2020), no. 39 24994–24999.

[125] C.-K. Mai, H. Zhou, Y. Zhang, Z. B. Henson, T.-Q. Nguyen, A. J. Heeger, and G. C. Bazan, *Facile doping of anionic narrow-band-gap conjugated polyelectrolytes during dialysis*, *Angewandte Chemie International Edition* **52** (2013), no. 49 12874–12878.

[126] C.-K. Mai, B. Russ, S. L. Fronk, N. Hu, M. B. Chan-Park, J. J. Urban, R. A. Segalman, M. L. Chabinyc, and G. C. Bazan, *Varying the ionic functionalities of conjugated polyelectrolytes leads to both p- and n-type carbon nanotube composites for flexible thermoelectrics*, *Energy & Environmental Science* **8** (2015), no. 8 2341–2346.

[127] Q. Cui and G. C. Bazan, *Narrow band gap conjugated polyelectrolytes*, *Accounts of Chemical Research* **51** (2018), no. 1 202–211.

[128] A. Dreuw, J. L. Weisman, and M. Head-Gordon, *Long-range charge-transfer excited states in time-dependent density functional theory require non-local exchange*, *The Journal of Chemical Physics* **119** (2003), no. 6 2943–2946.

[129] B. Baumeier, D. Andrienko, and M. Rohlfing, *Frenkel and charge-transfer excitations in donor–acceptor complexes from many-body green's functions theory*, *Journal of Chemical Theory and Computation* **8** (2012), no. 8 2790–2795. PMID: 26592120.

[130] F. Giustino, S. G. Louie, and M. L. Cohen, *Electron-phonon renormalization of the direct band gap of diamond*, *Phys. Rev. Lett.* **105** (2010) 265501.

[131] G. Antonius, S. Poncé, P. Boulanger, M. Côté, and X. Gonze, *Many-body effects on the zero-point renormalization of the band structure*, *Phys. Rev. Lett.* **112** (2014) 215501.

[132] G. Antonius, S. Poncé, E. Lantagne-Hurtubise, G. Auclair, X. Gonze, and M. Côté, *Dynamical and anharmonic effects on the electron-phonon coupling and the zero-point renormalization of the electronic structure*, *Phys. Rev. B* **92** (2015) 085137.

[133] F. Karsai, M. Engel, E. Flage-Larsen, and G. Kresse, *Electron–phonon coupling in semiconductors within the gw approximation*, *New Journal of Physics* **20** (2018), no. 12 123008.

[134] D. B. Dougherty, W. Jin, W. G. Cullen, G. Dutton, J. E. Reutt-Robey, and S. W. Robey, *Local transport gap in* c_{60} *nanochains on a pentacene template*, *Phys. Rev. B* **77** (2008) 073414.

Chapter 11

Conclusions

This dissertation is dedicated to developing efficient and accurate electronic structure methods for large-scale simulations of functional materials and realistic chemical systems. Chapter 1 states the background and motivations, followed by the relevant theories for electronic problems in Chapter 2. Chapter 3 introduces the perturbative approach to calculate quasiparticle energies in practice and the linear-scaling stochastic method for *GW* and beyond. Chapters 5–10 present my research work as six peer-reviewed publications, with individual conclusion section provided in each chapter.

For all the systems of interest, multiscale theoretical approaches are employed to treat the ground-state and excited-state properties. The investigation normally starts with preparing the molecular equilibrium structures or sampling the system geometries through molecular dynamics. For finite molecular systems, the structures are optimized by DFT calculations using the NWChem package.[1] The geometries of solid-state systems, e.g., diamond solids or polymeric assemblies, are relaxed with van der Waals corrections to DFT using the Quantum Espresso package.[2, 3] For molecules in the liquid phase, molecular dynamics simulations are performed to equilibrate and sample the system geometries with the Gromacs package.[4] The second step is to perform the ground-state

calculation for a system with fixed nuclei. Mean-field methods, especially KS-DFT with the PBE functional,[5, 6, 7] are used to determine the electronic ground state and obtain the single-particle eigenstates. Finally, many-body Green's function calculations within the stochastic formalism[8, 9, 10] utilize the eigenstates and the information of the ground-state Hamiltonian to compute quasiparticle energies that correspond to ionization potentials and electron affinities.

The multiscale approach described above is first applied to model the highly-ordered nanodomains of a donor–acceptor copolymer (Chapter 5). Three signature bands near the Fermi level are identified for this particular class of materials with alternating donor and acceptor units. Ambipolar charge transport is found possible in the crystalline domains. Furthermore, the dynamical screening effects from the highly polarizable solid-state environment are resolved on the band structures: the transport gap is found to be renormalized by $\sim$3 eV; the nonlocal polarization effects lead to bandwidth reduction and thus hinder the charge transport.

Chapter 6 introduces a powerful linear-scaling orbital localization approach for regionally localized states. This approach applies further to almost all my following work. Based on the generalized Pipek–Mezey scheme,[11, 12] individual atoms of interest are identified from a complex and giant system to form a fragment, leading to a modified cost function for obtaining localized orbitals on the fragment only. To further lower the cost-scaling of the iterative unitary transformations, the total orbital space is divided into blocks that are sequentially exhausted. When exemplified on the nitrogen-vacancy (NV) center in diamond solids, the maximum speedup observed is from eights days to half an hour. The resulting approach is applied to partition a wide range of systems either in the real space or in the orbital space. For the NV^- center, localized basis is used to isolate the defect from the bulk host environment, which is follwoed by the downfolding in the Hubbard model Hamiltonian. The downfolding approach with localized electronic states

and dynamically screening agrees excellently with experiments on the optical transition energies of the NV center in diamond solids.[13]

In Chapter 7, localized molecular orbitals, i.e., chemical bonds, are utilized to describe molecular ionizations in the liquid phase. The utilization is two-fold: (1) the localized orbitals of a solvated molecule resemble those of the isolated counterpart, providing a way to reconstruct molculear ionization states like the HOMO and LUMO of the isolated molecule; (2) the correlation self-energy of a quasiparticle excitation is decomposed and evaluated as two contributions, the molecular part and the environmental part. Three representative small molecules, including phenol, thymine, and phenyalanine, are chosen as solutes and solvated by water. The geometries of these solvated systems are sampled by snapshots extracted from molecular dynamics simulations. Significant and consistent destabilization effects due to solvation are observed for all investigated molecules, and the shifts in ionization potentials show quantitative agreements with reference data. Upon the decomposition of the self-energy, ∼40% of the polarization effects come from the solvent environment. The molecular part accounts for ∼60% due to a shorter distance to the localized excitation. Furthermore, the full valence spectrum is also accessible through the orbital reconstruction scheme for an arbitrary molecule in the liquid phase.

Chapter 8 continues on the solvated systems and focuses more on the environment. The energy shifts of molecular ionization potential do not depend only on the polarizable solvent environment but also on the spatial decay of the solute–solvent interactions. Using localized molecular orbitals, the solvent environment fragments into multiple solvation shells characterized by their distance away from the solute molecule. The fragment correlation self-energy is then computed for each solvation shell and plotted as a function of the distance. At the GW level, the density–density interactions between solute and solvent represent the direct screening effects from the solvent environment. These dynamical and nonlocal interactions are found to vanish at ∼9 Å, and the decaying

pattern is insensitive to the change of solvent. The 9 Å cutoff distance is interpreted as an effective interacting radius, within which the average energy shift per solvent molecule is found proportional to the macroscopic solvent polarizability.

In solid-state or consensed-phase systems, dynamical screening accounts for a large portion of electron–electron correlation. However, in molecular systems with low charge density, higher order couplings than density–density interactions can be essential to describe quasiparticle excitations. Chapter 9 benchmarks the established $G_0W_0^{\text{tc}}\Gamma_{\text{X}}$[10] approach with respect to a nearly full CI method on the molecular photoemssion spectra. Going beyond GW to density matrix interactions, the vertex corrections are introduced to successfully capture multiquasiparticle interactions induced by a high-energy molecular ionization. These effects are shown as shake-up satellites in the bottom valence region of the spectra. Chapter 10 presents another vertex-corrected approach that is generalized to one-dimensional and two-dimensional periodic systems. The vertex corrections are embedded in the GW correlation self-energy through an electronic active space. This active space consists of single-particle states describing low-energy optical transition for electron–hole pairs. For π-conjugated systems, localized occupied and virtual orbitals, especially π and π^* bonds, are chosen to form the active space. In principle, the active space constructed by π and π^* bonds can be considered complete in dimension due to a finite number of these chemical bonds. Such a completeness is not guaranteed if canonical orbital basis is used. Remarkable and consistent vertex effects are observed on correcting the G_0W_0 gaps of a wide range of donor–acceptor systems. The problem of underesmating the fundamental gap is alleviated by introducing the embedded vertex corrections.

In summary, the research projects completed in this dissertation have extended the application of highly accurate many-body Green's function approach to intriguing systems in chemistry and materials. New ideas have been proposed to treat localized excitations in an arbitrary complex environment, which are supported by partioning the system

with localized orbitals. Developing low-scaling algorithm further facilitates my research progress and enables an ecosystem for simulations, where multi-level methods share the same or a simliar scaling in cost. I believe the physical insight provided in this dissertation is informative and valuable for the community interested in how an environment affect the quasiparticle excitations. I am also confident that the established methods and algorithms will benefit the further development in electronic structure theory.

Bibliography

[1] E. Aprà, E. J. Bylaska, W. A. de Jong, N. Govind, K. Kowalski, T. P. Straatsma, M. Valiev, H. J. J. van Dam, Y. Alexeev, J. Anchell, V. Anisimov, F. W. Aquino, R. Atta-Fynn, J. Autschbach, N. P. Bauman, J. C. Becca, D. E. Bernholdt, K. Bhaskaran-Nair, S. Bogatko, P. Borowski, J. Boschen, J. Brabec, A. Bruner, E. Cauët, Y. Chen, G. N. Chuev, C. J. Cramer, J. Daily, M. J. O. Deegan, T. H. Dunning, M. Dupuis, K. G. Dyall, G. I. Fann, S. A. Fischer, A. Fonari, H. Früchtl, L. Gagliardi, J. Garza, N. Gawande, S. Ghosh, K. Glaesemann, A. W. Götz, J. Hammond, V. Helms, E. D. Hermes, K. Hirao, S. Hirata, M. Jacquelin, L. Jensen, B. G. Johnson, H. Jónsson, R. A. Kendall, M. Klemm, R. Kobayashi, V. Konkov, S. Krishnamoorthy, M. Krishnan, Z. Lin, R. D. Lins, R. J. Littlefield, A. J. Logsdail, K. Lopata, W. Ma, A. V. Marenich, J. Martin del Campo, D. Mejia-Rodriguez, J. E. Moore, J. M. Mullin, T. Nakajima, D. R. Nascimento, J. A. Nichols, P. J. Nichols, J. Nieplocha, A. Otero-de-la Roza, B. Palmer, A. Panyala, T. Pirojsirikul, B. Peng, R. Peverati, J. Pittner, L. Pollack, R. M. Richard, P. Sadayappan, G. C. Schatz, W. A. Shelton, D. W. Silverstein, D. M. A. Smith, T. A. Soares, D. Song, M. Swart, H. L. Taylor, G. S. Thomas, V. Tipparaju, D. G. Truhlar, K. Tsemekhman, T. Van Voorhis, Á. Vázquez-Mayagoitia, P. Verma, O. Villa, A. Vishnu, K. D. Vogiatzis, D. Wang, J. H. Weare, M. J. Williamson, T. L. Windus, K. Woliński, A. T. Wong, Q. Wu, C. Yang, Q. Yu, M. Zacharias, Z. Zhang, Y. Zhao, and R. J. Harrison, *Nwchem: Past, present, and future*, *The Journal of Chemical Physics* **152** (2020), no. 18 184102.

[2] P. Giannozzi, S. Baroni, N. Bonini, M. Calandra, R. Car, C. Cavazzoni, D. Ceresoli, G. L. Chiarotti, M. Cococcioni, I. Dabo, A. D. Corso, S. de Gironcoli, S. Fabris, G. Fratesi, R. Gebauer, U. Gerstmann, C. Gougoussis, A. Kokalj, M. Lazzeri, L. Martin-Samos, N. Marzari, F. Mauri, R. Mazzarello, S. Paolini, A. Pasquarello, L. Paulatto, C. Sbraccia, S. Scandolo, G. Sclauzero, A. P. Seitsonen, A. Smogunov, P. Umari, and R. M. Wentzcovitch, *QUANTUM ESPRESSO: a modular and open-source software project for quantum simulations of materials*, *Journal of Physics: Condensed Matter* **21** (2009), no. 39 395502.

[3] P. Giannozzi, O. Andreussi, T. Brumme, O. Bunau, M. B. Nardelli, M. Calandra, R. Car, C. Cavazzoni, D. Ceresoli, M. Cococcioni, N. Colonna, I. Carnimeo, A. D. Corso, S. de Gironcoli, P. Delugas, R. A. DiStasio, A. Ferretti, A. Floris, G. Fratesi,

G. Fugallo, R. Gebauer, U. Gerstmann, F. Giustino, T. Gorni, J. Jia, M. Kawamura, H.-Y. Ko, A. Kokalj, E. Küçükbenli, M. Lazzeri, M. Marsili, N. Marzari, F. Mauri, N. L. Nguyen, H.-V. Nguyen, A. O. de-la Roza, L. Paulatto, S. Poncé, D. Rocca, R. Sabatini, B. Santra, M. Schlipf, A. P. Seitsonen, A. Smogunov, I. Timrov, T. Thonhauser, P. Umari, N. Vast, X. Wu, and S. Baroni, *Advanced capabilities for materials modelling with quantum ESPRESSO*, *Journal of Physics: Condensed Matter* **29** (2017), no. 46 465901.

[4] H. J. C. Berendsen, D. van der Spoel, and R. van Drunen, *Gromacs: A message-passing parallel molecular dynamics implementation*, *Computer Physics Communications* **91** (1995), no. 1 43–56.

[5] P. Hohenberg and W. Kohn, *Inhomogeneous electron gas*, *Physical Review* **136** (1964), no. 3B B864–B871.

[6] W. Kohn and L. J. Sham, *Self-consistent equations including exchange and correlation effects*, *Physical Review* **140** (1965), no. 4A A1133–A1138.

[7] J. P. Perdew, K. Burke, and M. Ernzerhof, *Generalized gradient approximation made simple*, *Phys. Rev. Lett.* **77** (1996) 3865–3868.

[8] D. Neuhauser, Y. Gao, C. Arntsen, C. Karshenas, E. Rabani, and R. Baer, *Breaking the theoretical scaling limit for predicting quasiparticle energies: The stochastic GW approach*, *Physical Review Letters* **113** (2014), no. 7 076402.

[9] V. Vlček, W. Li, R. Baer, E. Rabani, and D. Neuhauser, *Swift GW beyond 10,000 electrons using sparse stochastic compression*, *Physical Review B* **98** (2018), no. 7 075107.

[10] V. Vlček, *Stochastic vertex corrections: Linear scaling methods for accurate quasiparticle energies*, *Journal of Chemical Theory and Computation* **15** (2019), no. 11 6254–6266.

[11] G. Knizia, *Intrinsic atomic orbitals: An unbiased bridge between quantum theory and chemical concepts*, *Journal of Chemical Theory and Computation* **9** (2013), no. 11 4834–4843. PMID: 26583402.

[12] S. Lehtola and H. Jónsson, *Pipek–mezey orbital localization using various partial charge estimates*, *Journal of Chemical Theory and Computation* **10** (2014), no. 2 642–649.

[13] M. Romanova, G. Weng, A. Apelian, and V. Vlcek, *Dynamical downfolding for localized quantum states*, *arXiv preprint arXiv:2211.05966* (2022).

Appendix A

Supporting information for "Quasiparticles and Band Structures in Organized Nanostructures of Donor−Acceptor Copolymers"

Guorong Weng, Vojtěch Vlček

A.1 Computational details

A.1.1 Geometries

Each polymer is considered to be straight and infinitely periodic. For D-A copolymers, the conventional alkyl groups attached to the fluorene unit are replaced with hydrogen atoms for computational convenience. The geometry and lattice constans of each periodic system are fully relaxed by employing Quantum-Espresso package [1, 2] with Kohn-Sham density functional theory (DFT) within the generalized gradient approximation (GGA)

[3] combined with Tkachenko-Scheffler treatment of the van der Waals interactions.[4] The lattice parameters of rectangular cells used throughout this study are summarized in Table A.1 together with the k–point meshes used to sample the Brillouin zones. In the optimization, π-π stacking without displacement is energetically the most favorable; the structures are illustrated in Figure A.1.

system	lattice constants			k-point
	a [Å]	b [Å]	c [Å]	mesh
1D FBT	12.774	-	-	4×1×1
2D FBT	12.759	3.836	-	1×4×1
3D FBT	12.759	3.802	7.109	4×4×4
1D FB-Ox	12.774	-	-	4×1×1
1D FB-Se	12.774	-	-	4×1×1

Table A.1: Lattice constants of various systems of interest and the k-point meshes for geometry optimization used in the Quantum-Espresso package.

A.1.2 Electronic structure and excitation energies

The many-body calculations are performed on polymer geometries obtained from first-principles structural optimizations with 0D, 1D, 2D, and 3D periodic boundary conditions.[5] The details of the structural relaxation are provided the previous section. The QP energies are obtained from perturbation theory using the Kohn-Sham density functional theory (DFT) with generalized gradient approximation as a starting point. The DFT step was performed using supercells that correspond to the k-point meshes in Table A.1; the supercells are illustrated in Figure A.1. The parameters of our DFT calculations are in Table A.2&A.3. From the DFT step, we obtain a set of eigenvalues

$\left\{\varepsilon^{\mathrm{KS}}\right\}$ and corresponding eigenstates $\{\phi\}$. The quasiparticle energies are computed as

$$\varepsilon = \varepsilon^{\mathrm{KS}} + \left\langle \phi \middle| \hat{\Sigma}(\omega = \varepsilon) - \hat{v}_{xc} \middle| \phi \right\rangle \tag{A.1}$$

where v_{xc} is the mean-field exchange-correlation potential and $\Sigma(\omega)$ is the dynamical and non-local self-energy operator. In the space-time domain (represented by coordinates $1 \equiv (r_1, t_1)$, the self-energy is approximated as [6]

$$\Sigma(1,2) = iG_0(1,2)W_0(1,2^+) \tag{A.2}$$

where G is the KS Green's function, W is the screened Coulomb interaction computed within the random-phase approximation, and 2^+ is infinitesimally later than 2.[7] The total self-energy is further decomposed to the static exchange and frequency-dependent correlation contribution. The evaluation of the self-energy employs the stochastic approach in which the expectation value of the self-energy is computed through a randomized sampling of wave functions and stochastic decomposition of quantum mechanical operators.[8, 9, 10] The parameters of the stochastic G_0W_0 calculations are in Table A.4.

For periodic systems, Brillouin-zone unfolding [11, 12, 13, 14, 15] is performed to generate the band structure. Then many-body calculations are performed on LCB, AIB and UCB at the k-points accessible by the choice of the supercell to give QP energies that form QP bands. The exchange and correlation energies are extracted from our GW calculations. The bands structures are interpolated by cubic splines.

System	Grid	Gridpoint Spacing (bohr)	Cutoff (hartree)
1D	482×76×76	dx=0.400664 dy=dz=0.4	26
2D	74×144×480	dx=0.4 dy=0.402778 dz=0.401852	26
3D	244×72×136	dx=0.395264 dy=0.399167 dz=0.395112	26
single molecule	76×76×50 (F) 80×50×56 (BT) 56×90×96 (FBT)	0.4	28

Table A.2: Setups in the DFT calculations of all systems containing F and BT. Note: The system is periodic in x direction in 1D calculations but in y and z directions in 2D calculations.

System	Grid	Grid Spacing (bohr)	Cutoff (hartree)
1D fluorene	320×76×76	dx=0.397250 dy=dz=0.4	26
O-substituted 1D strand	482×74×74	dx=0.400664 dy=dz=0.4	26
Se-substituted 1D strand	482×74×74	dx=0.400664 dy=dz=0.4	26
1D polyacetylene	126×100×100	dx=0.298107 dx=dz=0.3	26
1D polyethylene	130×100×100	dx=0.297060 dy=dz=0.3	26

Table A.3: Setups in the DFT calculations of the other systems.

Parameter	Value
plane wave cut-off (hartree)	26/28 (same in DFT calculations)
number of random vectors used for sparse stochastic compression	20000
number of random vectors characterizing the screened Coulomb interaction (per each vector sampling the Green's function)	15
number of vectors sampling the Green's function	1000
maximum time for real-time propagation of the dynamical self-energy	50 a.u.

Table A.4: Setups in the GW calculations of all systems.

A.2 Supplementary figures and tables

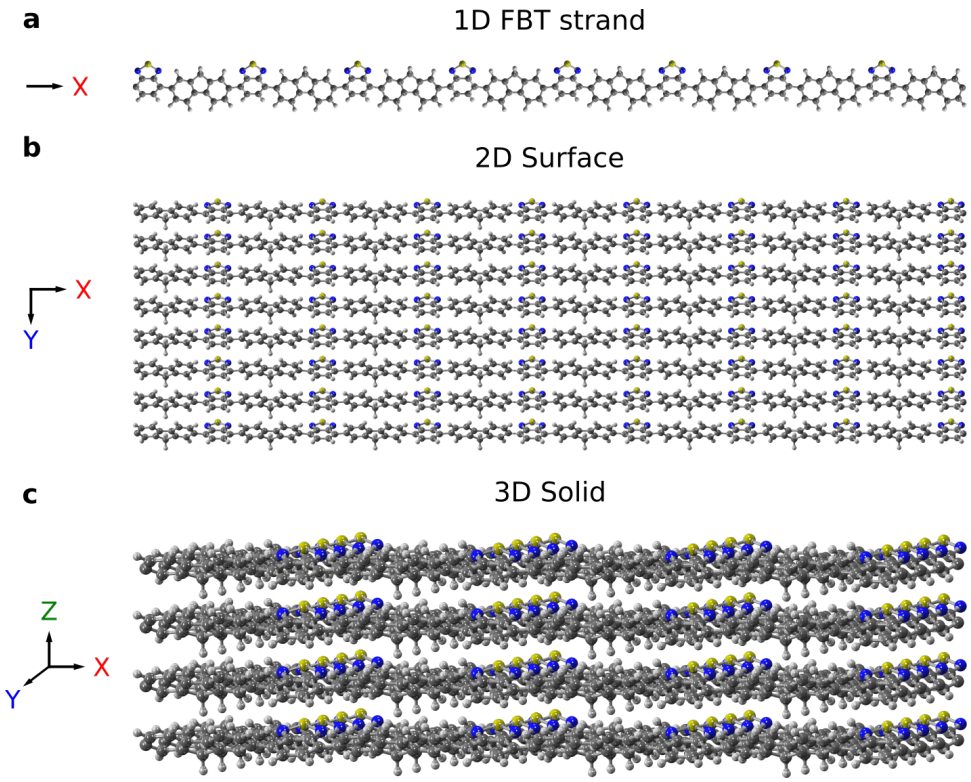

Figure A.1: The supercells of periodic systems in our DFT and GW calculations. (a) A supercell of the 1D system containing 8 repeated units in the periodic direction, the polymer axis which is defined as the X direction. (b) An 8×8 supercell of the 2D system that is periodic in two directions. The X direction is defined as in 1D and the Y axis denotes the polymer π-π stacking direction. (c) A 4×4×4 supercell of the 3D system that is periodic in three directions. The X and Y directions are defined as in 2D. The Z direction the edge-to-edge stacking direction.

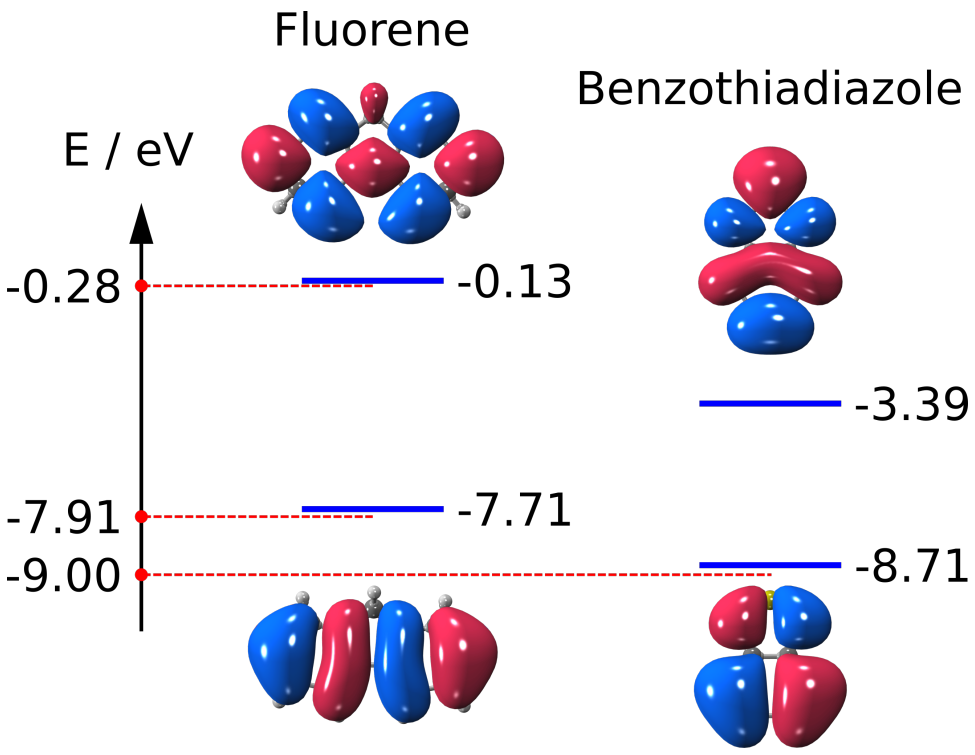

Figure A.2: Charge excitation energies, the highest occupied molecular orbitals (HOMO), and lowest unoccupied orbitals (LUMO) of the fluorene unit and the benzothiadiazole unit, respectively. Red and blue colors distinguish the wave function phase. The computed results are from the GW MB calculations, while the experimental results are available from the NIST database as indicated by the red dots on the energy axis.

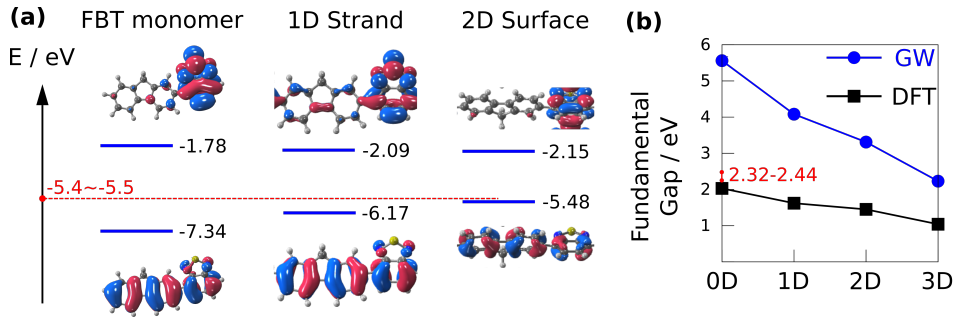

Figure A.3: Calculated QP energies and fundamental gaps of different systems. (a) Ionization potentials and electron affinities computed from GW for the FBT monomer, 1D FBT strand, and 2D FBT surface. The plotted frontier orbitals show that in the periodic systems, the valence band maximum state inherits the delocalized characteristic from the HOMO of the monomer and the conduction minimum state inherits the localized feature from the LUMO. Red and blue colors distinguish the wave function phase. (b) The fundamental gap as a function of the dimensionality of the system. Both the DFT gap and QP gap collapse as the system evolves from 0D (monomer) to 3D, while the QP gap shows a much more responsive contraction with respects to the system's topology. The red dots on the axes are available experimental results.[16]

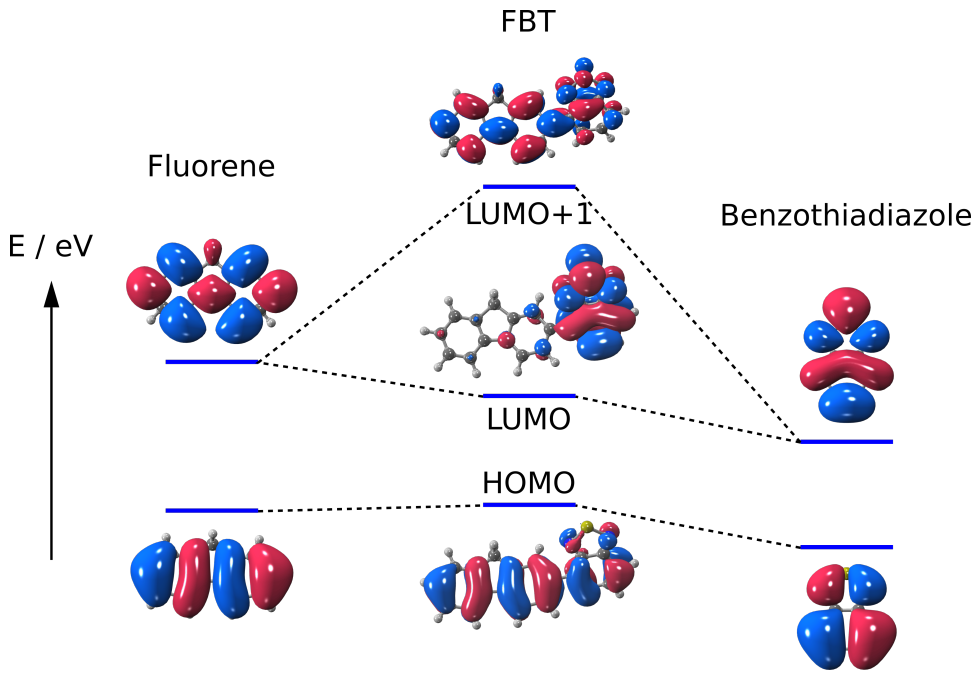

Figure A.4: Formations of molecular orbitals of the FBT monomers from the donor and the acceptor units. Red and blue colors distinguish the wave function phase. The FBT HOMO retains the delocalized feature of the fluorene and the benzothiadiazole HOMO, which represents the signature of the lower conjugated band (LCB). The FBT LUMO, however, retain the acceptor LUMO only being highly localized on the acceptor unit, which is responsible for the formation of the acceptor impurity band (AIB) in the periodic system. The LUMO+1 behaves similarly to the HOMO, accounting for the formation of the upper conjugated band (UCB).

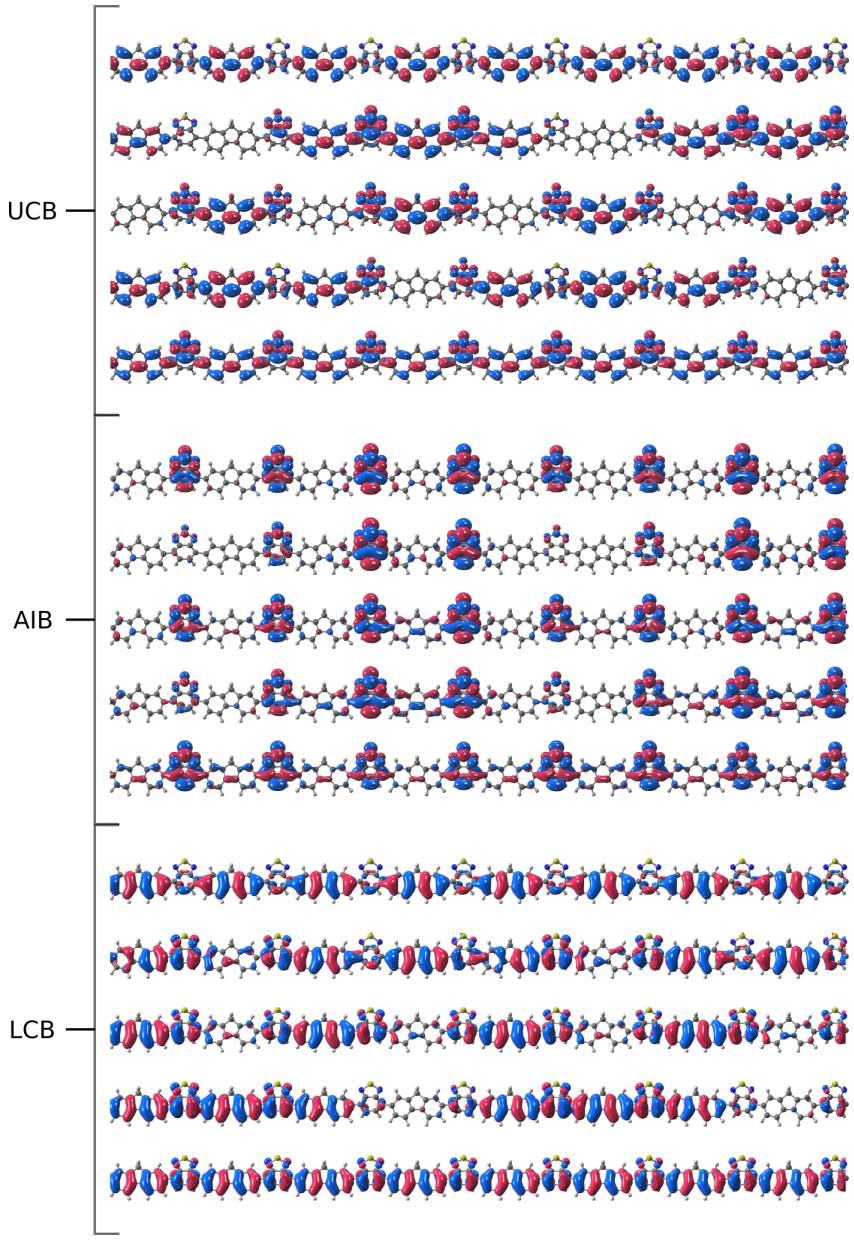

Figure A.5: Selected orbitals from the bands of interest in the 1D FBT system. The periodicity of the orbital correspond to the crystal momentum of the state. Red and blue colors distinguish the wave function phase. The lower block presents 5 states from the LCB and they feature delocalized orbitals along the backbone. The middle block presents 5 states from AIB where the orbitals are highly localized on the acceptor unit regardless the change in periodicity. The upper block presents 5 states from the UCB, which are qualitatively similar to those from LCB (the lower block).

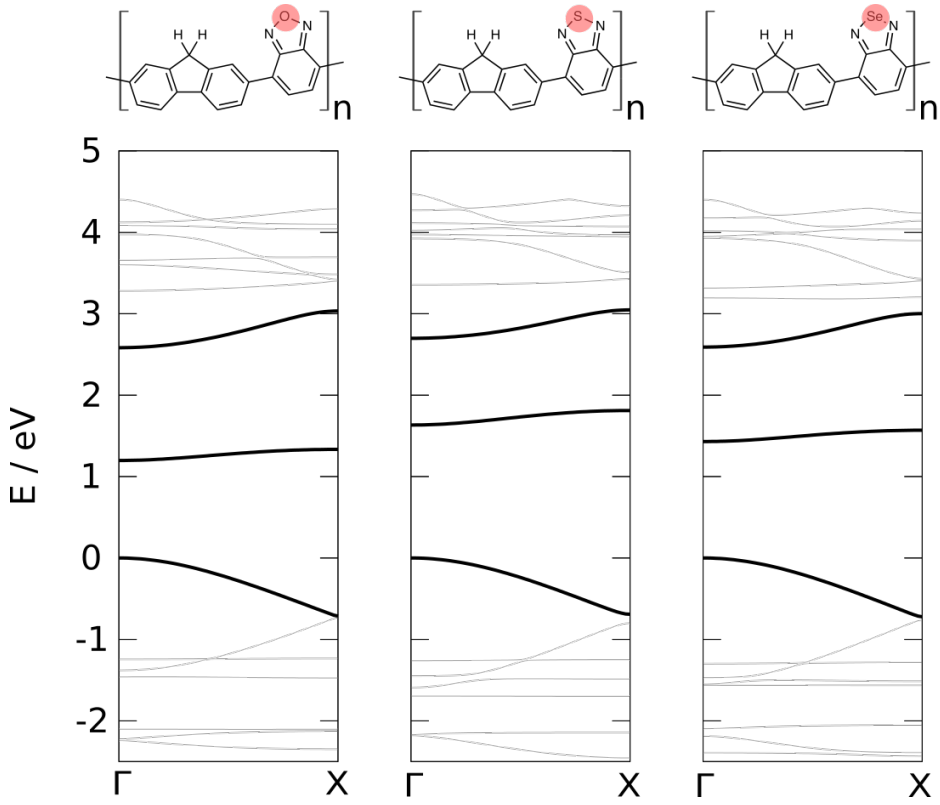

Figure A.6: Band structures of three D-A copolymers that have different heteratoms on the acceptor unit obtained from the Quantum-Espresso package. These three copolymers share very similar geometries (Table A.5). The highlighted bands from the bottom to the top correspond to LCB, AIB, and UCB, which shows the presence of AIB regardless of the chemical modifications (highlighted in the chemical structures) on the acceptor.[17]

system	torsion angle (°)		C-to-C distance (Å)	
	ϕ_1	ϕ_2	d_1	d_2
FBOX	41.80	43.05	1.467	1.466
FBT	42.37	43.92	1.470	1.471
FBSE	41.68	42.75	1.471	1.471

Table A.5: Torsion angles and C-to-C distances between the fluorene unit and three different acceptor units.

Decomposition	Contribution (meV)	
single-electron interactions	-249	
classical Coulomb interactions	1227	
exchange-correlation	-292 (mean-field)	-120 (non-local)
total bandwidth	686 (DFT)	858 (GW)

Table A.6: Individual contribution to the LCB width of 1D FBT.

system	VBW GW/DFT (meV)		
	x	y	z
1D chain	858±(38)/686	-	-
2D surface	363±(26)/393	626±(24)/625	-
3D solid	588±(33)/533	711±(32)/661	43±(32)/23

Table A.7: Valence bandwidths (VBW) of different FBT systems in each periodic direction by DFT and GW.

system	CBW GW/DFT (meV)		
	x	y	z
1D chain	265±(46)/182	-	-
2D surface	142±(29)/111	115±(32)/55	-
3D solid	164±(34)/143	123±(35)/132	302±(33)/256

Table A.8: Conduction bandwidths (CBW) of different FBT systems in each periodic direction by DFT and GW.

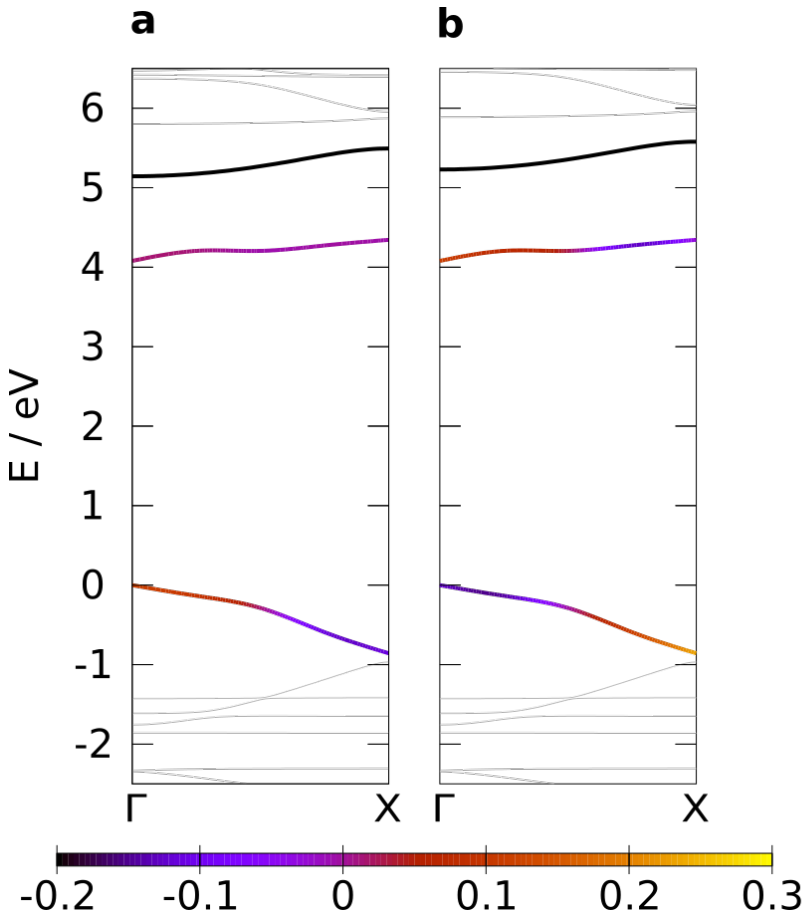

Figure A.7: Band structures with exchange and correlation energies of the 1D FBT system. Exchange and correlation energies are plotted relative to the band average. The Γ to X portion stands for the transport in the polymer direction. (a) The QP energy and exchange energy are plotted as a function of the crystal momentum for the highlighted lower and middle bands (colored). UCB is plotted in black. In LCB, the exchange grows more and more negative going from the Γ point to the X point due to the increase in orbital overlaps, which indicates the exchange interactions broaden the valence bandwidth in the conjugated direction. In AIB, however, the exchange energy is almost insensitive to the change in states due to the fact that all the orbitals are highly localized. (b) The QP energy and correlation energy are plotted as a function of the crystal momentum for the highlighted lower and middle bands (colored). UCB is plotted in black. In both LCB and AIB, the correlation energy suppresses the bandwidth due to the fact that the higher the QP energy, the more negative the correlation energy (Figure A.8).

system	Exchange energy (eV)		Difference (meV)
	Center state	Boundary state	
1D PAE	-14.59	-16.65	2069
1D PEE	-19.77	-19.41	-363

Table A.9: The exchange energies of the states at the Brillouin center and boundary of the highest valence bands for 1D polyacetylene and polyethylene systems.

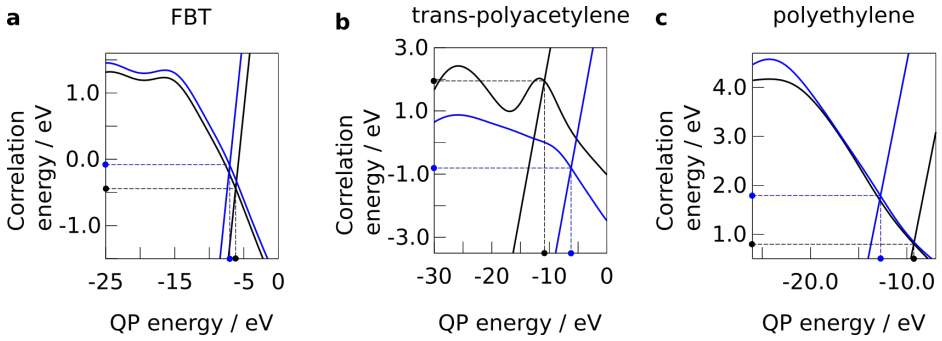

Figure A.8: Correlation energy plotted as a function of the QP energy of the Γ state (black) and the X state (blue) for systems: (a) 1D FBT strand, (b) 1D trans-polyacetylene, and (c) 1D polyethylene. The intersection between the curve and the straight line of the same color represents both the QP energy (x-coordinate) and the correlation energy (y-coordinate). All systems show the same rule that the correlation energy increases as the QP energy decreases.

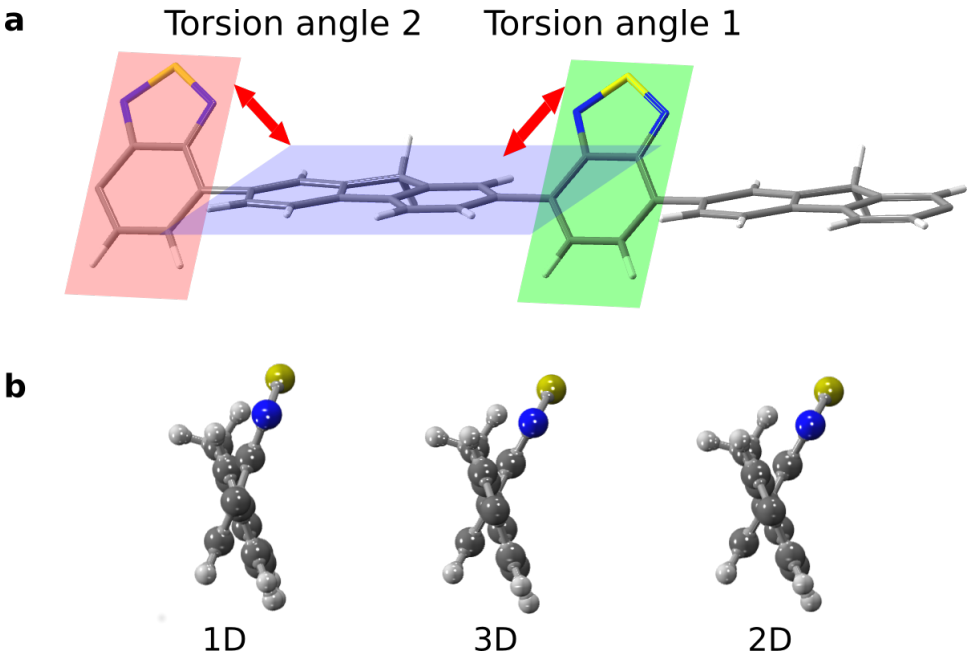

Figure A.9: Molecular geometries of FBT single strands optimized in periodic systems with different dimensionalities. (a) The donor subunit and the acceptor subunit retain a rigid planar structure with unaltered bond lengths and bond angles in three systems. The main geometrical difference among the single strands is the torsion angles, ϕ_1 and ϕ_2, between the donor and the acceptor, which are slightly different from each other (Table A.10). (b) The average torsion angle $(\phi_1+\phi_2)/2$ of the single strands from the optimized 1D, 3D, and 2D system in the order of the magnitude being 43°, 49°, and 56°.

system	torsion angle (°)		
	ϕ_1	ϕ_2	average
strand of 1D chain	42.37	43.92	43
strand from 3D solid	49.79	49.36	49
strand from 2D surface	55.67	56.16	56

Table A.10: Torsion angles between the fluorene unit and the benzothiadiazole unit in three FBT systems.

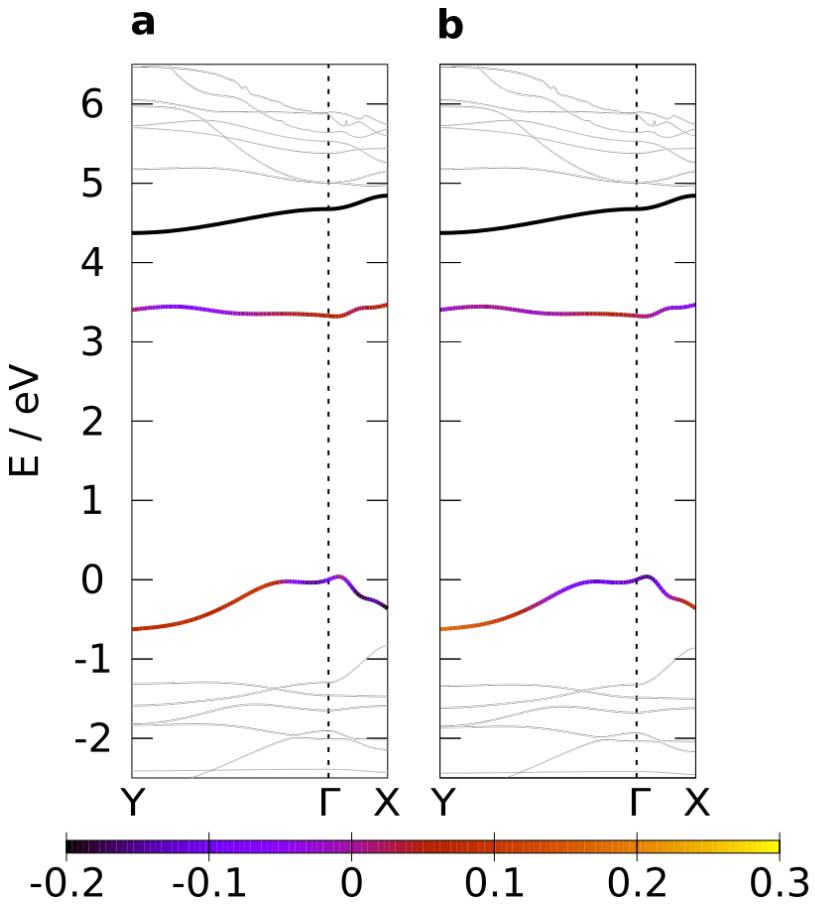

Figure A.10: Band structures with exchange and correlation energies of the 2D FBT system. Exchange and correlation energies are plotted relative to the band average. The Γ to Y portion stands for the transport in the polymer π-π stacking direction while the Γ to X portion stands for the transport along the polymer backbone. (a) The QP energy and exchange energy are plotted as a function of the crystal momentum for the highlighted lower and middle bands (colored). UCB is plotted in black. In the polymer direction, the exchange causes the same effects as found in the 1D system, while in the π-π stacking direction, the exchange behave oppositely. The exchange suppresses the both AIB and LCB widths. (b) The QP energy and correlation energy are plotted as a function of the crystal momentum for the highlighted lower and middle bands (colored). UCB is plotted in black.In both AIB and LCB and both directions, the correlation suppresses the widths due to the fact that the correlation energy increases as the QP energy decreases (Figure A.8).

supercell size	HOMO (eV)		Transport gap (eV)	
	DFT	GW	DFT	GW
2×2×1	-4.51	-5.12±(0.03)	1.52	3.02±(0.05)
4×4×1	-4.53	-5.52±(0.03)	1.52	3.34±(0.04)
6×6×1	-4.54	-5.45±(0.02)	1.45	3.31±(0.04)
interactions 8×8×1	-4.54	-5.48±(0.02)	1.52	3.33±(0.03)

Table A.11: Convergence of HOMO energy levels and transport gaps to the supercell size in 2D calculations.

Bibliography

[1] P. Giannozzi, S. Baroni, N. Bonini, M. Calandra, R. Car, C. Cavazzoni, D. Ceresoli, G. L. Chiarotti, M. Cococcioni, I. Dabo, A. D. Corso, S. de Gironcoli, S. Fabris, G. Fratesi, R. Gebauer, U. Gerstmann, C. Gougoussis, A. Kokalj, M. Lazzeri, L. Martin-Samos, N. Marzari, F. Mauri, R. Mazzarello, S. Paolini, A. Pasquarello, L. Paulatto, C. Sbraccia, S. Scandolo, G. Sclauzero, A. P. Seitsonen, A. Smogunov, P. Umari, and R. M. Wentzcovitch, *QUANTUM ESPRESSO: a modular and open-source software project for quantum simulations of materials*, *Journal of Physics: Condensed Matter* **21** (2009), no. 39 395502.

[2] P. Giannozzi, O. Andreussi, T. Brumme, O. Bunau, M. B. Nardelli, M. Calandra, R. Car, C. Cavazzoni, D. Ceresoli, M. Cococcioni, N. Colonna, I. Carnimeo, A. D. Corso, S. de Gironcoli, P. Delugas, R. A. DiStasio, A. Ferretti, A. Floris, G. Fratesi, G. Fugallo, R. Gebauer, U. Gerstmann, F. Giustino, T. Gorni, J. Jia, M. Kawamura, H.-Y. Ko, A. Kokalj, E. Küçükbenli, M. Lazzeri, M. Marsili, N. Marzari, F. Mauri, N. L. Nguyen, H.-V. Nguyen, A. O. de-la Roza, L. Paulatto, S. Poncé, D. Rocca, R. Sabatini, B. Santra, M. Schlipf, A. P. Seitsonen, A. Smogunov, I. Timrov, T. Thonhauser, P. Umari, N. Vast, X. Wu, and S. Baroni, *Advanced capabilities for materials modelling with quantum ESPRESSO*, *Journal of Physics: Condensed Matter* **29** (2017), no. 46 465901.

[3] J. P. Perdew, K. Burke, and M. Ernzerhof, *Generalized gradient approximation made simple*, *Phys. Rev. Lett.* **77** (1996) 3865–3868.

[4] A. Tkatchenko and M. Scheffler, *Accurate molecular van der waals interactions from ground-state electron density and free-atom reference data*, *Phys. Rev. Lett.* **102** (2009) 073005.

[5] C. A. Rozzi, D. Varsano, A. Marini, E. K. U. Gross, and A. Rubio, *Exact coulomb cutoff technique for supercell calculations*, *Phys. Rev. B* **73** (2006) 205119.

[6] L. Hedin, *New method for calculating the one-particle green's function with application to the electron-gas problem*, *Phys. Rev.* **139** (1965) A796–A823.

[7] R. M. Martin, L. Reining, and D. M. Ceperley, *Interacting Electrons: Theory and Computational Approaches*. Cambridge University Press, 2016.

[8] D. Neuhauser, Y. Gao, C. Arntsen, C. Karshenas, E. Rabani, and R. Baer, *Breaking the theoretical scaling limit for predicting quasiparticle energies: The stochastic gw approach*, *Phys. Rev. Lett.* **113** (2014) 076402.

[9] V. Vlček, W. Li, R. Baer, E. Rabani, and D. Neuhauser, *Swift gw beyond 10,000 electrons using sparse stochastic compression*, *Phys. Rev. B* **98** (2018) 075107.

[10] V. Vlček, *Stochastic vertex corrections: Linear scaling methods for accurate quasiparticle energies*, *Journal of Chemical Theory and Computation* **15** (2019), no. 11 6254–6266.

[11] V. Popescu and A. Zunger, *Extracting e versus $\vec{k}$ effective band structure from supercell calculations on alloys and impurities*, *Physical Review B* **85** (2012), no. 8 085201.

[12] H. Huang, F. Zheng, P. Zhang, J. Wu, B.-L. Gu, and W. Duan, *A general group theoretical method to unfold band structures and its application*, *New Journal of Physics* **16** (2014), no. 3 033034.

[13] T. B. Boykin and G. Klimeck, *Practical application of zone-folding concepts in tight-binding calculations*, *Phys. Rev. B* **71** (2005) 115215.

[14] T. B. Boykin, N. Kharche, G. Klimeck, and M. Korkusinski, *Approximate bandstructures of semiconductor alloys from tight-binding supercell calculations*, *Journal of Physics: Condensed Matter* **19** (2007), no. 3 036203.

[15] J. Brooks, G. Weng, S. Taylor, and V. Vlček, *Stochastic many-body perturbation theory for moiré states in twisted bilayer phosphorene*, *Journal of Physics: Condensed Matter* (2020).

[16] C.-K. Mai, B. Russ, S. L. Fronk, N. Hu, M. B. Chan-Park, J. J. Urban, R. A. Segalman, M. L. Chabinyc, and G. C. Bazan, *Varying the ionic functionalities of conjugated polyelectrolytes leads to both p- and n-type carbon nanotube composites for flexible thermoelectrics*, *Energy & Environmental Science* **8** (2015), no. 8 2341–2346.

[17] M. H. Chua, Q. Zhu, T. Tang, K. W. Shah, and J. Xu, *Diversity of electron acceptor groups in donor-acceptor type electrochromic conjugated polymers*, *Solar Energy Materials and Solar Cells* **197** (2019) 32–75.

Appendix B

Supporting information for "Reduced Scaling of Optimal Regional Orbital Localization via Sequential Exhaustion of the Single-Particle Space"

Guorong Weng, Mariya Romanova, Arsineh Apelian,[a] Hanbin Song,[b] Vojtěch Vlček

B.1 Downfolded effective Hamiltonian

In large systems with a certain anisotropy (defects in semiconductors, molecules in solvent environments) all physical phenomena can be attributed to a small active space embedded in a host environment. Thus, it is common to map the problem onto the

[a]Department of Materials, University of California, Santa Barbara, CA 93106, USA
[b]Current institution: University of California, Berkeley, Berkeley, CA 94720, USA

effective Hamiltonian, defined within an active space.

$$\begin{aligned}\hat{H} = &\sum_{i\sigma} \varepsilon_i \hat{c}^{\dagger}_{i\sigma}\hat{c}_{i\sigma} - \sum_{i\neq j,\sigma} t_{ij}\hat{c}^{\dagger}_{i\sigma}\hat{c}_{j\sigma} \\ &+ \sum_{i\sigma} U\hat{n}^{\dagger}_{i\uparrow}\hat{n}_{i\downarrow} + \sum_{i>j,\sigma,\sigma'} V\hat{n}^{\dagger}_{i\sigma}\hat{n}_{j\sigma'}\end{aligned} \tag{B.1}$$

where $\hat{c}^{\dagger}_{i\sigma}$ and $\hat{c}_{i,\sigma}$ are creation and annihilation operators in site i with spin σ and $\hat{n}^{\dagger}_{i\sigma}$ is a particle number operator. The ε_i, t_{ij} are the on-site and hopping energies.

We extract the Hamiltonian parameters ε, t U_i and V_{ij} from the first-principles calculations employing large supercells. To compute the onsite and hopping parameters we calculate the integral containing kinetic and ionic potential terms:

$$\begin{aligned}\varepsilon_i &= \int \varphi^*_i(\mathbf{r})[-\frac{1}{2}\nabla^2 + V^{\text{ion}}]\varphi_i(\mathbf{r})d\mathbf{r} \\ t_{ij,i\neq j} &= \int \varphi^*_i(\mathbf{r})[-\frac{1}{2}\nabla^2 + V^{\text{ion}}]\varphi_j(\mathbf{r})d\mathbf{r}\end{aligned} \tag{B.2}$$

The U_i represents Coulomb on-site interactions of electrons with a different spin, while V_{ij} is the Coulomb inter-site interaction, which we compute as:

$$\begin{aligned}U_i &= \int \varphi^*_i(\mathbf{r})\varphi_i(\mathbf{r})V(\mathbf{r},\mathbf{r}')\varphi^*_i(\mathbf{r}')\varphi_i(\mathbf{r}')d\mathbf{r}d\mathbf{r}' \\ V_{ij} &= \int \varphi^*_i(\mathbf{r})\varphi_i(\mathbf{r})V(\mathbf{r},\mathbf{r}')\varphi^*_j(\mathbf{r}')\varphi_j(\mathbf{r}')d\mathbf{r}d\mathbf{r}'\end{aligned} \tag{B.3}$$

where, the $V(\mathbf{r},\mathbf{r}')$ is the bare Coulomb interaction.

Table B.1: Comparison of the excited-state transition energies of the NV^- center in the 511-atom system with various truncated orbital space for the localization.

Symmetry	10 eV	20 eV	full space
$^3E - {}^3A_2$	0.121	1.003	1.556
$^1A_1 - {}^3A_2$	0.156	0.947	1.324
$^1E - {}^3A_2$	0.039	0.259	0.378
$\mathcal{P}'$ (%)	49.5	86.6	100

B.2 Excited states of the NV^- center

Table B.1 shows the excited states of the NV^- center computed in the basis of the Wannier functions that were obtained with different energy windows. The full space energy window is ~ 24 eV below the Fermi energy. One can see that even 20 eV window results in an extremely underestimated result, while for 10 eV window the order of states is reversed. As a measure of the localization we report the value of the objective functional $\mathcal{P}'$ (see main text). The $\mathcal{P}'$ is set to 100% for case where the full space is used in the energy window.

B.3 Preparation of stochastic basis using deterministic eigenstates

The stochastic basis representing the complement (rest) space in our sF-PMWF calculations is prepared in a three-step manner. First, a random vector is constructed in the full space

$$|\zeta_i^m\rangle = \sum_{j=1}^{N_s} \alpha_{ij}^m |\phi_j\rangle \tag{B.4}$$

where m denotes the m^{th} iteration in the outer-loop and $|\phi_j\rangle$ is the eigenstate in the full space. The set of random coefficients $\{\alpha_{ij}^m\}$ are associated with the outer-loop step m,

i.e., a different m corresponds to a different set of coefficients.

The second step is to perform Gram-Schmidt orthogonalization such that the stochastic basis is orthogonal to the core space

$$|\zeta_i^m\rangle = |\zeta_i^m\rangle - \sum_{k=1}^{N_c} \frac{\langle\psi_k^c|\zeta_i^m\rangle}{\langle\psi_k^c|\psi_k^c\rangle} |\psi_k^c\rangle \tag{B.5}$$

where $|\psi_k^c\rangle$ represents the state in the core space. The stochastic basis is then made mutually orthogonal

$$|\zeta_i^m\rangle = |\zeta_i^m\rangle - \sum_{j=1}^{i-1} \frac{\langle\zeta_j^m|\zeta_i^m\rangle}{\langle\zeta_j^m|\zeta_j^m\rangle} |\zeta_j^m\rangle \qquad i \geq 2 \tag{B.6}$$

The last step is to normalize the stochastic basis such that

$$\langle\zeta_i^m|\zeta_j^m\rangle = \delta_{ij} \tag{B.7}$$

and

$$\langle\psi_i^c|\zeta_j^m\rangle = 0. \tag{B.8}$$

After these three steps, the construction of stochastic basis for the m^{th} step is completed and it is ready to enter the work space.

B.4 Supplementary Tables and Figures

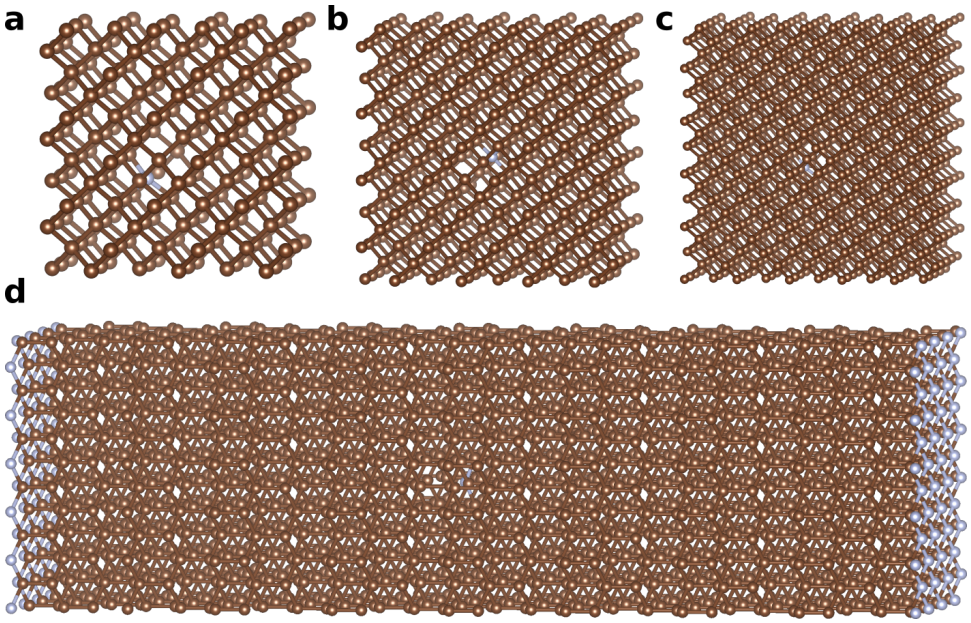

Figure B.1: Chemical structures of the four investigated diamond with NV^- center systems: (a) 215-atom supercell; (b) 511-atom supercell; (c) 999-atom supercell; (d) 2303-atom slab.

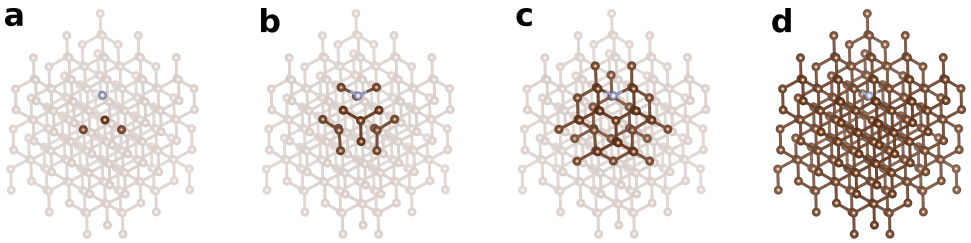

Figure B.2: Composition of the three fragments as well as the all-atom system: (a) 4-atom fragment; (b) 16-atom fragment; (c) 40-atom fragment; (d) all-atom system. The fragments are exemplified using the 215-atom cell while each fragment is found extremely similar around the NV^- center in the other investigated systems.

Table B.2: Comparison of sF-PMWF and F-PMWF with different combinations of N_c and N_r for orbital localization on the 215-atom system

Method	N_c	N_r	N_w	N_b	N_{it}^{outer}	Converged $\mathcal{P}'$	Converged $\mathcal{P}$	$\mathcal{P}'$ after 1st cycle (percentage gained)	t^{outer} (s)	t^{macro} (s)	n^{macro}	Total wall time (s)
F-PMWF	-	-	-	-	1	4.9345	4.6656	-	-	-	-	308
sF-PMWF	16	4	20	104	520	4.9436	4.6656	4.7882 (97%)	0.09	9.07	5	47
sF-PMWF	16	8	24	42	260	4.9436	4.6656	4.8366 (98%)	0.11	5.87	5	31
sF-PMWF	16	16	32	26	156	4.9435	4.6655	4.6533 (94%)	0.17	4.65	6	29
sF-PMWF	16	32	48	13	65	4.9436	4.6656	4.7039 (95%)	0.32	4.19	5	22
sF-PMWF	16	48	64	9	54	4.9436	4.6656	4.6888 (95%)	0.50	4.51	6	28
sF-PMWF	16	64	80	7	35	4.9436	4.6656	4.7348 (96%)	0.73	5.09	5	27
sF-PMWF	24	24	48	17	68	4.9346	4.6656	4.7523 (96%)	0.37	6.31	4	26
sF-PMWF	32	16	48	25	100	4.9346	4.6657	4.8425 (98%)	0.29	7.21	4	30
sF-PMWF	40	8	48	49	245	4.9346	4.6657	4.8868 (99%)	0.29	14.06	5	72
sF-PMWF (stochastic)	16	32	48	-	216	4.9346	4.6656	-	3.47	-	-	729

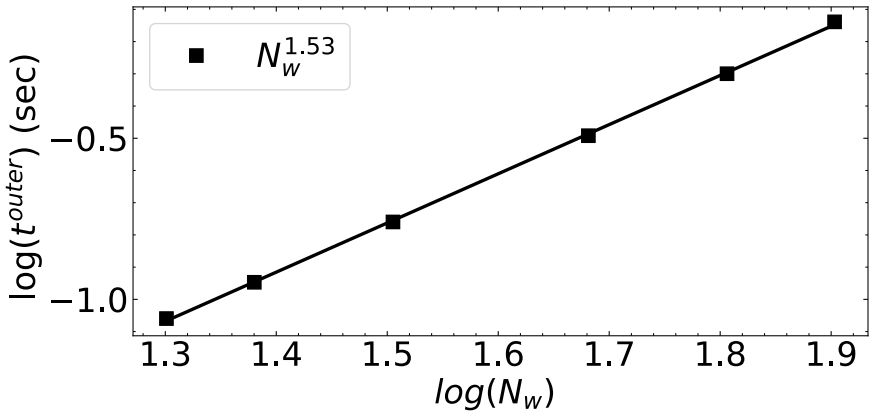

Figure B.3: The log of the time per outer-loop iteration (t^{outer}) as a function of the log of the number of states in the work space (N_w). The scaling of t^{outer} with N_w is derived from the slope of the linear fitting.

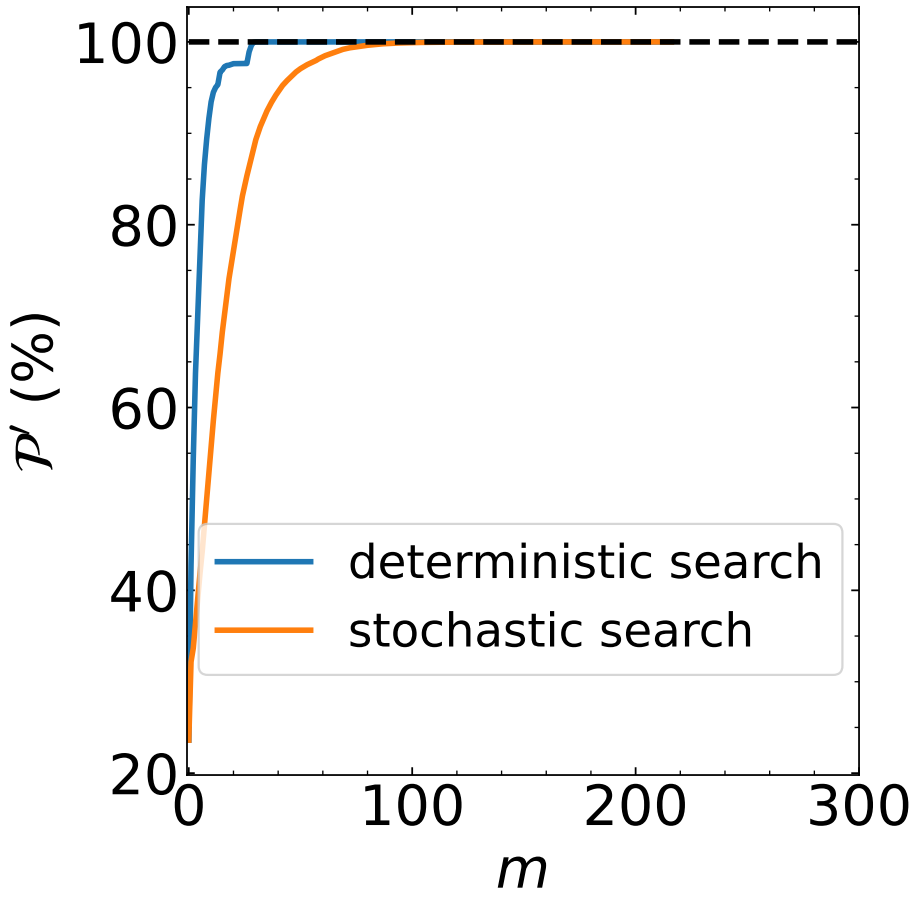

Figure B.4: Convergence of the functional $\mathcal{P}'$ with respect to the outer-loop step m for the NV^- center of the 215-atom system. Blue curve: localization performed with deterministic basis in the rest space. Orange curve: localization performed with stochastic basis in the rest space. The (16,32) combination is employed in both calculations.

Table B.3: Comparison of sF-PMWF and F-PMWF with different combinations of N_c and N_r for orbital localization on the 511-atom system

Method	N_c	N_r	N_w	N_b	N_{it}^{outer}	Converged $\mathcal{P}'$	Converged $\mathcal{P}$	$\mathcal{P}'$ after 1st cycle (percentage gained)	t^{outer} (s)	t^{macro} (s)	n^{macro}	Total wall time (s)
F-PMWF	-	-	-	-	1	4.9222	4.6498	-	-	-	-	7360
sF-PMWF	16	4	20	252	1512	4.9223	4.6498	4.6254 (94%)	0.26	64.97	6	397
sF-PMWF	16	8	24	126	630	4.9223	4.6498	4.6392 (94%)	0.35	44.65	5	230
sF-PMWF	16	16	32	63	315	4.9223	4.6498	4.6074 (94%)	0.53	34.44	5	175
sF-PMWF	16	32	48	21	128	4.9223	4.6498	4.634 (94%)	0.83	26.67	4	114
sF-PMWF	16	48	64	21	126	4.9223	4.6498	4.7189 (96%)	1.12	23.52	6	148
sF-PMWF	24	24	48	42	252	4.9223	4.6498	4.8208 (98%)	0.86	36.75	6	224
sF-PMWF	32	16	48	62	310	4.9223	4.6498	4.8476 (98%)	0.83	51.56	5	265
sF-PMWF	40	8	48	123	738	4.9223	4.6498	4.8791 (99%)	0.83	102.13	6	621

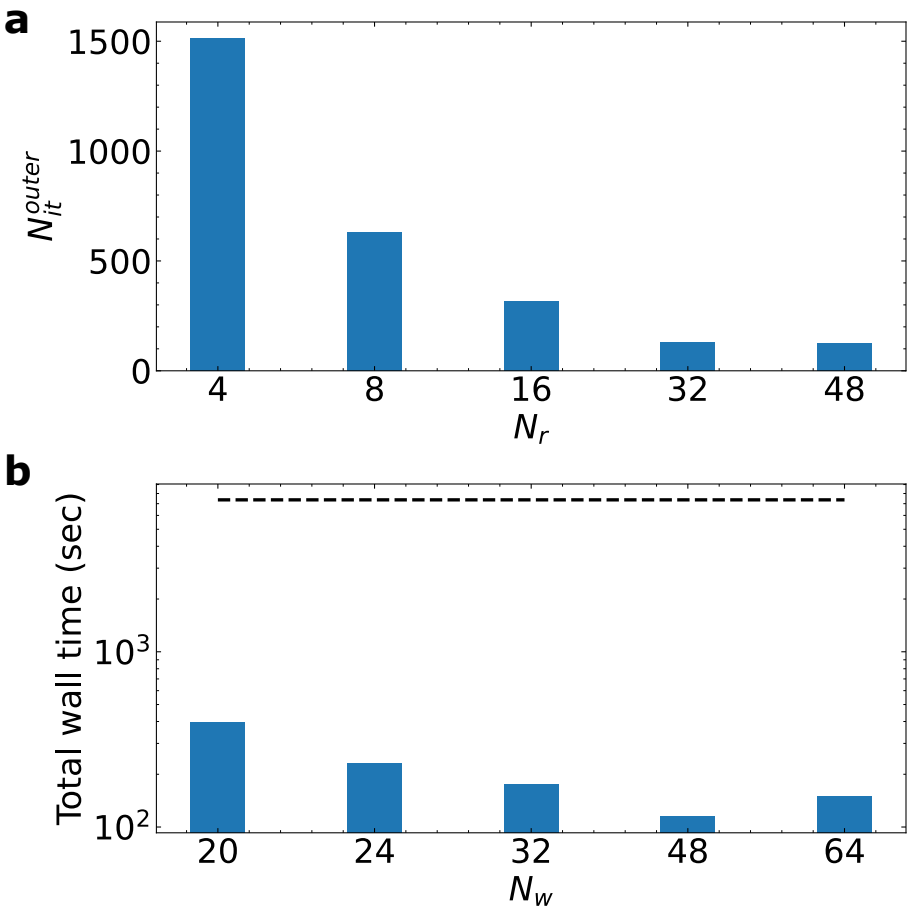

Figure B.5: Investigation of different combinations of N_c and N_r for the localization on the NV^- center of the 511-atom cell. N_c is fixed at 16. (a) Total number of iteration steps in the outer-loop as a function of the N_r. (b) Total wall time of the calculation as a function of N_w. Dashed line indicates the total wall time from the F-PMWF method using the full orbital space.

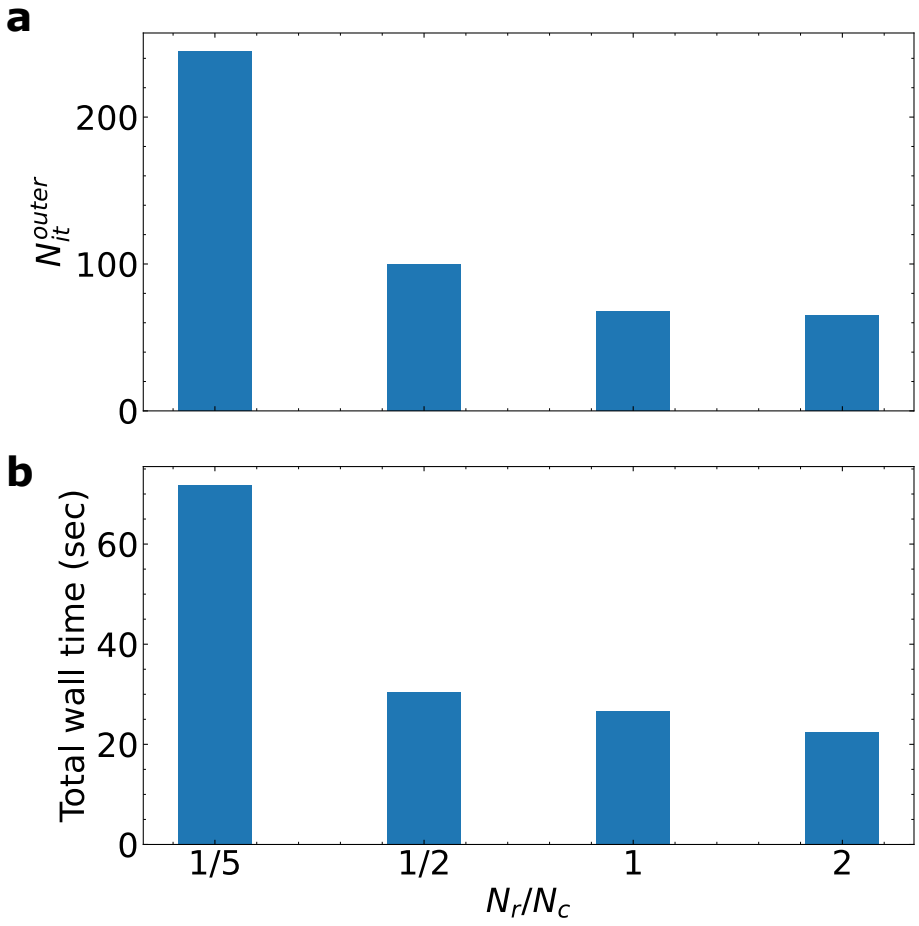

Figure B.6: Investigation of different combinations of N_c and N_r for the localization on the NV^- center of the 511-atom cell. N_w is fixed at 48. (a) Total number of iteration steps in the outer-loop as a function of the N_r/N_c ratio; (b) The total wall time as a function of the N_r/N_c ratio.

Table B.4: Comparison of sF-PMWF and F-PMWF with different combinations of N_c and N_r for orbital localization on the 999-atom system

Method	N_c	N_r	N_w	N_b	N_{it}^{outer}	Converged $\mathcal{P}'$	Converged $\mathcal{P}$	$\mathcal{P}'$ after 1st cycle (percentage gained)	t^{outer} (s)	t^{macro} (s)	n^{macro}	Total wall time (s)
F-PMWF	-	-	-	-	1	4.9194	4.6447	-	-	-	-	42006
sF-PMWF	16	16	32	124	620	4.9194	4.6446	4.6175 (94%)	0.89	109.89	5	575
sF-PMWF	16	32	48	62	310	4.9194	4.6446	4.6089 (94%)	1.50	92.81	5	489
sF-PMWF	16	48	64	42	210	4.9195	4.6446	4.0349 (82%)	2.22	93.47	5	493
sF-PMWF (stochastic)	16	32	48	-	999	4.9194	4.6446	-	23.78	-	-	24172

Table B.5: Comparison of sF-PMWF and F-PMWF with different combinations of N_c and N_r for orbital localization on the 2303-atom slab system

Method	N_c	N_r	N_w	N_b	N_{it}^{outer}	Converged $\mathcal{P}'$	Converged $\mathcal{P}$	$\mathcal{P}'$ after 1st cycle (percentage gained)	t^{outer} (s)	t^{macro} (s)	n^{macro}	Total wall time (s)
F-PMWF	-	-	-	-	1	4.9414	4.6731	-	-	-	-	695370
sF-PMWF	16	16	32	290	1740	4.9414	4.6731	3.7145 (75%)	1.11	333.03	6	2644
sF-PMWF	16	32	48	145	870	4.9414	4.6731	3.6976 (75%)	1.84	266.02	6	1683
sF-PMWF	16	48	64	97	582	4.9414	4.6731	3.8859 (79%)	2.50	241.98	6	1538

Table B.6: Time spent on the folding and unfolding steps of the four investigated systems. The unfolding step of each calculation employs the (16,32) combination.

System	Time (s)	
	Folding step	Unfolding step
215-atom cell	22	0.52
511-atom cell	114	1.85
999-atom cell	489	6.90
slab	1683	17.79

Table B.7: Information of the four investigated systems as well as the time and normalized time per outer-loop iteration and per macro-cycle.

System	N_e	N_s	N_g	t^{outer} (s)	t_n^{outer} (s)	t^{macro} (s)	t_n^{macro} (s)	n^{macro}
215-atom cell	864	432	314432	0.32	1.99	4.19	25.83	5
511-atom cell	2048	1024	778688	0.83	2.08	26.67	66.45	4
999-atom cell	4000	2000	1404928	1.50	2.07	92.81	128.16	5
slab	9312	4656	1940120	1.89	1.89	266.02	266.02	6

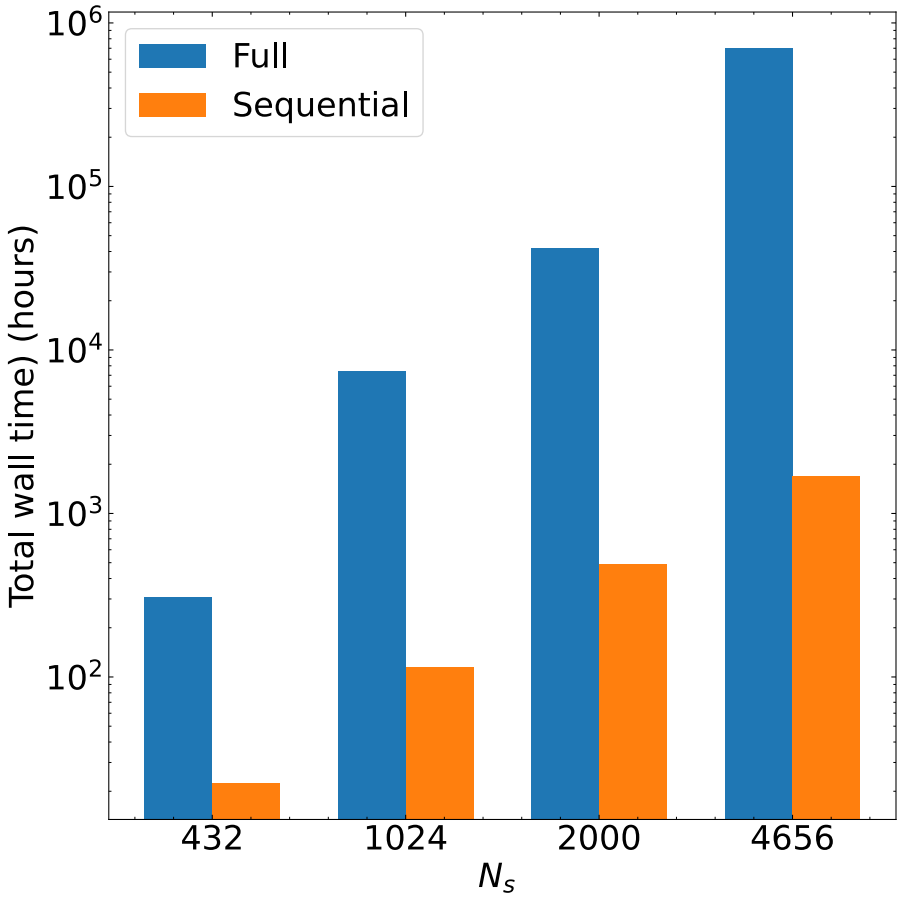

Figure B.7: Total wall time of orbital localization on each system with respect to the number of occupied states N_s. Blue bar: F-PMWF using the full orbital space. Orange Bar: sF-PMWF using the work space.

Table B.8: Total wall time and normalized total wall time of four investigated systems.

System	Total wall time (s)		Normalized total wall time (s)	
	F-PMWF	sF-PMWF	F-PMWF	sF-PMWF
215-atom cell	308	22	1903	139
511-atom cell	7360	114	18339	284
999-atom cell	42006	489	58007	675
slab	695370	1683	695370	1683

Table B.9: Time per SA iteration step in F-PMWF and sF-PMWF calculations for the four investigated systems

System	Time per SA iteration (s)	
	F-PMWF	sF-PMWF
215-atom cell	0.29	5.28×10^{-4}
511-atom cell	8.62	5.11×10^{-4}
999-atom cell	61.80	5.13×10^{-4}
slab	1056.26	4.94×10^{-4}

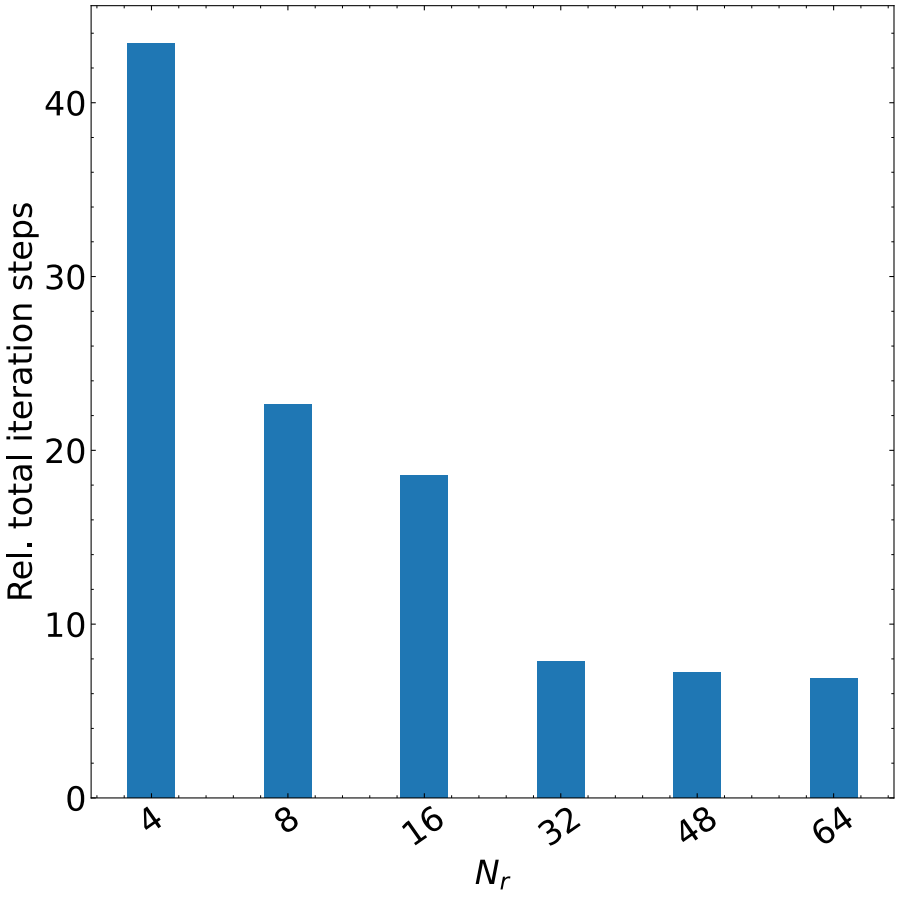

Figure B.8: Number of total SA iteration steps in sF-PMWF calculation relative to the number of total SA iteration steps in the F-PMWF calcuation for the 215-atom system using different N_r. The N_c is fixed at 16.

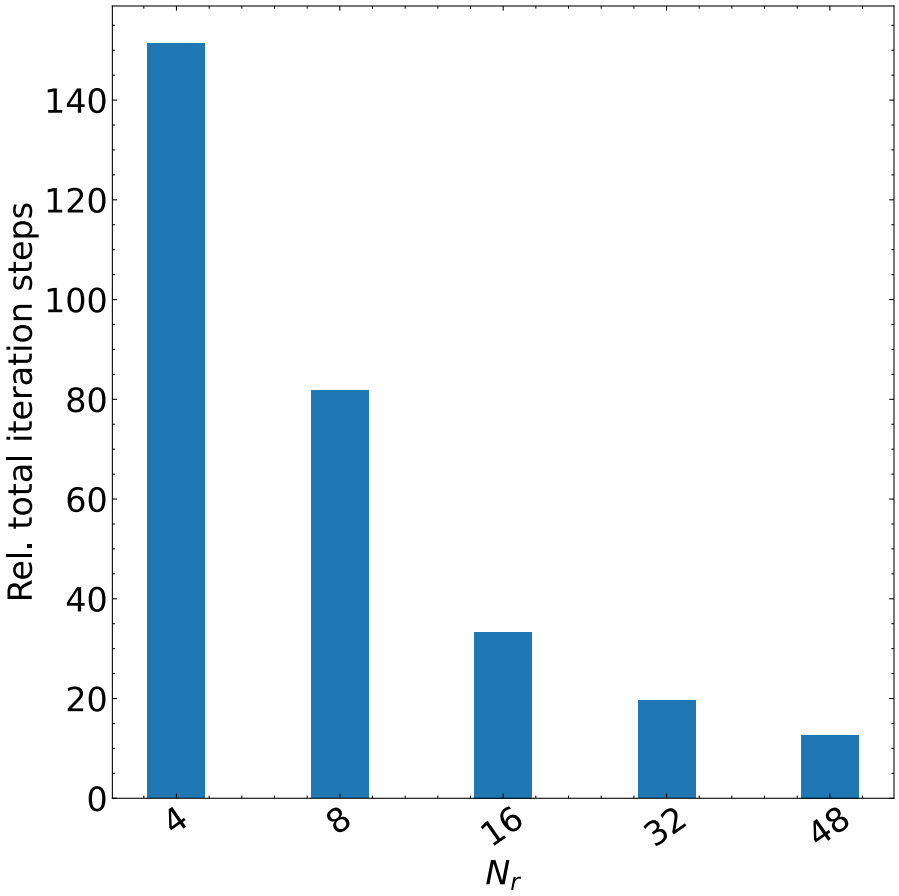

Figure B.9: Number of total SA iteration steps in sF-PMWF calculation relative to the number of total SA iteration steps in the F-PMWF calculation for the 511-atom system using different N_r. The N_c is fixed at 16.

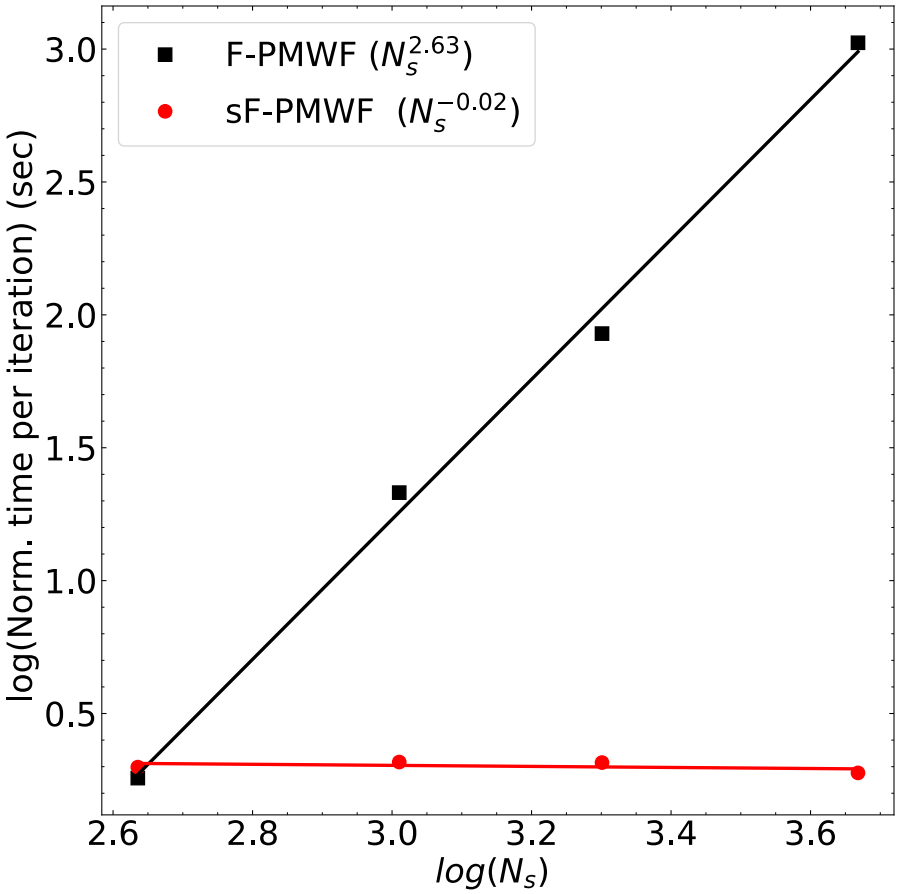

Figure B.10: The log of the normalized time per iteration plotted as a function of the log of number of occupied states N_s for the four investigated systems. The black line and square points represent the normalized t^{SA} obtained from the F-PMWF method using the full orbital space. The red line and circle points represent the normalized t^{outer} obtained from the sF-PMWF method using the constructed work space. The time per iteration is normalized to the largest grid (2303-atom system). The scaling is derived from the slope of each fitting.

Table B.10: Number of iterations required to reach convergence in F-PMWF and sF-PMWF calculations.

System	N_{it}^{SA} in F-PMWF	N_{it}^{outer} in sF-PMWF
215-atom cell	637	65
511-atom cell	700	128
999-atom cell	586	310
slab	650	870

Table B.11: Converged maximized $\mathcal{P}'$ from F-PMWF and sF-PMWF calculations. The (16,32) combination is used in the sF-PMWF calculations.

system	Converged $\mathcal{P}'$	
	F-PMWF	sF-PMWF
215-atom cell	4.9345	4.9346
511-atom cell	4.9222	4.9223
999-atom cell	4.9194	4.9195
slab	4.9414	4.9414

Table B.12: Converged maximized $\mathcal{P}$ from F-PMWF and sF-PMWF calculations.

system	Converged $\mathcal{P}$	
	F-PMWF	sF-PMWF
215-atom cell	4.6656	4.6656
511-atom cell	4.6498	4.6498
999-atom cell	4.6447	4.6446
slab	4.6731	4.6731

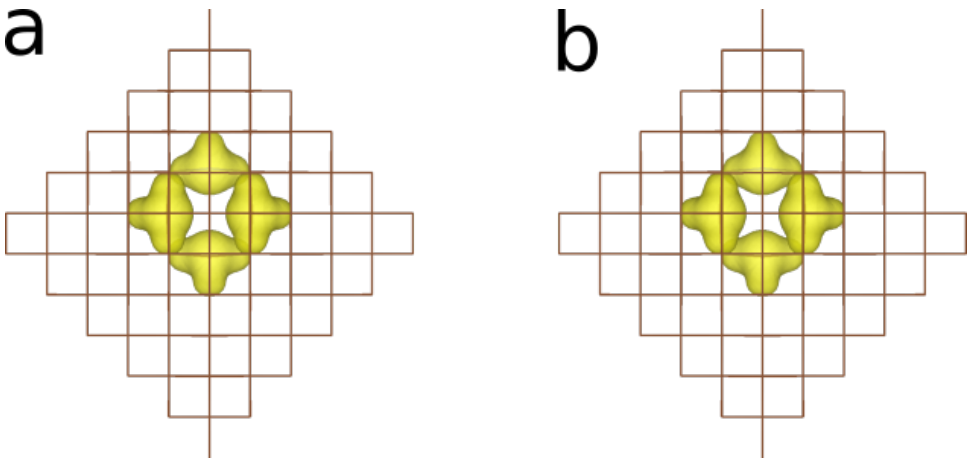

Figure B.11: Electron density constructed from the 16 regionally localized states on the NV^- center of the 215-atom system: (a) F-PMWF; (b) sF-PMWF. The isosurface value is set at 0.05 for all the plots.

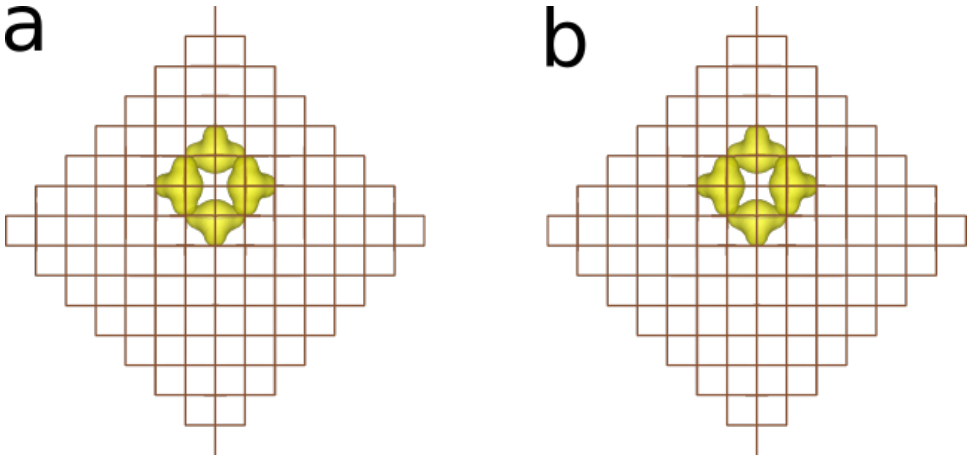

Figure B.12: Electron density constructed from the 16 regionally localized states on the NV^- center of the 511-atom system: (a) F-PMWF; (b) sF-PMWF. The isosurface value is set 0.05 for all the plots.

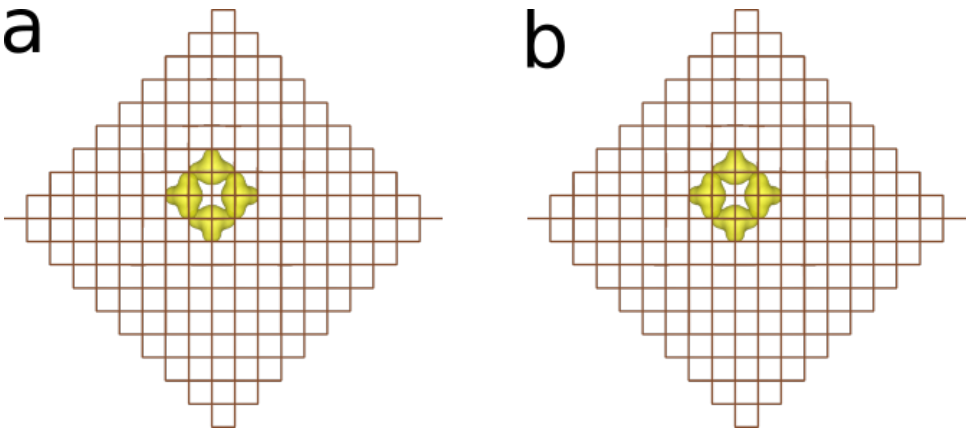

Figure B.13: Electron density constructed from the 16 regionally localized states on the NV^- center of the 999-atom system: (a) F-PMWF; (b) sF-PMWF. The isosurface value is set at 0.05 for all the plots.

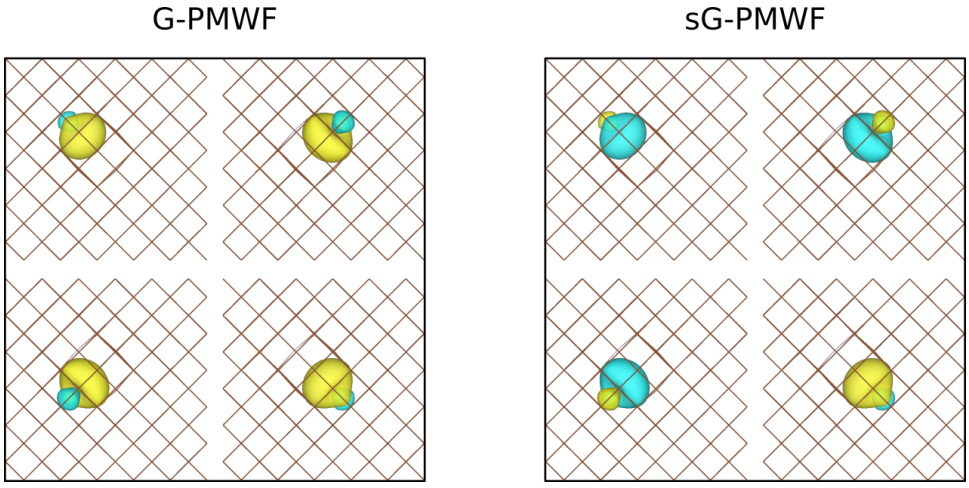

Figure B.14: The 4 regionally localized "p"-like states around the NV^- center of the 215-atom system. The left 4 states are obtained from F-PMWF and the right 4 are obtained from sF-PMWF. The yellow and blue colors represent the phases of the single-particle wavefunction. The isosurface value is set 0.05 for all the plots.

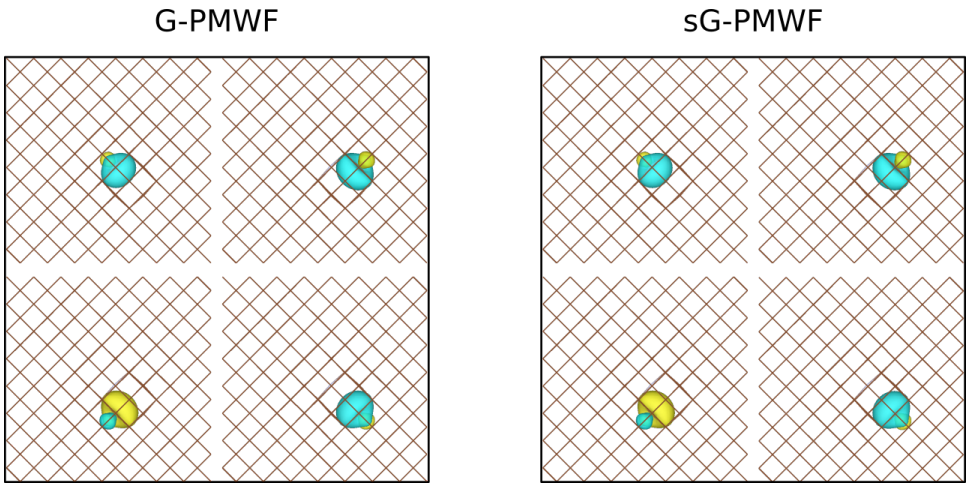

Figure B.15: The 4 regionally localized "p"-like states around the NV^- center of the 511-atom system. The left 4 states are obtained from F-PMWF and the right 4 are obtained from sF-PMWF. The yellow and blue colors represent the phases of the single-particle wavefunction. The isosurface value is set at 0.05 for all the plots.

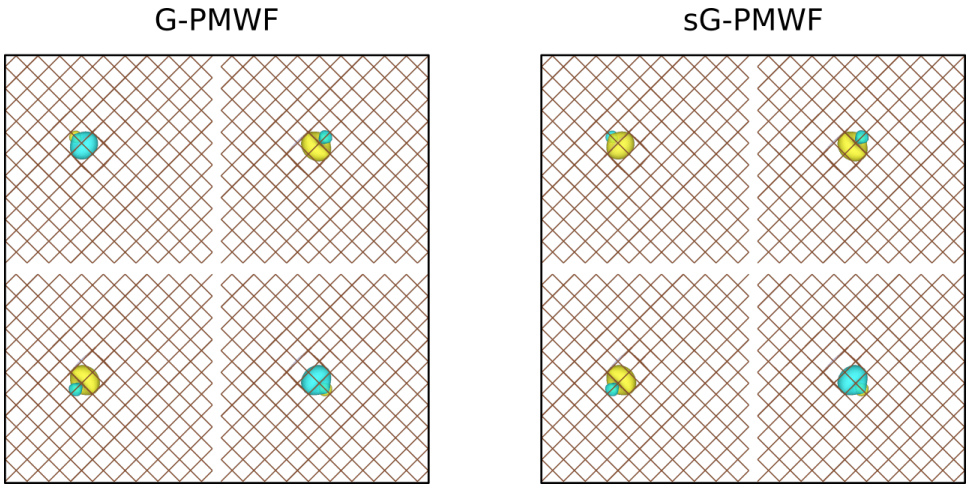

Figure B.16: The 4 regionally localized "p"-like states around the NV^- center of the 999-atom system. The left 4 states are obtained from F-PMWF and the right 4 are obtained from sF-PMWF. The yellow and blue colors represent the phases of the single-particle wavefunction. The isosurface value is set at 0.05 for all the plots.

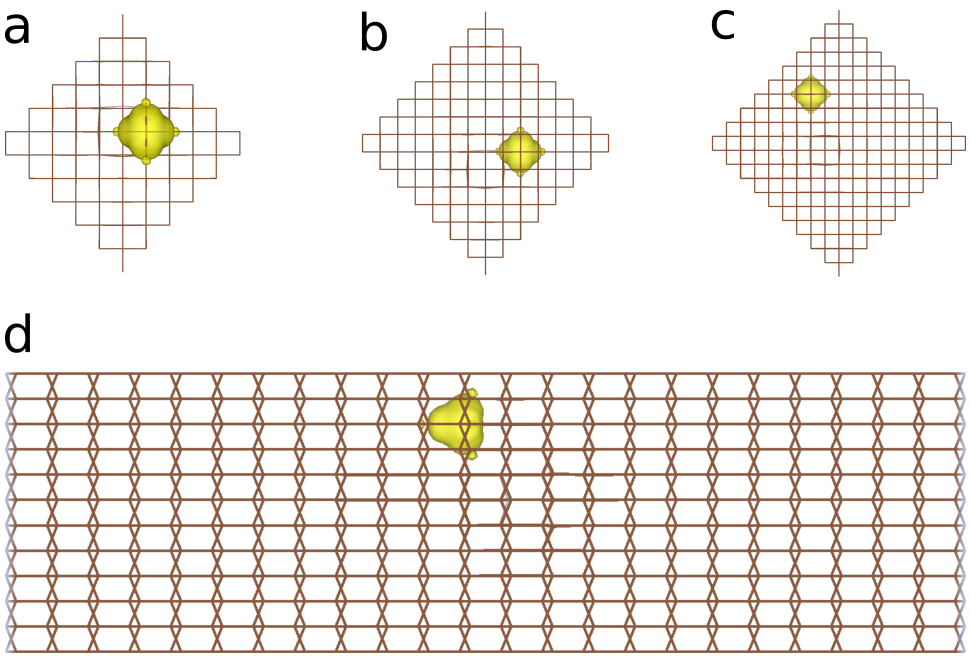

Figure B.17: Electron density constructed from the 4 regionally localized states on an arbitrary carbon of the four investigated systems: (a) 215-atom system; (b) 511-atom system; (c) 999-atom system; (d) 2303-atom system. The isosurface value is set at 0.01 for all the plots.

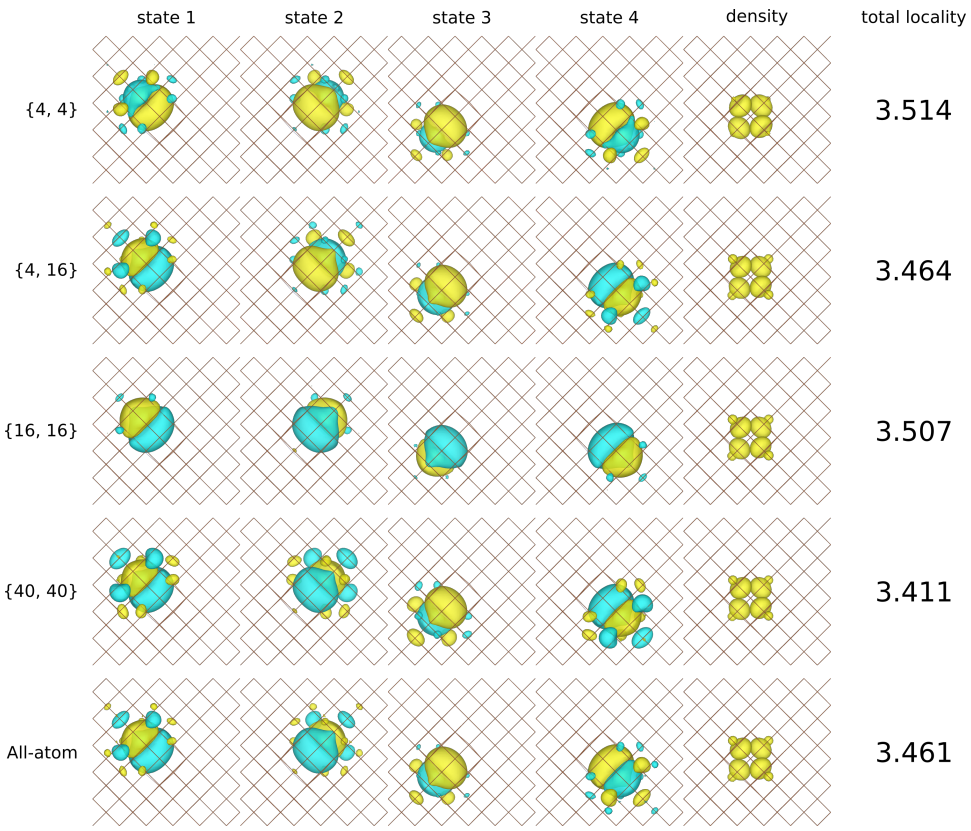

Figure B.18: The 4 regionally localized "p"-like states around the NV^- center of the 215-atom system using different sizes of the fragment or using all the atoms. The last column shows the electron density constructed from these 4 states in each calculation. The isosurface value is set at 0.02 for all the plots.

Table B.13: The spatial overlap between the set of Wannier basis from the fragment approaches and the set from the all-atom calculation.

Entry	state 1	state 2	state 3	state 4
{4, 4}	0.981877	0.978799	0.978799	0.978799
{4, 16}	0.999874	0.999704	0.999704	0.999704
{16, 16}	0.991859	0.985258	0.985259	0.985259
{40, 40}	0.997118	0.993832	0.993832	0.993789

Table B.14: The locality of each set of Wannier function basis on the corresponding atom plus the neighoring bonded atoms.

Entry	state 1	state 2	state 3	state 4	$\sum L_i$
{4, 4}	0.925726	0.862677	0.862680	0.862677	3.513760
{4, 16}	0.915932	0.849211	0.849211	0.849209	3.463562
{16, 16}	0.922626	0.861534	0.861534	0.861534	3.507228
{40, 40}	0.908731	0.834126	0.833826	0.834018	3.410700
all-atom	0.915629	0.848489	0.848488	0.848488	3.461094

Table B.15: Excited-state transition energies of the NV^- center in the four investigated systems using the Wannier function basis obtained from F-PMWF calculations. The numbers with and without the parenthesis correspond to the {4, 4} and {16, 16} fragment, respectively.

Transition	Energy (eV)			
symmetry	215-atom cell	511-atom cell	999-atom cell	slab
$^3E - {}^3A_2$	2.108 (1.560)	2.279 (1.695)	2.312 (1.710)	1.343 (0.399)
$^1A_1 - {}^3A_2$	1.433 (1.325)	1.310 (1.270)	1.202 (1.193)	1.159 (0.324)
$^1E - {}^3A_2$	0.447 (0.378)	0.435 (0.381)	0.413 (0.368)	0.329 (0.101)

Table B.16: The spatial overlap between the two sets of "p-like" Wannier functions obtained from the sF-PMWF (ψ^s) method and the F-PMWF (ψ) method for the 2303-atom system.

	ψ_1^s	ψ_2^s	ψ_3^s	ψ_4^s
ψ_1	0.9999798	1.11×10^{-3}	2.68×10^{-4}	7.89×10^{-4}
ψ_2	1.11×10^{-3}	0.9999992	9.19×10^{-6}	1.33×10^{-6}
ψ_3	2.64×10^{-4}	9.33×10^{-6}	0.9999997	7.12×10^{-6}
ψ_4	7.93×10^{-4}	2.65×10^{-6}	6.89×10^{-6}	0.9999995

Table B.17: Comparison of sF-PMWF and F-PMWF with different combinations of N_c and N_r for orbital localization on the 215-atom system with 16 atoms in the fragment

Method	N_c	N_r	N_w	N_b	N_{it}^{outer}	Converged $\mathcal{P}'$	Converged $\mathcal{P}$	$\mathcal{P}'$ after 1st access (percentage gained)	t^{outer} (s)	Total wall time (s)
F-PMWF	-	-	-	-	1	13.9402	6.7472	-	-	356
sF-PMWF	16	4	20	104	1664	13.9403	6.7472	12.3286 (88%)	0.10	170
sF-PMWF	16	8	24	42	676	13.9398	6.7471	12.3630 (87%)	0.14	96
sF-PMWF	16	16	32	26	182	13.9381	6.7466	11.9140 (85%)	0.23	43
sF-PMWF	16	32	48	13	104	13.9361	6.7463	11.9952 (86%)	0.43	46
sF-PMWF	16	48	64	9	81	13.9398	6.7471	12.5275 (90%)	0.58	48
sF-PMWF	16	64	80	7	42	13.9400	6.7471	12.9316 (93%)	1.02	44
sF-PMWF	16	80	96	6	36	13.9402	6.7471	13.5550 (97%)	1.36	51
sF-PMWF	32	48	80	9	90	13.9403	6.7472	13.6312 (98%)	0.72	66
sF-PMWF	48	32	80	12	108	13.9403	6.7472	13.9004 (99%)	0.75	82
sF-PMWF	64	16	80	23	184	13.9403	6.7472	13.9268 (99%)	0.71	132

Table B.18: Comparison of sF-PMWF and F-PMWF with different combinations of N_c and N_r for orbital localization on the 511-atom system with 16 atoms in the fragment

Method	N_c	N_r	N_w	N_b	N_{it}^{outer}	Converged $\mathcal{P}'$	Converged $\mathcal{P}$	$\mathcal{P}'$ after 1st access (percentage gained)	t^{outer} (s)	Total wall time (s)
F-PMWF	-	-	-	-	1	13.9227	6.7261	-	-	10631
sF-PMWF	16	8	24	126	2142	13.9227	6.7260	11.2259 (81%)	0.34	732
sF-PMWF	16	16	32	63	882	13.9226	6.7261	11.1987 (80%)	0.46	416
sF-PMWF	16	32	48	32	352	13.9225	6.7260	11.3184 (81%)	0.74	269
sF-PMWF	16	48	64	21	210	13.9216	6.7258	12.3472 (89%)	1.21	263
sF-PMWF	16	64	80	16	160	13.9222	6.7260	11.5273 (83%)	1.57	259
sF-PMWF	16	80	96	13	104	13.9225	6.7260	12.0496 (86%)	2.13	230
sF-PMWF	16	96	112	11	77	13.9226	6.7261	12.6309 (91%)	3.00	240
sF-PMWF	16	112	128	9	90	13.9225	6.7260	13.2126 (95%)	4.06	374
sF-PMWF	32	48	80	21	252	13.9226	6.7260	13.6220 (98%)	1.54	398
sF-PMWF	48	32	80	31	186	13.9226	6.7260	13.8586 (99%)	1.47	283
sF-PMWF	64	16	80	60	300	13.9227	6.7260	13.8899 (99%)	1.42	434

Table B.19: Comparison of sF-PMWF and F-PMWF with different combinations of N_c and N_r for orbital localization on the 999-atom system with 16 atoms in the fragment

Method	N_c	N_r	N_w	N_b	N_{it}^{outer}	Converged $\mathcal{P}'$	Converged $\mathcal{P}$	$\mathcal{P}'$ after 1st access (percentage gained)	t^{outer} (s)	Total wall time (s)
F-PMWF	-	-	-	-	1	13.9167	6.7200	-	-	58937
sF-PMWF	16	32	48	62	1178	13.9169	6.7198	11.0295 (79%)	1.53	1832
sF-PMWF	16	48	64	42	672	13.9172	6.7199	11.1849 (80%)	2.09	1435
sF-PMWF	16	64	80	31	310	13.9159	6.7195	11.3795 (82%)	3.06	978
sF-PMWF	16	80	96	25	200	13.9161	6.7195	11.6643 (84%)	4.06	840
sF-PMWF	16	96	112	21	189	13.9160	6.7195	12.1530(87%)	5.52	1074
sF-PMWF	16	128	144	16	128	1.9169	6.7198	12.2390 (88%)	8.74	1148

Table B.20: Comparison of sF-PMWF and F-PMWF with different combinations of N_c and N_r for orbital localization on the 2303-atom system with 16 atoms in the fragment

Method	N_c	N_r	N_w	N_b	N_{it}^{outer}	Converged $\mathcal{P}'$	Converged $\mathcal{P}$	$\mathcal{P}'$ after 1st access (percentage gained)	t^{outer} (s)	Total wall time (s)
F-PMWF	-	-	-	-	1	13.9451	6.7539	-	-	761005
sF-PMWF	16	32	48	145	1595	13.9451	6.7539	12.2360 (88%)	1.75	2888
sF-PMWF	16	48	64	97	970	13.9451	6.7539	12.3156 (88%)	2.44	2454
sF-PMWF	16	64	80	73	730	13.9450	6.7540	12.2248 (88%)	3.66	2761
sF-PMWF	16	80	96	58	580	13.9451	6.7539	12.0172 (86%)	4.73	2837

Appendix C

Supplementary material for "Efficient treatment of molecular excitations in the liquid phase environment via stochastic many-body theory"

Guorong Weng, Vojtěch Vlček

C.1 Computational Details

C.1.1 Geometry Preparation

The molecular structures of the three molecules studied in this work are shown in Fig. C.1. To obtain the ground-state geometries of these molecule in the gas phase, we perform energy optimization at the MP2/cc-pVDZ level using the NWChem package.[1] The relaxed molecule is place at the center of a simulation box, which is then filled by water molecules. The resulting homogeneous aqueous solution has a concentration of

$0.4 \sim 0.5$ mmol/g. The system geometries are then prepared by molecular dynamics simulations using Gromacs 5 package.[2] A generalized amber force field[3] is employed in the simulations with charge method AM1-bcc for the solute molecule and TIP4P for the water molecules.[4] The system is treated periodically in x, y, and z directions. An energy minimization step is performed to relax the structures, which is followed by the NVT equilibration, NPT equilibration, and MD simulation at 300K. The dynamics run 10,000,000 relaxation steps with a time interval 0.0005 ps, resulting in 5,000 ps in total. Then 5 snapshots are extracted from the 10,000,000 steps every 1,000 ps as representative configurations of the system for the following DFT calculations and many-body calculations. Fig. C.2 shows one of the snapshots for each system. The geometries of the isolated molecules are taken directly from these snapshots by simply removing all the water molecules.

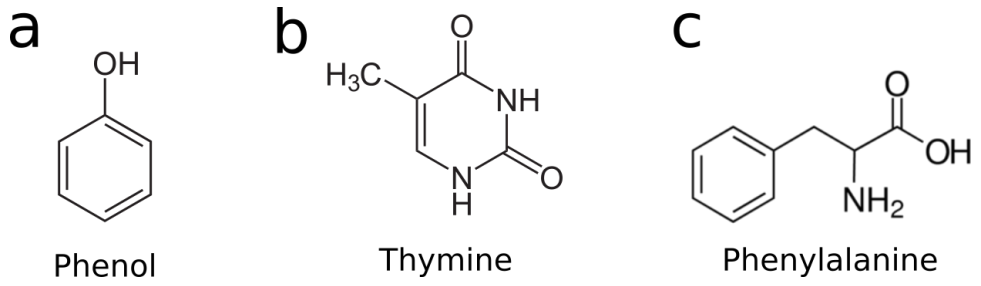

Figure C.1: Molecular structures of the three molecules studied in this work: (a) phenol; (b) thymine; (c) phenylalanine.

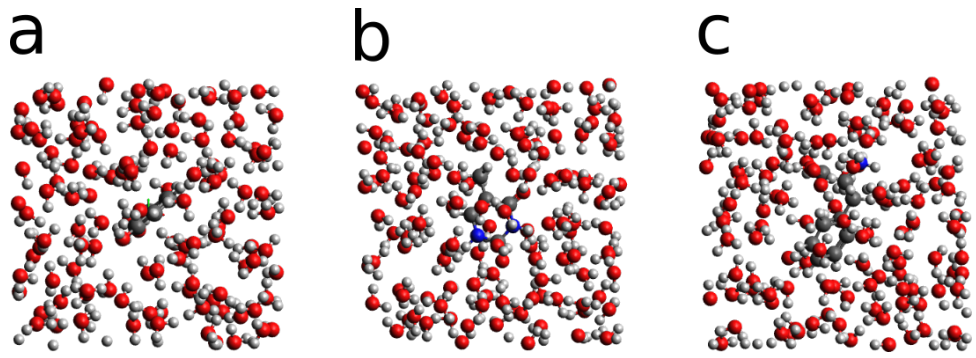

Figure C.2: Selected snapshots from MD simulations of three systems: (a) phenol; (b) thymine; (c) phenylalanine.

C.1.2 Pipek-Mezey Wannier Functions

The objective function $\mathcal{P}$ that evaluates the orbital localization is implicitly a functional of the unitary matrix W. The unitary matrix W transforms the original set of Kohn-Sham (KS) eigenstates into another set of states that lead to a larger value of $\mathcal{P}$. Steepest descent (ascent) algorithm is employed to maximize the value of $\mathcal{P}$ and find the corresponding unitary matrix W. The objective function is expressed as

$$\mathcal{P}(W) = \sum_{i}^{N_{occ}} \sum_{\mathcal{A}}^{N_{\mathcal{A}}} [Q_{ii}^{\mathcal{A}}(W)]^2 \tag{C.1}$$

Here, the matrix Q is given by

$$Q_{ij}^{\mathcal{A}} = \langle \psi_i | \, w_{\mathcal{A}} \, | \psi_j \rangle \, , \tag{C.2}$$

where ψ_i is an unitary-transformed state defined as

$$|\psi_k\rangle = \sum_{j} W_{jk} \, |\phi_j\rangle \, . \tag{C.3}$$

Here, W is the unitary matrix that is iteratively updated.

$w_{\mathcal{A}}$ in Eq. (C.2) represents the weight function for each atom type $\mathcal{A}$:

$$w_{\mathcal{A}}(\mathbf{r}) = \frac{\bar{n}_{\mathcal{A}(\mathbf{r})}}{\sum_{\mathcal{A}'}^{N_{\mathcal{A}'}} \bar{n}_{\mathcal{A}'}(\mathbf{r})}, \tag{C.4}$$

where $\bar{n}_{\mathcal{A}}(\mathbf{r})$ is the density function of atom type $\mathcal{A}$ using the simple Gaussian model density

$$\bar{n}_{\mathcal{A}}(\mathbf{r}) = \frac{N_{el,\mathcal{A}}}{\gamma_{\mathcal{A}}\sqrt{2\pi}} e^{\{-\frac{(\mathbf{r}-\mathbf{R}^{\mathcal{A}})^2}{2\gamma_{\mathcal{A}}^2}\}}. \tag{C.5}$$

Here, the parameter $\gamma_{\mathcal{A}}$ is set 0.5 bohr in our calculation. $\mathbf{R}^{\mathcal{A}}$ is the spatial coordinates of atom $\mathcal{A}$.

In practice, the $\mathcal{P}$ is maximized iteratively. In the zeroth step (represented by the superscript 0), the Q matrix is constructed using the KS eigenstates

$$Q_{ij}^{\mathcal{A},0} = \langle \phi_i | \, w_{\mathcal{A}} \, | \phi_j \rangle \, . \tag{C.6}$$

In the first and following iteration step n, the Q matrix is given by the unitary matrix W

$$Q^{\mathcal{A},n} = (W^{n\dagger}) \mathcal{Q}^{\mathcal{A},n-1} (W^n), \tag{C.7}$$

where the unitary matrix W is defined as the exponential of the anti-Hermitian matrix A

$$W^n = e^{A^n}. \tag{C.8}$$

Here, the anti-Hermitian matrix A is generated by the functional derivative of the objective function $\mathcal{P}$

$$A^n = \Delta t (\frac{\mathrm{d}\mathcal{P}}{\mathrm{d}A})^{(n-1)}, \tag{C.9}$$

where Δt is the "time-ste" parameter and the derivative $(\frac{\mathrm{d}\mathcal{P}}{\mathrm{d}A})^{(n-1)}$ is in fact a matrix whose

element is given by

$$(\frac{\mathrm{d}\mathcal{P}}{\mathrm{d}A})^{(n-1)}_{ij} = \sum_{\mathcal{A}}[\mathcal{Q}^{\mathcal{A},n-1}_{ij}(\mathcal{Q}^{\mathcal{A},n-1^*}_{ii} - \mathcal{Q}^{\mathcal{A},n-1^*}_{jj}) - \mathcal{Q}^{\mathcal{A},n-1^*}_{ij}(\mathcal{Q}^{\mathcal{A},n-1}_{jj} - \mathcal{Q}^{\mathcal{A},n-1}_{ii})]. \quad \text{(C.10)}$$

Once the $\mathcal{P}$ is maximized, the set $\{\psi\}$ corresponds to the localized PMW functions.

C.1.3 Stochastic GW Approach

Ground state DFT calculations with periodic boundary conditions at the PBE level serve as the starting point for the subsequent many-body calculations. 3-dimensional periodic boundary condition is employed with a cubic cell for the solute-solvent systems and 0-dimensional periodic boundary condition is employed for the single molecule systems. Troulller-Martins pseudopotentials and real space grids are adopted in our calculations with a kinetic energy cutoff of 28 hartrees. The cell parameters of each solute-solvent systems are listed in Table C.1.

system	grid	spacing [bohr]
phenol	72*72*72	0.40621
thymine	76*76*76	0.40756
phenylalanine	76*76*76	0.40347

Table C.1: Cell parameters in DFT calculations

Using the KS-DFT (PBE) starting point, the quasiparticle energies are computed as

$$\varepsilon_i = \varepsilon_i^{\mathrm{KS}} + \left\langle \phi_i \middle| \hat{\Sigma} - v_{xc} \middle| \phi_i \right\rangle, \quad \text{(C.11)}$$

where $\varepsilon_i^{\mathrm{KS}}$ is the Kohn-Sham eigenvalue and v_{xc} is the mean-field exchange-correlation potential calculated with generalized gradient approximation. The self energy Σ is

further split into exchange (Σ_x) and correlation (Σ_c). The exchange term is treated with Hartree-Fock exchange, while the Σ_c is approximated by the GW method.

For the particular eigenstate $|\phi_i\rangle$ of a mean-field Hamiltonian H_0, the correlation self energy within GW approximation is expressed as

$$\langle\phi_i|\,\Sigma_c(t)\,|\phi_i\rangle = \langle\phi_i|\,iG_0(t)W_P(t)\,|\phi_i\rangle\,, \tag{C.12}$$

where W_P is the time-ordered polarization potential expressed using a two-point polarizability χ and the bare Coulomb kernel ν

$$\begin{aligned} W_P(\mathbf{r},&\mathbf{r}',t) = \\ &\int\int \nu(\mathbf{r},\mathbf{r}'')\chi(\mathbf{r}''\mathbf{r}''',t)\nu(\mathbf{r}''',\mathbf{r}')\mathrm{d}\mathbf{r}''\mathrm{d}\mathbf{r}''' \end{aligned} \tag{C.13}$$

G_0 is the non-interacting Green's function. In the stochastic formalism, G_0 is sampled using a set of random vectors ζ

$$G_0(\mathbf{r},\mathbf{r}',t) = \frac{1}{N_\zeta}\sum_l^{N_\zeta}\zeta_l(\mathbf{r},t)\bar{\zeta}_l(\mathbf{r}'), \tag{C.14}$$

where N_ζ denotes the number of random vectors and the vector $\bar{\zeta}$ spans the entire Hilbert space. The vector ζ is either in the occupied or unoccupied subspace depending on the time argument

$$|\zeta(t)\rangle = \begin{cases} e^{-iH_0t}\hat{P}^{occ}\,|\bar{\zeta}\rangle & t<0, \\ e^{-iH_0t}(I-\hat{P}^{occ})\,|\bar{\zeta}\rangle & t>0. \end{cases} \tag{C.15}$$

Here, Negative time argument denotes hole propagation while positive denotes electron propagation. $\hat{P}^{occ}$ is the projection operator projecting on the occupied subspace and I is

the identity operator. And hence the perturbative correction becomes

$$\langle\phi|\,\Sigma_c(t)\,|\phi\rangle \simeq \frac{1}{N_\zeta}\sum_\zeta \int \phi(\mathbf{r})\zeta(\mathbf{r},t)u_{\bar{\zeta}}(\mathbf{r},t)\mathrm{d}\mathbf{r} \tag{C.16}$$

Here, $u_{\bar{\zeta}}(\mathbf{r},t)$ is the induced charge density potential defined as

$$u_{\bar{\zeta}}(\mathbf{r},t) = \int W_P(\mathbf{r},\mathbf{r}',t)\bar{\zeta}(\mathbf{r}')\phi(\mathbf{r}')\mathrm{d}\mathbf{r}' \tag{C.17}$$

Practically $u_{\bar{\zeta}}(\mathbf{r},t)$ is computed from the retarded response potential

$$\tilde{u}_{\bar{\zeta}}(\mathbf{r},t) = \int \tilde{W}_P(\mathbf{r},\mathbf{r}',t)\bar{\zeta}(\mathbf{r}')\phi(\mathbf{r}')\mathrm{d}\mathbf{r}', \tag{C.18}$$

The retarded response potential can be further written in terms of the induced charge density fluctuation δn

$$\begin{aligned}\tilde{u}_\zeta(\mathbf{r},t) &= \int\int\int \nu(\mathbf{r},\mathbf{r}'')\chi(\mathbf{r}'',\mathbf{r}''',t)\delta v(\mathbf{r}''',\mathbf{r}')\mathrm{d}\mathbf{r}'\mathrm{d}\mathbf{r}''\mathrm{d}\mathbf{r}''' \\ &= \int \nu(\mathbf{r},\mathbf{r}')\delta n(\mathbf{r}',t)\mathrm{d}\mathbf{r}'\end{aligned} \tag{C.19}$$

Here, we define a perturbing potential

$$\delta v(\mathbf{r},\mathbf{r}') = \nu(\mathbf{r},\mathbf{r}')\bar{\zeta}(\mathbf{r}')\phi(\mathbf{r}'). \tag{C.20}$$

The time-dependent retarded response potential $\tilde{u}_\zeta(\mathbf{r},t)$ is Fourier transformed into the frequency domain and expanded for the whole frequency domain

$$u_\zeta(\mathbf{r},\omega) = \begin{cases} \tilde{u}_\zeta(\mathbf{r},\omega), & \omega \geq 0 \\ (\tilde{u}_\zeta(\mathbf{r},\omega))*, & \omega < 0 \end{cases}. \tag{C.21}$$

The parameters of the stochastic many-body calculations are listed in Table. C.2.

Parameters	value
plane wave cut-off (hartree)	28
number of random vectors used for sparse stochastic compression	20000
number of random vectors characterizing the screened Coulomb interaction (per each vector sampling the Green's function)	16
number of vectors sampling the Green's function	1000
maximum time for real-time propagation of the dynamical self-energy (a.u.)	50

Table C.2: Parameters in the GW calculations of all systems.

C.2 Supplementary tables and figures

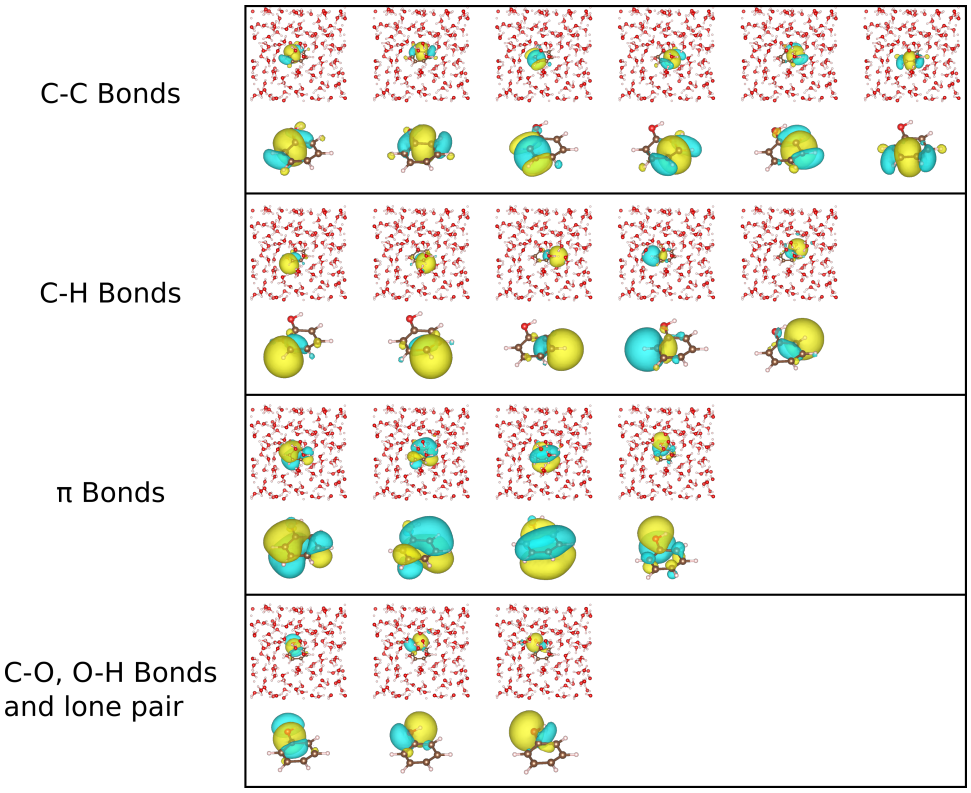

Figure C.3: PMW functions of the solvated and isolated phenol molecule. There exits a one-to-one correspondence between these two sets of PMW functions labelled by chemical bonds or lone pair electrons.

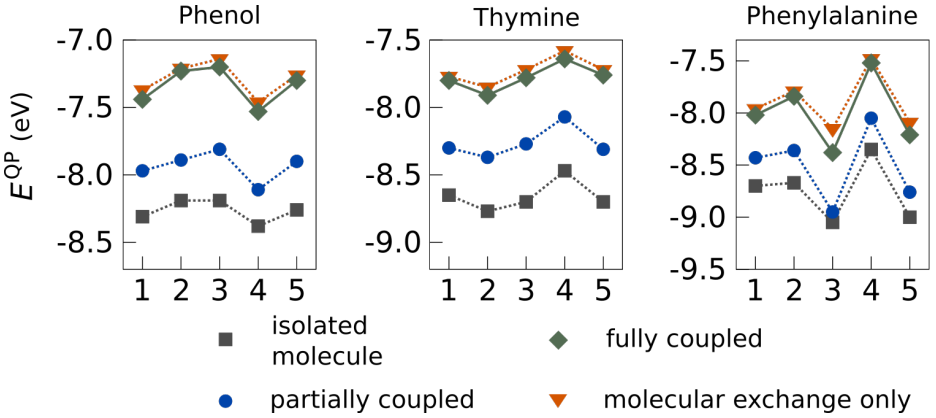

Figure C.4: HOMO QP energies with respect to the system snapshots along the MD trajectory of the three molecules. Here, "isolated molecule" means the QP energies are calculated for the HOMO of the molecules without the solvent, while the others are calculated for the reconstructed HOMO with the solvent.

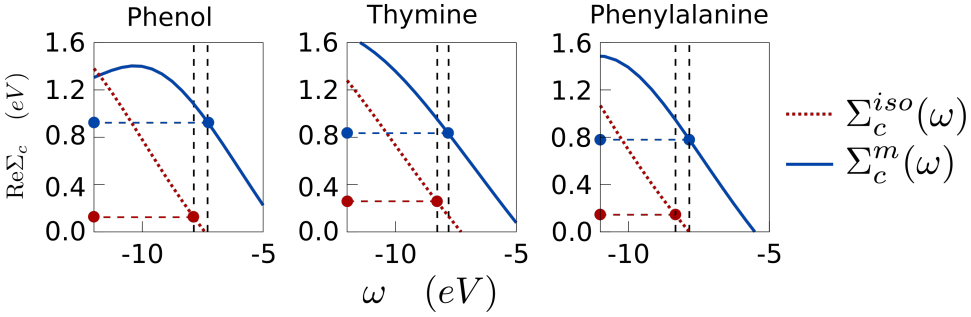

Figure C.5: Correlation energy contribution from the solvated molecule (Σ_c^m) compared with the isolated one (Σ_c^{iso}) at the QP energy solution.

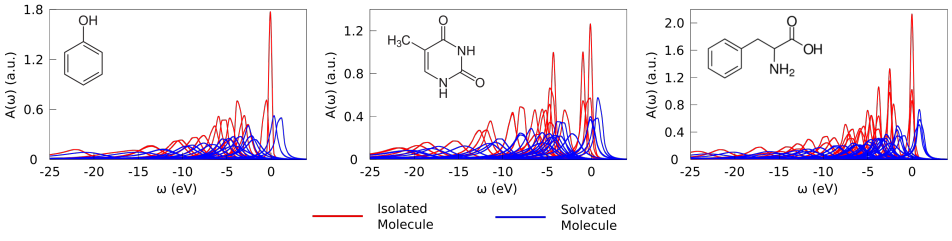

Figure C.6: Spectral functions of each individual QP excitation for the three molecules. The color distinguishes the solvated molecule from its isolated counterpart.

	ψ_1^m	ψ_2^m	ψ_3^m	ψ_4^m	ψ_5^m	ψ_6^m	ψ_7^m	ψ_8^m	ψ_9^m	ψ_{10}^m	ψ_{11}^m	ψ_{12}^m	ψ_{13}^m	ψ_{14}^m	ψ_{15}^m	ψ_{16}^m	ψ_{17}^m	ψ_{18}^m
ψ_1^{ao}	0.0004	**0.9997**	0.0002	0.0002	0.0010	0.0001	0.0006	0.0001	0.0002	0.0008	0.0013	0.0002	0.0015	0.0058	0.0005	0.0011	0.0013	0.0002
ψ_2^{ao}	0.0002	0.0007	0.0004	0.0000	0.0006	0.0000	**0.9995**	0.0003	0.0001	0.0053	0.0006	0.0021	0.0006	0.0011	0.0003	0.0000	0.0063	0.0002
ψ_3^{ao}	0.0038	0.0008	0.0009	0.0001	0.0000	0.0001	0.0001	0.0001	0.0005	0.0003	0.0002	0.0005	**0.9984**	0.0002	0.0033	0.0000	0.0016	0.0002
ψ_4^{ao}	0.0002	0.0000	0.0013	0.0004	0.0000	**0.9997**	0.0001	0.0039	0.0065	0.0002	0.0003	0.0001	0.0003	0.0004	0.0007	0.0007	0.0004	0.0022
ψ_5^{ao}	0.0006	0.0048	0.0003	0.0004	0.0043	0.0002	0.0001	0.0000	0.0005	0.0024	0.0002	0.0003	0.0000	**0.9975**	0.0002	0.0049	0.0001	0.0001
ψ_6^{ao}	0.0002	0.0001	0.0001	0.0000	0.0001	0.0000	0.0048	0.0001	0.0002	**0.9971**	0.0002	0.0027	0.0004	0.0003	0.0003	0.0004	0.0125	0.0003
ψ_7^{ao}	0.0001	0.0011	0.0001	0.0011	**0.9995**	0.0002	0.0001	0.0002	0.0020	0.0009	0.0064	0.0001	0.0001	0.0057	0.0001	0.0018	0.0007	0.0004
ψ_8^{ao}	0.0002	0.0001	0.0011	0.0074	0.0015	0.0060	0.0001	0.0002	**0.9983**	0.0000	0.0009	0.0000	0.0000	0.0003	0.0001	0.0001	0.0006	0.0022
ψ_9^{ao}	**0.9997**	0.0008	0.0006	0.0001	0.0002	0.0003	0.0000	0.0007	0.0003	0.0014	0.0000	0.0001	0.0045	0.0018	0.0009	0.0008	0.0003	0.0003
ψ_{10}^{ao}	0.0000	0.0004	0.0002	0.0000	0.0001	0.0001	0.0021	0.0003	0.0001	0.0032	0.0001	**0.9988**	0.0006	0.0001	0.0027	0.0031	0.0023	0.0033
ψ_{11}^{ao}	0.0006	0.0001	**0.9998**	0.0002	0.0000	0.0015	0.0000	0.0029	0.0015	0.0001	0.0003	0.0002	0.0015	0.0001	0.0003	0.0002	0.0010	0.0002
ψ_{12}^{ao}	0.0001	0.0009	0.0001	0.0021	0.0055	0.0002	0.0004	0.0002	0.0006	0.0002	**0.9986**	0.0001	0.0001	0.0002	0.0013	0.0019	0.0001	0.0024
ψ_{13}^{ao}	0.0006	0.0001	0.0027	0.0006	0.0001	0.0036	0.0002	**0.9993**	0.0000	0.0002	0.0001	0.0002	0.0003	0.0001	0.0004	0.0005	0.0002	0.0009
ψ_{14}^{ao}	0.0001	0.0000	0.0000	**0.9997**	0.0006	0.0004	0.0002	0.0008	0.0083	0.0007	0.0023	0.0000	0.0001	0.0012	0.0001	0.0002	0.0002	0.0009
ψ_{15}^{ao}	0.0003	0.0001	0.0009	0.0009	0.0005	0.0024	0.0002	0.0010	0.0032	0.0000	0.0032	0.0029	0.0000	0.0003	0.0094	0.0004	0.0003	**0.9976**
ψ_{16}^{ao}	0.0001	0.0004	0.0005	0.0001	0.0003	0.0001	0.0051	0.0001	0.0004	0.0097	0.0005	0.0021	0.0001	0.0000	0.0005	0.0002	**0.9977**	0.0003
ψ_{17}^{ao}	0.0007	0.0005	0.0000	0.0001	0.0003	0.0011	0.0004	0.0005	0.0002	0.0001	0.0019	0.0024	0.0032	0.0002	**0.9981**	0.0040	0.0007	0.0095
ψ_{18}^{ao}	0.0005	0.0009	0.0002	0.0005	0.0024	0.0008	0.0002	0.0005	0.0000	0.0001	0.0026	0.0030	0.0000	0.0064	0.0057	**0.9979**	0.0000	0.0008

Table C.3: Spatial overlaps $|\langle\psi_i^g|\psi_j^m\rangle|$ between two sets of PMW functions of phenol molecule.

	Phenol	Thymine	Phenylalanine
snapshot 1	-8.31 ± 0.06	-8.65 ± 0.06	-8.70 ± 0.06
snapshot 2	-8.19 ± 0.06	-8.77 ± 0.06	-8.67 ± 0.06
snapshot 3	-8.19 ± 0.06	-8.70 ± 0.07	-9.05 ± 0.06
snapshot 4	-8.38 ± 0.06	-8.47 ± 0.06	-8.35 ± 0.06
snapshot 5	-8.26 ± 0.06	-8.70 ± 0.06	-9.00 ± 0.05
average	-8.27	-8.66	-8.75
standard deviation	0.08	0.11	0.28
relaxed geometry	-8.21	-8.88	-8.60
exp.	-8.51[5]	-9.18[6]	-8.82[7]

Table C.4: HOMO QP energies of five selected snapshots for the three isolated molecules. The average values and standard deviations over the five snapshots are provided for comparisons with the gas-phase relaxed geometry and the experimental values. Unit: eV

	state 30	state 31	state 32
snapshot 1	-8.37±0.09	**-8.02**±0.06	-8.17±0.10
snapshot 2	**-7.84**±0.07	-7.91±0.08	-8.11±0.07
snapshot 3	**-8.38**±0.06	-8.43±0.08	-8.61±0.10
snapshot 4	-8.44±0.10	-7.81±0.09	**-7.52**±0.06
snapshot 5	-8.95±0.12	-8.27±0.10	**-8.21**±0.05

Table C.5: QP energies of five selected snapshots for the first three highest occupied states of solvated phenyalalanine. The state number represents the order of PBE eigenstates. Numbers in bold stand for the reordered HOMO QP energies. Unit: eV

	Phenol	Thymine	Phenylalanine
snapshot 1	-5.65	-6.00	-5.87
snapshot 2	-5.53	-6.05	-5.77
snapshot 3	-5.51	-6.14	-6.17
snapshot 4	-5.75	-5.87	-5.96
snapshot 5	-5.60	-6.04	-6.37
average	-5.61	-6.02	-6.03
standard deviation	0.10	0.10	0.24
relaxed geometry	-5.75	-6.25	-5.78

Table C.6: PBE HOMO eigenvalues of five selected snapshots for the three isolated molecules. The average values and standard deviations over the five snapshots are provided for comparisons with the gas-phase relaxed geometry. Unit: eV

	Phenol	Thymine	Phenylalanine
snapshot 1	-7.44 ± 0.06	-7.80 ± 0.07	-8.02 ± 0.06
snapshot 2	-7.23 ± 0.06	-7.91 ± 0.07	-7.84 ± 0.07
snapshot 3	-7.20 ± 0.07	-7.78 ± 0.07	-8.38 ± 0.06
snapshot 4	-7.53 ± 0.06	-7.64 ± 0.07	-7.52 ± 0.06
snapshot 5	-7.30 ± 0.07	-7.76 ± 0.07	-8.21 ± 0.05
average	-7.34	-7.78	-7.99
standard deviation	0.14	0.10	0.33

Table C.7: HOMO QP energies of five selected snapshots for the three solvated molecules. The energies are computed with the fully-coupled correlation. The standard deviations over the five snapshots are provided for comparisons with the QP energy shifts. Unit: eV

molecule	Phenol		Thymine		Phenylalanine	
phase	gas	aqueous	gas	aqueous	gas	aqueous
experiment[a]	8.508 ± 0.001[5]	7.6 ± 0.1[8]	9.18[6]	8.50[9]	8.80 to 9.15[10, 7]	8.70[11]
calculation[b]	8.55[12]	7.90[12]	9.20[13]	8.30[13]	9.16[14]/8.72[14]	7.66[14]
this work[c]	8.27 ± 0.08	7.34 ± 0.14	8.66 ± 0.11	7.78 ± 0.10	8.75 ± 0.28	7.99 ± 0.33
this work[d]	8.21 ± 0.05	-	8.88 ± 0.05	-	8.60 ± 0.05	-

Table C.8: Comparisons of our computed IPs for the three molecules with available experimental and computational references. Unit: eV
[a] experimental data are obtained by pump-probe photoionization threshold,[5] UV photoelectron spectroscopy,[6] resonant two-photon ionization,[10] liquid-microjet photoelectron spectroscopy,[8, 11] and electron impact ionization.[9]
[b] computational data are obtained by EOM-IP-CCSD/EFP method[12, 13], electron propagator in the partial third-order (P3) approximation,[14] and DFT/NEPCM method.[14]
[c] these IPs values are averaged over 5 system snapshots.
[d] these IPs values are obtained for the relaxed molecular geometry in the gas phase.

	Phenol	Thymine	Phenylalanine
snapshot 1	0.87	0.85	0.68
snapshot 2	0.96	0.86	0.82
snapshot 3	0.99	0.92	0.67
snapshot 4	0.85	0.83	0.83
snapshot 5	0.96	0.94	0.79
average	0.93	0.88	0.76
standard deviation	0.06	0.05	0.08
reference value	0.91[12]	0.90[13]	-

Table C.9: HOMO QP energy shifts of five selected snapshots for the three solvated molecules. The energies are computed with the fully-coupled correlation. The average values and standard deviations over the five snapshots are provided for comparisons with the references and the QP energy, respectively. Unit: eV

	Phenol	Thymine	Phenylalanine
snapshot 1	-0.09	-0.04	-0.13
snapshot 2	-0.03	-0.12	-0.10
snapshot 3	-0.07	-0.08	-0.12
snapshot 4	-0.09	-0.07	-0.06
snapshot 5	-0.05	-0.05	-0.16
average	-0.07	-0.07	-0.12
standard deviation	0.03	0.03	0.04

Table C.10: The environment subspace exchange energy Σ_x^{env} of the five selected snapshots for the three solvated molecules. The values are extracted from the calculations of the HOMO QP energies. Unit: eV

	Phenol	Thymine	Phenylalanine
snapshot 1	43	38	47
snapshot 2	37	35	36
snapshot 3	43	30	37
snapshot 4	34	40	44
snapshot 5	38	39	33
average	39	36	39
standard deviation	4	4	6

Table C.11: The ratio of the environment subspace correlation energy Σ_c^{env} to the total correlation energy Σ_c of the five selected snapshots for the three solvated molecules. The values are extracted from the calculations of the HOMO QP energies. Unit: %

	Phenol	Thymine	Phenylalanine
snapshot 1	0.34	0.35	0.27
snapshot 2	0.30	0.40	0.31
snapshot 3	0.38	0.43	0.10
snapshot 4	0.27	0.40	0.30
snapshot 5	0.36	0.39	0.24
avaerage	0.33	0.39	0.24
standard deviation	0.04	0.03	0.08

Table C.12: HOMO QP energy shifts of five selected snapshots for the three solvated molecules without the solute-to-solvent feedback mechanism. Unit: eV

state number	isolated [eV]	solvated [eV]	QP energy shift [eV]
1	-30.78 ± 0.29	-29.85 ± 0.31	0.93 ± 0.43
2	-24.57 ± 0.14	-23.89 ± 0.16	0.68 ± 0.22
3	-22.03 ± 0.14	-20.94 ± 0.15	1.09 ± 0.20
4	-22.00 ± 0.13	-20.78 ± 0.13	1.22 ± 0.19
5	-19.06 ± 0.11	-18.01 ± 0.13	1.05 ± 0.17
6	-18.59 ± 0.11	-17.40 ± 0.13	1.19 ± 0.17
7	-17.00 ± 0.11	-16.02 ± 0.13	0.98 ± 0.17
8	-16.02 ± 0.11	-15.05 ± 0.12	0.97 ± 0.16
9	-14.74 ± 0.11	-13.73 ± 0.12	1.01 ± 0.16
10	-14.22 ± 0.09	-13.18 ± 0.10	1.04 ± 0.14
11	-13.60 ± 0.10	-12.64 ± 0.11	0.96 ± 0.15
12	-13.09 ± 0.13	-12.65 ± 0.14	0.44 ± 0.20
13	-12.85 ± 0.13	-11.92 ± 0.14	0.93 ± 0.18
14	-11.91 ± 0.09	-10.88 ± 0.10	1.03 ± 0.14
15	-11.43 ± 0.09	-10.61 ± 0.10	0.82 ± 0.14
16	-11.02 ± 0.10	-10.28 ± 0.11	0.74 ± 0.16
17	-8.94 ± 0.09	-8.00 ± 0.09	0.94 ± 0.13
18	-8.26 ± 0.06	-7.30 ± 0.07	0.96 ± 0.09
average	-	-	0.94
standard deviation	-	-	0.18

Table C.13: QP energies and QP energy shifts of all valence states of isolated and solvated phenol molecule. Unit: eV

state number	isolated [eV]	solvated [eV]	QP energy shift [eV]
1	-30.97 ± 0.21	-30.27 ± 0.22	0.70 ± 0.31
2	-30.65 ± 0.20	-29.79 ± 0.22	0.86 ± 0.30
3	-28.49 ± 0.18	-27.28 ± 0.20	1.21 ± 0.27
4	-27.38 ± 0.17	-26.15 ± 0.19	1.23 ± 0.26
5	-24.21 ± 0.15	-23.26 ± 0.15	0.95 ± 0.21
6	-21.44 ± 0.12	-20.47 ± 0.13	0.97 ± 0.18
7	-20.69 ± 0.11	-19.70 ± 0.12	0.99 ± 0.16
8	-20.12 ± 0.14	-19.13 ± 0.16	0.99 ± 0.21
9	-17.65 ± 0.10	-16.67 ± 0.12	0.98 ± 0.16
10	-17.63 ± 0.10	-16.65 ± 0.11	0.98 ± 0.15
11	-16.52 ± 0.12	-15.55 ± 0.13	0.97 ± 0.17
12	-14.98 ± 0.11	-14.43 ± 0.12	0.55 ± 0.16
13	-15.09 ± 0.12	-14.30 ± 0.13	0.79 ± 0.18
14	-14.27 ± 0.10	-13.55 ± 0.11	0.72 ± 0.14
15	-13.97 ± 0.15	-13.22 ± 0.18	0.75 ± 0.23
16	-13.46 ± 0.21	-12.87 ± 0.23	0.59 ± 0.32
17	-13.28 ± 0.11	-12.43 ± 0.12	0.85 ± 0.16
18	-13.17 ± 0.10	-12.37 ± 0.11	0.80 ± 0.15
19	-12.91 ± 0.11	-11.96 ± 0.13	0.95 ± 0.17
20	-11.60 ± 0.11	-10.89 ± 0.12	0.71 ± 0.16
21	-9.60 ± 0.14	-8.74 ± 0.15	0.86 ± 0.20
22	-9.52 ± 0.15	-8.79 ± 0.16	0.73 ± 0.22
23	-8.97 ± 0.15	-8.17 ± 0.16	0.80 ± 0.22
24	-8.65 ± 0.06	-7.80 ± 0.07	0.85 ± 0.09
average	-	-	0.87
standard deviation	-	-	0.17

Table C.14: QP energies and QP energy shifts of all valence states of isolated and solvated thymine molecule. Unit: eV

state number	isolated [eV]	solvated [eV]	QP energy shift [eV]
1	-33.29 ± 0.24	-32.34 ± 0.26	0.95 ± 0.35
2	-30.52 ± 0.22	-29.29 ± 0.25	1.23 ± 0.33
3	-26.17 ± 0.19	-25.19 ± 0.20	0.98 ± 0.28
4	-24.48 ± 0.15	-24.18 ± 0.15	0.30 ± 0.21
5	-22.94 ± 0.12	-21.98 ± 0.13	0.96 ± 0.17
6	-21.69 ± 0.14	-20.73 ± 0.15	0.96 ± 0.21
7	-21.72 ± 0.11	-20.73 ± 0.12	0.99 ± 0.16
8	-20.42 ± 0.11	-19.38 ± 0.12	1.04 ± 0.16
9	-18.59 ± 0.10	-17.44 ± 0.12	1.15 ± 0.16
10	-18.48 ± 0.11	-17.48 ± 0.13	1.00 ± 0.17
11	-17.64 ± 0.09	-16.67 ± 0.10	0.97 ± 0.13
12	-16.21 ± 0.10	-15.41 ± 0.12	0.80 ± 0.16
13	-16.00 ± 0.10	-15.19 ± 0.13	0.81 ± 0.14
14	-15.75 ± 0.09	-15.03 ± 0.10	0.72 ± 0.13
15	-15.66 ± 0.15	-14.90 ± 0.17	0.76 ± 0.22
16	-14.75 ± 0.11	-14.03 ± 0.12	0.72 ± 0.16
17	-14.36 ± 0.09	-13.54 ± 0.09	0.82 ± 0.13
18	-14.55 ± 0.09	-13.74 ± 0.10	0.81 ± 0.13
19	-13.68 ± 0.09	-12.81 ± 0.10	0.87 ± 0.13
20	-13.43 ± 0.08	-12.64 ± 0.09	0.79 ± 0.12
21	-13.25 ± 0.09	-12.34 ± 0.10	0.91 ± 0.14
22	-12.74 ± 0.08	-12.09 ± 0.09	0.65 ± 0.12
23	-12.64 ± 0.08	-11.85 ± 0.09	0.79 ± 0.12
24	-12.54 ± 0.09	-11.65 ± 0.10	0.89 ± 0.13
25	-11.68 ± 0.08	-11.27 ± 0.09	0.41 ± 0.12
26	-11.40 ± 0.07	-10.50 ± 0.08	0.90 ± 0.11
27	-11.25 ± 0.13	-10.30 ± 0.14	0.95 ± 0.19
28	-11.15 ± 0.08	-10.31 ± 0.08	0.84 ± 0.12
29	-10.73 ± 0.15	-9.82 ± 0.16	0.91 ± 0.22
30	-8.67 ± 0.10	-7.84 ± 0.07	0.88 ± 0.14
31	-8.75 ± 0.08	-7.91 ± 0.08	0.84 ± 0.12
32	-8.90 ± 0.09	-8.11 ± 0.10	0.79 ± 0.13
average	-	-	0.86
standard deviation	-	-	0.18

Table C.15: QP energies and QP energy shifts of all valence states of isolated and solvated phenylalanine molecule

state number	QP energy (solvated) [eV]	$\mathrm{Im}\Sigma_c$	$\mathrm{Im}\Sigma_c^{iso}$	$\mathrm{Im}\Sigma_c^{iso}/\mathrm{Im}\Sigma_c$
1	-32.34 ± 0.26	4.09	2.80	0.68
2	-29.29 ± 0.25	3.10	2.27	0.73
3	-25.19 ± 0.20	2.85	1.81	0.64
4	-24.18 ± 0.15	3.77	3.1	0.82
5	-21.98 ± 0.13	2.56	1.75	0.68
6	-20.73 ± 0.15	2.83	2.11	0.75
7	-20.73 ± 0.12	2.17	1.41	0.65
8	-19.38 ± 0.12	1.87	1.08	0.58
9	-17.44 ± 0.12	1.59	0.90	0.57
10	-17.48 ± 0.13	1.74	1.32	0.76
11	-16.67 ± 0.10	1.60	1.01	0.63
12	-15.41 ± 0.12	1.34	0.60	0.45
13	-15.19 ± 0.13	1.50	0.85	0.57
14	-15.03 ± 0.10	1.55	1.01	0.65
15	-14.90 ± 0.17	1.48	0.65	0.44
16	-14.03 ± 0.12	1.46	0.70	0.48
17	-13.54 ± 0.09	1.09	0.62	0.57
18	-13.74 ± 0.10	1.23	0.75	0.61
19	-12.81 ± 0.10	1.01	0.40	0.40
20	-12.64 ± 0.09	1.04	0.49	0.47
21	-12.34 ± 0.10	1.01	0.44	0.44
22	-12.09 ± 0.09	1.10	0.66	0.60
23	-11.85 ± 0.09	1.04	0.48	0.46
24	-11.65 ± 0.10	0.86	0.29	0.34
25	-11.27 ± 0.09	1.37	0.93	0.68
26	-10.50 ± 0.08	0.74	0.21	0.28
27	-10.30 ± 0.14	0.87	0.20	0.23
28	-10.31 ± 0.08	0.58	0.15	0.26
29	-9.82 ± 0.16	0.86	0.30	0.35
30	-7.84 ± 0.07	0.46	0.05	0.11
31	-7.91 ± 0.08	0.43	0.05	0.12
32	-8.11 ± 0.10	0.56	0.17	0.30
Average	-	-	-	0.51

Table C.16: Imaginary parts of the self energy at the QP energy of all valence states for solvated ($\mathrm{Im}\Sigma_c$) and isolated ($\mathrm{Im}\Sigma_c^{iso}$) phenyalanine and the ratio between these two.

Bibliography

[1] E. Aprà, E. J. Bylaska, W. A. de Jong, N. Govind, K. Kowalski, T. P. Straatsma, M. Valiev, H. J. J. van Dam, Y. Alexeev, J. Anchell, V. Anisimov, F. W. Aquino, R. Atta-Fynn, J. Autschbach, N. P. Bauman, J. C. Becca, D. E. Bernholdt, K. Bhaskaran-Nair, S. Bogatko, P. Borowski, J. Boschen, J. Brabec, A. Bruner, E. Cauët, Y. Chen, G. N. Chuev, C. J. Cramer, J. Daily, M. J. O. Deegan, T. H. Dunning, M. Dupuis, K. G. Dyall, G. I. Fann, S. A. Fischer, A. Fonari, H. Früchtl, L. Gagliardi, J. Garza, N. Gawande, S. Ghosh, K. Glaesemann, A. W. Götz, J. Hammond, V. Helms, E. D. Hermes, K. Hirao, S. Hirata, M. Jacquelin, L. Jensen, B. G. Johnson, H. Jónsson, R. A. Kendall, M. Klemm, R. Kobayashi, V. Konkov, S. Krishnamoorthy, M. Krishnan, Z. Lin, R. D. Lins, R. J. Littlefield, A. J. Logsdail, K. Lopata, W. Ma, A. V. Marenich, J. Martin del Campo, D. Mejia-Rodriguez, J. E. Moore, J. M. Mullin, T. Nakajima, D. R. Nascimento, J. A. Nichols, P. J. Nichols, J. Nieplocha, A. Otero-de-la Roza, B. Palmer, A. Panyala, T. Pirojsirikul, B. Peng, R. Peverati, J. Pittner, L. Pollack, R. M. Richard, P. Sadayappan, G. C. Schatz, W. A. Shelton, D. W. Silverstein, D. M. A. Smith, T. A. Soares, D. Song, M. Swart, H. L. Taylor, G. S. Thomas, V. Tipparaju, D. G. Truhlar, K. Tsemekhman, T. Van Voorhis, Á. Vázquez-Mayagoitia, P. Verma, O. Villa, A. Vishnu, K. D. Vogiatzis, D. Wang, J. H. Weare, M. J. Williamson, T. L. Windus, K. Woliński, A. T. Wong, Q. Wu, C. Yang, Q. Yu, M. Zacharias, Z. Zhang, Y. Zhao, and R. J. Harrison, *Nwchem: Past, present, and future*, *The Journal of Chemical Physics* **152** (2020), no. 18 184102.

[2] H. J. C. Berendsen, D. van der Spoel, and R. van Drunen, *Gromacs: A message-passing parallel molecular dynamics implementation*, *Computer Physics Communications* **91** (1995), no. 1 43–56.

[3] J. Wang, R. M. Wolf, J. W. Caldwell, P. A. Kollman, and D. A. Case, *Development and testing of a general amber force field*, *Journal of computational chemistry* **25** (2004), no. 9 1157–1174.

[4] W. L. Jorgensen and J. D. Madura, *Temperature and size dependence for monte carlo simulations of tip4p water*, *Molecular Physics* **56** (1985), no. 6 1381–1392.

[5] R. J. Lipert and S. D. Colson, *Accurate ionization potentials of phenol and*

phenol-(h2o) from the electric field dependence of the pump–probe photoionization threshold, *The Journal of Chemical Physics* **92** (1990), no. 5 3240–3241.

[6] S. Urano, X. Yang, and P. R. LeBreton, *Uv photoelectron and quantum mechanical characterization of dna and rna bases: valence electronic structures of adenine, 1,9-dimethyl-guanine, 1-methylcytosine, thymine and uracil*, *Journal of Molecular Structure* **214** (1989) 315–328.

[7] K. T. Lee, J. Sung, K. J. Lee, S. K. Kim, and Y. D. Park, *Conformation-dependent ionization of l-phenylalanine: structures and energetics of cationic conformers*, *Chemical Physics Letters* **368** (2003), no. 3 262–268.

[8] J. W. Riley, B. Wang, J. L. Woodhouse, M. Assmann, G. A. Worth, and H. H. Fielding, *Unravelling the role of an aqueous environment on the electronic structure and ionization of phenol using photoelectron spectroscopy*, *The Journal of Physical Chemistry Letters* **9** (2018), no. 4 678–682.

[9] S. K. Kim, W. Lee, and D. R. Herschbach, *Cluster beam chemistry: hydration of nucleic acid bases; ionization potentials of hydrated adenine and thymine*, *The Journal of Physical Chemistry* **100** (1996), no. 19 7933–7937.

[10] K. T. Lee, J. Sung, K. J. Lee, Y. D. Park, and S. K. Kim, *Conformation-dependent ionization energies of l-phenylalanine*, *Angewandte Chemie International Edition* **41** (2002), no. 21 4114–4117.

[11] A. Roy, R. Seidel, G. Kumar, and S. E. Bradforth, *Exploring redox properties of aromatic amino acids in water: Contrasting single photon vs resonant multiphoton ionization in aqueous solutions*, *The Journal of Physical Chemistry B* **122** (2018), no. 14 3723–3733.

[12] D. Ghosh, A. Roy, R. Seidel, B. Winter, S. Bradforth, and A. I. Krylov, *First-principle protocol for calculating ionization energies and redox potentials of solvated molecules and ions: Theory and application to aqueous phenol and phenolate*, *The Journal of Physical Chemistry B* **116** (2012), no. 24 7269–7280.

[13] D. Ghosh, O. Isayev, L. V. Slipchenko, and A. I. Krylov, *Effect of solvation on the vertical ionization energy of thymine: From microhydration to bulk*, *The Journal of Physical Chemistry A* **115** (2011), no. 23 6028–6038.

[14] D. M. Close, *Calculated vertical ionization energies of the common α-amino acids in the gas phase and in solution*, *The Journal of Physical Chemistry A* **115** (2011), no. 13 2900–2912.

Appendix D

Supporting information for "Spatial Decay and Limits of Quantum Solute–Solvent Interactions"

Guorong Weng, Amanda Pang,[a] Vojtěch Vlček

D.1 Theory and Methodology

This section summarizes the theories involved in the main text and the corresponding computational details. Technical information about the stochastic *GW* approach can be found in refs 1, 2, 3. For the fragment-Pipek-Mezey localization, please refer to ref 4 for more details.

[a]Current institution: University of Pennsylvania, PA, 19104, USA

D.1.1 Molecular Dynamics Simulations

Molecular dynamics (MD) simulations are employed to generate snapshots for each solvated systems. Throughout this work, we use the Gromacs 5 package[5] with the generalized Amber force field, AM1-bcc charge method, and three-dimensional (3D) periodic boundary conditions for all MD calculations. The solute molecule, phenol, is structurally relaxed at the MP2/cc-pVDZ using the NWchem package. For the H_2O case, we employ the TIP4P water model.[6] For the other four organic solvents, we first build the solvent-only systems using their mass-density at room temperature under 1 atmosphere. These systems are then equilibrated using the NVT ensemble. Finally, these solvents with equilibrated geometries are used to solvate the phenol molecule. The solvated systems are treated with the following: energy minimization, NVT equilibrium, NPT equilibrium, and MD simulations at 300 K. All the MD simulations run 10,000,000 relaxation steps with a time interval of 0.0005 ps, resulting in a total simulation time of 5,000 ps. From the MD trajectory of each solvated system, we extract a snapshot every 1,000 ps and obtain five representative system geometries. These five extracted snapshots are further used in the Density Functional Theory (DFT) calculations and many-body calculations.

D.1.2 Density Functional Theory Calculations

DFT calculations in this work employ a real-space implementation with 3D periodic boundary conditions (for the solvated systems), the PBE exchange-correlation functional,[7] and Troullier-Martines pseudopotentials.[8] The resulting canonical eigenstates are used in the following orbital localization and many-body calculations. Parameters of the DFT calculations are provided in Table D.1-D.5. For all the calculations, the plane-wave kinetic energy cut-off is set at 26 E_h.

D.1.3 Fragment-Pipek-Mezey Localization

Pipek-Mezey (PM) orbital localization is performed on the set of occupied canonical orbitals to obtain the localized electronic subspace. The original PM cost function $\mathcal{P}$ reads

$$\mathcal{P}(\mathbf{U}) = \sum_{i=1}^{N_s} \sum_{A=1}^{N_A} [Q_{ii}^{A}(\mathbf{U})]^2 \tag{D.1}$$

where $\mathbf{U}$ is the unitary matrix that transforms the basis, N_s is the number of states considered in the transformation, N_A denotes the number of atoms involved in the transformation, and Q is the atomic partial charge matrix. When $\mathcal{P}$ is maximized, the corresponding $\mathbf{U}$ yields the PM localized orbitals. The Q matrix is computed by

$$Q_{ij}^{A,n} = \int \psi_i^{n*}(\mathbf{r}) w_A(\mathbf{r}) \psi_j^{n}(\mathbf{r}) \mathrm{d}\mathbf{r} \tag{D.2}$$

where ψ_i^n represents the transformed states at the n^{th} iteration step of maximization. $w_A(\mathbf{r})$ in eq (D.2) denotes the atomic weight function, for which we employ the real-space partitioning scheme with the Gaussian form.

If all the atoms are included in eqs. (D.1) and (D.2), the $\mathcal{P}$ will reach a global maximum, and localized orbitals will be obtained for the whole system. However, the cost of localization depends linearly on the N_A, and this will suffer from a cost overhead if one is interested only in a single fragment of the system. Herein, we employ the modified $\mathcal{P}$, as introduced in ref 4, for orbital localization of a selected fragment. The fragment weight function is defined as

$$F^k(\mathbf{r}) = \sum_{i}^{N_A^k} w_i^k(\mathbf{r}) \tag{D.3}$$

Here, $F^k(\mathbf{r})$ is the weight function of the k^{th} fragment, N_A^k is the number of atoms constituting the k^{th} fragment, and $w_i^k(\mathbf{r})$ is the atomic weight function of each atom

belonging to the k^{th} fragment. The Q matrix for the selected fragment is thus written as

$$Q_{ij}^{k,n} = \int \psi_i^{n*}(\mathbf{r}) F^k(\mathbf{r}) \psi_j^n(\mathbf{r}) \mathrm{d}\mathbf{r} \tag{D.4}$$

which is in fact a fragment partial charge matrix. The modified PM cost function with the fragment partial charge matrix reads

$$\mathcal{P}'(\mathbf{U}) = \sum_{i=1}^{N_s'} [Q_{ii}^k(\mathbf{U})]^2 \tag{D.5}$$

where N_s' denotes the number of localized states that are being sought on the k^{th} fragment. Note that maximization of $\mathcal{P}'$ leads to only N_s' states that are localized on the fragment but not maximally-localized on each atom of the fragment. Yet, these N_s' states are sufficient to define the electronic subspace for the k^{th} fragment. If one is interested in the real PM localized orbitals on each atom of the fragment, these N_s' can be used as input states to maximize the original cost function $\mathcal{P}$ in eq (D.1).

D.1.4 Stochastic G_0W_0 Calculations

In this work, quasiparticle (QP) energies are computed by applying the non-local and dynamical self-energy as a perturbative correction to the DFT eigenvalue. The QP energy reads

$$\varepsilon_j^{QP} = \varepsilon_j^0 + \langle \phi_j | \hat{\Sigma}_{\text{X}} + \hat{\Sigma}_{\text{C}}(\omega = \varepsilon_j^{QP}) - \hat{v}_{xc} | \phi_j \rangle \tag{D.6}$$

Here, ε_j^0 represents the eigenvalue of the eigenstate ϕ_j using the mean-field exchange functional $\hat{v}_{xc}$. The non-local exchange interaction $\hat{\Sigma}_{\text{X}}$ is equivalent to the Fock operator. The frequency-dependent correlation self-energy $\hat{\Sigma}_{\text{C}}$ is obtained by fourier transforming the time-dependent counterpart.

In the stochastic G_0W_0 formalism, the Green's function (G_0) is sampled by a set of random vectors

$$G_0(\mathbf{r},\mathbf{r}';t) = -i\{\zeta(\mathbf{r};t)\bar{\zeta}(\mathbf{r}')\} \tag{D.7}$$

where the brackets $\{\dots\}$ denote averaging over the number of random vectors used in sampling. The random function $\bar{\zeta}(\mathbf{r})$ is given by

$$\bar{\zeta}(\mathbf{r}) = \pm\frac{1}{\mathrm{dV}} \tag{D.8}$$

Here, dV is the unit volume of the real-space grid, and the plus-minus sign represents the randomness. The time-evolved projected random function $\zeta(\mathbf{r};t)$ is written as

$$\zeta(\mathbf{r};t) = \begin{cases} \langle\mathbf{r}|e^{-i\hat{H}_0 t}\hat{P}^{occ}|\bar{\zeta}\rangle & t<0 \\ \langle\mathbf{r}|e^{-i\hat{H}_0 t}(\hat{I}-\hat{P}^{occ})|\bar{\zeta}\rangle & t>0 \end{cases} \tag{D.9}$$

In eq (D.9), $\hat{H}_0$ is the static mean-field Hamiltonian used in DFT calculations, $\hat{P}^{occ}$ is the projector composed of all the occupied states, and $\hat{I}$ is the identity.

The stochastic form of the G_0W_0 correlation self-energy reads

$$\langle\phi_j|\hat{\Sigma}_{\mathrm{C}}(t)|\phi_j\rangle = \{\int \phi_j(\mathbf{r})\zeta(\mathbf{r};t)u(\mathbf{r};t)\mathrm{d}\mathbf{r}\} \tag{D.10}$$

Here, $u(\mathbf{r};t)$ is the time-dependent potential due to the induced charge density. It is derived from the following retarded potential $\tilde{u}(\mathbf{r};t)$

$$\tilde{u}(\mathbf{r};t) = \int \nu(\mathbf{r},\mathbf{r}')\delta n(\mathbf{r}';t)\mathrm{d}\mathbf{r}' \tag{D.11}$$

where $\nu(\mathbf{r},\mathbf{r}') = \frac{1}{|\mathbf{r}-\mathbf{r}'|}$ is the Coulomb kernel, and the time-dependent induced charge

density fluctuations ($\delta n(\mathbf{r};t)$) is also sampled by another set of random vectors. Further details of deriving the $\delta n(\mathbf{r};t)$ are provided in the next section.

D.1.5 Generalized Decomposition of GW Correlation Self-energy

D.1.6 Fragment Electronic Subspace

For solute-solvent systems, localized orbitals provide a straightforward and convenient way to separate the solute from the environment. As mentioned above, the set of regionally PM localized orbitals on a specific molecule can be obtained directly by constructing a fragment. Moreover, the localization can be done by sequentially exhausting the orbital space.[4] Here, we first demonstrate the construction of an electronic subspace for the solute molecule, and then generalize it to any fragment in the system.

For the solute molecule, the fragment is defined by the following weight function

$$F^{mol}(\mathbf{r}) = \sum_{i}^{N_A^{mol}} w_i(\mathbf{r}) \tag{D.12}$$

where N_A^{mol} represents the number of atoms of the molecule and $w_i(\mathbf{r})$ is the atomic weight function of each atom using the real-space partitioning. This fragment weight function is used in the orbital localization (see eqs. (D.4) and (D.5)), which leads to regionally localized orbitals. The localization is essentially broken into two steps: (1) search for N_s localized states on the molecule; (2) localize these N_s states on each atom of the molecule. This work focuses on the occupied subspace, and N_s includes all the valence electrons of the molecule. Note that only the second step provides the PM localized orbitals. However, the first step is sufficient to separate the solute from the environment. Mathematically,

the molecular electronic subspace is defined by the following projector

$$\hat{P}^{mol} = \sum_{i}^{N_s} |\psi_i^{mol}\rangle \langle \psi_i^{mol}| \tag{D.13}$$

where ψ_i^{mol} represents a localized orbital on the solute molecule. This set of localized basis is also used to reconstruct the molecular state ϕ_j^R

$$|\phi_j^R\rangle = \sum_{i}^{N_s} \alpha_{ji} |\psi_i^{mol}\rangle \tag{D.14}$$

Here, α_{ji} is the coefficient obtained from decomposing the ϕ_j^{iso} of the isolated molecule in its localized basis. There is a one-to-one correspondence between the localized basis of the solvated molecule and that of the isolated molecule. The full recipe can be found in our previous work.[9] The superscript "R" in eq (D.14) is omitted for clarity in this work.

Analogously, we can define a weight function of any fragment in the system for the orbital localization

$$F^k(\mathbf{r}) = \sum_{i}^{N_A^k} w_i^k(\mathbf{r}) \tag{D.15}$$

Here, N_A^k denotes the number of atoms that constitute the k^{th} fragment. In a multi-molecule system, a fragment can be a single molecule or a cluster of molecules. The corresponding electronic subspace is then given by

$$\hat{P}^k = \sum_{i}^{N_s'} |\psi_i^k\rangle \langle \psi_i^k| \tag{D.16}$$

where ψ_i^k is a localized orbital and N_s' represents the number of localized occupied orbitals on the k^{th} fragment.

In our solute-solvent systems, we first separate the solute molecule from the solvent environment, and then fragment the environment into multiple solvent shells. The solvent

molecules within the same shell are (ideally) of the same distance away from the solute. The shell weight function F_s^k has the following form

$$F_s^k(\mathbf{r};\mathbf{R}^k) = \sum_i^{N_A^k} w_i^k(\mathbf{r}) \tag{D.17}$$

Here, the k^{th} shell is characterized by the distance $\mathbf{R}^k$. The shell weight function sums over all the N_A^k atoms in the k^{th} shell. Accordingly, the electronic subspace of the k^{th} shell is defined by the projector in eq D.16.

D.1.7 Fragment Correlation Self-energy

The frequency-dependent correlation self-energy $\hat{\Sigma}_{\text{C}}(\omega)$ in eq (D.6) is practically obtained from the Fourier transformation of the time-dependent counterpart $\hat{\Sigma}_{\text{C}}(t)$ (eq (D.10)). In the *GW* approximation, the $\Sigma_{\text{C}}(t)$ (expectation value) stems from the time-dependent charge density fluctuations $\delta n(t)$ (see eqs. (D.10) and (D.11)) induced by the electron removal/addition

$$\Sigma_{\text{C}}(t) = \Sigma_{\text{C}}\left[\delta n(t), t\right] \tag{D.18}$$

In a real-time and real-space implementation, $\delta n(t)$ is computed by

$$\delta n(\mathbf{r}, t) = n(\mathbf{r}, t) - n_0(\mathbf{r}) \tag{D.19}$$

where $n(\mathbf{r}, t)$ is computed from the time-evolved single-particle states and $n_0(\mathbf{r})$ denotes the ground-state (GS) density. The deterministic $n_0(\mathbf{r})$ is usually obtained from all the

N_{occ} occupied canonical KS orbitals

$$n_0(\mathbf{r}) = \sum_i^{N_{occ}} \phi_i^*(\mathbf{r})\phi_i(\mathbf{r}) \tag{D.20}$$

Alternatively, the GS density can also be expressed by a set of unitary transformed states, e.g., localized orbitals

$$n_0(\mathbf{r}) = \sum_i^{N_{occ}} \psi_i^*(\mathbf{r})\psi_i(\mathbf{r}) \tag{D.21}$$

where ψ_i represents a localized orbital. Upon the fragmentation of a system, the GS density can be further written as

$$n_0(\mathbf{r}) = \sum_k^{N_{frag}} \sum_i^{N_{occ}^k} \psi_i^{k*}(\mathbf{r})\psi_i^k(\mathbf{r}) = \sum_k^{N_{frag}} n_0^k(\mathbf{r}) \tag{D.22}$$

Here, N_{occ}^k is the number of occupied states on the k^{th} fragment. ψ_i^k and $n_0^k(\mathbf{r})$ denote an orbital and the density localized on the k^{th} fragment, respectively.

In contrast to $n_0(\mathbf{r})$, the time-dependent density $n(\mathbf{r}, t)$ is calculated by a set of time-evolved states that are perturbed by the electron addition/removal at $t = 0$. In order to express $n(\mathbf{r}, t)$ in the same form of eq (D.22), we make the following assumption in this work: the perturbed and time-evolved ψ^k stay localized on the k^{th} fragment. In other words, we assume no intermolecular charge transfer happens and all the density fluctuations remain on the fragment. This "local density fluctations" assumption is reasonable when there is no apparent donor-acceptor character found in a van-der Waals bound molecular system. Upon this assumption, $n(\mathbf{r}, t)$ is written as

$$n(\mathbf{r}, t) = \sum_k^{N_{frag}} \sum_i^{N_{occ}^k} \psi_i^{k*}(\mathbf{r}, t)\psi_i^k(\mathbf{r}, t) = \sum_k^{N_{frag}} n^k(\mathbf{r}, t) \tag{D.23}$$

where ψ_i^k represents a time-evolved localized orbital on the k^{th} fragment, and $n^k(\mathbf{r}, t)$ is

the time-evolved density localized on the k^{th} fragment.

Plugging eqs. (D.22) and (D.23) in Eq (D.19), the induced density fluctuation $\delta n(\mathbf{r}, t)$ is thus fragmented

$$\delta n(\mathbf{r}, t) = \sum_{k}^{N_{frag}} n^k(\mathbf{r}, t) - \sum_{k}^{N_{frag}} n_0^k(\mathbf{r}) = \sum_{k}^{N_{frag}} \delta n^k(\mathbf{r}, t) \tag{D.24}$$

where $\delta n^k(\mathbf{r}, t)$ denotes the local density fluctuation on the k^{th} fragment. The fragmented $\delta n(\mathbf{r}, t)$ further leads to the fragment correlation energy Σ_{C}

$$\Sigma_{\text{C}}[\delta n(t), t] = \sum_{k}^{N_{frag}} \Sigma_{\text{C}}^k \left[\delta n^k(\mathbf{r}, t), t\right] \tag{D.25}$$

For a specific molecular state ϕ_j, the fragmentation of Σ_{C} in the frequency domains reads

$$\Sigma_{\text{C}}(\omega = \varepsilon_j^{QP}) = \sum_{k}^{N_{frag}} \Sigma_{\text{C}}^k(\omega = \varepsilon_j^{QP}) \tag{D.26}$$

In this work, we do not aim to prove the equivalence shown in eq (D.26). Instead, we first compute the correlation energy contributed from a specific fragment, e.g., a solvation shell at distance $\mathbf{R}^k$, and then study the decay of Σ_{C}^k as a function of $\mathbf{R}^k$.

In our stochastic GW formalism, both $n(\mathbf{r}, t)$ and $n_0(\mathbf{r})$ are stochastically sampled by a set of random functions, and $n_0(\mathbf{r})$ also becomes time-dependent due to its stochastic nature

$$n(\mathbf{r}, t) = \{\eta^*(\mathbf{r}, t)\eta(\mathbf{r}, t)\} \tag{D.27}$$

At $t = 0$, $\eta(\mathbf{r})$ is a random vector projected onto the occupied subspace

$$\eta(\mathbf{r}) = \langle \mathbf{r}|\hat{P}^{occ}|\bar{\eta}\rangle \tag{D.28}$$

where $\bar{\eta}$ is a random function in real space: $\bar{\eta}(\mathbf{r}) = \pm\frac{1}{\mathrm{dV}}$ (dV is the unit volume). The stochastic resolution of identity is satisfied by the constructed $\bar{\eta}$.[1, 2] The projector $\hat{P}^{occ}$ consists of all the occupied states. Similar to the deterministic case, $\eta(\mathbf{r})$ is perturbed at $t = 0$ by the electron addition/removal and then time-evolved, which gives $n(\mathbf{r}, t)$ equivalent to the one in eq (D.19). Without perturbation, the time-evolved η instead leads to $n_0(\mathbf{r}, t)$. And the induced density fluctuation $\delta n(\mathbf{r}, t)$ is then generated via eq (D.19) using the stochastic $n(\mathbf{r}, t)$ and $n_0(\mathbf{r}, t)$

$$\delta n(\mathbf{r}, t) = n(\mathbf{r}, t) - n_0(\mathbf{r}, t) \tag{D.29}$$

In the previous section, we introduce the electronic subspace for the k^{th} solvation shell. The stochastic sampling of $\delta n^k(\mathbf{r}, t)$ in eq (D.24) can be achieved by replacing the operator $\hat{P}^{occ}$ in eq D.28 with $\hat{P}^k$ (eq D.16)

$$\eta^k(\mathbf{r}) = \langle \mathbf{r}|\hat{P}^k|\bar{\eta}\rangle \tag{D.30}$$

Here, $\eta^k(\mathbf{r})$ represents a localized random function on the k^{th} solvation shell. $\delta n^k(\mathbf{r}, t)$ can then be readily calculated by using $\eta^k(\mathbf{r})$ in eqs. (D.27) and (D.29). Finally, the correlation energy contributed from the k^{th} solvation shell is computed by the $\delta n^k(\mathbf{r}, t)$. Again, the stochastic implementation can easily treat any fragment with up to thousands of electrons. In the Results and Discussion section of the main text, we demonstrate the $\mathbf{R}^k$-dependence of Σ_{C}.

D.2 Supplementary Tables and Figures

Table D.1: Parameters of the simulation box used in DFT calculations for the H_2O solvated system. All lengths are provided in Bohr unit.

snapshot	small cell			large cell		
	lattice constant	grid spacing	grid size	lattice constant	grid spacing	grid size
1	29.663	0.3903	76^3	38.360	0.3996	96^3
2	30.366	0.3996	76^3	38.868	0.4049	96^3
3	29.646	0.3901	76^3	38.503	0.4011	96^3
4	29.982	0.3945	76^3	38.700	0.4031	96^3
5	29.525	0.3885	76^3	38.915	0.4054	96^3

Table D.2: Parameters of the simulation box used in DFT calculations for the ACN solvated system. All lengths are provided in Bohr unit.

snapshot	small cell			large cell		
	lattice constant	grid spacing	grid size	lattice constant	grid spacing	grid size
1	26.946	0.3963	68^3	33.991	0.3952	86^3
2	26.473	0.3893	68^3	34.047	0.3959	86^3
3	26.742	0.3933	68^3	34.215	0.3979	86^3
4	27.159	0.3994	68^3	34.824	0.4049	86^3
5	26.566	0.3907	68^3	34.157	0.3972	86^3

Table D.3: Parameters of the simulation box used in DFT calculations for the DCM solvated system. All lengths are provided in Bohr unit.

snapshot	small cell			large cell		
	lattice constant	grid spacing	grid size	lattice constant	grid spacing	grid size
1	29.126	0.3936	74^3	39.257	0.4006	98^3
2	29.196	0.3945	74^3	38.857	0.3965	98^3
3	29.051	0.3926	74^3	38.208	0.3899	98^3
4	29.680	0.4011	74^3	38.460	0.3924	98^3
5	29.170	0.3942	74^3	38.845	0.3954	98^3

Table D.4: Parameters of the simulation box used in DFT calculations for the THF solvated system. All lengths are provided in Bohr unit.

snapshot	small cell			large cell		
	lattice constant	grid spacing	grid size	lattice constant	grid spacing	grid size
1	30.547	0.3916	78^3	37.740	0.3931	96^3
2	31.103	0.3988	78^3	37.899	0.3948	96^3
3	30.449	0.3904	78^3	38.129	0.3972	96^3
4	30.665	0.3931	78^3	37.744	0.3932	96^3
5	31.124	0.3990	78^3	37.626	0.3919	96^3

Table D.5: Parameters of the simulation box used in DFT calculations for the BEN solvated system. All lengths are provided in Bohr unit.

snapshot	small cell			large cell		
	lattice constant	grid spacing	grid size	lattice constant	grid spacing	grid size
1	31.868	0.3984	80^3	40.264	0.3947	102^3
2	32.167	0.4021	80^3	40.822	0.4002	102^3
3	31.918	0.3990	80^3	41.221	0.4041	102^3
4	32.386	0.4048	80^3	40.979	0.4018	102^3
5	31.353	0.3919	80^3	40.452	0.3966	102^3

Parameters	value
plane wave cut-off (hartree)	26
number of random vectors used for sparse stochastic compression	20000
number of random vectors characterizing the screened Coulomb interaction (per each vector sampling the Green's function)	16
number of vectors sampling the Green's function	2000
maximum time for real-time propagation of the dynamical self-energy (a.u.)	50

Table D.6: Parameters in the *GW* calculations of all systems.

solvent	small cell	large cell
H_2O	118	273
ACN	33	64
DCM	31	73
THF	31	59
BEN	30	62

Table D.7: Number of solvent molecules in the two simulation cells of each solvated system.

solvent	small cell			large cell			α_m (Å^3)
	ε^{iso} (σ)	$\varepsilon^{\text{solv}}$ (σ)	$\Delta\varepsilon$ (σ)	ε^{iso} (σ)	$\varepsilon^{\text{solv}}$ (σ)	$\Delta\varepsilon$ (σ)	
H_2O	-8.26 (0.08)	-7.34 (0.14)	0.92 (0.06)	-8.16 (0.16)	-7.11 (0.17)	1.05 (0.06)	1.48
ACN	-8.21 (0.07)	-7.15 (0.08)	1.06 (0.05)	-8.21 (0.15)	-7.11 (0.14)	1.10 (0.05)	4.41
DCM	-8.42 (0.23)	-7.14 (0.27)	1.28 (0.06)	-8.18 (0.15)	-6.75 (0.14)	1.43 (0.08)	6.50
THF	-8.16 (0.09)	-7.02 (0.04)	1.14 (0.08)	-8.16 (0.07)	-6.83 (0.10)	1.33 (0.07)	7.93
BEN	-8.18 (0.07)	-6.98 (0.07)	1.20 (0.06)	-8.22 (0.10)	-6.83 (0.14)	1.39 (0.05)	10.38

Table D.8: HOMO QP energies of isolated and solvated phenol and the ionization potential (IP) shifts. All energy values are averaged over five snapshots and reported in eV unit. Standard deviations (σ) are provided in parenthesis. The mean polarizability (α_m) of each solvent is provided for comparing the solvation many-body effects.

solvent	snapshot1	snapshot2	snapshot3	snapshot4	snapshot5	average
H_2O	99	98	99	90	97	97
ACN	31	32	31	32	34	32
DCM	20	25	23	27	24	24
THF	21	18	18	19	20	19
BEN	18	19	15	15	14	16

Table D.9: Number of *effective* solvent molecules in each snapshot of each solvated system. The results are obtained from the large simulation cells.

solvent	N_{eff}^0	$\Delta\varepsilon^0$	N_{eff}^m	$\overline{\Delta\varepsilon}^m$	$N_{\text{eff}}^m \times \overline{\Delta\varepsilon}^m$	$N_{\text{eff}}^0 \times \overline{\Delta\varepsilon}^m$
H_2O	97	1.05	96	0.0122	1.16	1.17
ACN	32	1.10	33	0.0374	1.23	1.20
DCM	24	1.43	27	0.0553	1.49	1.32
THF	19	1.33	21	0.0676	1.43	1.30
BEN	16	1.39	19	0.0887	1.73	1.44

Table D.10: Number of effective solvent molecules and average energy shift per solvent molecule derived from the proposed solvation model. The resulting QP energy shifts are compared with the first-principle results labelled by the superscript 0.

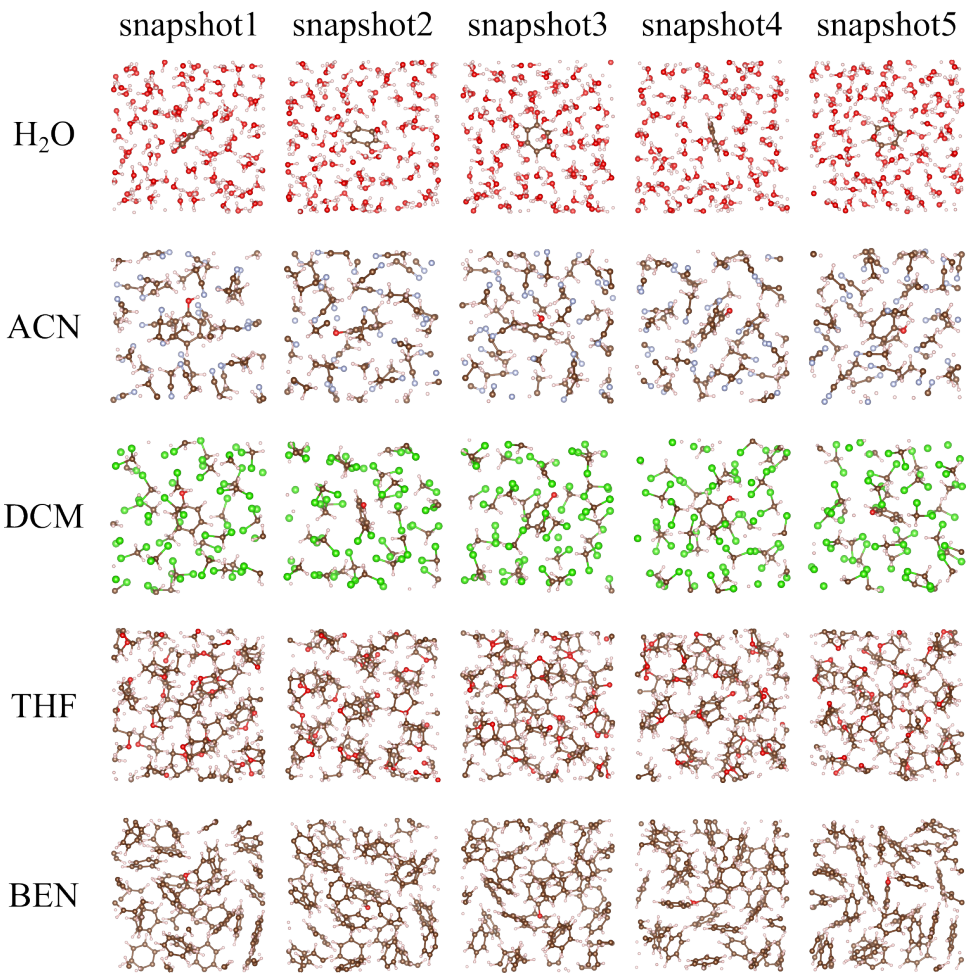

Figure D.1: Five extracted snapshots from the MD trajectories of each solvated system using the small simulation cell.

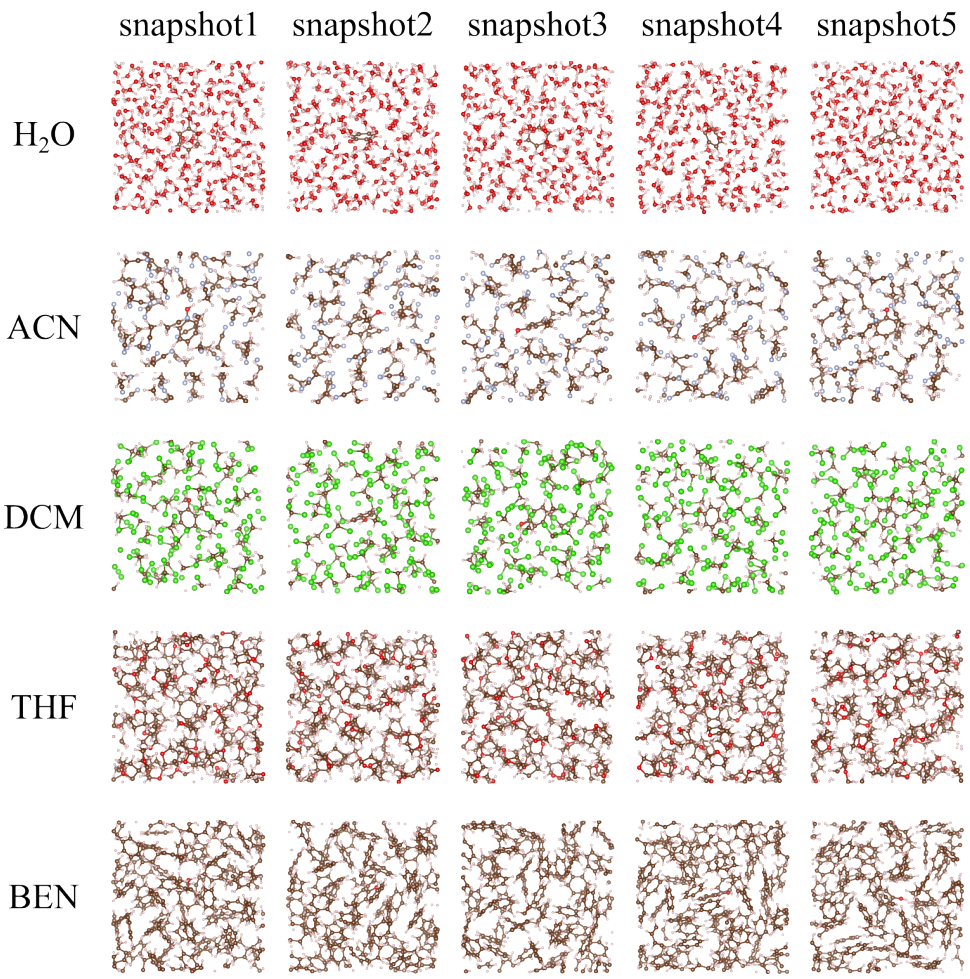

Figure D.2: Five extracted snapshots from the MD trajectories of each solvated system using the large simulation cell.

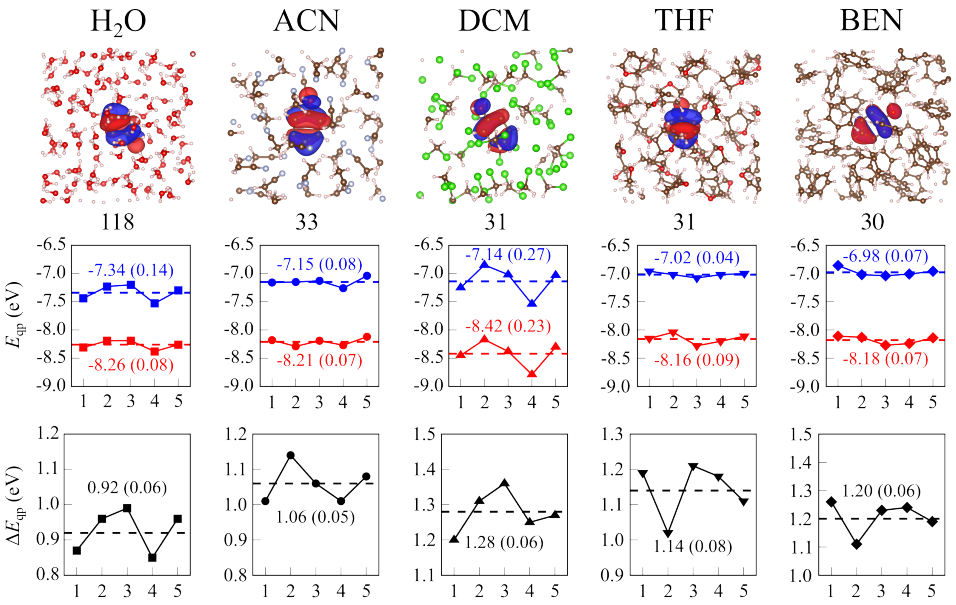

Figure D.3: Computational results for each solvated system using the small simulation cell: representative solvated HOMO (upper part), HOMO QP energies of each selected snapshot (middle part), and QP energy shifts between the isolated and solvated HOMO of each selected snapshot (lower part). The blue color represents the solvated HOMO while the red color represents the isolated counterpart. The dashed line indicates the average value over the five snapshots with the standard deviation provided in parenthesis.

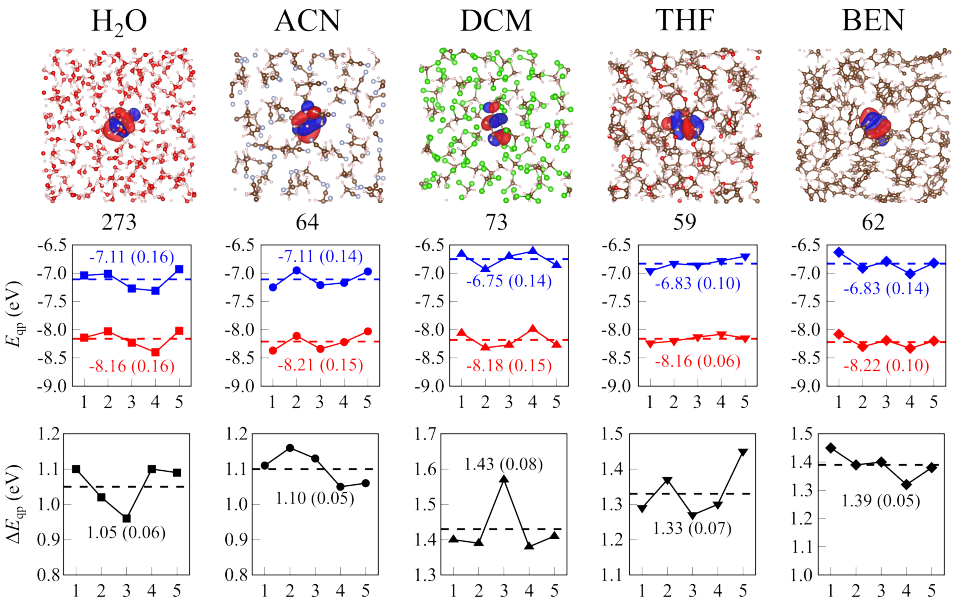

Figure D.4: Computational results for each solvated system using the large simulation cell: representative solvated HOMO (upper part), HOMO QP energies of each selected snapshot (middle part), and QP energy shifts between the isolated and solvated HOMO of each selected snapshot (lower part). The blue color represents the solvated HOMO while the red color represents the isolated counterpart. The dashed line indicates the average value over the five snapshots with the standard deviation provided in parenthesis.

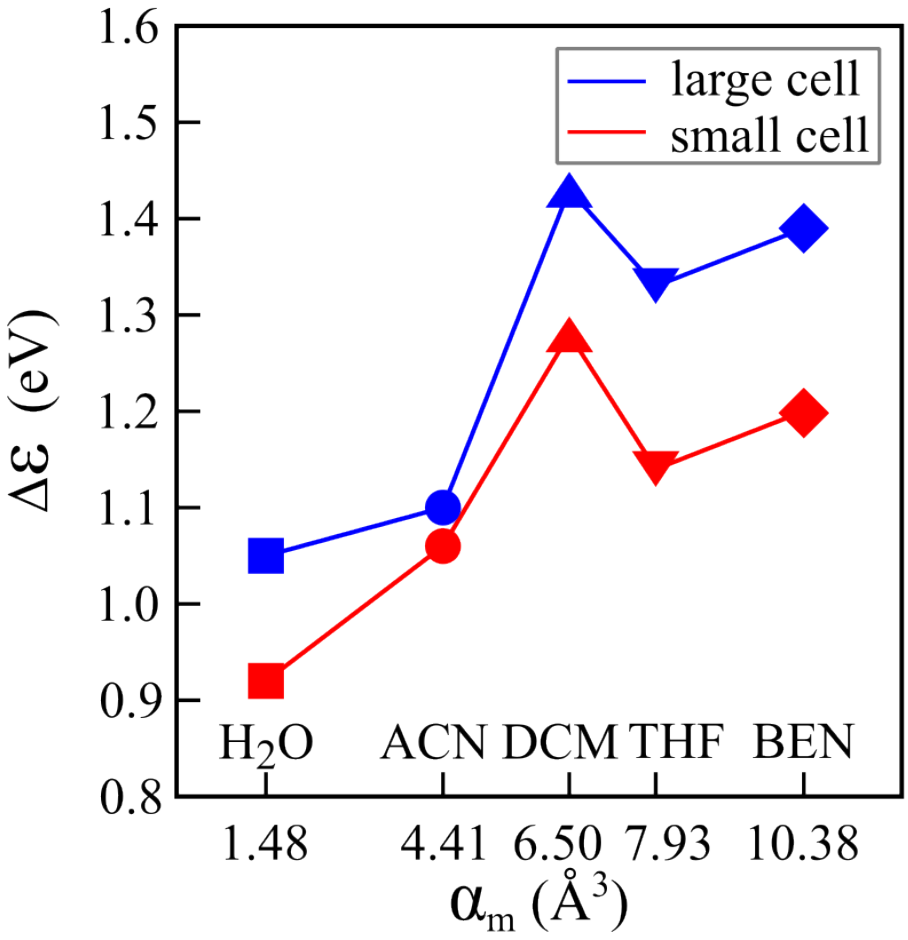

Figure D.5: IP shifts $\Delta\varepsilon$ plotted as a function of the mean polarizability; the two colors denote the two simulation cells with different number of solvent molecules.

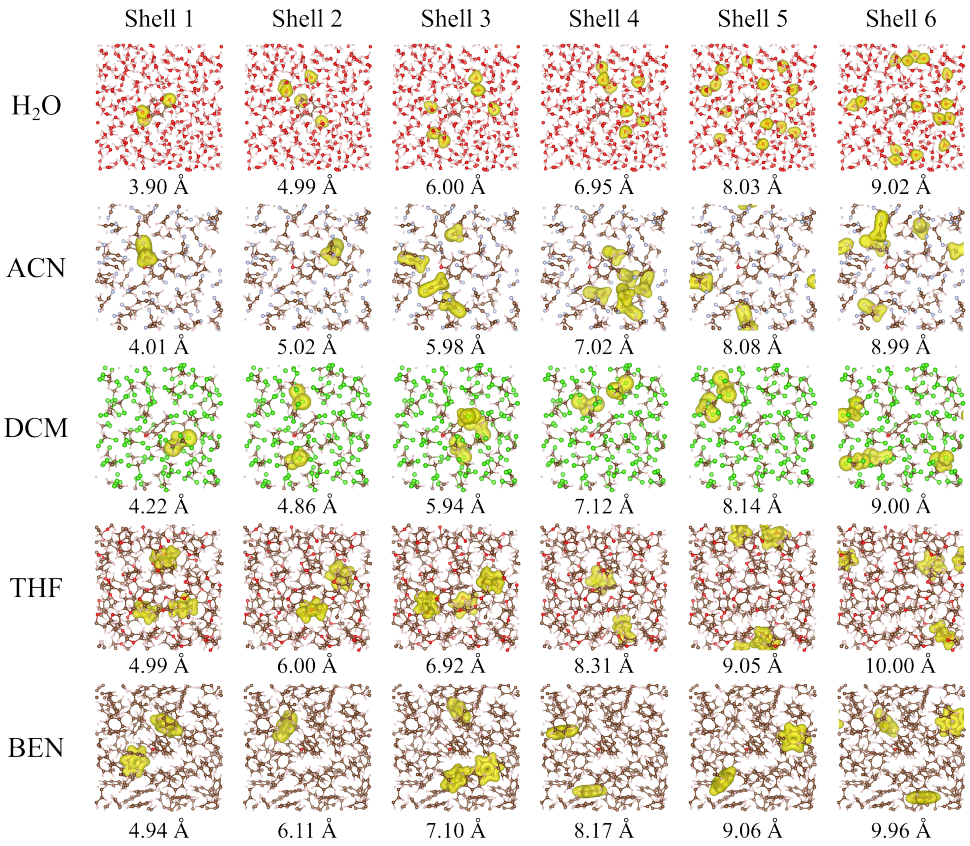

Figure D.6: Solvation shells represented by the electron density at six different distances for each solvated system.

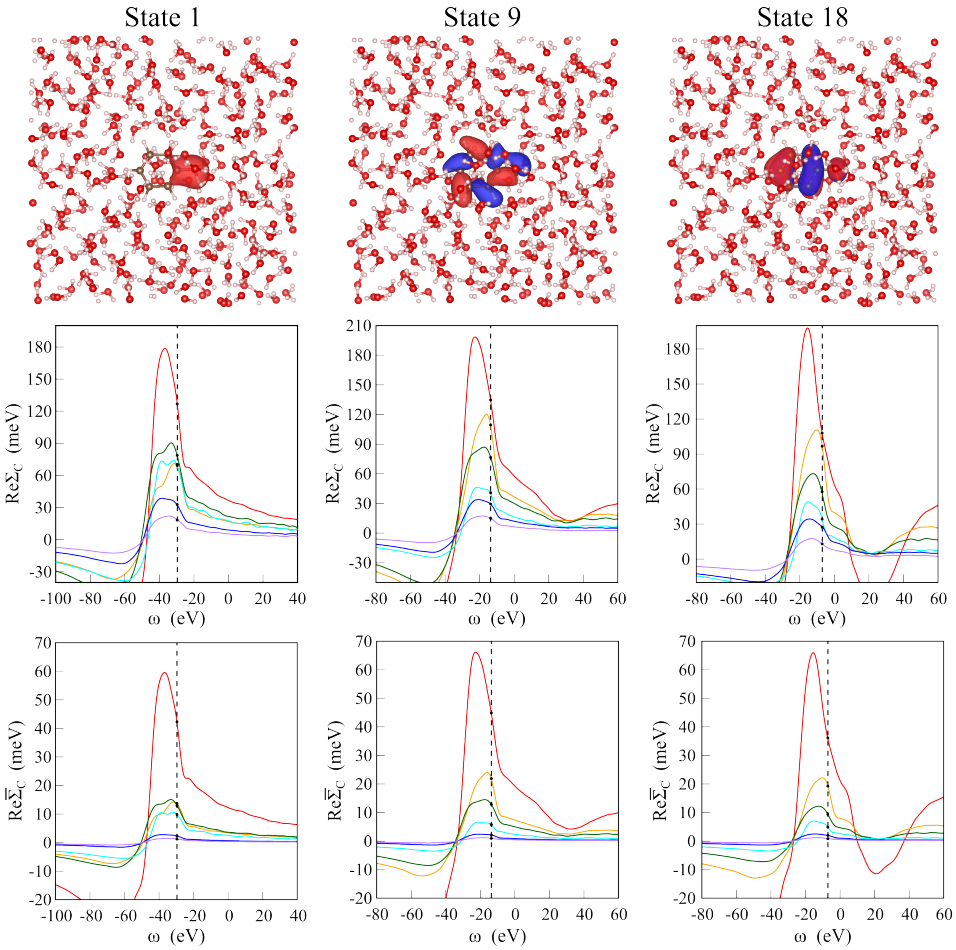

Figure D.7: Computational results for phenol in H_2O using the large simulation cell: the 1^{st}, 9^{th}, and 18^{th} ionization states (upper part), real part of the fragment correlation self-energy (before normalization) induced by the corresponding ionization state (middle part), and real part of the fragment correlation self-energy (after normalization) induced by the corresponding ionization state (lower part). The dashed line indicates the QP energy.

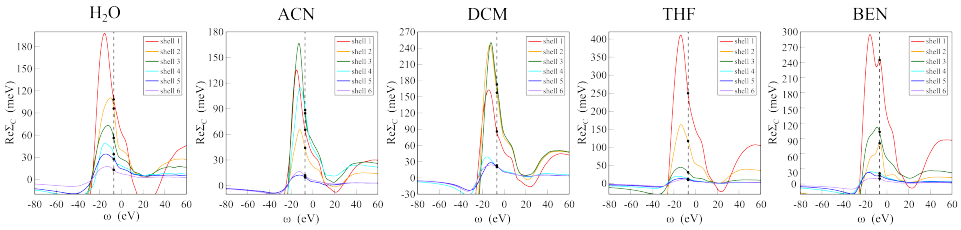

Figure D.8: Real part of the fragment correlation self-energy (before normalization) contributed from the six solvation shells of each solvated system. The dashed line indicates the QP energy.

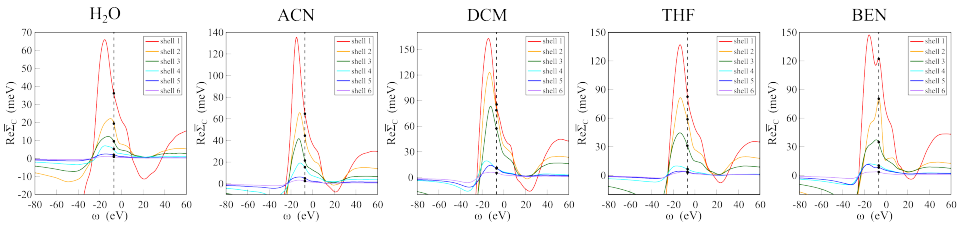

Figure D.9: Real part of the fragment correlation self-energy (after normalization) contributed from the six solvation shells of each solvated system. The dashed line indicates the QP energy.

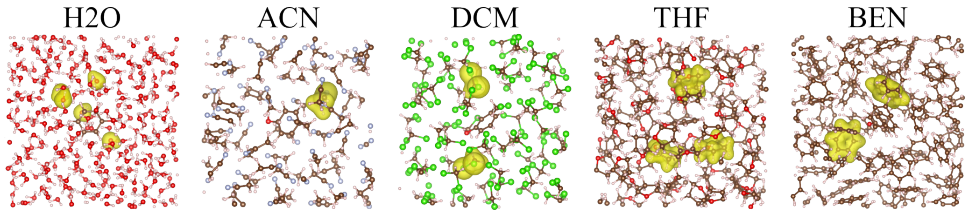

Figure D.10: Solvation shells represented by the electron density at ∼5 Å of each solvated system.

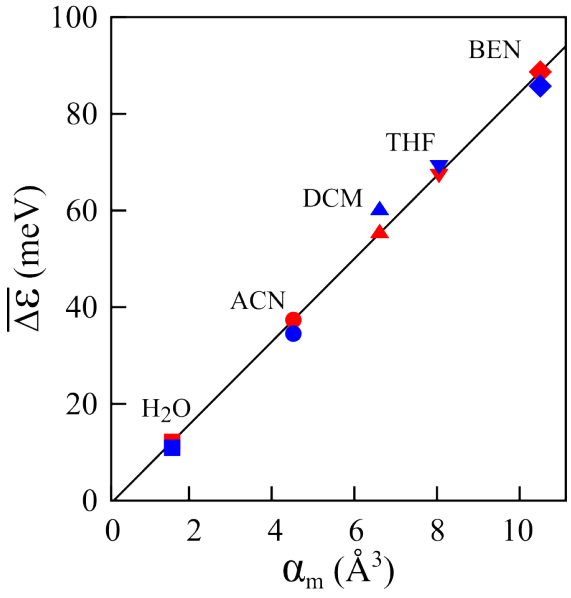

Figure D.11: Comparisons between the derived $\overline{\Delta\varepsilon}$ (red) using the straight line and the first-principle ones (blue).

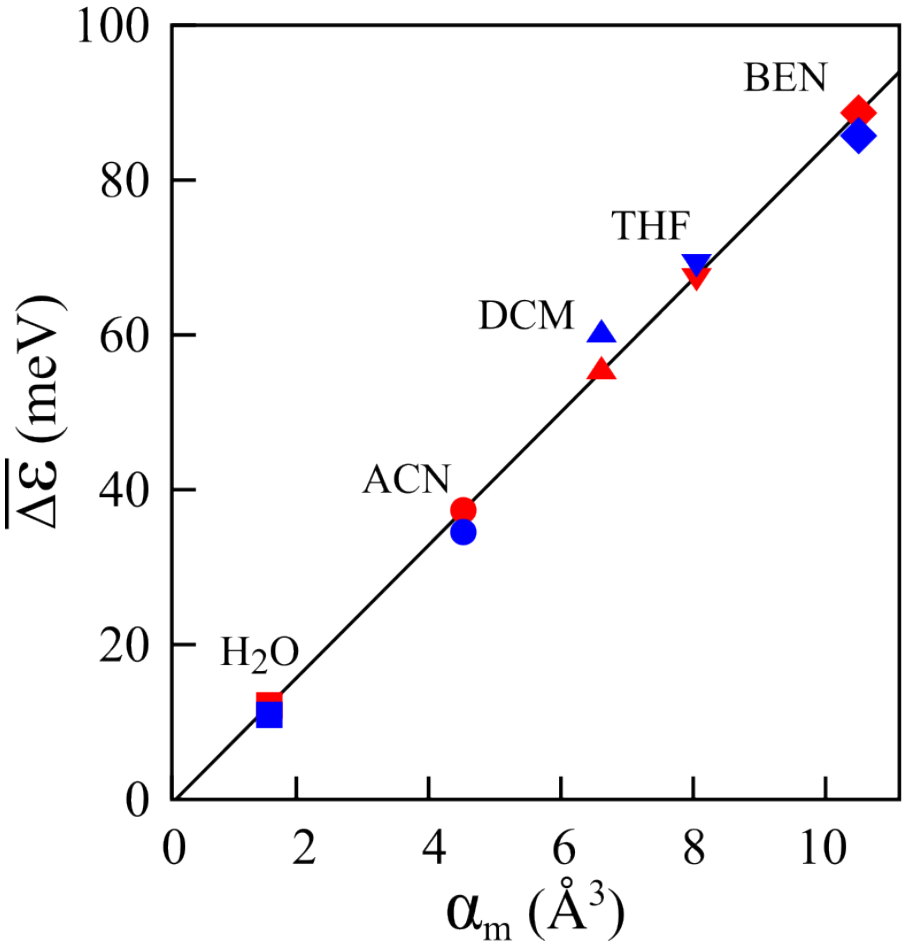

Figure D.12: Graphical solutions to the QP energy for phenol in H_2O using the small simulation cell: the red curve represents the isolated HOMO and the blue curve represents the solvated HOMO. The intersection between each curve and the straight black line indicates the QP energy. Snapshots 1-5 are provided from left to right.

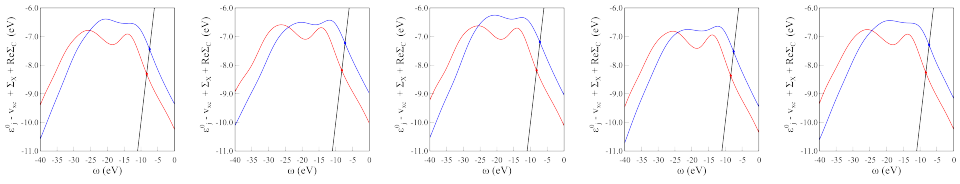

Figure D.13: Graphical solutions to the QP energy for phenol in H_2O using the large simulation cell: the red curve represents the isolated HOMO and the blue curve represents the solvated HOMO. The intersection between each curve and the straight black line indicates the QP energy. Snapshots 1-5 are provided from left to right.

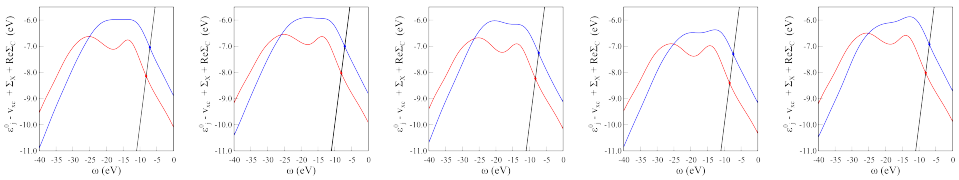

Figure D.14: Graphical solutions to the QP energy for phenol in ACN using the small simulation cell: the red curve represents the isolated HOMO and the blue curve represents the solvated HOMO. The intersection between each curve and the straight black line indicates the QP energy. Snapshots 1-5 are provided from left to right.

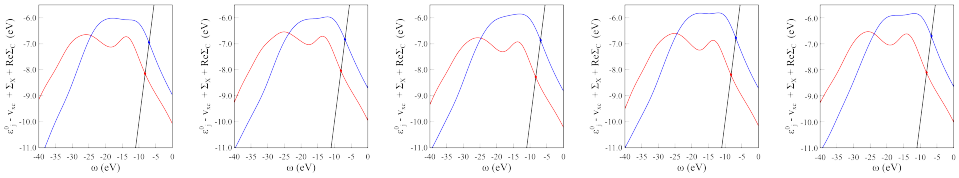

Figure D.15: Graphical solutions to the QP energy for phenol in ACN using the large simulation cell: the red curve represents the isolated HOMO and the blue curve represents the solvated HOMO. The intersection between each curve and the straight black line indicates the QP energy. Snapshots 1-5 are provided from left to right.

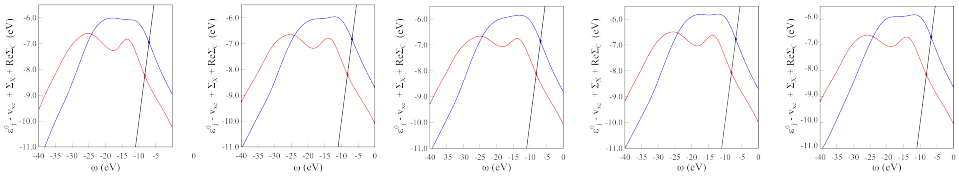

Figure D.16: Graphical solutions to the QP energy for phenol in DCM using the small simulation cell: the red curve represents the isolated HOMO and the blue curve represents the solvated HOMO. The intersection between each curve and the straight black line indicates the QP energy. Snapshots 1-5 are provided from left to right.

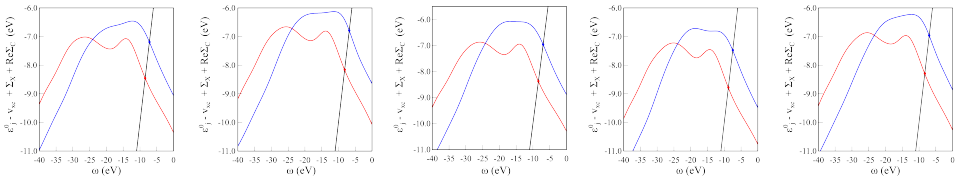

Figure D.17: Graphical solutions to the QP energy for phenol in DCM using the large simulation cell: the red curve represents the isolated HOMO and the blue curve represents the solvated HOMO. The intersection between each curve and the straight black line indicates the QP energy. Snapshots 1-5 are provided from left to right.

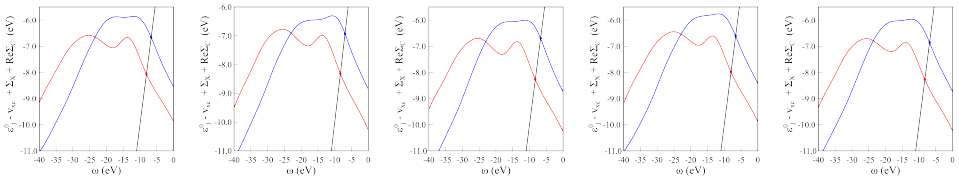

Figure D.18: Graphical solutions to the QP energy for phenol in THF using the small simulation cell: the red curve represents the isolated HOMO and the blue curve represents the solvated HOMO. The intersection between each curve and the straight black line indicates the QP energy. Snapshots 1-5 are provided from left to right.

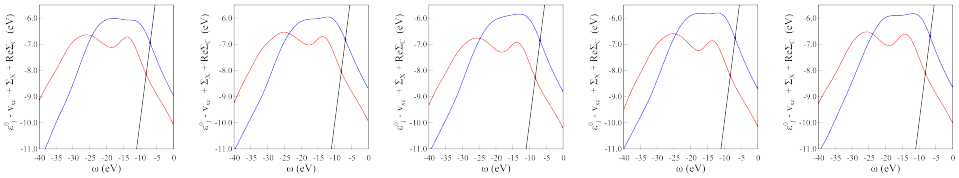

Figure D.19: Graphical solutions to the QP energy for phenol in THF using the large simulation cell: the red curve represents the isolated HOMO and the blue curve represents the solvated HOMO. The intersection between each curve and the straight black line indicates the QP energy. Snapshots 1-5 are provided from left to right.

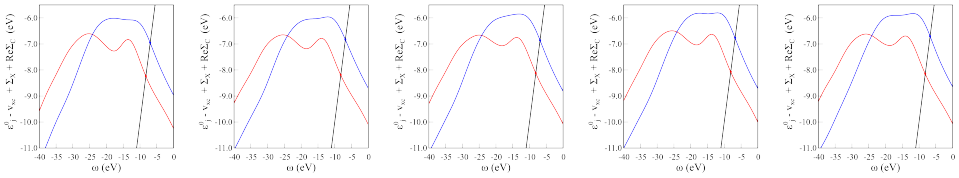

Figure D.20: Graphical solutions to the QP energy for phenol in BEN using the small simulation cell: the red curve represents the isolated HOMO and the blue curve represents the solvated HOMO. The intersection between each curve and the straight black line indicates the QP energy. Snapshots 1-5 are provided from left to right.

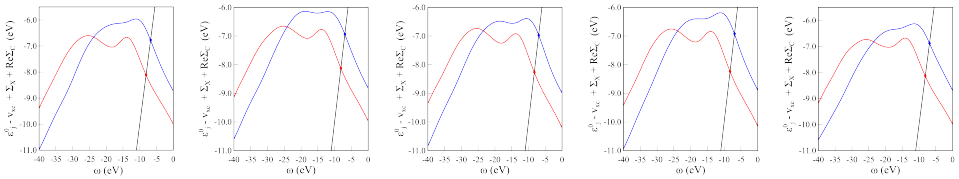

Figure D.21: Graphical solutions to the QP energy for phenol in BEN using the large simulation cell: the red curve represents the isolated HOMO and the blue curve represents the solvated HOMO. The intersection between each curve and the straight black line indicates the QP energy. Snapshots 1-5 are provided from left to right.

Bibliography

[1] D. Neuhauser, Y. Gao, C. Arntsen, C. Karshenas, E. Rabani, and R. Baer, *Breaking the theoretical scaling limit for predicting quasiparticle energies: The stochastic GW approach*, *Physical Review Letters* **113** (2014), no. 7 076402.

[2] V. Vlček, W. Li, R. Baer, E. Rabani, and D. Neuhauser, *Swift GW beyond 10,000 electrons using sparse stochastic compression*, *Physical Review B* **98** (2018), no. 7 075107.

[3] V. Vlček, *Stochastic vertex corrections: Linear scaling methods for accurate quasiparticle energies*, *Journal of Chemical Theory and Computation* **15** (2019), no. 11 6254–6266.

[4] G. Weng, M. Romanova, A. Apelian, H. Song, and V. Vlček, *Reduced scaling of optimal regional orbital localization via sequential exhaustion of the single-particle space*, *Journal of Chemical Theory and Computation* **18** (2022), no. 8 4960–4972.

[5] H. J. C. Berendsen, D. van der Spoel, and R. van Drunen, *Gromacs: A message-passing parallel molecular dynamics implementation*, *Computer Physics Communications* **91** (1995), no. 1 43–56.

[6] W. L. Jorgensen and J. D. Madura, *Temperature and size dependence for monte carlo simulations of tip4p water*, *Molecular Physics* **56** (1985), no. 6 1381–1392.

[7] J. P. Perdew, K. Burke, and M. Ernzerhof, *Generalized gradient approximation made simple*, *Phys. Rev. Lett.* **77** (1996) 3865–3868.

[8] N. Troullier and J. L. Martins, *Efficient pseudopotentials for plane-wave calculations*, *Phys. Rev. B* **43** (1991) 1993–2006.

[9] G. Weng and V. Vlček, *Efficient treatment of molecular excitations in the liquid phase environment via stochastic many-body theory*, *The Journal of Chemical Physics* **155** (2021), no. 5 054104.

Appendix E

Supplementary material for "Are multi-quasiparticle interactions important in molecular ionization?"

Carlos Mejuto-Zaera,[a] Guorong Weng, Mariya Romanova, Stephen J. Cotton,[b,c] K. Birgitta Whaley,[1] Norm M. Tubman,[d] Vojtěch Vlček

E.1 Methodological details

E.1.1 ASCI - Ground State

The idea behind the ASCI algorithm is to find an optimal truncation $\mathcal{T}^N$ of a given size $\left|\mathcal{T}^N\right|$ of the full Hilbert space, in order to accurately describe the ground state of a many-

[a]University of California, Berkeley, California 94720, USA
[b]Quantum Artificial Intelligence Laboratory (QuAIL), Exploration Technology Directorate, NASA Ames Research Center, Moffett Field, California 94035, USA
[c]KBR, 601 Jefferson St., Houson, Texas 77002, USA
[d]Quantum Artificial Intelligence Laboratory (QuAIL), Exploration Technology Directorate, NASA Ames Research Center, Moffett Field, California 94035, USA

body Hamiltonian. ASCI has previously been shown to be able to successfully identify optimal truncations for a wide variety of systems across the fields quantum chemistry and condensed matter physics, including several molecular systems, the uniform electron gas, the two-dimensional square lattice Hubbard model and Hubbard-Anderson impurity models of the sort typically found in dynamical mean-field theory calculations [1, 2]. Effectively, we specify as input the size $\left|\mathcal{T}^N\right|$ of the truncation that we can afford, i.e., a number of Slater determinants into which the full Hilbert space is truncated, as well as the Hamiltonian of interest H in some single-particle basis. The ASCI algorithm returns the most important $\left|\mathcal{T}^N\right|$ many-body Slater determinants for the description of the ground state wave function $|\Psi_0\rangle$ of H. We can then project the Hamiltonian H onto that truncation space, and compute the approximate ground state wave function $|\psi_0\rangle$ and the approximate ground state energy E_0.

The key element in the ASCI algorithm is the introduction of a ranking criterion, which given two determinants allows to estimate which one is more important for the ground state wave function. Using this ranking criterion, the identification of the optimal truncation space is performed iteratively, exploring regions of the Hilbert space connected through H to a given reference truncation $\mathcal{T}^N$. After the exploration staga, all new determinants together with the determinants in $\mathcal{T}^N$ are ranked. Finally, we build a new truncation $\mathcal{T}'^N$ by keeping only the $\left|\mathcal{T}^N\right|$ most important determinants in the ranking. The Hamiltonian is then diagonalized in the new truncation $\mathcal{T}'^N$, getting new ground state energy and wave function estimates. The process is repeated until the ground state energy E_0 converges to the desired accuracy.

The ASCI algorithm performs best for systems with (a) a high Hamiltonian connectivity, which accelerates the search, and (b) a true ground state that is well described by a few states in some one-body basis. Both of these conditions are usually fulfilled in molecular systems. The dense two-body term in the molecular Hamiltonian in typical quantum

chemistry basis-sets accounts for point (a). An optimal one-body basis, in the sense described by condition (b), can be found by introducing rotation to natural orbitals through the ASCI calculation. These rotations are usually performed in the first few iterations and are crucial to achieving a compact truncation, i.e. an accurate truncation that is a small as possible. For more detailed on the ASCI algorithm, see [1, 3, 4].

E.1.2 ASCI - Green's Function

Having determined the optimal truncation $\mathcal{T}^N$ and the corresponding ground state wave function $|\psi_0\rangle$ and energy E_0, one can compute the Green's function by evaluating eq 1. In [5] we showed that the fast convergence of the ground state energy with the size $\left|\mathcal{T}^N\right|$ of $\mathcal{T}^N$ is inherited by the Green's function, which also converges rapidly with the number of determinants in the truncated space. The particle and hole components of the Green's function are computed separately using the Lanczos algorithm [6, 7]. The Green's function evaluation can be conceptually split into two steps: identifying a truncated basis in the particle (hole) sector and evaluation of the ref in that truncated basis.

We want to build the truncated basis in the particle (hole) sector $\mathcal{T}^{N+1}$ ($\mathcal{T}^{N-1}$) on top of the truncated space in the N particle sector $\mathcal{T}^N$, that is returned by ASCI. Unlike in previous studies [5], where a different basis was built for each Green's function matrix element, here we build a single basis in the particle (hole) sector that is common to all elements of the Green's function. For this, we build a partial basis $\mathcal{T}_i^{N\pm1}$ for each orbital i, and then form the total basis as the union of these partial bases, i.e.

$$\mathcal{T}^{N\pm1} = \cup_i \mathcal{T}_i^{N\pm1}. \tag{E.1}$$

In order to form $\mathcal{T}_i^{N\pm1}$, we build an initial "naive" truncated space $\mathcal{T}_i^{N+1,0}$ by applying the corresponding creation (annihilation) operator $c_i^\dagger$ (c_i) to all determinants in $\mathcal{T}^N$. The

union of these naive spaces, which will be at most p times as large as $\mathcal{T}^N$, where p is the number of orbitals, would be enough to compute matrix elements like $\langle\psi_0|c_i H c_j^\dagger|\psi_0\rangle$ within ASCI accuracy. However, the Green's function requires inverting the Hamiltonian and thus more determinants are needed in general. We expand the naive truncations by adding "layers" of single and double excitations of the determinants in $\mathcal{T}_i^{N+1,0}$. If we apply m layers, we add new determinants that are $1, 2, \ldots, m$ single or double excitations away form the determinants in $\mathcal{T}_i^{N+1,0}$. In general, we do not add these layers of excitations on top of all the determinants in a given naive space, but only on top of those generated from determinants in $\mathcal{T}^N$ that possess a ground state wave function coefficient above some threshold. For the computations presented in this work, we choose this threshold to be 10^{-3}. In [5] we showed that for the typical impurity models found in dynamical mean-field theory calculations on the Hubbard model, two layers of excitations were sufficient to converge the spectral functions along the real frequency axis. In the small molecular examples in this work, one layer was enough. Furthermore, in these layers we add only single excitations and no doubles.

Using only a small number of layers is fundamental, since the size of the truncated spaces increases exponentially with the number of applied layers. To further reduce the size of each $\mathcal{T}_i^{N+1}$ without compromising accuracy, we exploit the active space structure of the orbital space $\{c_i\}$, identifying those orbitals with occupation close to 2 or 0 as inactive, and the rest as active. When adding layers of excitations, we then only consider excitations from and to active orbitals. This can significantly reduce the size of $\mathcal{T}_i^{N+1}$. We consider an orbitals as "active" if it's average occupation in the ground state wave function $\langle n_i\rangle_0$ fufills $10^{-4} \leq \langle n_i\rangle_0 \leq 2 - 10^{-4}$. The natural orbital rotations introduced in the ground state calculation optimize this active space, since they tend to maximize the number of inactive orbitals.

We note that due to the way in which the naive truncations $\mathcal{T}_i^{N+1}$ ($\mathcal{T}_i^{N-1}$) are built,

using the corresponding creation (annihilation) operators, the final truncation spaces for different orbitals will in general be different. In the exact diagonalization limit (the full configuration interaction limit), i.e., when the ASCI truncation $\mathcal{T}^N$ is equal to the full Hilbert space in the N particle sector, then all the partial truncations $\mathcal{T}_i^{N+1}$ for all orbitals become equal and identical to the full Hilbert space in the $(N+1)$ particle sector. It is then unnecessary to build more than one of the "partial" truncations in this limit. Moreover, it is only necessary to apply one layer of excitations on top of the naive truncation space to recover the full Hilbert space.

For a given orbital i, the sizes of the particle and hole truncations, $\left|\mathcal{T}_i^{N+1}\right|$ and $\left|\mathcal{T}_i^{N-1}\right|$, can be very different. In particular, an orbital that is full, or mostly full, in the ground state will have a much smaller $\left|\mathcal{T}_i^{N+1}\right|$ than $\left|\mathcal{T}_i^{N-1}\right|$. This is because most important determinants in the ground state wave function will likely have that orbital occupied, such that when applying $c_i^\dagger$ these determinants do not contribute to $\mathcal{T}_i^{N+1}$. Conversely, an orbital that is empty or mostly empty will have a much smaller $\left|\mathcal{T}_i^{N-1}\right|$ than $\left|\mathcal{T}_i^{N+1}\right|$. For partially occupied orbitals, i.e. orbitals with an average occupation in the ground state $\langle n_i \rangle_0$ close to 1, both spaces will be of comparable size. As a result of these differences, for the small molecular systems studied in this work and also when using a large basis set, $\left|\mathcal{T}_i^{N+1}\right|$ will be much larger than $\left|\mathcal{T}_i^{N-1}\right|$, because there are far more orbitals than electrons. Since the systems studied here are not particularly strongly correlated, there are at most of the order of 30-40 active orbitals in the ground state of any of the five systems. Of those, only $n_{el}/2$ spatial orbitals are substantially occupied, where n_{el} is the number of electrons. Consequently, the full hole truncated bases $\mathcal{T}^{N-1}$ built as explained above only have relevant contributions of $n_{el}/2$ orbitals (in this work between 5-7), while $\mathcal{T}^{N+1}$ has relevant contributions from all unoccupied virtual orbitals. The number of the latter in an augmented quadruple zeta basis is of the order of 100, so $\mathcal{T}^{N+1}$ will be about two orders of magnitude larger than $\mathcal{T}^{N-1}$. This makes computing the particle

component of the Green's function much more computationally demanding than the hole component. In this work we have concentrated on the negative frequency part of the spectral function $A(\omega)$. This simplifies the calculations, since, for any many-body system, the particle component of the ground state Green's function has all diagonal elements equal to zero for $\omega < 0$. Thus, to compute the spectral function $A(\omega)$, we do not need the particle Green's function. Once the full truncated basis $\mathcal{T}^{N+1}$ (or $\mathcal{T}^{N-1}$ for the hole component) has been determined, we evaluate the particle component of eq 1 using the Lanczos algorithm [6, 7]. In our previous work [5] we used the simple one-band Lanczos method [6] to compute all elements of the Green's function one at a time. This strategy, amenable to trivial parallelization, is ideal if one is interested in the different elements of the Green's function independently, for example when one only wants to determine the spectral function $A(\omega) = -\frac{1}{\pi}\Im G(\omega)$. In these cases, it is sufficient to find for each Green's function element the optimal truncations $\mathcal{T}^{N\pm1}$, which as noted above will be in general different for each element $G(\omega)^p_{i,j}$.

This can become an issue when using a truncated Hilbert space, as is the case in ASCI, for systems in which different orbitals show a significant degree of coupling. This was the case for the molecules studied in this work, since as discussed in the main paper the orbital resolved spectral function $A(\omega)_i = -\frac{1}{\pi}\Im\left[G(\omega)_{i,i}\right]$ for orbital i showed satellites resonant with the main quasiparticle energies of another orbital j. In order to capture these features accurately, we used a common basis for all elements of the Green's function, by building the union of the partial truncations corresponding to each orbital. Instead of computing each Green's function element in parallel, we employed the band Lanczos algorithm [7] to determine all at the same time, reducing the computational time significantly. Using band Lanczos, and a common truncation basis for all Green's function elements, ensured an accurate description of inter-orbital resonant features with modest sized truncations. The price for the time saving using band Lanczos is in memory, since it requires storing more

vectors simultaneously than the two that are formally needed in the one-band formulation. Thanks to the compactness of the $\mathcal{T}^{N\pm1}$ spaces, we could afford the memory demands, since each vector had at most $\sim$7 million elements (in the case of N_2 in the aug-cc-pvqz basis). The band Lanczos method has received relative little attention in the many-body literature, and thus we briefly summarize the main idea and properties of the method here, following the presentation of [7].

The band Lanczos method is a natural generalization of the common Lanczos algorithm, which uses several linearly independent initial vectors instead of only one. In n band Lanczos, one starts thus with an orthonormal set of vectors $\left\{\tilde{\psi}_i\right\}_{i=1}^{n}$.[e] Then, one builds a Krylov space formed by actions of the Hamiltonian H on this starting set. In each iteration, one acts with H on a vector in the Krylov space, and makes it orthogonal to the previous ones using a recursion relation. Unlike in one-band Lanczos, where the recursion relation involves only three vectors at a time, this band Lanczos verison involves $2n+1$ vectors. Thus, one needs to store in memory the last $2n$ vectors in the Krylov space, resulting in the higher memory demand of the band Lanczos method compared to simple Lanczos. During the iterative process, the Hamiltonian matrix in the Krylov basis is evaluated. While in one-band Lanczos the Hamiltonian is tridiagonal in the Krylov basis, in n band Lanczos the Hamiltonian is band-diagonal, with n non-vanishing upper- and lower-diagonals. After j iterations, during which one has gone over the span of each of the original $\left\{\tilde{\psi}_i\right\}_{i=1}^{n}$ vectors $J = \lfloor \frac{j}{n} \rfloor$ times, one has formed the Hamiltonian $H^{(j)}$. Similarly to one-band Lanczos, this Krylov Hamiltonian fulfills the following relations with respect to the set $\left\{\tilde{\psi}_i\right\}_{i=1}^{n}$ [7]:

[e]For the Green's function calculation, e.g. in the particle sector, n equals the number of orbitals and the starting vectors are orthonormalized linear combinations of $\left\{c_i^\dagger |\psi_0\rangle\right\}_{i=1}^{n}$. This orthonormalization is performed by QR factorization.

$$\left(H^{(j)}\right)^k |\widetilde{\psi}_i\rangle = \quad H^k |\widetilde{\psi}_i\rangle\,, \quad \text{for } 1 \le i \le n, \tag{E.2}$$
$$\text{for } 0 \le k \le J-1$$
$$\langle\widetilde{\psi}_i| \left(H^{(j)}\right)^k |\widetilde{\psi}_h\rangle = \langle\widetilde{\psi}_i|H^k|\widetilde{\psi}_h\rangle\,, \quad \text{for } 1 \le i,h \le n, \tag{E.3}$$
$$\text{for } 0 \le k \le 2J-1,\ k \text{ odd}$$
$$\text{for } 0 \le k \le 2J-2,\ k \text{ even}.$$

Thus the first $2J-2$ powers of the Krylov Hamiltonian have the exact same matrix elements with the initial set $\left\{\tilde{\psi}_i\right\}_{i=1}^{n}$ as does the full Hamiltonian. This equivalence of Hamiltonian powers provides a fast convergence of the Green's function with the number of Lanczos iterations, which can also be understood in terms of the moments of the spectral function [6].

It should be noted that for the same number of iterations j, the one-band Lanczos method equates more expectation values than n band Lanczos, since $J = \lfloor \frac{j}{n} \rfloor$.

If necessary, the same number of powers can be recovered in the band Lanczos method by increasing the number of iteration by a factor linear with the number of orbitals, although this is rarely necessary. For the calculations presented in this work, due to the weakly correlated ground state structure of the closed-shell molecules considered here, we only need to consider the $n_{el}/2$ lowest orbitals when determining the Green's function. Effectively, we only computed an at most 7×7 block of the full Green's function matrix. Thus, a standard number of 4000 band Lanczos iterations was sufficient to obtain reliable Green's functions.

E.1.3 ASCI - Simulation Parameters

For the small closed-shell molecular systems studied in this work, we performed an ASCI ground state calculation with $\left|\mathcal{T}^N\right| = 5 \cdot 10^5$ determinants using cc-pvXz and aug-cc-pvXz basis sets, where X = D,T,Q. For CH_4, we were not able to use the aug-cc-pvQz basis set, so we only report results for the other five basis sets. To determine the spectral function $A(\omega)$ for $\omega < 0$, we subsequently constructed the hole truncated space $\mathcal{T}^{N-1}$. We proceed as described above, using one layer of single excitations and a frequency spacing of 0.05 eV.

E.1.4 ASCI - $A(\omega)$ convergence with the truncation space size

Fig. E.1 shows the hole component of the spectral function $A(\omega)$ for select systems and different basis sets. We see that the main quasiparticle energies show excellent convergence with the number of states, with no appreciable change over a wide range of values of $\left|\mathcal{T}^N\right|$.

While different systems and basis sets show slightly different convergence behavior, in general the position of the QPEs could be always be converged within 0.15 eV, in the sense that results shown in the main paper would change by no more than 0.15 eV on increasing the truncation space size by a factor of 5. The satellite features also show a satisfactory qualitative convergence with respect to the size of the target space.

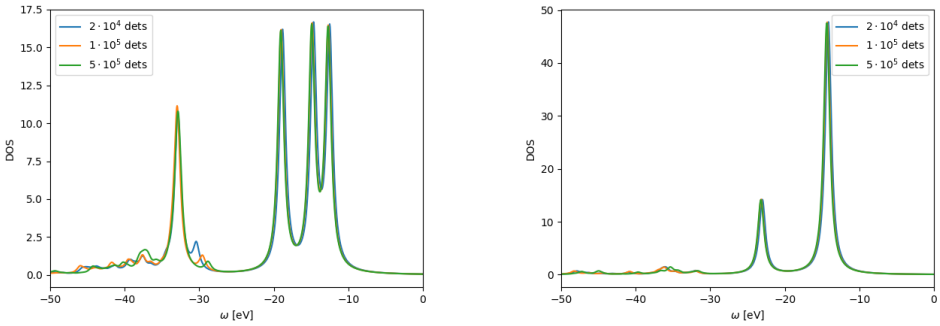

(a) H_2O.

(b) CH_4.

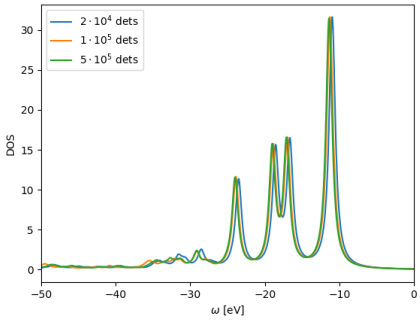

(c) C_2H_2.

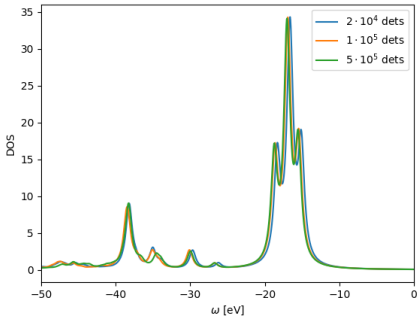

(d) N_2.

Figure E.1: Hole component of the spectral function for the occupied orbitals of the molecules studied with aug-cc-pvqz basis sets and different ASCI truncations. We use a broadening factor of 0.5 eV.

E.1.5 ASCI - $A(\omega)$ convergence with basis set

Fig. E.2 shows the convergence of the hole component of spectral function as a function of the basis set for all five molecular systems presented in the main paper. We extrapolated the quasiparticle energies to the complete basis set limit following the prescription in [8]. Here as well, the qualitative convergence of the satellite features is satisfactory.

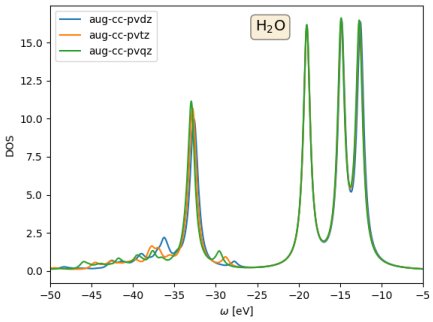

(a) H_2O.

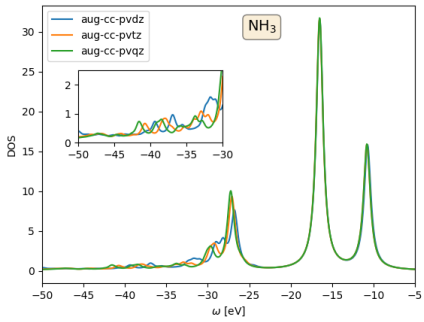

(b) NH_3.

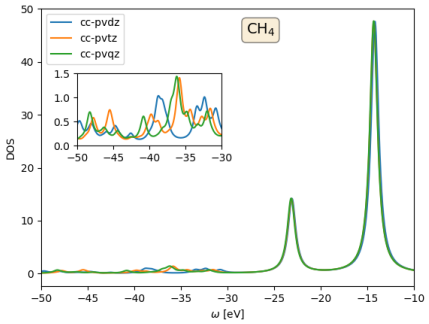

(c) CH_4.

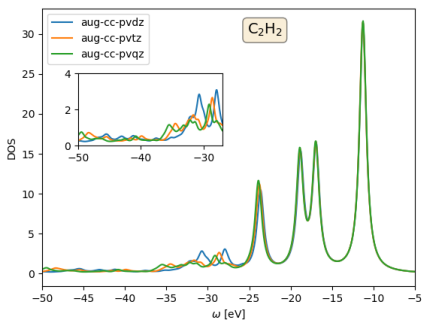

(d) C_2H_2.

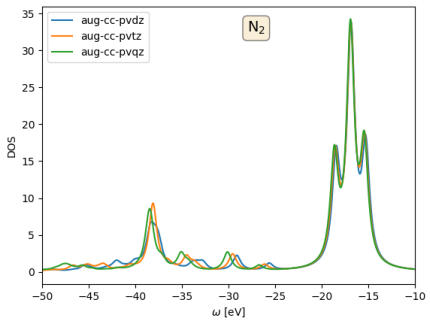

(e) N_2.

Figure E.2: Hole component of the spectral function for the molecules studied with different augmented, correlation consistent basis sets and an ASCI truncation of 10^5 determinants. We use a broadening factor of ~ 0.5 eV.

E.1.6 ASCI - quasiparticle Energies

In Table E.1 we report the quasiparticle energies for all valence orbitals and all molecules studied in the main paper with different basis sets. We also show the results with basis set extrapolation using the prescription in [8]. These results are computed with ASCI using a truncated space of $5 \cdot 10^5$ states, using a broadening of 0.50 eV. For the lowest lying valence orbital of N_2 we report only the position of the highest peak. The apparent jumps in the QP energies for this lowest lying orbital in N_2 when going from double to triple zeta basis are due to weight redistribution among these peaks, which changes the identity of the largest contribution. As discussed above, the quasiparticle energy convergence with the size of the truncated space appears to be reached within a confidence interval of ± 0.15 eV. The extrapolated quasiparticle energies from the augmented and non-augmented basis sets are in good agreement with each other.

We note that, similar to the inter-orbital resonances in the $GW\Gamma$ self-energies discussed in the main paper, the orbital resolved ASCI spectral functions also present resonances. Fig. E.3 shows the orbital resolved spectral functions $A(\omega)_i$ for all molecules. With the exception of CH_4, all show small resonant peaks between the orbital furthest from the HOMO and at least one of the other orbitals. The $A(\omega)_i$ for the orbital furthest from the HOMO is emphasized with an arrow. However, this resonances appear in the ASCI spectral functions due to the mixed character of the natural orbital basis in which they are computed. Rotating the ASCI Green's functions to the HF basis eliminates the resonances. This leaves the question whether the resonances observed in the $GW\Gamma$ self-energies have a similar "artificial" origin, i.e. related to a physically inconsequential orbital basis rotation. While all MBPT calculations where performed in the HF basis, which would thus suggest a different origin, we must consider the fact that using a space grid instead of a Gaussian basis set (see below) may induce some degree of orbital mixing, akin to the one obtained

from natural orbital rotations. Thus, it is unclear whether the self-energy resonances have an actual physical, or in contrast purely computational origin.

orbital	cc-pvdz	cc-pvtz	cc-pvqz	cc-extrapol.	aug-cc-pvdz	aug-cc-pvtz	aug-cc-pvqz	aug-extrapol.
H_2O-1	-32.57	-32.67	-32.87	-33.05	-32.57	-32.72	-32.87	-32.99
H_2O-2	-18.51	-18.86	-19.01	-19.15	-19.01	-19.01	-19.06	-19.10
H_2O-3	-14.26	-14.71	-14.86	-14.95	-14.81	-14.91	-14.91	-14.90
H_2O-4	-11.96	-12.46	-12.66	-12.79	-12.56	-12.66	-12.71	-12.75
NH_3-1	-27.51	-27.31	-27.36	-27.48	-27.36	-27.31	-27.31	-27.36
NH_3-2	-16.21	-16.46	-16.56	-16.61	-16.51	-16.56	-16.51	-16.51
NH_3-3	-16.21	-16.46	-16.56	-16.63	-16.51	-16.56	-16.51	-16.51
NH_3-4	-10.31	-10.71	-10.86	-10.95	-10.76	-10.86	-10.81	-10.81
CH_4-1	-23.06	-23.16	-23.21	-23.25	-23.06	-23.16		
CH_4-2	-14.21	-14.36	-14.36	-14.35	-14.26	-14.36		
CH_4-3	-14.21	-14.36	-14.36	-14.35	-14.26	-14.36		
CH_4-4	-14.21	-14.36	-14.36	-14.35	-14.26	-14.36		
C_2H_2-1	-23.66	-23.81	-24.01	-24.14	-23.66	-23.86	-24.01	-24.13
C_2H_2-2	-18.71	-18.91	-19.01	-19.08	-18.86	-18.96	-19.01	-19.05
C_2H_2-3	-16.86	-17.01	-17.11	-17.18	-16.96	-17.06	-17.11	-17.15
C_2H_2-4	-11.21	-11.31	-11.41	-11.48	-11.31	-11.36	-11.41	-11.45
C_2H_2-5	-11.21	-11.31	-11.41	-11.48	-11.31	-11.36	-11.41	-11.45
N_2-1	-38.12	-38.02	-38.27	-38.47	-38.12	-37.97	-38.27	-38.56
N_2-2	-18.26	-18.56	-18.71	-18.82	-18.46	-18.61	-18.76	-18.88
N_2-3	-16.66	-16.91	-17.01	-17.08	-16.86	-16.96	-17.01	-17.05
N_2-4	-16.66	-16.91	-17.01	-17.08	-16.86	-16.96	-17.01	-17.05
N_2-5	-15.06	-15.36	-15.51	-15.64	-15.31	-15.46	-15.51	-15.54

Table E.1: QPE's of the valence orbitals for H_2O, NH_3, CH_4, C_2H_2 and N_2 in different basis sets. The QPE's correspond to the maxima of the negative part of the imaginary hole component Green's function for the valence orbitals. These were computed with ASCI using 10^5 states.

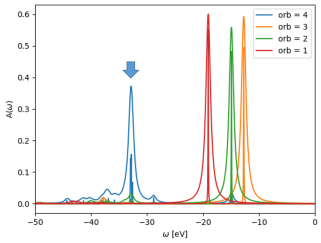

(a) H_2O. Resonance between orbtial 4 and 2.

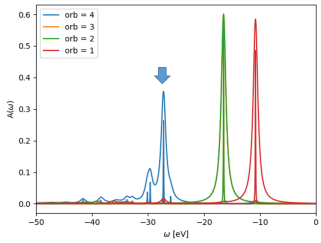

(b) NH_3. Resonance between orbital 4 and 1.

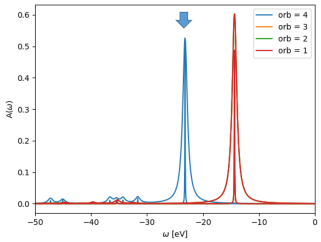

(c) CH_4. No appreciable resonance.

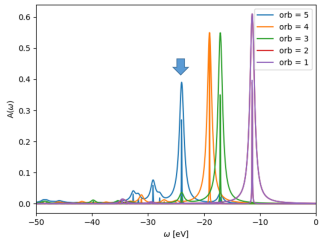

(d) C_2H_2. Resonance between orbital 5 and 3.

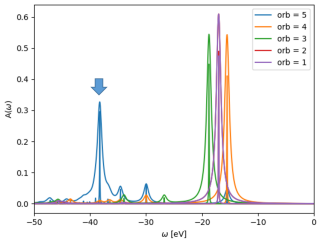

(e) N_2. Resonance between orbital 5 and 4.

Figure E.3: Hole component of the spectral function for the molecules studied, orbital resolved, using the largest basis set. We use a broadening factor of ~ 0.5 eV. All molecules except for CH_4 show small resonances between the orbital furthest away from the HOMO (shown with an arrow) and another orbital.

E.1.7 Quasiparticle energies and spectra for all methods

In Table E.2 we summarize the quasiparticle energies obtained from all methods used in the paper (HF, GW, $GW\Gamma$ and ASCI) that are presented in Fig. (2) of the main paper. The ASCI results correspond to the values obtained by basis set extrapolation in the augmented basis set for all molecules except for CH_4, where the non-augmented basis set was used for the extrapolation. In Fig. E.4 we show the spectral functions and self-energies for H_2O, CH_4, C_2H_2 and N_2.

H_2O	HF	GW	$GW\Gamma$	ASCI	NH_3	HF	GW	$GW\Gamma$	ASCI
orb 1	-36.82	-35.06	-32.02	-32.99	orb 1	-31.08	-29.22	-27.58	-27.36
orb 2	-19.51	-19.62	-19.20	-19.10	orb 2	-17.12	-17.11	-16.70	-16.51
orb 3	-15.92	-15.44	-15.03	-14.90	orb 3	-17.12	-17.11	-16.70	-16.51
orb 4	-13.88	-13.36	-12.94	-12.75	orb 4	-11.70	-11.69	-10.85	-10.81
CH_4	HF	GW	$GW\Gamma$	ASCI					
orb 1	-25.69	-24.21	-22.74	-23.25					
orb 2	-14.83	-15.03	-14.61	-14.35					
orb 3	-14.83	-15.03	-14.61	-14.35					
orb 4	-14.83	-15.03	-14.61	-14.35					
C_2H_2	HF	GW	$GW\Gamma$	ASCI	N_2	HF	GW	$GW\Gamma$	ASCI
orb 1	-28.06	-25.88	-24.31	-24.13	orb 1	-40.19	-37.57	-39.12	-38.56
orb 2	-20.90	-20.04	-19.62	-19.05	orb 2	-21.14	-20.04	-19.62	-18.88
orb 3	-18.53	-18.37	-17.95	-17.15	orb 3	-16.82	-17.53	-17.11	-17.05
orb 4	-11.18	-12.11	-11.27	-11.45	orb 4	-16.82	-17.53	-17.11	-17.05
orb 5	-11.18	-12.11	-11.27	-11.45	orb 5	-17.28	-16.96	-16.28	-15.54

Table E.2: QPE's of the valence orbitals for all molecules and the different methods presented in Fig. 2 in the main paper.

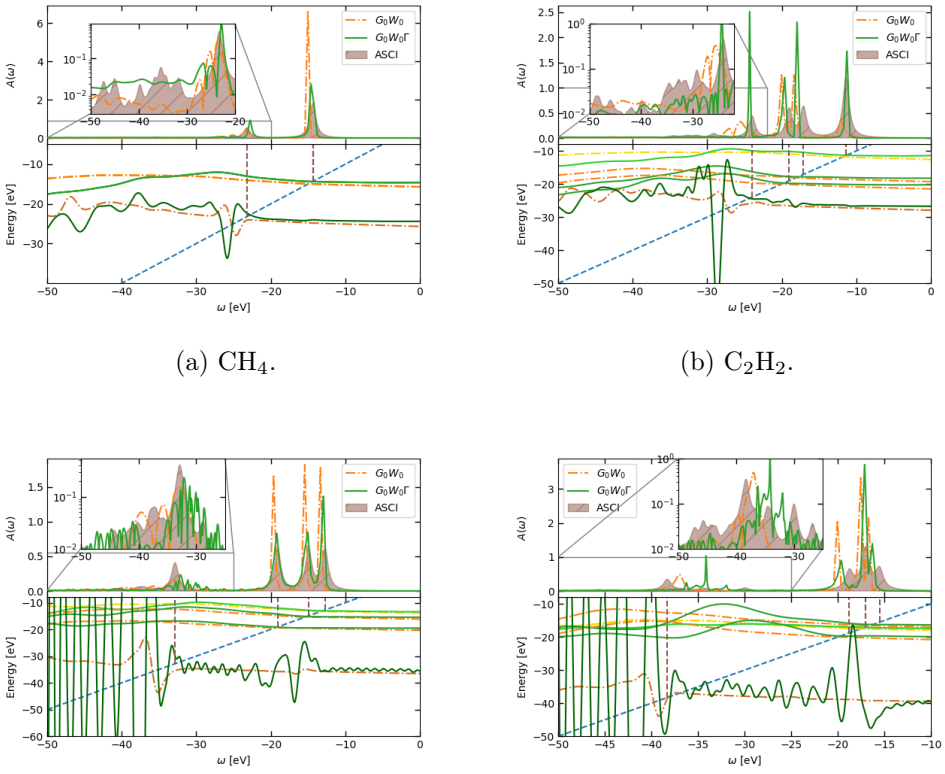

(a) CH_4. (b) C_2H_2.

(c) H_2O. (d) N_2.

Figure E.4: Upper panels: Spectral functions for several molecules as computed with ASCI (filled curve), G_0W_0 (dot-dashed line) and $G_0W_0\Gamma$ (solid line). Lower panels: Corresponding real part of the diagonal self-energy terms, with graphical solution of the QP equation (2) of the main paper.

E.1.8 Stochastic Many-body Perturbation Theory Calculations

The starting point calculations for the MBPT ground state calculations are performed with a real-space Hartree-Fock (HF) implementation. The formalism and implementations of the real-space and real-time stochastic many-body calculations are provided in Refs [9, 10]. We employ Troullier-Martins pseudopotentials [11] and a kinetic energy cutoff of 28 E_h. The real-space grid parameters adopted in our calculations for each molecule are listed in Table E.3.

system	grid	grid spacing (a_0)
H_2O	72×60×70	0.30
NH_3	66×66×60	0.30
CH_4	72×72×72	0.30
C_2H_2	72×72×90	0.30
N_2	50×50×60	0.35

Table E.3: Parameters of the HF calculations.

The quasipariticle energies are computed as

$$\varepsilon^{\mathrm{QP}} = \varepsilon^{\mathrm{HF}} + \left\langle \phi \middle| \hat{\Sigma}(\omega = \varepsilon^{\mathrm{QP}}) \middle| \phi \right\rangle \tag{E.4}$$

where $\varepsilon^{\mathrm{HF}}$ and $|\phi\rangle$ are the HF eigenvalue and the eigenstate. The Σ is the self-energy term, yielding the electron correlation. Our MBPT calculations avoid the self-consistent renormalization [12]. Instead, we employ a one-shot correction on top of a HF starting point, whose single-electron orbitals are close to the true Dyson orbitals [13]. The Green's function in the HF basis is thus nearly diagonal (see the description of ASCI results). Most importantly, HF prevents the appearance of spurious MQP peaks in GW [14, 15, 16]. Note, however, that the one-shot treatment translates to an unscreened vertex term [17, 18, 10], potentially overestimating the MQP couplings.

The self energies are computed via the one-shot G_0W_0 and the vertex-corrected $G_0W_0\Gamma$ method. In G_0W_0, the self-energy is expressed as

$$\Sigma(1,2) = i\nu(1,\bar{4})G(1,2)\nu(2,\bar{5})\chi(\bar{5},\bar{4}) \tag{E.5}$$

where $\chi(1,2)$ represents the two-point polarizability and ν the Coulomb kernel. The bar over the number means integrating over the space and time. In $G_0W_0\Gamma$, the expression

reads

$$\Sigma(1,2) = i\nu(1,\bar{4})G(1,2)\nu(2,\bar{5})\chi(\bar{5},\bar{4}) - i\nu(1,\bar{4})G(1,\bar{3})\nu(\bar{3},2)^3\chi(\bar{3},2,\bar{4}) \tag{E.6}$$

Compared to G_0W_0, the extra term involving the three-point polarizability ${}^3\chi(1,2,3)$ in the expression accounts for higher order electron correlation. See Refs. [19, 10] for full discussion of the meaning of the higher order effects.

In the stochastic formalism, the Green's function is sampled by selecting random vectors ζ, which sample the occupied and unoccupied subspace (propagated backward and forward in time). To make the expression for the self-energy separable, we use the sparse stochastic compression technique with additional set of sparse random vectors ξ[20, 9]. The random vectors spanning the entire Hilbert space are constructed as $\pm \mathrm{d}V^{-1/2}$ (with uniform distribution on each real space grid point). Here, $\mathrm{d}V$ is the volume element of the grid. Occupied subspace sampling is achieved by projecting the random vectors on all occupied states of the underlying mean-field calculation [9]. The unoccupied subspace represents the complementary part of the random vector. For all systems we used a number of random vectors $N_\zeta = 1000$ and $N_\xi = 20000$. No other stochastic sampling is employed (unlike in calculations for large systems).

The real-time propagation limits the frequency resolution of the self-energy. In practice, we employ 50 a.u. maximum propagation time for excitations in the SQP regime. This value is consistent with our previous work for molecules and solids.[21, 9, 22, 10] Resolution of the spectral features in the MQP regime requires (at least) three times larger propagation time (150 a.u.). Longer time evolution is subject to a large stochastic fluctuation and sampling bias. The longest simulations reported are thus based on the 150 a.u. propagation time. The convergence of the spectral features is illustrated in Fig. E.6.

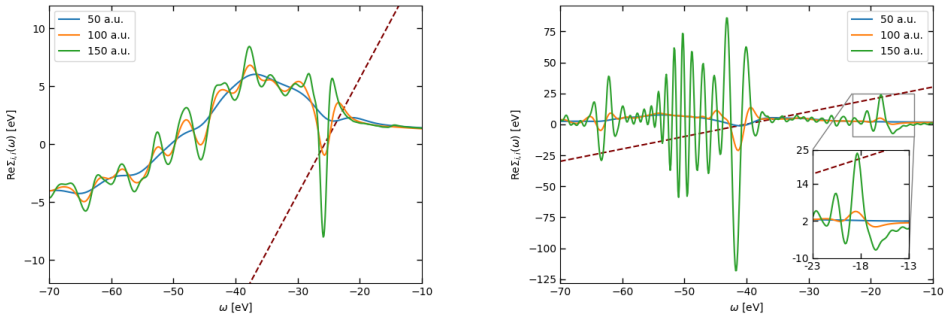

(a) CH_4. (b) N_2.

Figure E.5: Upper panels: Spectral functions for several molecules as computed with ASCI (filled curve), G_0W_0 (dot-dashed line) and $G_0W_0\Gamma$ (solid line). Lower panels: Corresponding real part of the diagonal self-energy terms, with graphical solution of the QP equation (2) of the main paper.

Figure E.6: Diagonal self energy components for the valence orbital furthest away from the HOMO for N_2 and CH_4 computed with vertex corrected $G_0W_0\Gamma$. Results are shown for different propagation times. The dashed line corresponds to the frequency line $y(\omega) = \omega$. See text for discussion.

Bibliography

[1] N. M. Tubman, J. Lee, T. Y. Takeshita, M. Head-Gordon, and K. B. Whaley, *A deterministic alternative to the full configuration interaction quantum monte carlo method*, *J. Chem. Phys.* **145** (2016), no. 4 044112.

[2] N. M. Tubman, C. Mejuto-Zaera, J. M. Epstein, D. Hait, D. S. Levine, W. Huggins, Z. Jiang, J. R. McClean, R. Babbush, M. Head-Gordon, and K. B. Whaley, *Postponing the orthogonality catastrophe: efficient state preparation for electronic structure simulations on quantum devices*, 2018.

[3] N. M. Tubman, C. D. Freeman, D. S. Levine, D. Hait, M. Head-Gordon, and K. B. Whaley, *Modern approaches to exact diagonalization and selected configuration interaction with the adaptive sampling ci method*, *Journal of Chemical Theory and Computation* **16** (2020), no. 4 2139–2159.

[4] N. M. Tubman, D. S. Levine, D. Hait, M. Head-Gordon, and K. B. Whaley, *An efficient deterministic perturbation theory for selected configuration interaction methods*, 2018.

[5] C. Mejuto-Zaera, N. M. Tubman, and K. B. Whaley, *Dynamical Mean-Field Theory Simulations with the Adaptive Sampling Configuration Interaction Method*, *Phys. Rev. B* **100** (2019) 125165.

[6] E. Pavarini, E. Koch, D. Vollhardt, and A. Lichtenstein, eds., *The LDA+DMFT approach to strongly correlated materials*, ch. 8, pp. 235–264. Verlag des Forschungszentrum Jülich, 2011.

[7] H. D. Meyer and S. Pal, *A band-lanczos method for computing matrix elements of a resolvent*, *J. Chem. Phys.* **91** (1989) 6195.

[8] T. Rangel, S. M. Hamed, F. Bruneval, and J. B. Neaton, *Evaluating the GW approximation with ccsd(t) for charged excitations across the oligoacenes*, *J. Chem. Theory Comput.* **12** (2016) 2834–2842.

[9] V. Vlček, W. Li, R. Baer, E. Rabani, and D. Neuhauser, *Swift GW beyond 10,000 electrons using sparse stochastic compression*, *Phys. Rev. B* **98** (2018) 075107.

[10] V. Vlček, *Stochastic vertex corrections: Linear scaling methods for accurate quasiparticle energies*, *J. Chem. Theory Comput.* **15** (2019) 6254.

[11] N. Troullier and J. L. Martins, *Efficient pseudopotentials for plane-wave calculations*, *Phys. Rev. B* **43** (1991) 1993–2006.

[12] L. Hedin, *New method for calculating the one-particle green's function with application to the electron-gas problem*, *Phys. Rev.* **139** (1965) A796–A823.

[13] M. Díaz-Tinoco, H. H. Corzo, F. Pawłowski, and J. V. Ortiz, *Do dyson orbitals resemble canonical hartree–fock orbitals?*, *Mol. Phys.* **117** (2019) 2275.

[14] M. Véril, P. Romaniello, J. A. Berger, and P. Loos, *Unphysical discontinuities in GW methods*, *J. Chem. Theory Comput.* **14** (2018) 5220.

[15] D. Golze, J. Wilhelm, M. J. van Setten, and P. Rinke, *Core-level binding energies from GW: An efficient full-frequency approach within a localized basis*, *J. Chem. Theory Comput.* **14** (2018) 4856.

[16] D. Golze, L. Keller, and P. Rinke, *Accurate absolute and relative core-level binding energies from GW*, *J. Phys. Chem. Lett.* **11** (2020) 1840.

[17] P. Romaniello, F. Bechstedt, and L. Reining, *Beyong GW approximation: Combining correlation channels*, *Phys. Rev. B* **85** (2012) 155131.

[18] E. Maggio and G. Kresse, *GW vertex corrected calculations for molecular systems*, *J. Chem. Theory Comput.* **13** (2017) 4765.

[19] R. M. Martin, L. Reining, and D. M. Ceperley, *Interacting Electrons: Theory and Computational Approaches*. Cambridge University Press, 2016.

[20] D. Neuhauser, Y. Gao, C. Arntsen, C. Karshenas, E. Rabani, and R. Baer, *Breaking the theoretical scaling limit for predicting quasiparticle energies: The stochastic GW approach*, *Phys. Rev. Lett.* **113** (2014) 076402.

[21] V. Vlček, D. Neuhauser, E. Rabani, and R. Baer, *Stochastic GW calculations for molecules*, *J. Chem. Theory Comput.* **13** (2017) 4997.

[22] V. Vlček, E. Rabani, and D. Neuhauser, *Quasiparticle spectra from molecules to bulk*, *Phys. Rev. Materials* **2** (2018) 030801(R).

Appendix F

Supplementary material for "Embedding vertex corrections in GW self-energy: Theory, implementation, and outlook"

Guorong Weng, Rushil Mallarapu,[a] Vojtěch Vlček

F.1 Theory and Computation

The stochastic GW and vertex-corrected GW formalism are formulated in detail in our previous work.[1, 2] The Pipek-Mezey localizaed orbitals and Wannier functions, especially the unoccupied states, are generated by our recent development,[3] where technical details are provided.

[a]Current institution: Harvard University, Cambridge, MA, 02138, USA

F.1.1 Green's Function and Self-Energy

The single-particle Green's Function is defined as

$$G(1,2) = -i \langle \Psi | \hat{\mathcal{T}} \hat{\psi}(1) \hat{\psi}^{\dagger}(2) | \Psi \rangle , \tag{F.1}$$

where Ψ represents the ground-state many-body wavefunction of a N-electron system, $\hat{\mathcal{T}}$ is the time-ordering operator, and $\hat{\psi}$ and $\hat{\psi}^{\dagger}$ denote the electron annihilation and creation operators. In this material, we use a short-hand notation for space-time coordinates: $(\mathbf{r}_1, t_1) \equiv 1$. Throughout this material, we introduce a bar symbol above these short-hand notations, e.g. $\bar{1}$, where the space-time coordinates are integrated.

The total self-energy, Σ_T, contains all the electron-electron interactions and is written as

$$\Sigma_{\mathrm{T}}(1,2) = \Sigma_{\mathrm{H}}(1)\delta(1,2) + \Sigma_{\mathrm{XC}}(1,2). \tag{F.2}$$

The Σ_{H} on the right-hand-side (RHS) is the Hartree self-energy while the Σ_{XC} denotes the exchange-correlation self-energy. The delta function represents the locality in space and instantaneity in time: $\delta(1,2) = \delta(\mathbf{r}_1 - \mathbf{r}_2)\delta(t_1 - t_2)$. The Σ_{H} in the Green's function formalism is expressed as

$$\Sigma_{\mathrm{H}}(1) = -i\nu(1,\bar{2})G(\bar{2},\bar{2}^{+}). \tag{F.3}$$

Here, ν is the instantaneous Coulomb interaction written as

$$\nu(1,2) = \frac{1}{|\mathbf{r}_1 - \mathbf{r}_2|}\delta(t_1 - t_2). \tag{F.4}$$

The equal-time Green's function $G(2,2^{+})$ is directly related to the electron density

$$n(\mathbf{r}_2) = -iG(2,2^{+}), \tag{F.5}$$

where 2^+ represents a time argument t_2^+ that is infinitesimal after t_2.

The exchange-correlation self-energy contains all the nonlocal and dynamical electron-electron interactions

$$\Sigma_{\mathrm{XC}}(1,2) = -i\nu(1,\bar{4})G(1,\bar{3})\frac{\delta G^{-1}(\bar{3},2)}{\delta U(\bar{4})}, \tag{F.6}$$

where U is an external potential. The solution to Eq. (F.6) includes a three-point irreducible vertex function Γ that needs to be approximated.

F.1.2 Exchange-Correlation Self-Energy

The exchange-correlation self-energy in the total self-energy is the most important and challenging term to tackle. To simplify the expression of Σ_{XC}, the Green's function G can be expressed by the Dyson equation

$$G^{-1}(1,2) = G_0^{-1}(1,2) - \Sigma_{\mathrm{T}}(1,2), \tag{F.7}$$

where G_0 is the Green's function derived from the Hamiltonian ($\hat{h}$) with single-particle terms (kinetic energy and external field) only. Inserting Eq. (F.7) to Eq. (F.6), the expression of Σ_{XC} becomes

$$\Sigma_{\mathrm{XC}}(1,2) = -i\nu(1,\bar{4})G(1,\bar{3})\frac{\delta G_0^{-1}(\bar{3},2)}{\delta U(\bar{4})} + i\nu(1,\bar{4})G(1,\bar{3})\frac{\delta \Sigma_{\mathrm{T}}(\bar{3},2)}{\delta U(\bar{4})}. \tag{F.8}$$

Note that $\frac{\delta G_0^{-1}(3,2)}{\delta U(4)} = -\delta(3,2)\delta(3,4)$. The first term on the left-hand-side (LHS) of Eq. (F.8) is further written as

$$\Sigma_{\mathrm{X}}(1,2) = i\nu(1,2)G(1,2). \tag{F.9}$$

Notice that $iG(1,2)\delta(t_1-t_2) = -\rho(\mathbf{r}_1,\mathbf{r}_2;t_1)$, the first term on LHS of Eq. (F.8) ultimately recovers the instantaneous nonlocal exchange Σ_{X}, which is equivalent to the Fock operator in the Hartree-Fock approximation. The second term on the LHS of Eq. (F.8) is instead denoted Σ_{C}

$$\Sigma_{\mathrm{C}}(1,2) = i\nu(1,\bar{4})G(1,\bar{3})\frac{\delta\Sigma_{\mathrm{T}}(\bar{3},2)}{\delta U(\bar{4})}. \tag{F.10}$$

By introducing a generalized three-point reducible polarizability ${}^3\chi(6,5,4) := -i\frac{\delta G(6,5)}{\delta U(4)}$, the final expression of Σ_{C} reads

$$\Sigma_{\mathrm{C}}(1,2) = -\nu(1,\bar{4})G(1,\bar{3})\frac{\delta\Sigma_{\mathrm{T}}(\bar{3},2)}{\delta G(\bar{6},\bar{5})}{}^3\chi(\bar{6},\bar{5},\bar{4}). \tag{F.11}$$

F.1.3 GW Approximation

Due to the functional derivative of the total self-energy Σ_{T} in Eq. (F.10), the correlation energy Σ_{C} needs to be solved self-consistently. Given that the exact solution is nearly intractable, several approximations have been proposed for the functional derivative of Σ_{T}. The GW approximation takes

$$\Sigma_{\mathrm{T}}(3,2) \approx \Sigma_{\mathrm{H}}(3)\delta(3,2). \tag{F.12}$$

Inserting Eqs. (F.12) and (F.3) to Eq. (F.11), the functional derivative becomes

$$\frac{\delta\Sigma_{\mathrm{T}}(\bar{3},2)}{\delta G(\bar{6},\bar{5})} \approx -i\nu(2,5)\delta(6,5)\delta(3,2) \tag{F.13}$$

The three-point polarizability is also reduced to a two-point one

$$\chi(5,4) := -i\frac{\delta G(5,5^+)}{\delta U(4)} = \frac{\delta n(5)}{\delta U(4)}. \tag{F.14}$$

Plugging Eqs. (F.13) and (F.14) into Eq. (F.11), the correlation energy essentially becomes the GW polarization energy

$$\Sigma_{\mathrm{C}}^{GW}(1,2) = i\nu(1,\bar{4})G(1,2)\nu(2,\bar{5})\chi(\bar{5},\bar{4}). \tag{F.15}$$

Adding Eq. (F.9) to Eq. (F.15), the GW exchange-correlation self-energy reads

$$\Sigma_{\mathrm{XC}}^{GW}(1,2) = iG(1,2)W(1,2), \tag{F.16}$$

where W is the screened Coulomb interaction defined as

$$W(1,2) = \nu(1,2) + \nu(1,\bar{3})\chi(\bar{3},\bar{4})\nu(\bar{4},2). \tag{F.17}$$

F.1.4 $GW\Gamma_{\mathrm{X}}$ Approximation with Bare Exchange

Beyond the GW approximation, one can consider both the Σ_{H} and Σ_{X} in Eq. (F.11) while neglect completely the Σ_{C}. This leads to a vertex correction term to the GW self-energy, where the vertex comes from the derivative of the nonlocal exchange interaction. For convenience, the derived vertex (Γ) is denoted Γ_{X}. Assuming the bare exchange interaction is used, the total self-energy is approximated as

$$\Sigma_{\mathrm{T}}(3,2) \approx \Sigma_H(3)\delta(3,2) + \Sigma_{\mathrm{X}}(3,2). \tag{F.18}$$

The functional derivative in Eq. (F.11) thus becomes

$$\frac{\delta\Sigma_{\mathrm{T}}(\bar{3},2)}{\delta G(\bar{6},\bar{5})} \approx -i\nu(2,5)\delta(6,5)\delta(3,2) + i\nu(3,2)\delta(5,2)\delta(6,3). \tag{F.19}$$

Apparently, the first term on the RHS of Eq. (F.19) leads to the GW correlation energy associated with a two-point polarizability. The second term is a correction to GW known as the vertex. The resulting $GW\Gamma_{\mathrm{X}}$ correlation energy is written as

$$\begin{aligned}\Sigma_{\mathrm{C}}^{GW\Gamma_{\mathrm{X}}}(1,2) &= i\nu(1,\bar{4})G(1,2)\nu(2,\bar{5})\chi(\bar{5},\bar{4}) - i\nu(1,\bar{4})G(1,\bar{3})\nu(\bar{3},2)^3\chi(\bar{3},2,\bar{4}) \\ &= \Sigma_{\mathrm{C}}^{GW} + \Sigma_{\mathrm{C}}^{\Gamma_{\mathrm{X}}}.\end{aligned} \tag{F.20}$$

For convenience, the Γ_{X} correction to the correlation self-energy is denoted $\Sigma_{\mathrm{C}}^{\Gamma}$, which involves an irreducible three-point polarizability. In practice, the two-point polarizability in Σ_{C}^{GW} yields the time-dependent induced density, while the three-point polarizability in $\Sigma_{\mathrm{C}}^{\Gamma}$ yields the time-dependent induced density matrix. Both induced density and density matrix fluctuations are computed using real-time propagation.

F.1.5 $GW\Gamma_{\mathrm{X}}$ with Rescaled Exchange

A simple coefficient-self-consistency scheme can be introduced to the $GW\Gamma_{\mathrm{X}}$ approximation. The coefficient acts a pre-factor that rescales the nonlocal exchange interaction to approximate the correlation effect. The rescaling factor is denoted β and this approach is denoted $GW\Gamma_{\beta}$ approximation. The total self-energy approximated by the rescaled exchange is written as

$$\Sigma_{\mathrm{T}}(3,2) \approx \Sigma_{\mathrm{H}}(3)\delta(3,2) + \beta\Sigma_{\mathrm{X}}(3,2), \tag{F.21}$$

where $\beta\Sigma_{\mathrm{X}} \approx \Sigma_{\mathrm{X}}+\Sigma_{\mathrm{C}}$. In principle, the Σ_{C} functional has to be solved self-consistently. By introducing a factor β, the problem is reduced to solving the coefficient β self-consistently.

The initial guess of β comes from the GW approximation

$$\beta^0 = \frac{\Sigma_{\mathrm{X}} + \Sigma_{\mathrm{C}}^0}{\Sigma_{\mathrm{X}}}. \tag{F.22}$$

Here, Σ_{C}^0 denotes the GW self-energy. All the self-energies on the right-hand side of Eq. (F.22) are the expectation values for a specific quasiparticle state. The same notations apply to the following derivation. The $GW\Gamma_{\beta^0}$ correlation self-energy reads

$$\Sigma_{\mathrm{C}}^{GW\Gamma_{\beta^0}} = \Sigma_{\mathrm{C}}^{GW} + \beta^0 \Sigma_{\mathrm{C}}^{\Gamma_{\mathrm{X}}} \tag{F.23}$$

Note that the frequency-dependent Σ_{C}^{GW} and $\Sigma_{\mathrm{C}}^{\Gamma}$ are computed one time only, but the value of them are solved self-consistently based on the value of β. The value of β is iteratively updated until self-consistence

$$\beta^n = \frac{\Sigma_{\mathrm{X}} + \Sigma_{\mathrm{C}}^{n-1}}{\Sigma_{\mathrm{X}}}, \tag{F.24}$$

where $\Sigma_{\mathrm{C}}^{n-1}$ is the $GW\Gamma_{\beta}$ correlation energy using β^{n-1} in Eq. (F.23). The self-consistent correlation energy is written as

$$\Sigma_{\mathrm{C}}^{GW\Gamma_{\beta^{sc}}} = \Sigma_{\mathrm{C}}^{GW} + \beta^{sc} \Sigma_{\mathrm{C}}^{\Gamma_{\mathrm{X}}}, \tag{F.25}$$

where β^{sc} is the self-consistent rescaling factor.

In this work, we starts with the one-shot GW (G_0W_0) correlation self-energy and apply vertex corrections on top. Only the diagonal terms of the self-energy matrix are evaluated. The QP energy is obtained by

$$\varepsilon_i^{QP} = \varepsilon_i^0 + \langle \phi_i | \hat{\Sigma}_{\mathrm{XC}} - \hat{v}_{\mathrm{xc}} | \phi_i \rangle \,, \tag{F.26}$$

where ε_i^0 is the eigenvalue of eigenstate ϕ_i from the starting-point calculation using the following Kohn-Sham (KS) DFT Hamiltonian

$$\hat{H}^0 = \hat{h} + \hat{\Sigma}_{\mathrm{H}} + \hat{v}_{\mathrm{xc}}. \tag{F.27}$$

Here, $\hat{h}$ is the single-particle term containing the kinetic energy and the electron-nuclear attraction. v_{xc} (as in Eq .(F.26)) represents the local or semi-local exchange-correlation potential. In this work, the v_{xc} is approximated by the PBE functional.

F.1.6 Stochastic Formalism of Σ_{C}

As introduced above, the exchange self-energy is computed by the Hatree-Fock form, while the correlation part requires calculating the time-dependent induced density fluctuation (δn) and time-dependent induced density-matrix fluctuation ($\delta\rho$). In the stochastic formalism, the Green's function G, δn, and $\delta\rho$ are all sampled by random functions. On a real space grid, a random function is prepared as follows

$$\bar{\zeta}(\mathbf{r}) = \pm\frac{1}{\sqrt{\mathrm{d}V}}, \tag{F.28}$$

where $\mathrm{d}V$ is the unit volume of each grid point. The sign of the value at each grid point is randomly chosen between "+" and "-", which gives rise to the stochastic resolution of identity

$$\hat{\mathcal{I}} = \{|\bar{\zeta}\rangle\langle\bar{\zeta}|\}. \tag{F.29}$$

The brackets $\{\dots\}$ denote an average over the whole set of random functions, which are used in the following texts. The stochastic form of the KS Green's function reads

$$G_0(\mathbf{r}_1, \mathbf{r}_2, t_1 - t_2) = \{\zeta(\mathbf{r}_1, t_1)\bar{\zeta}(\mathbf{r}_2, t_2)\}. \tag{F.30}$$

Note that the Green's function depends only on the difference between t_1 and t_2 and thus we set $t_2 = 0$. The vector ζ is a projected vector from $\bar{\zeta}$ by the projector $\hat{P}$ or $\hat{\mathcal{I}} - \hat{P}$. The projector $\hat{P}$ depneds on the chemical potential and the Hamiltonian $\hat{H}_0$, representing the occupied subspace for "hole" states. Its complement $\hat{\mathcal{I}} - \hat{P}$ represents the unoccupied subspace for "electron" states. The time-evolved projected random vectors are prepared by

$$\zeta(\mathbf{r}, t) = \begin{cases} \langle \mathbf{r}| e^{-i\hat{H}^0 t} \hat{P} |\bar{\zeta}\rangle & t < 0 \\ \langle \mathbf{r}| e^{-i\hat{H}^0 t} (\hat{\mathcal{I}} - \hat{P}) |\bar{\zeta}\rangle & t > 0 \end{cases} . \tag{F.31}$$

In practice, the time propagation is discretized. Using the projected random functions, the density and density matrix are constructed by

$$n(\mathbf{r}) = \{\eta^*(\mathbf{r})\eta(\mathbf{r})\}, \tag{F.32}$$

and

$$\rho(\mathbf{r}_1, \mathbf{r}_2) = \{\eta^*(\mathbf{r}_2)\eta(\mathbf{r}_1)\}. \tag{F.33}$$

Here, η is a projected random vector in the occupied subspace

$$|\eta\rangle = \hat{P} |\bar{\zeta}\rangle . \tag{F.34}$$

The stochastic G_0W_0 correlation self-energy is written as

$$\Sigma_{\mathrm{C}}^{G_0W_0}(t) = \{\phi_i(\bar{\mathbf{r}})\zeta(\bar{\mathbf{r}}, t)W_{\mathrm{P}}(\bar{\mathbf{r}}, t)\}, \tag{F.35}$$

where $W_{\mathrm{P}}(t) = \hat{\nu}\hat{\chi}(t)\hat{\nu} |\bar{\zeta}\phi_i\rangle$ is a time-ordered polarization potential obtained from a retarded potential W_{P}^r. The retarded potential is computed by the induced density

fluctuation

$$W_{\mathrm{P}}^{r}(\mathbf{r},t)=\nu(\mathbf{r},\bar{\mathbf{r}}_2)\delta n(\bar{\mathbf{r}}_2,t). \tag{F.36}$$

The time-dependent induced density fluctuation has the following form

$$\delta n(\mathbf{r},t)=\chi(\mathbf{r},\bar{\mathbf{r}}_2,t)\nu(\bar{\mathbf{r}}_2,\bar{\mathbf{r}}_3)\bar{\zeta}(\bar{\mathbf{r}}_3)\phi_i(\bar{\mathbf{r}}_3). \tag{F.37}$$

In the $G_0W_0\Gamma_{\mathrm{X}}$ approximation, we first assume the nonlocal exchange functional is bare. The stochastic Γ_{X} term in the self-energy is expressed as

$$\Sigma_{\mathrm{C}}^{\Gamma_{\mathrm{X}}}(t)=\{\phi_i(\bar{\mathbf{r}}_1)\zeta(\bar{\mathbf{r}}_2,t)W_{\mathrm{X}}(\bar{\mathbf{r}}_1,\bar{\mathbf{r}}_2,t)\}. \tag{F.38}$$

Due to the linearity relation, the screened Γ_{X} contribution to the self-energy is simply written as

$$\Sigma_{\mathrm{C}}^{\Gamma_\beta}(t)=\beta\{\phi_i(\bar{\mathbf{r}}_1)\zeta(\bar{\mathbf{r}}_2,t)W_{\mathrm{X}}(\bar{\mathbf{r}}_1,\bar{\mathbf{r}}_2,t)\}=\beta\Sigma_{\mathrm{C}}^{\Gamma_{\mathrm{X}}}(t). \tag{F.39}$$

And therefore, one can always first compute $\Sigma_{\mathrm{C}}^{\Gamma_{\mathrm{X}}}(t)$ and then multiply it by β.

In Eq. (F.38), $W_{\mathrm{X}}(t)=\hat{\nu}^3\hat{\chi}(t)\hat{\nu}\,|\bar{\zeta}\phi_i\rangle$ and is a time-ordered exchange potential obtained from a retarded potential W_{X}^{r}. The retarded potential is computed by the induced density matrix fluctuation

$$W_{\mathrm{X}}^{r}(\mathbf{r}_1,\mathbf{r}_2,t)=\nu(\mathbf{r},\mathbf{r}_2)\delta\rho(\mathbf{r}_2,\mathbf{r}_2,t), \tag{F.40}$$

where the induced density matrix fluctuation is

$$\delta\rho(\mathbf{r}_1,\mathbf{r}_2,t)={}^3\chi(\mathbf{r}_1,\mathbf{r}_2,\bar{\mathbf{r}}_3,t)\nu(\bar{\mathbf{r}}_3,\bar{\mathbf{r}}_4)\bar{\zeta}(\bar{\mathbf{r}}_4)\phi_i(\bar{\mathbf{r}}_4). \tag{F.41}$$

In practice, both the induced density and density matrix fluctuations are computed by taking the difference between the perturbed and unperturbed system at a certain time

t. In the following derivation, we focus on the time-dependent induced density matrix fluctuation, which can be trivially generalized to the density one. At $t = 0$, the random vectors η within the occupied subspace are perturbed

$$|\eta_\lambda\rangle = e^{i\hat{v}_\lambda} |\eta\rangle \,, \tag{F.42}$$

where v_λ is a perturbing potential due to the addition/removal of an electron

$$v_\lambda(\mathbf{r}_1) = \lambda\nu(\mathbf{r}_1, \bar{\mathbf{r}}_2)\bar{\zeta}(\bar{\mathbf{r}}_2)\phi_i(\bar{\mathbf{r}}_2). \tag{F.43}$$

Here, λ controls the strength of the perturbation and we take $\lambda = 10^{-4}E_h^{-1}$. These perturbed states are then evolved in time

$$\eta_\lambda(\mathbf{r}, t) = \langle \mathbf{r}|e^{-i\hat{H}(t)t}|\eta_\lambda\rangle \,. \tag{F.44}$$

The Hamiltonian here is a generic one. If one takes $\hat{H}(t) = \hat{H}^0(t)$, i.e., KS-DFT Hamiltonian, the only time-dependent term in $\hat{H}^0(t)$ is the Hartree term and the resulting G_0W_0 correlation energy is computed at the random phase approximation (RPA) level. Vertex correction to the polarizability requires a time-dependent nonlocal exchange term in $\hat{H}(t)$ and the corresponding correlation energy is known as the $G_0W_0^{tc}$ approximation. In the next section, we demonstrate the construction of an effective QP Hamiltonian with a rescaled time-dependent nonlocal exchange. With the time-evolved random vectors, the time-dependent density matrix is constructed as

$$\rho_\lambda(\mathbf{r}_1, \mathbf{r}_2, t) = \{\eta^*_\lambda(\mathbf{r}_2, t)\eta_\lambda(\mathbf{r}_1, t)\}, \tag{F.45}$$

and the induced density matrix fluctuation is computed as

$$\delta\rho(\mathbf{r}_1, \mathbf{r}_2, t_1) = \frac{\rho_\lambda(\mathbf{r}_1, \mathbf{r}_2, t_1) - \rho_0(\mathbf{r}_1, \mathbf{r}_2, t_1)}{\lambda}, \tag{F.46}$$

where ρ_0 is the unperturbed density matrix exhibiting time-dependence due to the stochastic nature of η.

F.1.7 Embedded Vertex Correction

Vertex correction applies to the polarizability and directly to the correlation self-energy ($\Sigma_{\mathrm{C}}^{\Gamma\mathrm{x}}$). THis works aims to handle the vertex corrections within an electronic active space through the proposed *separation-propagation-recombination* (SPR) process.

The separation step utilizes an active space projector that is performed on the random vectors. Regarding the electron-hole pair formation in an charge-excitation process, we select the energetically active states to form the active space. The projector is given by

$$\hat{P}^A = \sum_{i=1}^{N_{\mathrm{act}}} |\psi_i^A\rangle \langle\psi_i^A| . \tag{F.47}$$

Here, N_{act} denotes the number of active states and ψ_A represent a projector state in the active state. The projector states can be gap-edge states, e.g., HOMO and LUMO. They can also be π and π^* bonds when using the localized basis. We use $\hat{P}^R = \hat{I} - \hat{P}^A$ to represent the complement of the active space ($\hat{I}$ is the identity). At $t = 0$, the random vector η, either perturbed or not, is separated by into the active component and the rest

$$|\eta^A\rangle = \hat{P}^A |\eta\rangle , \tag{F.48}$$

and

$$|\eta^R\rangle = \hat{P}^R |\eta\rangle \,. \tag{F.49}$$

These two components are then time-evolved by two different operators in the descretized propagation step

$$|\eta^{A'}(\mathrm{d}t)\rangle = e^{-i\hat{H}^{\mathrm{eff}}(0)\mathrm{d}t} |\eta^A\rangle \,, \tag{F.50}$$

and

$$|\eta^{R'}(\mathrm{d}t)\rangle = e^{-i\hat{H}^{0}(0)\mathrm{d}t} |\eta^R\rangle \,, \tag{F.51}$$

where $\mathrm{d}t$ is the time interval in each discrete propagation step. The $\hat{H}^{\mathrm{eff}}$ in Eq. (F.50) is a *space-specific* effective QP Hamiltonian with a rescaled time-dependent nonlocal exchange

$$\hat{H}^{\mathrm{eff}}(t) = \hat{h} + \hat{\Sigma}_{\mathrm{H}}(t) + \alpha\hat{\Sigma}_{\mathrm{X}}(t), \tag{F.52}$$

where the rescaling factor α is similar to the β mentioned above. The α represents the entire active space, i.e., a set of projector states, and is thus derived as the average of β_i for each ψ_i^A in Eq. (F.47)

$$\alpha = \frac{1}{N_{\mathrm{act}}} \sum_{i}^{N_{\mathrm{act}}} \beta_i, \tag{F.53}$$

where β_i is computed by Eq. (F.22) at the G_0W_0 level. In contrast to $\hat{H}^{\mathrm{eff}}$, the $\hat{H}_0$ in Eq (F.51) is simply the mean-field Hamiltonian with only the time-dependent Hartree

$$\hat{H}_0(t) = \hat{h} + \hat{\Sigma}_H(t) \tag{F.54}$$

The treatment of the active component introduces vertex correction through the time-dependent nonlocal exchange, while the treatment of the rest component is equivalent to RPA. Note that the time-evolution may cause leakage of the $\eta^{A'}$ to the rest space. To

recover the "real" active component at $t = dt$, the following operations are required

$$|\eta^A(\mathrm{d}t)\rangle = \hat{P}^A\,|\eta^{A'}(\mathrm{d}t)\rangle + \hat{P}^A\,|\eta^{R'}(\mathrm{d}t)\rangle\,, \tag{F.55}$$

and

$$|\eta^R(\mathrm{d}t)\rangle = \hat{P}^R\,|\eta^{A'}(\mathrm{d}t)\rangle + \hat{P}^R\,|\eta^{R'}(\mathrm{d}t)\rangle\,. \tag{F.56}$$

These two operations are performed in each propagation step.

After obtaining $\eta^A(dt)$ and $\eta^R(dt)$, the last step of the SPR process is to recombine these two components and give the time-evolved embedded vector

$$|\eta^{\mathrm{emb}}(\mathrm{d}t)\rangle = |\eta^A(\mathrm{d}t)\rangle + |\eta^R(\mathrm{d}t)\rangle\,. \tag{F.57}$$

The set of $\eta^{\mathrm{emb}}(t)$ then leads to $n^{\mathrm{emb}}(t)$ and $\rho^{\mathrm{emb}}(t)$ through Eqs. (F.32) and (F.33), and also $\delta n^{\mathrm{emb}}(t)$ and $\delta\rho^{\mathrm{emb}}(t)$ through Eq. (F.46). Finally, the $G_0W_0^{tc}\Gamma_\beta$ correlation energy with embedded vertex corrections is computed from the $\delta n^{\mathrm{emb}}(t)$ and $\delta\rho^{\mathrm{emb}}(t)$.

The same SPR treatment applies also to the random vectors ζ for the time propagation of the Green's function.

F.2 Supplementary figures and tables

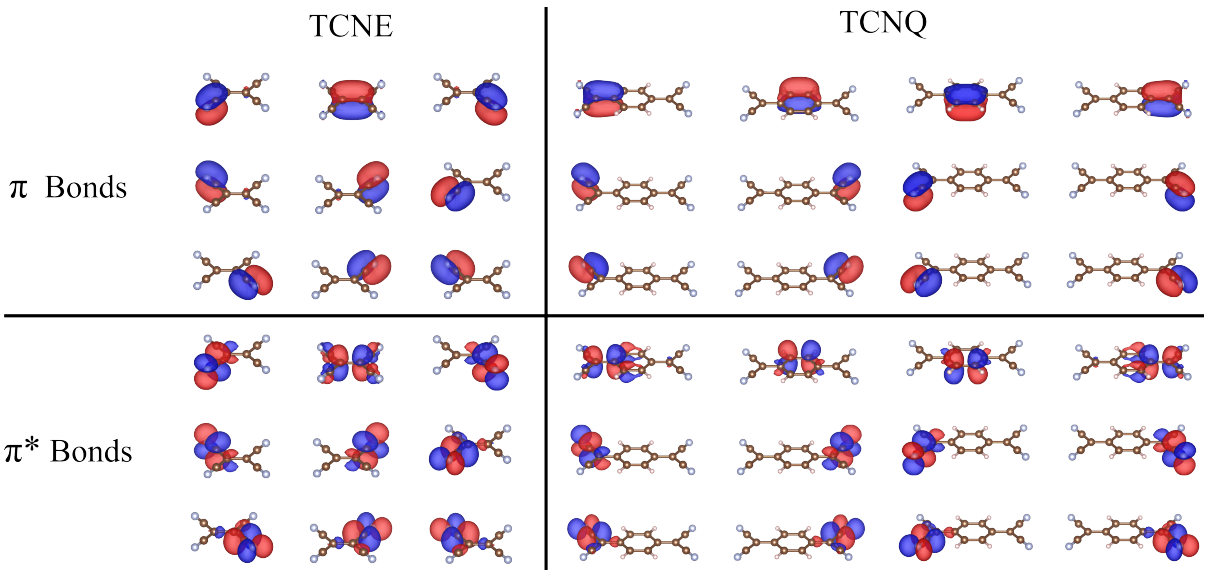

Figure F.1: The full set of basis orbitals that defines the active occupied (upper half) and unoccupied (lower half) spaces of the TCNE and TCNQ molecules.

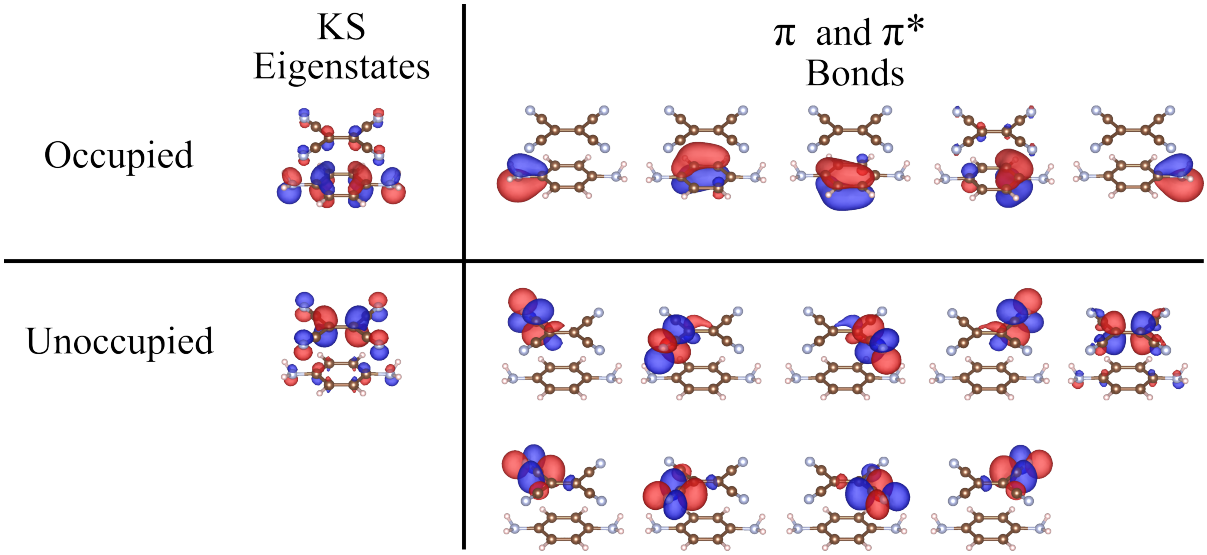

Figure F.2: The full set of basis orbitals that defines the active occupied (upper half) and unoccupied (lower half) spaces of the B-T dimer: Kohn-Sham eigenstates representation (left) and π and π^* bonds representation (right).

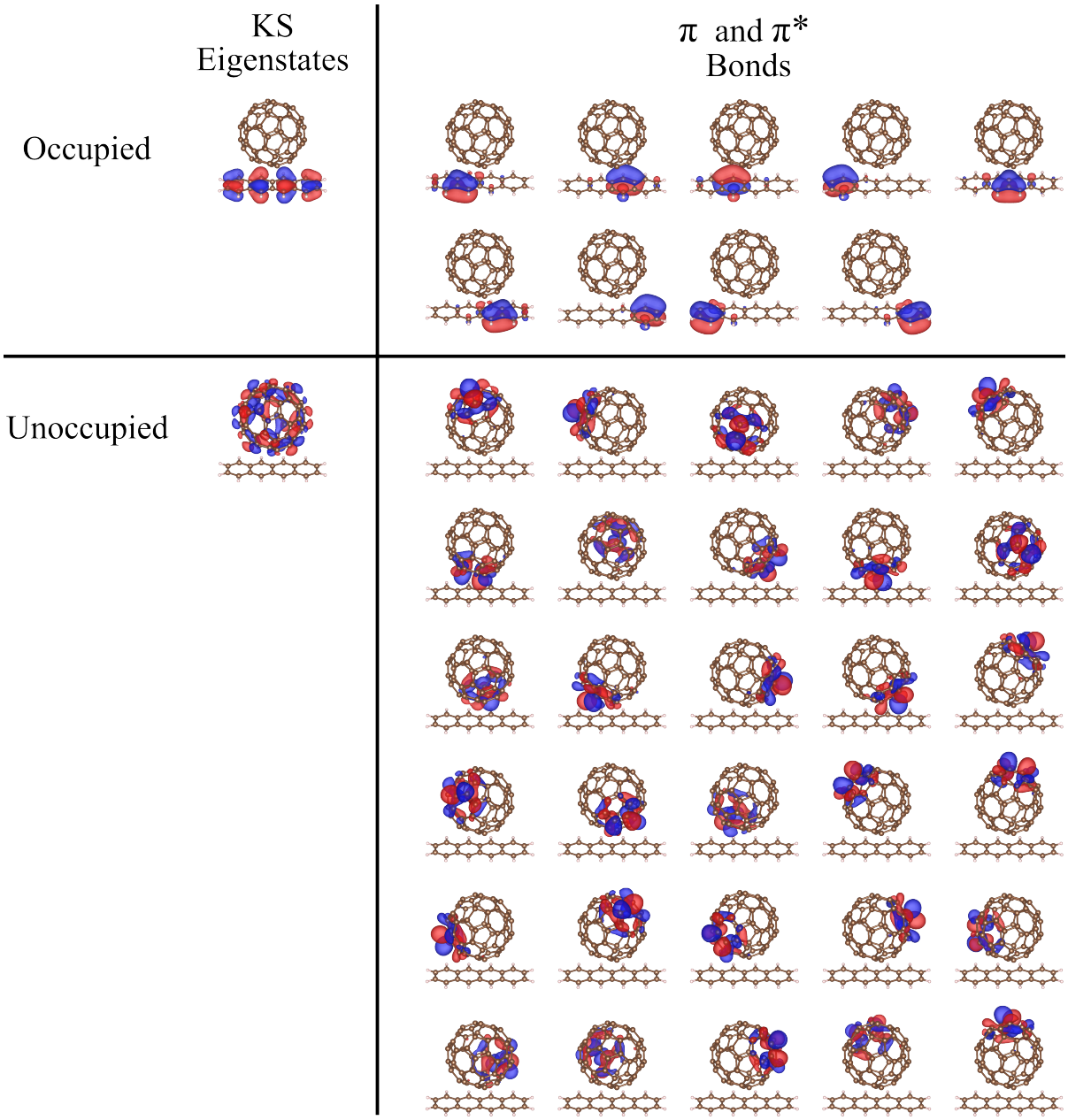

Figure F.3: The full set of basis orbitals that defines the active occupied (upper half) and unoccupied (lower half) spaces of the D-T dimer: Kohn-Sham eigenstates representation (left) and π and π^* bonds representation (right).

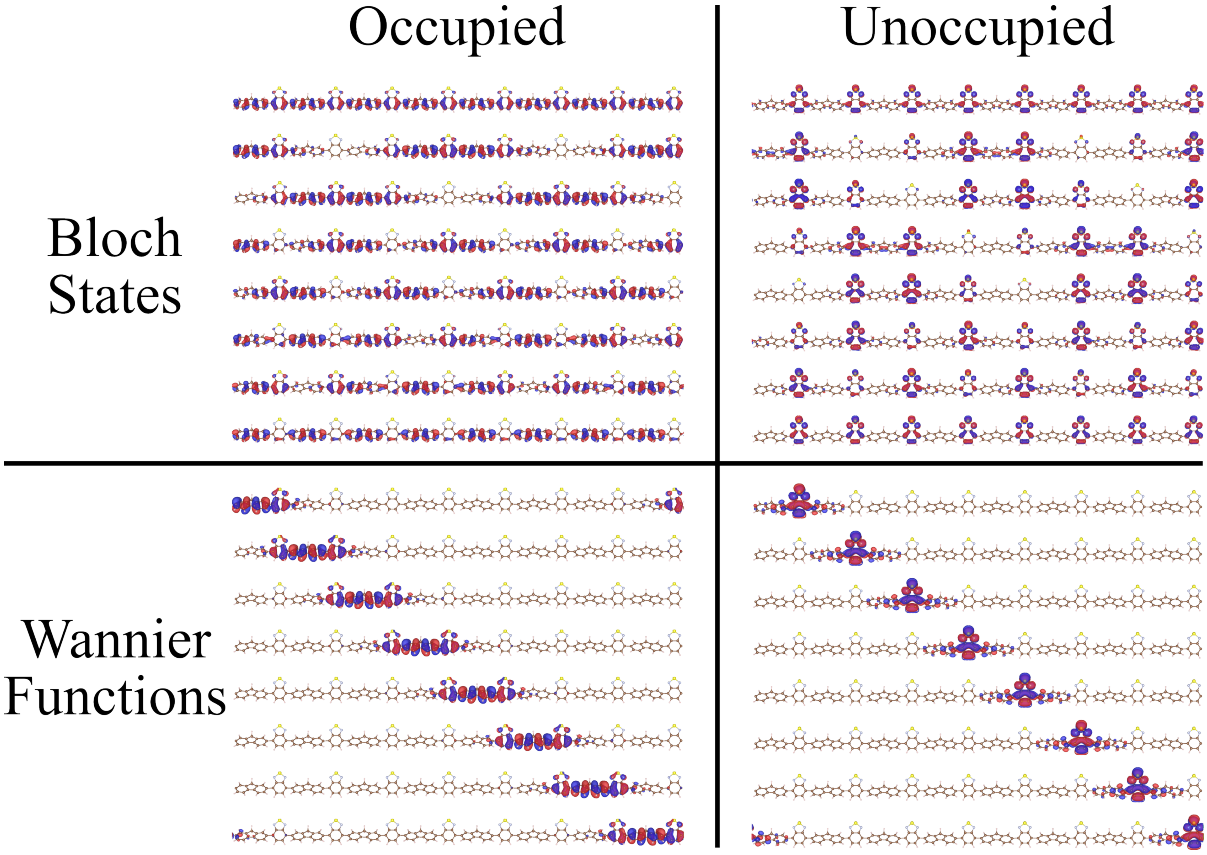

Figure F.4: The full set of basis orbitals that defines the active occupied (left) and unoccupied (right) spaces of the p-FBT polymer: Bloch states representation (upper half) and Wannier functions representation (lower half).

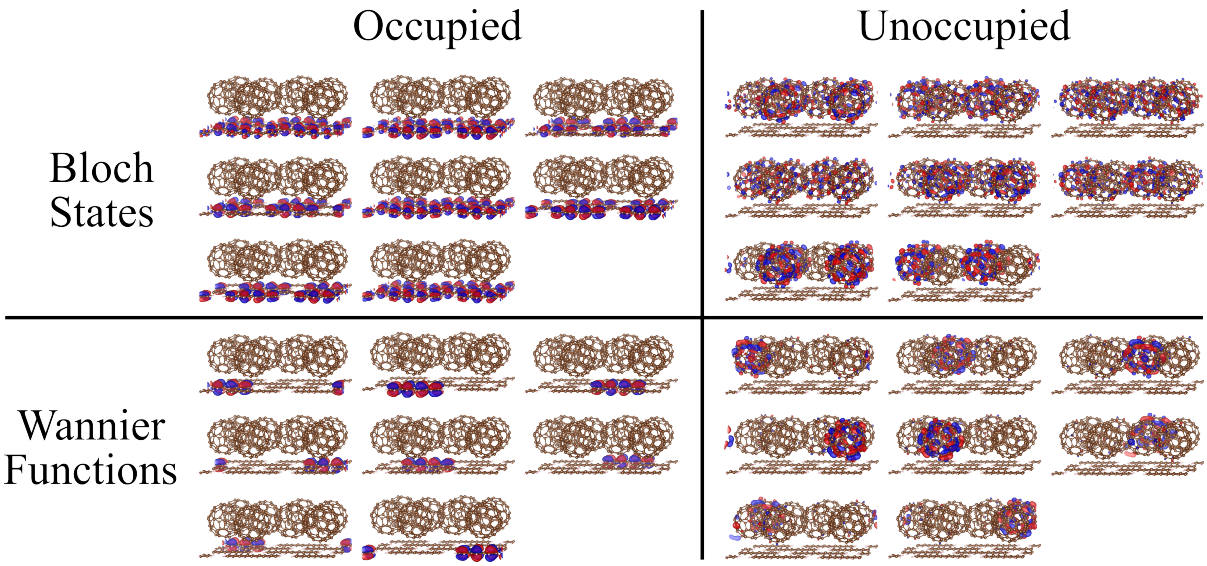

Figure F.5: The full set of basis orbitals that defines the active occupied (left) and unoccupied (right) spaces of the Tc-C double layers: Bloch states representation (upper half) and Wannier functions representation (lower half).

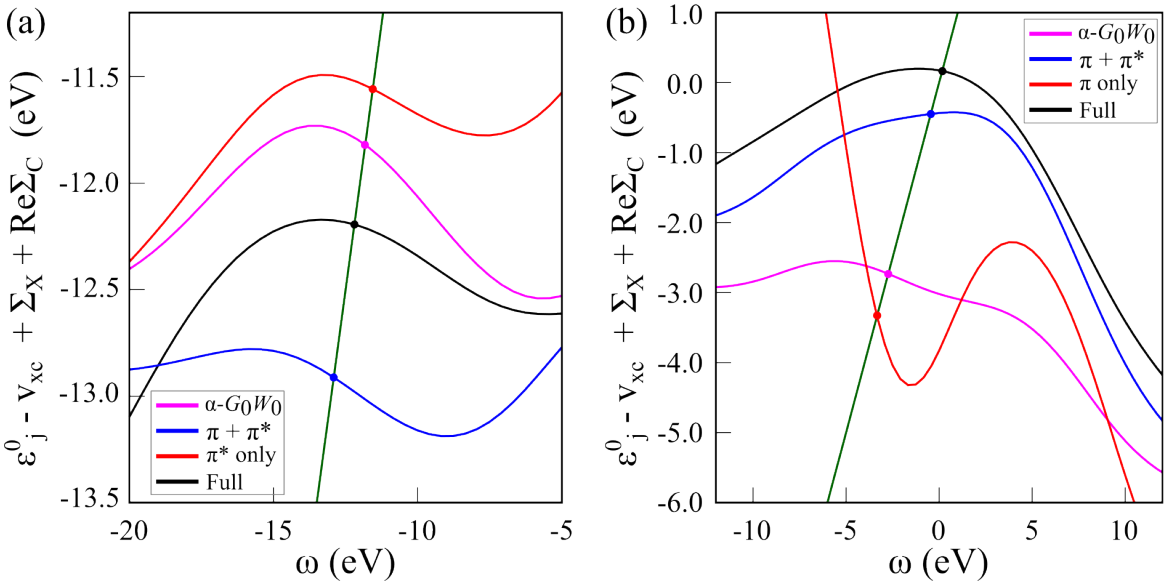

Figure F.6: Graphical solutions to the QP energies for the (a) HOMO and the (b) LUMO of the TCNE molecule. The magenta curve represents the self-energy computed using the π and π^* active space without the Γ term. The blue curve denotes the self-energy computed using the π and π^* active space with the Γ term. The red and black curves represent the Γ term computed using the π (or π^*) active space and the full electronic space, respectively. The intersections between the straight line and the curves denote the QP energy.

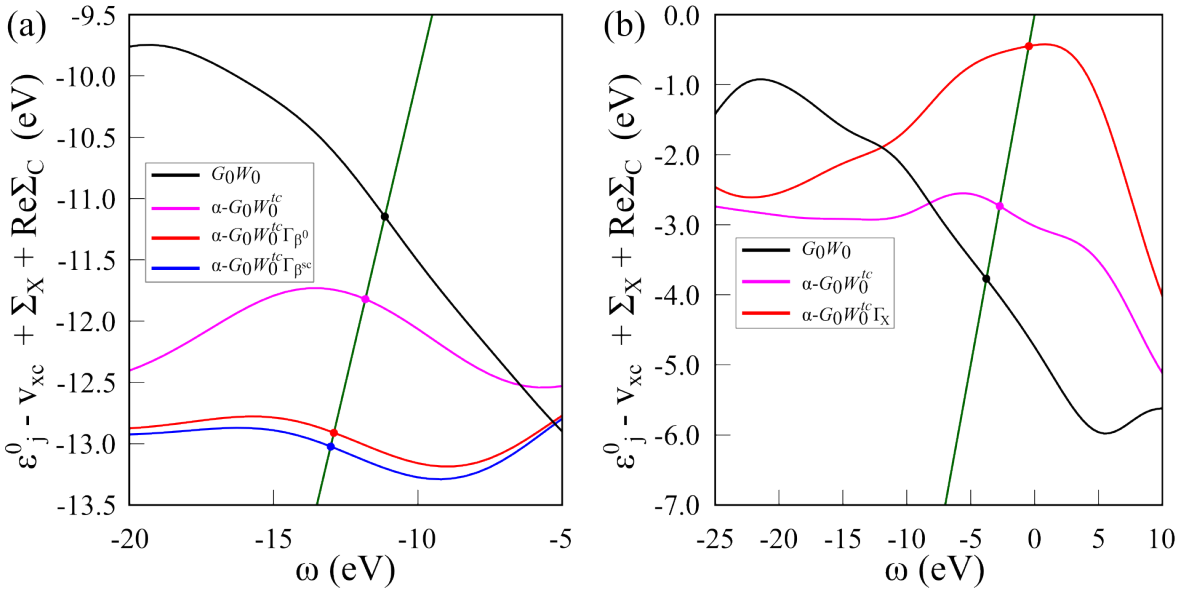

Figure F.7: Graphical solutions to the QP energies of the TCNE molecule: (a) the HOMO QP energy solutions using the augmented active space where $\beta^0 = 0.998$ and $\beta^{sc} = 1.103$; (b) the LUMO QP energy solutions using the augmented active space where Γ is derived from bare Σ_X. The intersections between the straight line and the curves denote the QP energy.

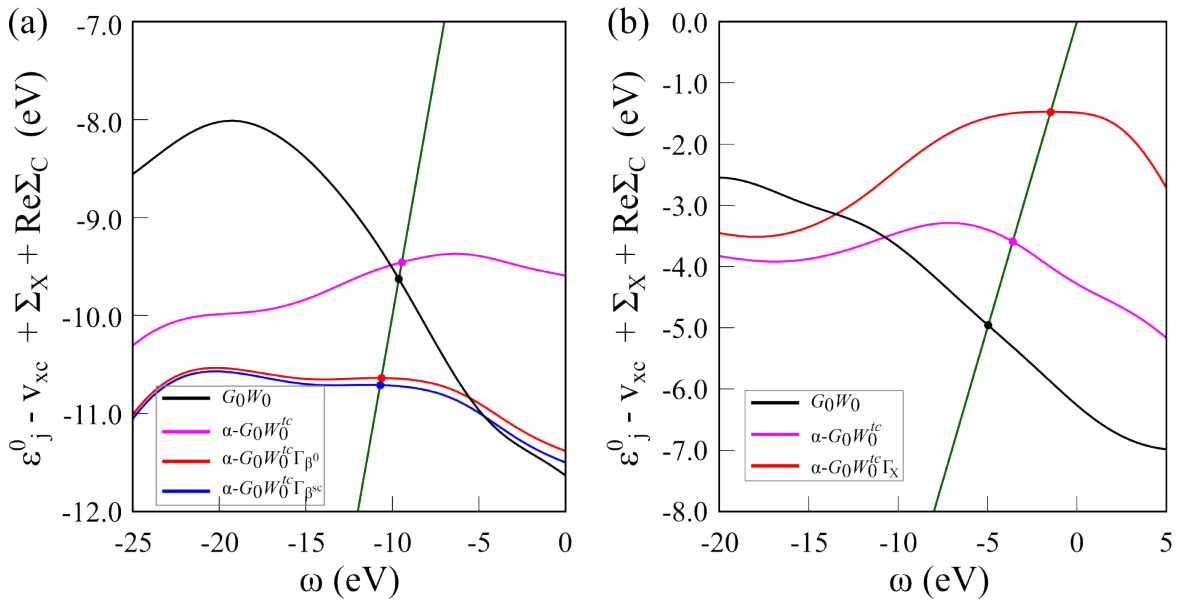

Figure F.8: Graphical solutions to the QP energies of the TCNQ molecule: (a) the HOMO QP energy solutions using the augmented active space where $\beta^0 = 1.029$ and $\beta^{sc} = 1.096$; (b) the LUMO QP energy solutions using the augmented active space where Γ is derived from bare Σ_X. The intersections between the straight line and the curves denote the QP energy.

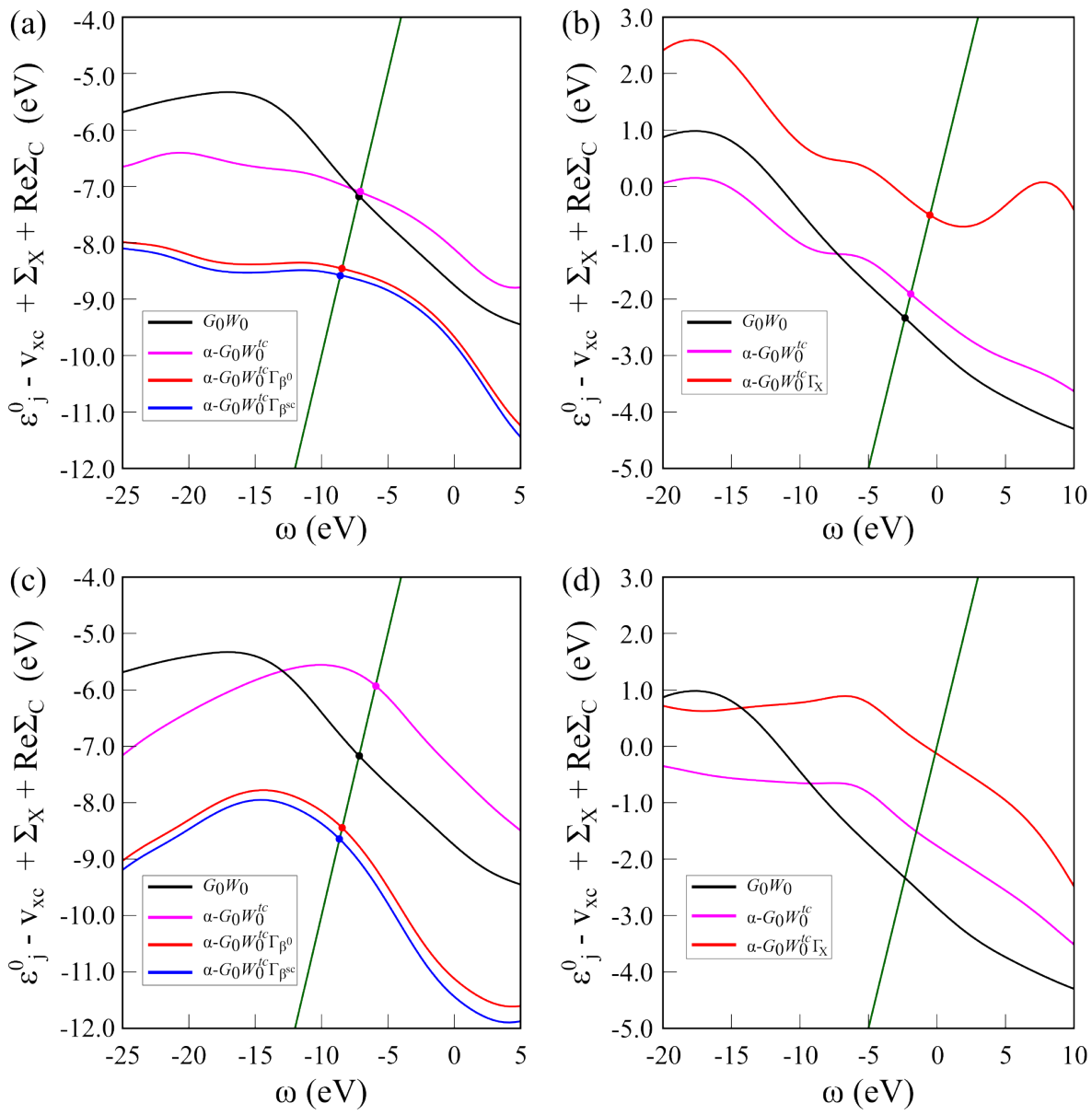

Figure F.9: Graphical solutions to the QP energies of the B-T dimer: (a) the HOMO QP energy solutions using the minimal active space where $\beta^0 = 0.996$ and $\beta^{sc} = 1.097$; (b) the LUMO QP energy solutions using the minimal active space where Γ is derived from bare Σ_X; (c) the HOMO QP energy solutions using the augmented active space where $\beta^0 = 0.996$ and $\beta^{sc} = 1.082$; (d) the LUMO QP energy solutions using the augmented active space where Γ is derived from bare Σ_X. The intersections between the straight line and the curves denote the QP energy.

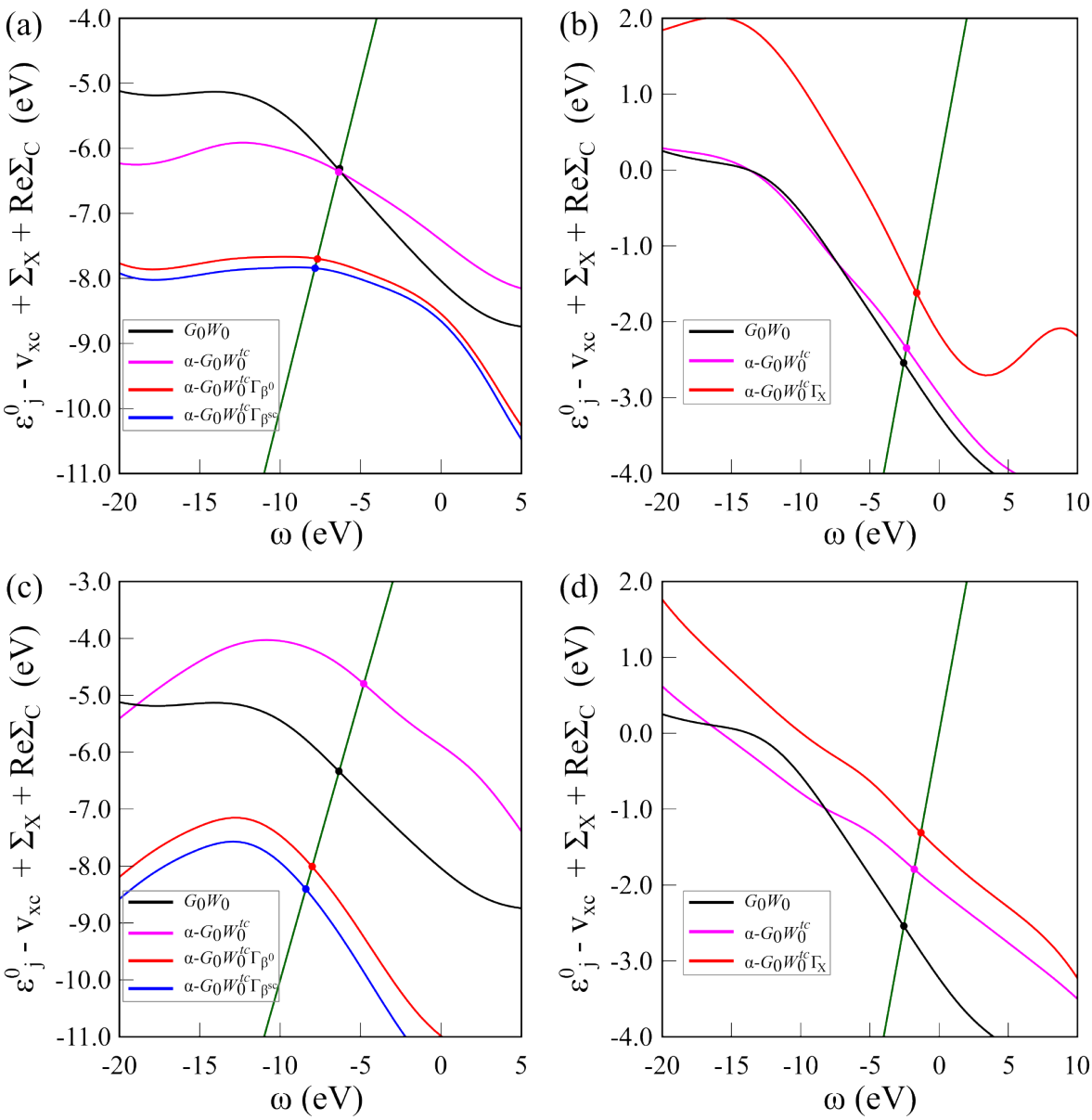

Figure F.10: Graphical solutions to the QP energies of the Tc-C dimer: (a) the HOMO QP energy solutions using the minimal active space where $\beta^0 = 1.039$ and $\beta^{sc} = 1.142$; (b) the LUMO QP energy solutions using the minimal active space where Γ is derived from bare Σ_X; (c) the HOMO QP energy solutions using the augmented active space where $\beta^0 = 1.039$ and $\beta^{sc} = 1.183$; (d) the LUMO QP energy solutions using the augmented active space where Γ is derived from bare Σ_X. The intersections between the straight line and the curves denote the QP energy.

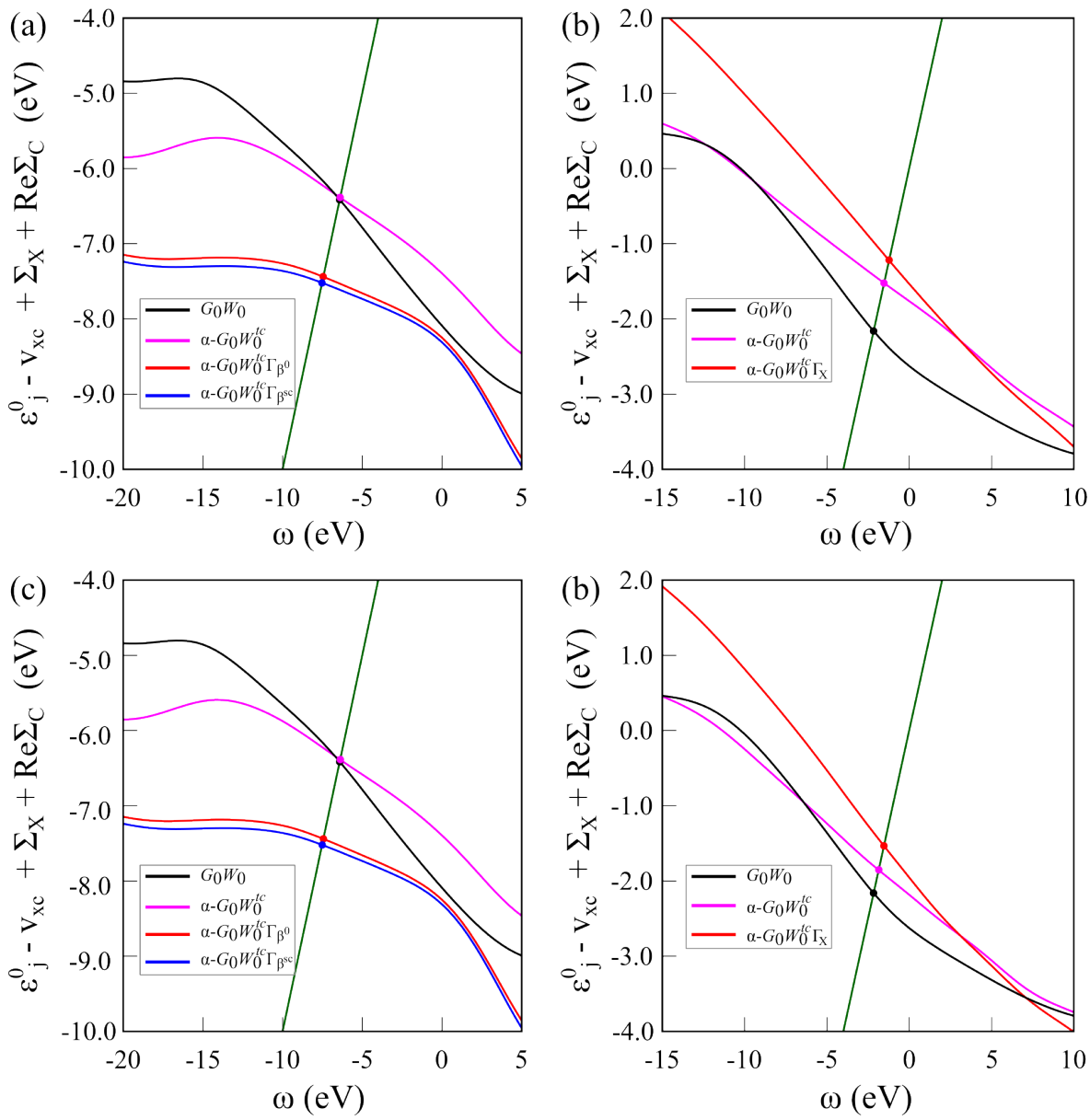

Figure F.11: Graphical solutions to the QP energies of the p-FBT polymer: (a) the VBM QP energy solutions using the Bloch representation where $\beta^0 = 1.025$ and $\beta^{sc} = 1.098$; (b) the CBM QP energy solutions using the Bloch representation where Γ is derived from bare Σ_X; (c) the VBM QP energy solutions using the Wannier representation where $\beta^0 = 1.025$ and $\beta^{sc} = 1.096$; (d) the CBM QP energy solutions using the Wannier representation where Γ is derived from bare Σ_X. The intersections between the straight line and the curves denote the QP energy.

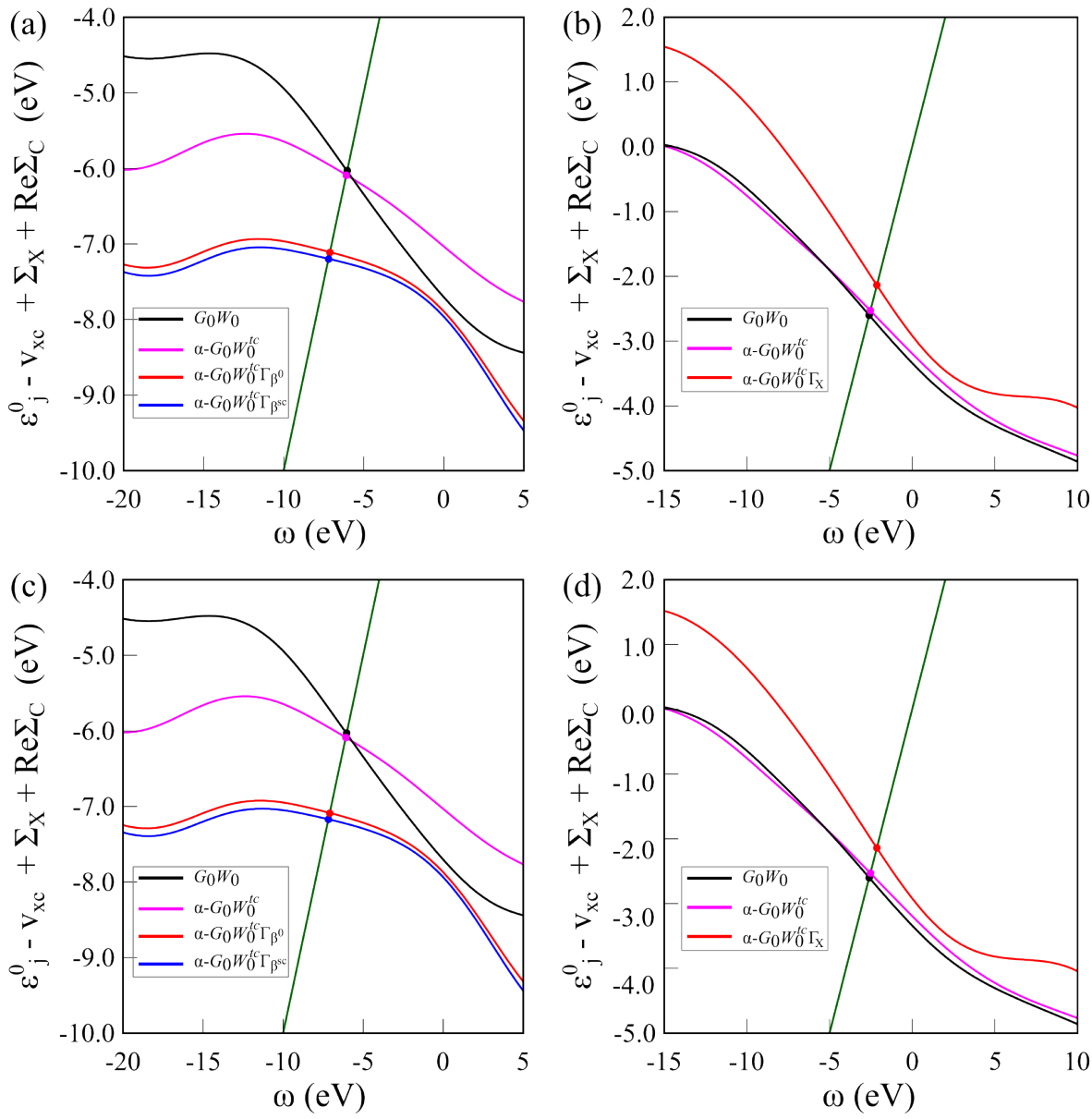

Figure F.12: Graphical solutions to the QP energies of the Tc-C double layers: (a) the VBM QP energy solutions using the Bloch representation where $\beta^0 = 1.033$ and $\beta^{sc} = 1.116$; (b) the CBM QP energy solutions using the Bloch representation where Γ is derived from bare Σ_X; (c) the VBM QP energy solutions using the Wannier representation where $\beta^0 = 1.033$ and $\beta^{sc} = 1.114$; (d) the CBM QP energy solutions using the Wannier representation where Γ is derived from bare Σ_X. The intersections between the straight line and the curves denote the QP energy.

system	grid	spacing [bohr]
TCNE	88*88*76	0.35
TCNQ	86*68*46	0.35
B-T Dimer	86*98*80	0.35
Tc-C Dimer	136*112*96	0.35
p-FBT	480*76*76	0.4023333
Tc-C double layers	136*150*150	0.353774

Table F.1: Cell parameters in DFT calculations

Parameters	value
plane wave cut-off (hartree)	28
number of random vectors used for sparse stochastic compression	20000
number of random vectors characterizing the screened Coulomb interaction (per each vector sampling the Green's function)	16
number of vectors sampling the Green's function	2000
maximum time for real-time propagation of the dynamical self-energy (a.u.)	50

Table F.2: Parameters in the GW calculations of all systems.

Table F.3: Screening factors α of the active space defined for the single TCNE molecule. All values are in arbitrary unit.

Basis Type	α	
	occ.	unocc.
π and π^* Bonds	0.979 (0.004)	1.176 (0.006)

Table F.4: HOMO/LUMO energies and fundamental gaps of the single TCNE molecule computed by different methods. All energy values are in eV unit.

System	Method	HOMO/LUMO/Gap
TCNE	DFT	-8.61/-5.85/2.76
	G_0W_0	-11.15/-3.77/7.38
	α^1-$G_0W_0^{tc}$	-11.82/-2.73/9.09
	α^1-$G_0W_0^{tc}\Gamma_{\beta_j^0}$	-12.91/-2.73*/10.18
	α^1-$G_0W_0^{tc}\Gamma_{\beta_j^{sc}}$	-13.02/-2.73*/10.29

[1] Screening factor computed from the localized orbitals basis

* The LUMO energy is taken from the $G_0W_0^{tc}$ result

Table F.5: Screening factors α of the active space defined for the single TCNE molecule. All values are in arbitrary unit.

Basis Type	α	
	occ.	unocc.
π and π^* Bonds	0.983 (0.006)	1.158 (0.010)

Table F.6: HOMO/LUMO energies and fundamental gaps of the single TCNQ molecule computed by different methods. All energy values are in eV unit.

System	Method	HOMO/LUMO/Gap
TCNQ	DFT	-7.78/-6.27/1.51
	G_0W_0	-9.63/-4.96/4.66
	α^1-$G_0W_0^{tc}$	-9.46/-3.59/5.86
	α^1-$G_0W_0^{tc}\Gamma_{\beta_j^0}$	-10.70/-3.59*/7.11
	α^1-$G_0W_0^{tc}\Gamma_{\beta_j^{sc}}$	-10.71/-3.59*/7.12

[1] Screening factor computed from the localized orbitals basis

[*] The LUMO energy is taken from the $G_0W_0^{tc}$ result

Table F.7: Comparisons of the computed IP of TCNE between references (60 and 64 in the main text) and this work. The references of the experimental data are also from the main text.

IP (eV)	G_0W_0@PBE	G_0W_0+SOSEX	α-$G_0W_0^{tc}$	α-$G_0W_0^{tc}\Gamma_\beta$	Exp. (vertical)
Ref. 60	11.1	11.3	NA	NA	
Ref. 64	11.19	11.32	NA	NA	11.77-11.79[114,118]
This work	11.15	NA	11.82	12.91/13.02	

Table F.8: Comparisons of the computed EA of TCNE between references (60 and 64 in the main text) and this work. The references of the experimental data are also from the main text.

EA (eV)	G_0W_0@PBE	G_0W_0+SOSEX	α-$G_0W_0^{tc}$	α-$G_0W_0^{tc}\Gamma_\beta$	Exp. (vertical/adiabatic)
Ref. 60	3.8	3.3	NA	NA	
Ref. 64	3.78	3.22	NA	NA	2.30[115]/3.16[116,117]
This work	3.77	NA	2.73	0.45 ($\beta = 1$)	

Table F.9: Screening factors α of the active space defined for the DAB-TCNE dimer system. All values are in arbitrary unit.

Basis Type	α	
	occ.	unocc.
KS Eigenstates	0.996	1.100
π and π^* Bonds	0.975 (0.012)	1.135 (0.025)

Table F.10: Screening factors α of the active space defined for the Tc-C dimer system. All values are in arbitrary unit.

Basis Type	α	
	occ.	unocc.
KS Eigenstates	1.039	1.214
π and π^* Bonds	0.980 (0.004)	1.154 (0.010)

Table F.11: HOMO/LUMO energies and fundamental gaps of the donor-acceptor complexes computed by different methods. All energy values are in eV unit.

System	Method	HOMO/LUMO/Gap
B-T dimer	DFT	-5.45/-4.77/0.68
	G_0W_0	-7.17/-2.33/4.84
	α^1-$G_0W_0^{tc}$	-7.10/-1.91/5.19
	α^1-$G_0W_0^{tc}\Gamma_{\beta_j^0}$	-8.45/-1.91*/6.54
	α^1-$G_0W_0^{tc}\Gamma_{\beta_j^{sc}}$	-8.57/-1.91*/6.66
	α^2-$G_0W_0^{tc}$	-5.92/-1.51/4.41
	α^2-$G_0W_0^{tc}\Gamma_{\beta_j^0}$	-8.44/-1.51*/6.93
	α^2-$G_0W_0^{tc}\Gamma_{\beta_j^{sc}}$	-8.64/-1.51*/7.13
Tc-C dimer	DFT	-4.65/-4.10/0.55
	G_0W_0	-6.34/-2.54/3.79
	α^1-$G_0W_0^{tc}$	-6.36/-2.35/4.01
	α^1-$G_0W_0^{tc}\Gamma_{\beta_j^0}$	-7.70/-2.35*/5.35
	α^1-$G_0W_0^{tc}\Gamma_{\beta_j^{sc}}$	-7.84/-2.35*/5.49
	α^2-$G_0W_0^{tc}$	-4.80/-1.79/3.01
	α^2-$G_0W_0^{tc}\Gamma_{\beta_j^0}$	-8.03/-1.79*/6.24
	α^2-$G_0W_0^{tc}\Gamma_{\beta_j^{sc}}$	-8.43/-1.79*/6.64

[1] Screening factor computed from the KS eigenstates basis

[2] Screening factor computed from the localized orbitals basis

[*] The LUMO energy is taken from the $G_0W_0^{tc}$ result

Table F.12: Screening factors α of the active space defined for the 1D p-FBT system. All values are in arbitrary unit.

Basis Type	α	
	TVB	BCB
Bloch States	1.016 (0.010)	1.260 (0.009)
Wannier Functions	1.002	1.082

Table F.13: Screening factors α of the active space defined for the 2D Tc-C double-layer system. All values are in arbitrary unit.

Basis Type	α	
	TVB	BCB
Bloch States	1.034 (0.000)	1.193 (0.005)
Wannier Functions	1.010	1.061

Table F.14: VBM/CBM energies and fundamental gaps of the 1D p-FBT and 2D Tc-C double layers computed by different methods. All energy values are in eV unit.

System	Method	VBM/CBM/Gap
p-FBT	DFT	-4.97/-3.35/1.62
	G_0W_0	-6.42/-2.09/4.33
	α^1-$G_0W_0^{tc}$	-6.39/-1.52/4.86
	α^1-$G_0W_0^{tc}\Gamma_{\beta_j^0}$	-7.44/-1.52*/5.92
	α^1-$G_0W_0^{tc}\Gamma_{\beta_j^{sc}}$	-7.52/-1.52*/6.00
	α^2-$G_0W_0^{tc}$	-6.38/-1.86/4.52
	α^2-$G_0W_0^{tc}\Gamma_{\beta_j^0}$	-7.41/-1.86*/5.55
	α^2-$G_0W_0^{tc}\Gamma_{\beta_j^{sc}}$	-7.49/-1.86*/5.63
Tc-C Double Layers	DFT	-4.97/-4.27/0.70
	G_0W_0	-6.04/-2.60/3.44
	α^1-$G_0W_0^{tc}$	-6.09/-2.53/3.56
	α^1-$G_0W_0^{tc}\Gamma_{\beta_j^0}$	-7.11/-2.53*/4.58
	α^1-$G_0W_0^{tc}\Gamma_{\beta_j^{sc}}$	-7.20/-2.53*/4.67
	α^2-$G_0W_0^{tc}$	-6.09/-2.53/3.56
	α^2-$G_0W_0^{tc}\Gamma_{\beta_j^0}$	-7.09/-2.53*/4.56
	α^2-$G_0W_0^{tc}\Gamma_{\beta_j^{sc}}$	-7.17/-2.53*/4.64

[1] Screening factor computed from the KS eigenstates basis

[2] Screening factor computed from the localized orbitals basis

[*] The LUMO energy is taken from the $G_0W_0^{tc}$ result

Bibliography

[1] V. Vlček, W. Li, R. Baer, E. Rabani, and D. Neuhauser, *Swift GW beyond 10,000 electrons using sparse stochastic compression*, *Physical Review B* **98** (2018), no. 7 075107.

[2] V. Vlček, *Stochastic vertex corrections: Linear scaling methods for accurate quasiparticle energies*, *Journal of Chemical Theory and Computation* **15** (2019), no. 11 6254–6266.

[3] G. Weng, M. Romanova, A. Apelian, H. Song, and V. Vlček, *Reduced scaling of optimal regional orbital localization via sequential exhaustion of the single-particle space*, *Journal of Chemical Theory and Computation* **18** (2022), no. 8 4960–4972.